THE BRITTLE AND PLASTIC RESPONSE OF QUARTZ

GRAHAM JOHN GLOVER

A THESIS PRESENTED TO FULFIL THE REQUIREMENTS

FOR THE DEGREE OF DOCTOR OF PHILOSOPHY

OF THE

UNIVERSITY OF CAPE TOWN

1980

ACKNOWLEDGEMENTS

It is a great pleasure to thank the various people and organisations who have been involved in this project and who made possible its successful outcome. Firstly I owe a debt of gratitude to my supervisor Professor Tony Ball, for his critical guidance and interest and for making available laboratory facilities. The Director and staff of the Mining Technology Laboratory, Chamber of Mines of South Africa, are thanked for their interest and valuable discussion at various stages. Professor R. E. Smallman, University of Birmingham, United Kingdom made available the HVEM facility. Drs. P. Lilley and N. Gay are especially thanked for their assistance with the deformation of the quartz crystals in the Griggs apparatus. Dr. D. Crawford, Director, Electron Microscope Unit, University of Cape Town, gave generous assistance with Scanning Electron Microscopy. Mr. N. Dreze constructed the scratching apparatus and environmental chamber. Mr. B. Greeves gave valuable help with the photography and is particularly thanked for his efforts with the X-ray topographic plates. Mrs. E. Simonse skillfully assisted with polishing the quartz samples and helped with the preparation of this manuscript. Mrs. J. Parsons typed the manuscript. Finally I wish to acknowledge generous financial support both from the University of Cape Town and the Chamber of Mines of South Africa.

ABSTRACT

Quartz is the principal mineral constituent of the earth's upper crust and a knowledge of the deformation characteristics of quartz are of geological and technological importance. In common with many ceramic materials, quartz may not satisfy the Von Mises independent slip system criterion and clarification is required on the exact response to an imposed stress system at a given temperature.

Single crystal synthetic quartz ('water' content in the range 50-150 ppm H/Si) has been compressed parallel to c[0001] at moderate temperatures ($T \approx 800$-1000 K) and slow strain rates ($\dot{\varepsilon} \approx 10^{-6} - 10^{-7}\ s^{-1}$). The resulting dislocation structures were analyzed and were found consistent with the mechanism of climb of a and c type dislocations. The application of the theory of Nabarro (Philos. Mag., 16, 231-237, 1967) indicated that the diffusivity was of the order $10^{-22}\ m^2\ s^{-1}$ at 1000 K, and that the activation energy for creep corresponded closely with that for the diffusion of hydroxyl (OH^-) ions. To investigate further the important role of lattice water on the plastic deformation of quartz, a series of heat treatments were attempted. It was found that at low temperatures ($\lesssim$ 1000 K) numerous dislocation loops were formed while at elevated temperatures (T > 1100K) these loops climbed rapidly, interacting to form a three dimensional network. In addition, a strain free precipitate formed which resisted coarsening. The impurity defect structure is modelled in terms of a hydrogen defect, probably involving an hydroxyl ion and an oxygen vacancy, and the hydrolytic weakening mechanism in quartz may be visualized

as the rapid climb motions of dislocations by a vacancy absorption mechanism.

The room temperature Vickers indentation of quartz is elastic-plastic, with a constraint factor $C' \approx 1.3$. An HVEM analysis was consistent with this. The resolved shear stress during indentation was of the order of the theoretical shear strength of quartz and the $\underline{a}$, $\underline{c}$ and $\langle \underline{a} + \underline{c} \rangle$ slip systems were all equally difficult to operate at room temperature. A fracture mechanics analysis of the cracks radiating from the corners of the Vickers hardness impression indicated that $\gamma \approx 10$ J m^{-2} for quartz. The cutting of quartz with a vertically loaded Vickers pyramid at slow speeds revealed that quartz cuts by the mechanism of delamination. The sharp diamond cutting point was found to rapidly blunt, and a directional anisotropy of cutting quartz found in these conditions. The scratching results have been interpreted in terms of the stress distribution for a sliding Hertzian contact. In such an analysis the coefficient of friction and position of maximum shear stress are important parameters. Results obtained in dry, moist and wet conditions, as well as at elevated temperatures suggest that there is a 'competition' between the energy input into the partial cone-cracks formed to the rear of the sliding contact, and the development of a sub-surface shear crack. The dominating influence of lubrication lowering the coefficient of friction is emphasized. A reduction in friction reduces the tendency to form cone-cracks and enhances a cutting action.

On the basis of this study, the deformation of quartzite in the earth's crust is discussed, and the implications for large scale diamond drilling operations are analysed.

C O N T E N T S

NOMENCLATURE

$\underline{b}$	Burgers vector
C'	Constraint factor
D	Diffusion coefficient
e	Electronic charge
eV	Electron volt
E	Young's modulus
F_H	Horizontal force
F_V	Vertical force
f	Force ratio
G	Energy release rate
h	Planck's constant
H_V	Vickers hardness
H_K	Knoop hardness
HVEM	High voltage electron microscope
k	Boltzmann constant
K	Stress intensity factor
K_C	Critical stress intensity factor (fracture toughness)
n	Logarithmic index
P_C	Critical cone-crack formation load
P	Applied load
Q	Activation energy
R	Gas constant
S_e	Specific energy
SEM	Scanning electron microscopy
T_M	Melting temperature
T_C	Hydrolytic weakening temperature
TEM	Transmission electron microscope
v_a	Activation volume
V	Voltage
XRT	X-ray diffraction topography

γ	Surface energy
ε	Strain
$\dot{\varepsilon}$	Strain rate
θ_B	Bragg angle
θ	Indentor half angle
λ	Wavelength
μ	Friction coefficient
ν	Poisson's ratio
ξ_g	Extinction distance
ρ	Radius
σ	Stress
σ_f	Fracture Stress
σ_i	Principal stress
σ_y	Yield stress
τ	Shear stress

CHAPTER 1

GENERAL INTRODUCTION

1.1 Overview

Quartz is the principal mineral constituent of the earth's upper crust and a knowledge of the deformation properties of this material are of vital importance to a wide range of disciplines. A detailed understanding of the brittle fracture of quartz is essential to those industries which are engaged in the extraction of useful minerals, so that the efficiency and safety of mining operations may be improved. Geological science requires the conditions under which quartz may deform plastically in order to develop theories of crustal deformation, and to provide a more detailed understanding of tectonic sequences. At the same time, however, a brittle or a plastic response may occur simultaneously. For example earthquake phenomena are evidently brittle fracture events, although taking place within a broad plastic field, while in mining operations tool bit temperatures may develop to a sufficient extent to allow the rock to display local ductility. It is thus apparent that any study of quartz must include a consideration of both the plastic and brittle behaviour, and the conditions under which these two extremes are manifest, if it is to be of practical benefit.

The process of drilling, cutting and grinding can all be regarded as forms of comminution in which unbroken material is converted into small fragments. Comminution presently involves the use of a rapidly applied force to achieve efficient fragmentation, and it is anticipated that the dominant mechanical response of a rock under these conditions will indeed be brittle fracture. However, the tool work-piece area is a complex zone and there is increasing recognition that high temperatures may

be generated by frictional heating with a resulting plastic deformation of the rock. Hydrostatic conditions may be induced which also favour plastic deformation. These plasticity processes may cause the blunting of sharp cracks, or simply the ploughing of the rock surface by the bit, as a result of which material is deformed but not removed. In either case the energy expenditure is increased and the overall efficiency of cutting reduced. It is clearly desirable to keep the plastic response to a minimum.

The nature of material removal by drill or cutting bits is still imperfectly understood, and considering the global expenditure on such processes small improvements in efficiency would result in large-scale savings when considered as a whole. Because of the complexity of the drilling operation ideas from modern physics, rock mechanics and fracture mechanics should all be effectively utilized in understanding more completely how material is removed.

Brittle solids are stronger in compression than in tension, and a cutting tool must operate by creating a tensile stress field in the workpiece if it is to be effective at comminuting material. If a cutting tool is considered to be constructed from a number of point indentors it is evident that the results of indentation fracture mechanics should provide some clues as to the mode of material removal.

Optimization can be approached by researching three aspects. These are:

1. The mechanical response of the material being drilled.
2. The design of the tool bit.
3. External parameters such as lubricants and chemo-mechanical environments.

It is obvious, however, that in practice all three must be considered together. Such a task may appear daunting at first sight because of the large number of variables, and many different types of rock. However, by the use of well-defined

cutting geometries (particularly single-point cutting tools), cutting parameters (speeds, normal force, temperature) and lubricants and/or environments, it may be possible to determine precisely those factors which most influence the cutting process.

The earth's upper crust extends to a depth of ≈ 35 Km, (Fig.1.1) and in this zone quartzitic rocks are dominant. Maximum temperatures are relatively low (< 900 K), and differential pressures are of the order 0.3 - 3 Kbar. Geological data suggests strain rates encompassing the range 10^{-12} -10^{-16} s^{-1}, so that a geological plate 1000 Km long deforming at the lower bound of strain rate would shorten by approximately 3 mm per year. Quartz in common with many ceramic materials may not satisfy the Von Mises independent slip system criterion under crustal conditions of temperature and stress. Laboratory compression tests have shown that the activation of the requisite five slip systems requires high stresses, and temperatures in excess of 1000 K. Thus on this basis a polycrystal of quartz within the crust cannot deform comformably, and extensive shattering or cataclasis is to be expected. However, evidence from HVEM investigations of quartzite (Fig.1.2) suggests the opposite. It can be seen that dislocation lines are smooth and loops are visible, consistent with the operation of dislocation climb mechanisms. Under the creep deformation conditions in the earth's crust, it may be possible that the Von Mises restriction can be overcome.

There is a remarkable similarity between the dislocation structures observed in ceramic materials and those of metals. While a detailed understanding of the deformation mechanisms of the former materials is still in its infancy, good progress has been made by utilising the models which metallurgists have developed and refined to explain the mechanical properties of metals. Dislocation slip, creep and climb are common to both classes of solid, but care has to be taken, since charge neutrality requirements in ceramics can provide an additional restriction on deformation which takes place by the transport of ionic species. With a correct interpretation of these differences there should be no difficulty in adapting the current deformation theories of metals tc ceramic materials.

To induce plasticity during the indentation or cutting of a solid which does not satisfy the Von Mises criterion the pressures under the tool must be sufficient to activate all the requisite slip systems. The fact that hardness impressions can be made in quartz (Fig.1.3) suggests that this is the case, even at room temperature. However, to confirm this conclusively evidence for dislocation nucleation and slip is required from transmission electron microscopy and additionally there must be no tendency for a pressure induced transformation to denser phases.

1.2 Scope of the Present Investigations

The aim behind the investigations described in this thesis was to investigate the brittle and plastic response of single crystal quartz, and to attempt to relate these to important practical applications. The brittle response was investigated using a single point scratching apparatus, using a well defined tool geometry and a controlled environment. Both room temperature, and high temperature scratches were made. The microfractures and deformation were examined, and evidence for a plastic response assessed. Measurements were also made of the forces acting during scratching to evaluate the energetics of cutting under different conditions. An important parallel study was the investigation of room temperature hardness impressions over the same load range as the scratching tests, to provide information on the similarities and differences in deformation between static indentation and dynamic (scratching) indentation. The results of these tests are related to the operation of large rock drilling and cutting bits.

The plastic response was investigated in a series of slow strain rate uniaxial compression tests. A crystal of quartz orientated such that the easy slip systems do not experience any resolved shear stress can only deform by slip

with the operation of the hard slip systems. If the hard systems do not operate and if the crystal does strain, then this strain must be accommodated by the climb motions of dislocations of the easy slip systems. Within the framework of the Von Mises criterion this suggests that the restriction on deformation can be overcome, and the necessity for hard slip system operation relaxed. Such tests were performed, and the resulting dislocation structures analysed by HVEM. The implications of the results for geological science are discussed.

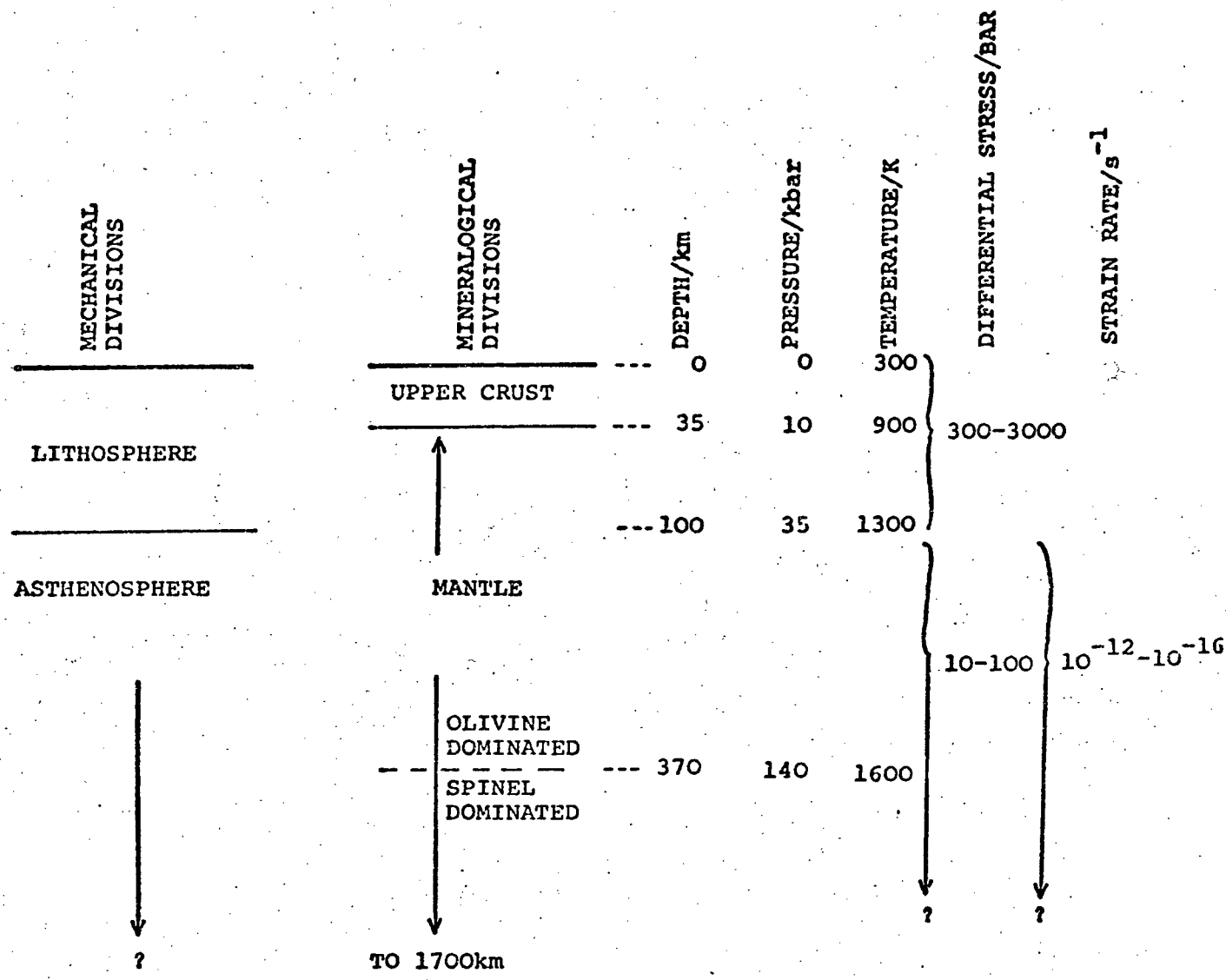

Fig.1.1 Sketch of the principal subdivisions of the Earth in the first 400km. (after: Goetze, C.; Phil. Trans. R. Soc. Lond. A.288, 99-119, 1978).

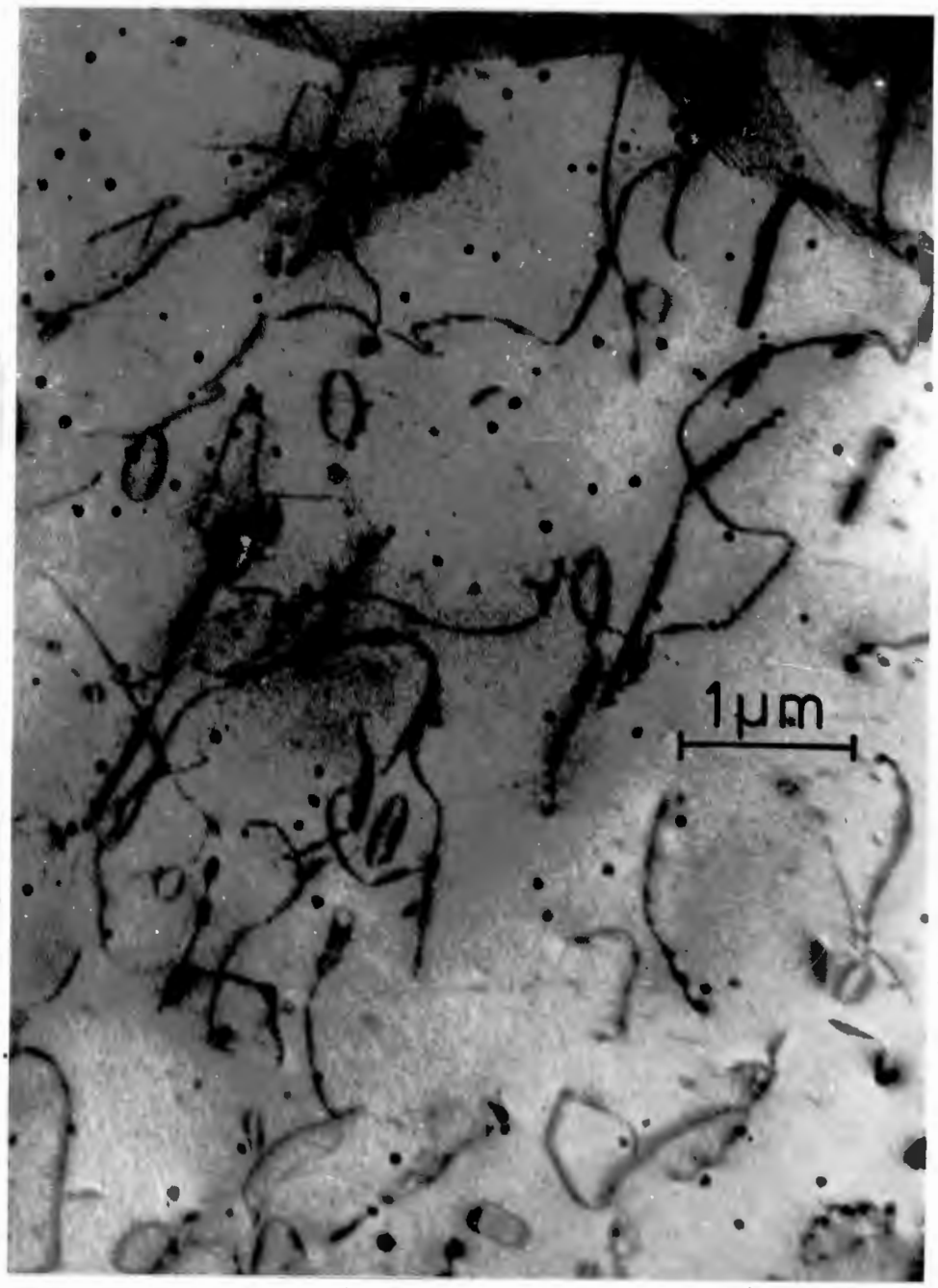

Fig.1.2 An example of the dislocation structure of a naturally deformed quartzite. Note the dislocation loops and smooth segments, typical of climb. (High voltage electron micrograph, 1000KeV).

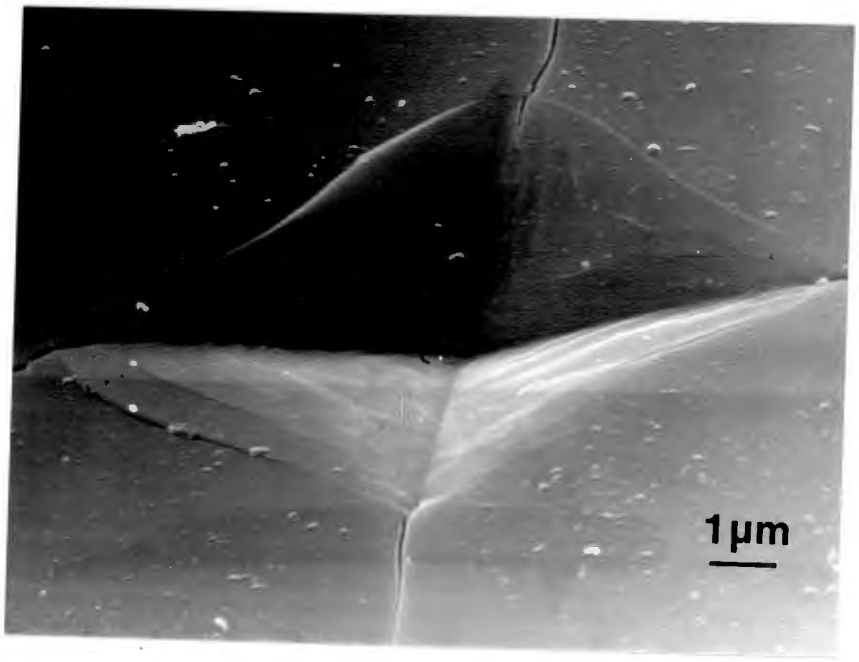

Fig.1.3 Vickers hardness impression on single crystal synthetic quartz. The smooth appearance of the impression suggests that plastic processes may operate at room temperature in this brittle solid.

CHAPTER 2

THE CRYSTALLOGRAPHY AND STRUCTURE OF QUARTZ

2.1 Phase Relationships

Quartz is pure silicon dioxide, SiO_2, and is the most abundant member of the family of silica minerals. Quartz can exist in two different polymorphs. The phase that is stable at room temperature and atmospheric pressure is designated low or α-quartz. At 846K α-quartz transforms to a higher symmetry form, designated high or β-quartz. α-quartz undergoes no further phase transformations on cooling from room temperature to 4.2K. β-quartz is stable from 846K to 1143K and upon reaching this temperature transforms to tridymite. However, in contrast to the α→β quartz transformation which is extemely rapid over a narrow temperature range, the β-quartz→tridymite transformation is slow, and β-quartz may exist metastably to the melting temperature (≈1700K). Fig.2.1 indicates the pressure-temperature diagram for the silica polymorphs. An important point to notice is that β-quartz can be transformed to α-quartz by the application of a suitable pressure.

The basic structural unit of the silica minerals is the $[SiO_4]$ tetrahedron. In quartz, cristobalite, low tridymite and silica glass this tetrahedron is perfect, with O-Si-O angles equal to the tetrahedral value of 109.5°. However, differences do exist between the Si-O-Si angle, which lead to structural variations; in α-quartz the Si-O-Si angle is 143.5°, while in silica glass it can vary from 120-180°, to give the glass a random spatial network of tetrahedra units.

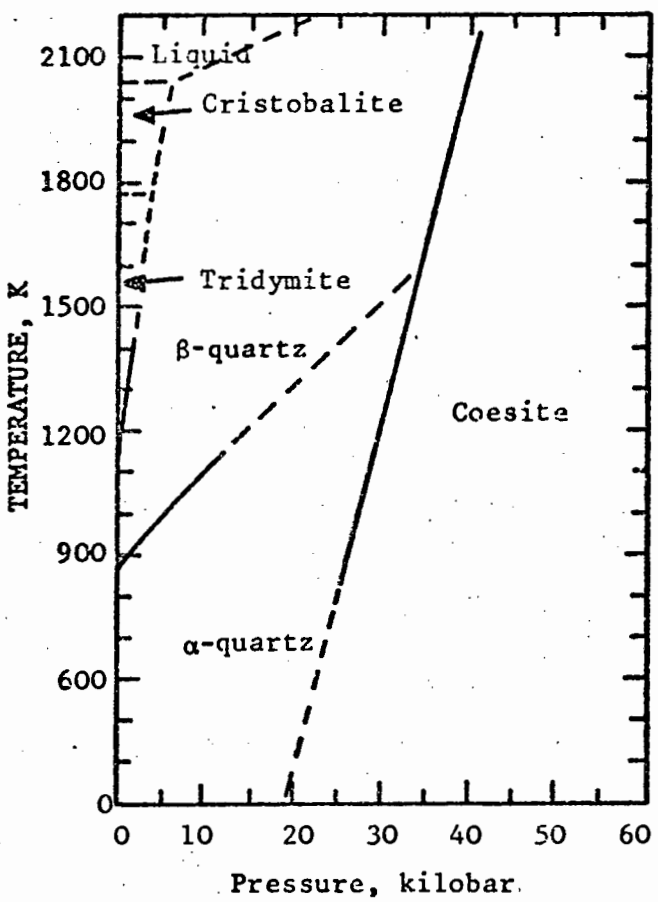

Fig.2.1 Pressure-temperature diagram for SiO_2 polymorphs.

2.2 The Structure of α-quartz

α-quartz crystallizes in the trigonal trapezohedral crystal glass (32) of the rhombohedral subsystem, with an hexagonal lattice type. There is one axis of three-fold symmetry, and perpendicular to this axis are three axes of two-fold symmetry, separated by 120^{o}. The Miller and Bravais axes for the hexagonal and rhombohedral cells, respectively, of the trigonal system are shown schematically in Fig.2.2, drawn with reference to quartz. The three pyramidal faces ABC, ADE and AFG belong to the primary positive first order rhombohedron (r-faces), while the remaining pyramidal faces are z-faces. The Bravais axes are a_1, a_2 and a_3 and C, parallel to OG, OC, OE and OA respectively.

If the r-faces are extended they meet at M_1, M_2 and M_3. The projection of these large planes on the basal plane (e.g. M_1 N) defines the Y-axes. The Y-axes are also the projection of the Miller axes on the basal plane. The X-axes are the Bravais axes, and are the two-fold axes. The principle axis is the Z-axis, also known as the optic axis. The X, Y and Z notation is common to piezo-electric descriptions; accordingly, samples cut with major faces normal to these axes are known as X-cuts, Y-cuts and Z-cuts respectively (Fig.2.3). A stereographic projection of α-quartz constructed along the Z-axis is shown in Fig.2.4.

The crystal class to which α-quartz belongs has the property of enantiomorphism. That is, the crystal may exist in two forms which are mirror images of one another. These two types are illustrated in Fig.2.5. On each diagram the characteristic faces are shown.

The enantiomorphous space groups have been determined or described in terms of morphological, optical and structure dependent characteristics. As discussed by Frondel (1962) and Cady (1946) this has led to much confusion in the actual placing of the crystallographic axes. The space group which either form belongs to is determined structurally: $C3_12$ for

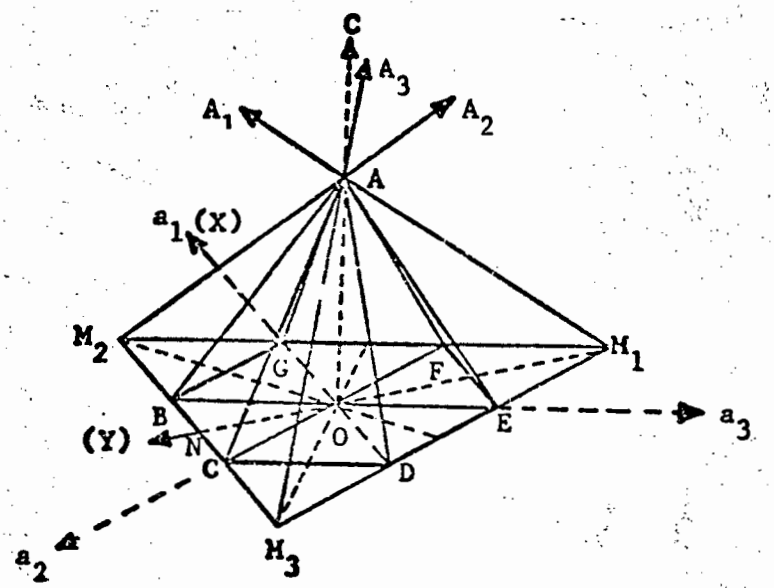

Fig.2.2 Schematic diagram of the unit cell of the trigonal crystal system. The Miller axes (A_1,A_2,A_3) and Bravais axes (a_1,a_2,a_3,C) are indicated.

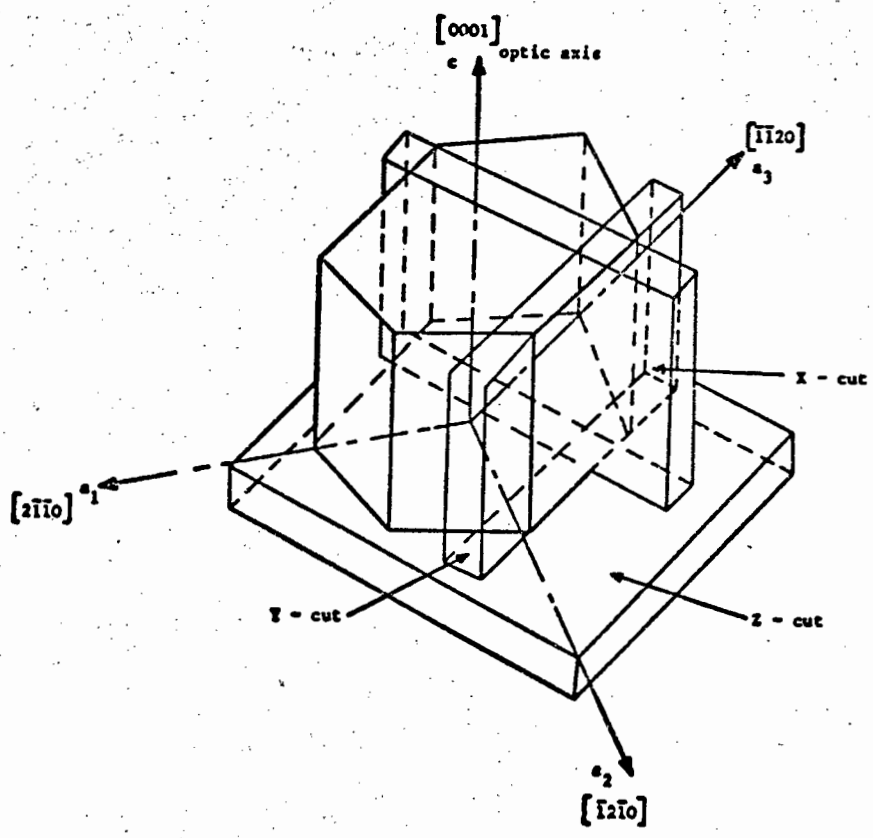

Fig.2.3 Schematic diagram of the orientation of the three principal quartz cuts with reference to the quartz crystal lattice. (after: Hartley, N.E.W., and Wilshaw, T.R, 1973).

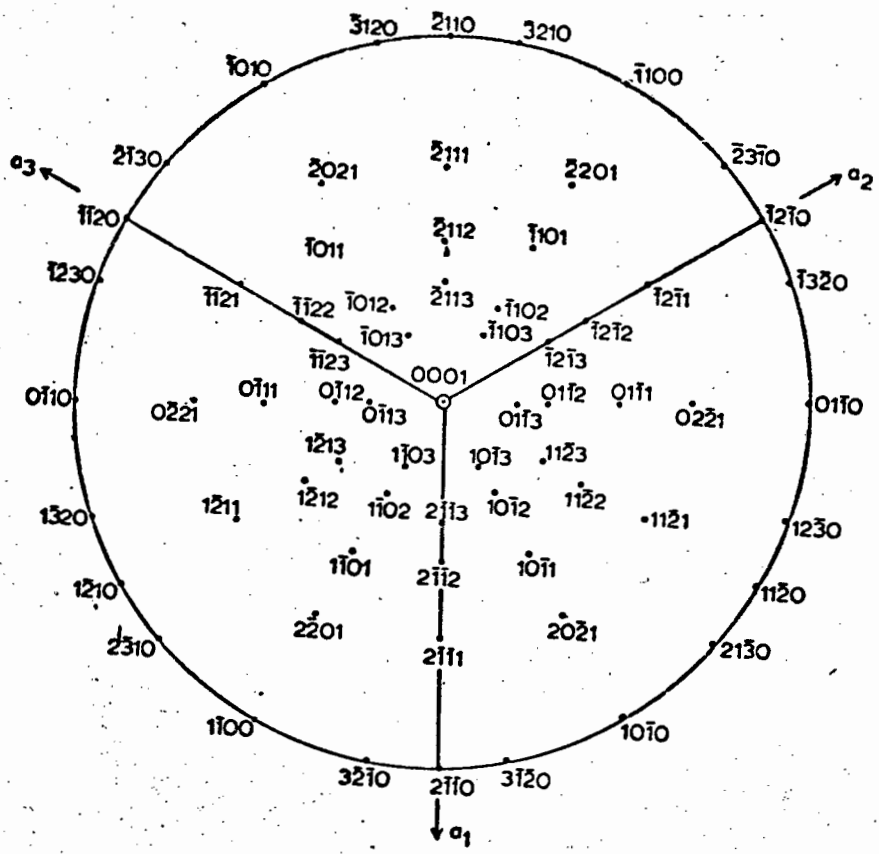

Fig.2.4 Stereographic projection of α-quartz constructed along c [0001] .

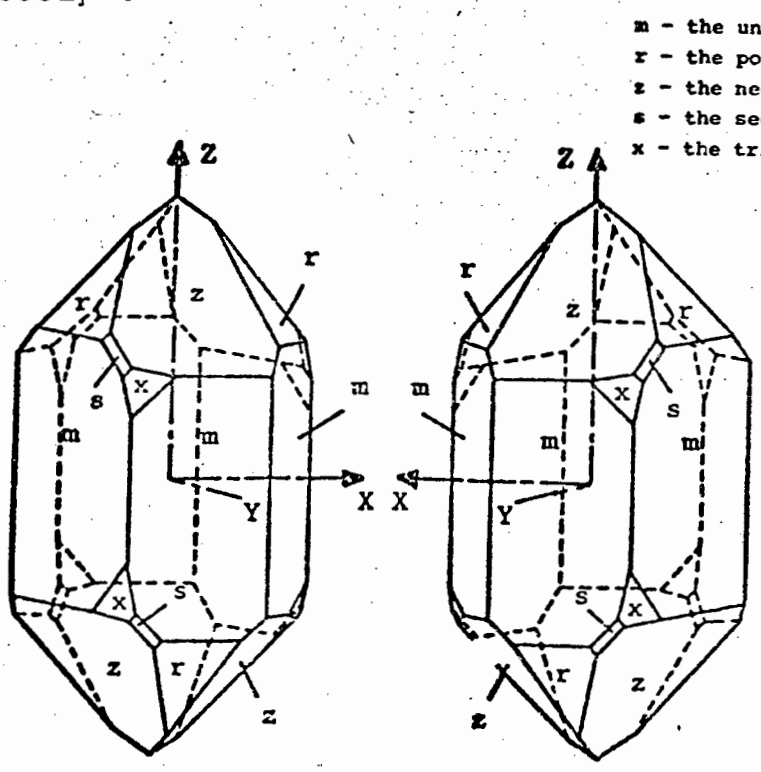

Fig.2.5 The two enantiomorphic forms of α-quartz.

for right-handed crystals and $C3_22$ for left-handed crystals. However, the morphological or conventional hand of quartz is opposite to the structural hand. Quartz has the ability to rotate the plane of polarization of light propagating parallel to the optic axis, either to the left or to the right, and Biot in 1814 termed quartz right-handed if the plane of polarization is rotated clockwise when the observer looks towards the light source through an analyzer. Biot's definition is now formally accepted. This means that a crystal that is right-handed on the basis of optical rotation is also right-handed crystallographically as determined by the position of the s and x faces (Fig.2.5).

The unit cell of α-quartz contains three SiO_2 units, with nominal room temperature lattice parameters a_o = 4.913 Å and c_o = 5.405 Å. The atomic positions for the space group $C3_12$ are:

Si : $\bar{u}, \bar{u}, \frac{1}{3}$; u, o, o; $o, u, \frac{2}{3}$

O : x, y, z; $y-x, \bar{x}, z+\frac{1}{3}$; $\bar{y}, x-y, z+\frac{2}{3}$;
$x-y, \bar{y}, \bar{z}$; $y, x, \frac{2}{3}-z$; $\bar{x}, x-y, \frac{1}{3}-z$.

with the parameters

$u = 0.465$

$x = 0.415$

$y = 0.272$

$z = 0.120$

X-ray diffraction data gathered by Smith & Alexander (1963) from single crystal natural quartz and by Young and Post (1962) from synthetic quartz gives the following average values for the bond angles and lengths.

Bond Angles		Bond Lengths	
O - Si - O	109.5°	Si - O	1.61 Å
Si - O - Si	144.0°	O - O	2.62 Å
		Si - Si	3.06 Å

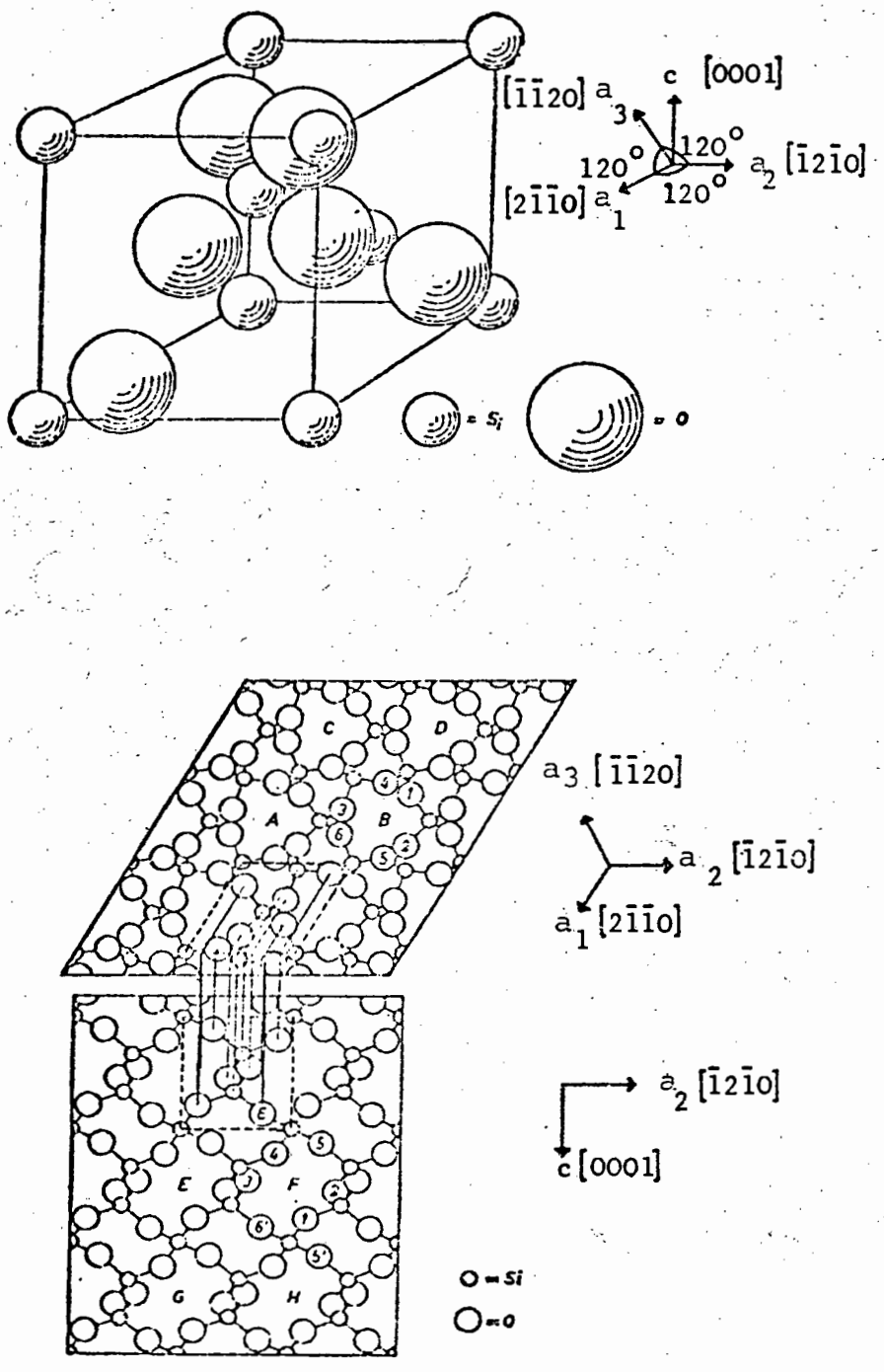

Fig.2.6. Atomic positions in right handed α-quartz structure (a) the unit cell, (b) projection onto (0001) and (10$\bar{1}$0). (after Kats, 1962).

The Si - O bond is of an intermediate type, being half covalent and half ionic.

The actual atomic arrangements, determined by X-ray diffraction, is complicated and difficult to visualize. A three-dimensional representation of the α-quartz unit cell is shown in Fig.2.6. Projections of the atoms (strictly ions) onto the basal and prismatic planes are also shown. These projections clearly demonstrate an important feature of the quartz crystal structure, which are the relatively open 'tunnels' (e.g. A, B, C, D) parallel to the C[0001] axis. There is one tunnel per unit cell. There are also rhombic 'tunnels' (e.g. E, F, G, H) running parallel to each of the a-axes, making three a-axis tunnels per unit cell. We shall show later that these open tunnels have an important influence on the incorporation and mobility of impurities in quartz.

2.3 The Structure of β-quartz

β-quartz belongs to the hexagonal trapezohedral (622) crystal class. It is enantiomorphous with the space groups $C6_22$ or $C6_42$, and the unit cell contains three SiO_2 units. At 848 K, $a_o \approx 5.0$ Å and $c_o \approx 5.4$ Å.

The atomic positions for the $C6_22$ space group are:

Si : $\frac{1}{2}\ \frac{1}{2}\ \frac{1}{3}$; $\frac{1}{2}$, O, O; O, $\frac{1}{2}$, $\frac{2}{3}$

O : $u,\bar{u},\frac{5}{6}$; $\bar{u}$, $u,\frac{5}{6}$; $u,2u,\frac{1}{2}$; $\bar{u},2\bar{u},\frac{1}{2}$; $2u,u,\frac{1}{6}$; $2\bar{u},\bar{u},\frac{1}{6}$;

with $u = 0.197$.

The structure of β-quartz is more symmetrical than α-quartz.

2.4 The α-β Phase Transformation in Quartz

At 846K α-quartz undergoes a rapid, displacesive phase transformation to β-quartz. The transformation does not involve the breaking of any atomic bonds and may simply be visualized as small cooperative rotations of the SiO_4 tetrahedra by 19° about their two-fold axes. The temperature at which β-quartz transforms to α-quartz is usually a few degrees below α→β transformation temperature. The actual transformation temperature is sensitive to the impurity content of the crystal, and variations of several degrees can occur in natural quartz, while a considerably greater variation occurs in synthetic quartz (Keith & Tuttle, 1952).

Young (see Coe & Paterson, 1969) examined in detail the phase transformation by X-ray diffraction techniques. This author found that structurally the transition is marked by a discontinuous shift of the equilibrium positions of the atoms, an increase in the amplitude of vibration of the oxygen atoms perpendicular to the Si - O - Si planes, and an abrupt increase in the Si - O - Si bond angle by 2°. Also, there is a dramatic increase in the development of small scale Dauphiné twins, which may start from a few degrees to many tens of degrees below the transition, and may or may not achieve a maximum (50% by volume) throughout the sample. An increase in the scattering of light at the phase transition may be attributable to these twin boundaries.

The α→β transition temperature is affected by an applied stress. Coe and Paterson (1969) found that a hydrostatic pressure increases the transition temperature by 25°/Kbar. Under a confining pressure of 3Kbar a directed stress, applied perpendicular to $\underline{C}$[0001] raises the transition temperature by $\approx 11^{\circ}$/Kbar and by 5°/Kbar when applied parallel to $\underline{C}$[0001]. This effect of pressure must be considered when compression tests are undertaken on single crystal quartz at elevated temperatures. It is clearly desirable that the crystal should remain either within the α, or the β stability field for the duration of the experiment.

2.5 Twinning in quartz

Several modes of twinning may occur in quartz. The major types are:

(a) Dauphiné law twinning (electrical twinning)

(b) Brazil law twinning (optical twinning)

(c) A combination of Dauphiné/Brazil twinning

(d) Japan law twinning

Dauphiné Twinning

This twin is formed by a lattice rotation of π radians around the [0001] axis. The hand of the crystal remains the same, but the polarity of the a-axis is reversed in the twinned regions. It cannot be recognized by optical means but shows up on polished and etched crystals. X-ray diffraction can also be used to detect Dauphiné twins, by monitoring the intensity of diffracted radiation. X-ray diffraction topography has also been successfully used to map the twinned regions in α-quartz (Lang, 1965).

Dauphiné twinning may be induced by a mechanical stress, by cooling a crystal down through the α-β transition point, or by thermal shock. Dauphiné twinning disappears in the β-quartz polymorph since the twin operation around the three-fold axis is an identity operation around the six-fold axis of β-quartz.

Brazil Twinning

The twinned portions of the crystal are related by a reflection across $\{11\bar{2}0\}$, and are of opposite hand. The crystal axes are parallel, but the electrical polarity of the a-axes is reversed in the twinned regions. The presence of Brazil twinning can be detected optically because the twinned regions rotate plane polarised light in opposite directions. Brazil twinning cannot be induced artificially, and is not removed by heating past the α-β transition temperature.

Combined Dauphiné - Brazil Twinning

This combination twinning is rare, and consists of a π rotation about [0001] and a reflection over $\{11\bar{2}0\}$. The crystal axes are parallel, but the electrical polarity of the a-axis is not reversed.

Japan Twinning

There are four related types of Japan twinning. Briefly, they are contact twins with c-axes inclined at $84^{\circ}33'$. The twin plane is $(11\bar{2}2)$.

2.6 Piezoelectric Response

If a mechanical stress (either compressive or tensile) is applied to a crystal of α or β quartz, directed along certain crystallographic directions, electrical charges are induced on the crystal faces. The induced electrical polarisation is known as the piezoelectric effect, and is a direct result of the lack of a centre of symmetry of the crystal. Conversely, an applied electric field produces a mechanical strain in the crystal. It is this latter phenomenon that is exploited in the electronics industry for the construction of high stability oscillators and ultrasonic drives.

Compression along an a-axis of α-quartz produces a negative charge on the end of the a-axis terminated by the x and s faces, and a positive charge on the opposite end. Compression perpendicular to a $\{10\bar{1}0\}$ prism face induces charges on the ends of the a-axes identical to those produced by a tension directed along the a-axis. No induced charge is developed by a stress applied along the c[0001] optic axis.

2.6.1 Influence of Twinning on Electrical Properties

The use of quartz for piezoelectric oscillators requires that there are no twinned regions with opposite electric axes in the crystals. Thus, both Dauphiné and Brazil twinning (but not the combined twinning) will influence the oscillator. Crystals containing Dauphiné twins usually have a completely twinned volume, whereas Brazil twinning involves only relatively small volumes. Consequently much research work has been performed on the elimination of Dauphiné twins. Thomas and Wooster (1951), found that the application of a stress gradient or torsion may in some circumstances reduce the extent of twinning.

The stress fields around dislocation lines may also produce an intense, short range electric field in Piezoelectric

crystals. From theoretical calculations on α-quartz, Saada (1971) found that field strengths of $\approx 5\ 10^8\ Vm^{-1}$ were possible near straight dislocations, and that the electrical interaction between a charge carrier and a dislocation could be very strong. This may have an important bearing on those deformation mechanisms which involve the diffusion of ionic species through the lattice.

2.7 Single Crystal Growth of Quartz

Single crystal quartz can be artificially grown using a hydrothermal technique. The first attempts at growing quartz crystals by this method were successfully made by Spezia in the early 1900's. However, the size of the crystals was small and growth took a long time. Because of the importance of crystalline quartz to the electronics industry, and due to the interruption of supplies of natural quartz crystals during World War II, major attempts were made by a number of groups in the United States and the United Kingdom to develop more precise growth techniques which could produce good quality quartz in reasonable quantities. Today the combined world production of synthetic quartz is approximately 750 000 Kg/year.

In the hydrothermal technique (Laudise, 1973) a steel autoclave with a lower and an upper chamber (Fig.2.7) is filled with a mineralizer (usually a NaOH or Na_2CO_3 solution). The lower chamber contains a relatively finely divided quartz nutrient, while the upper chamber contains the suspended quartz seed plates. Both chambers are temperature-controlled independently and care is taken to ensure isothermal conditions. A baffle plate separate the two zones.

A typical growth profile would be:

Lower chamber	:	673K
Upper chamber	:	623K
Pressure	:	2 Kbar

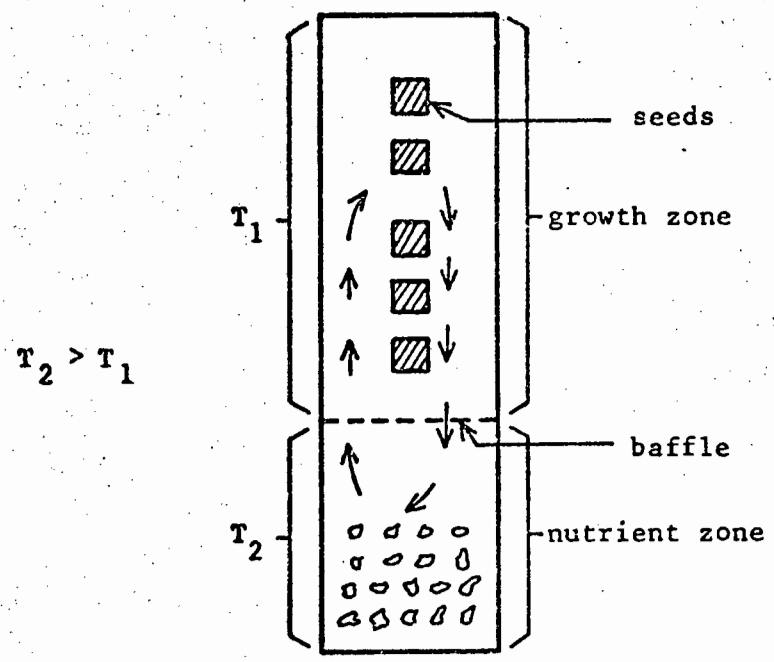

Fig.2.7 Schematic diagram of the hydrothermal technique for the growth of synthetic quartz crystals.

The solution saturates at 673K and moves by convection to the growth zone where, because the solution is now supersaturated quartz is deposited on the seed plates. The solution then returns to the lower chamber.

Advantages of a hydrothermal method include the fact that the growth takes place in the α-quartz stability field, and crystals of good homogeneity and high quality may be consistently produced.

A seed plate will grow in all directions but the growth does not proceed at an equal rate. Growth in the Z-direction (Z-growth) is the fastest, while it is slower in the +X-direction (X- growth). In the Y-direction (Y-growth) the growth rate is very slow. Growth also occurs in directions perpendicular to the major and minor rhombohedra (major and minor growth, respectively). The impurity levels of the various growth zones will be different. Z-growth has the lowest concentration, followed by +X and -X, while the rhombohedral zones contain the maximum impurity concentration. At high growth rates the crystals become flawed or cloudy. An (0001) seed plate would grow typically at a rate of 2 mm per day.

Deliberate doping of quartz with impurities can also reduce the quality of the final crystal. In general the major inclusion in synthetic quartz is acmite (Na_2O . Fe_2O_3 . $4SiO_2$), and commercial crystals are carefully checked prior to component synthesis for these particles. The Fe is picked up from the steel autoclave, which also becomes lined with acmite by the action of Na^+.

One interesting feature of crystal growth in the Z-direction is the development of a 'cobble' texture (Fig.2.8). Each cobble represents an 'impurity cell', and X-ray diffraction topography (Fig.2.9) clearly shows that at the cell wall the impurity atoms produce a lattice mismatch, visible as fault surface fringe contrast. It has been found (Lang & Miuscov, 1967) that the X-ray fringe contrast corresponds to the grooves between the cobbles.

Fig.2.8 Typical Z-growth synthetic quartz, showing the rough face, or 'cobble texture'.

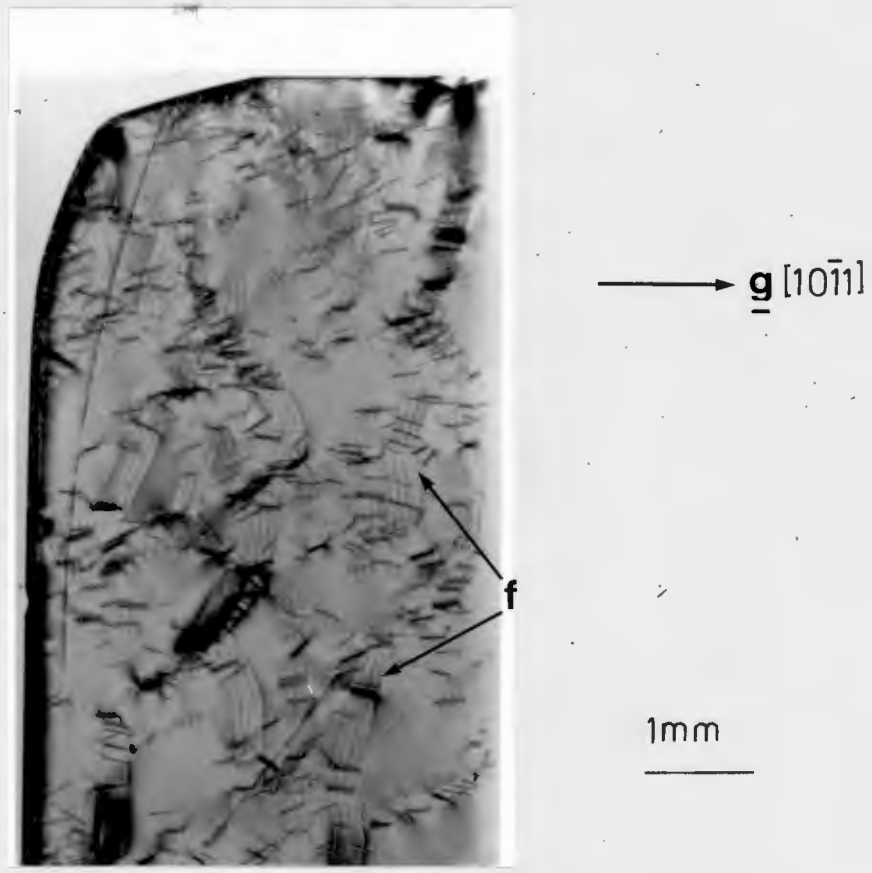

Fig.2.9 X-ray topograph of basal section of above crystal. The cobble grooves are visible as fringe contrast (f).

2.8 Defect Structure

2.8.1 General Impurities

Quartz is an electrical insulator with a fundamental band-gap in the vacuum ultra-violet (≈ 9eV). At $0^{o}K$ in the defect free state, the valence band is completely filled with electrons, and the conduction band empty. However, defects may introduce energy levels into the band-gap.

The major impurity species in quartz are the alkali ions (Li^{+}, Na^{+}, K^{+}), $A\ell^{3+}$, Fe^{3+} and also H^{+}. $A\ell^{3+}$ can substitute for Si^{4+} although the radius of the trivalent $A\ell^{3+}$ ion (0.57 $\mathring{A}$) is somewhat larger than Si^{4+} (0.39 $\mathring{A}$). It is believed that the alkali and hydrogen ions may be charge compensators for $A\ell^{3+}$ to preserve electrical neutrality in the crystal. The impurity ions are probably located within the open channels of the quartz lattice.

The low probability of electrons occupying levels in the conduction band suggests that the low temperature electrical conductivity observed in quartz will be due to impurity ions which can drift through the crystal lattice, along an imposed potential gradient. Both Verhoogen (1952) and Wenden (1957) have investigated the ionic diffusion and electrical conductivity in natural quartz.

Wenden found that the electrical conductivity of quartz displays several different regimes of behaviour, with a strong dependence on the length of time for which the field has been applied. On initial application of the electric field transient currents can be detected, as impurities trapped in the lattice during crystal growth are activated to contribute to the total current flowing. After the electric field has been applied for a considerable length of time, all of the mobile

impurity carriers have been removed from the lattice and steady state conditions prevail.

Since the change of resistivity with reciprocal temperature can be used to obtain an activation energy for ionic diffusion, it is vital that the various conduction regimes should be understood in order that pure ionic diffusion alone is measured, and not some transient effect. In diffusion experiments where known ionic species are injected into the lattice under the action of an electric field the measurement of conductivity must be undertaken only on specimens that have been completely cleared of mobile defects of uncertain origin, i.e. steady-state conditions must have been achieved prior to injection.

The conductivity is significantly affected by the direction of the applied field. Thus conductivity is high in a direction parallel to c[0001], implying that the c-axis channels allow ions to readily diffuse along them. Conductivity perpendicular to c[0001] is much lower. However, when steady-state conditions have been reached, the conductivity both parallel and perpendicular to c[0001] is essentially equivalent, indicating that the mechanism of charge transport may be the same. Verhoogen drew attention to the fact that if the field was removed for several days, the initial high conductivity could be regained.

The diffusion coefficient of the ions is more sensitive to the charge carried by the ions than their absolute size. Thus univalent ions can drift more easily than polyvalent species. The c-axis channels are 2Å in diameter, implying that the maximum radius of a diffusing ion is ≈ 1Å. However, it is found that the large K^+ ion (radius = 1.33Å) can diffuse more rapidly than smaller polyvalent ions. Verhoogen (1952) therefore suggested that the mechanism of diffusion may involve pre-existing 'holes' in the lattice, such as oxygen vacancies. This vacancy carries an effective positive charge, which would tend to repel any positively-charged ions. Thus the larger the charge carried by an ion

the greater the repulsive force experienced, corresponding to a reduction in the diffusion rate.

Verhoogen obtained the following activation energies for ionic diffusion along c[0001]:

Li^+ : 0.90 eV

Na^+ : 1.05 eV

K^+ : 1.38 eV

Wenden made measurements of the activation energy for conduction when all impurities had been removed from the lattice. After eight weeks of passing current the intrinsic activation energy was 1.72 eV.

An alternative, but equally effective, method for determining the activation energies of defects in solids is to use acoustic loss techniques. In a perfectly elastic solid the applied stress and strain are in phase and no energy is dissipated. However, if there is a time dependence the stress and strain are no longer in phase and energy losses occur. The internal friction, Q^{-1}, is equal to tan δ, where δ is the phase angle. Internal friction will result when defects are activated. Thus, by measuring the internal friction as a function of temperature it is possible to find activation energies for particular defect species. This technique is particularly effective, and was developed for quartz because of the use of this crystal as a piezoelectric oscillator and the need to keep energy losses to a minimum.

Loss peaks occur from very low temperature until well into the β-quartz field. The reason for the low temperature peaks is shown in Fig.2.10. In this particular example an Al^{3+} ion has substituted for the Si^{4+} ion. The overall potential well associated with Al^{3+} is ≈leV. Superimposed om this potential are a series of relatively low potential barriers due to binding forces, the influence of ionic size and steric hindrance. The passage of Li^+, Na^+ and K^+ ion is shown, along with the corresponding small barriers that the ions must overcome while drifting along the c-axis

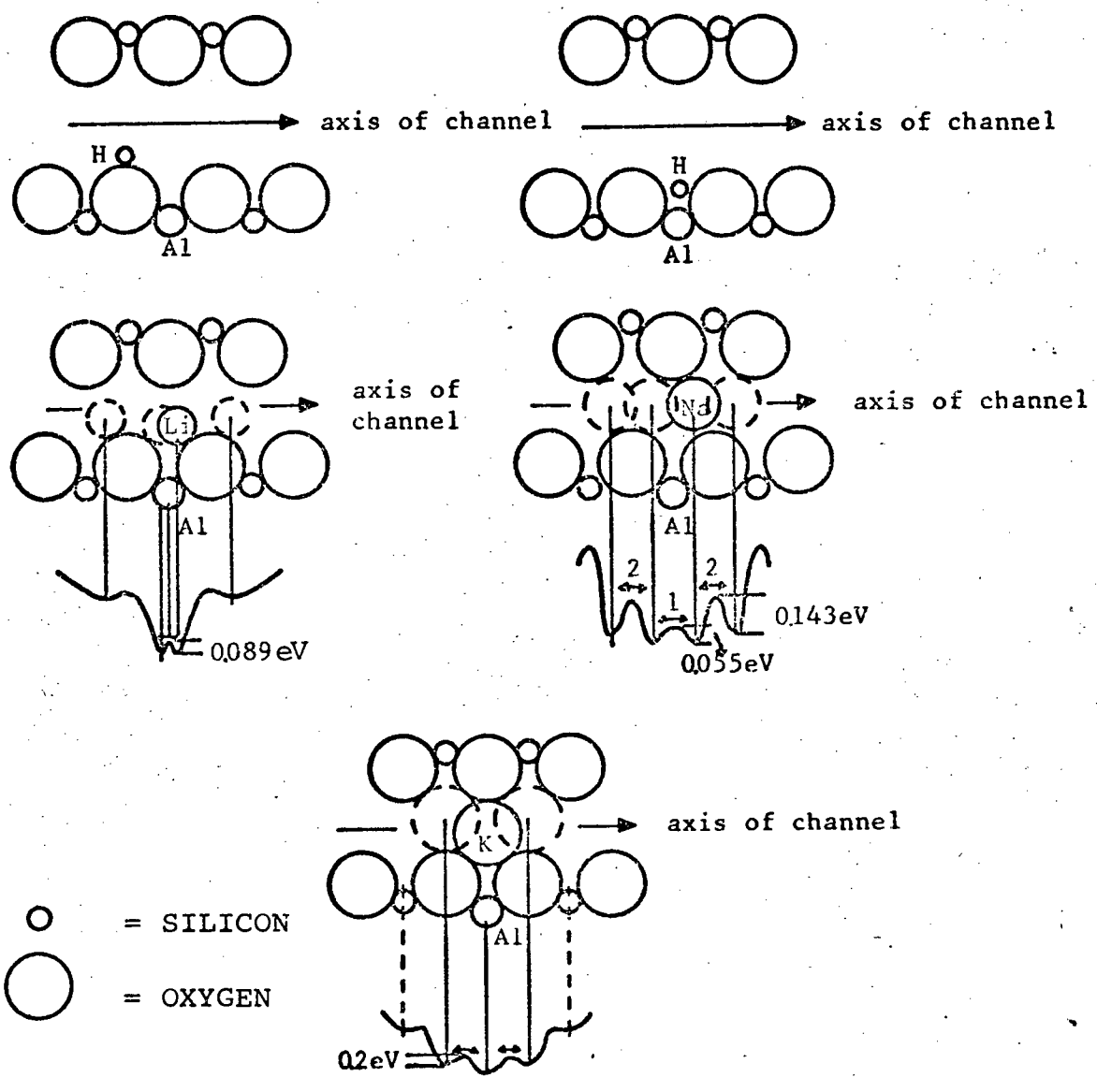

Fig.2.10 Models of the position of H^+ and alkali ions in the channels of quartz crystals. The potential energy curves are also shown. (after: Stevels, J.M., and Volger, J.: Philips Res. Repts., 17, 283-314, 1962).

channels. The activation energy of these small barriers can be measured at low temperatures before high temperature diffusion has set in, which will mask the effect.

The activation energies Li^+, Na^+ and K^+ determined by acoustic loss analysis are as follows (Fraser 1968):

Li^+ : 0.72 eV

Na^+ : 0.77 eV

K^+ : 0.92 eV

There is poor agreement with the results obtained by conductivity measurements.

2.8.2 Hydrogen Defects in Quartz

A group of specimen dependent absorption bands exist in the infra-red spectrum of quartz. It has been established (Kats, 1962) that the 3400 cm^{-1} bands in the spectrum are due to hydrogen defects (hydrogen bonded OH) in the lattice.

The various infra-red absorption bands can be classified into three distinct types of hydrogen defects.

1. Sharp bands attributable to (OH) in well-defined structural sites, associated with Al^{3+} or alkali impurity ions (Na^+, Li^+, K^+).

2. A broad absorption band which does not sharpen to ice bands at low temperatures. This is due to a gel-type hydroxyl, involving silanol SiOH groups.

3. Molecular water (that sharpens to ice bands for experimental measurements made at low temperatures) at approximately 3200 cm^{-1}.

A significant feature of the infra-red spectrum of synthetic quartz is a broad absorption band from 3600 - 3100 cm^{-1} whereas natural quartz shows considerably less absorption over this range. Since it has been established (Dodd & Fraser, 1965)

that the absorption at 3500 cm^{-1} is proportional to the concentration of hydrogen defects, the above results suggest that synthetic quartz contains a higher concentration of these defects. Kats (1962) has examined the infra-red spectrum of quartz in detail. In order to discover the way in which the hydrogen defects were incorporated, and the influence of other impurity ions, he performed annealing, diffusion and electrolysis experiments on synthetic and natural quartz crystals. He was unable to give a specific model in the case of synthetic quartz, but suggested the following possibilities:

(a) The hydrogen may be present in the form of H_2O molecules in occlusions in the lattice, which may explain the presence of a characteristic broad absorption band.

(b) The hydrogen may be present in locally disturbed parts of the lattice (formed by uncontrolled crystal growth). Broken Si - O - Si bonds occur, which capture (OH) groups with the possibility of hydrogen bonding. Thus at high temperatures the bonds may close and (OH) be driven off.

(c) The hydrogen may be present as H_2O molecules located interstitially in the c-axis tunnels.

The hydrogen ions were found to diffuse slowly, and there was no correlation between the number of hydrogen ions and alkali ions.

In natural quartz the absorption bands were found to be sensitive to heat treatments. Prior to a heat treatment the alkali ions were found to exert an influence, whereas after annealing (T > 900K), the bands were insensitive to the alkali ions. It is evident that at elevated temperatures the alkali ions must diffuse to unspecified sites which are not associated with hydrogen defects.

CHAPTER 3

THE PLASTICITY OF QUARTZ

3.1 Introduction

In common with many ceramic materials quartz may not possess the requisite number of slip systems to satisfy the Von Mises (1928) criterion. This is a consequence of the large values of Burgers vector found in such materials and the associated high energy of such dislocations. Von Mises deduced that for a polycrystal to undergo a general homogeneous change of shape without discontinuous phenomena such as cracking, five independent 'shear modes' must be available to the individual grains. In terms of present day dislocation theory, a slip system is equivalent to a shear mode. Quartz may deform by slip on prismatic, rhombohedral and pyramidal planes in the direction $\underline{a}$, $\underline{c}$ and $\langle \underline{a} + \underline{c} \rangle$ in addition to (0001) $\langle 11\bar{2}0 \rangle$, the most common slip system. The $\underline{a}$ and $\underline{c}$ systems together do not possess the requisite number of independent members to produce a homogeneous change of shape, and such a deformation is only possible with, in addition, the operation of $\langle \underline{a} + \underline{c} \rangle$.

The Burgers vector of an $\langle \underline{a} + \underline{c} \rangle$ dislocation is 7.3 $\mathring{A}$, which is extremely high and energetically unfavourable and it is not likely to operate except at high temperatures (> 1000 K) and under conditions of high applied stress. This has been confirmed experimentally (Baëta and Ashbee, 1969a), and suggests that in the earth's crust quartzite can only deform with associated fracturing.

However, a relaxation of the Von Mises criterion is allowed if a dislocation climb component is added to slip on the restricted systems (Groves and Kelly, 1969). Climb is a process which is important in the solid-state deformation of materials at elevated temperatures ($T > 0.5\ T_M$), and low strain rates. It is thus possible that climb mechanisms may play a vital role in the deformation of quartzite in the

earth's crust. Evidence for this comes from electron microscope studies of naturally deformed quartzites (Fig.1.2), and it is observed that rather than the dislocation structure being knotted and tangled (typical of a cold-worked structure) the appearance is that in which dislocation climb has continuously operated. The dislocation segments are smooth and numerous loops are visible. It is evident that the Von Mises restriction may thus be overcome under geological creep conditions.

A further feature of crustal deformation is the large quantities of water that exist in equilibrium within the rock. This water may either be pore-water, located in fissures, or held in solution within the crystal lattice. We shall show that water can lead to a drastic reduction in the strength of quartz, by the mechanism of hydrolytic weakening (Griggs 1967). Indeed no description of the deformation of quartz, either in the laboratory or in the field, is complete without some consideration of the effect of water on deformation history.

3.2 Hydrolytic Weakening

The laboratory strength of quartz tested in compression at temperatures $\lesssim$ 1200 K is in excess of 20 Kbar (McClaren et al., 1967). This is true only of pure dry natural quartz. To prevent premature fracture it is usual to apply a confining pressure around the specimen. In this way plasticity can be induced in favourable cases at elevated temperatures and slow strain rates. The confining medium often used is mineral talc, which becomes unstable under these experimental conditions and de-hydrates. The first indication that water could in fact weaken quartz was discovered in this way. It was found that there was a dramatic reduction in strength when 'water' diffused into the lattice. It was subsequently found that synthetic quartz was considerably weaker than natural quartz.

Since quartz is grown artificially under hydrothermal conditions there is a high probability that 'water' can be incorporated in the lattice, especially when there are fluctuations in growth conditions. Since the discovery of water weakening most studies have concentrated on synthetic quartz, firstly to unravel the mechanism of hydrolytic weakening and secondly the ease with which plasticity can be induced enables the slip systems in quartz to be more readily ascertained. We must note, however, that because of the different impurity concentrations, synthetic quartz and natural quartz may behave as two entirely different materials mechanically. Accordingly, care must be taken in assessing likely geological deformation on the basis of studies on synthetic quartz.

A 'wet' weak sample of quartz may be strengthened by prolonged annealing (> 100 hours) at elevated temperatures ($\approx$ 1100K) (Kekulawala et al., 1978). It is postulated that water held in solution precipitates out, denuding the lattice of its potential weakening agent. This water precipitation is accompanied by an optical milkiness, often systematically arranged about either side of the seed plate in the form of 'growth-bands'.

The water weakening mechanism was originally investigated by David Griggs who, in collaboration with F.C. Frank F.R.S., suggested that the most likely cause was bond hydrolysis at dislocation lines. Thus, we have in the presence of lattice water the reaction

$$Si - O - Si + H_2O \rightarrow Si - OH : HO - Si \quad .$$

The strong covalent Si - O - Si bonds have been replaced by weaker hydrogen bonding, and slip of the dislocation is now correspondingly easier due to the reduction in lattice friction.

However, further investigations by McClaren & Retchford (1969) revealed that such a mechanism was untenable. It had initially been supposed that the linear portion of the stress-strain curve of natural quartz was elastic and hence recoverable

on unloading. However, this is not the case and at the end of the linear slope a high density ($\approx 10^{14}$ m^{-2}) of tangled dislocations was observed. There is no clear delineation between the elastic and post-yield portions of the stress-strain curve, suggesting that more than one slip system is operative, and that subsequent tangling of dislocations produces extreme work hardening. It was clear that dislocation generation and multiplication was equally possible in dry samples and that the measured 'strength' was much lower than had initially been assumed.

Griggs (1967) had determined the hydrolytic weakening temperature T_c (that is, the temperature at which a sample suddenly becomes weak under compression) by a stress relaxation technique. By loading the crystal to $\approx$ 45 Kbar at 473K, subsequently raising the temperature by 50^{o} increments, and following the resulting relaxation of stress ($\Delta\sigma/\sigma$), he determined as T_c the temperature at which the slope of $\Delta\sigma/\sigma$ vs temperature showed an inflexion. The critical weakening temperature was found to decrease with increasing water content (measured by infra-red absorption spectroscopy at $\approx$ 3500 cm^{-1}) is given by the expression (Paterson & Kekulawala, 1979):

$$T_c = \alpha/(\beta + \log H/Si),$$

where T_c is measured in degrees Kelvin. The constants α and β depend on the imposed strain rate, and average values for these are α = 3600, β = 7.7. Griggs (1967) measured an activation energy of 0.42 eV for hydrolytic weakening.

Thus a 'dry' crystal (60 ppm H/Si) has a weakening temperature of $\approx$ 1000 K while a 'wet' crystal (5000 ppm H/Si) has $T_c \approx$ 700 K. Dry natural quartz crystals weaken at T $\approx$ 1300 K, and by using the above relationship for T_c, we may show that the water content is $\approx$ 10 ppm H/Si.

TEM investigations by McClaren and Retchford (1969) on synthetic quartz specimens compressed above and below T_c ($\approx$ 673K in this experiment), and on specimens that had been annealed prior to deformation demonstrated that the climb of dislocations

was responsible for the observed behaviour of the water rich samples. Deformation below T_c produced a high density of tangled dislocations, whereas above T_c the density was lower and the dislocation structures were those typical of climb. Their conclusion was that T_c was the temperature at which the rate of recovery exceeds the rate of work-hardening. It was found that on annealing deformed crystals at 698 K and atmospheric pressure the density of dislocation reduced and precipitates ('bubbles') formed. These bubbles were thought to be formed by the reaction:

$$Si - OH : HO - Si \overset{T \gtrless T_c}{\rightleftharpoons} Si - O - Si + H_2O,$$

with the H_2O precipitating out. After an anneal of 1023 K, only occasional bubbles and dislocations were seen. Little change was observed for $T = 573\,K$ ($T < T_c$).

The strengthening of initially weak synthetic quartz has been quantified by Paterson, Kekulawala and Boland (1978). Their crystal had a water content of 400 ppm H/Si ($T_c = 873\,K$) and the strength was defined as the stress at 1.5% strain. The heat treatment was carried out at 1173 K and atmospheric pressure. Full strengthening was not achieved until 100 hours, where it had increased by approximately six times its unannealed strength. However, it is surprising that these authors noted that all the infra-red changes (used to monitor the water content) were complete after the relatively short interval of five hours.

It is worthwhile to recapitulate on the various hydrogen defects and the corresponding infra-red spectrum in quartz. The three main types of infra-red absorption bands are:

1. A group of sharp bands attributable to OH^- in well defined structural sites, commonly associated with impurity ions such as Al^{3+} or alkalis.

2. A broad absorption band which does not sharpen into ice bands at low temperatures. This is a gel-type hydroxyl defect involving (SiOH) groups.

3. Ice bands (for measurements made at 77 K) due to molecular water.

On heating the broad band (2) is replaced by an ice band (3) as water is precipitated. This broad band is the only one which can be correlated with the high temperature weakness of quartz. Thus it can be interpreted that the effective weakening agent is removed at elevated temperatures by the precipitation of 'water' from the SiOH group defects.

The precipitation phenomenon has been studied optically and by TEM. The original investigation linking both techniques was by McClaren and Phakey (1966), who studied the amethyst, citrine and milky variations of quartz. After annealing at 900 K for 50 hours amethyst and citrine became optically milky or turbid, and TEM revealed large numbers of precipitates (in the form of faceted bubbles) and a high density of dislocations. Neither defects were originally present in the unannealed samples. It was suggested that the dislocations formed to relieve the high stress fields around the bubbles. The optical milkiness of amethyst and citrine quartz was attributed to light scattering by the bubbles.

Optical studies of precipitation in synthetic quartz have been by Bastin and Mitchell (1961) and Bambauer et al. (1969). Bastin and Mitchell were able to quantify the light scattering due to the developing precipitates and found an activation energy of $\approx$ 1.1 eV. Their results also led them to the suggestion that an aluminium impurity was the constituent of the precipitates, since regions of high precipitate density and also radiation darkening (often attributed to Al) occurred together. Also the extent of optical absorption was proportional to the Al content of the crystals. Optical examination revealed that the scattering centres were open clusters on specific planes, and that the spatial extent of these planes increased with annealing temperature.

However, Bambauer et al. argued that the scattering centres were 'gel-defects', i.e. a special type of H-containing defect. Increased infra-red absorption occurred in regions

where subsequent anneal treatments rendered the quartz milky. Autoradiographic studies demonstrated that Na was also relatively more abundant in the milky regions, while Al was less abundant. In the non-milky regions the concentration of H was ≈ 1000 ppm H/Si, rising to 3500 ppm H/Si in the milky bands. The corresponding concentration of Na was ≈ 400 ppm Na/Si rising to ≈ 700 ppm Na/Si.

The 'gel-defect' suggested was in the form of a locally disordered and less dense region of the lattice, consisting of H_2O, and SiOH together with Na^+, NaOH, and Al^{3+}. During heat treatment the reaction

$$2\ (Si - OH) \rightarrow Si - O - Si \quad + H_2O$$

occurred. These gel regions were hence assumed to form "into a more dense 'glassy' structure rich in trace elements and into cavities in which H_2O is enriched".

It is clear that a detailed understanding of precipitation is far from complete, and it is necessary to form some link between this phenomenon and the mechanism of hydrolytic weakening. The above discussion would suggest that the diffusion of 'water' from structural sites to dislocation lines can only take place over a certain range of temperature leading to precipitation. The application of a hydrostatic pressure does not prevent precipitation (Jones 1978), and often bubbles are visible in micrographs taken of deformed samples.

Kirby and McCormick (1979), demonstrated that in samples orientated for $(2\bar{1}\bar{1}0)$ <0001> slip the activation energy for creep was independent of water content, while dislocation velocity was dependent. They suggested that the tertiary stage of creep (i.e. hardening) was caused either by the reduction in available water for weakening or by precipitation hardening, although there were indications that the former mechanism predominated. Knowledge of the kinetics of precipitation is desirable.

We emphasise that no detailed transmission electron microscope studies have been made of the precipitation process

in quartz, although on the basis of indirect optical and infra-red studies the case for water precipitation at elevated temperatures is well established. Furthermore, the experimental evidence indicates that the precipitation is sufficient to reduce the availability of the weakening agent in quartz, resulting in a strengthening of 'weak' crystals.

3.3 Deformation of Single Crystal Quartz

3.3.1 Theoretical Considerations of Slip Systems in Quartz

On the basis of energy arguments (i.e. dislocation energy proportional to the square of the Burgers vector) the expected Burgers vectors are the shortest lattice vectors. In quartz these vectors are:

$\underline{a}$	(4.913 Å)
$\underline{c}$	(5.405 Å)
$\langle \underline{a} + \underline{c} \rangle$	(7.304 Å)

These values of $\underline{b}$ are however large and dissociations are expected.

The Frank energy criterion and the Peierls stress criterion predicts that the slip direction corresponds to the shortest perfect dislocation Burgers vector, while the glide plane should be the plane with the lowest Peierls stress (largest d-spacing). However, as discussed by Baëta and Ashbee (1969,b) in a complex structure such as quartz other structural factors must be considered. These include

(1) Slip directions

During slip the direction must be such as to avoid strong electrostatic repulsive forces. Also, the minimum disturbance to the tetrahedral SiO_4 units results in the breaking of the least number of bonds.

(2) Slip planes

Because directional bonding is important in quartz the plane with the lowest Peierl's stress may not necessarily have the largest d-spacing. On the basis of this argument it is suggested that the easiest slip plane is that which has the lowest Si-O bond density. The bond density for various crystal planes are shown in Table 3.1. From this the rhombohedral $\{10\bar{1}1\}$ planes are expected to be the easiest slip planes. Slip across (0001) is the most difficult. Prismatic slip $\{10\bar{1}0\}$ is also favoured over (0001) slip.

3.3.2 Experimental Determination of Slip Systems in Quartz

Laboratory compression tests made on orientated single crystal quartz have revealed that this material can deform by dislocation slip on a number of slip systems. The active systems for a particular stress orientation depend on such factors as the imposed strain rate, temperature and concentration of lattice water.

A major complicating factor in plasticity studies of quartz is the inhomogeneous distribution of water in synthetic crystals. It now appears that the dominant slip system depends critically on the water content of the crystal. A worthwhile goal is the homogenisation of the lattice water throughout the crystal, since it is often reported that during compression most of the strain is accommodated in the water-rich bands. However, the tendency for water to precipitate at elevated temperatures (> 1100 K) probably makes this impossible. The problems associated with homogenisation have been summarised by Paterson and Kekulawala (1979).

Extensive investigations of the operative slip systems under compression have been made by a number of authors. Originally the focus of interest was the form of the stress-strain curve and details of the yield point. Only optical observations were made to determine slip directions. Later a

significant advance was made when routine ion-beam thinning facilities became available for the preparation of electron transparent specimens. This enabled the dislocation structures to be examined in detail and analytical diffraction contrast experiments were used to determine the dislocation Burgers vectors. However, in common with other silicate materials, quartz suffers from extensive electron beam irradiation damage, reducing considerably the time available for viewing a particular area. This fact has hampered electron microscope studies of quartz, and will be discussed in a later section.

The identification of slip systems in quartz has been derived from several approaches (Morrison-Smith et al., 1976):

(a) Structural energy arguments that the most probable Burgers vector is the shortest crystal lattice vector.

(b) Optical observations of lattice rotations or of the orientation of deformation lamellae.

(c) Optical observation of slip line outcrops on specimen surfaces.

(d) Electron microscope analysis using the $\underline{g} \cdot \underline{b} = 0$, $\underline{g} \cdot \underline{b} \times \underline{u} = 0$ criteria.

Baëta and Ashbee (1969a, 1970) deformed single crystals of synthetic quartz (water content 163 ppm H/Si) in various orientations at different temperatures to determine the operative slip systems. These experiments were made with no confining pressure and were the first to demonstrate that quartz can deform plastically at atmospheric pressure. Slip occurred in the crystallographic directions $\underline{a}$, $\underline{c}$ and $\langle \underline{a} + \underline{c} \rangle$ and on many low index planes co-zonal with these directions. The determination of slip systems was made by optical examination of slip traces after deformation. Table 3.2 lists the slip systems that were found in these experiments. Slip was found to be equally easy in the $\underline{a}$ and $\underline{c}$ directions, but in the $\langle \underline{a} + \underline{c} \rangle$ direction approximately three times harder than

TABLE 3.1

BOND DENSITIES AND INTERPLANAR SPACINGS FOR THE DIFFERENT SLIP SYSTEMS OF QUARTZ (BAËTA AND ASHBEE, 1969b)

Slip Plane	Bond Density (Si-O Bonds Å^{-2})	Interplanar Spacing (Å)
$\{10\bar{1}1\}$	0.057	3.34
$\{11\bar{2}2\}$	0.063	1.82
$\{10\bar{1}0\}$	0.073	4.25
$\{11\bar{2}1\}$	0.077	2.24
$\{10\bar{1}2\}$	0.078	2.28
$\{11\bar{2}0\}$	0.084	2.46
$\{10\bar{1}3\}$	0.085	1.66
(0001)	0.092	5.40

TABLE 3.2

SLIP DIRECTIONS AND SLIP PLANES IN SYNTHETIC QUARTZ (BAËTA & ASHBEE, 1969,a).

Slip Direction	b (Å)	Slip Plane
$\langle 11\bar{2}0\rangle$	5.02	(0001) $\{1\bar{1}00\}$ $\{1\bar{1}01\}$ $\{1\bar{1}02\}$ $\{1\bar{1}03\}$
[0001]	5.48	$\{1\bar{1}00\}$ $\{11\bar{2}0\}$
$\langle 11\bar{2}3\rangle$	7.44	$\{1\bar{1}01\}$ $\{11\bar{2}1\}$ $T \gtrsim 1000K$ $\{11\bar{2}2\}$

for $\underline{a}$ or $\underline{c}$ slip and then only for temperatures > 1023 K. This was attributed to the large value of the $<\underline{a} + \underline{c}>$ Burgers vector.

Details of the stress-strain curve showed that there was a characteristic yield point, a region of easy glide and a subsequent strain hardening portion. This latter effect was due to the exhaustion of dislocation sources in the regions of rapid dislocation multiplication. After the initial strain hardening, further dislocation sources become operative in regions of the test samples where little previous deformation had occurred. A higher rate of strain hardening was observed for crystals compressed parallel to $[\bar{1}011]$, where the operation of multiple slip systems caused dislocation interaction and locking.

Differences in the stress-strain behaviour over different temperature intervals was attributed to variations in deformation characteristics in either the α- or β- quartz stability field. Also, the extensive stress field about dislocations can obviously affect the α-β transition point in the vicinity of dislocations. Baëta and Ashbee found a large scatter in their yield point data below 923 K which they considered to be caused by the anomalous mechanical behaviour of quartz near the α-β transition point. At temperatures > 923 K deformation was entirely in the β-quartz field and less scatter resulted.

Baëta and Ashbee concluded that the specimens were unstable with respect to the β-quartz structure above ≈ 1100 K. The assumed mechanism was the phase transformation of β-quartz to tridymite, at dislocation lines. The precipitation of this new phase could lead to a form of precipitation hardening. Direct experimental evidence showed cristobalite had formed instead of tridymite, while coesite was also present in some cases. Since coesite only forms under a high stress (15-40 Kbar) (T ≈ 600-2000 K) it was assumed that high stress concentrations were present due to dislocation pile-ups. For example, the mean hydrostatic pressure associated with a pure edge dislocation ($\underline{b} = \underline{a}$) is ≈ 7 Kbar at a distance 10 $|\underline{a}|$ above the

dislocation. This stress increases as the number of dislocations increases, conditions that are typical of a pile-up.

Turning to the role of water, Baëta and Ashbee considered that the nucleation of glide dislocations was easier in 'wet' samples than in 'dry' samples, while the subsequent glide of dislocations through the lattice was equally difficult in all samples regardless of the water content. The measured water content of these crystals (163 ppm H/Si) leads to a value of $T_c \approx 923$ K. This corresponds to the temperature at which the rate of drop in yield stress (of crystals compressed parallel to $[\bar{1}\bar{1}22]$) as a function of temperature reduced considerably. Thus an alternative explanation of the large scatter in results for $T < T_c$ is the inhomogeneous nature of slip in quartz. At $T > T_c$ deformation is controlled by the climb motion of dislocations, a process by which slip plane obstacles can be overcome, hence facilitating continual slip.

In another major study Morrison-Smith, Paterson and Hobbs (1976) deformed synthetic quartz crystals along $[\bar{1}101]$ at a strain rate of 10^{-5} s^{-1}, and undertook detailed investigations of the dislocation structures using TEM. Below 823 K the structures observed were typical of a low temperature behaviour (tangles of dislocation and straight sided loops) while above this temperature climb processes were active.

In the initial stages of deformation loops were observed to nucleate and expand. These loops formed at low temperatures grew by glide and thus permitted identification of the slip system, since the loop plane defines the slip plane. The most common loops lay on the $(10\bar{1}0)$, $(01\bar{1}1)$ and $(10\bar{1}\bar{1})$ planes. Other loops lay on the (0001), $(01\bar{1}0)$, $(10\bar{1}0)$, $(21\bar{1}0)$ and $(\bar{1}2\bar{1}0)$ planes. (0001) loops were more common at the higher test temperatures. The $(1\bar{1}00)$ loops had $\underline{b} = [0001]$, while loops on $(01\bar{1}1)$ had $\underline{b} = [2\bar{1}\bar{1}0]$ or $[\bar{1}210]$.

Difficulties were encountered with the identification of slip planes at higher temperatures because the loops were less well-defined.

There were indications that Burgers vectors of the type $\langle \underline{a} + \underline{c} \rangle$ $\langle 11\bar{2}3 \rangle$ existed for T > 850 K. However, only indirect inference of $\langle \underline{a} + \underline{c} \rangle$ was presented by Morrison-Smith et al., in a specimen deformed at ≈ 1100 K. From the findings of Baëta and Ashbee (1969a) the existence of $\langle \underline{a} + \underline{c} \rangle$ is not unexpected for deformation at T > 1000 K.

The inhomogeneous distribution of water led to differences in deformation in 'wet' and 'dry' zones. For example, in specimens deformed between 900-1000 K recovery processes (e.g. climb) were proceeding at a significantly faster rate in the water-rich zones (which were determined prior to deformation by infra-red spectroscopy), while in the dry zones the dislocation structures were more typical of low temperature deformation (straight sided loops). However, the water content did not appear to affect the various slip systems differently.

These results are consistent with the fact that the most significant feature of lattice water is to assist the climb motions of dislocations rather than their slip motions.

Spherical 'bubbles' were observed in samples deformed at temperatures in excess of 1100 K and the precipitation of water was proposed. The bubbles were not faceted indicating that they had not reached an equilibrium configuration.

The average water content of the crystals used in these experiments was 800 ppm H/Si indicating a value of T_c = 783 K. Since the water is distributed inhomogeneously then it may be expected that the local water content in 'wet' bands is much higher. It is thus surprising that the transition temperature from low temperature to high temperature dislocation structures was ≈ 900 K for these water-rich bands. Since the imposed strain rate was low (≈ 10^{-5} s^{-1}) this apparent discrepancy cannot be explained by a strain rate effect on T_c.

3.4 Polycrystal Deformation

3.4.1 The Von Mises Problem

Von Mises (1928) demonstrated theoretically that five independent shear modes (slip systems) are required for a polycrystal to undergo a general plastic deformation by slip. When a polycrystal deforms a grain within it is constrained to deform generally. If five independent slip systems are not available then pore formation, grain boundary sliding, twinning or fracture of the crystal will occur.

The method to determine if slip systems are independent involves a consideration of strain tensors. We shall not describe this in detail but merely state the result. Infinitesimal plastic deformation involves slip on k slip systems, with strain $E_{ij}^{(k)}$. Summation over the k systems (referred to a common set of axes) gives the total strain with the six strain components $E_{ij}^{(T)}$:

$$E_{ij}^{(T)} = \Sigma E_{ij}^{(k)} .$$

Only five of the strain components $E_{ij}^{(T)}$ are independent, since pure glide processes do not change the volume of the deforming elements. Mathematically this is equivalent to:

$$E_{11}^{(T)} + E_{22}^{(T)} + E_{33}^{(T)} = 0.$$

Thus there are only five independent total strain components to be determined, and five independent slip systems producing strains. Only five independent slip systems are required for a general slip and no more than five independent slip systems can exist in a given crystal. By the term 'independent slip system' we mean that the shear cannot be achieved by any combination of the other available slip systems.

It is found by calculation and experiment that there are a large number of slip systems available to both FCC and

BCC metals. Thus the general observation that these materials are ductile is in accord with this. In HCP metals, on the other hand, a ductile response is limited. Basal glide in HCP metals is insufficient to allow a general deformation; the slip system $\langle 11\bar{2}0\rangle$ (0001) yields three distinct systems, only two of which are independent. The same is true of prismatic $\langle 11\bar{2}0\rangle$ $(10\bar{1}0)$ slip. A combination of slip in the $\langle 11\bar{2}0\rangle$ direction on the (0001) and $\{10\bar{1}0\}$ planes gives four independent slip systems. Only with the operation of pyramidal slip $\langle 11\bar{2}3\rangle$ $\{11\bar{2}3\}$ can a general deformation be produced. In this case there are six systems of which five are independent. Thus, this system alone, or in combination with the basal and prismatic systems enables a polycrystal to deform uniformly. However, because of the large values of Burgers vector associated with $\underline{a} + \underline{c}$ systems the Peierl's stress is high and their operation is only probable at elevated temperatures, and at high values of resolved shear stress.

The necessity of five independent slip systems is relaxed when we have crystals with free surfaces. The extreme example of this is a single crystal, deformed in tension or compression, in which case a single slip system is sufficient to produce the strain.

Groves and Kelly (1969) discussed the change of shape of a crystal deforming by the operation of dislocation climb mechanisms. The addition of a climb component relaxes the Von Mises criterion, such that fewer than five independent slip systems suffice for a general deformation.

For the case of change of shape by <u>climb alone</u>, six independent climb systems are necessary. (The condition of zero volume change is <u>not</u> automatically satisfied for climb as it is for slip). This implies that such a crystal must possess six different Burgers vectors. The number of crystals for which such a condition is satisfied is few, but cubic crystals and the hexagonal crystal Al_2O_3 do have this required number of Burgers vectors.

To achieve plastic flow in polycrystalline quartz a combination of glide plus climb is essential. Thus the addition of climb to the system $\langle 11\bar{2}0\rangle$ (0001) and either $\{10\bar{1}0\}$ or $\{11\bar{2}0\}$ in the [0001] direction is sufficient for homogeneous deformation.

It is clear that if we attempt to deform a single crystal, stressed such that the resolved shear stress is zero on the active slip planes, than any change of shape must be accomplished by climb alone.

3.4.2 Creep Deformation

Under conditions of low applied stress and low temperatures most ceramic materials display a time-dependent deformation known as creep. Strain rates under creep conditions are low, and it is probable that rock in the earth's mantle deforms by creep mechanisms.

At values of applied stress that are insufficient to cause dislocations to slip, or under conditions where a deforming grain of a polycrystal lacks the necessary number of independent slip systems the mechanism of dislocation climb enables a change of shape to occur. In order that a dislocation can climb, ions or atoms must be transported from, or to, the end of the dislocation half plane. It is usual to consider the motion of lattice vacancies; the direction of the vacancy flux is opposite to the mass transport flux.

Creep by dislocation climb is just one of a number of creep processes in materials, and is important in single crystal deformation. In fine-grained polycrystals alternative mechanisms are possible. In this case the grain boundaries act as efficient sources and sinks of vacancies, and a change of shape is effected by diffusion transport either along the grain boundary interface or across the grains.

3.4.3 Diffusion Controlled Climb

Consider an edge dislocation in a body which is subjected to an applied (non-hydrostatic) stress σ_{xx} (Fig.3.1). In the stress-free state ($\sigma_{xx} = 0$) an equilibrium concentration (C_o) of vacancy defects exists in the solid. We may define the chemical potential (G) of the vacancies by (Hirth & Lothe, 1968)

$$G = kT \ln(C/C_o) \quad .$$

C is a vacancy concentration that is <u>different</u> from C_o. For example, the local equilibrium vacancy concentration close to the dislocation is

$$C_{DISLOC} = C_o \exp(\sigma_{xx} V_a/kT)$$

where V_a is the activation energy for formation of the vacancy. The elastic force per unit length of dislocation acting on a dislocation of length ℓ is

$$\frac{F_y}{\ell} = \sigma_{xx}|\underline{b}| \quad .$$

In the presence of a stress σ_{xx} at the dislocation, and a vacancy concentration that is different from C_o, the total force on the dislocation is

$$\frac{F_y}{\ell} = \sigma_{xx}|\underline{b}| + \left[\frac{kT|\underline{b}|}{V_a} \ln\left(\frac{C}{C_o}\right)\right] \quad .$$

The term $(kT|\underline{b}|/v_a) \ln(C/C_o)$ is an osmotic force acting on the dislocation, and is due to point defect emission or annihilation on the dislocation line.

If the chemical potential of the vacancies is different from that at a position far from the dislocation, then there will be a diffusive flow of vacancies down the gradient of chemical potential, and the dislocation will climb in order to maintain the local equilibrium concentration.

Under the action of a pure hydrostatic pressure the chemical potential at the surface of the body is equal to that in the interior. Under these conditions the dislocation will not climb. However, if the stress is non-hydrostatic the chemical potential at the surface and near the dislocation is different. At surface A (Fig.3.1), where the applied stress is directed, the chemical potential is the same as that at dislocation ($G = \sigma_{xx} v_a$), while at surface B the value of G is zero. There will be a net flow of vacancies from surface B to the dislocation in addition to vacancy flow from B to A. The dislocation will thus climb in this stress condition.

Since vacancy concentration gradients can exist between free surfaces of a body under the action of an applied differential stress, then it may be expected that grain boundaries can also act in the same manner, within a polycrystal. The grain boundary can supply, annihilate and transport vacancies in a manner that depends on the stress system, chemical potential gradient, and microstructure.

Three types of grain boundary creep can be discerned:

(1) The diffusing flux of vacancies passes through the crystal grain from one surface to another.

(2) The vacancies diffuse within the grain boundary region around the grain.

Mechanism (1) is termed Nabarro-Herring creep while (2) is termed Coble creep. The mechanism of Nabarro-Herring creep is outlined in Fig.3.2. A polycrystalline solid has a differential stress (σ) applied to it, the stress state altering the chemical potential. Vacancy diffusion currents (indicated by the arrows in Fig.3.2) are generated. Thus over a period of time the grain will change shape. The Nabarro-Herring analysis predicts a strain rate $\dot{\varepsilon}_{NH}$ depending on the first power of the stress as

$$\dot{\varepsilon}_{NH} = B\sigma\Omega D/d^2 kT.$$

$B \approx 2$, and is dependent on the exact grain geometry, Ω the atomic volume, D the diffusion coefficient of the slowest moving atomic species and d the grain diameter.

A change of shape by diffusion through the grain boundary region is analogous to Nabarro-Herring creep. It is a type of short-circuit diffusion and has a lower activation energy than bulk diffusion. Consequently, it is more important at lower temperatures. The strain rate is given by

$$\dot{\varepsilon}_{COBLE} = B'\sigma\Omega\omega D_g/d^3kT$$

$B' \approx 150/\pi$, ω is the effective grain boundary width, D_g the grain boundary diffusion coefficient and d the grain edge length. Nabarro-Herring and Coble creep contribute independently to the overall strain-rate and are additive.

It should be noted that accurate predictions of creep rate rely heavily upon a knowledge of the diffusion coefficient of the ionic species in the solid. Experimentally, D can be measured using radioactive tracer techniques yielding the tracer diffusion coefficient. Most materials of technological importance, and rock forming minerals, contain more than one atomic species and the choice of which diffusion coefficient to utilise in the creep equations is difficult. In general the slowest diffusing species is the rate determining ion for the following reason. A charged ion which diffuses faster than its counter-ion will electrically charge any grain boundary to which it diffuses. Charge neutrality breaks down and an electric field is established, which opposes any further segregation of the faster moving ion. A steady flux is quickly restored, and it can be easily seen that the slowest moving ion controls the overall mass flux and hence diffusional climb or creep rate.

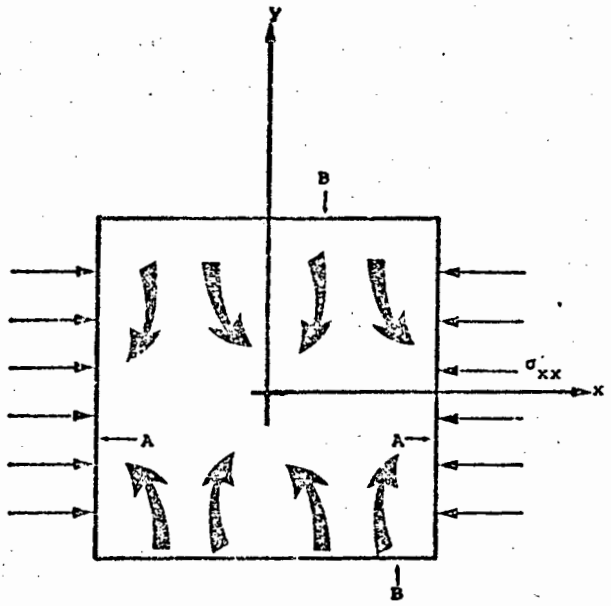

Fig.3.1 Edge dislocation in a solid subject to an applied compressive stress σ_{xx}. Vacancy diffusion currents are indicated.

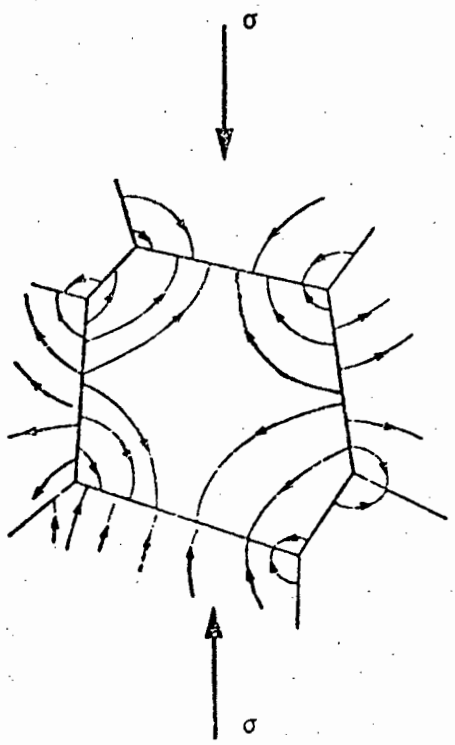

Fig.3.2 The mechanism of Nabarro-Herring creep in a polycrystal. The vacancy diffusion currents due to an applied stress σ are shown.

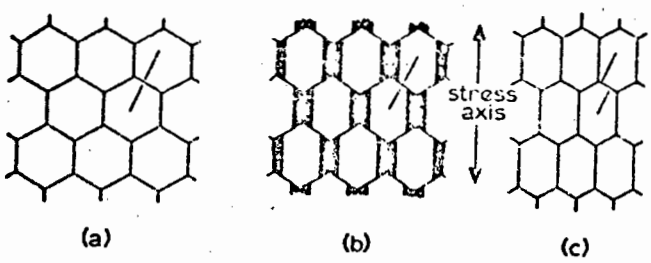

Fig.3.3 Schematic diagram of grain boundary sliding during the creep deformation of a polycrystal (a) unstressed state (b) during deformation voids will open up (c) to prevent void formation sliding (indicated by the marker offset) will occur. (After Burton, 1977).

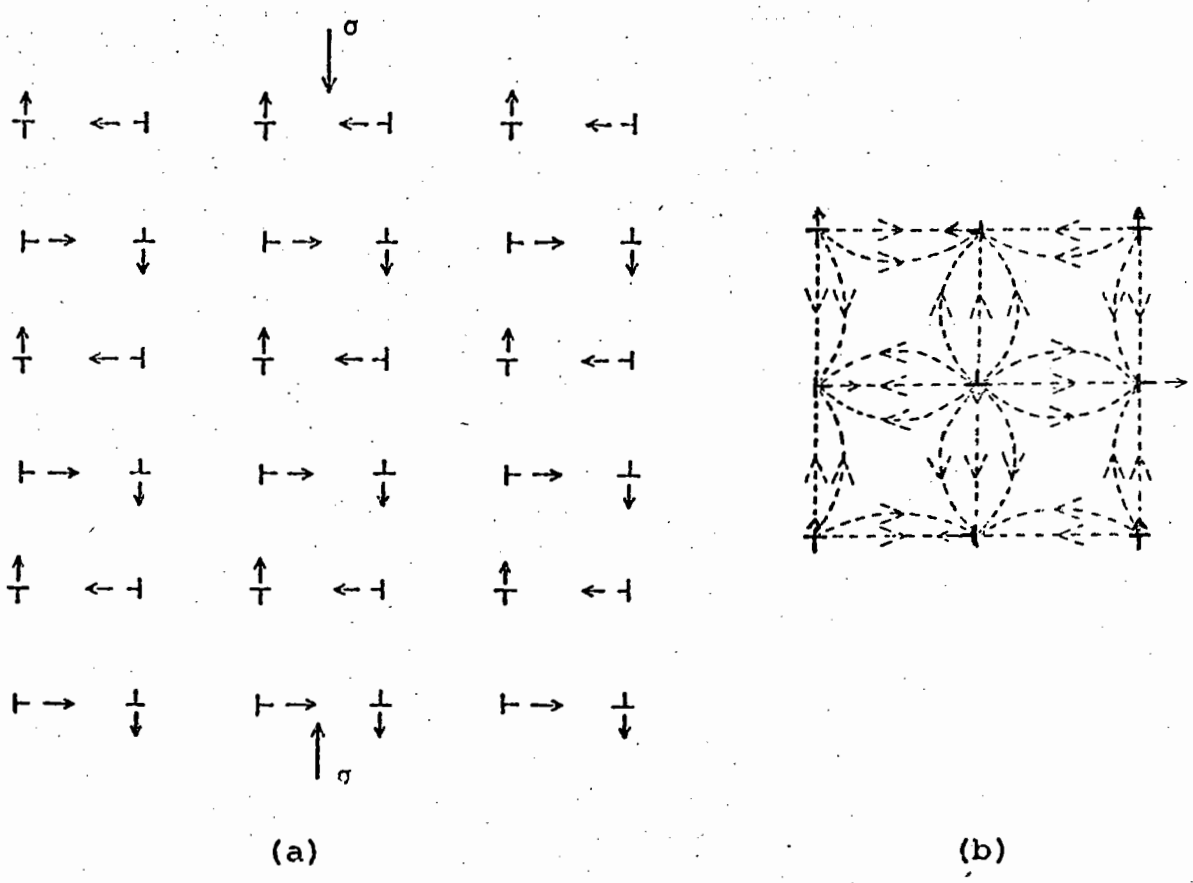

Fig.3.4 The Nabarro creep model (a) an array of dislocations indicating the direction of climb (b) diffusion currents (vacancy flow).

Tracer diffusion studies performed as a function of temperature enable an activation energy to be determined. The identification of the rate determining ion under creep conditions in multi-component systems can be made by comparing the tracer activation energy with the activation energy for creep. In many oxides O^{2-} is often found to be the slowest moving species and is hence rate determining.

A further complication with polycrystal deformation is the mechanism of grain boundary sliding. Fig.3.3 is a schematic representation of such sliding during diffusional creep. We consider an array of hexagonal grains (Fig.3.3a), subject to a differential stress. The grains change shape, but if they do not slide relative to one another, cavities must open up (Fig.3.3b). Thus to maintain material coherency sliding must occur, and this is indicated by the displacement of the marker on the figure (Fig.3.3c). Sliding and diffusion do not contribute independently to the strain. For a more complete discussion of this see Burton (1977).

Since dislocations can act as sources and sinks of vacancies diffusional creep can arise if a vacancy diffusion between dislocation allows the applied stress to do work. Nabarro (1967) developed such a model for dislocation creep (Fig.3.4). The crystal has an established stable dislocation network. The dislocations are heavily jogged and cannot multiply by glide so that the deformation is controlled entirely by climb. Nabarro assumed that the dislocations operated as Bardeen-Herring climb sources (see Hirth and Lothe 1968)such that the total length of dislocation remains at a constant equilibrium value. The chemical potential produced by the applied stress provides the driving force for vacancy migration and the flux of vacancies causes the dislocations to climb in the manner shown in Fig.3.4. The strain-rate supported by this climb mechanism is:

$$\dot{\varepsilon}_N = \frac{Db\sigma^3}{\pi kTG^2} \Big/ \ell n\left(\frac{4G}{\pi\sigma}\right) \quad ,$$

where G is the shear modulus. The strain rate is proportional to the third power of the applied stress, and is known as power-law creep.

At lower temperatures short-circuit diffusion along the dislocation cores will predominate over homogeneous diffusion through the crystal. In this case the strain rate is:

$$\dot{\varepsilon} = 4D_c b\, \sigma^5/\pi^4 kTG^4 \quad .$$

D_c is the core diffusion coefficient.

Nabarro's (1967) model has recently been criticized by Evans and Knowles (1977, 1978). They put forward the argument that Nabarro's treatment was unrealistic because he assumed his dislocations to be sessile in slip. Thus the only contribution to strain was from pure climb processes. In metals this was held to be an unrealistic restriction since glide is relatively easy. Non-metallic materials generally have a high Peierl's lattice stress and the Nabarro climb model is probably more accurate.

The typical values of strain rate deduced by the Evans & Knowles theory are typically 2-3 orders of magnitude higher than that predicted by the Nabarro creep equation, and they provide experimental evidence from the literature that supports their equation. Thus the role of climb is simply to release dislocations from their pinning points and glide provides the only significant contribution to the overall strain. In essence their theory closely follows that of Weertman (1957), except that they model a three-dimensional network of dislocations rather than the dislocation pile-ups assumed by Weertman.

Unfortunately Evans & Knowles make no reference in the development of their theory to the Von Mises restriction on polycrystal change of shape. Groves and Kelly (1969) considered that the creep theory of Weertman (1957) (i.e. climb assisted glide), could not be used for the very reason that climb now makes no direct contribution to the macroscopic strain of the deforming polycrystal, and allows no change of shape which is not

produced by glide. Thus this theory cannot be applied to any material which lacks the necessary five independent slip systems.

Al_2O_3 is a material which lacks five independent slip systems except for very high temperature deformation and Evans and Knowles (1978) utilise (among other materials) the polycrystal Al_2O_3 creep data of Cannon & Sherby (1977) to demonstrate that the form of their creep equation is correct. Dislocation core diffusion was assumed negligible at the test temperature (> 1873K, $\approx 0.85T_M$). Similar creep data was obtained by Warshaw & Norton (1962) on coarse grained Al_2O_3 and by Chang (1960) on single crystal Al_2O_3. Warshaw and Norton utilised Weertman's theory to analyse their data, a step which was criticized by Groves and Kelly for the reasons given above. Groves and Kelly in fact suggested that the Nabarro creep model was more appropriate to the experiments of Norton and Warshaw and also of Chang, and concluded that a dislocation climb mechanism could provide a strain rate of the order of magnitude of that found in single crystal Al_2O_3, unfavourably orientated for slip.

From this discussion it is clear that when a polycrystalline material lacks the requisite number of slip systems, the Nabarro model has good applicability. The climbing dislocations thus contribute directly to the overall strain. The release of pinned dislocations by a climb component cannot allow a change of shape (Groves and Kelly, 1969), unless five independent slip systems are active. We suggest that the Evans & Knowles (1977, 1978) model is not applicable to materials such as Al_2O_3 or quartz because of the restricted slip systems.

CHAPTER 4

THE BRITTLE FRACTURE OF QUARTZ

4.1 Historical Introduction

The nature of fracture in solids classified as brittle is such that their strengths in tension are appreciably lower than their theoretical or ideal strength. This may be rationalized by understanding that flaws or defects in such solids exert a dominating influence upon the maximum stress the material may sustain, and in essence a study of brittle fracture is a study of flaws. The theoretical basis, and experimental methods, of quantifying brittle fracture are well established, although the nature of failure in polycrystalline solids is complex and methods of analysis are under development.

Historically, the founder of modern brittle fracture theory was A.A. Griffith who, in 1920, perceived that sharp cracks can reduce the strength of solids under stress. His theoretical approach was backed by experimental verification that the predictions of his theory were correct. However, Griffith's work went largely unnoticed until the 1940's when there was considerable interest in designing metallic structures which were fail-safe with regard to fracture phenomena. This led to the development of unique testing techniques for materials which could be carried out on a laboratory scale, yet retain applicability at a macroscopic level.

It was found that Griffith's predictions failed for those materials which displayed ductility under stress, yet the basic principles of fracture developed by the Griffith approach did retain applicability. That is, provided due regard is made for plastic processes at the crack tip the fracture stress can be predicted. Such an approach forms the basis for the 'fracture toughness' treatment of failure.

Central to the fracture toughness approach is the fact that regardless of specimen geometry or loading configuration, a certain critical stress level at a crack tip must be achieved for rapid propagation of a crack in a given material. The critical stress parameter defines the fracture toughness, and is a material constant.

The concepts of fracture toughness have been developed to a high level of expertise and are quite general. They can be applied to brittle solids displaying little or no plasticity at fracture, enabling valuable predictions to be made of failure modes in these solids under complex loading conditions, such as indentation.

4.2 The Theoretical Strength of a Solid

The theoretical, or ideal strength of a solid under tension is determined solely by considering the chemical forces acting between a pair of atomic planes. To estimate this strength we wish to know how the stress (σ) between two atoms varies as a function of their separation (x) (Fig.4.1a). At the equilibrium separation (x_o) the interatomic stress is zero, but this rises as the separation between the atoms increases, eventually decreasing and falling to zero at large separations. Let the maximum value of this force be σ_{max}.

Following Kelly, (1971), this curve can be approximated to a sine function (the dotted line in Fig.4.1b) such that

$$\sigma = \sigma_{max} \sin \frac{2\pi}{\lambda} (x - x_o) \quad , \tag{4.1}$$

where λ is the wavelength of the function.

To evaluate σ_{max} we first differentiate σ with respect to x, to obtain

$$\frac{d\sigma}{dx} = \sigma_{max} \frac{2\pi}{\lambda} \cos \frac{2\pi}{\lambda} (x - x_o) \tag{4.2}$$

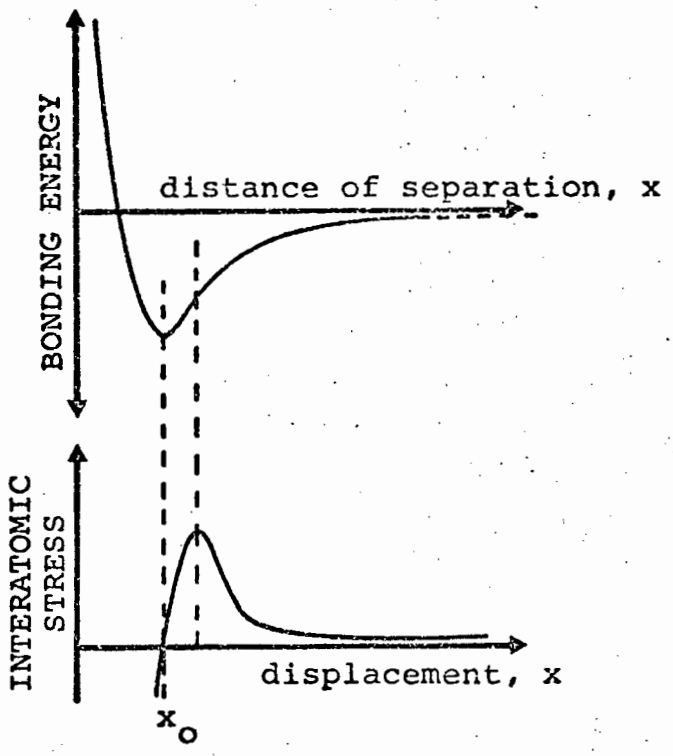

Fig.4.1(a) Bonding energy and interatomic stress as a function of distance of separation.

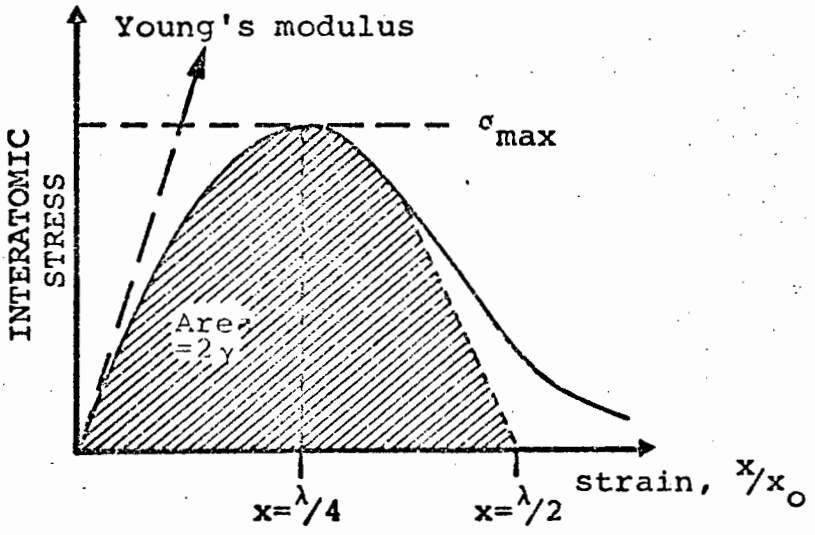

Fig.4.1(b) Atomic stress - strain curve, showing the sine curve approximation.

When $x - x_o$ is small eq.(4.2) gives

$$\frac{d\sigma}{dx} = \sigma_{max}\left(\frac{2\pi}{\lambda}\right) .$$

For a displacement x the strain is dx/x_o, and since the Young's modulus (E) is given by the stress divided by the strain we may write

$$E = \frac{d\sigma}{dx} \cdot x_o = \sigma_{max} \frac{2\pi}{\lambda} x_o$$

or

$$\sigma_{max} = \frac{E\lambda}{2\pi x_o} \qquad (4.3)$$

As we are concerned with fracture, we assume that the energy supplied to force the atoms completely apart is equal to the work of fracture. The work of fracture must not be less than the surface energy γ of the <u>two</u> new surfaces created, and is hence at least equal to 2γ. The energy supplied to cause the complete separation is simply the area under the stress - strain curve in Fig.4.1b and hence

$$\int_{x_o}^{x_o + \lambda/2} \sigma \, dx = 2\gamma$$

Using eq.(4.1) and evaluating the integral

$$\int_{x_o}^{x_o + \lambda/2} \sigma \, dx = \sigma_{max} \int_{x_o}^{x_o + \lambda/2} \sin \frac{2\pi}{\lambda} (x - x_o) \, dx$$

$$= -\sigma_{max} \frac{\lambda}{2\pi} \cos \frac{2\pi}{\lambda} (x - x_o) \Big]_{x_o}^{x_o + \lambda/2}$$

$$= -\sigma_{max} \frac{\lambda}{2\pi} \left[\cos \frac{2\pi}{\lambda} \left(x_o + \frac{\lambda}{2} - x_o\right) - \cos \frac{2\pi}{\lambda}(x - x_o)\right]$$

$$= 2\gamma \left[(x - x_o \to 0)\right]$$

Thus $\lambda = \frac{2\pi\gamma}{\sigma_{max}}$

Substituting this value for λ into eq.(4.3), and equating σ_{max} to σ_f (the fracture stress) we may show

$$\sigma_f = \sqrt{\frac{E\gamma}{x_o}}$$

Letting x_o equal the lattice parameter a, we obtain

$$\sigma_f = \sqrt{\frac{E\gamma}{a}} \qquad (4.4)$$

It is possible to make a very approximate estimate of the surface energy γ.

By letting $\lambda/2 \rightarrow a$, the lattice parameter, eqn. 4.3 becomes

$$\sigma_{max} \approx E/\pi \ .$$

Again, equating σ_{max} to σ_f and substituting in eqn.4.4 we find

$$\sigma_f = \frac{E}{\pi} = \sqrt{\frac{E\gamma}{a}}$$

hence

$$\gamma = \frac{Ea}{\pi^2} \approx \frac{Ea}{10}$$

We can use these estimates for the particular example of α-quartz at room temperature. Since we are considering the breaking of an unconstrained solid we take the reciprocal of the S_{11} elastic compliance component (instead of C_{11}) for E (Kelly 1973, page 8).

Considering cleavage across (0001),

$$a \approx 5\ 10^{-10}\ m,$$

and $S_{11} \approx 1.27\ 10^{-11}\ m^2\ N^{-1}$ (Nye, 1957, page 148)

we find $\gamma \approx 3.8\ Jm^{-2}$, and $\sigma_{max} \approx 2.4\ 10^{10}\ Nm^{-2}$.

4.3 Stress Concentrations About Holes

We have already noted that materials classified as brittle fail from pre-existing flaws in their structure. These flaws act as stress concentrators and hence under the action of an applied macroscopic tensile stress the crack-tip stress can rise to a value equal to the atomic bond fracture stress, estimated in the previous section, even though the applied stress is considerably below this value. The development of theories of fracture draw upon this idea of a crack-tip stress concentration.

Inglis (1913) determined the stress distribution about an elastically deformed elliptical crack, length 2c, width 2b, subject to an applied body stress σ_L (Fig.4.2). The radius ρ of the crack-tip is b^2/c and Inglis calculated that the stress σ_{yy} acting in the plane perpendicular to the crack was

$$\sigma_{yy} = 2\sigma_L (c/\rho)^{\frac{1}{2}} \qquad (c \gg b) \quad .$$

The ratio $\sigma_{yy}/\sigma_L = 2(c/\rho)^{\frac{1}{2}}$ is known as the elastic stress concentration factor.

The variation in stress about the crack is shown in Fig.4.3, for the case c = 3b. The stress concentration is localised within a region approximately c, and high stress gradients within a distance approximately ρ, from the tip.

In terms of a fracture criterion we may set $\sigma_y = \sigma_{max}$ and use the ideal strength approximation (eq.4.4) to show that:

$$\sigma_{max} = \sqrt{E\gamma/a} = 2\sigma_L\sqrt{c/\rho} \quad .$$

Thus at fracture $\sigma_{max} = \sigma_f$ and hence

$$\sigma_f = \sqrt{\frac{E\gamma\rho}{4ac}} \quad . \qquad (4.5)$$

If we make the assumption that the radius of the crack tip is

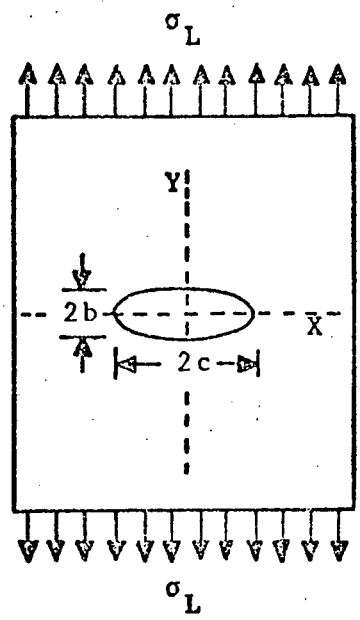

Fig.4.2 Plate containing elliptical hole, semi-axes b,c, subjected to uniform applied tension σ_L.

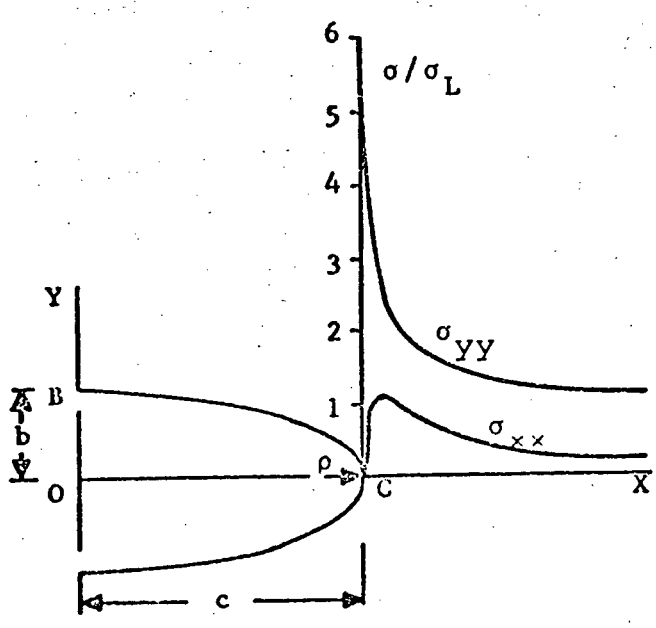

Fig.4.3 Stress concentration at elliptical hole, c=3b.

of atomic dimensions and $\approx$ a we can write eq.(4.5) as

$$\sigma_f = \sqrt{\frac{E\gamma}{4c}} \quad . \tag{4.6}$$

We can now estimate the effect of crack length on the fracture stress. Our value for the theoretical strength α-quartz is $2.4\ 10^{10}\ Nm^{-2}$. Consider a crack length c = 1 μm in such a crystal. Inserting this value of c into eq.(4.6) we can show that

$$\sigma_f \approx 3\ 10^{8}\ Nm^{-2} \quad ,$$

which is approximately 1% of the theoretical strength. This amply demonstrates the dominating influence of microscopic cracks or flaws on the strength of such a solid.

4.4 The Griffith Analysis of Brittle Fracture Phenomena

Griffith (1920) in his fracture analysis, conceived the problem in terms of a thermodynamic energy balance; that is, a crack is unstable if the stored energy released by crack extension is greater than the energy consumed due to the creation of new surface area. The stored energy is that supplied by the loading system, and we should carefully note that we may have a loading geometry which gives either constant load or constant strain conditions.

Consider an infinite body containing a crack, length 2c, subject to an applied tensile stress σ (Fig.4.4). We wish to determine the stored energy released by a crack extension δc, at both ends of the crack. Following Jayatilaka (1979, p.57), the total strain energy associated with a cracked body, of Young's modulus E, is the sum of two terms. The first is the stored energy in the absence of the crack, and this is equal to $\sigma^2/2E$ per unit volume. The second is the stored energy in the presence of the crack. In a body containing

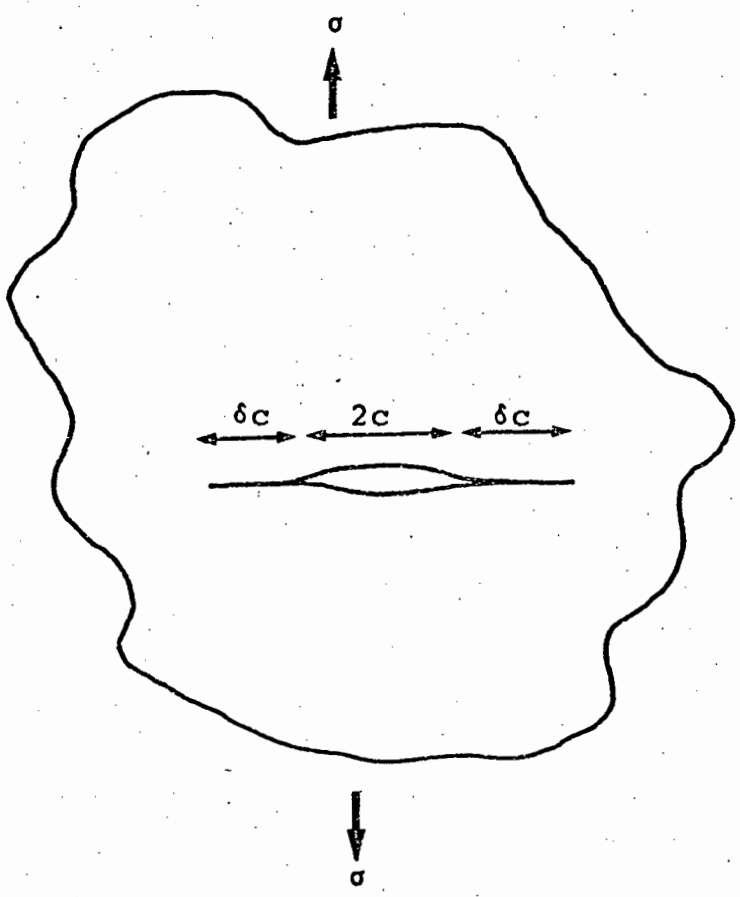

Fig. 4.4 An infinite two-dimensional body containing a through-the-thickness Griffith crack, length 2c. Applied body load σ.

an elliptical crack, the stored energy is

$$W = \frac{\sigma^2 \pi c^2}{4E} (1 + \nu) (K + 1),$$

where ν is the Poisson's ratio and $K = (3 - 4\nu)$ for plane strain conditions (a thin plate) and $K = (3 - \nu)/(1 + \nu)$ for plane stress conditions (a thin plate).

For the cracked body there are three energy terms contributing to the total energy of the system:

(1) $U = \sigma^2/2E$ — the stored strain energy which is independent of the crack.

(2) $W = \frac{\sigma^2 \pi c^2}{4E} (1+\nu)(K+1)$ — the stored strain energy in the presence of the crack.

(3) S, the surface energy of the crack. If γ is the surface energy per unit area of the body then the surface energy due to the crack is

$S = 4c\gamma$.

The total energy of this system is equal to the sum of the surface and crack terms, minus the strain energy released by the crack. Thus

$$U_{TOT} = S + U - W \quad .$$

Griffith was concerned with the conditions under which a crack would just become unstable. As an energy criterion this is equivalent to $dU_{TOT}/dc = 0$. That is the mechanical and surface energy terms are balanced. Hence

$$\frac{dU_{TOT}}{dc} = \frac{d}{dc} (S + U - W) = 0 \quad . \qquad (4.7)$$

Inserting the appropriate energy terms into eq.(4.7) we obtain

$$\frac{dU_{TOT}}{dc} = \frac{d}{dc}\left\{4\gamma c + \frac{\sigma^2}{2E} - \frac{\sigma^2\pi c^2}{4E}(1+\nu)(K+1)\right\} = 0$$

$$= 4\gamma - \frac{\sigma^2\pi c}{2E}(1+\nu)(K+1) = 0$$

$$\text{or } \sigma = \sqrt{\frac{8E\gamma}{\pi c(1+\nu)(K+1)}}$$

Letting $\sigma = \sigma_f$, and substituting for K we obtain

$$\sigma_f = \sqrt{\frac{2E\gamma}{(1-\nu^2)\pi c}} \quad \text{(plane strain)} \qquad (4.8)$$

$$\text{and } \sigma_f = \sqrt{\frac{2E\gamma}{\pi c}} \quad \text{(plane stress)} \qquad (4.9)$$

Up to this point we have described the general solution to the Griffith crack system. During crack extension the loading system may or may not be contributing work. Two extremes can be cited (Fig.4.5):

(1) Constant load conditions

(2) Constant strain conditions

The elastic load/displacement curves for a plate with cracks of length c, and (c + δc) are shown in Fig.4.6. The body with the longer crack is more compliant and hence has a smaller slope. Now, in the general solution the strain energy in the absence of the crack is independent of the loading system, and we focus our attention on the energy terms in the presence of the crack.

During infinitesimal crack extension δc the change in total free energy δU is given by

$$\delta U = -\delta W_b + \delta U_e + \delta U_s \ ,$$

where δW_b is the work done by the external load, δU_e is the change in strain energy, and δU_s the change in the surface energy of the crack.

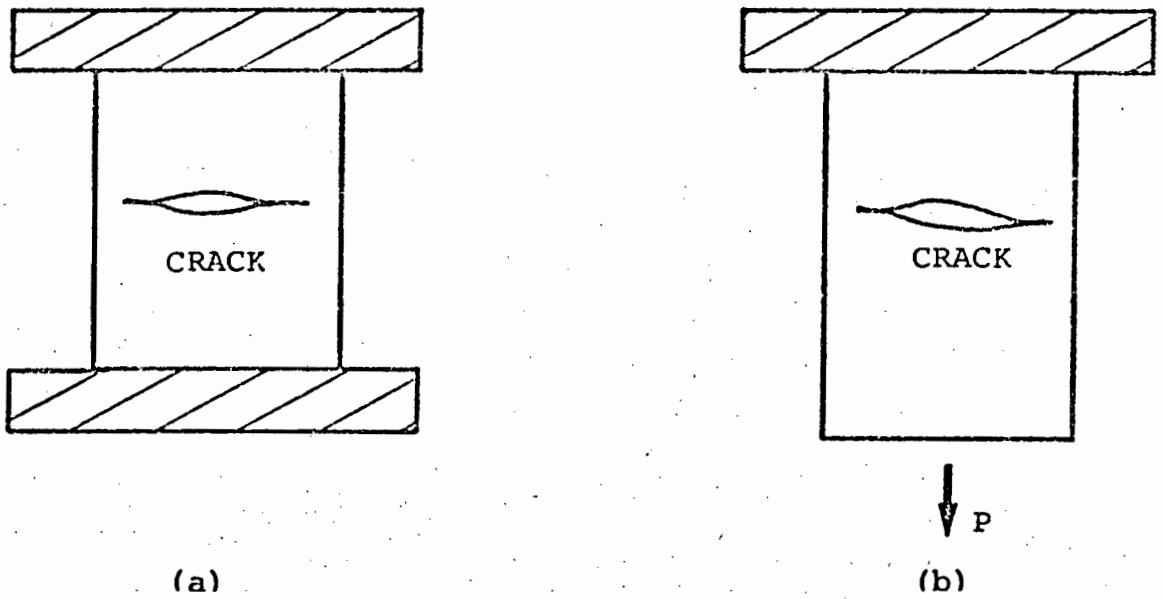

Fig.4.5 Loading systems considered in the Griffith analysis (see text): (a) constant strain (b) constant load.

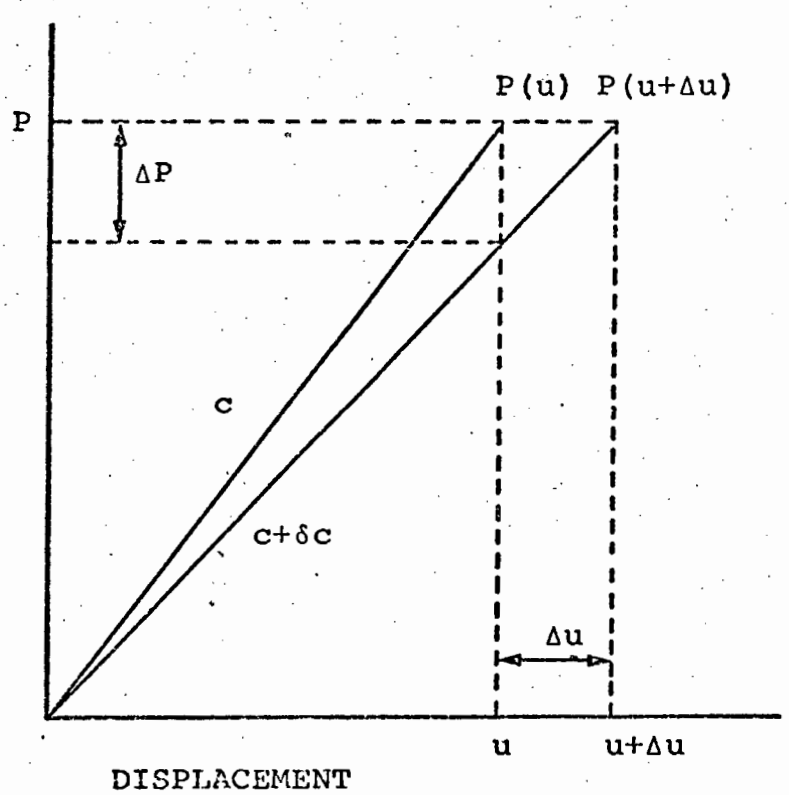

Fig.4.6 The load-displacement curve for cracks of length c and c+δc in a body. In fixed grip (constant strain) conditions crack extension is accompanied by a load drop ΔP. In constant load conditions the displacement increases by Δu.

(1) Fixed grip loading (Fig.4.5a)

The crack extension is accompanied by a decrease in load ΔP and a decrease in the amount of stored elastic energy δU_e equal to:

$$\delta U_e = \tfrac{1}{2} (P - \Delta P)\, u - \tfrac{1}{2} P u = - \tfrac{1}{2} u \Delta P$$

Since the displacement is fixed, there is no external work ($\delta W_b = 0$) and hence:

$$\delta U = - \tfrac{1}{2} u \Delta P + \delta U_s \qquad (4.10)$$

(2) Constant load (Fig.4.5b)

The external work done is $P\Delta u$, while the stored energy increases by the amount:

$$\tfrac{1}{2} P (u + \Delta u) - \tfrac{1}{2} P u = \tfrac{1}{2} P \Delta u$$

Thus,

$$\delta U = - P\Delta u + \tfrac{1}{2} P\Delta u + \delta U_s$$

$$\delta U = - \tfrac{1}{2} P\Delta u + \delta U_s \qquad (4.11)$$

To compare the energy changes under these sets of conditions we make use of the fact that the displacement (u) of the body is related to the applied load (P) by the compliance (A) of the system; viz: $u = AP$. The reciprocal of the load - deflection curve, at a particular value of crack length c, defines A. For the limit of small crack extensions ($\delta c \to 0$) the values of A for cracks of length c and $c + \delta c$ are constant and hence

$$\Delta u = A\Delta P \quad .$$

For constant strain conditions, using $u = AP$, eqn.(4.10) becomes

$$\delta U = -\tfrac{1}{2} u\Delta P + \delta U_s = -\tfrac{1}{2} AP\Delta P + \delta U_s$$

For constant load conditions using $\Delta u = A\Delta P$, eqn.(4.11) becomes

$$\delta U = -\tfrac{1}{2} P\Delta u = -\tfrac{1}{2} PA\Delta P + \delta U_s$$

Thus for a small crack extension δc the decrease in the strain energy of a cracked body under fixed grip conditions is identical to the decrease in potential energy under constant loading conditions. The Griffith formulation is thus independent of the loading system used.

4.5 The Energy Release Rate

The energy (either strain energy or potential energy) released (dW) per unit extension of the crack front (dc) is known as the energy release rate G and is defined (for a crack, length 2c, which extends at both ends) as:

$$G = \tfrac{1}{2} \frac{dW}{dc} \quad .$$

Fig.4.7a shows the way in which the various energy terms vary as a function of crack length. The total energy reaches a maximum at the critical crack length C_{crit} for catastrophic propagation. Fig.4.7bindicates the variation of G with c. At $c = c_{crit}$ the energy release rate exceeds the surface energy term; more energy is available than is consumed and the crack extends unstably.

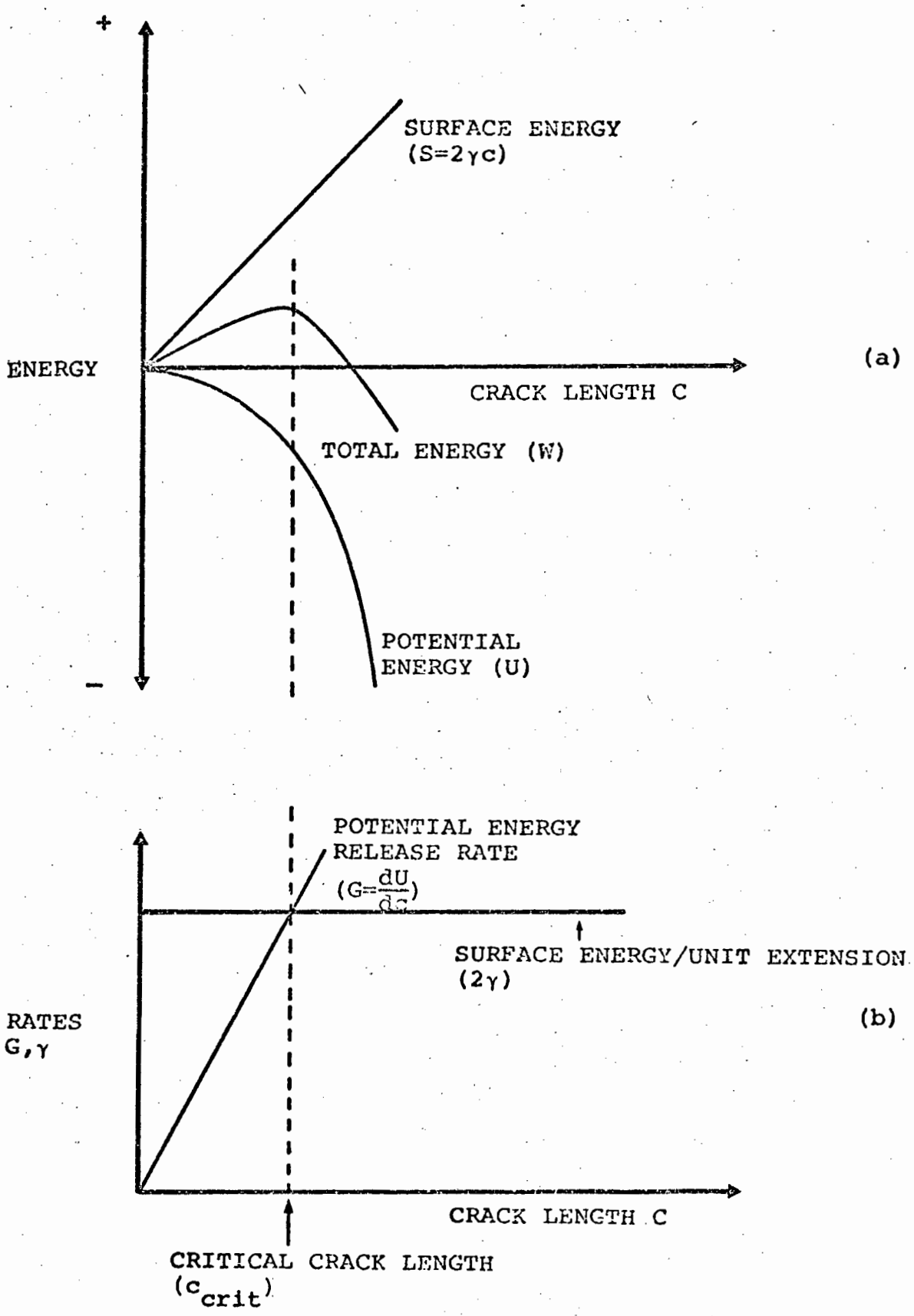

Fig.4.7 (a) Variation of energy terms with crack length.
(b) Variation of energy rates with crack length.

4.6 Fracture Mechanics : The Engineering Approach to Fracture

The previous analysis of fracture based on reversible thermodynamics suffers from the disadvantage that the energy criterion may be satisfied for unstable crack extension, yet the concentrated crack-tip stresses may be insufficient to break interatomic bonds (Knott, 1973). Thus the Griffith criterion is a necessary, though not sufficient condition for fracture. We now develop a more general approach to fracture that has practical use in engineering situations, ensuring that the fracture criterion is both a necessary and sufficient condition for failure.

4.6.1 Modes of Crack Propagation

There are three modes of crack opening displacement (Fig.4.8). These are:

(1) Mode I (opening mode), the normal separation of the crack walls under the action of a tensile force.

(2) Mode II (sliding mode), the shearing of the crack walls in a direction normal to the crack front.

(3) Mode III (tearing mode), the shearing of the crack walls parallel to the crack front.

The shearing modes are particularly important in rock fracture processes where hydrostatic pressures can suppress the tensile mode.

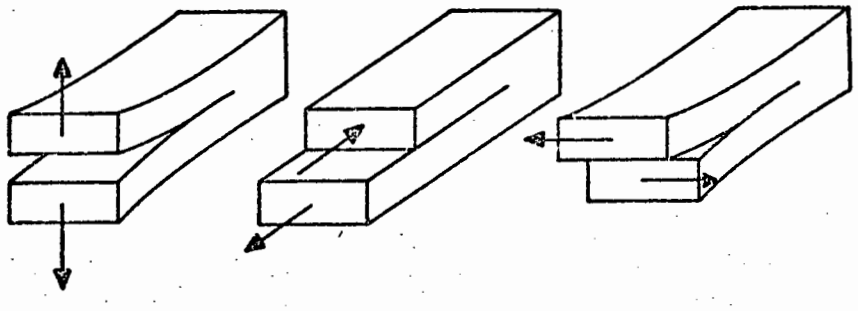

Fig.4.8 The three modes of fracture: I opening mode; II sliding mode; III tearing mode.

4.6.2 Stress Intensity Factors

For each of the modes it is possible to calculate the crack tip stresses. For Mode I conditions it is found that a function of the form

$$\begin{bmatrix} \sigma_x \\ \sigma_y \\ \tau_{xy} \end{bmatrix} = \frac{K_I \cos(\theta/2)}{\sqrt{2\pi r}} \begin{bmatrix} 1 - \sin\frac{\theta}{2} \cdot \sin\frac{3}{2}\theta \\ 1 + \sin\frac{\theta}{2} \cdot \sin\frac{3}{2}\theta \\ \sin\frac{\theta}{2} \cdot \cos\frac{3}{2}\theta \end{bmatrix}$$

describes the stress state at the crack tip. K is the stress intensity factor describing the intensity of the local field, and depends on the loading configuration and specimen geometry. r and θ are co-ordinates relative to the crack tip. In general we may write

$$K_I = \sigma\sqrt{\pi c} \quad \text{x geometrical factor} \quad .$$

The geometrical factor is a function of crack length c, and specimen dimensions. Irwin suggested that the stress field near a crack tip could be used as a means of characterising the resistance of a material to fracture. For a given material at fracture the crack tip stress state must be a constant i.e. it is independent of loading geometry. The value of K_I for catastrophic fracture is called K_{IC}, the critical value of stress intensity. K_{IC} is also the 'fracture toughness' parameter.

To incorporate the stress intensity factor approach into a fracture criterion we may again calculate the strain energy released by a crack extending an amount δc. Utilising the value of K for a specific loading geometry it may be shown that

$$G_I = \frac{K_I^2}{4E} (1 + \nu) (K + 1),$$

where K has been defined previously. At fracture $K_I = K_{IC}$ and hence

$$G_{IC} = K_{IC}^2/E \quad \text{(plane stress)}$$

and $$G_{IC} = \frac{K_{IC}^2}{E}(1-\nu^2) \quad \text{(plane strain)}$$

demonstrating the equivalence of the G and K parameters.

Consider an elastic material which fails by brittle failure. $G.\delta c$ or $(K^2/E)\delta c$ is the energy per unit thickness which would be released if the crack advances by a distance δc. In terms of Griffith's criterion this energy must exceed 2γ for propagation. Thus (in plane strain)

$$G_{IC}\,\delta c = \frac{K_{IC}^2}{E}(1-\nu^2)\,\delta c = 2\gamma\,\delta c \quad .$$

Letting $K = \sigma\sqrt{\pi c}$, and $\sigma = \sigma_f$ we can show:

$$\sigma_f = \sqrt{\frac{2E\gamma}{\pi c(1-\nu^2)}} \quad .$$

This expression for fracture stress is exactly the same as that derived previously (eq.4.8), from the Griffith approach. We may summarise the fracture toughness approach by stating that it includes non-linear processes at the crack-tip. In the ideal brittle solid $G_{IC} = 2\gamma$. In brittle solids where there may be limited ductility at the crack tip, $G_{IC} > 2\gamma$. In ductile materials $G_{IC} \gg 2\gamma$. G_{IC} is thus a convenient parameter to assess the 'brittleness' of a solid.

Since the stress intensity factor for many loading configurations, specimen geometries and crack shapes have been computed, laboratory values of K_{IC} can be incorporated into the equations for stress intensity describing engineering scale structures. In this way safe operating conditions can be calculated to prevent catastrophic failures. We should note that the concept of fracture toughness is a well developed subject and the interested reader should refer to books (e.g. Knott, 1973) developing this theme in more detail.

4.7 Failure from Cracks under Complex Stress States

Generally, a body is subjected to a state that is more complex than uniaxial. Thus, a crack may propagate under Mode II or Mode III loading conditions. To model such a situation the complex stress state is reduced to a biaxial stress system with the crack orientated at an angle to the principle stresses (Fig.4.9). The general (and somewhat simplified procedure) is to then calculate the stresses at the crack, and to determine at which position on the crack front the tensile stress reaches the theoretical strength. Thus the crack does not extend in its own plane (as under Mode I loading) but at some angle to this plane (Fig.4.10). Even under a biaxial compressive stress it is possible to find regions of tensile stress about a crack, and hence propagation will initiate in these regions. A crack loaded in shear has regions of tension and compression at the tip (Fig.4.11). Propagation accordingly initiates in the tensile field. Complete analyses of these problems are complex, but we may state several important results.

(i) The fracture strength in compressive loading is eight times the strength in uniaxial tension.*

(ii) The magnitude of the shear stress required to propagate a crack in pure shear loading (Mode II) is less than the uniaxial Mode I fracture tensile stress.

(iii) For compressive loading with an applied hydrostatic pressure superimposed, the fracture stress (in shear) is increased.

The superimposition of a hydrostatic pressure is exploited in laboratory compression testing of brittle solids at elevated temperatures. By doing this, premature brittle fracture is avoided, allowing a plastic response to develop.

---

*In practice friction between crack faces increases this factor by many times (Bieniawski, Int. J. Rock Mech. Min. Sci., 4, 407 - 423, (1967).

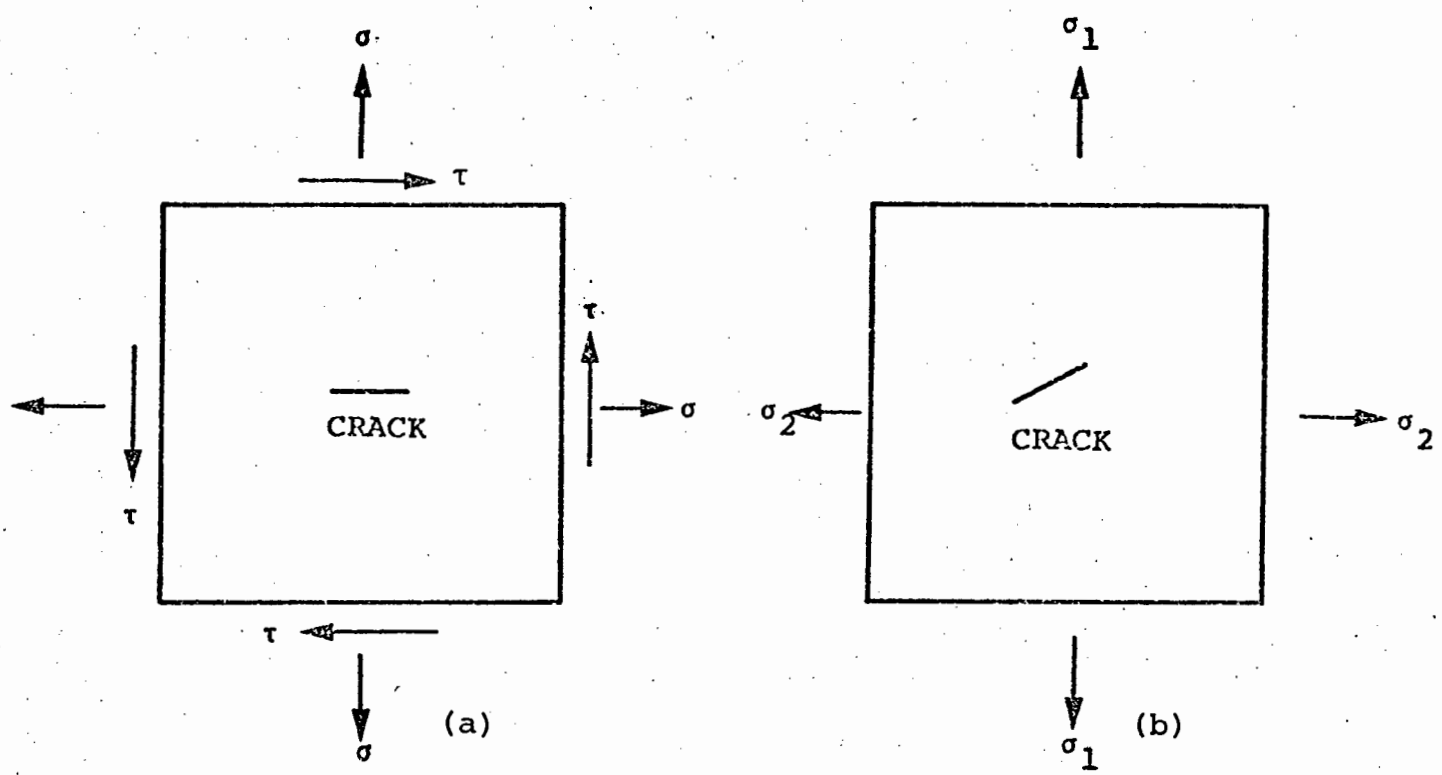

Fig.4.9 (a) Body containing a crack subject to a complex stress state (b) the stress state in (a) can be reduced to a biaxial stress system with the crack inclined at an angle.

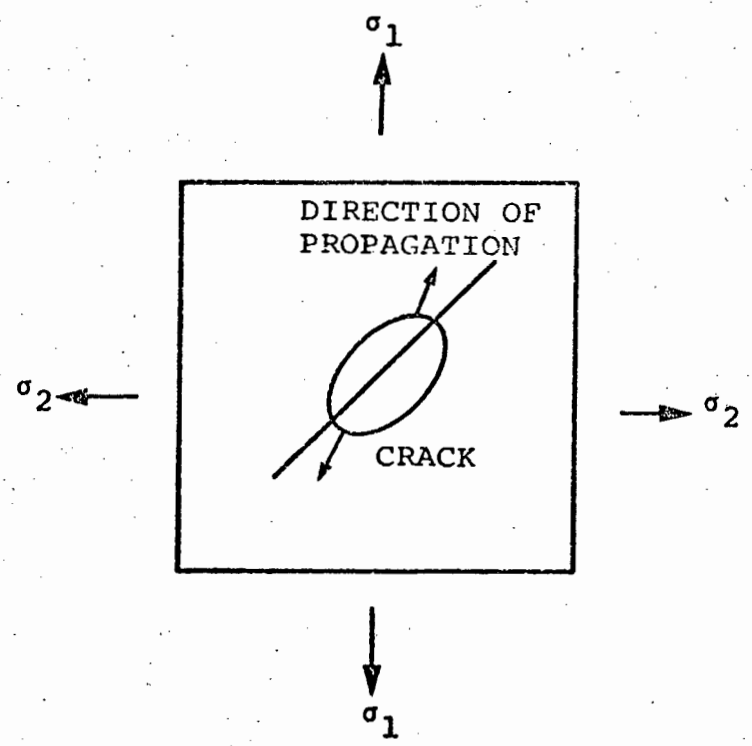

Fig.4.10 Initiation direction of an elliptical crack in a biaxially stressed body. Note that the crack does not extend in its own plane.

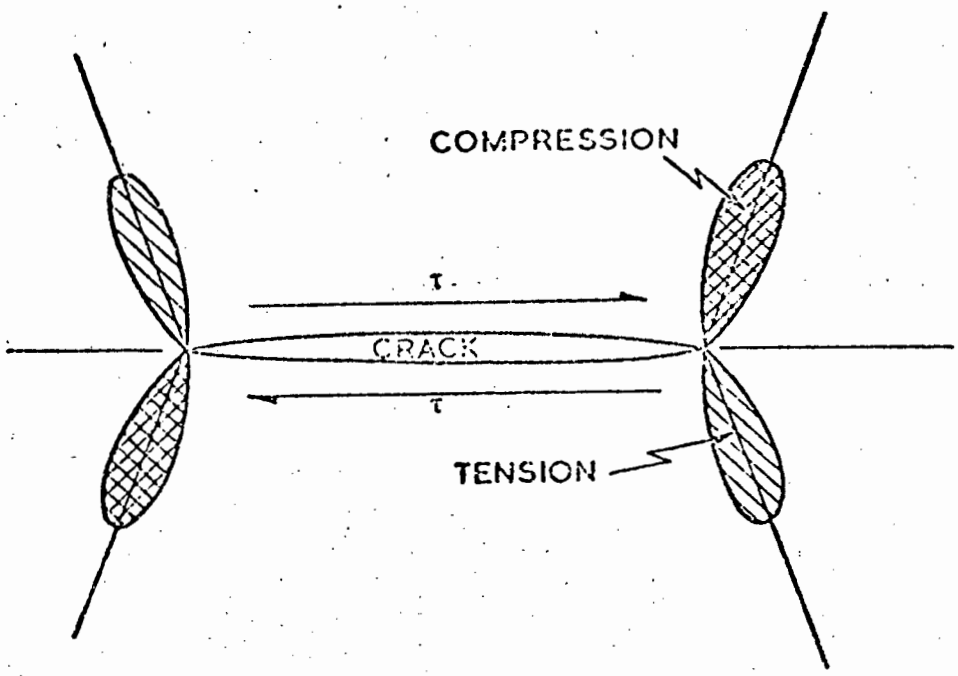

(a)

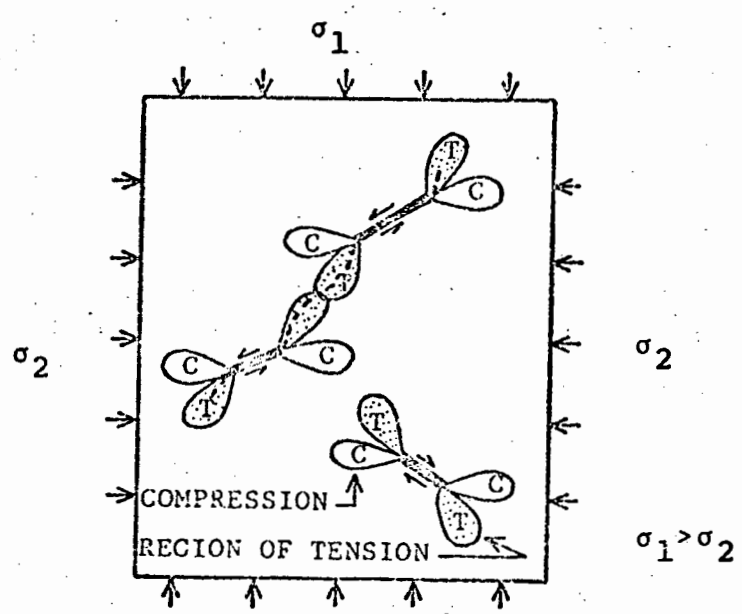

(b)

Fig.4.11 (a) Crack loaded in shear develops regions of tension and compression at the tip (b) an array of shear loaded cracks (for example in a rock) develops into a macroscopic crack through the body by coalesence.

4.8 Microstructural Aspects of Brittle Fracture

A polycrystalline material has grains that are crystallographically misorientated relative to one another. The interfaces between the grains (grain boundaries) can be surfaces of weakness. A crack propagating through a polycrystal may either cut across the crystal boundaries (transgranular fractures) or follow the grain boundary itself (intergranular fracture) (Fig.4.12). Transgranular fracture is favoured by solids that have strong grain boundaries and small misorientations. At the interface there can be a substantial reduction in the cohesive forces (for example, due to atomic bond misorientations or impurities) and in this case there is an increased tendency for a propagating crack to follow the grain boundary. It is obvious that intergranualr fracture results in a rather circuitous fracture path. One result of intergranular fracture is to reduce the fracture energy by up to half. However, since the crack path changes direction abruptly, the overall effect is to increase the apparent fracture energy, since the crack length is considerably increased.

4.9 The Influence of Environmental Factors on Fracture

There is currently considerable interest in enhancing the fracture of brittle solids through the action of environmental agents (e.g. see Westwood, 1974). In this way it is hoped that a reduction in the large energy expenditure made, for example, during the drilling and cutting of rock, or the grinding of semiconductor ceramic substrates can be achieved. Two major types of environmental action may be discerned. The first of these is known as static fatigue by which a crack may propagate at low speed under an applied stress which is insufficient to allow catastrophic fracture under inert conditions. It is found that the strength decreases with an increase in time-at-load. The action of water vapour on glass is a

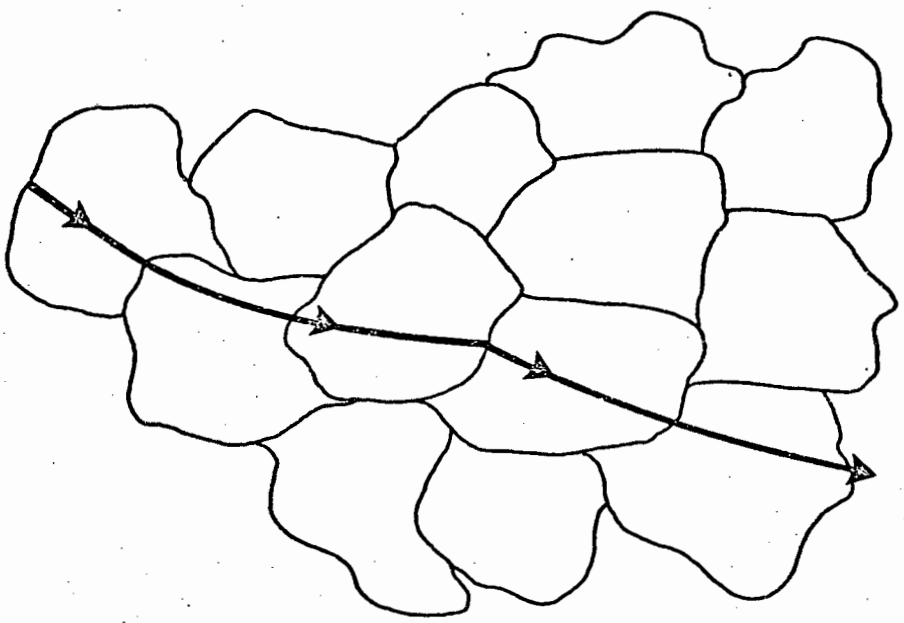

TRANSGRANULAR FRACTURE

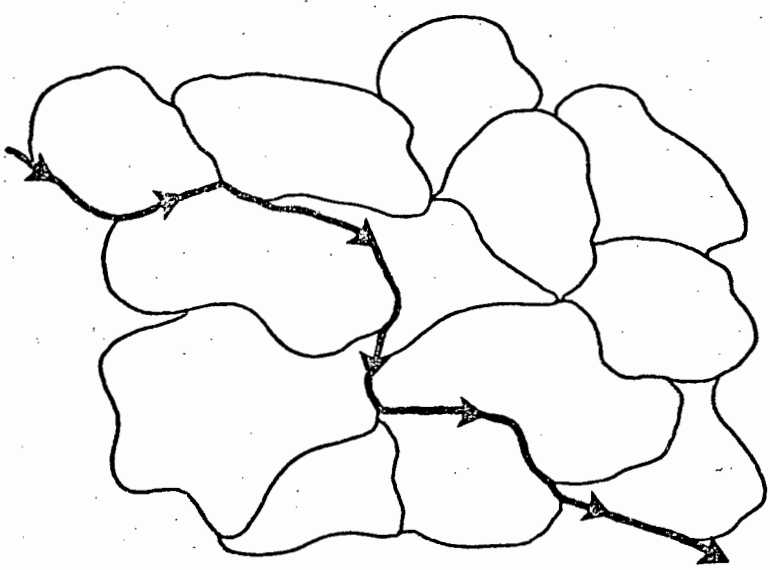

INTERGRANULAR FRACTURE

Fig.4.12 Microstructural control of fracture.

good example of this gradual deterioration in residual strength. The second type of environmental effect is chemomechanical in origin; the flow properties of a solid may be so altered by the presence of the environment that the initiation of a fracture event is correspondingly easier. For example, the adsorption induced changes in the hardness of non-metals is thought to be related to the ease with which dislocations either nucleate or glide. The essential difference between these two types of behaviour is that static fatigue may take place over a considerable time-scale, whereas chemomechanical effects are far more immediate.

4.9.1 Static Fatigue

The classic example of a static fatigue effect is the glass/water system. The mechanism of strength reduction is stress-enhanced chemical dissolution at the crack tip, leading to flaw sharpening, which enables the crack to propagate at applied stresses that are considerably below those determined by experiment under inert or quasi-instantaneous loading. The active chemical species are H^+ or OH^- ions and the fracture strength is found to be a function of the relative humidity of the test environment. Static fatigue effects are absent at low temperatures where water is inert, under vacuum conditions or for very short duration loading. If the tests are carried out as a function of temperature an activation energy can be deduced; for pure silicate glasses this is approximately 3.5 eV which is close to the theoretical Si - O bond strength (4.4 eV). In soda-lime-silicate glasses, activation energies are found that are near to that for Na^+ ion diffusion, emphasizing the role of this relatively mobile 'network modifier' in fracture events.

The enhanced chemical reactions occurring at the highly stressed region of the crack tip have been examined by Hillig and Charles (1964). They considered three specific examples

of chemical action (Fig.4.13)

(a) The rate of chemical attack is uniform everywhere in which case the crack tip will increase in radius. Hence the solid is strengthened. This process will occur if the rate of chemical attack is stress-insensitive, or if no stress is applied.

(b) The corrosion rate is stress-enhanced. In this situation the rate of chemical attack will be greater at the tip region which decreases the radius of the tip, resulting in a reduced fracture stress.

(c) The rounding of the tip by corrosion is balanced by an increase in the length of the flaw, leading to flaw growth. In other words this is equivalent to the fatigue limit for which the stress concentration remains constant with time.

Extensive experimental investigations of the static fatigue of the glass-water system have been undertaken by Wiederhorn (1967). A strong dependence of crack velocity as a function of applied load (or stress intensity K_I) is observed (Fig.4.14), which varies with the environmental relative humidity. Wiederhorn's experimental results show three distinct regions of behaviour

(a) Region 1: the crack velocity is exponentially dependent on the applied load, suggesting that fracture is controlled by chemisorption or other chemical reactions at the crack tip.

(b) Region II: the crack velocity is independent of applied load; here the rate of diffusion of water to the crack tip controls fracture, since it is assumed that diffusion is not affected by the state of stress at the surface.

(c) Region III: crack propagation is independent of the environmental condition. The Griffith criterion has not yet been met which occurs at K_{IC}. Region III may not always be present.

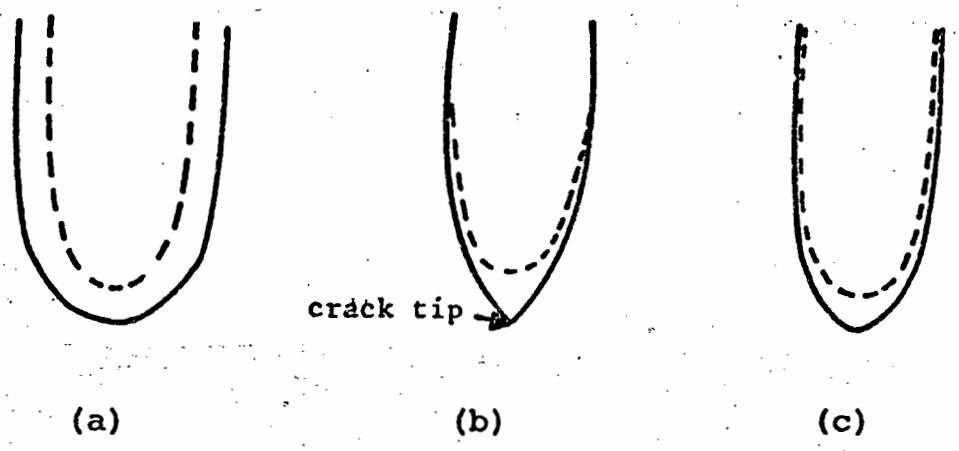

Fig.4.13 Hillig and Charles model of stress enhanced corrosion at a crack tip. See text for a description of the three different possibilities.

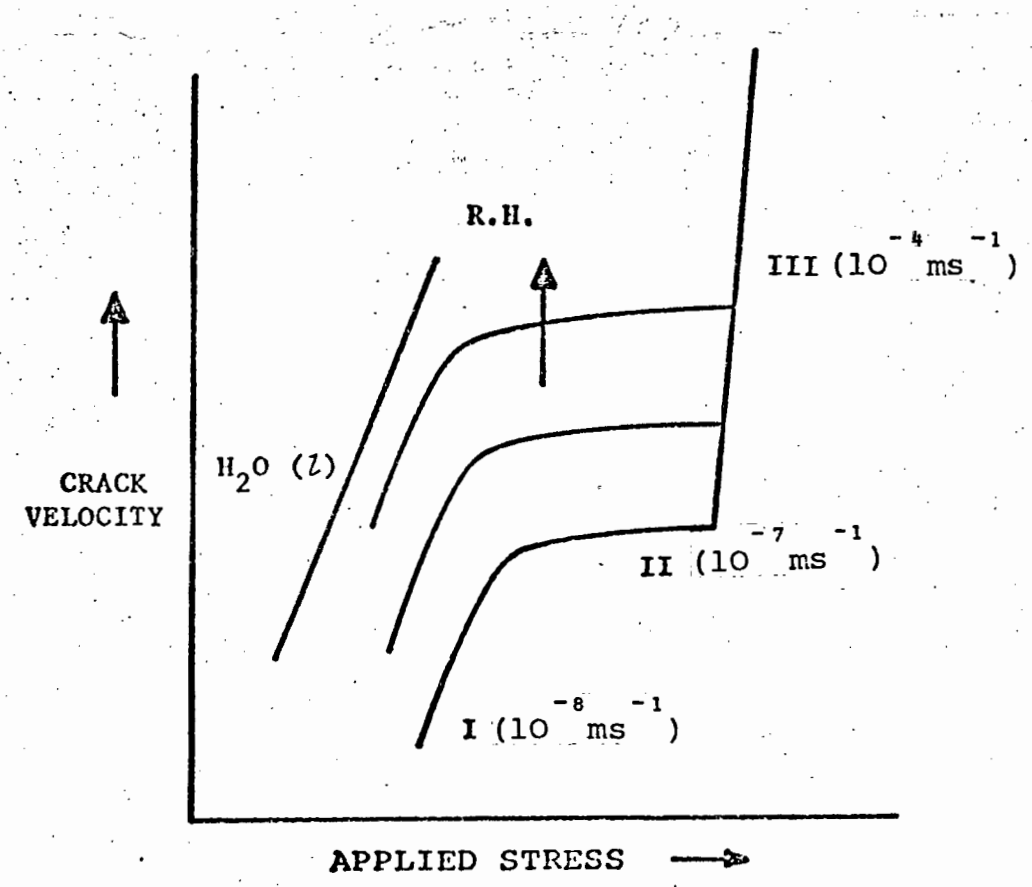

Fig.4.14 Schematic representation of crack velocity data as a function of applied stress and relative humidity (R.H.). Three different crack propagation stages can be discerned (see text). Typical values of crack velocity are shown. (after: Wiederhorn, S.M., 1967).

4.9.2 Static Fatigue in Quartz

Both Martin (1972) and Scholz (1972) have examined static fatigue effects in quartz. Scholz compressed crystals of natural quartz parallel to the c-axis and to the a-axis, and monitored the time-to-failure as a function of applied stress, humidity and temperature. For crystals submerged in water at $25^{o}C$ and compressed parallel to c, failure occurred after $\approx$ 100 secs, at a stress of $\approx$ 20 Kbar, while at a reduced stress of 15 Kbar the failure time increased to $\approx 10^{5}$ s. Crystals compressed parallel to the a-axis showed a longer time-to-failure at the lowest stress levels. In atmospheric moisture the failure times were at least an order of magnitude longer, while in a vacuum (10^{-3} torr) failure times were increased by two to three orders of magnitude, compared to the results from the submerged samples. The failure time reduced as the temperature was raised.

The number of cracking events was measured using an ultrasonic detector system. It was found that the sudden application of water dramatically increased the number of acoustic events. An important point to emerge from this study was that immediately after the application of stress the acoustic event count was high, but then decayed as the test progressed. There was no sudden increase in crack events just prior to failure, indicating that only a few cracks cause complete failure. No strain within the experimental sensitivity could be detected during the loading and failure sequence.

Scholz performed one failure test in an atmosphere of dry hydrogen. No enhancement of fracture was noticed, indicating that the weakening mechanism was not hydrogen embrittlement. However, Williams & Lawn (1973) did find that the fracture load (in a Hertzian test) was reduced at elevated temperatures in proton irradiated quartz. Surface microcracks in a state of tension were thought to provide preferential sinks for diffusing hydrogen, and the strong Si - O - Si

bond was replaced by weaker hydrogen bonding according to the scheme:

$$(Si - O - Si) + H \rightarrow Si - OH: - Si$$

$$+ H \rightarrow (-Si - OH : H - Si -)$$

Fracture was correspondingly easier. The failure of Scholz to observe static fatigue in the hydrogen atmosphere must be attributable to the high energy required to dissociate the hydrogen molecule.

4.9.3 Chemo-mechanical Effects

It has frequently been proposed, and experimental evidence has convincingly demonstrated, that environments which increase the hardness of a solid give increased drillability. These are known as ζ-potential effects, and are related to the surface charge of a solid in a particular environment. A.R.C. Westwood and co-workers in the United States have made a substantial research effort into the effects of these chemo-mechanical environments on drilling performance. (For a review see Westwood, 1974). For the case of quartz single crystals drilled in water, toluene (which has a low residual water content) and normal alcohols, a clear correlation is found between the pendulum hardness, (P.H.)*, and drillability, and a maximum in the value of P.H. corresponds to a maximum in the drilling rate. Additionally, a zero in the ζ-potential corresponds to a maximum in the P.H. The

---

*The pendulum hardness (P.H.) is a measure of the rate of damping of a pendulum with a diamond fulcrum (e.g. cone or Vickers pyramid). The measured rate of damping is related to the energy absorbed by near surface flow and fracture processes occurring beneath the fulcrum. For a hard, brittle solid relatively little energy is absorbed and the P.H. is large. For a ductile solid, more energy is absorbed and the P.H. is smaller (Westwood, MacMillan and Kalyoncu, 1973).

drilling rate in the n-alcohols was significantly increased over the rate for water or toluene. Heptanol and decanol gave the most dramatic improvements (≈ 3000% increase in drilling rate : this corresponds to a small 16% increase in P.H.). Both heptanol and decanol give a ζ-potential equal to zero for quartz.

In a study of the abrasion and drilling of $A\ell_2O_3$, Swain et al. (1975) drew attention to the fact that while a $\zeta = 0$ was best for a maximum drilling rate, this corresponded to a minimum in wear by abrasion. The abrasive wear experiments were performed with 45 μm grit impregnated on a metallographic wheel, rotating at 500 rpm, while the drilling studies were made with a diamond core bit, diameter 3.2 mm, wall thickness 1 mm; the normal load was 5 kg and the speed of rotation 2200 rpm. The liquid environments in the experiments were water and the normal alcohols. Thus, from these tests, the penetration rates of diamond bits was greatest when the material was hardest (measured by Knoop hardness testing) and presumably most brittle at $\zeta = 0$. By contrast, the abrasive wear rate was least when $\zeta = 0$.

A model proposed by Lawn (1975) was used to explain these results. The suggestion was that material removal by abrasion occurs by a mechanism that is primarily dependent on flow properties (i.e. hardness), while material removal in drilling is considered to be dependent primarily on brittle fracture processes. Assuming the particles in the abrasive wheel to be fixed, it is not clear at all why any distinction is made for abrasion and drill-cutting wear processes.* Attention was drawn to the fact that wear of the diamond cutting particles may be affected by the environment, a point which has been emphasized by Cooper & Berlie (1976). These later authors studied the penetration rate of a diamond drill-bit in water and normal alcohols cutting Granite Bolus. There was no dramatic increase in penetration rate when changing from an alcohol to a water environment and vice-versa. An interpretation was made in terms of the diamond cutting points suffering reduced wear in alcohol environments, allowing cutting to continue.

*It could be argued that in abrasion there is a cycle of loading and unloading, while in drilling the load is maintained until failure.

CHAPTER 5

THE INDENTATION OF BRITTLE SOLIDS

5.1 Introduction

If a particle is loaded against the surface of a brittle solid several things may happen. The solid may deform inelastically and a permanent impression may be left on the surface. Alternatively, microfracturing events will occur which will leave the solid in a weakened state. More frequently both inelastic and fracturing processes prevail together. Since many material removal operations involve the use of sharp or blunt cutting particles it is anticipated that the results obtained from an investigation of the indentation of a brittle solid may provide some quantitative information on the mechanisms of the wear of these solids. Such a study forms the basis of indentation fracture mechanics.

5.2 Static Loading with a Sharp Indentor

The sub-surface stress field distribution for an isotropic, linear elastic solid, subject to a surface point load P was determined by Boussinesq in 1885. The magnitude of the stresses are proportional the the applied load, and inversely proportional to the square of the radial distance from the point of application.

In the Boussinesq analysis the point is considered to be infinitely sharp, the contact area is zero, and hence there will be a stress infinity at the point of contact. In practice, when a sharp indentor is loaded against a solid, non-linear deformation processes (such as plastic flow or densification)

will operate to relieve this high stress and, as a result, the indentor sinks in, distributing the load over a finite contact area. When this occurs the characteristic hardness impression is formed.

The mean contact pressure, p_o, for a hardness indentation is defined (Lawn & Wilshaw, 1975) as

$$p_o = P/\alpha\pi a^2 \qquad (5.1)$$

where α is a constant and depends on the indentor geometry, and 'a' is the characteristic dimension of the impression. Consider the specific case of a Vickers hardness test. The indentor is a pyramid and the Vickers hardness value H_v (load/area of contact) is given by

$$H_v = \frac{1.8544.\ P}{d^2} \qquad (5.2)$$

where d is the length of the impression diagonal, and P the indentation load. Assume now that the mean contact pressure is equal to the Vickers hardness H_v. Equating eqns.5.1 and 5.2, and letting the characteristic dimension (a), of the impression be d/2, we may show that $\alpha = 4/(1.8544\pi) \approx 2/\pi)$. For the convenience of calculation α is taken to be $2/\pi$, and hence $p_o \approx H_v$.

The operation of the non-linear processes has been described in terms of 'blunting' of the indentor tip and the stress field is not described by the Boussinesq solution in the vicinity of the deformed region. However, we expect that the Boussinesq solution will become increasingly accurate in areas away from this zone.

An idealised picture of the processes occurring in a in a solid during indentation is as follows. Immediately below the indentor there is a zone of hydrostatic pressure which expands as the indentor sinks into the material. The hydrostatic zone exerts a pressure onto the surrounding material, generating an annular region in which plastic flow

processes operate, although constrained by the elastic matrix. To obtain general yielding the pressure in the outer areas of the contact zone must reach the yield stress for the solid.

During the indentation of a solid the indentor imposes an arbitrary change of shape on the material (Gilman, 1973). Thus the Von Mises (1928) five independent slip system criterion must be met if fracturing is to be avoided, and a plastic impression made. As already discussed, this criterion may not be met at room temperature in quartz. However, if plastic hardness impressions can be made then this suggests that the hard $\langle \underline{a} + \underline{c} \rangle$ slip system must be activated.

The hardness (H) and yield stress (σ_Y) of a solid are related by the general expression $H = C'\sigma_Y$, where C' is a constant known as the constraint factor. For most metals indented with a Vickers Pyramid, C' is approximately equal to 3 and the indentation is regarded as fully plastic.

Provided that the constraint factor is known, hardness data can be used to compute the yield strength of materials as a function of temperature. This method is particularly exciting for brittle materials showing evidence for plasticity during indentation. In conventional compression experiments it is generally impossible to induce plasticity in such solids over the temperature range 300 - 800 K.

5.2.1 Crack Geometry generated by the Static Sharp Indentor

The stress field has components of tension in it, and the orientation of these tensile components is responsible for the crack geometry. Experimentally, it is found that the crack formation in a brittle material occurs in the following sequence (Fig.5.1):

(a) Initial Loading: an irreversible zone of deformation about the contact point is produced, increasing in size with load.

(b) Critical Zone Formation: at a critical load a crack is nucleated in the zone under the indentor, lying on a plane of symmetry which depends upon the geometry of the indentor and also crystal anisotropy. This crack is known as a median vent.

(c) Stable Crack Growth: on increasing the load further the median vent extends stably downwards.

(d) Initial Unloading: the median vent begins to close, but does not heal.

(e) Residual Stress Cracking: prior to complete removal of the indentor the elastic matrix relaxes, creating an additional tensile component superimposed on the applied field. This process generates sideways-extending cracks that are known as lateral vents.

(f) Complete Unloading: the lateral vents continue extending and may intersect the specimen surface. This will cause chipping or spalling and the removal of material. In some cases radial cracks form.

The overall crack pattern is influenced by many additional factors, for example

1. The rate of loading and unloading
2. Environmental conditions
3. Crystal structure (particularly a strong cleavage tendency)
4. Indentor geometry (for example, loading with a Vickers pyramid causes cracks to radiate from the diagonal corners)
5. Contact point - specimen lubrication (interfacial friction)

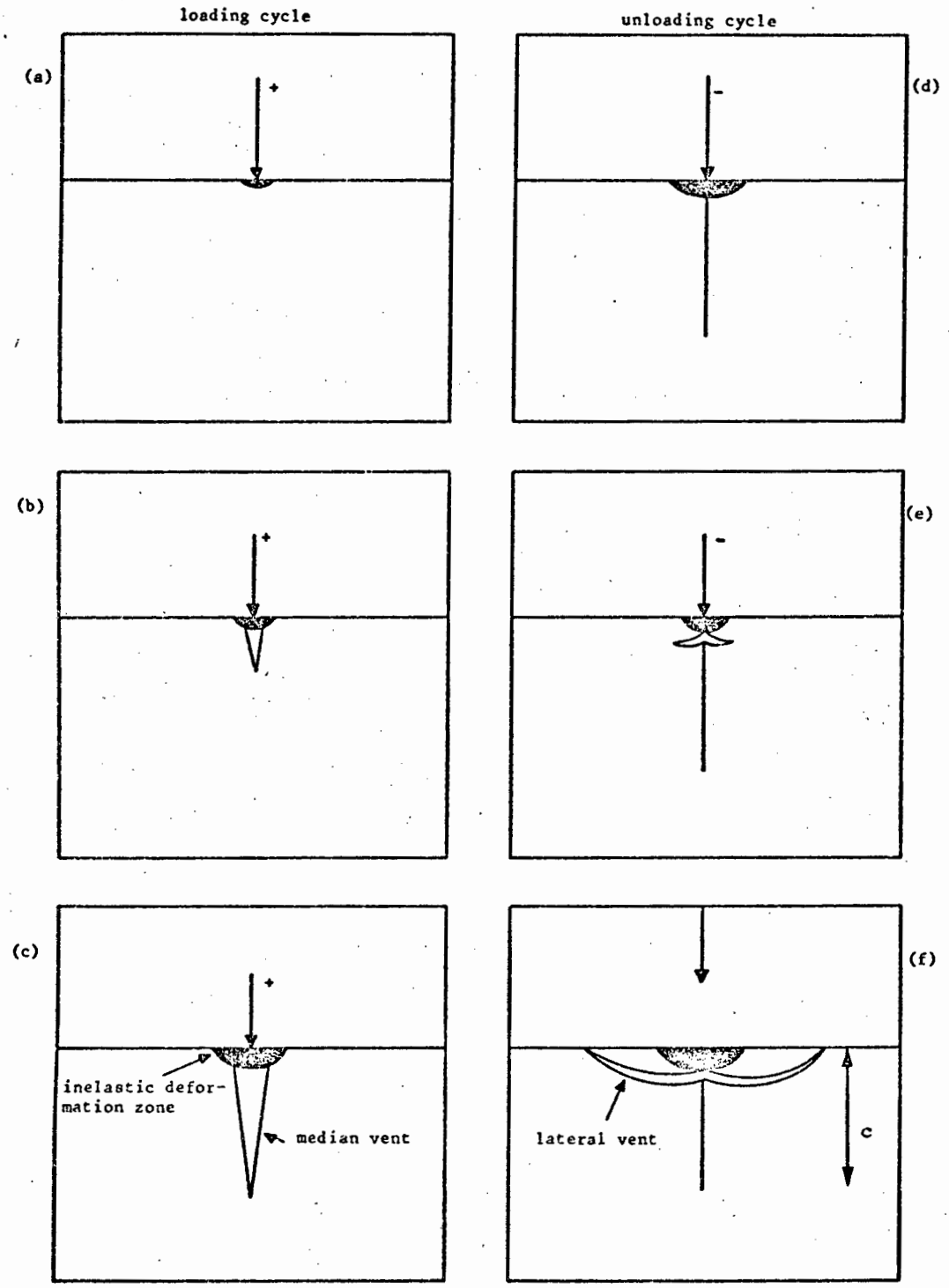

Fig.5.1 Sequence of crack formation during indentation with the sharp particle.

The above crack sequence must therefore be considered as the ideal situation, and probably rarely observed except under special conditions.

To place this crack sequence within an indentation fracture mechanics formulation it is neccessary to calculate the stress intensity factor K at the crack tip.

As an example, consider that we have a well developed median vent, diameter c, below the indentor (Fig.5.1f.) For this configuration Swain & Lawn (1976) showed that for a sharp indentor, half angle θ:

$$c = (K'P^2/2\gamma E)^{\frac{1}{3}} \qquad (5.3)$$

where $K' = (1 - \nu^2)/\pi^3 \tan^2 \theta$

Thus, by knowing the material contents ν and E, and measuring the crack length c for a particular load, a plot of c^3 against P^2 enables the fracture toughness of the material to be evaluated. This test can conveniently be made using a Vickers pyramid. The median cracks are defined from the indentor centre and a simple measurement of the radial length of these cracks, for a series of loads is a remarkably easy way to obtain fracture toughness information. It is particularly valuable for small specimens, or in situations where it may be impossible to machine specimens for a conventional fracture toughness test configuration. For a more detailed discussion on the merits of this technique as a measure of fracture toughness the reader should refer to Evans (1979).

5.3 Static Loading with a Blunt Indentor

The elastic contact between a flat specimen and a loaded smooth sphere (Fig.5.2) is an example of the classical Hertzian contact configuration. The stress distribution was first deduced by Hertz (1881). The contact pressure depresses the surface of the solid and flattens the spherical indentor. A region of surface compression exists in the centre of the contact circle, surrounded by a region of tension. At the surface the radial tensile stress varies as

$$\sigma_t = \frac{1-2\nu}{2} \frac{P}{\pi x^2} \qquad (x > a) \tag{5.4}$$

where P is the applied compressive load and a is the radius of the contact circle given by

$$a = \sqrt[3]{\frac{4}{3}\left(\frac{K'PR}{E}\right)} \quad . \tag{5.5}$$

R is the radius of the sphere and

$$K' = \frac{9}{16}\left\{(1-\nu^2) + (1-\nu'^2)\frac{E}{E'},\right\} \quad .$$

E, E', ν, ν' refer to the indented medium and indentor respectively.

The distribution of the pressure over the contact area is hemispherical in form (Fig.5.3), and given by:

$$p' = \frac{3P}{2\pi a^2}\left(1 - \frac{x^2}{a^2} - \frac{z^2}{a^2}\right)^{\frac{1}{2}} \quad .$$

At $x = 0$, $z = 0$ the pressure is a maximum (p_o) and equal to $3P/2\pi a^2$. Also drawn on Fig.5.3 are the lines of constant shear stress (τ) in the sub-surface regions.

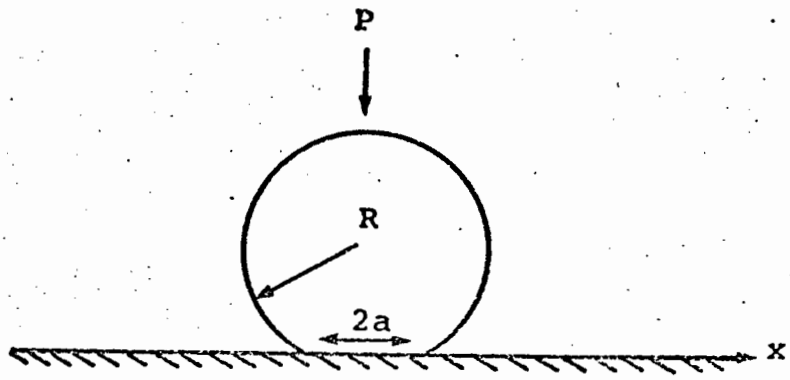

Fig.5.2 Hertzian contact between a flat specimen and a loaded sphere.

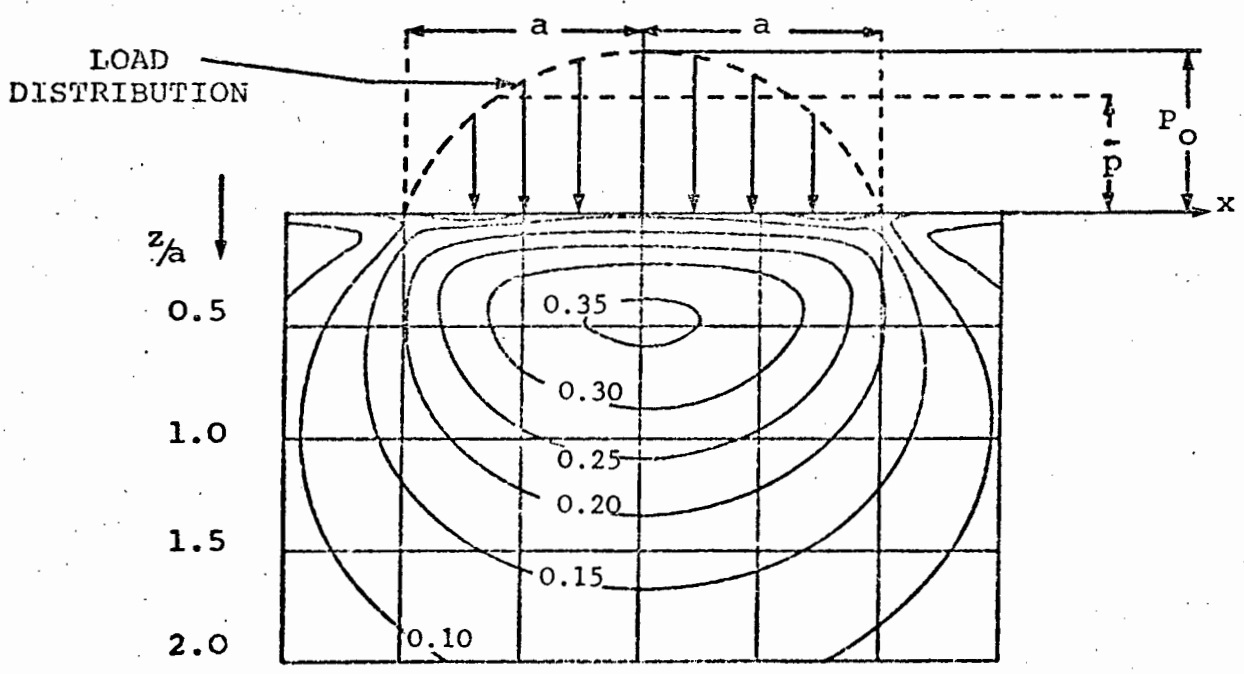

Fig.5.3 Distribution of surface pressure and sub surface maximum shear stress. The shear stress is in units of P_o/τ. P_o is the maximum Hertzian pressure and p the average pressure.

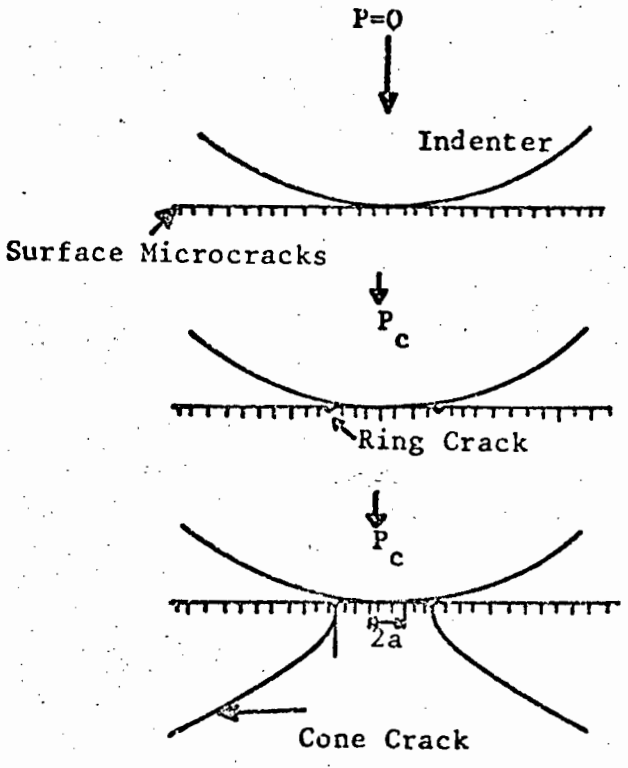

Fig.5.4(a) Development of the Hertzian cone-crack.

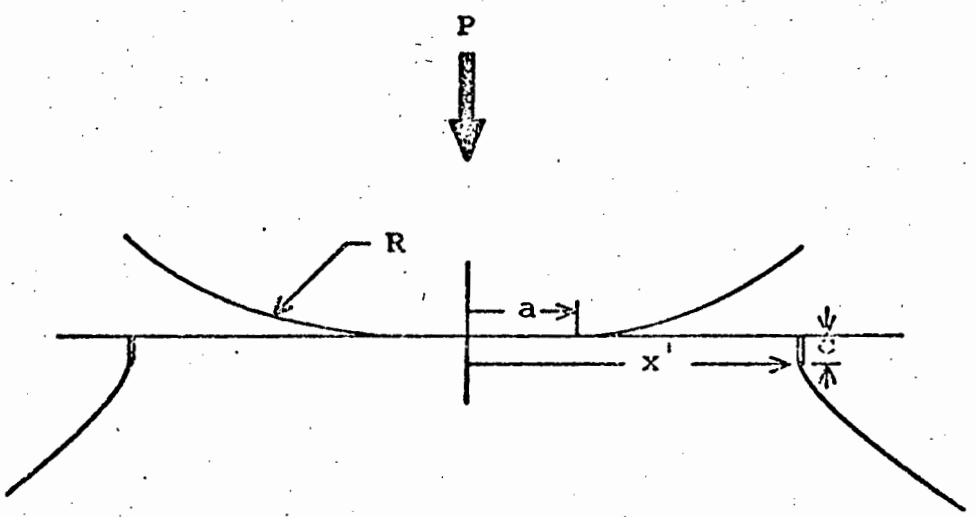

Fig.5.4(b) Parameters used in the description of the cone-crack formation. (see text).

5.3.1 Crack Geometry Generated by the Static Blunt Indentor

As the normal load on the indentor is increased, a cone-shaped crack suddenly develops into the surface of a brittle solid, (Fig.5.4a). Qualitatively, the mechanism of cone-crack formation is rather simple. The cone-crack is initiated at some favourably orientated surface flaw on the specimen, which experiences an increasing tensile stress as the applied load is increased. At a critical applied load, P_c, the Griffith criterion for fracture is exceeded and a precursor ring crack initiates at this flaw and runs around the contact area. The circular surface stress field diminishes rapidly with distance below the surface, limiting the depth of the ring crack. Further crack extension is now downwards with increasing load, to form the fully developed truncated cone-crack.

Crystal anisotropy will obviously play a role in determining the exact morphology of the conical crack surface, and there is a compromise between the tendency for the crack to follow stress trajectories and cleavage planes (Lawn & Wilshaw, 1975).

As high shear stresses (max $0.31p_o$ at $z = 0.5a$) exist under the indentor (Timoshenko & Goodier, 1970) it is possible that most materials will undergo some form of inelastic deformation. By analogy with the sharp indentor case, this produces a residual stress field on unloading which gives rise to further crack nucleation and propagation. The extent of this residual field extends up to several contact diameters.

Depending on the indentor sphere radius and applied force a contact situation that is initially 'blunt' will become effectively 'sharp' as the sphere is pushed further into the specimen (Lawn and Wilshaw, 1975). On increased loading a median crack forms, growing in size in the form of a 'half-penny', while the lateral cracks form on unloading. Radial cracks that are shallower than the lateral cracks may also develop. The cracking events for the idealised case are shown in Fig.5.5. On complete unloading a permanent impression has formed.

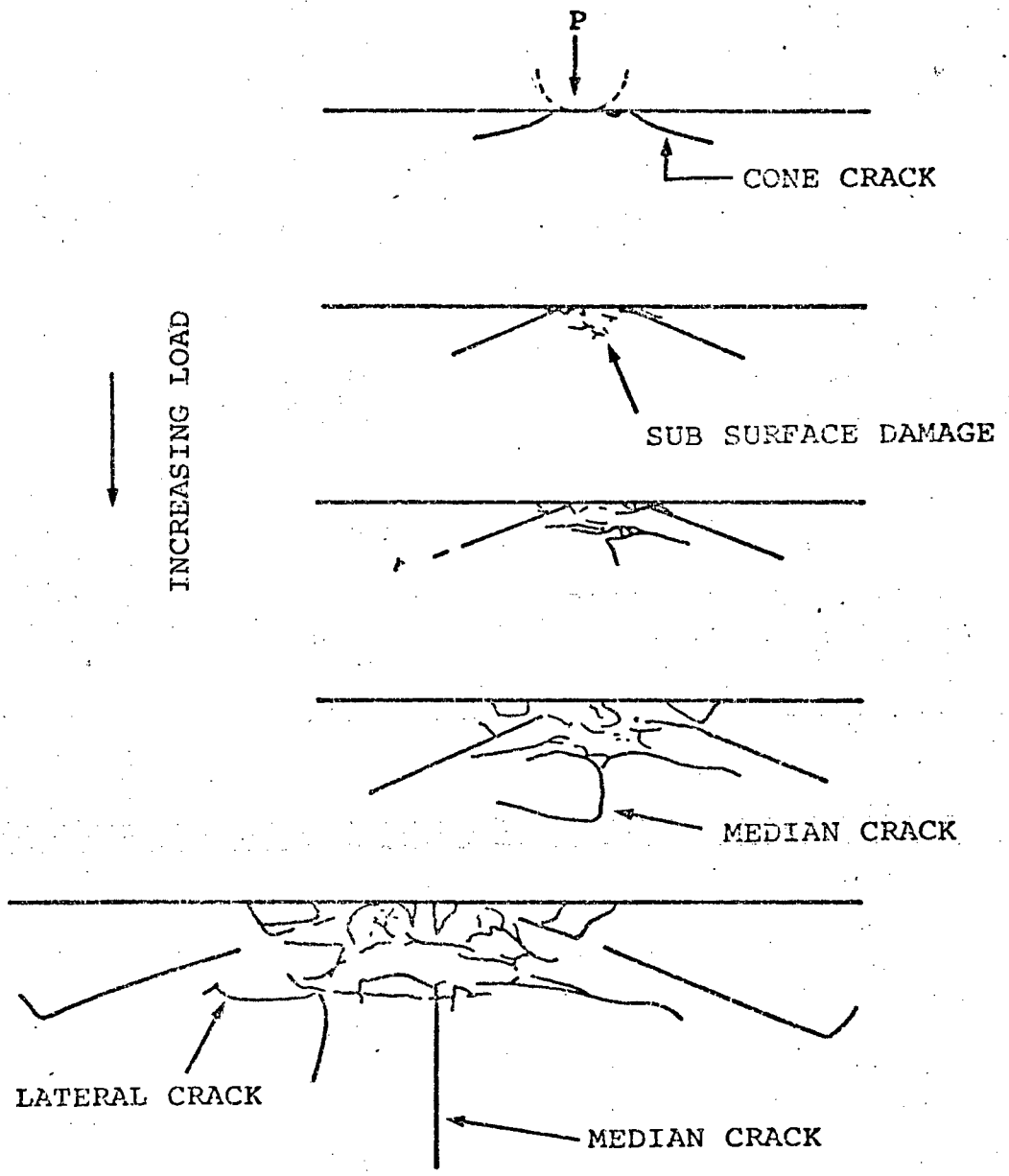

Fig.5.5 Cracking sequence for a loaded sphere indenting the surface of a solid. The development of cone-cracks, median and lateral cracks is indicated. (after: Lawn and Wilshaw, 1975).

It is possible (Hartley & Wilshaw, 1973) to develop an expression relating the fracture toughness of the indented solid to the critical formation load (P_c) of the cone-crack. Using the schematic diagram (Fig.5.4b) for Hertzian instability, we assume that the cone-crack initiates from a surface flaw of length c at x'. This crack feels an increasing tensile stress as the load is applied. If the flaw is considered to be equivalent to a single edge crack in tension then the fracture criterion for this crack to extend is

$$\sigma_f = \frac{1}{1.12} \left\{ \frac{2E\gamma}{(1-\nu^2)\pi c} \right\}^{\frac{1}{2}} \qquad (5.6)$$

Substituting for E from eqn.(5.5), and equating eqs.(5.6) and (5.4) we can show that at instability ($P = P_c$)

$$P_c = \frac{32\pi}{3(1.12)^2} \frac{K'^4 R\gamma}{(1-\nu^2)(1-2\nu)^2} \left(\frac{x'}{a}\right)^4 \left(\frac{a}{c}\right) .$$

If this flaw is situated at the edge of the circle of contact ($x' = a$):

$$P_c = \frac{32\pi}{3(1.12)^2} \frac{K'^4 R\gamma}{(1-\nu^2)(1-2\nu)^2} \left(\frac{a}{c}\right) \qquad (5.7)$$

As discussed by Hartley & Wilshaw (1973) the exact values of c are difficult to measure but provided all samples receive an identical surface abrasion treatment then the fracture toughness is proportional to the fracture load P_c.

We can appreciate that the idea of flaw statistics will enter the complete description of Hertzian cracking in brittle materials since both the distribution and orientation of the surface flaws are controlling fracture initiation. This is unlike the case of a pointed indentor, where the cracks are probably generated by the developing sub-surface deformation.

5.3.2 The Auerbach Law

The Hertzian analysis shows that the fracture load varies as the square of the radius R of the sphere. However, it is found experimentally (e.g. Langitan & Lawn, 1969) that the fracture load is more nearly proportional to R, at least for small radius spheres, and this apparent breakdown of the Hertzian analysis is known as the Auerbach law.

As discussed by Langitan & Lawn (1969) two schools of thought have evolved to explain the Hertzian fracture problem. The first suggests that since fracture is initiated from surface flaws, the fracture load is governed by the size and also location of the flaws. The second contends that the fracture criterion is governed by a balance between the strain energy released, and the surface energy gained by the growing cone-crack. In this second theory fracture still originates at a surface flaw, but the statistical distribution of the flaws does not control the fracture load and lead to the Auerbach Law behaviour. A short summary of the Auerbach law problem has recently been given by Harrison & Wilks (1978).

5.4 The Sliding Sharp Indentor

The exact formulation of this problem is complex, but has recently been attempted by Swain (1979). He employs the solution developed by Mindlin (1936), in which an elastic half space is subjected to a static normal, as well as a horizontal point load.

The stress components are found to be of the form

$$\sigma_{ij} = \left(\frac{P}{\pi a^2}\right)\left[\lambda F_{ij}(\phi)_v + \mu F_{ij}(\phi)_h\right]_\nu \quad ,$$

where $F_{ij}(\phi)_v$ and $F_{ij}(\phi)_h$ are the vertical and horizontal components respectively, and λ, μ are the relative ratios of these

two components. In a sliding friction test $\lambda = 1$, and μ is the coefficient of friction. The resultant of the vertical and horizontal forces is inclined at an angle to the vertical. Swain's calculation showed that there was an asymmetry in the stress field as compared to the static sharp indentor with a strong tensile component in the wake of the sliding contact.

5.4.1 Crack Geometry Generated by the Sliding Sharp Indentor

We may expect the median crack, and lateral cracks to translate along with the sliding indentor (Swain 1979). The lateral cracks are formed on unloading. Fig.5.6 shows the crack geometry.

Utilizing a fracture mechanics formulation Swain (1979) was able to find expressions for the depth of median cracks and the width of lateral cracks. Concerning the rates of material removal, the lateral cracks are more important since they intersect the surface and cause spalling and chipping. The lateral cracks are an unloading phenomenon and are driven by the residual stress field about the scratch (or indentation). The formation of the residual stress is caused by the inelastic deformation zone about the scratch particle, in an exactly analogous manner to the static sharp indentor.

The stress intensity factor for a lateral crack is given as

$$K = \beta H \pi^{\frac{1}{2}} a (c^2 - a^2)^{\frac{1}{2}} c^{-3/2} \qquad (5.8)$$

where c is the width of the crack and (a) the scratch half width (see Fig.5.6). β is related to the residual stress about the scratch and typically has values of $\frac{1}{15} - \frac{1}{30}$.

If we now assume that $c \gg a$, then eqn.(5.8) reduces to

$$K = \beta H \pi^{\frac{1}{2}} a c^{-\frac{1}{2}} \quad .$$

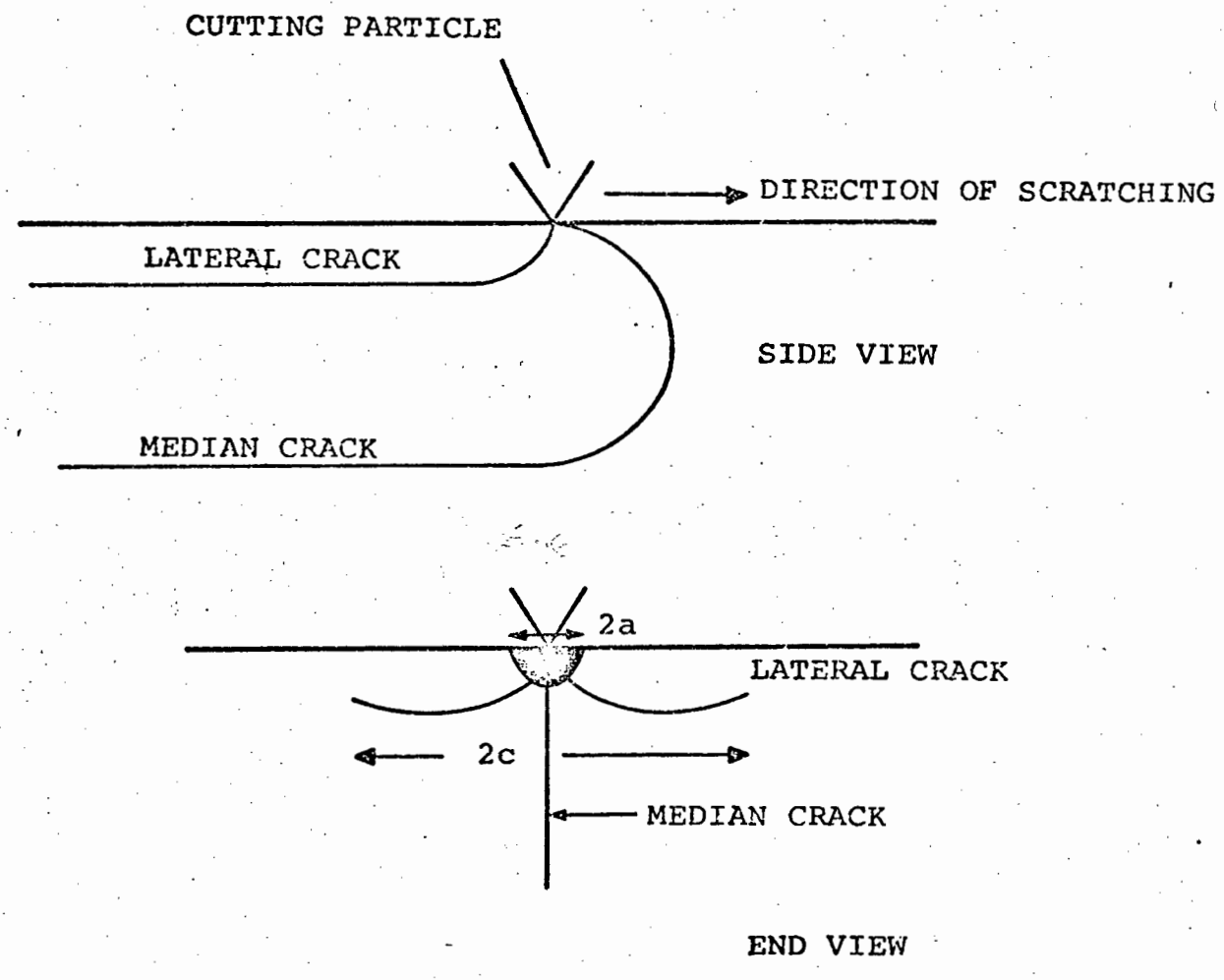

Fig.5.6 Crack geometry expected from a sliding sharp particle. The median and lateral cracks translate along with the particle. (after: Swain, 1979).

Since $K^2 = G_c E = 2\gamma E$ for a brittle solid, then

$$K^2 = \frac{\beta^2 H^2 \pi a^2}{c} = 2\gamma E$$

$$\text{or} \quad c = \frac{\beta^2 H^2 \pi a^2}{2\gamma E} \tag{5.9}$$

For scratching with a Vickers pyramid a further simplification can be made if we relate the scratch half width (a) to the hardness of the solid, viz. $H \approx P/2a^2$. Thus eqn. (5.9) becomes

$$c = \frac{\beta^2 H \pi P}{4\gamma E} \quad . \tag{5.10}$$

Applying this result to α-quartz, for values of $\beta \approx \frac{1}{15}$ (Swain, 1979), $H \approx 10^{10}$ N m^{-2}, $E \approx 10^{11}$ N m^{-2}, γ(theoretical) ≈ 4 Jm^{-2}, and a vertical load P = 1N we may calculate a value for $c \approx 87$ μm. Using the accepted experimental value of $\gamma \approx 11$ Jm^{-2} (Hartley & Wilshaw, 1973) then $c \approx 32$ μm, and the ratio of lateral crack width to scratch half width is equal to ≈ 4.5. Swain (1979) presents results on scratching on quartz, and gives a c/a ratio of 5.

5.5 The Sliding Blunt Indentor

The stress field created by a circular sliding contact has been analysed by Hamilton and Goodman (1966) and it is found that the form of the static Hertzian stress field is changed by the sliding contact. The most important feature is that the surface tensile stress at the rear of the contact is enhanced to a value:

$$\sigma_{(dy)} = \frac{3P}{2\pi a^2} \left\{ \tfrac{1}{3}(1 - 2\nu) + \mu\pi\left(\frac{4 + \nu}{8}\right) \right\} \tag{5.11}$$

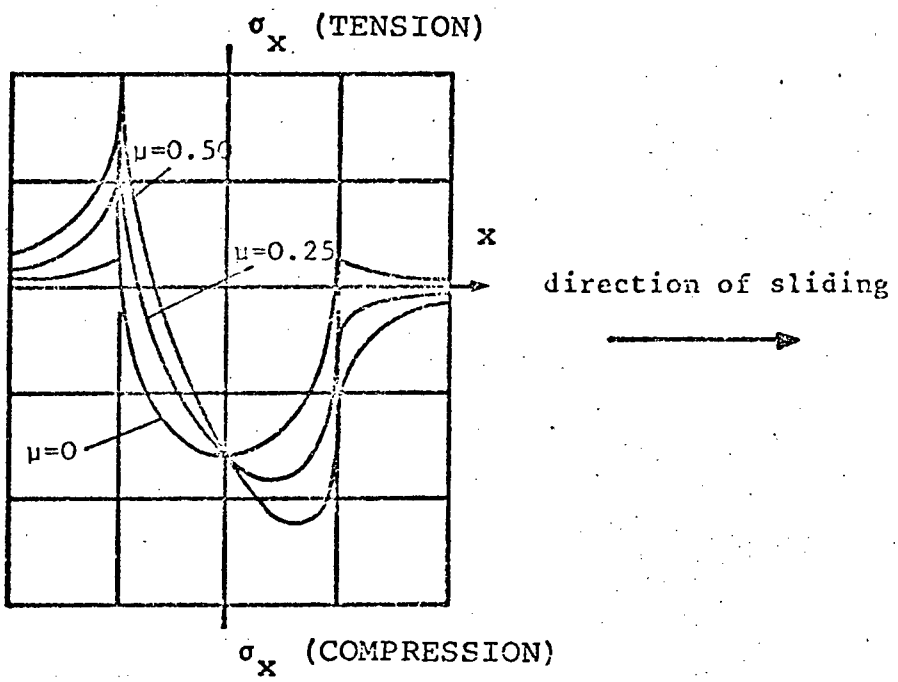

Fig.5.7 The surface stress caused by a sliding circular contact for different values of the coefficient of friction μ. (after: Hamilton and Goodman, 1966).

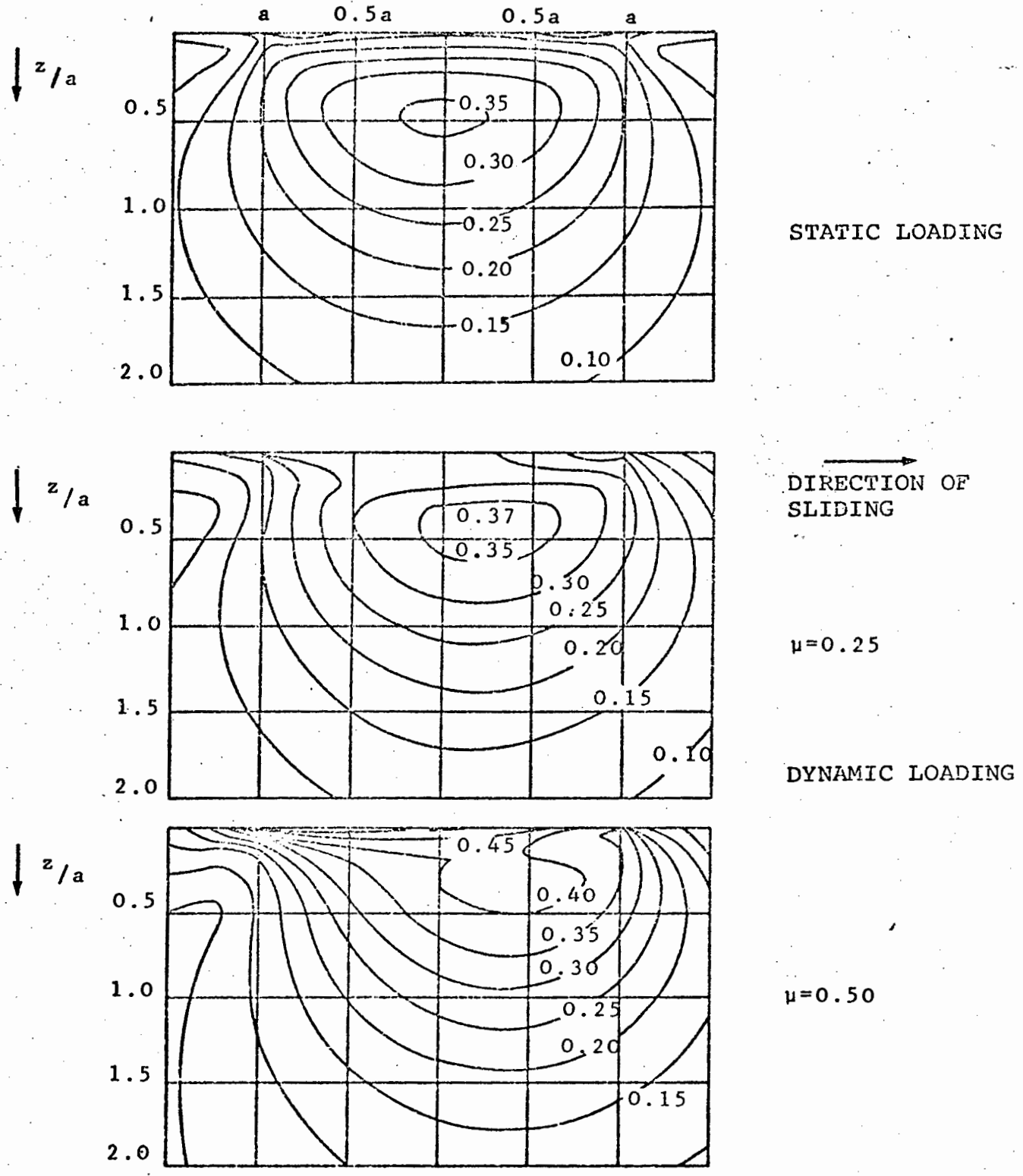

Fig.5.8 Comparison of the sub-surface maximum shear stress for the static and sliding Hertzian contact. The shear stress is in units of P_o/τ. (after: Hamilton and Goodman, 1966).

where P is the normal load, a the radius of contact and μ the coefficient of friction.

This should be compared to the tensile stress at the edge of the static circle of contact

$$\sigma_{(st)} = \frac{1-2\nu}{2} \cdot \frac{P}{\pi a^2} \qquad (5.12)$$

The dramatic manner in which the tensile stresses are enhanced is shown in Fig.5.7. The dependence on μ is clearly depicted. Also notice how the tensile force at the contact front changes to a compressive force for $\mu \geq 0.079$.

Fig.5.8 compares the shear stress distribution for the static and dynamic indentors. In the dynamic case the position of maximum shear stress ($z = 0.5a$ for $\mu = 0$) shifts upwards and slightly forwards, increases, and is eventually located at the surface for $\mu \approx 0.27$.

5.5.1 Crack Geometry Generated by the Sliding Blunt Indentor

Because of the enhanced tensile field at the rear of the contact, it is found that the critical load to form a cone-crack is considerably reduced over the static value of P_o. A spherical indentor sliding over a surface will produce a series of 'horseshoe-shaped' cone cracks (corresponding to the regions of maximum tensile stress) along the track.

If we assume that the material fails at the same tensile stress regardless of whether or not the contact is static or dynamic we may find the ratios of the static P_{st} and dynamic P_{dy} failure loads (Gilroy & Hirst, 1969).

Since $a^3 = \frac{4K'PR}{3E}$

where R is the radius of the sphere and K' has been defined previously (eqn.5.5), then for the static indentor

$$a_{st} = P_{st}^{\frac{1}{3}}/N^{\frac{1}{3}}$$

and for the sliding indentor

$$a_{dy} = P_{dy}^{\frac{1}{3}}/N^{\frac{1}{3}}$$

where $N = 3E/4K'R$ and is independent of the static or sliding formulation. Substituting a_{st} for a in eqn.5.12 we find

$$\sigma_{st} = \frac{1 - 2\nu}{2} \frac{P_{st}^{\frac{1}{3}}}{\pi} N^{\frac{2}{3}} \qquad (5.13)$$

and, likewise, a_{dy} for a in eqn.(5.11)

$$\sigma_{dy} = \frac{3}{2} \frac{P_{dy}^{\frac{1}{3}} N^{\frac{2}{3}}}{\pi} \left\{\frac{1}{3}(1 - 2\nu + \mu\pi \left(\frac{4 + \nu}{8}\right)\right\} . \qquad (5.14)$$

Equating (5.13) and (5.14) we obtain the relationship

$$\frac{P_{st}}{P_{dy}} = \left\{1 + \frac{3\pi}{8} \frac{(4 + \nu)}{(1 - 2\nu)} \cdot \mu\right\}^3 \qquad (5.15)$$

P_{st} is the load to produce the cone crack, and P_{dy} the load to produce an equivalent crack during sliding.

In a complex fracture mechanics analysis of cone-crack formation under a sliding blunt indentor Lawn (1967) derived the expression

$$\frac{P_{st}}{P_{dy}} = (1 + 15.5\ \mu)^3 /0.2 \qquad (5.16)$$

where μ is the coefficient of friction.

For a coefficient of friction $\mu = 0.1$ and $\nu = \frac{1}{3}$ we may calculate that the Gilroy & Hirst analysis (eq.5.15) yields a ratio $P_{st}/P_{dy} \approx 20$ while the Lawn analysis (eq.5.16) predicts $P_{st}/P_{dy} \approx 83$.

The central factor in the Lawn (1967) analysis is the validity of the Auerbach law (P_c α indentor radius R) (see section 5.3.2) and the range of μ for which this law holds. Lawn predicted that the Auerbach law would break down at a coefficient of friction $\approx$ 0.02. For values of μ greater than this the critical fracture load is proportional to the square of the radius and hence considerably reduced.

On the other hand, Gilroy & Hirst (1969), find experimental evidence from sliding tests on glass that the reduction in the fracture load is more in agreement with the Hamilton-Goodman formula (eqn.(5.15)) than with Lawn's prediction, eqn. (5.16). The Hamilton-Goodman formula assumes the fracture load αR^2, and Gilroy & Hirst suggest that the critical coefficient of friction when the Auerbach law breaks down is greater than Lawn's by at least an order of magnitude. Even when μ = 0.5 and the Auerbach law does not hold, the fracture load is several times larger than that predicted by Lawn.

Despite the disagreement between Gilroy and Hirst (1969) and Lawn (1967) on the exact value of this reduction in fracture load, it is clear that fracture is considerably favoured in the sliding situation. This suggests that the extent of surface damage by a sliding contact may be considerably reduced by using a lubricant which lowers the coefficient of friction, and hence suppresses the tendency to form partial cone-cracks.

CHAPTER 6

SPECIMEN PREPARATION AND ANALYTICAL TECHNIQUES

6.1 Introduction

The success and repeatability of most experiments in materials science relies upon well-prepared specimens. In particular, single crystals should be accurately orientated with respect to the crystallographic axes, and in the majority of cases the surface must be very finely polished, with little or no residual work-hardened layer. This is a particularly important consideration in our experiments on the microhardness and scratch deformation of quartz, where the extent of the imposed deformation lies within approximately five microns of the surface. Poor specimen preparation would in these cases probably inform us of the role of sub-surface damage, and mask the intrinsic crystal response.

The standard observational techniques of transmission electron microscopy (TEM), scanning electron microscopy (SEM), X-ray diffraction topography(XRT) and optical microscopy, likewise depend upon a good surface finish if detail is not to be lost or obscured. Surface damage introduces large strain fields which are readily detected, both in TEM and XRT, although the former technique is not as strain-sensitive as the X-ray method. In the optical microscopy of transparent materials a finely-polished surface enables the extent of sub-surface microcracking to be clearly detected. It is thus apparent that the combined use of the above techniques, coupled with well-defined specimen preparation, represents a powerful analytical system for determining both the brittle and plastic response of quartz under a variety of conditions.

6.2 Starting Material

Single crystal synthetic quartz was used exclusively in this work. Lumbered Z-growth bars were obtained from STC (Pty) Ltd., Johannesburg. This material was a standard commercial grade quartz, with a 'water' content in the range 50-150 ppm H/Si. No analysis could be made for other trace impurities. Specimens were also obtained in the form of pre-orientated platelets, with approximate dimensions 10 mm × 10 mm × 1 mm. These crystals had a ground finish. The three principal cuts of quartz were obtained (X-cut, Y-cut, Z-cut), machined to a tolerance of $\pm 2^{o}$. Some of these crystals were checked with a back reflection X-ray technique and found to be within specification.

6.3 Specimen Preparation

In this section the grinding and polishing procedure for quartz is discussed. No claims to a definitive programme are made, since many variations and combination of grits, polishing preparations and techniques are possible. The procedure that has been finally adopted evolved over the course of this study and was found to be well-suited to the available equipment. It represents the fastest means of obtaining a well-polished sample with extremely consistent results.

Because a large number of samples were used it was found advantageous to prepare several specimens together, by mounting them on a brass block and grinding and then polishing them together. A suitable mounting glue was a low melting-point thermo-plastic cement, which was alcohol soluble. Specimens were removed from the block by heating, and the excess glue dissolved from the surface.

6.3.1 Grinding Procedure

A range of SiC grits was available (grades 120-1000), and these were used for all the grinding (fast material removal) operations. The grinding plattern was a cast iron wheel, to which a SiC/water slurry was added. The specimens were ground by hand, using a figure-of-eight motion. Care was taken not to apply too much hand pressure since this tended to break up the edges of the specimens.

In cases where it was required to remove a considerable quantity of material (as for example preparation of the thin transmission electron microscope specimens) the full range of grits was used. However, when the as-received quartz specimens were to be polished, a preliminary grinding operation with 600 and 1000 grit was found to be advantageous prior to the polishing stage. The 1000 grit was especially useful since this shortened considerably the time required to polish the specimens.

The SiC/water slurry was frequently replenished, and the specimens carefully cleaned in an ultrasonic bath between each change of grit.

6.3.2 Polishing Procedure

Both diamond paste (various grit size 6 μm - 0.1 μm) and an alumina ($A\ell_2O_3$)/water slurry were tried. It was found that with the use of diamond paste polishing took a longer time and gave less consistent results than with the alumina slurry. Accordingly, alumina was chosen as the most satisfactory medium for polishing quartz. Two particle sizes were used; for rough polishing 0.3 μm α-alumina and for fine polishing 0.05 μm γ-alumina.

The polishing suspensions incorporating CeO and CrO particle (size 0.05 μm) were also used. It was found that these compounds also produced good results, although no

quantitative information is available on their relative merits over the alumina suspensions from this work. It was noted, however, that the polishing time could be reduced. Often, after the final polish using 0.05 μm alumina, an additional five minutes polish with 0.50 μm CeO/CrO was made.

A satisfactory polishing cloth was one which is usually designated for diamond paste polishing (DP cloth) with an oil lubricant. Despite the use of alumina/water these cloths had a long life, and were used throughout.

Both hand and automatic polishing techniques were used. Manual polishing was accomplished by mounting DP cloths on a glass plate and polishing in a figure-of-eight motion. The time to achieve a good finish was surprisingly short. Approximately twenty minutes for rough polishing and thirty minutes for the final polishing produced an excellent surface finish. It has the obvious disadvantage that the operation must be attended to all the time, but in view of the good results this was judged extremely worthwhile.

An attempt was made to speed up the operation by mounting the DP cloths on a Knuth rotary polisher. In this case between five to ten minutes was sufficient to produce a good surface. To prevent directional polishing the block was rotated in a direction opposite to that of the wheel.

Also tried were a Buehler Vibromet vibratory polisher and a Metals Research Ltd multipol machine. Polishing on the Vibromet was accomplished by mounting the specimens on special aluminium blocks and adding weights, determined by trial and error, to produce a satisfactory rotary operation. However, this technique takes a relatively long time (polishing at each stage for up to 72 hours). One curious feature which was observed on several occasions was extensive surface crazing. Frequently the outer surface areas of the specimens were not polished, while the inner areas had a good finish. Because of the variability of this technique it was used infrequently. We should note, however, that if polishing conditions are correct a large number of specimens (up to 24) can be polished at one time, and the surface finish is excellent with no strain hardening in the surface layers.

The multipol machine can only polish one block of specimens at a time, and gave excellent results. Polishing times were of the order of several hours. To ensure that the pad did not dry out a water drip feed was attached. The usual speed of rotation was 1 rps and the applied pressure approximately 300 gm./cm^2.

After the polishing operation the specimens were ultrasonically cleaned in alcohol, and then etched in a 10% HF acid solution for 10 minutes with continuous agitation. The specimens were then thoroughly washed in water, alcohol and ether using the ultrasonic cleaner, dried by air blowing, and stored in a dessicator until required for use.

6.3.3 Preparation of TEM Specimens

Problems were encountered in preparing the thin transmission electron microscopy specimens. The specimen must be only $\approx$ 30 μm - 50 μm thick, with a polished surface, prior to ion-beam thinning. It was found that the specimens wore unevenly during grinding so that only the edges of the specimen were thin enough. To overcome this problem the specimens were mounted onto a brass block which fitted snugly into an outer annular ring. In this way the specimen surface remained parallel to the grinding wheel at all times, and even wear resulted.

6.4 Ion-beam Thinning

A notable advance in the understanding of the deformation of ceramic materials was made when ion-beam thinning facilities became available for preparing specimens for the transmission electron microscope. Prior to this it was customary to crush the material and hope that thin flakes were produced, and also that the crushing operation did not introduce

any additional damage. The ion-beam thinning technique ensures that relatively large electron transparent areas of refractory crystals can be prepared.

The method operates by allowing a narrow beam of charged Ar^+ ions, accelerated to 5-6 KeV to impinge upon a sample at a grazing angle of incidence ($\approx 20^\circ$), (Fig.6.1). The ions erode the surface layers of the sample which becomes dished and eventually holes through. To prevent any directional etching the specimen is slowly rotated. Conditions for the most efficient thinning must be determined by trial and error for each material. It should be noted that the fastest material removal rate may not correspond to the production of large thin areas, since a thin tapering edge is required. At large angles of incidence of the beam (which corresponds to high rates of material removal) the ideal taper will not be produced.

Two ion-beam thinning units were used, both manufactured by Ion-Tech Ltd., Teddington, U.K. A conventional 'Microlap' thinner (Fig.6.2) with twin electrodes was originally the instrument of choice. The operating conditions to produce good electron transparent areas in quartz were as follows:

Accelerating voltage	:	5-6 KeV
Beam Current	:	50 μA
Angle of incidence	:	20°
Erosion rate	:	0.5 μm/hr/beam

It was found advantageous to continue thinning for 60 minutes after 'hole-through' at a reduced angle of incidence ($\approx 10\text{-}15^\circ$). The thinning rate is relatively slow and with a specimen starting thickness of 50 μm, up to two days thinning were required. Results were, however, excellent and extremely consistent.

A fast single beam 'Microrapid' thinner (Fig.6.3) was also employed. The specimen is positioned closer to the ion-source, which is water cooled and can operate at higher beam

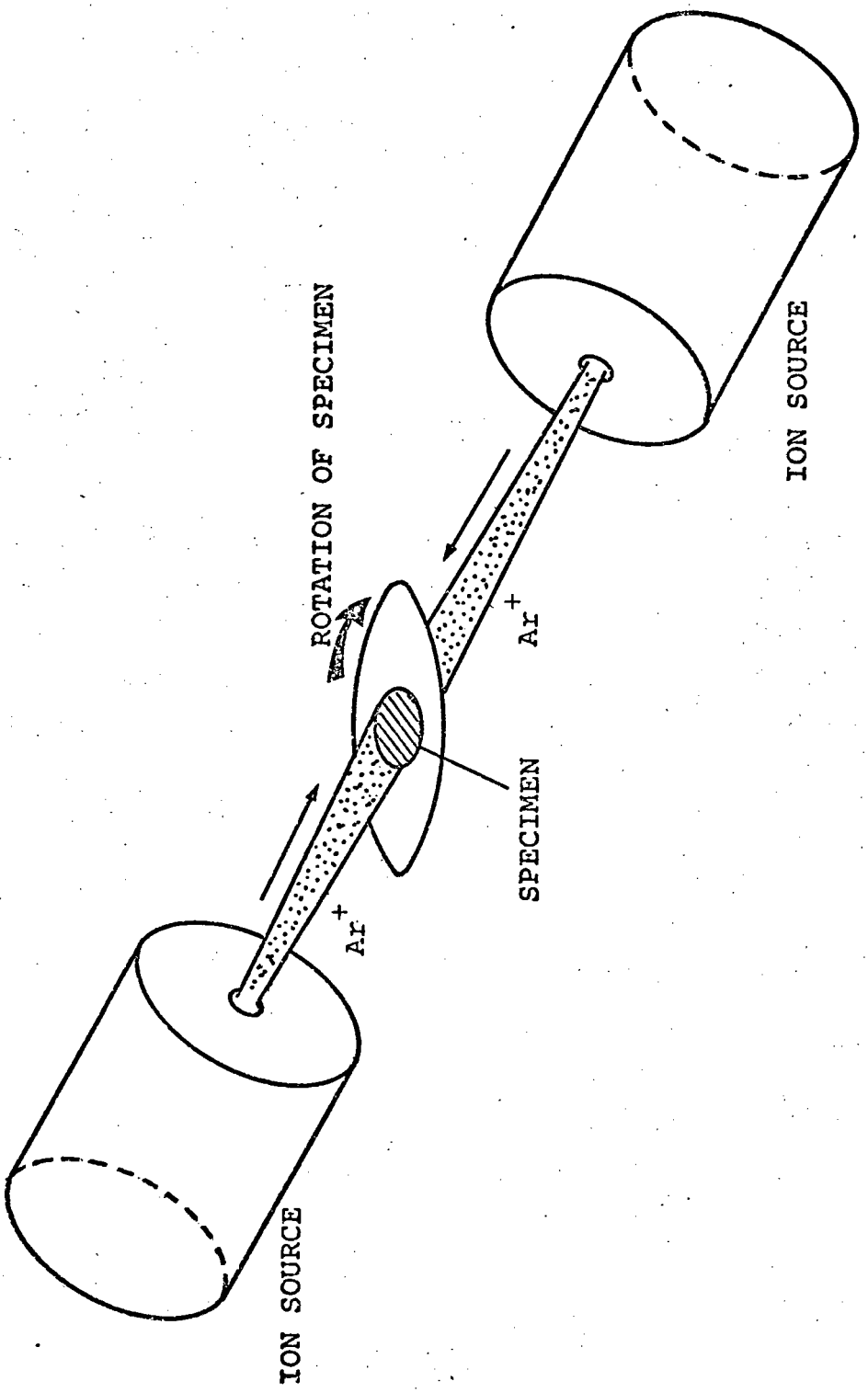

Fig.6.1 Principle of ion-beam thinning.

Fig.6.2 'Microlap' ion-beam thinning unit.

I=ION SOURCE
S=SPECIMEN HOLDER

Fig.6.3 'Microrapid' ion-beam thinning unit.

currents. Specimen holders were available at 0°, 35° and 90° incidence. The 90° (normal) incidence was found to be unsatisfactory since the quartz sample shattered under the action of the ion-beam. Presumably the erosion rate is so high that considerable heat is produced, which cannot be dissippated quickly enough. Thus the quartz fractures by thermal shock. However, the 35° holder gave good results, and no shattering occurred. Typical operating conditions were:

Accelerating voltage	:	5-6 KeV
Beam current	:	200 μA
Erosion rate	:	100 μm/hr

Large electron transparent areas were formed with the Microrapid. Even thick (≈ 100 μm) specimens could be thinned with success.

6.5 Transmission Electron Microscopy

The experimental confirmation of the de Broglie hypothesis, which states that material particles (e.g. electrons, protons) have an associated wave nature (wavelength $\lambda = h/p$), coupled with the fact that electrons can be focussed by suitably orientated magnetic fields, laid the groundwork for the development of transmission electron microscopy (TEM). The first transmission microscope was constructed by Knoll & Ruskin in 1931, and commercial instruments became available in 1939. In principle the optics of the TEM is similar to optical microscopy, in that condenser and objective lenses are used to form an image of a specimen.

Compared to the wavelength of light, the de Broglie wavelength of electrons is exceedingly small. The relativistic de Broglie wavelength, λ, is given by the relationship

$$\lambda = \frac{h}{[2m_o eE(1 + eE/2m_o c^2)]^{\frac{1}{2}}} \quad .$$

h is Planck's constant, m_o the rest mass of the electron, e the electronic charge, and E the accelerating voltage. Electrons accelerated to 100 KeV have λ = 0.037 Å, while at 1000 KeV, λ = 0.0087 Å. These values of wavelength are several orders of magnitude smaller than X-ray photons of crystallographic interest.

In common with X-ray diffraction, the electron beam produces a diffraction pattern when it passes through a specimen. This pattern reflects the symmetry of the crystal lattice.

Since electrons can be readily focussed (unlike X-rays) it is possible to utilize information contained in the diffracted beams to obtain an image of the crystal structure at high magnification. The phenomenon of diffraction involves the establishment of a coherent phase relationship from a periodic structure (crystal lattice). Any deviation from periodicity will accordingly result in a loss of coherence, and a change in diffracting conditions. Since dislocations introduce atomic displacements away from equilibrium positions the loss of coherency produces images of dislocations in crystals.

To understand image contrast quantitatively it was found necessary to develop a 'dynamical' theory, which is able to describe this amplitude of the transmitted and diffracted beams at various depths in the crystal. We shall not describe this theory in detail, but merely note several important results that are of importance in understanding image contrast.

The central equations of the dynamical theory are of differential form and known as the Darwin-Howie-Whelan equations. These are expressions linking the amplitude of the transmitted beam (ϕ_o), and diffracted beam (ϕ_g); as a function of depth z, through the crystal. They are of the form

$$\frac{d\phi_o}{dz} = \frac{i\pi}{\xi_o}\phi_o + \frac{i\pi}{\xi_g}\phi_g \exp(2\pi i \underline{s} z) \qquad (6.1)$$

$$\frac{d\phi_g}{dz} = \frac{i\pi}{\xi_o}\phi_o \exp(-2\pi i \underline{s} z) + \frac{i\pi}{\xi_g}\phi_g \quad . \qquad (6.2)$$

$\underline{s}$ is the deviation from the Bragg angle and ξ_o, ξ_g are constants.

Dynamical theory shows that the energy of the incident beam continually changes from the incident beam direction to the diffracted beam direction at periodic distances thoughout the crystal depth. The distance from the position where all the energy is in the incident beam to where it is again in the incident beam is termed the extinction distance ξ_g and given by

$$\xi_g = \frac{\pi\Omega\cos\theta_B}{\lambda f(\theta)} \quad .$$

$f(\theta)$ is the atomic scattering amplitude, θ_B the Bragg angle, Ω the unit cell volume and λ the electron wavelength.

If we have a wedge-shaped specimen it is possible to observe variations in intensity over the viewing area because of this interchange of energy. Consider we have two-beam conditions and we focus our attention on the bright-field image (i.e. the image formed by the transmitted beam). We shall find a dark fringe (going in from the specimen edge) at $\frac{1}{2}\xi_g$, $1\frac{1}{2}\xi_g$ ... ; this corresponds to energy being wholly in the diffracted beam. If absorption is allowed for the fringes eventually become damped out in thick regions of the sample. The fringes are useful in electron microscopy because a knowledge of ξ_g enables the thickness of the specimen to be determined.

The use of the dynamical theory enables images of defects to be theoretically determined for a particular set of diffraction conditions. The theory is complex, but well documented (e.g. Hirsch et al. 1965). In particular it enables the experimenter to adjust his diffraction conditions to perform quantitative analysis and to be certain that there are no abnormal conditions.

6.5.1 Dislocation Contrast

Dislocation can be of either pure edge or pure screw character, or some combination of edge and screw (mixed dislocation). In an elastically isotropic material the displacement fields due to these dislocations are:

(a) Edge dislocation

$$R_{EDGE} = \frac{1}{2\pi}\left[\underline{b}\,\frac{\sin 2\theta}{4(1-\nu)} + (\underline{b}\times\underline{u})\left(\frac{1-2\nu}{2(1-\nu)}\right)\ln r + \frac{\cos 2\theta}{4(1-\nu)}\right]$$

u is a unit vector in the direction of the dislocation, $\underline{b}$ the Burgess vector, ν Poissons ratio and r,θ polar coordinates of R relative to the dislocation core.

(b) Screw dislocation

$$R_{SCREW} = \underline{b}\,\theta/2\pi .$$

(c) Mixed dislocation

$$R_{mixed} = \frac{1}{2\pi}\left[\underline{b}\,\theta + \underline{b}\,\frac{\sin 2\theta}{4(1-\nu)} + (\underline{b}\times\underline{u})\left(\frac{1-2\nu}{2(1-\nu)}\right)\ln r + \frac{\cos 2\theta}{4(1-\nu)}\right].$$

In the presence of a strain field $\underline{R}$ the dynamical equations (6.1) and (6.2) become:

$$\frac{d\phi_o}{dz} = \frac{i\pi\phi_o}{\xi_o} + \frac{i\pi}{\xi_g}\,\phi_g \exp(2\pi i\underline{s}z + 2\pi i\ \underline{g}\cdot\underline{R})$$

$$\frac{d\phi_g}{dz} = \frac{i\pi\phi_o}{\xi_g} \exp(-2\pi i\underline{s}z - 2\pi i\ \underline{g}\cdot\underline{R}) + \frac{i\pi}{\xi_o}\,\phi_g$$

The distortion of the lattice causes a phase factor $\exp(-i\alpha)$,

where $\alpha = 2\pi\ \underline{g}\cdot\underline{R}$, to be superimposed upon the normal scattering process for the perfect crystal. This results in enhanced deflection of energy into the diffracted beam close to the dislocation line. Thus a bright field image of a dislocation in a specimen will show a general light background with dark regions arising from the enhanced diffraction into the diffracted beam. It is now possible to understand how a dislocation can be analysed in the TEM and a value of the relevant Burgers vector obtained. Inserting the value of R for a screw dislocation, (Burgers vector $\underline{b}$), into the expression for $\alpha = 2\pi g\cdot\underline{R}$ we find that $\alpha = \underline{g}\cdot\underline{b}\ \theta$. The contrast from this dislocation will depend on the value of $\underline{g}\cdot\underline{b}$. For a perfect dislocation this is either 1 or 0, corresponding to enhanced diffraction or no diffraction respectively. $\underline{g}\cdot\underline{b} = 0$ is the invisibility criterion of the screw dislocation.

For an edge dislocation, Burgers vector $\underline{b}$, contrast depends on both $\underline{g}\cdot\underline{b}$, and $\underline{g}\cdot\underline{b} \times \underline{u}$. Thus even though $\underline{g}\cdot\underline{b} = 0$, $\underline{g}\cdot\underline{b} \times \underline{u}$ may be none-zero and contrast will be observed. However, contrast from the $\underline{g}\cdot\underline{b} \times \underline{u} \neq 0$ term is generally small, and $\underline{g}\cdot\underline{b} = 0$ can safely be used for edge dislocations. Calculation shows that a dislocation will show no residual contrast for $\underline{g}\cdot\underline{b} \times \underline{u} \lesssim 0.64$. For both $\underline{g}\cdot\underline{b}$ and $\underline{g}\cdot\underline{b} \times \underline{u}$ to be zero the electron beam must lie in the plane containing both the dislocation line and Burgers vector. To analyse unambiguously the dislocation Burgers vector it is necessary to obtain two $\underline{g}\cdot\underline{b} = 0$ conditions. Since $\underline{b}$ is common to both the reflecting planes, $\underline{b}$ must be the zone axis of the two planes.

In elasticity anisotropic materials, the $\underline{g}\cdot\underline{b} = 0$ criterion is often inapplicable because lattice planes perpendicular to the reflecting planes are distorted. Under these conditions it is often necessary to perform an image matching analysis. The experimental dislocation image is compared to a computed image with known values of $\underline{g}$, $\underline{u}$ and $\underline{b}$. In this way $\underline{b}$ can be determined for particular diffracting conditions.

The effect of a large value of ξ_g is to make the dislocation image diffuse. There is also the additional problem that very small deviations from the exact Bragg angle can put

the dislocation out of contrast, and care must be exercised in obtaining precise diffracting conditions.

6.5.2 Burgers Vector Determination of Dislocations in Quartz

Because of the low atomic scattering factor of oxygen, quartz has large values of extinction distance, ξ_g. This results in diffuse images, making Burgers vector analysis difficult. Values of ξ_g for various reflections in quartz at accelerating voltages of 100 KeV and 1000 KeV are shown in Table 6.1. Since quartz is elastically anisotropic the $\underline{g}\cdot\underline{b} \times \underline{u}$ invisibility criterion may not be fulfilled.

Dislocation images in quartz have been computer simulated by McCormick (1976) for 120 KeV electrons as a function of $\underline{b}$, $\underline{u}$, beam direction, foil normal, and deviation from the exact Bragg angle. His principal conclusions from the simulation were that the anisotropy of quartz had a negligible effect on dislocation images. Computed images with $\underline{g}\cdot\underline{b} = 0$ and $\underline{g}\cdot\underline{b} \times u \neq 0$ indicated that an edge dislocation would be effectively out of contrast if $g\cdot b \times u < 0.64$. The same was true of mixed dislocations.

However, McCormick drew attention to the narrow angular reflecting range for ξ_g large, so that dislocations in quartz could easily be put out of contrast for small deviations from the exact Bragg condition. As an example, for 120 KeV electrons diffracting from the (0003) plane ξ_g = 10 171 Å and a misorientation of $\approx 0.06^{\circ}$ could put the dislocations out of contrast.

Quartz is known to undergo severe electron beam degradation in the electron beam. This means that there is often not enough time to take a full set of micrographs from one particular area to analyse the dislocation Burgers vectors. Often the value of $\underline{b}$ must be determined by inference.

TABLE 6.1

VALUES OF EXTINCTION DISTANCE (ξ_g) FOR THE VARIOUS REFLECTIONS IN α-QUARTZ AT 100 KeV AND 1000 KeV

Plane	ξ_g (100 KeV) Å	ξ_g (1000 KeV) Å
$(10\bar{1}1)$	1050	1784
$(\bar{1}011)$	680	1158
$\{10\bar{1}0\}$	1530	2601
$\{11\bar{2}0\}$	1720	2924
$\{11\bar{2}2\}$	1520	2435
(0003)	9530	16230

[Values of ξ_g calaculated from the 120 KeV data of Ardell, A.J., Christie, J.M., McCormick, J.W., Philos. Mag., 29, 1399-1411, (1974].

6.6 X-ray Diffraction Topography

Complementary to transmission electron microscopy is an X-ray diffraction technique which allows the examination of (low density) dislocation structures in thick single crystals. This technique is known as X-ray diffraction topography (Lang, 1959) and since it inception has provided a considerable body of useful data on defect structures. The ability of X-rays of crystallographic wavelength ($\lambda \approx 0.5$ Å - 1.5 Å) to penetrate to large depths ($\approx$ 1 mm) ensures that the dislocation structures observed are typical of the bulk crystal, and this overcomes the restriction of TEM, where the maximum electron beam penetration of material of low atomic number is $\approx$ 1-2 μm at 1000 KeV.

An additional bonus of the X-ray technique if the ability to perform in-situ experiments (deformation tests, heat treatments, oxidation, etc.), on the same specimen, and without the problem of introducing additional damage into the specimen. Furthermore the equipment needed to perform these experiments is simpler than that required for the restricted space of TEM stages.

However, the relative complexity of the basic experimental procedure, long exposure and film processing times and perhaps the more important fact that resolution is low and limited to the examination of crystals with dislocation densities $\lesssim 10^{8} m^{-2}$ has not been conducive to the widespread use of X-ray diffraction topography. The restriction to specimens of single crystals has also been a limiting factor. Regardless of these problems many worthwhile and significant research studies have been undertaken with X-ray topography as a central theme, and the review by Tanner (1976) should be consulted for these applications.

6.6.1 Image Formation in X-ray Diffraction Topography

The mechanism of image formation in X-ray diffraction topography can be understood by referring to Fig.6.4. Assume that the crystal is orientated at the Bragg condition, and that a dislocation line is located at some depth below the surface. The incident beam has a divergence ϕ which is greater than the perfect crystal reflecting range $\Delta\theta$ The perfect crystal reflecting range is the angle over which the crystal accepts an incident beam for the diffraction process; it may simply be visualised as an 'uncertainty' in the Bragg angle θ_B, and typically $\Delta\theta \approx 10^{-5}$ radians (Tanner, 1976). The beam divergence ϕ is $\approx 10^{-4}$ radians, depending on the experimental set-up. At the dislocation line the crystal planes are rotated away from their normal positions. Thus that part of the incident beam which is being diffracted experiences a loss of coherency. The part of the beam which is not being diffracted, but passing straight through the crystal enters the dislocation strain field and may satisfy the Bragg condition. Thus, an excess of beam energy is directed into the diffracted beam and as a result an image (the direct image) of the dislocation can be recorded by a suitable recording medium. Images are also formed by the beam losing coherency (the dynamical and intermediary images), but these have a poor spatial resolution. In most X-ray diffraction topographs it is the direct images which we associate with the dislocation lines in the crystal.

The experimental set-up to achieve defect imaging by X-rays is shown in Fig.6.5. A collimated X-ray beam is incident upon a crystal orientated at the Bragg angle θ_B. A diffracted beam is produced which is detected at a photographic plate. The crystal and plate scan together through the beam and a 'picture' of the crystal can be produced.

The Burgers vectors of dislocations can be determined by diffracting from several sets of crystal planes in sequence. This is similar to the analysis of dislocations in the TEM (Section 6.5.1).

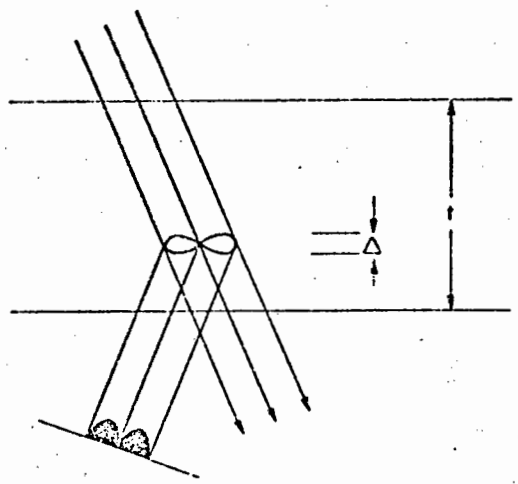

Fig.6.4(a) Cylinders of misorientation around an edge dislocation. The thickness of material having misorientation greater than the perfect crystal range is denoted Δ. The two parts of the image arise from the two lobes of opposite misorientation.

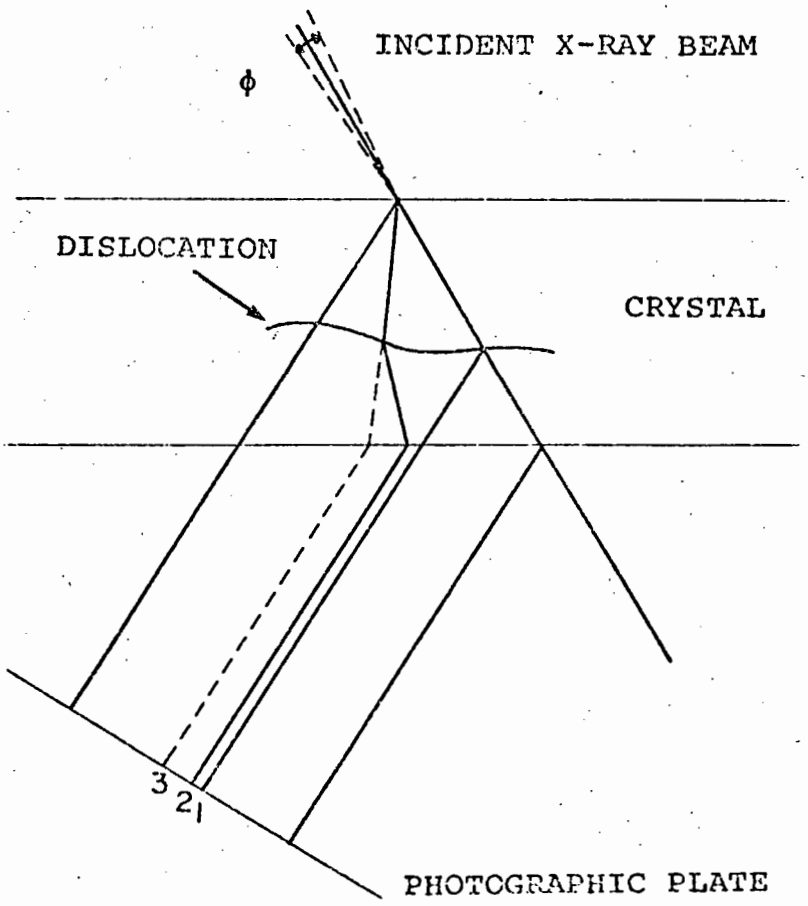

Fig.6.4(b) Formation of the three types of image in topographs: 1, Direct image, 2, Intermediary image, 3, Dynamical image.

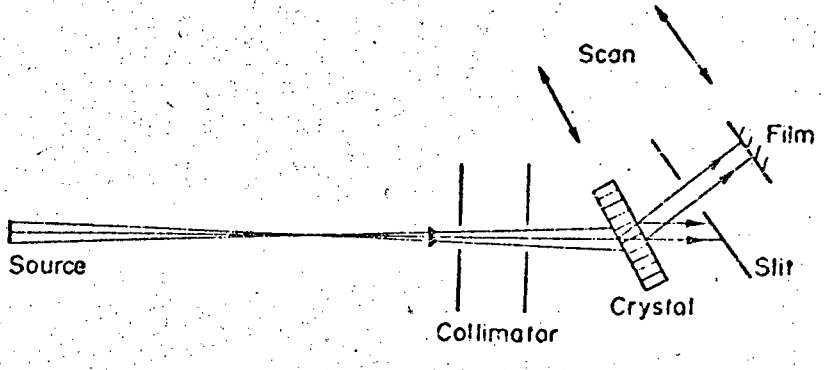

Fig.6.5 Principle of X-ray diffraction topography (Lang's transmission technique).

6.6.2 X-ray Diffraction Topography Image Resolution

There is no magnification on an X-ray topograph and attention must be paid to instrumental resolution. If the projected height of the X-ray source is h, the source to crystal distance L and crystal to photographic plate distance x, then the vertical resolution is given by $\delta = xh/L$. That is, each point in the crystal will be smeared out vertically to a line of length xh/L. In the horizontal plane the most important factor is to ensure that simultaneous diffraction of $K\alpha_1$ and $K\alpha_2$ components of radiation does not occur. If the width of the X-ray source is ω and the divergence slits have a width L_1, then the horizontal divergence of the beam is $(\omega + L_1)/L$. The angular separation of the $K\alpha_1$ and $K\alpha_2$ components must be less than this.

Consider we use an X-ray source height 0.1 mm, projected width 0.1 mm (say a 1 mm wide focus, take-off angle $\approx 5^{\circ}$). For a molybdenum target the intense monochromatic X-ray lines are $K\alpha_1$ ($\lambda = 0.70930$ Å) and $K\alpha_2$ ($\lambda = 0.71359$ Å). Let the source to crystal distance be 50 cm and crystal to plate distance be 1 cm. Thus the vertical resolution is $\delta \approx 2$ μm. If the divergence slits have a width of 0.1 mm, then the beam divergence is $\approx 10^{-4}$ radians. Let the d-spacing of the diffraction planes be 3 Å, so that the $K\alpha_1$ $K\alpha_2$ separation is $\approx 7\ 10^{-4}$ radians. Hence the $K\alpha_1$, $K\alpha_2$ images will not diffract simultaneously, since the beam divergence is less than the $K\alpha_1$ $K\alpha_2$ angular separation.

Since there is no inherent magnification in X-ray topographic imaging the photographic plate must give a good spatial resolution, and nuclear emulsion plates are preferred. However, the small grain size (undeveloped $\approx$ 0.14μm) results in a slow exposure time which is typically several hours per mm of crystal scanned. Developing procedures are time consuming as well. To obtain a uniform development processing is performed at low temperatures ($\approx 0^{\circ}$ C). Consequently it takes approximately three hours to process the emulsion plate.

In this work a JEOL microfocus X-ray generator (type JMX - 8H) was used. The focal spot size was 1mm x 0.1mm. The X-ray topography camera was an Elliott Bros., Bristol Lang camera (Fig.6.6). The focus-crystal distance was ≈50cm, and the divergence slit had a width of 100μm. At a 5^{o} take-off angle the effective focal spot size is 0.1mm x 0.1mm. For a crystal-plate distance of 1cm the vertical resolution was ≈2μm. Ilford L4 plates were used, and exposures times for quartz were ≈4hours/mm, with Mo $K\alpha_1$ radiation. The processing schedule for the nuclear emulsion plates are given in Table 6.2.

C=COLLIMATOR

D=DIFFRACTED BEAM SLIT

P=PHOTOGRAPHIC PLATE

T=TRAVERSE STAGE

X=CRYSTAL

A=DETECTOR

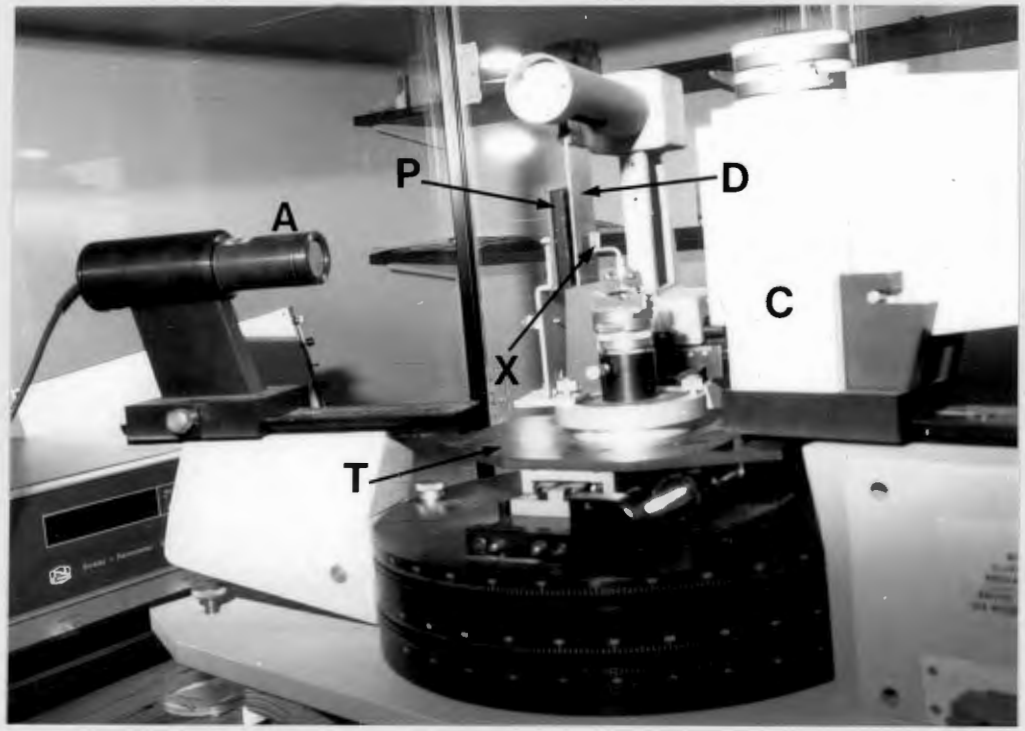

Fig.6.6 The Lang X-ray topography camera.

Table 6.2: Processing times for Ilford L4 emulsions

Thickness	25 μm
Soak in filtered deionized water	10 mins.
Develop (1:3 D19b to deionized water)	15-30 mins.
Stop (1% glacial acetic acid in deionized water)	10 mins.
Fix (300g sodium thiosulphate 30g sodium bisulphite in 1 litre deionized water)	30 mins.
Wash (filtered tap-water)	2 hrs.

CHAPTER 7

DISLOCATION CLIMB DEFORMATION IN QUARTZ

7.1 Introduction

A crystal grain of quartz stressed parallel to c[0001] does not experience any resolved shear stress on the easy slip systems ([0001]{11$\bar{2}$0} or {10$\bar{1}$0} and <11$\bar{2}$0>(0001) or {10$\bar{1}$0}), and strain cannot be accommodated by slip, if slip systems involving dislocations with Burgers vectors of the type a + c <11$\bar{2}$3> do not operate. However the climb of an initially nucleated system of a and c dislocations enables deformation to proceed (Groves and Kelly, 1969).

The success of the Nabarro (1967) diffusional creep model in predicting the creep rates of solids that can only deform if climb makes a direct contribution to the total strain, prompted Ball & White (1978) to propose that the deformation of quartzite in the earth's crust may also occur by the climb motion of dislocations, and accordingly utilised the Nabarro equation to predict likely strain rates.

Consider we have a quartz crystal stressed along c[0001]. This configuration is schematically represented in Fig.7.1. Dislocations with Burgers vectors a <11$\bar{2}$0> provide the necessary sources and sinks of vacancies for the climb of the c [0001] dislocations.

Recalling the Nabarro equation:

$$\dot{\varepsilon} = \frac{Db\sigma^3}{\pi kTG^2} / \ell n \left(\frac{4G}{\pi\sigma}\right) ,$$

and inserting typical values of b ($\approx 5.10^{-10}$ m), of shear modulus G ($\approx$ 33 GPa) for quartz, at typical crustal-temperatures (800K) and stress (10 MPa) we can calculate a strain rate $\dot{\varepsilon} \approx 4.5\ 10^{9} D\ s^{-1}$. D is unfortunately not clearly defined,

since the activation energy Q_c for diffusional creep is believed to depend on the lattice water concentration and hence may not correlate with that of oxygen ion diffusion, which is the slowest moving species and hence rate determining. A general expression for D has been derived by White (1976) and is equal to $5.10^{-18}\exp(-Q_c/KT)$. Ball & White (1978) utilize an average value of Q_c(0.87 eV) and hence:

$$D(800K) = 1.55\ 10^{-23}\ m^2s^{-1} ,$$

resulting in a strain rate of $2.5\ 10^{-14}\ s^{-1}$. Such a value is reported to be similar to that obtained by other methods of estimating crustal strain rates. A climb mechanism can thus make the essential contribution to rock deformation under creep conditions.

It is instructive to see if this model can be tested under laboratory conditions of stress and strain rate. Applying the same procedure as above, at stress levels ~ 500 MPa and temperatures ~ 773K we can show that the strain rate under these testing conditions is $\approx 4.5\ 10^{-9}s^{-1}$. At 600 MPa and 1173K, $\dot{\varepsilon} \approx 4\ 10^{-7}s^{-1}$. This is well within the capabilities of conventional slow testing apparatus provided due care is taken.

7.2 Experimental Methods

A single crystal of Z-growth commercial grade synthetic quartz was used in these experiments. The water water content of this grade of material is in the range 50 - 150 ppm H/Si, and is consequently relatively 'dry'. Lang X-ray diffraction topographs were taken of a 0.5 mm thick basal slice of this crystal and the measured grown-in dislocation density was $\approx 10^7\ m^{-2}$.

The orientation of the crystal was checked by a Laue back reflection X-ray photograph, and cylindrical specimens, 20 mm in length and 6 mm diameter were cored with the [0001] axes aligned accurately along the cylindrical stress axis. The end faces were ground flat and parallel, while the cylindrical surface was left in the as-cored stated.

Deformation of the crystals was performed in a solid-medium Griggs machine. This is a piston cylinder device capable of attaining confining pressures of up to 15 Kb and temperatures of about 1600K at constant strain rates ranging from 10^{-4} to $10^{-9}s^{-1}$. The maximum differential stress attainable is 45 Kb.

The sample assembly is shown in Fig.7.2. This consists of a muscovite insulator (resting on the base plate) through which the pyrophyllite base and its tungsten carbide core protrude. Above this is the talc confining pressure jacket containing the furnace and specimen. The thermocouple leads pass through the talc jacket and a porcelain rod supports the thermocouple bead next to the specimen. This assembly is then contained in the pressure cylinder, and a copper disc and a lead disc are pressed into the open end of the pressure cylinder.

The furnace comprises a hollow carbon cylinder with an inner talc lining in which the specimen stands. The thermocouple is chromel-alumel. Current flows through the tungsten carbide base in the centre of the pyrophyllite cylinder the carbon jacket (heating the inner talc lining and the specimen) and out through the copper disc into the pressure cylinder. The muscovite insulates the pressure cylinder from the base plate.

The piston assembly is annular consisting of an inner load piston and an outer confining pressure piston. The confining pressure is applied, using a hydraulic ram, to the lead disc and the talc confining pressure jackets. The inner load piston penetrates the lead before impinging on the specimen and axial force is measured with an external load cell.

Some of the problems associated with such a solid-medium apparatus will now be briefly considered.

In the specimen, fairly large thermal gradients exist so that the temperature used in an experiment refers strictly to the temperature pertaining at the middle of the specimen, near the thermocouple bead.

Friction between the pressure cylinder wall and the confining pressure or talc jackets can contribute to disparities between actual confining pressure and the value seen on the gauge. This was minimised by lubricating this interface with a thin layer of high temperature grease. The talc confining pressure medium itself has a finite strength and may not distribute the confining pressure evenly to the specimen.

The middle portions of the specimen undergo far more deformation than the ends, so that meaningful observations are generally restricted to those taken in the middle of the specimen.

For experiments run at strain rates slower than, or equal to, $10^{-4}s^{-1}$ the standard procedure for the Griggs apparatus was used. First, the confining pressure ram is lowered until a very small pressure registers on the gauge. The load piston is lowered until some force shows on the recorder. The confining pressure is then raised slowly to its desired level and the load motor is set for a strain rate of $10^{-4}s^{-1}$ and switched on. Once the load piston has penetrated the lead, the load motor is stopped. The temperature is increased to the desired value, the load motor is set up for the particular strain rate required and a note is made of the reading on the dial gauge (which measures displacement). The load motor is started and the experiment is allowed to procede until the desired displacement is achieved. The displacement is measured at intervals during the run.

To unload the specimen, the motor is run in reverse at $10^{-4}s^{-1}$, and the temperature reduced rapidly to about 500K. When the load pressure and the confining pressure are nearly equal, the confining pressure is allowed to reduce slowly, always maintaining a small axial load on the specimen.

When the confining pressure and load pressure are zero and temperature reduced to ambient, the pressure cylinder was removed and the sample assembly pressed out into a cylindrical teflon mould. This was filled with epoxy, placed in an evacuated bell jar for a few minutes and allowed to set. After the epoxy had set, the sample assembly was removed from the mould and cut lengthways using a diamond saw. The axial strain was calculated from the length of the deformed specimen.

Two experimental conditions were tested:

(a) $T = 973K$, $\dot{\varepsilon} = 10^{-7}s^{-1}$ (code PAL 9)

(b) $T = 773K$, $\dot{\varepsilon} = 10^{-6}s^{-1}$ (code PAL 7)

In both cases a confining pressure of 3Kbar (300 MPa) was applied to the specimen.

After deformation the samples were cut into basal (0001) and longitudinal $\{11\bar{2}0\}$ sections $\approx$ 250 μm thick using an annular diamond saw. Care was taken to ensure that only sections from the centre of the deformed samples were used for the optical and HVEM analysis.

Optical examination was performed by making standard 30 μm thin sections, while HVEM studies were made in an AEI Ltd EM7 equipped with a goniometer stage and anticontamination device. The operating voltage was 1000 KeV in all cases.

7.3 Results

7.3.1 Stress-Strain Relationships

Stress-strain curves were computed from the read-out of displacement and load while the specimens were straining. These are shown in Fig.7.3 for both PAL 7 and PAL 9. It should be emphasized that quantitative data from these curves is difficult to obtain (Lilley, Private Communication). In particular, during long experiments the displacement is not a true linear

function of time, and sometimes large errors can be introduced into the strain axis. Because of the nature of the Griggs machine there is a large axial stress on the specimen at zero strain. In Pal 9 this was 5.2 Kbar, with a differentail stress of 2.2 Kbar, while in PAL 7, the axial stress was 9.1 Kbar with a differential stress of 6.1 Kbar.

A rounded yield point was observed for both specimens; σ_y (PAL 7) $\cong$ 950 MPa and σ_y (PAL 9) $\cong$ 500 MPa, and at 2% strain the flow stress had risen to σ (PAL 7) $\cong$ 1000 MPa and σ (PAL 9) $\cong$ 900 MPa. As the temperature of the α-β transition is raised by 10.6°/Kbar for a stress applied parallel to $\underline{c}$ [0001] under a confining pressure of 3 Kbar (Coe & Paterson, 1969), specimen PAL 9 remained in the β-quartz stability field, while PAL 7 remained in the α-quartz stability field, for the duration of the deformation tests.

7.3.2 Optical Examination

Optical examination of the deformed samples was made after slicing them perpendicular to $[11\bar{2}0]$. Minor fracturing was observed (Fig.7.4), predominantly along the traces of the basal planes. It is thought that this is due to a momentum effect on unloading the specimen after deformation (Gay, Private communication). Although the unloading rate was fairly slow ($10^{-4}s^{-1}$), the stored elastic energy in the system is still released too rapidly and fracturing results. Alternatively this may be an indication of the difficulty of slip and climb at these strain rates.

Standard 30 μm slices of both basal (0001) and longitudinal $(11\bar{2}0)$ sections is transmitted light revealed no deformation features.

An attempt to determine the dislocation density by an etch-pitting technique was not successful, and no pits which could be associated with dislocations were observed in the microscope; the overall appearance was one of general macroscopic etching.

7.3.3 High Voltage Electron Microscopy

Both basal and longitudinal sections were examined in the EM 7 and an analysis of the Burgers vectors of the dislocations was attempted. The foil planes were basal (0001) and longitudinal $(11\bar{2}0)$.

The general appearance of the dislocation structures in both PAL 7 and PAL 9 appears to be consistent with a deformation mechanism in which dislocation climb has been predominant (Fig. 7.5). The structure does not have the knotted appearance of a cold-worked material, nor the angular appearance of a recovered material. Loops are visible and the dislocation segments are curved. There was no significant difference between the dislocation structures and densities of both PAL 7 and PAL 9 and no distinction is made when presenting these results. The dislocation density n was measured by the method due to Ham (1961); random lines were drawn on the micrographs and the number of dislocation line intercepts N counted. If t is the thickness of the foil and L the total length of the drawn lines then

$$n = 2N/Lt \quad .$$

The foil thickness was estimated by counting the number of thickness fringes and knowing ξ_g for the particular reflexion. Because of the high dislocation density and overlapping images a lower estimate of $n = 10^{13}\ m^{-2}$ was obtained for both samples.

Basal (0001) Foils

1. With the beam direction close to [0001] segments of the dislocation network could be made to go out of contrast in turn as different $g = 1\bar{1}00$ type reflexions were used (Figs. 7.6 and 7.7a). The dislocation loops could not be imaged unless the specimen was tilted to a $\langle 1\bar{2}1\bar{3}\rangle$ zone axis and $\underline{g} = 1\bar{1}01$ used (Fig. 7.7b)

2. With the beam parallel to $[1\bar{2}1\bar{3}]$ a limited number of dislocation segments displayed good contrast for $g = 10\bar{1}0$ (Fig.7.8). The loops are out of contrast for this reflexion. All the dislocations and loops were in contrast for $g = 1\bar{1}01$ (Fig.7.9).

Longitudinal $(11\bar{2}0)$ Foils

1. With the beam parallel to the $[01\bar{1}0]$ zone axis, micrographs were taken with $\underline{g} = \bar{2}112$, $\bar{2}100$ and 0003 operating in turn (Fig.7.10). All the dislocations and loops were in good contrast for $\underline{g} = \bar{2}112$ and a marked alignment of loops can be seen along the traces of the basal planes (Fig.7.10a). With $\underline{g} = \bar{2}110$ the loops were out of contrast, while a number of segments crossing the basal plane remain in contrast (Fig.7.10b). With $\underline{g} = 0003$ the long extinction distance renders the contrast diffuse (Fig.7.10c). However, despite this, dislocation images of the loops lying along the basal traces are in contrast, while the dislocation segments are out of contrast. Contrast information is summarized in Table 7.1.

7.4 Discussion

7.4.1 Burgers Vector Analysis

For a climb deformation model to be applicable to this experiment, we may expect a dislocation structure which is consistent with the following:

Basal $\underline{c}[0001]$ vacancy loops

Prismatic $\underline{a}\langle 11\bar{2}0\rangle$ interstitial loops

Little or no evidence for $\underline{a} + \underline{c}$ $\langle 11\bar{2}3\rangle$ glide dislocations.

The 3-fold multiplicity of the {11$\bar{2}$0} planes suggests that expanding $\underline{a}$<11$\bar{2}$0> loops will readily intersect to form a three-dimensional dislocation network, and consequently an ill-defined loop structure. On the basis of this model (Fig.7.11a) predicted micrographs are shown in Fig.7.11b both basal and longitudinal sections.

Employing the $\underline{g}\cdot\underline{b} = 0$ invisibility criterion for the basal sections suggests that the basal loops have $\underline{b} = c$[0001] since [0001] [01$\bar{1}$0] = 0, [0001] [$\bar{1}$100] = 0 and [0001] [10$\bar{1}$0] = 0. For $\underline{g}$ = 1$\bar{1}$01, $\underline{g}\cdot\underline{b} \neq 0$ and basal loops are observed in contrast.

Since only limited numbers of dislocation segments go out of contrast for the different reflexions, several values of $\underline{b}$ exist in the network. If they are $\underline{a}$<11$\bar{2}$0> dislocations then there are the following choices of $\underline{b}$: $\underline{a}$[$\bar{2}$110], $\underline{a}$[$\bar{1}$2$\bar{1}$0] and $\underline{a}$[11$\bar{2}$0]. Values of $\underline{g}\cdot\underline{b}$ are calculated and presented in Table 7.2. We note that each type of $\underline{a}$<11$\bar{2}$0> dislocation should be out of contrast for one of the <01$\bar{1}$0> reflections. This is in agreement with experimental observations.

However, this does not rule out the possibility of <11$\bar{2}$3> dislocation, since they will also go systematically out of contrast for <01$\bar{1}$0> reflections.

For the reflection $\underline{g}$ = 1$\bar{1}$01, the dislocations $\underline{a}$[$\bar{2}$110] and $\underline{a}$[$\bar{1}$2$\bar{1}$0] should be in contrast ($\underline{g}\cdot\underline{b} \neq 0$) while $\underline{a}$[11$\bar{2}$0] out of contrast. Our initial deduction from the micrograph (Fig.7.9a) that all the dislocations are in contrast for $\underline{g}$ = [1$\bar{1}$01] is then mistaken if $\underline{a}$[11$\bar{2}$0] dislocations are present. However, the large number of dislocations in contrast for this reflection, and the overlapping images, is probably responsible for the lack of clear evidence for the out-of-contrast dislocations.

Micrographs taken along the [01$\bar{1}$0] zone axis show dislocation contrast consistent with the above analysis, and resolve the ambiguity of the <11$\bar{2}$3> dislocations. With $\underline{g}$ = 0003 only the loops lying along the basal traces are in contrast. This confirms the choice of b = $\underline{c}$[0001] for these dislocations. Similar confirmation comes from the lack of contrast for these loops with $\underline{g}$ = $\bar{2}$110.

The dislocation segments are in contrast for $\underline{g} = \bar{2}112$ and $\bar{2}110$, while out-of-contrast for $\underline{g} = 0003$, suggesting that $\underline{b} = \langle 11\bar{2}0 \rangle$.

If $\underline{a} + \underline{c}$ $\langle 11\bar{2}3 \rangle$ dislocations were present, good contrast would have been observed for these dislocations with $\underline{g} = 0003$ ($g.b \neq 0$). The observed lack of contrast indicates that $\underline{a} + \underline{c}$ $\langle 11\bar{2}3 \rangle$ are not present.

Although the above analysis is not unambiguous, the evidence suggests that a considerable number of dislocation loops and loop complexes lie on the basal planes of the deformed crystals with $b = \underline{c}[0001]$ normal to their plane. In addition a network of curved dislocations with Burgers vectors of the type $\underline{a}$ $\langle 11\bar{2}0 \rangle$ exists throughout the crystals.

In the absence of optical and TEM experimental evidence for dislocations with $b = \underline{a} + \underline{c}$ $\langle 11\bar{2}3 \rangle$, strain parallel to the compression $\underline{c}$-axis of the crystals must occur by the climb motions of the $\underline{a}$ $\langle 11\bar{2}0 \rangle$ and $\underline{c}[0001]$ dislocations as depicted in the schematic diagrams of Figs.7.1 and 7.11a). Strain will be accomplished by the climb of vacancy loops in the basal planes and the necessary sinks for the interstitial species produced will be the interstitial loops climbing on the various prism planes.

7.4.2 Application of the Nabarro Climb Model

The agreement of the predictions and observations suggests a quantitative examination of the climb model for the particular testing conditions. The expression for the strain rate deduced by Nabarro (1967) has the form:

$$\dot{\varepsilon} = \frac{Db\sigma^3}{\pi kTG^2} / \ln\left(\frac{4G}{\pi\sigma}\right) ,$$

and implicit in its derivation is the relationship, $n = \sigma^2/G^2b^2$, between dislocation density n and stress σ. The substitution of the experimental values of strain rate $\dot{\varepsilon}$ (10^{-6} s^{-1}), stress σ at 2 percent strain ($\approx$1000 MPa), temperature T (773K) and the

accepted values of shear modulus G(= 33 GPa), Burgers vector b(≈ 5A) and Boltzmann's constant k yields a value of the diffusion coefficient of approximately $10^{-22} m^2\ s^{-1}$ and a dislocation density of approximately $10^{15} m^{-2}$. The discrepancy between the measured (~ $10^{13}\ m^{-2}$) and calculated dislocation densities emphasises the difficulty of estimating high densities and may indicate that the theory requires some modification for the exact geometry of the dislocation loops in quartz. The imposed strain rate of $10^{-6}\ s^{-1}$ requires, according to the equation $\dot{\varepsilon} = \underline{b}n\bar{v}$, an average climb velocity $\bar{v}$ of less than 0.2 $\mathring{A}s^{-1}$ and at a strain (ε) of 2 percent these dislocations will have climbed distances, given by $\varepsilon/\underline{b}n$, of up to 4 μm. The diameters of the observed dislocation loops are compatible with this estimate of the upper limit.

The diffusivity must represent the movements of the ionic species through the lattice which control the climb rate of dislocations and hence the experimental strain rate. Data obtained by Baëta and Ashbee (1970) and Hobbs and coworkers (1968, 1972) from similar compression experiments performed on single crystals of quartz along their c axes has been used to calculate D from the Nabarro expression. These values are plotted, together with the present ones, as a function of the reciprocal of testing temperature in Fig.7.12. A least squares analysis on this data was made. A straight line can be fitted which has the equation:

$$D(m^2\ s^{-1}) = 0.8\ 10^{-16} \exp\left(\frac{82KJ}{RT}\right) ,$$

and the slope of this line yields Q_c, the value of the activation energy for diffusional creep in quartz. This experimental value of Q_c(0.85 eV) is similar to the average value assumed by Ball & White (1978). Also plotted on Fig.7.12 are the results of Haul and Dümbgen (1962) for O^{18} diffusion in natural quartz crystals. The tracer activation energy (2.4 eV) is considerably higher than the activation energy for diffusional creep. In fact Q_c more closely approximates to the activation energy for OH^- ion diffusion, found experimentally by White (1971) to be 0.65 eV.

Evidence for this effect of 'water' comes from creep experiments performed on quartz by Ayensu & Ashbee (1977). For testing at T < 900K these authors obtained a value of $Q_c \approx 0.7$ eV in synthetic quartz, and which rose to 1.35 eV for T > 900K. At temperatures > 900K precipitates, assumed to contain water, formed and were visible on electron micrographs. It was proposed by Ayensu & Ashbee that the precipitation of the water effectively denuded the lattice of its potential weakening agent and dislocation slip was correspondingly more difficult. To enable the crystal to continue deforming, the water must now be continuously extracted from the precipitates. Since this will involve the diffusion of oxygen (and silicon) an increased value of Q_c is to be expected. The scatter in the data in the present work does not allow us to clarify if such an increase in activation energy occurs during diffusional creep and considerably more experimental data, preferably on crystal with the same water content, is required. However, we do observe the occasional precipitate during electron microscope examination, (Fig.7.10c).

From the above it can be inferred that the water impurity within the quartz lattice influences the diffusion rate and hence the climb of dislocations. It is not possible, at present, to detail the nature of this influence but the observed hydrolytic weakening phenomenon (Griggs, 1967) must be associated with the increased diffusivity. This increased diffusivity is amply demonstrated by the value of $8 \times 10^{-18} m^2 s^{-1}$ for the diffusion of O^{18} in quartz measured by Choudhury et al. (1965) at 940 K under a pressure of 820 bar of water vapour as compared with the value of $1.3 \times 10^{-22} m^2 s^{-1}$ obtained by Haul and Dümbgen (1962) at 1273 K under 90 torr of pure oxygen. Impurities in other oxide materials (e.g. Al_2O_3) are known to affect the creep deformation parameters (for a review see Mitchell et al. 1979), but an understanding of these effects is complex. It is hoped that over the next few years critical experiments will be performed on quartz to help unravel the dominant effect that impurities have on the deformation properties of this material.

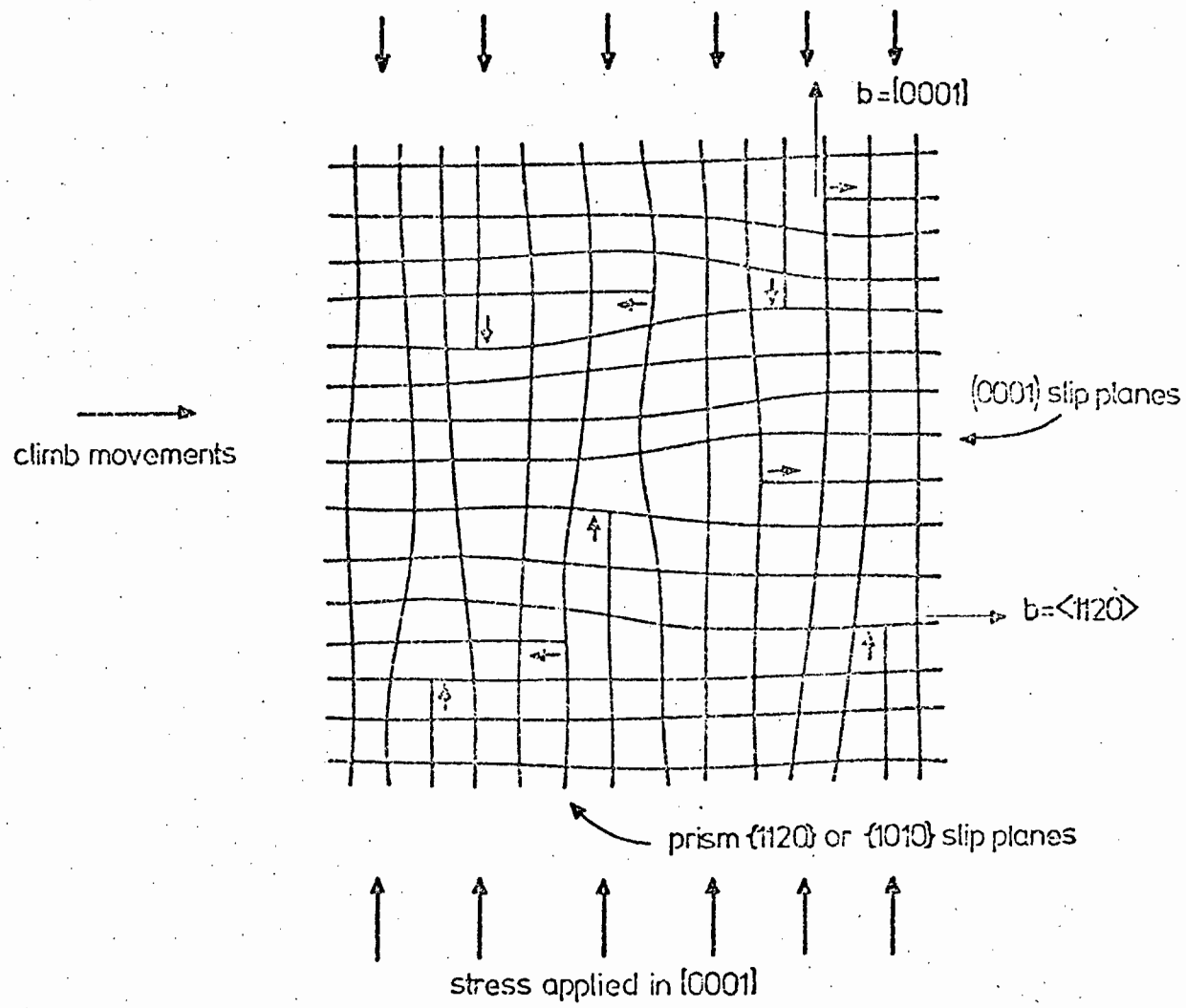

Fig.7.1 A schematic representation of the application of the dislocation climb model of Nabarro to the deformation of a quartz crystal in the [0001] direction.

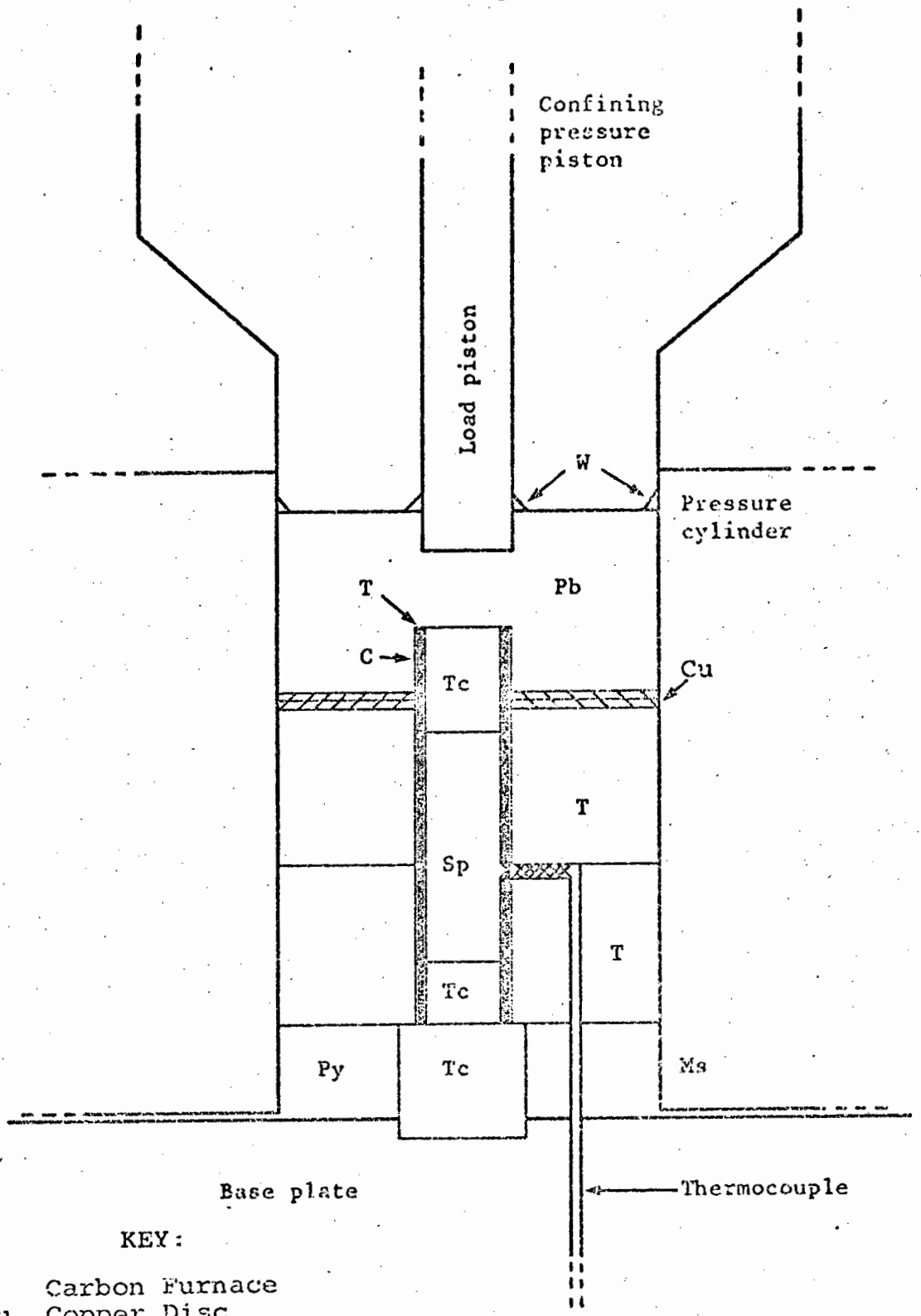

KEY:

C	Carbon Furnace
Cu	Copper Disc
Pb	Lead Disc
W	Anti-extrusion Rings
T	Talc Pressure Jacket
Sp	Specimen
Tc	Tungsten Carbide Core
Py	Pyrophyllite Base
Ms	Muscovite Insulator

Fig.7.2 The Griggs deformation apparatus.

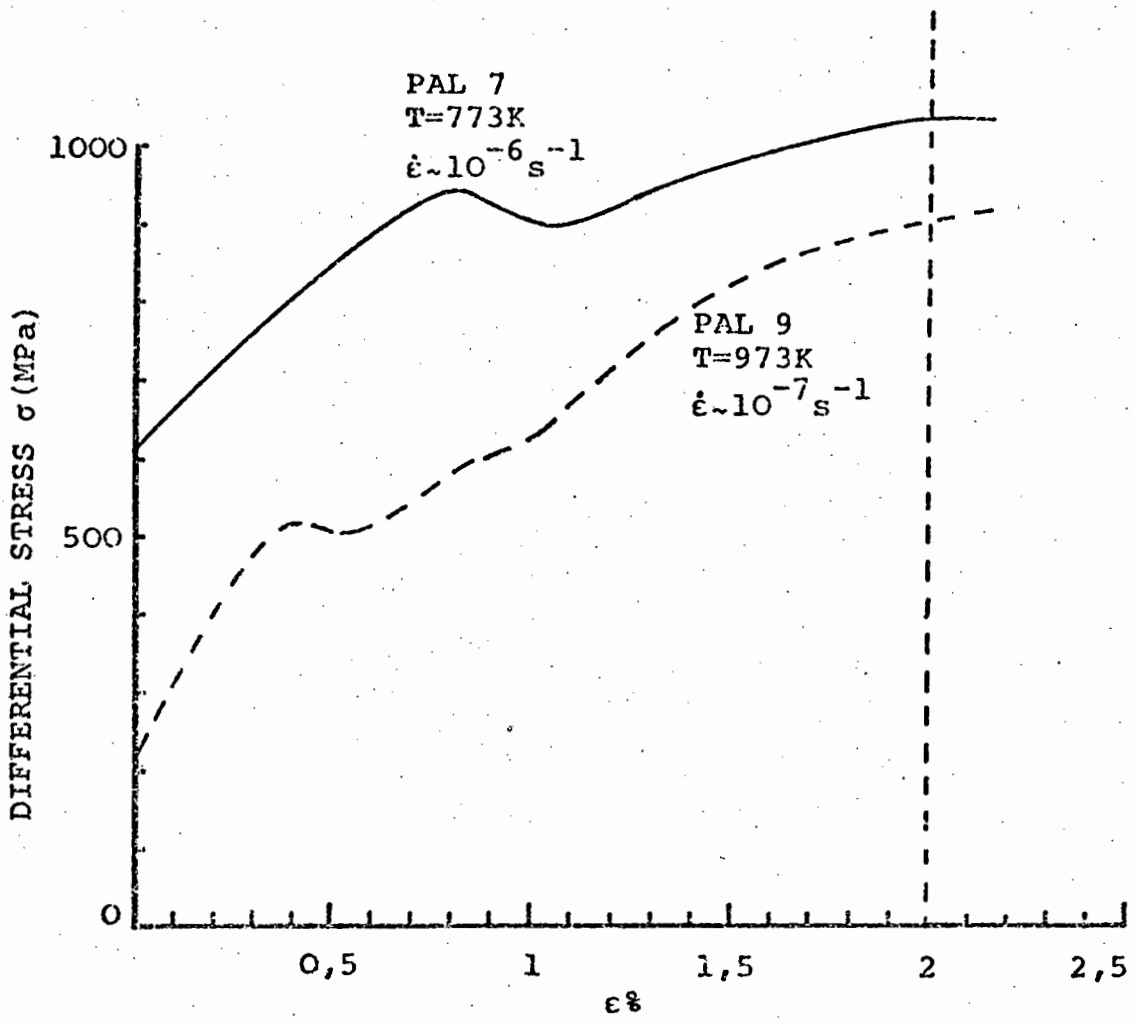

Fig.7.3 Stress-strain curves for deformed quartz crystals, (PAL 7 and PAL 9).

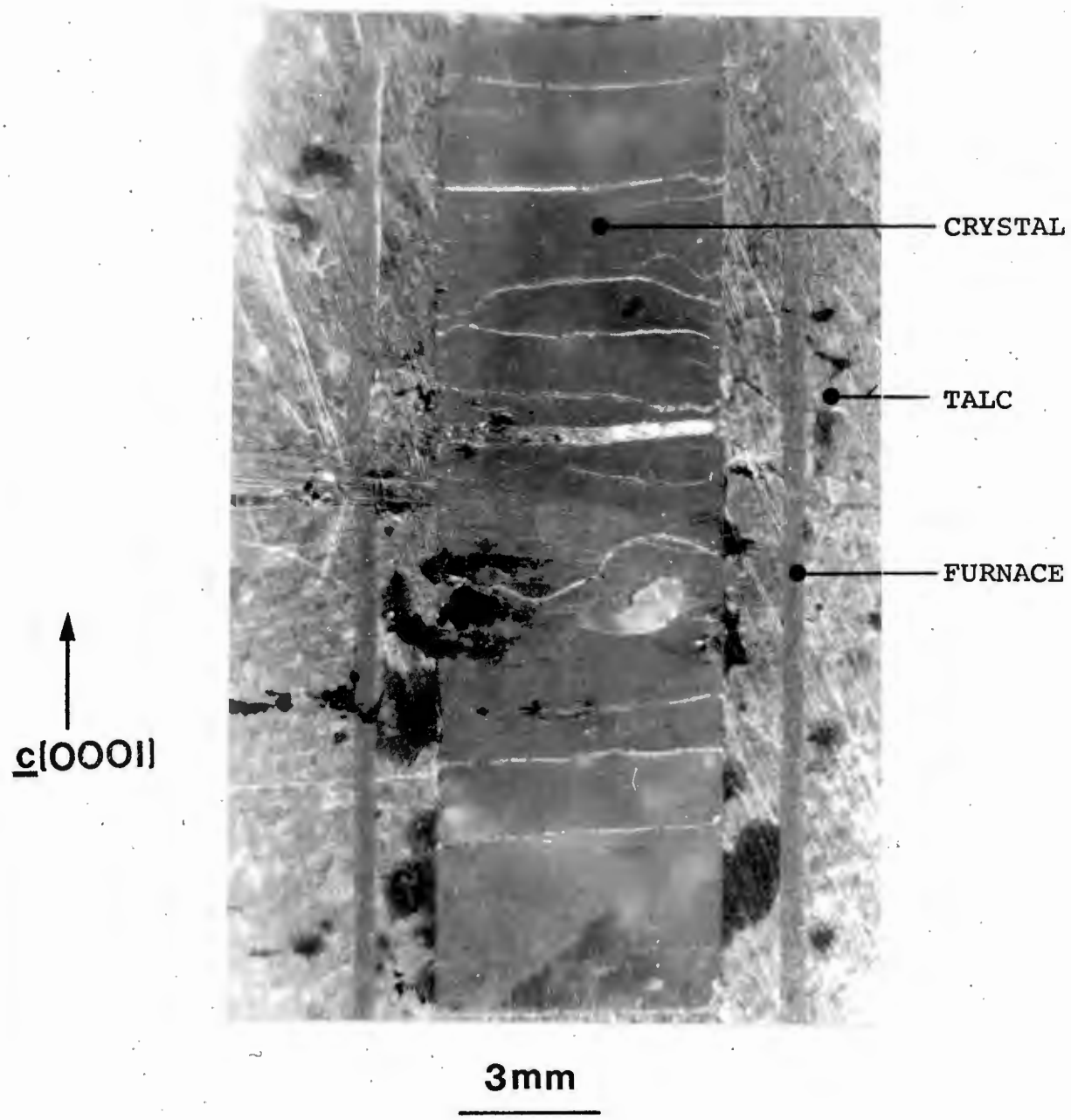

Fig.7.4 Optical micrograph of deformed crystal sliced longitudinally parallel to c [0001] .

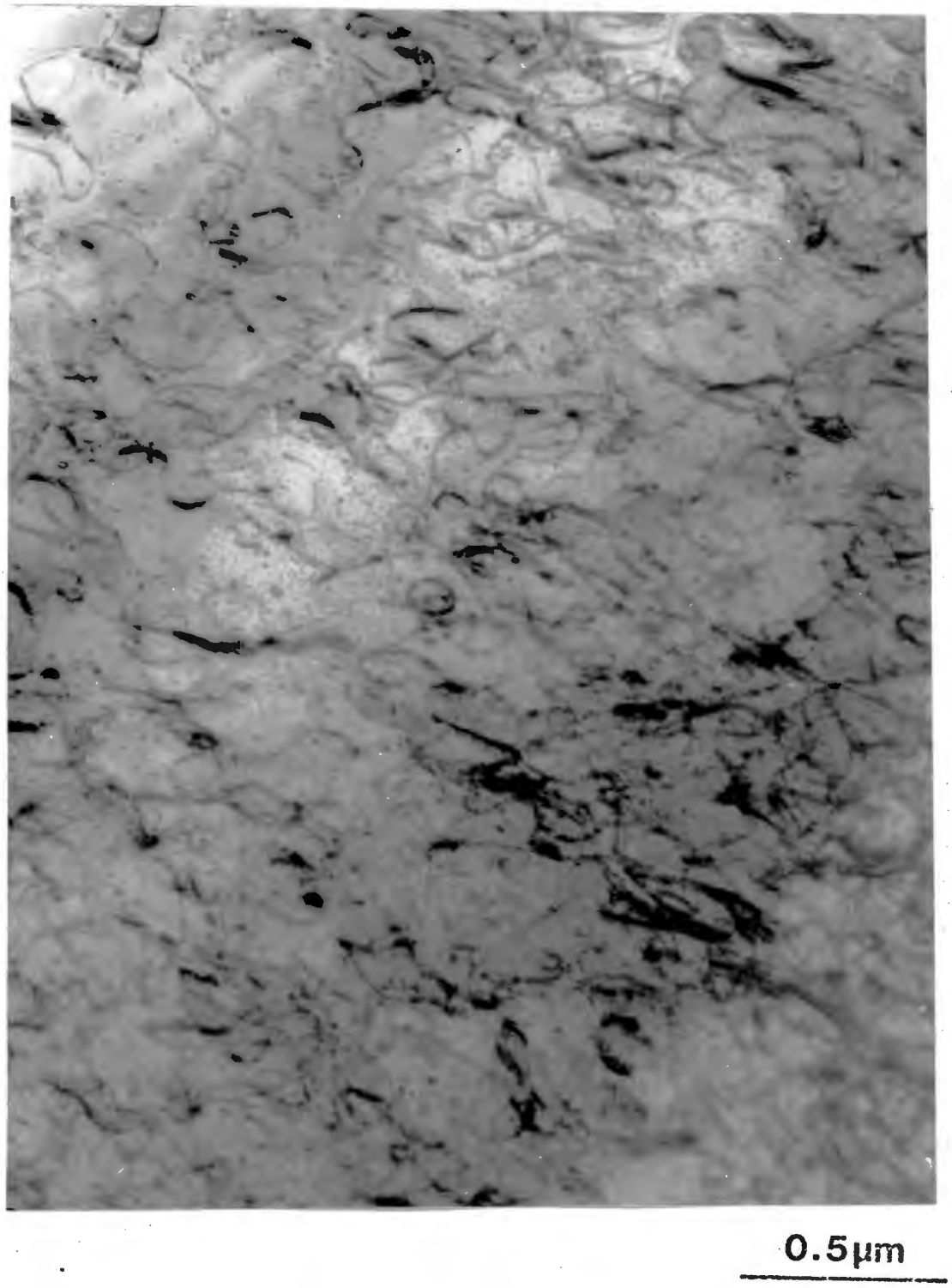

Fig.7.5 Dislocation structure of crystal of quartz compressed parallel to $\underline{c}$[0001] at 973K and $\dot{\varepsilon} \sim 10^{-7} s^{-1}$. Note the numerous dislocation loops and smooth dislocation segments, typical of a climb structure.

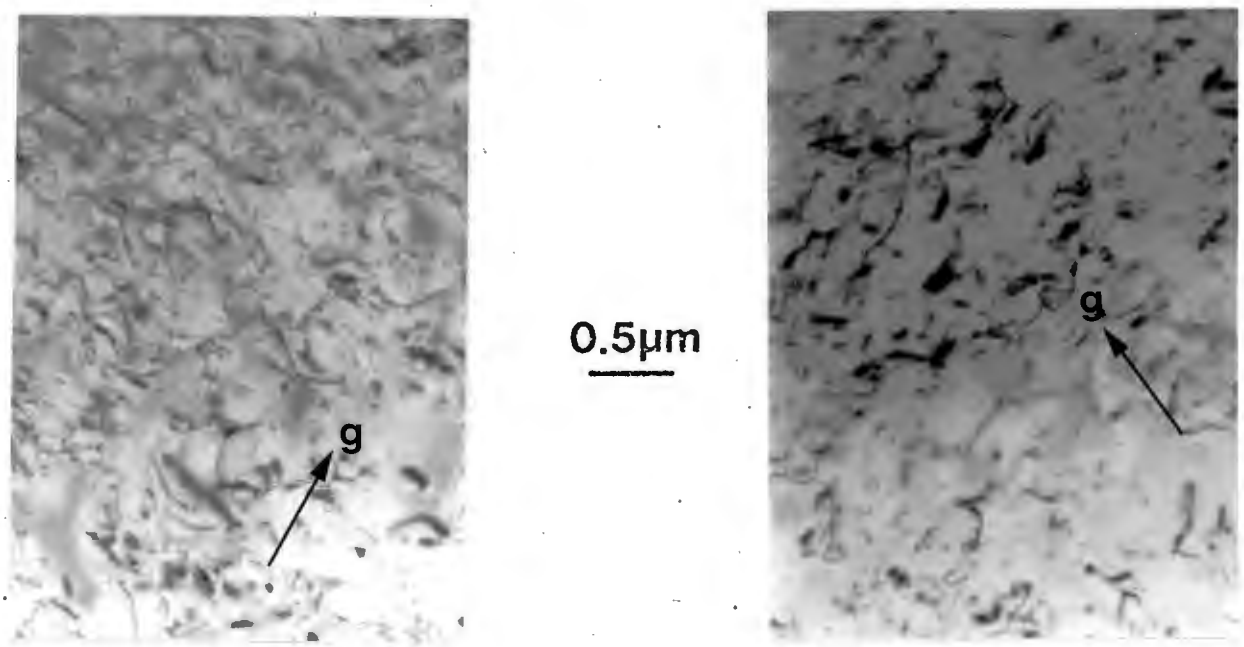

(a) (b)

Fig.7.6 Basal section with beam direction close to [0001]. Same areas imaged with different $[\bar{1}100]$ type reflecting vectors (a) $g=01\bar{1}0$ (b) $g=\bar{1}100$.

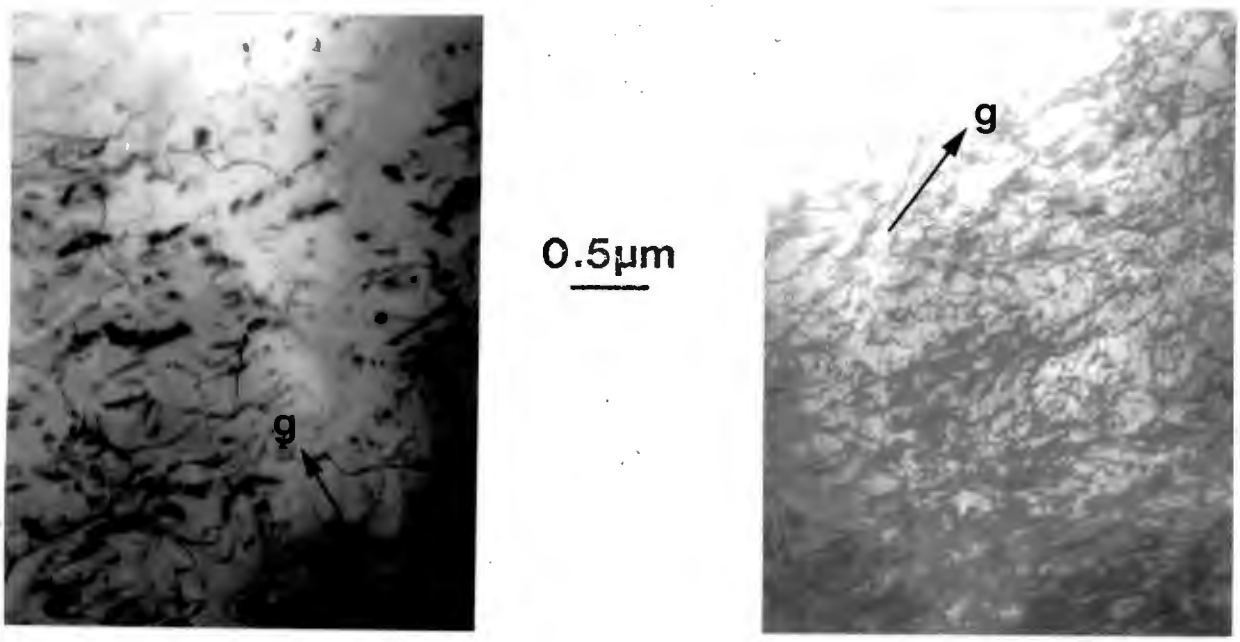

(a) (b)

Fig.7.7 Basal section (a) beam direction close to [0001], $g=1\bar{1}00$; (b) specimen rotated around $[10\bar{1}0]$ to bring beam direction close to $[1\bar{2}13]$ zone axis, $g=1\bar{1}01$.

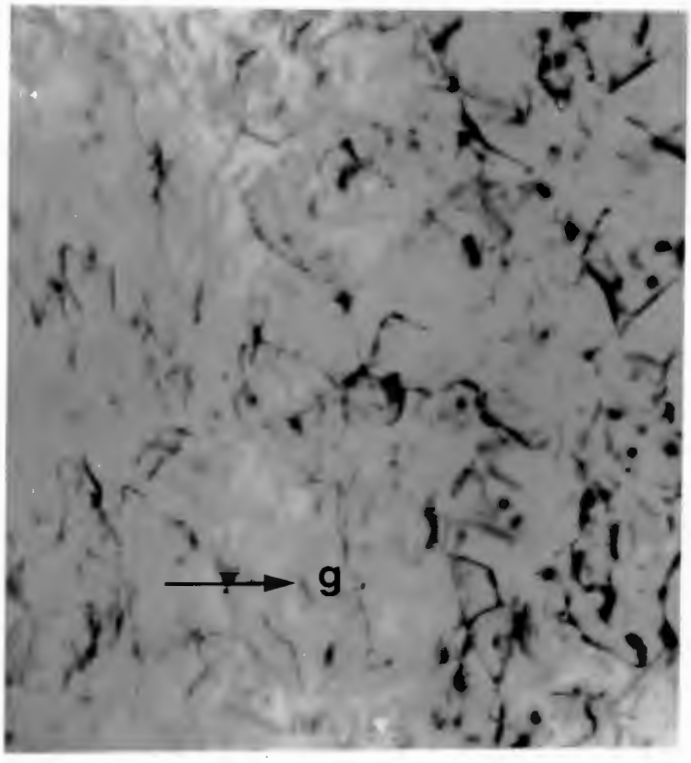

Fig.7.8 Basal section with beam direction close to $[12\bar{1}3]$, $g=10\bar{1}0$.

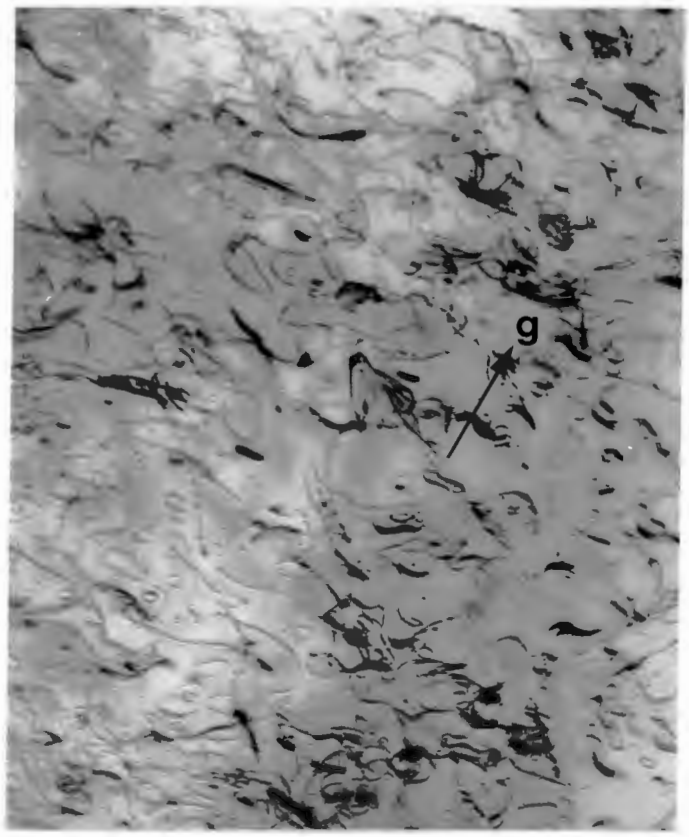

Fig.7.9 Basal section with beam direction close to $[12\bar{1}3]$, $g=1\bar{1}01$.

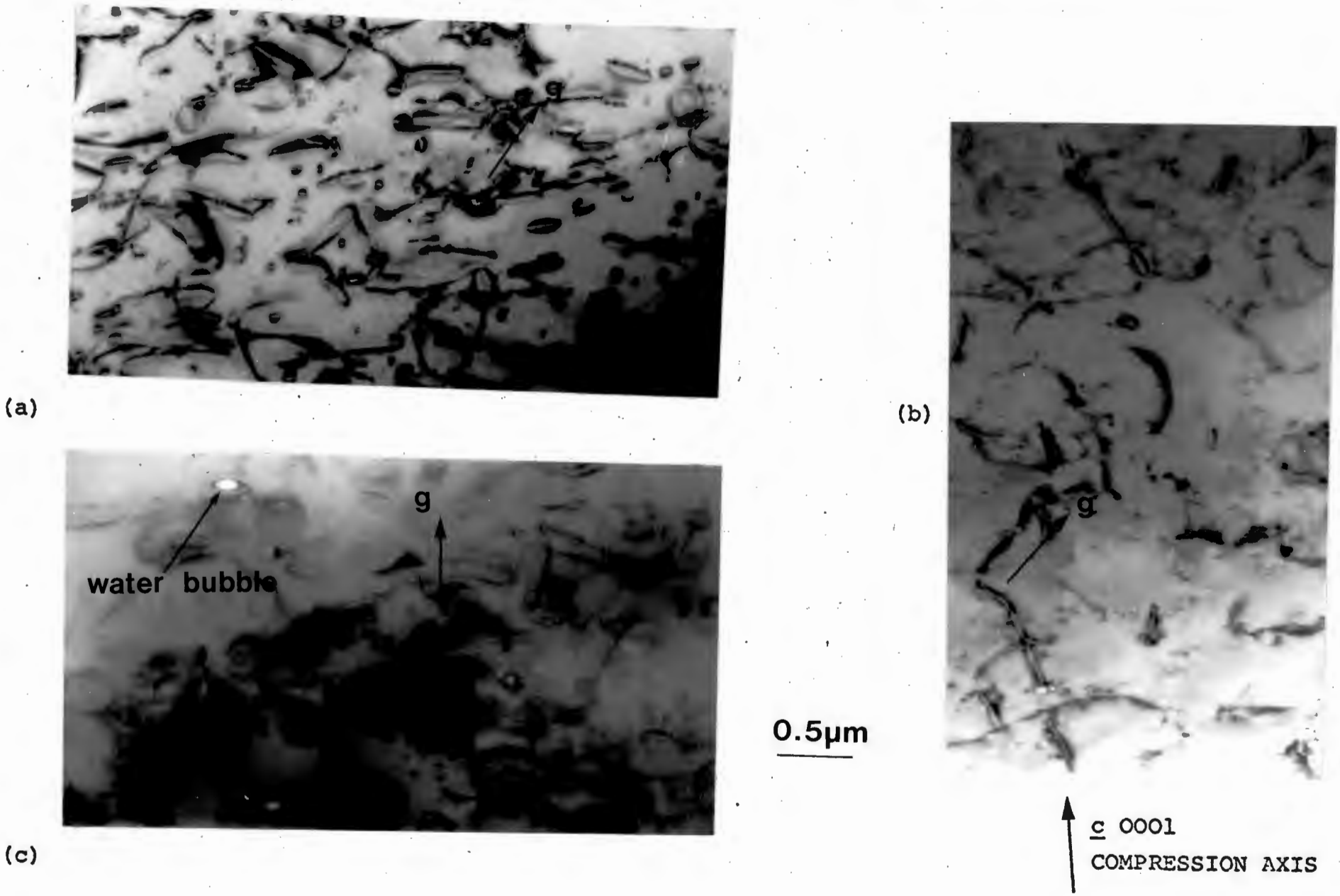

Fig.7.10 Longitudinal section with beam direction close to $[01\bar{1}0]$; (a) $g=\bar{2}112$; (b) $g=\bar{2}110$; (c) g=0003. Note the water bubble in (c).

TABLE 7.1

CONTRAST INFORMATION OBTAINED EXPERIMENTALLY FROM THE DISLOCATION LOOPS AND DISLOCATION SEGMENTS

g	Loops	Segments
$\{1\bar{1}00\}$	0	1 (Go systematically out of contrast for different g)
$(1\bar{1}01)$	1 (all loops)	1 (All in contrast)
$(\bar{2}112)$	1 (all loops)	1 (All in contrast)
$(\bar{2}110)$	0	1 (Only some segments in contrast)
(0003)	1 (all loops)	0

0 = Out of contrast

1 = In contrast

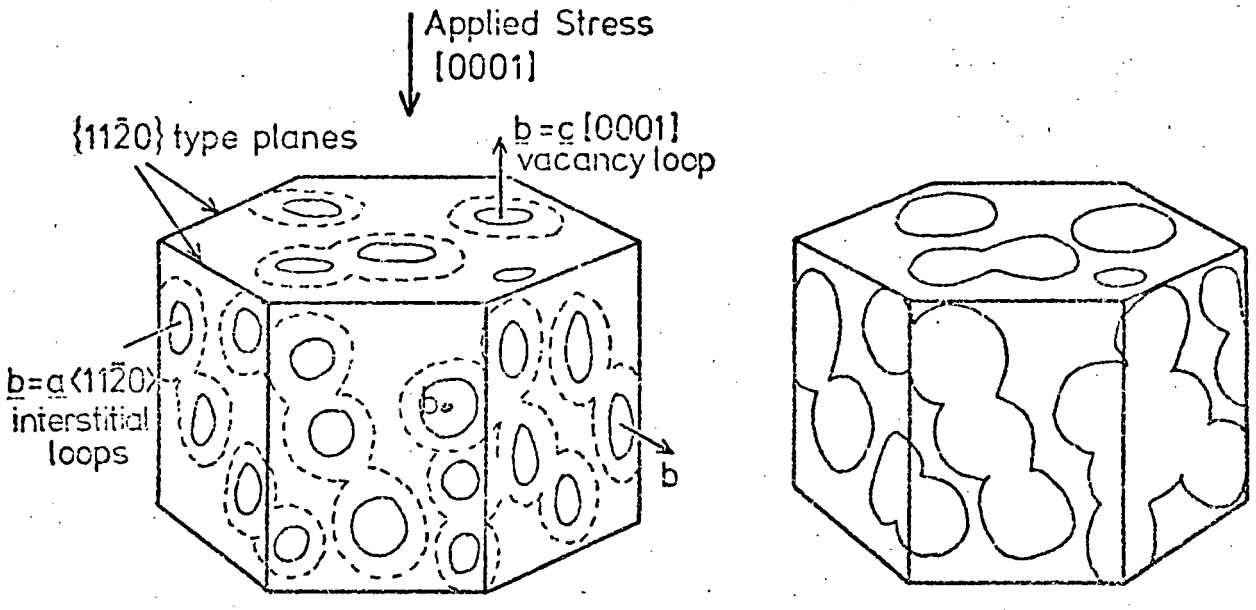

Fig.7.11(a) A schematic representation of the application of the dislocation climb model of Nabarro to the deformation of a quartz crystal in the [0001] direction. The growth and interaction of the vacancy and interstitial loops is indicated.

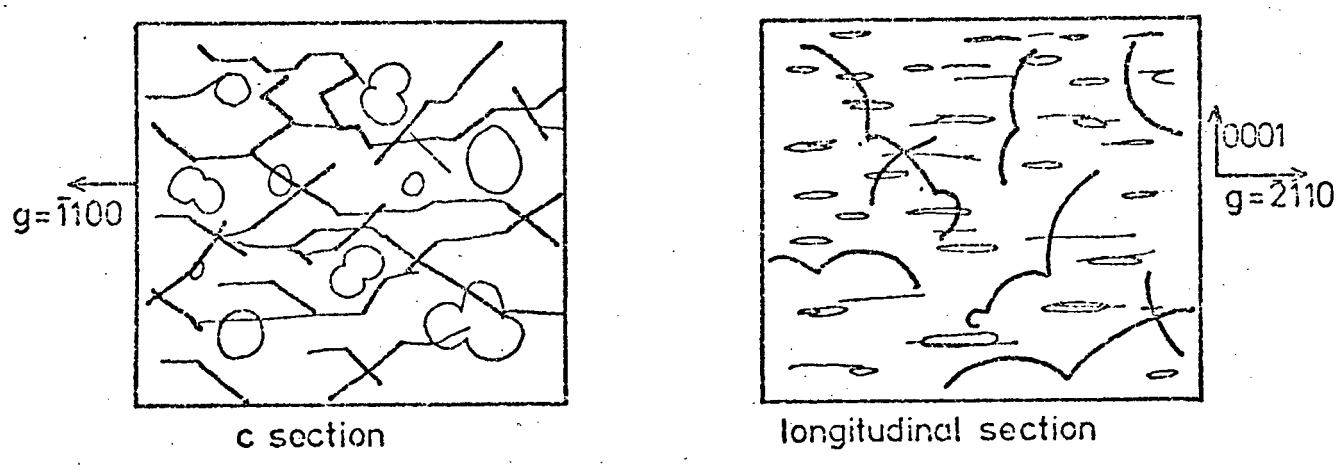

Fig.7.11(b) Predicted electron micrographs for the basal and longitudinal sections. The beams direction and reflecting vector for the basal micrograph are [0001] , g=$\bar{1}$100 and this picture should be compared with fig.7.6(b) and fig.7.7(a). The beam direction and reflecting vector for the longitudinal section are [01$\bar{1}$0] g=$\bar{2}$110 and this picture should be compared with fig.7.10(b).

TABLE 7.2

VALUES OF (g·b) FOR THE EXPERIMENTAL CONDITIONS

$\underline{b} = \langle 11\bar{2}0 \rangle$

$\underline{b} = \langle 11\bar{2}3 \rangle$

$\underline{b} = [0001]$

g	$\pm[11\bar{2}0]$	$\pm[\bar{1}2\bar{1}0]$	$\pm[\bar{2}110]$	$\pm[11\bar{2}3]$	$\pm[\bar{1}2\bar{1}3]$	$\pm[\bar{2}113]$	$\pm[11\bar{2}\bar{3}]$	$\pm[\bar{1}21\bar{3}]$	$\pm[\bar{2}11\bar{3}]$	$\pm[0001]$
$10\bar{1}0$	±3	0	$\mp$3	±3	0	$\mp$3	±3	0	$\mp$3	0
$01\bar{1}0$	±3	±3	0	±3	±3	0	±3	±3	0	0
$\bar{1}100$	0	±3	±3	0	±3	±3	0	±3	±3	0
0003	0	0	0	±9	±9	±9	$\mp$9	$\mp$9	$\mp$9	±3
$1\bar{1}01$	0	$\mp$3	$\mp$3	±3	0	0	$\mp$3	$\mp$6	$\mp$6	±2
$\bar{2}112$	$\mp$3	±3	±6	±3	±9	±12	$\mp$9	±9	0	±2
$\bar{2}110$	$\mp$3	±3	±6	$\mp$3	±3	± 3	$\mp$3	±3	±6	0

FRACTION OF PERFECT DISLOCATIONS INVISIBLE

Reflection	FRACTION OF DISLOCATIONS INVISIBLE		
	$\langle 11\bar{2}0 \rangle$	$\langle 11\bar{2}3 \rangle$	[0001]
$10\bar{1}0$	$\frac{1}{3}$	$\frac{1}{3}$	1
0003	1	0	0
$\bar{2}112$	0	$\frac{1}{6}$	0
$\bar{2}110$	0	0	1

0 = all visible

1 = all invisible

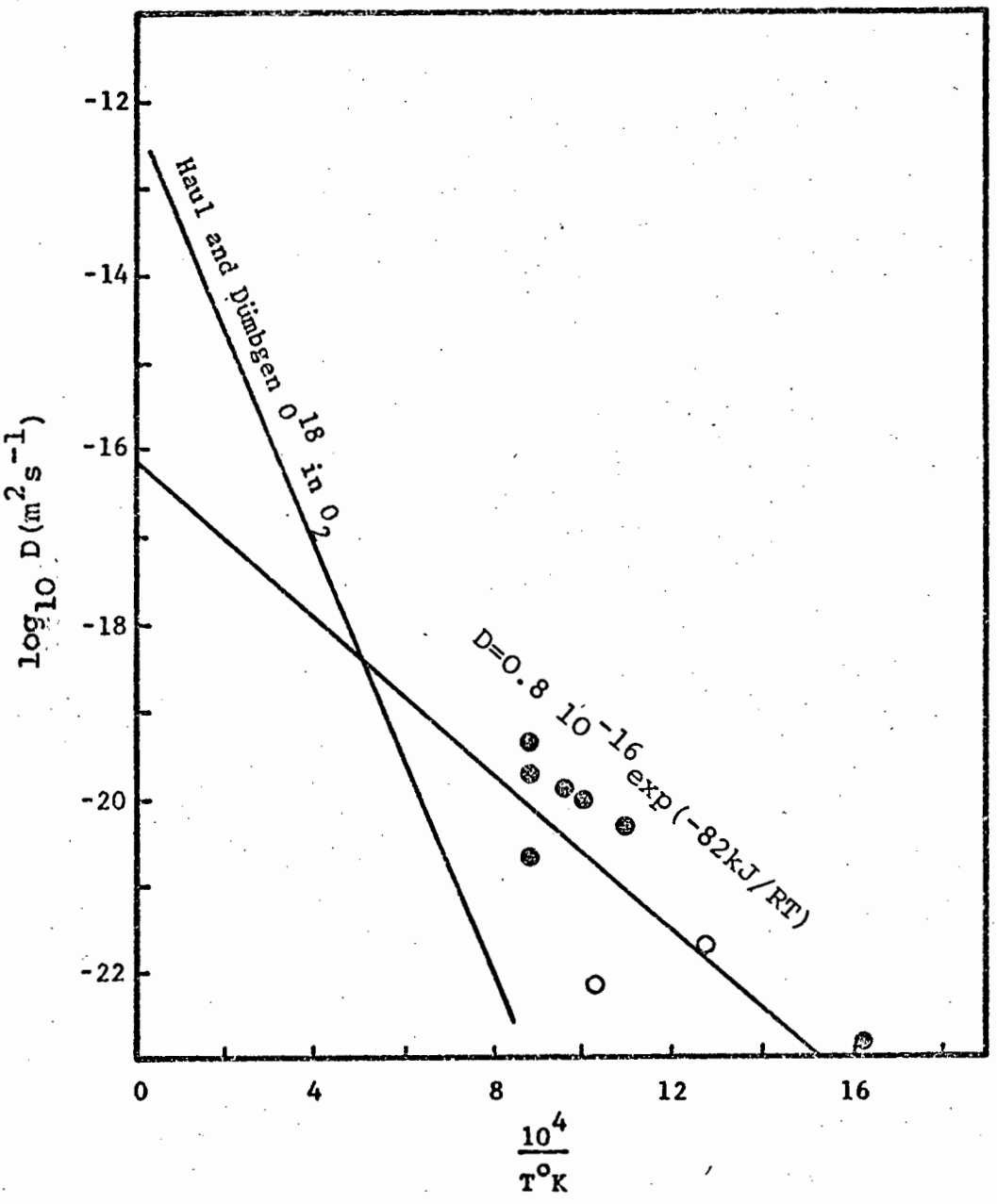

Fig.7.12 Diffusion coefficients calculated from the Nabarro equation using mechanical data obtained by Baëta and Ashbee (1970) (●), Hobbs et al. (1968,1972) (●) and the present work (○) for compression of quartz crystals along the [0001] direction. The fitted straight line is compared with the experimental results of Haul and Dümbgen (1962) for O^{18} diffusion in quartz crystals.

CHAPTER 8

DEFECTS IN ANNEALED SINGLE CRYSTAL QUARTZ

8.1 Introduction

The heat treatment of quartz at elevated temperatures results in the appearance of an optical milkiness or turbidity. The milkiness has been attributed to the growth of precipitates and the subsequent Tyndall light scattering from the particles. This scattering effect is particularly marked for anneals made on synthetic quartz crystals (Bastin and Mitchell, 1961). It is possible to quantify the development of the light scattering and hence determine an activation energy for precipitate growth. The results of Bastin and Mitchell (1961) for the annealing of synthetic quartz indicate an activation energy of 1.1 eV.

8.2 Identification of the Precipitating Species

The major impurities in synthetic quartz are alkali ions (Li^+, Na^+), aluminium (Al^{3+}) and hydrogen (H^+) ions, at concentrations ~ 10^{24} m^{-3}. The aluminium ions are believed to be incorporated substitutionally for silicon in the lattice. Fe^{3+} may also occupy substitutional lattice positions in a similar manner. Because of the difference in valence charge neutrality is maintained by the incorporation of a positive ion, such as an alkali or hydrogen, at an interstitial site in close proximity to the Al^{3+} ion. Defect configurations also include the following possibilities:

(a)

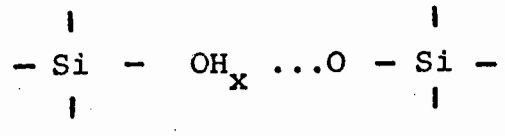

(b)

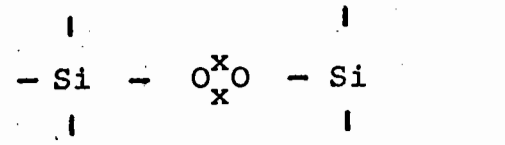

(x=Alkali ion)

(c)

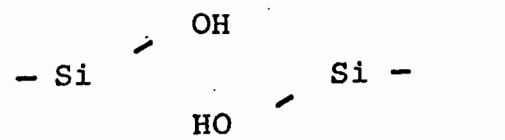

The alkali ions associated with (OH) show up as characteristic sharp absorption bands in the infra-red spectrum. The bonded (OH) is manifest as a broad background absorption, centred on 3500 cm^{-1}.

Upon heat treatment, the alkali bands reduce in intensity, indicating a rearrangement of the alkali ions. Other broad bands appear, which suggest the development of a bonded (OH) defect. It has been found (Dodd and Fraser, 1965) that there is a correlation between the milkiness and the bonded (OH) content (of an unannealed sample). In the milky regions there is a reduced concentration of alkali ions associated with (OH). Alkali ions are, however, still present in these regions; neutron activated analysis (Bambauer et al., 1969) showed that the concentration of Na is high in the milky bands.

Table 8.1 summarises the activation energy data for various defects in the quartz lattice, while Fig.8.1 shows the variation in diffusion coefficient as a function of reciprocal temperature for the mobile ionic species. Also included on Fig.8.1 is the mechanical data obtained from the diffusional creep experiments.

As previously discussed, (section 3.2), it is now generally accepted that the precipitates are 'water-bubbles'. On annealing, the hydrogen bonded (OH) can diffuse within the lattice, and at higher temperatures will precipitate as 'H_2O'.

We note from Table 8.1 and Fig.8.1 the following important points:

1. When all ionic species of uncertain origin have been cleared from the quartz lattice by an applied electric field, the conductivity becomes intrinsic, and is the same both parallel and perpendicular to [0001]. Wenden (1957) considers that the current is carried by oxygen vacancies. The activation energy for oxygen vacancy diffusion is 1.72 eV.

2. The diffusion experiments of Kats (1962) in which D_2O vapour was diffused into the quartz lattice in a direction parallel to [0001], yielded a high temperature (intrinsic) activation energy for hydrogen ion diffusion of 1.85 eV. At low temperatures ($\lesssim$ 900K) the activation energy was lower (0.84 eV). At 1000K the diffusion coefficient of H^+ was $\approx 1.7\ 10^{-13}\ m^2\ s^{-1}$.

3. A study of oxygen diffusion in quartz by Choudhury et al. (1965) gave the following results for O^{18} diffusion at 940K. In a direction parallel to [0001], $D \cong 4\ 10^{-16}\ m^2\ s^{-1}$ while perpendicular to [0001], $D \cong 8\ 10^{-18}\ m^2\ s^{-1}$. It is to be noted that the oxygen was diffused into the lattice by surrounding the crystal in O^{18} enriched water, at a pressure of 820 bar. In this respect the experiment is similar to that of Kats (1962). However, while Kats traced the motion of hydrogen ions, Choudhury et al. traced the motion of oxygen ions.

4. The activation energy for OH^- ion diffusion at low temperatures, (< 800K) measured by White (1971) is $\approx$ 0.65 eV.

From the above we find:

(a) There is a striking similarity between the activation energy for oxygen vacancies and hydrogen ions at elevated temperatures. ($\gtrsim$ 846 K)

(b) The low temperature ($\lesssim$ 800K) activation energy for hydrogen ion diffusion is (within experimental error) equivalent to that for OH^- ion diffusion.

(c) The diffusion coefficient for oxygen ions in the presence of water is similar to that for hydrogen ion diffusion.

We thus postulate that the hydrogen defects in quartz and oxygen vacancies are linked in some way and that the impurity defect structure of quartz can be understood from the standpoint of vacancy migration and interaction.

8.3 Effect of Impurities on Mechanical Properties

The precipitation mechanism ties in nicely with the hydrolytic weakening phenomenon (Griggs, 1967), since a prior heat treatment at high temperature (> 1100K) will strengthen a weak ('wet') crystal (Kekulawala et al., 1978). The active weakening agent (OH^-) is thus effectively removed from the lattice by precipitation. The use of infra-red absorption spectroscopy (see, for example, Paterson and Kekulawala, 1979) to monitor the changes in the hydrogen defect configuration during heat treatment sequences, and subsequent mechanical tests, has shown that it is the bonded OH defect which is common to samples of quartz showing an anomalous weakness.

Confirmation of the weakening effect of 'water' in solution came from the analysis of the creep deformation experiments described in the previous chapter. The indication was that the activation energy for creep ($\approx$ 0.85 eV) was approximately the same as that for OH^- ion diffusion, determined by White (1971) to be $\approx$ 0.65 eV. As previously mentioned the results of Bastin and Mitchell (1961) inducate that the OH^- precipitating species has an activation energy of 1.1 eV.

In view of these discrepancies, and the lack of any direct and detailed studies of the 'water' precipitation phenomenon, quartz has been heat treated and studied by optical microscopy, X-ray diffraction topography and high voltage electron microscopy (HVEM). In particular, it should be possible, using electron microscopy, to follow the growth of individual precipitates, and, from the rate of increase in size, with time and temperature, obtain an accurate value of activation energy for the diffusion process.

8.4 Experimental Methods

A single crystal of commercial grade Z-growth synthetic quartz (water content 50-150 ppm H/Si) was used in these experiments. This crystal was cut from the same bar used in the compression tests. In order to map optically the distribution of wet and dry bands the crystal was first sectioned parallel and perpendicular to c[0001] and annealed at 1100K in vacuo. The characteristic milkiness was observed, revealing the formation of the growth bands.

Small basal wafers 1 mm thick were than cut from both the wet and dry bands in the unannealed crystal, and heated in vacuo at various temperatures (800-1200K) for different periods of time (300 sec - 160 hours). A section was cut (0.5 mm thick) which included both dry and wet bands for parallel annealing experiments using optical microscopy and X-ray diffraction topography in order to monitor the defect distribution. The heating and cooling rates were kept constant at $\approx 0.1^{o}s^{-1}$.

After the annealing treatment the wafers were ground to a thickness of 100 μm, polished on both sides and ion-beam thinned to electron transparency. The HVEM observations were made in an AEI EM7 operated at 1000 KeV. Two beam conditions were used exclusively, and in all cases the operating g-vector was $10\bar{1}0$. X-ray diffraction topographic examination was made

using $MoK\alpha_1$ radiation. Optical observations were made using a Zeiss stereo microscope, with the light source and viewing direction positioned at 90° to one another. Additional observations were made by placing the crystals between crossed polars in the conventional metallurgical microscope.

8.5 Results

8.5.1 The Annealing Behaviour of Wet Bands

Optical examination (Fig.8.2) of a basal section which had been annealed for 45 min. at 900K revealed the characteristic 'milky' bands. The defects responsible for the dispersion can be resolved along the edges of the bands, and Fig.8.3 shows their crystallographic nature. They are linear in section with lengths of $\approx$ 50 μm and lie on the $\{10\bar{1}0\}$ prism planes. The 'milkiness' is evident within 5 min. of annealing at 900K.

Figs.8.4 and 8.5 are X-ray topographs taken of the same (0001) section in the unannealed condition, and after an anneal of 45 min. at 900K. The development of a milky band has produced extreme strain contrast in the left hand side band, whereas within the right hand side band, defects can be resolved. The size of these defects is compatible with those observed optically at the edge of the milky bands. The density of similar defects in the left hand side band is presumably so high that a general darkening has been produced.

Fig. 8.6 is an optical micrograph of the same basal section taken between crossed polars, corresponding to Fig.8.3. The stress fields of the defects are clearly visible as a stress birefringence effect. It is to be noted that both the optical milkiness and the X-ray topographic contrast persisted even after annealing treatments at high temperatures (1200K) and for long times ($\approx$ 150 hours).

The HVEM examination of the 'wet' bands prior to annealing showed no evidence for characteristic defects. A low temperature anneal ($\approx$ 900K) for short times ($\lesssim$ 60 min.) produces numerous dislocation loops (Fig.8.7) lying on the $\{10\bar{1}0\}$ prism planes. For longer annealing times these loops grow and become irregular in shape (Fig.8.8).

Annealing at higher temperatures (> 1100K) causes the rapid growth of the loops and their subsequent interaction creates a three dimensional network of dislocations (Figs. 8.9 and 8.10). A new defect can now be observed and which has the form of a thin hexagonal platelet lying on the basal plane. These defects, which do not produce strain contrast in the adjacent matrix, are distributed homogeneously throughout the 'wet' band but many are attached to the dislocation network. The density and mean diameter (Fig.8.11) of these platelets was measured as a function of time of annealing at 1100 K. An equilibrium density of $10^{13}m^{-2}$ and a mean diameter of 0.06 μm is attained after only 300s. The platelets are then extremely stable and no coarsening is observed after annealing times of 160 hr. at 1100K. Furthermore, their density and mean size are insensitive to temperature.

8.5.2 Annealing Behaviour of Dry Bands

The annealing of dry bands for long times at high temperatures produces a low density of dislocations on which a number of very small precipitates can be observed (Fig.8.12). The hexagonal platelets are apparently absent. No intense X-ray contrast or optical milkiness was evident in this case. However, upon careful optical examination, milky lines could be seen, which were found by a comparison with the X-ray diffraction topographs to correspond to the as-grown dislocation network. These dislocations could not be seen optically in the unannealed sample.

8.6 Discussion

8.6.1 The Mechanism of Diffusion and Precipitation

The rapidity ($t \lesssim 300s$) with which the platelet precipitates (water bubbles) grow, suggests that the diffusion coefficient of the precipitating species may be high but our inability to follow the growth of the precipitates to their equilibrium size, as a function of time and temperature, precludes a calculation of the activation energy for this process. We may, however, estimate the volume diffusion coefficient of 'water' in the matrix.

The lack of contrast in the water bubble itself indicates that they must be less than one extinction distance (ξ_g) thick. For the reflection used, this suggests a thickness $Z \lesssim 150$ nm, and hence the precipitate is, to a first approximation, spherical. Following the analysis given in Martin and Doherty (1976) for the growth of a spherical precipitate, we can show that the radius R of the precipitate at time t is given by the expression $R = \lambda(Dt)^{\frac{1}{2}}$. λ is a function of the degree of supersaturation (K), given by

$$K = 2(C_I - C_M)/(C_p - C_I) \qquad (8.1)$$

This expression may be evaluated from a knowledge of:

(a) The concentration (C_I) of the precipitating species in the matrix at the precipitate/matrix interface.

(b) The concentration (C_M) in the matrix at a point remote from the precipitate.

(c) The concentration (C_p) in the precipitate itself.

Applying the approximation $C_I = 0$, and noting that $C_p = 1$ for the case of water precipitating in quartz (i.e. the precipitate is assumed not to be a compound formation

with Si or O) then we can estimate that

$$K \approx -2C_M \quad . \qquad (8.2)$$

To evaluate C_M (the concentration of water is the matrix) we can adopt two approaches. Either assume that $C_M \cong$ 50-150 ppm H/Si (the average water content) or estimate C_M from the water bubble concentration. In this latter, more realistic, case we will assume that <u>all</u> of the water held in solution will precipitate at elevated temperatures.

The volume V of each spherical precipitate of radius r = 0.035 μm is:

$$V = \frac{4}{3} \pi r^3 = 1.8\ 10^{-22}\ m^3 \ .$$

The measured precipitate density on a projected area of 1 m^2 gave $10^{13}\ m^{-2}$.

The thickness of the quartz foil is ≈ 1.5 μm (measured using thickness fringes). Thus, the volume density of the precipitates is $10^{13}/(1 \times 1 \times 1.5\ 10^{-6})\ m^{-3}$, or $6.7\ 10^{18}$ precipitates m^{-3}.

Hence, the total volume of precipitates per cubic metre of quartz is $1.2\ 10^{-3} m^3$.

Assuming the density of the water in the precipitate to be 1 gm/cm^3, we have $1.2\ 10^3\ gm/m^3$ of water in this sample of quartz.

Using the fact that 1 mole of water contains ≈ $6\ 10^{23}$ molecules, and that 1 mole of water weighs 18 gm we estimate that the concentration of 'water' in the matrix is $4\ 10^{25}\ H/m^3$.

The density of SiO_2 (quartz) is 2.6 gm/cm^3. This is equivalent to $2.6\ 10^{28}\ SiO_2$ molecules/m^3. Thus, the atomic concentration (C_M) of water in the matrix is $(4\ 10^{25}/2.6\ 10^{28})$ or $C_M = 0.0015$. This is equivalent to 1500 ppm H/Si.

It is clear that the concentration of 'water' in the wet growth bands may be considerably higher than the average (infra-red) measurement would suggest.

Inserting this value of C_M in eqn.(8.2) we find that $K \approx -0.003$, yielding a value of $\lambda = 0.2$. Using the expression for the gorwth of the precipitate, $R = \lambda(Dt)^{\frac{1}{2}}$, with our values of R(0.035 10^{-6} m), λ(0.2) and t(300 secs), we can calculate that the volume diffusion coefficient of 'water' in the quartz matrix is $\approx 1.02\ 10^{-16}\ m^2s^{-1}$.

8.6.2 The Nucleation and Growth of the Dislocation Loops

The correlation in size, crystallography and the temperature of formation of the linear defects (Figs.8.2 and 8.6) suggests that the cause of the milkiness, and the strain contrast of the X-ray diffraction topographs are the dislocation loops observed by HVEM. The rapid climb motions of the dislocation loops (Fig.8.9) at T > 1100 K, is reminiscent of the mechanism by which an effective supersaturation of vacancies causes the climb of dislocations in metallic systems during a fast quench.

In view of the close correlation between the activation energy for hydrogen ion diffusion (Kats, 1962) and the activation energy for oxygen vacancy migration obtained electrically (Wenden, 1957) (see Table 8.1), it was suggested that a model based on a vacancy mechanism is appropriate to descriptions of the defect structure of quartz. Such a model enables us to propose that the addition of 'water' is equivalent to the generation of an excess number of vacancies over and above the thermal equilibrium concentration. Hence, an effective supersaturation of vacancies exists in the lattice.

The following sequence of events during heat treatments is proposed:

1. The mobile alkali ions can readily diffuse at low temperatures. These ions will aggregate to form the strain centres.

2. On continued annealing dislocation loops will be nucleated and punched out from these strain centres.

3. At a critical temperature (depending upon the exact concentration of 'water' held in solution within the lattice) vacancies will form and diffuse to the dislocation loops.

4. The loops climb rapidly but subsequently the vacancy supersaturation decays, and the dislocation loops will become immobile.

The excess vacancies due to 'water' may be formed as follows: We consider a bonded OH group, the hydrogen ion compensating for a substitutional aluminium ion located in close proximity:

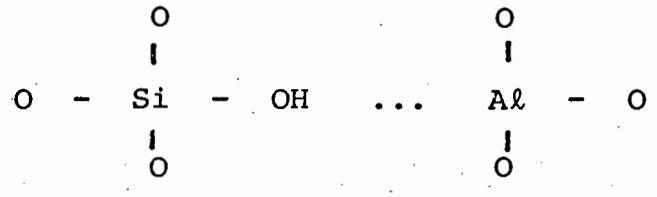

The Si-O bonding will be weakened by the presence of the hydrogen ion and at low temperatures the OH^- ion can assume a substitutional position, creating in the process an oxygen vacancy, which carries an effective positive charge. Both the OH^- ion and oxygen vacancy are now free to wander through the lattice.

Assuming all the hydrogen defects in our sample of quartz to be ionized, there will be $\sim 10^{25}$ vacancies/m^3. This should be compared to the equilibrium concentration of vacancies $[V]_{eq}$ which can be estimated from the expression $[V]_{eq} = (1/v_a)\exp -(W_f/kT)$. v_a is the activation volume ($\approx a^3$) and W_f is the vacancy formation energy. Using values of a ($= 5\ 10^{-10}$m) and W_f (≈ 1.7 eV) (Verhoogen, 1952) we may calculate that $[V]_{eq} \sim 10^{19} m^{-3}$. Quite clearly there is an effective supersaturation of vacancies in the presence of 'water'.

It is possible to calculate the total amount of climb produced in a quenching experiment, if all the vacancies are absorbed at dislocation lines. If the dislocation density is ρ, then the dislocations climb an average distance $\ell = 2cv_a/\rho b$, where c is the excess vacancy concentration to be quenched out (Hirth and Lothe, 1968). In the present experiments the density of loops is $\approx 4\ 10^{12}\ m^{-2}$ and $c = 10^{25} m^{-3}$, from which we may calculate that the loops will climb on average $\approx 1.25\ \mu m$. This is compatible with the experimental observations and suggests that such a mechanism can indeed account for the rapid dislocation climb motions in these annealing experiments.

8.6.3 The Optical Turbidity

Light scattering from crystals originates from several sources. The thermal vibrations of the lattice produce both Rayleigh scattering (acoustical branch phonons) and Raman scattering (optical branch phonons). The intensity of Raman scattering in quartz is $\lesssim$ 10% of the Rayleigh scattering (Taurel and Humphreys-Owen, 1960). The theory of Rayleigh scattering predicts an intensity proportional to the absolute temperature and inversely proportional to the fourth power of the wavelength of the incident radiation.

Defects or imperfections in the crystal cause additional scattering; in this case the scattering power is different between crystals of the same kind. Ultramicroscopic studies may then reveal dislocation networks, glide bands and a fine structure which can be interpreted as individual edge dislocations (Nabarro, 1967b). The scattering is caused by the change in the polarizability of the defect.

Such studies have been made particularly of the alkali halides. Impurity and vacancy clouds about charged dislocations in this class of materials produces a strong scattering,

while the subsequent precipitation of impurities in the vicinity of dislocation lines (self decoration) reduces the scattering power (Plint and Greig, 1964 and Vand et al., 1966).

An alternative approach to the study of defects by light scattering is the analysis of the characteristic stress birefringence (or double refraction) caused by the stress fields of individual dislocations (Fathers and Tanner, 1973). This method is equivalent to a study of photoelastic patterns. The dislocation contrast arising from stress birefringence microscopy is a strong function of the type of dislocation (screw, edge or mixed), and the exact orientation of the dislocation with respect to the crossed polars (Tanner and Fathers, 1974).

Recent observations on the light scattering of quartz (Moriya and Ogawa, 1978, 1980) have shown that dislocations can be observed in this material using light scattering tomography. The use of a laser source, with a fine pencil beam, ensured that the dislocations were seen with a minimum of background scattering. Images caused by undecorated dislocations were clear lines, while dislocations decorated by impurities displayed many dots along their length.

The images from the clean dislocations were strongly dependent upon the exact direction of the incident beam. It is to be noted that the image analysis undertaken by Moriya and Ogawa (1980) assumed that the photoelastic changes in the refractive index of the crystal were responsible for the contrast. Experimentally these authors did not use crossed polars.

Our observations of defects in quartz using optical techniques (Figs.8.3 and 8.6) are similar to those found by Moriya and Ogawa. In the absence of detailed work by us on the dependence of the visibility of the linear defects with light beam direction, we assume that these defects must be associated with impurity and vacancy clouds. These impurities cause a

change in polarizability, and hence scattering power. The as-grown dislocations in the dry bands only become visible upon heat treatment, and hence it is reasonable to assume that at elevated temperatures these dislocations attract mobile impurities to their vicinity. This will result in an impurity cloud about the dislocation. We assume an analogous mechanism for the case of the linear defects. We have suggested that the rapid growth of the loops (Fig.8.7) is associated with a vacancy mechanism, and the observation that we have a light scattering effect must be closely connected with the vacancy cloud about these loops.

It has been usual in the literature to attribute the optical milkiness in quartz solely to the water bubble precipitates. We find that the light scattering is apparent before the growth of the strain free precipitates. Using light of wavelength $\lambda \sim 5000$ Å (0.5 μm) it is evident that the size of the precipitates ($\approx$ 0.1 μm) is less than the λ of light. Under these conditions the precipitate particles cannot be resolved. However, we find that in circumstances where an electron microscopy study has been made in quartz displaying milkiness (e.g. McLaren and Phakey, 1966) dislocations have been visible in addition to water bubbles. We therefore feel that there is now strong evidence to suggest that the light scattering can be due to dislocations and not just to the water bubble precipitates. Thus the interpretation of the origin of milkiness in quartz crystals must be undertaken on the basis of a complete microstructural study.

8.6.4 The Precipitation Phenomenon

During high temperature annealing the new feature of interest which appeared was the hexagonal strain free platelet. The failure of these precipitates to grow in size is surprising since most precipitation systems show a tendency to coarsen. The mechanism of coarsening ('Ostwald Ripening') releases excess surface energy, and is energetically favourable : the

larger particles grow at the expense of the smaller ones because the latter have a larger surface area to volume ratio. Systems which resist coarsening show the following general features (Martin and Doherty, 1976):

(1) Low interfacial energy between the precipitate and the matrix.

(2) Low solubility.

(3) Low diffusion coefficient.

It is apparent that the detailed understanding of such systems is far from complete. However, in the case of quartz, the resistance of the platelets to coarsening must stem in part from the negligible interface energy which is indicated by their faceted nature and the lack of strain contrast.

On the other hand, Paterson & Kekulawala (1979) found that the bubbles in their synthetic quartz samples (water content ≈ 400 ppm H/Si) increased in number (many finer bubbles appeared) and decreased in average size during a prolonged heat treatment (several days) at 1200K. By way of explanation Paterson & Kekulawala suggest that the diffusion coefficient of 'water' may be dependent upon the concentration of water held in solid solution during earlier stages of precipitation. Thus, on continued annealing, the diffusion coefficient would decrease sufficiently to prevent the larger bubbles coarsening at the expense of the smaller ones. The water now precipitates at other sites located between the first-formed bubbles. However, why smaller precipitates should grow is unclear, since presumably the driving force for coarsening is the reduction of excess surface energy. Smaller precipitates should dissolve preferentially, not increase in size, if any larger precipitates are present.

Paterson & Kekulawala (1979), from an analysis of the precipitation phenomenon in quartz, suggest that the solid solubility of the OH species at atmospheric pressure and

1200 K is ~ 10 ppm H/Si.

The direction of ionic diffusion in the quartz lattice is, of course, highly anisotropic, and apart from oxygen vacancies, no ions diffuse in directions perpendicular to [0001]. Thus, in the annealing experiments the precipitates are effectively absorbing ions from within long, narrow tubes. Unless two precipitates lie along the same axis and overlap then the precipitates are effectively isolated, and Ostwald ripening may not occur. We could postulate that the new precipitates observed by Paterson and Kekulawala (1979) may be due to either vacancy condensation (void formation), or the slow nucleation of water bubbles located in c-axis channels which are relatively depleted of water.

Our annealing experiments demonstrated the rapid growth of the bubbles ($t \approx 300$ secs), and a diffusion coefficient of $10^{-16} m^2 s^{-1}$ was calculated for the precipitating species. This value of D is almost exactly the same as that obtained by Choudhury et al. (1965) for the diffusion of oxygen (in the presence of 820 bar water, at 940K) in quartz, parallel to [0001]. We believe that the equivalence emphasises the close correlation between the mechanism of diffusion of water (OH^-) and oxygen vacancies as proposed earlier.

8.6.5 Hydrolytic Weakening and the effect of 'Water' on the Deformation of Quartz

Hydrolytic weakening may be seen as a surfeit of dislocations (or potential dislocation sources) and their rapid climb by vacancy absorption. Since the vacancy concentration at any particular temperature is proportional to the 'water' content, a high water content is equivalent to a lower temperature at which climb may initiate. The hardening of wet quartz crystals by a prior heat treatment is evidently related to a lack of vacancies (by water precipitation) and the inhibition of climb motions.

Kekulawala et al. (1978) find that it takes annealing times of up to 100 hours at 1200 K to achieve a full strengthe-

ning of weak synthetic quartz. Our experiments have clearly shown that the effective hardening in a wet growth band takes place extremely rapidly ($t \approx 300$ secs) and it is evident that the changes taking place in the wet bands cannot account for dramatic changes in strength which occur for long anneals.

Since a specimen of quartz, tested in compression, is likely to include both wet and dry growth bands, it could well be the case that in a pre-annealed sample the so-called dry bands retain a higher concentration of dislocation climb promoting vacancies than the wet bands. In the wet bands the climb processes have occurred rapidly and no vacancies exist to allow the climb of the additional dislocations which will be nucleated during deformation. However, the precipitates in the wet band will harden the crystal by pinning these dislocations, and the overall response is evidently a complex interaction of different mechanisms.

Finally it is to be noted that during slow deformation testing a frequent observation is that the bubbles are not faceted (e.g. Morrison-Smith et al., 1976). This suggests that the bubbles are still in the process of achieving their equilibrium faceted nature, and that the diffusion coefficient of 'water' under such conditions is probably lower than during a normal anneal. This can explain why the diffusivity of 'water' calculated from creep data (Fig.8.1) is lower than the corresponding diffusion coefficient of 'water' found on annealing.

TABLE 8.1

THE ACTIVATION ENERGY (Q) OF SOME DEFECT SPECIES IN QUARTZ

DEFECT	Q (α-quartz) eV	Q (β-quartz) eV	SOURCE OF DATA*
Na^+ (// [0001])	0.89	0.5	Frischat (1970)
Na^+ (⊥ [0001])	1.8	1.2	
Li^+	0.72		Fraser (1968)
K^+	0.92		
OH^- (// [0001])	0.65		White (1971)
H^+ (// [0001])	0.84	1.85	Kats (1962)
O^{2-} vacancy ?	1.72	1.72	Wenden (1957)
O^{2-} (dry)		2.4	Haul & Dümbgen (1962)
O^{2-} (wet)	Not measured		
Diffusional Creep	0.85	0.85?	Present experiments

* Frischat, G. H., (1970) : J. Am. Ceram. Soc., 53 , 357.
Fraser, D. B., (1968) : Physical Acoustics, Vol. 5, ed. Mason,W.P., Academic Press, New York.
Haul, R., & Dümbgen,G., (1962) : Z. Elektrochemie, 66, 636 - 641.
Kats, A., (1962) : Philips Res. Repts., 17 , 133 - 195.
Wenden, H. E., (1962) : Amer. Mineral., 42, 859 - 886.
White, S., (1971) : Nature, 233, 63 - 64.

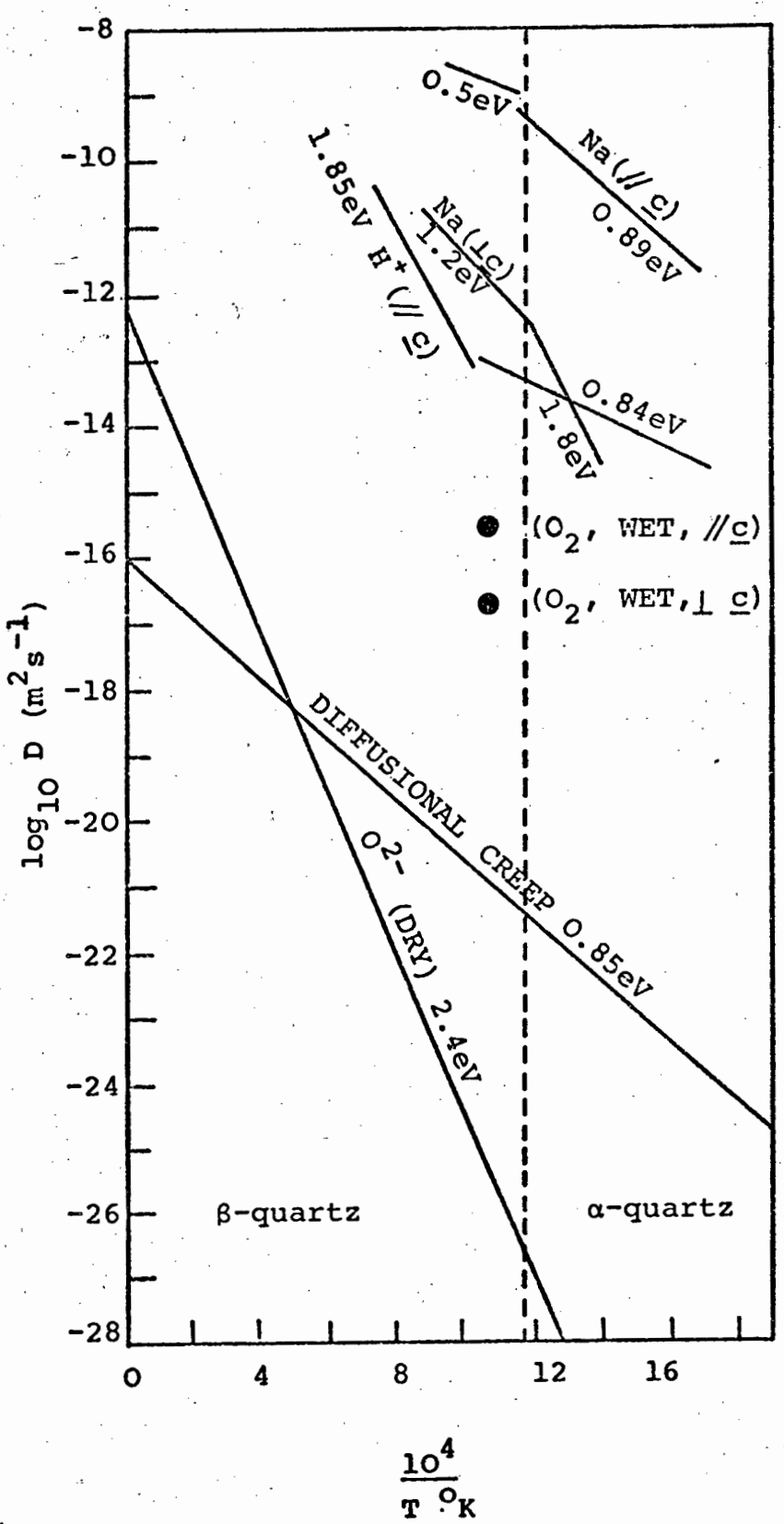

Fig.8.1 The diffusion coefficient and activation energy of some ionic species in quartz. Also shown are the data obtained from the creep deformation tests.

Fig.8.2 Optical micrograph of a basal section which has been annealed for 45 min. at 900K. A milky band on the L.H.S. is apparent.

Fig.8.3 Optical micrograph taken close to the edge of the milky band of fig.8.2. The defects can be resolved and lie on $(10\bar{1}0)$ planes.

Fig.8.4 X-ray topograph of above basal section prior to annealing.

Fig.8.5 X-ray topograph of same crystal which has been annealed for 45 min. at 900K. The defects which can be seen in fig.8.3 can be resolved close to the milky band.

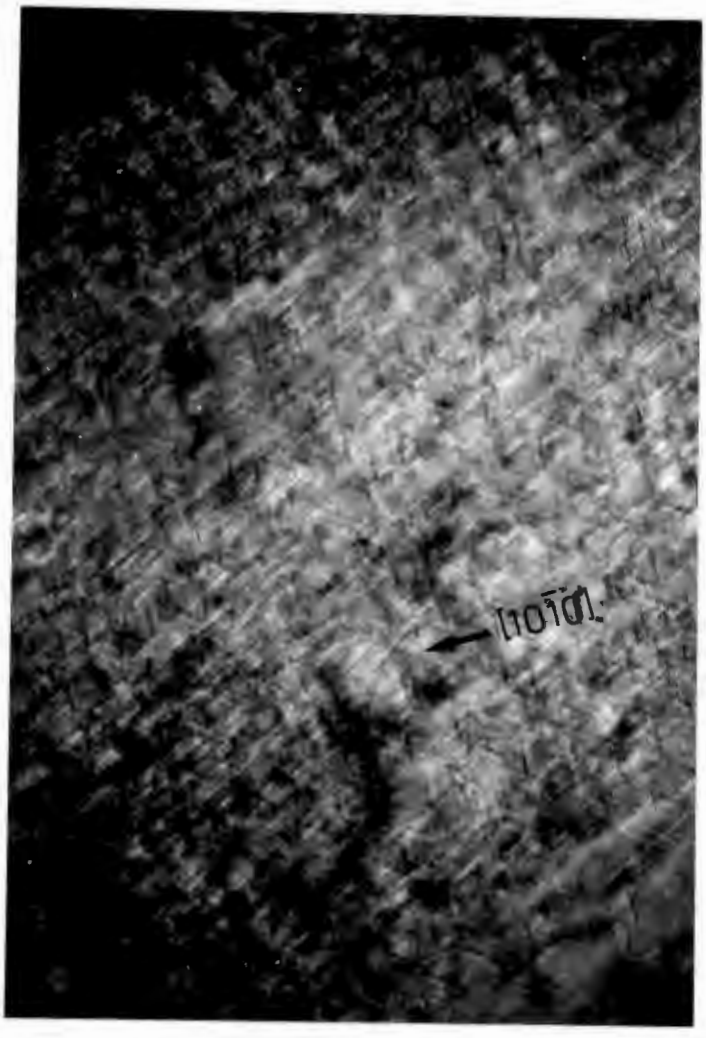

Fig.8.6 Optical micrograph of annealed sample taken between crossed polars. Note the linear structure, similar to that observed in fig.8.3.

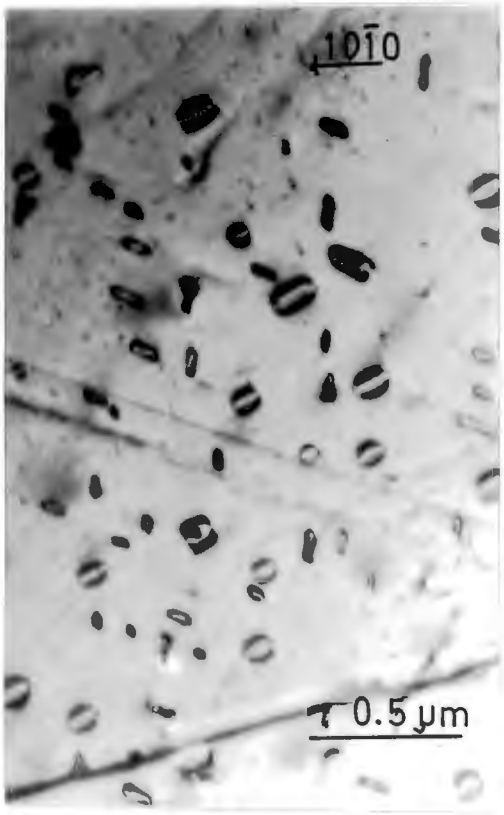

Fig.8.7 High voltage electron micrograph of a 'wet' band after an anneal at 900K for 30 min. The loops lie on $(10\bar{1}0)$ planes.

Fig.8.8 High voltage electron micrograph of a 'wet' band after an anneal at 900K for 80 min. The small defects in the background are radiation induced damage.

Fig.8.9 High voltage electron micrograph of a 'wet' band after an anneal at 1100K for 38 hrs. A network of dislocations and thin hexagonal precipitates are present.

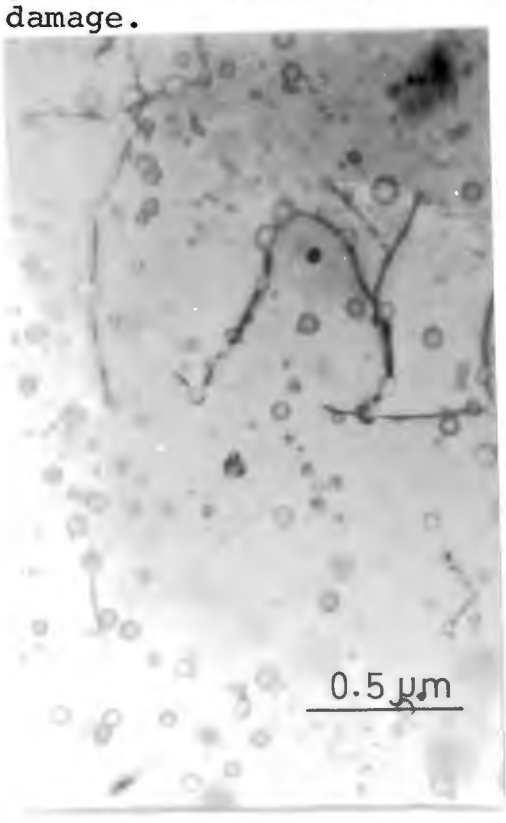

Fig.8.10 High magnification of features seen in fig.8.9.

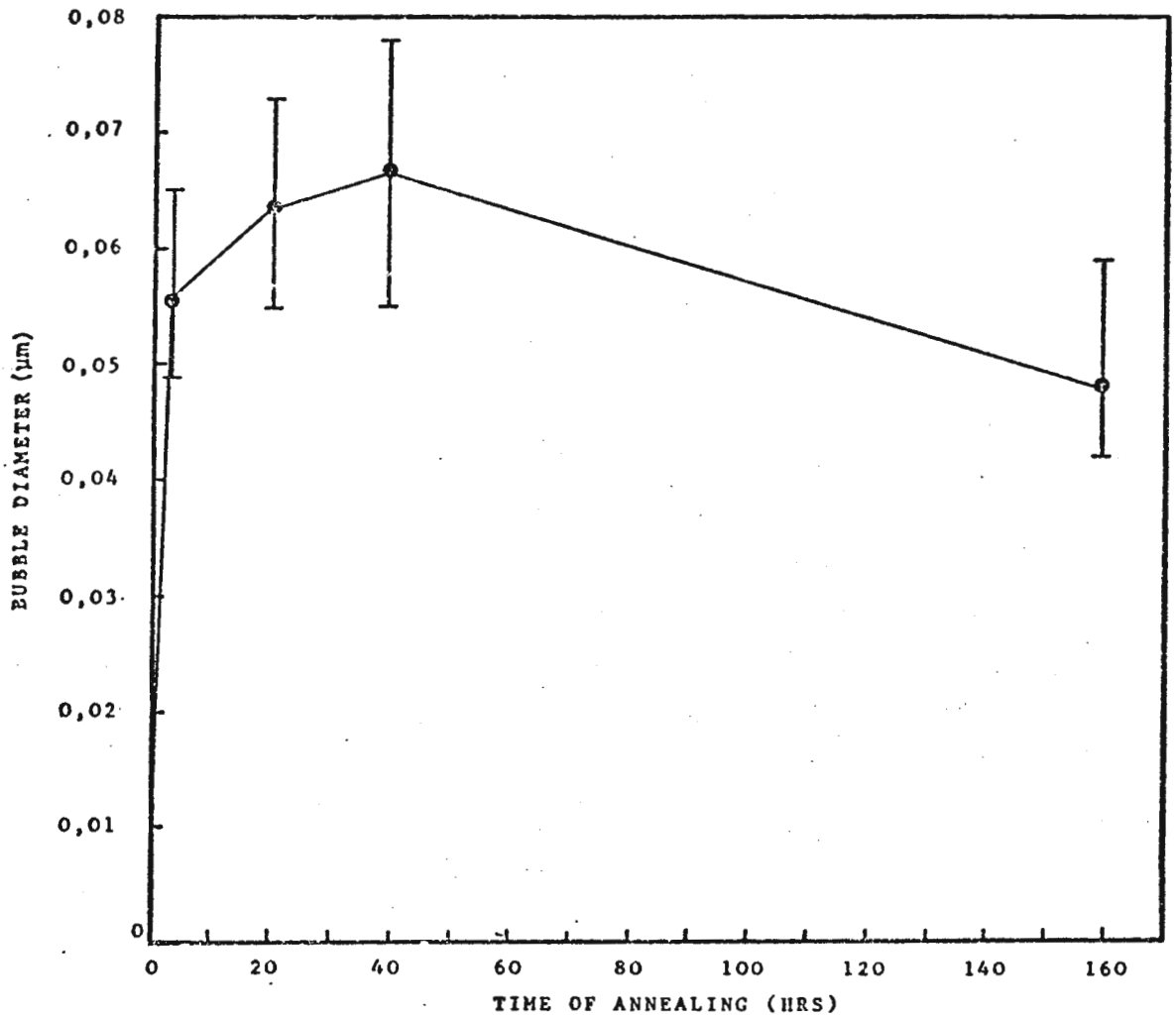

Fig.8.11 The mean diameter of the precipitates measured as a function of annealing time at 1100K.

Fig.8.12 HVEM of an annealed dry band. (1123K, 20hours). Note the low density of dislocation loops and the small precipitates (arrowed).

CHAPTER 9

MICROHARDNESS MEASUREMENTS ON QUARTZ

9.1 Introduction

The microhardness test is a comparatively simple and convenient method of investigating the near-surface mechanical properties of a solid. In the usual experimental configuration an indentor (made from diamond), with a known geometrical shape is forced against the surface of the solid under test. The indentor is held at a pre-determined load for a fixed period of time, then unloaded. Measurement of the resulting surface impression is made, and from a knowledge of the applied load and indentor shape the hardness value may be calculated, usually expressed in Kg mm^{-2}.

9.2 The Vickers Hardness Test

The Vickers hardness test utilises a square based pyramid (Fig.9.1) as the indentor. The angle between the opposite faces is 136^{o} (the A.S.T.M. specifies an accuracy in this angle to 30' of arc). The Vickers hardness value can be calculated as follows:

The surface area (M) of a square pyramid of apex angle θ, and base diagonal d is given by

$$M = d^2/2 \sin(\theta/2) \qquad (9.1)$$

For the Vickers pyramid $\theta = 136^{o}$ and hence eqn.(9.1) becomes

$$M = d^2/2 \sin 68^{o} = d^2/1.8544 \quad .$$

Hardness (H) is defined as load/projected surface area of indentation area, therefore, for an applied load, P, :

$$H = P/M, \text{ or}$$

$$H = \frac{1.8544 \cdot P}{d^2} \text{ Kg mm}^{-2} , \qquad (9.2)$$

for P measured in Kg and d in mm.

The indentation diagonals are measured optically. Due to crystal anistropy the two diagonals may be of slightly different lengths. In this case an average value is taken.

9.3 Errors in Microhardness Measurements

The microhardness test is subject to certain instrumental errors. These include (Mott, 1956)

1. Vibration during the test, resulting in a smaller H_v value than the correct one. Vibrations come from many sources, for example, machinery working in the vicinity of the tester, or doors slamming. Even the vibrations from illumination sources on the tester may cause problems. Inaccuracies due to vibrations increase as time-at-load is increased.

2. Incorrect shape of the indentor, either apex angle θ, or a chisel tip. These errors can be corrected provided the exact indentor geometry is known.

3. The accuracy of the applied load. (For microhardness tests this is certainly not a trivial source of error).

4. The accuracy of the diagonal measurements. It is extremely difficult to measure small indentations, and in addition the optics give only a finite resolution. Resolving power (defined as the minimum separation necessary between two lines, for each line to be observed individually) is given by the expression 0.5 λ/N.A. where λ is the wavelength of the light being used for the measurement and N.A. is the numerical aperture of the objective lens.

5. Calibration of the optical measuring scale may also contain errors. This calibration is normally performed using a stage micrometer with lines ruled at 0.01 mm intervals. It has been suggested that this is not accurate enough as the lines are coarsely ruled, and for the most exact measurements spectrographic gratings, having several hundred lines per mm, should preferably be used.

6. Instrument design problems. These depend on the actual construction of the hardness tester and will not be elaborated upon. A microhardness instrument should, however, only cover a hundred-fold increase in load from the minimum value to the maximum (i.e. 1 gm - 100 gm, 100 gm to 1000 gm etc.) if it is to give satisfactory results over the full load range.

9.4 Interpretation of Microhardness Data

In hardness testing three distinct loading ranges can be distinguished (Bückle, 1973), shown schematically in Fig. 9.2. For applied loads greater than approximately 3 Kg the hardness value is constant, and we obtain a measure of the standard hardness. In the range 200 gm to 3 Kg the hardness value increases with decreasing load. For both of these load ranges there is agreement amongst different investigators as to the hardness value of any particular solid. However, for loads less than 200 gm we enter the 'microhardness' field and here considerable disagreement exists between published results. The microhardness values have been reported to increase or decrease, with decreasing load for measurements made on the same material.

It is evident that the tried and tested techniques of standard hardness testing became invalid at low loads. Besides the problem of errors in the measurement of low loads and small distances, it is generally accepted that an increase in hardness at low loads is a real effect (Bückle, 1959), although the physical interpretation (apart from work-hardened surface layers) is still not resolved.

Theoretically the Vickers pyramid produces a geometrically similar impression, irrespective of the depth of penetration. This means that the mean pressure below the indentor should be independent of the indentation size. For such an indentor the Kick similarity law applies, viz.

$$P = ad^2 \quad , \qquad (9.3)$$

where P is the applied load, d is the impression diameter and 'a' is a constant which depends on the material and indentor shape.

The Kick law (eq.9.3) can be combined with the definition of Vickers hardness (eq.9.2) and we may show that

$$H_v = 1.8544\ a = \text{constant.}$$

Since in the microhardness region H_v is not a constant with load, Onitsch (see Mott, 1956) suggested that the Kick similarity law could be re-written as a Meyer power law, of the form

$$P = a\,d^n \qquad (9.4)$$

Hence in the macrohardness region n = 2, while in the microhardness region n ≠ 2. Comparing the Meyer power law (eq. 9.4) with the Vickers hardness (eq.9.2) we may show:

$$H_v = 1.8544.\ a.d^{n-2}\ , \qquad (9.5)$$

or

$$H_v = 1.8544.\ a^{2/n}.P^{(n-2)/n} \qquad (9.6)$$

If n = 2, then H_v is a constant and independent of either load or diagonal measurement.

The exponent n is known as the logarithmic index, and may be obtained by a plot of log d against log P. However, this plot frequently shows deviations from a straight line even over a restricted load range (e.g. 5 - 100 gm) and n can only generally be determined over much smaller intervals. However, it does not appear admissable to select a load range such that the highest load does not exceed the lowest load by more than ten times (e.g. 10 - 100 gm). It is definitely not allowable to extrapolate out to the higher standard hardness load range (≳ 3Kg), from microhardness measurements.

Bückle (1959) has determined from an analysis of many results (in the absence of errors) on 'metals or phases that are pure, homogeneous and have an undisturbed single crystal or very coarse grained structure' that the basic form of the log P - log d curve is as shown in Fig.9.3.

9.5 The Indentation of Brittle solids

The indentation of brittle solids presents a number of problems. Firstly a hardness impression is only considered 'good' if no cracking or fracturing occurs about the indent site. This evidently restricts the maximum applied load to relatively low values, and a high degree of error in measurement is likely. Secondly the diamond indentor itself may permanently deform if the material being tested is very hard, and hence this will result in anomalous results.

The observation that fracturing only occurs at high loads has been interpreted in terms of a size effect; that is, plastic deformation will result when the deformed volume is small. At higher load there is an increased chance of the stress field interacting with defects and then an increased probability of fracturing from microflaws in the solid. Such arguments are similar to those put forward to explain the tensile strength of brittle solids.

Some authors (see, for example, J.H. Westbrook, 1973) have commented on the use of an arbitrary scale for estimating the 'no-crack hardness' of brittle solids, tested by indentation. A brittleness number is defined, running from 0 to 5 (Fig. 9.4). Brittleness number = 0 corresponds to no visible cracks or chipping, while 5 corresponds to the shape of the impression being destroyed. Thus the hardness value is plotted against the brittleness number and the resulting curve extrapolated to zero brittleness for the no-crack hardness. It is suggested that only brittleness numbers 0, 1 and 2 should be used for determining microhardness values.

9.6 Experimental Methods

In these experiments a microhardness device fitted with a Vickers pyramid was used exclusively. The hardness tester (Fig.9.5) is an accessory to a Reichert MeF 2 optical microscope, and fits into position on the objective lens mounting. The load is applied by manually rotating the fine-focus control of the microscope, which moves the specimen stage, with the attached sample, down onto the pyramid. Thus, the loading rate can be controlled. Application of the load is vibrationless, provided care is taken and not too high a loading-rate attempted. The applied load is monitored continuously through the optical system. Before use, the loading system was calibrated using known weights within the range 5 gm - 100 gm and the occular diagonal length scale calibrated with a stage micrometer ruled at 0.01 mm intervals.

Measurements were made using unfiltered light (λ_{av} = 5500 Å). Since the Reichert microhardness tester utilises a × 63 objective lens, with a numerical aperture of 0.9, the resolving power is ≈ 0.3 μm. Thus the diagonal measurements are uncertain to ± 0.6 μm.

Microhardness tests were made at room temperatyre (300K) and in laboratory air (humidity ≈ 70%) on polished and etched sections of the X-, Y-, and Z-cut planes of single crystal synthetic quartz. The crystals were annealed at 800K in vacuo prior to testing. The indentor diagonals were aligned in the following crystallographic directions:

X $(11\bar{2}0)$: $[0001] - [10\bar{1}0]$

Y $(1\bar{1}00)$: $[0001] - [11\bar{2}0]$

Z (0001) : $[11\bar{2}0] - [10\bar{1}0]$.

Care was taken to ensure that the loading and unloading rate was kept approximately constant at 1.5 gm s^{-1}. The maximum load was held for fifteen seconds. At least five indentations were made at each load. No measurable difference in

hardness could be detected for variations in time-at-load from five seconds to three hundred seconds, over the full load range. Diagonal measurements were made in-situ immediately after indentation and unloading, using the occular eyepiece and normally incident illumination. In order to measure the length of the cracks radiating from the diagonal corners an optical micrograph was taken of each indentation. To achieve enhanced contrast on these micrographs slightly oblique illumination was used.

Scanning electron microscope specimens were prepared by mounting on aluminium stubs and coating with a conducting Au-Pd layer. Examination was made in a Cambridge Instruments S180 operated at 25 KeV.

Transmission electron microscopy samples were ion-beam thinned to electron transparency from the back side only (i.e. not the indented surface) and examination was performed in an A.E.I. (Ltd) EM7 with goniometer stage. Operation was at 1000 KeV, using two beam conditions.

To ascertain the consistency of the hardness measurements an experiment was undertaken in which fifty-two indentations were made on the same specimen (X-cut plane) at a load of 11 gm. A frequency histogram of these results (Fig.9.6) indicates that although the measured occular readings vary between the limits 20 - 26 divisions, the measurements are consistent with the majority falling close to the mean value of 23.6. From error theory we can show that the standard error in the mean is 0.15 units. However, the resolution imposed by the optical system is ± 0.6 μm which is equivalent to ± 4 occular divisions. These results apparently confirm the fact that any one observer can compare indentation diagonals to a higher degree of accuracy than that suggested by resolution consideration (Mott, 1956).

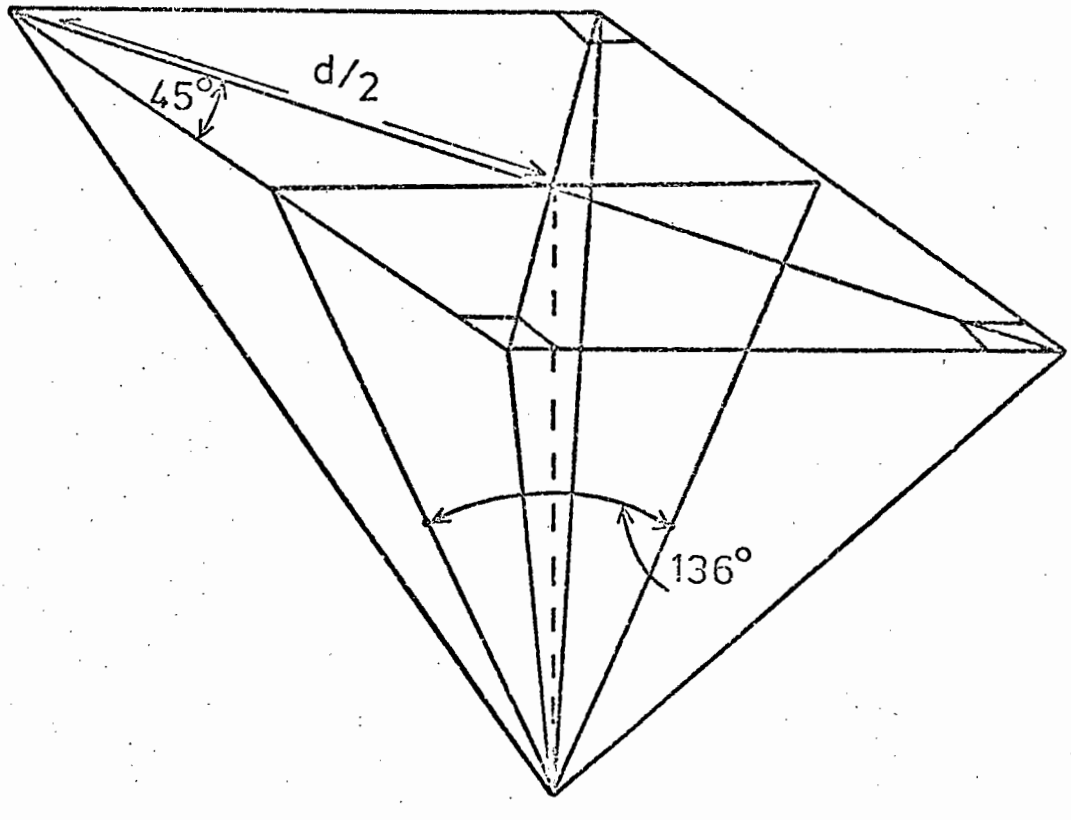

Fig.9.1 Schematic diagram of the Vickers hardness pyramid.

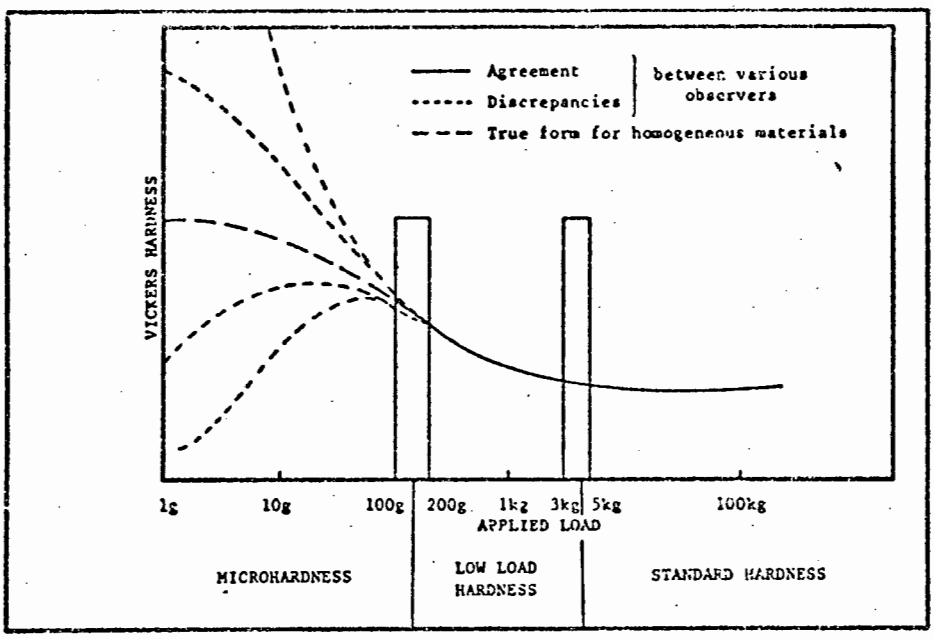

Fig.9.2 The three hardness loading ranges, indicating the basic form of the hardness/load curve. Note the disagreement for results in the microhardness regime. (after: Bückle, 1973).

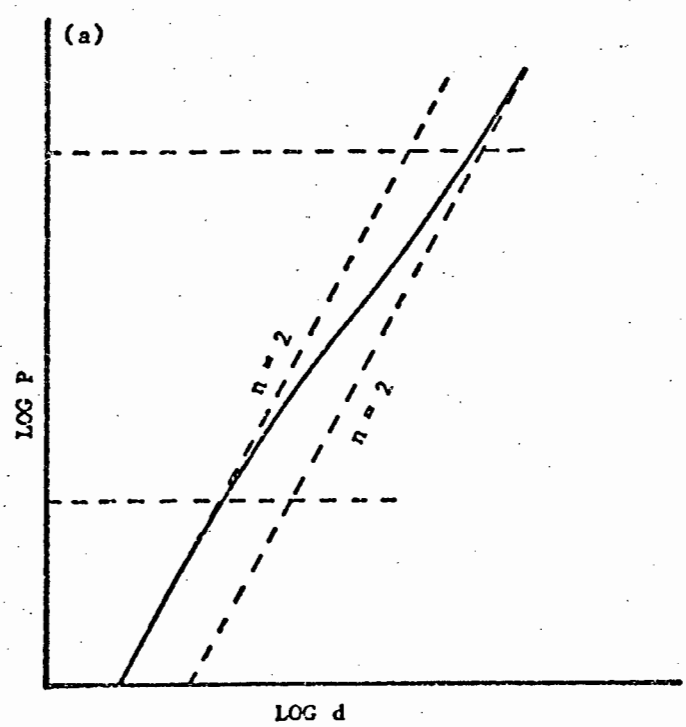

Fig.9.3 Basic form of the log P - log d curve in a homogenous material. The variation in logarithmic index (n) is indicated. (after: Bückle, 1959).

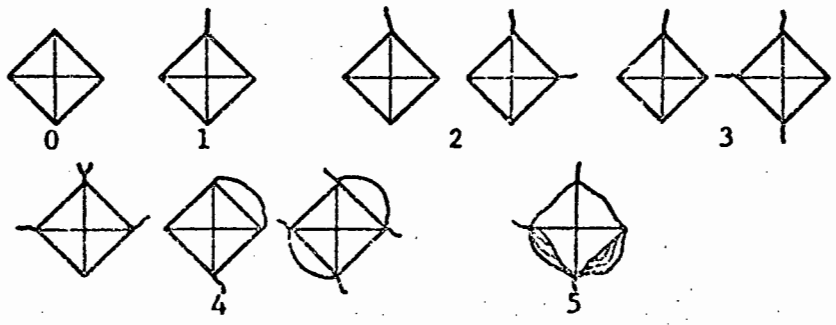

Arbitrary Scale for Estimating the Brittleness Number of Refractory Compounds

Brittleness number	Character of impression
0	No visible cracks or chipping
1	One small crack
2	One crack not coinciding with the continuation of the diagonal of the impression; two cracks in adjacent corners of the impression
3	Two cracks in opposite corners of the impression
4	More than three cracks; one or two chips at the sides of the impression
5	Shape of impression broken up

Fig.9.4 Schematic diagram of a proposed brittleness index (see text). (after: Westbrook, 1973).

Fig.9.5 Microhardness tester used in these experiments.

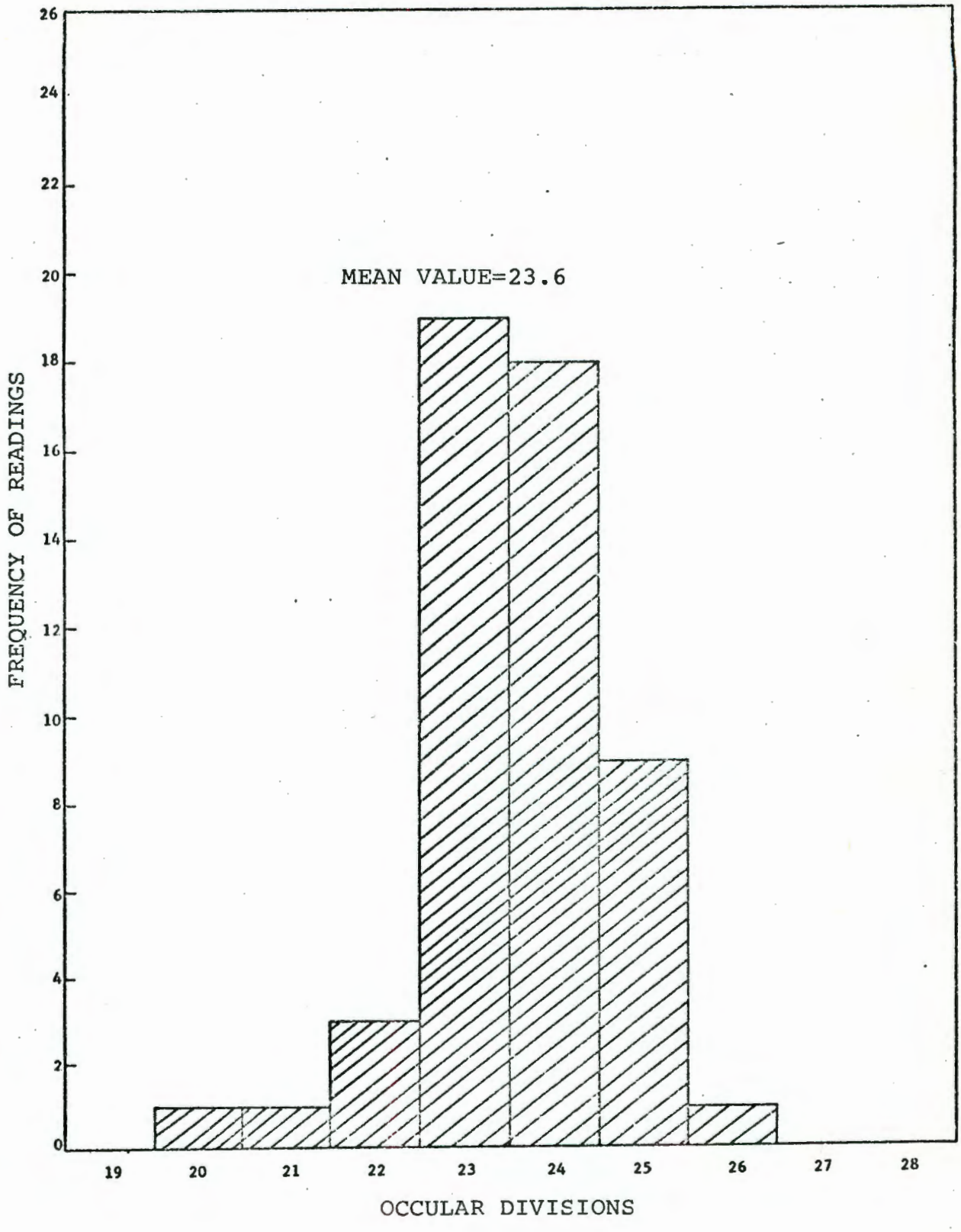

Fig.9.6 Frequency histogram of the results of 52 indentations made at a load of 11gm on the X-cut plane.

9.7 Results

9.7.1 Microhardness Data

The microhardness (MH) values obtained from the measurements are presented as a function of applied load (P) (Fig.9.7) and impression diagonal (d) (Fig.9.8) for all three crystal orientations. It is noted that the hardness value shows an increase as the load is decreased. Also evident are large fluctuations in hardness from load to load. The data on the diagonal lengths is included since this provides a clearer means of comparing results from different samples. This can be rationalised by considering that the imposed deformation volume is the same for a constant diagonal length, in this case, a higher hardness value indicates an increased pressure acting below the indentor.

9.7.2 The Logarithmic Index, n

The date was used to obtain a value for the logarithmic index n, of the Meyer power law (eqn.9.4). Log P/log d (Fig.9.9a-c) was plotted for each of the three crystal orientations and a least squares fit applied to the measurements. The slope of this curve yields n.

The calculated values of n were as follows:

X $(11\bar{2}0)$: n = 1.81

Y $(1\bar{1}00)$: n = 1.80

Z (0001) : n = 1.73

These values of n(<2) indicate that, as expected, the hardness increases with decreasing load. Using eq.(9.5) the MH can hence be represented over the load range 10 - 100 gm as:

X $(11\bar{2}0)$: MH = $991\ P^{-0.106}$ Kg mm^{-2}

Y $(1\bar{1}00)$: MH = $855\ P^{-0.113}$ Kg mm^{-2}

Z (0001) : MH = $818\ P^{-0.158}$ Kg mm^{-2}

These results are plotted in Fig.9.10.

The hardness can be expressed in terms of an indentation diagonal length d and the logarithmic index n as:

$$n_{MH_d} .$$

Choosing d = 10 μm we can show, via eqn.9.4, that:

X $(11\bar{2}0)$: MH = $^{1.81}1312_{10\mu m}$ Kg mm^{-2}

Y $(1\bar{1}00)$: MH = $^{1.80}1167_{10\mu m}$ Kg mm^{-2}

Z (0001) : MH = $^{1.73}1251_{10\mu m}$ Kg mm^{-2}

If it had been assumed that n = 2, a plot of P/d^2 would have given the following values for MH:

X $(11\bar{2}0)$: MH = 1346 Kg mm^{-2}

Y $(1\bar{1}00)$: MH = 1192 Kg mm^{-2}

Z $(000\bar{1})$: MH = 1297 Kg mm^{-2}

9.7.3 Microscopic Examination

(a) Optical Microscopy

Examination of the indentations at high magnification disclosed differences between the three crystal planes indented. Fig.9.11 shows a typical indent on the Z-cut plane. The median cracks, lying along the planes of symmetry of the pyramid, are clearly visible at the surface radiating from the diagonal corners in the $[10\bar{1}0]$ and $[11\bar{2}0]$ directions. These

cracks were formed at all loads, apart from the lowest ($\lesssim$ 10 gm), and no deviations from the trace of the pyramidal base diagonals was noted for this crystal orientation. During post indentation observation, one of these cracks was noted to rapidly develop.

Similar observations were made for the Y-cut plane (Fig.9.12). Well-developed cracks radiate from the diagonals for all loads $\gtrsim$ 10 gm. However, a new feature is observed (Fig.9.13), visible as white contrast on the optical micrograph, and which lies to the edges of the indentation crater. This feature was observed for all load $\gtrsim$ 40 gm, and was often present on only one or two sides of the impression (Fig.9.14).

On the X-cut plane the median cracks showed a departure from the expected indentor diagonal symmetry. Fig.9.15 shows clearly that along the trace of [0001] only one crack is produced; on the opposite side of the indent the crack has split into two directions. This was a general observation for the X-cut plane. A further example is shown in Fig.9.16. Note also now that the cracks in the $[10\bar{1}0]$ direction are not present. In Fig.9.17 a crack can be seen which has followed a 'zig-zag' path during development. Also visible are the regions of white contrast at the edges of the indent, similar to that observed for the Y-cut plane (c.f. Fig.9.14).

(b) Scanning Electron Microscopy

To achieve good revolution of the indentations it was found necessary to tilt the samples to an angle of between 50 - 70°. Fig.9.18 shows an indentation made on the Z-cut plane. The overall appearance is smooth, with no obvious fragmentation, fracturing or crushing. The median cracks are clearly visible, with a large opening displacement close to the indent crater. There is also evidence that relaxation of the indent may have occurred after unloading. Careful examination reveals that the walls of the crater have sprung back in towards the centre. The degree of relaxation

is greater at the mid-points between adjacent diagonal corners, and this is schematically represented in Fig.9.19. Fig.9.20 is a low load (5.4 gm) impression on the Z-cut plane. Note the rather indistinct shape, and the absence of median cracks.

It can be seen that the white contrast visible on the optical micrographs (e.g. 9.13) is associated with shallow lateral chips (Fig.9.21). This effect is further shown in Fig.9.22 for the X-cut plane; note particularly in this case the median cracks radiating out from the sides of the indentation. Visible within the indent walls are microcracks (marked C). Fig.9.23 (at higher magnification and at a larger SEM tilt angle) shows this microcracking phenomenon. It appears that the development of these cracks may be associated with the appearance of slip line outcrops (Fig.9.24). Fig.9.25 shows a further example of indentation microfracturing.

Investigation of etched indentation made on the Z-cut plane (Fig.9.26) showed no evidence for the development of either etch pits or crystallographic features, such as rhombohedral faceting.

However, there is one feature of interest, which is the development of a series of lines, having a distinct crystallographic nature, around the indentations. These lines are common to all of the indentations (only the Z-cut plane was investigated) and follows the same general pattern. A re-investigation of this effect using the Nomarski light interference technique shows the pattern clearly (Fig.9.27). It is tentatively suggested that this effect may be the development of secondary Dauphiné twins.

(c) High Voltage Electron Microscopy

Specimens which had been indented at 50 gm were examined by transmission electron microscopy. However, while there was no unambiguous evidence for dislocation nucleation and slip from this investigation, the results are clearly suggestive of such a process. Figs.9.28 and 9.29 are typical micrographs taken in two-beam conditions. The cracks extending from the indentation diagonals are clearly visible, and the theoretical

outline of the impression has been shown by dotted lines on Fig.9.28. From this it may be seen that the image contrast is coming from a localised region at the bottom of the impression. Since the thinning process did not remove any material from the surface which was indented, then this effect must be wholly due to dislocation nucleation and/or strain at the apex of the impression.

If plastic processes are operating during the indentation process then the number of dislocations generated must be extremely high, and hence not resolvable in the electron microscope due to overlapping images. In addition there was no evidence for twin formation or phase transformations from diffraction patterns.

(d) X-ray Diffraction Topography

To obtain an estimate of the extent of the strain field about the indentations, a series of impressions (5.4 gm - 100 gm) was made on the Z-cut and Y-cut planes, and examined by Lang X-ray diffraction topography.

Figs.9.30 and 9.31 show the resulting topographic images. The greatest spatial extent of the strain field (the black contrast on the topographic image) lies on the negative side of the diffraction vector ($\underline{g}$). The widths of the strain field were measured as shown in Fig.9.30b. These results, along with the corresponding diagonal size as determined optically, are given in Fig.9.32.

9.7.4 Fracture Toughness Measurements

Measurements were made of the lengths of the median cracks (c), as a function of applied load (P). No significant crystallographic anisotropy of crack length could be determined, and hence an average value was taken for each indent. In the case of the X-cut plane, the cracks extending from the indentation sides were not included. c^3 was plotted as a function

of P^2, and the slope of the least-squares linear relationship (P^2/c^3) (Fig.9.33) is given by:

$$\frac{2E\gamma\ \pi^3\ \tan^2\ (\theta/2)}{1-\nu^2}$$

Using average values of Poisson's ratio ν (≈ 0.1) and Young's modulus $E(\approx 10^{11}\ N\,m^{-2})$ we may calculate the fracture surface energy γ for each crystal plane indented. These results give for γ:

X-cut plane $(11\bar{2}0)$: 9.6 J m^{-2}

Y-cut plane $(1\bar{1}00)$: 8.2 J m^{-2}

Z-cut plane (0001) : 11.4 J m^{-2}

It should be noted that these values refer to room temperature, moist laboratory air conditions.

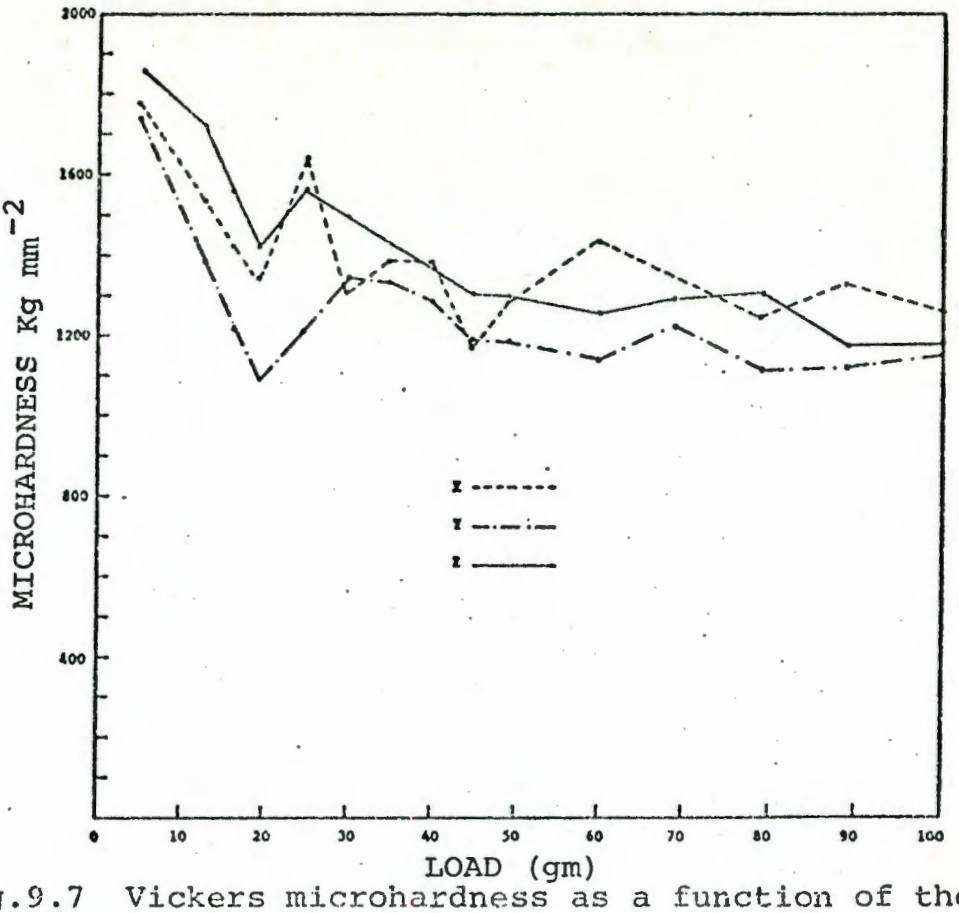

Fig.9.7 Vickers microhardness as a function of the applied load (X-, Y-, and Z-cut planes).

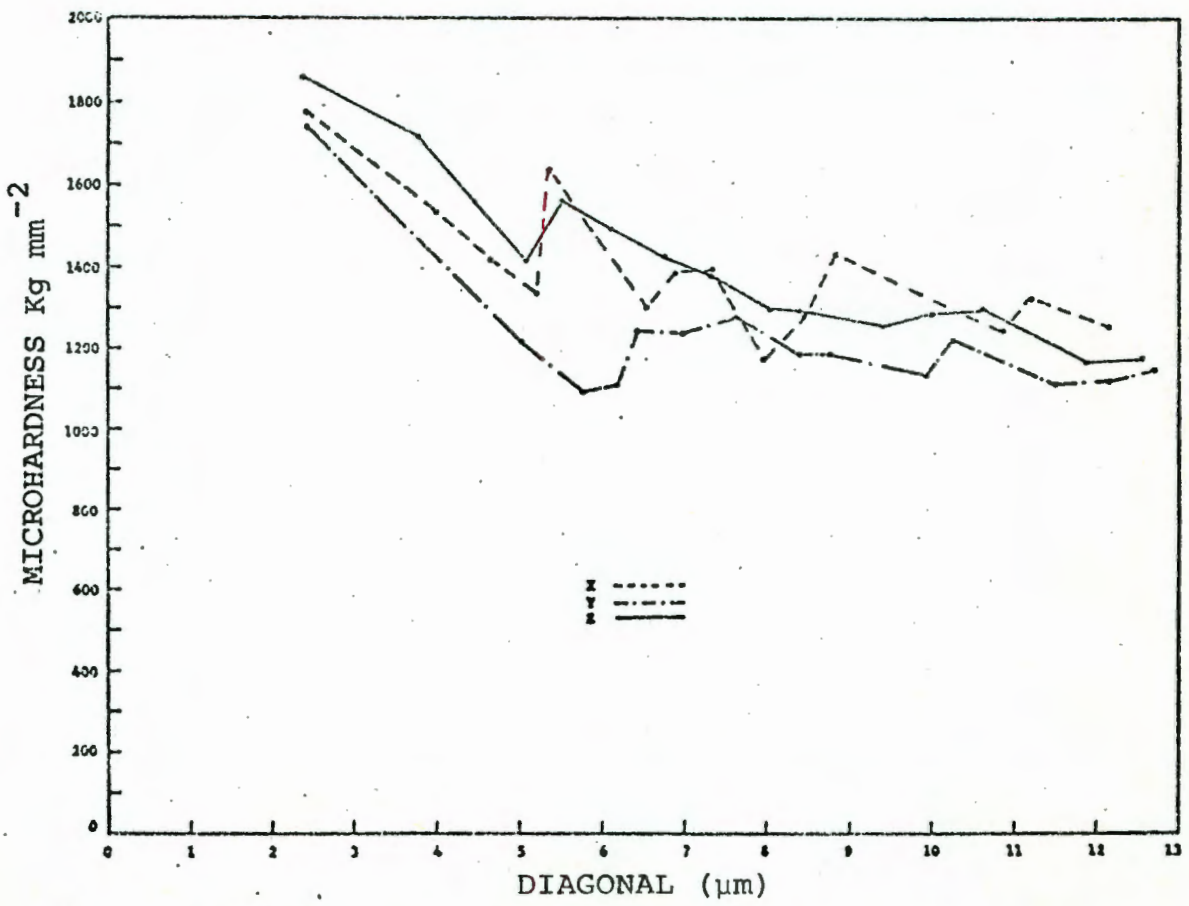

Fig.9.8 Vickers microhardness as a function of the impression diagonal length (X-, Y-, and Z-cut planes).

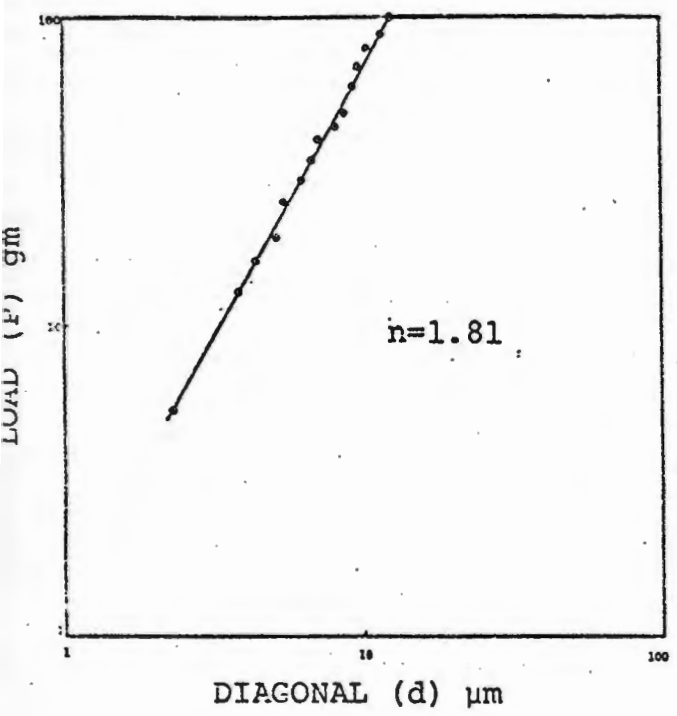

(a)

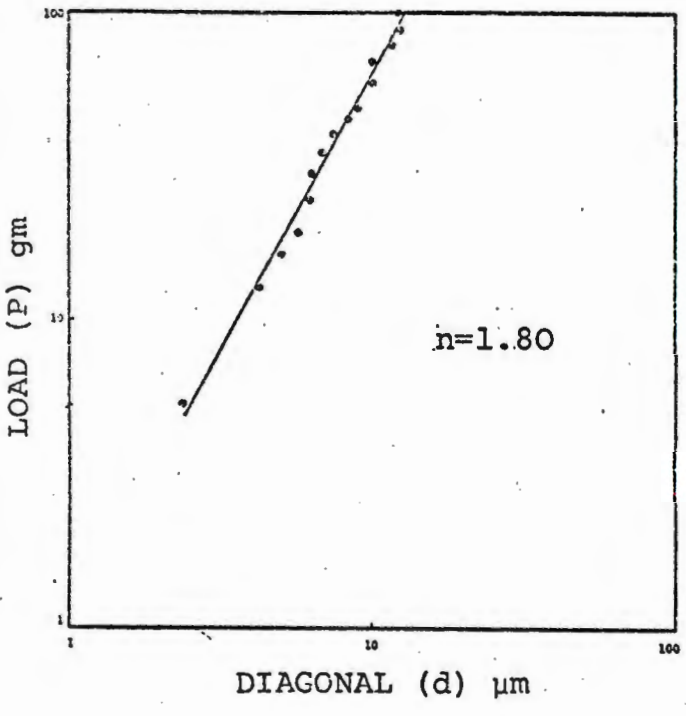

(b)

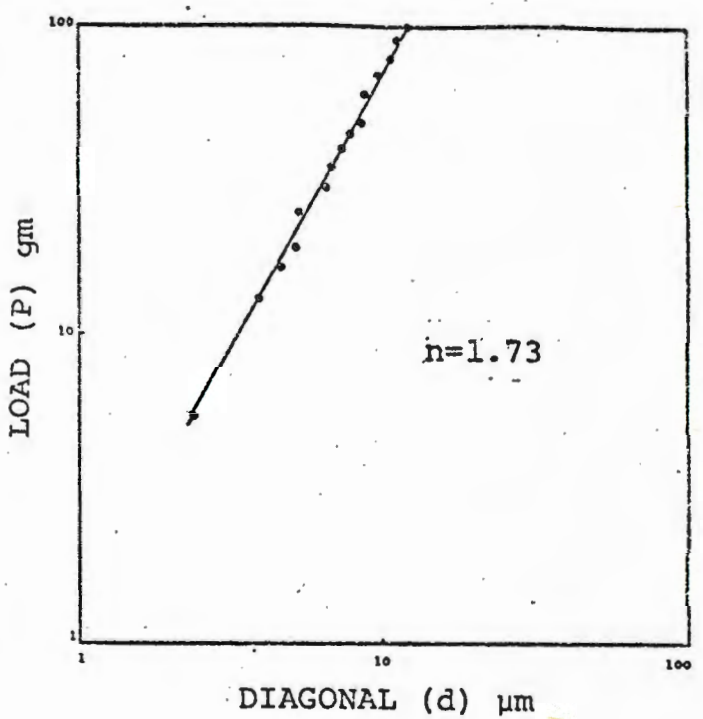

(c)

Fig.9.9 Log P/log d for (a) X-cut plane. (b) Y-cut plane. (c) Z-cut plane. The slope of the curve yields the logarithmic index, n.

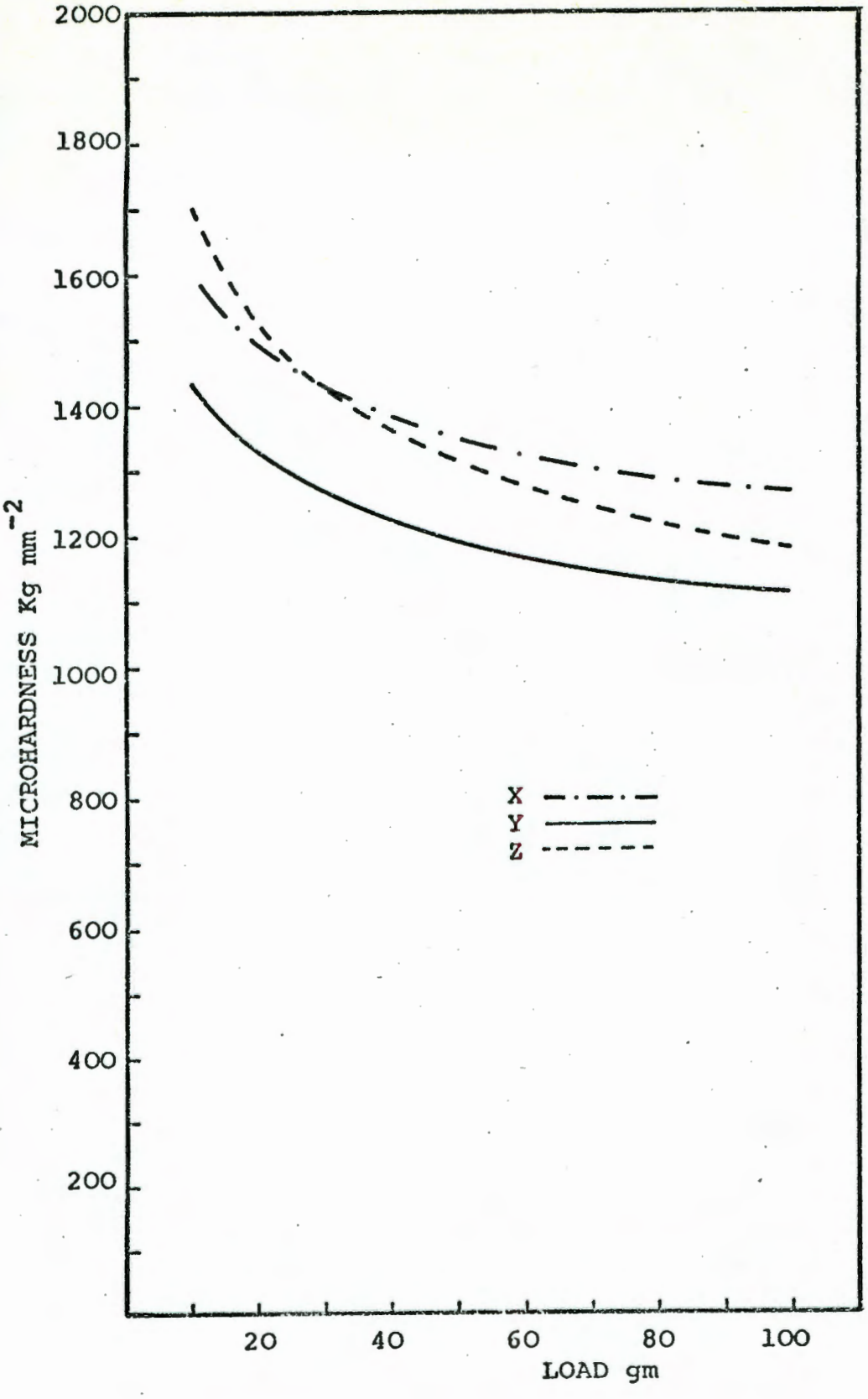

Fig.9.10 Hardness as a function of applied load. The hardness values are calculated using the logarithmic index (n) and the Meyer power law expression (eq. 9.5).

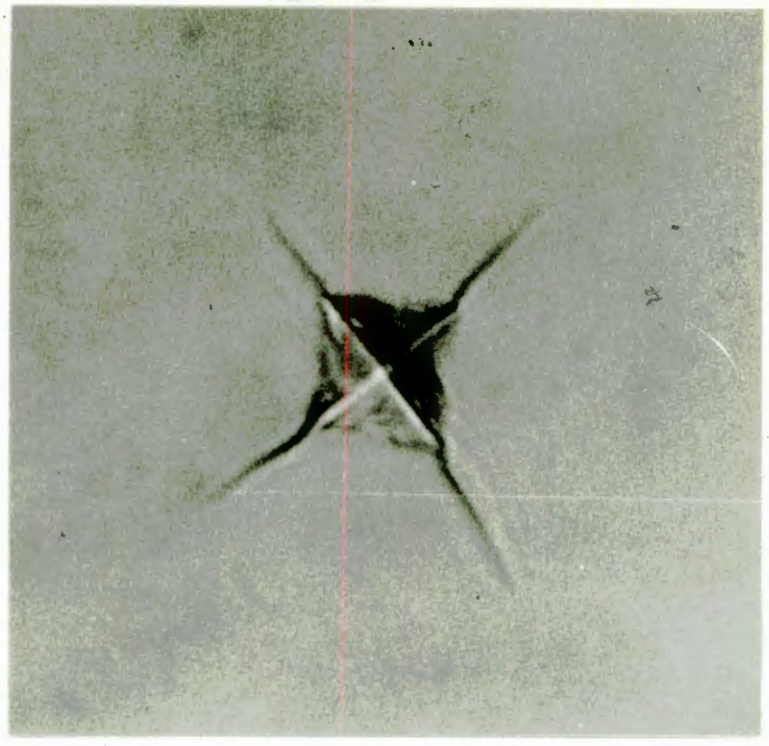

Fig.9.11 Optical micrograph of a 100gm indentation (Z-cut plane).

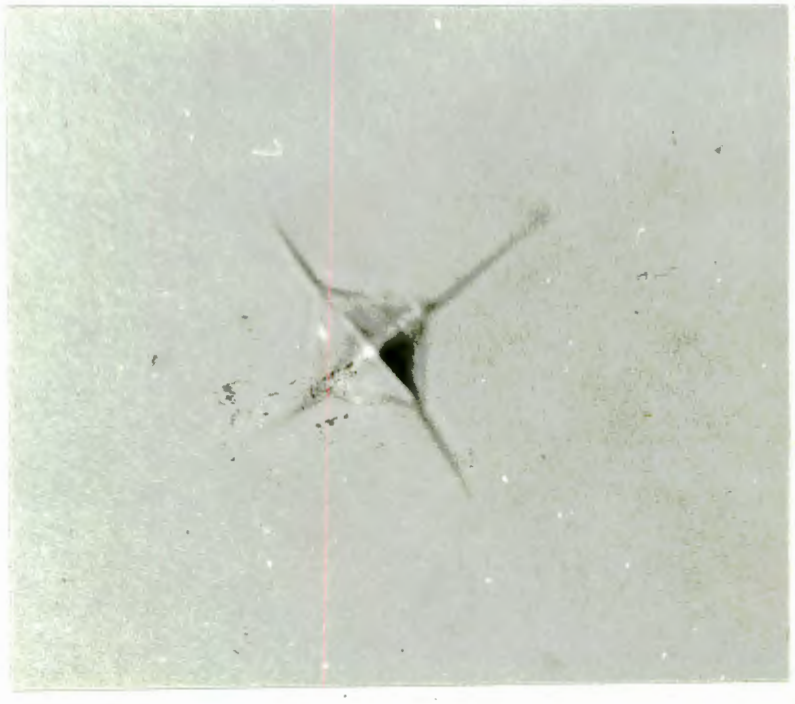

Fig.9.12 Optical micrograph of a 69gm Vickers indentation (Y-cut plane).

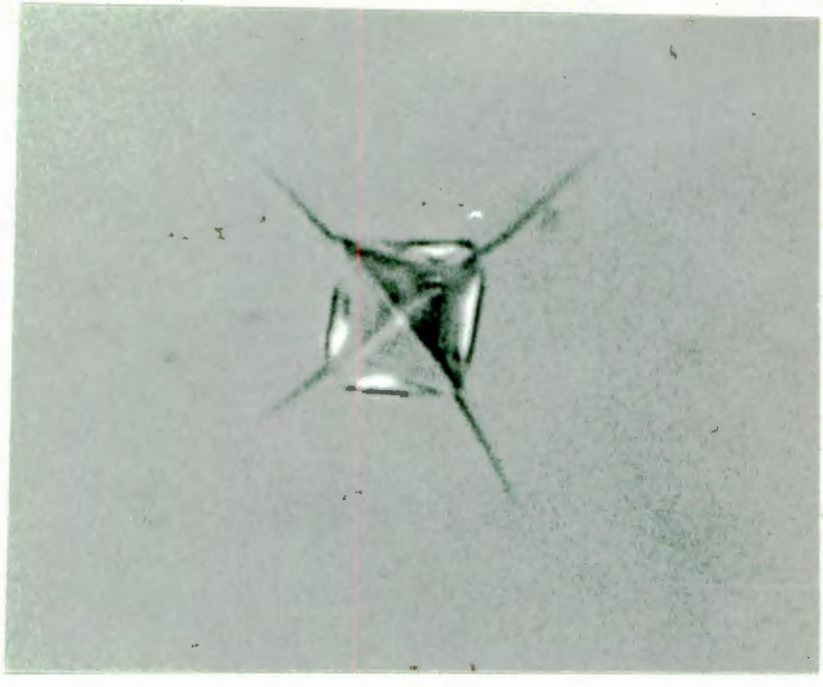

Fig.9.13 89gm Vickers indentation. Note the features at the edges of the impression visible as white contrast (Y-cut plane).

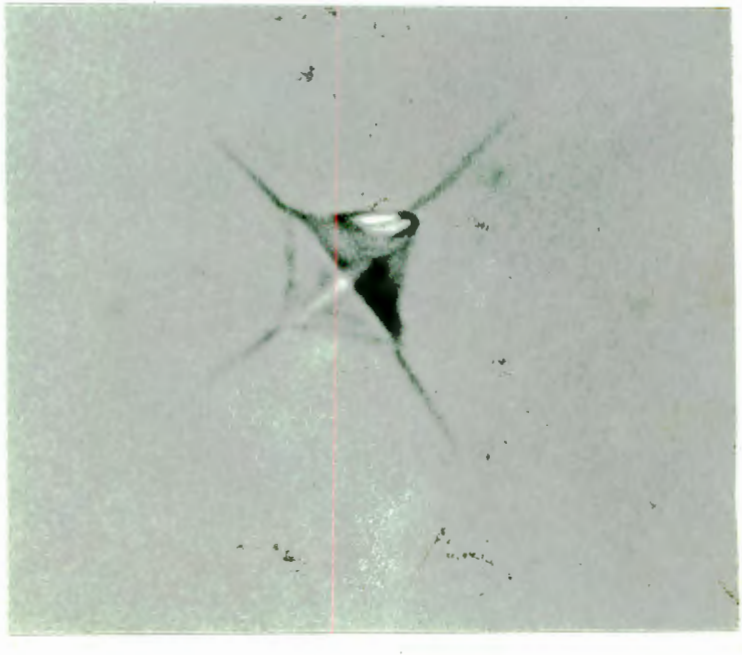

Fig.9.14 79gm Vickers indentation (Y-cut plane).

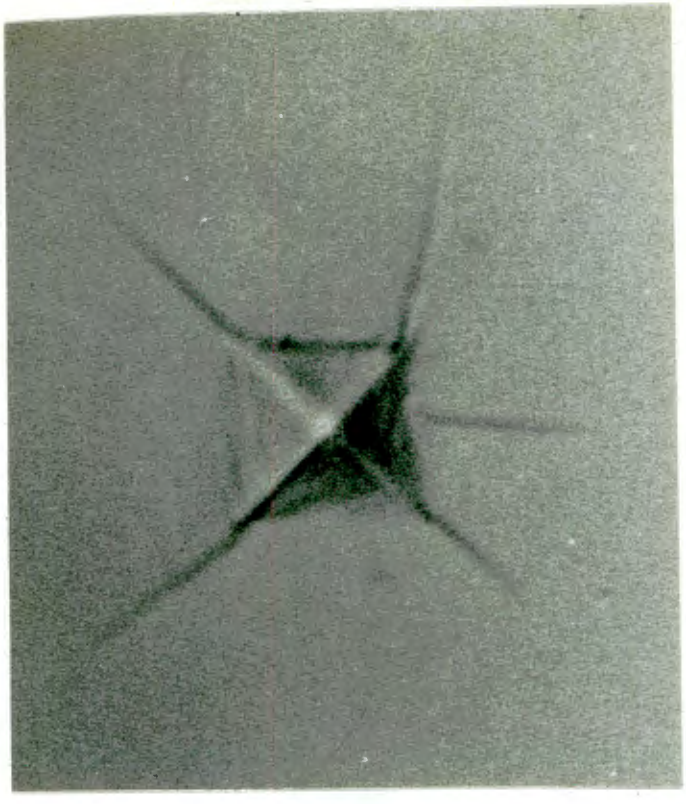

Fig.9.15 89gm Vickers indentation on the X-cut plane. Note the fact that the median crack does not follow the trace of the impression diagonal.

Fig.9.16 60gm Vickers indentation on X-cut plane.

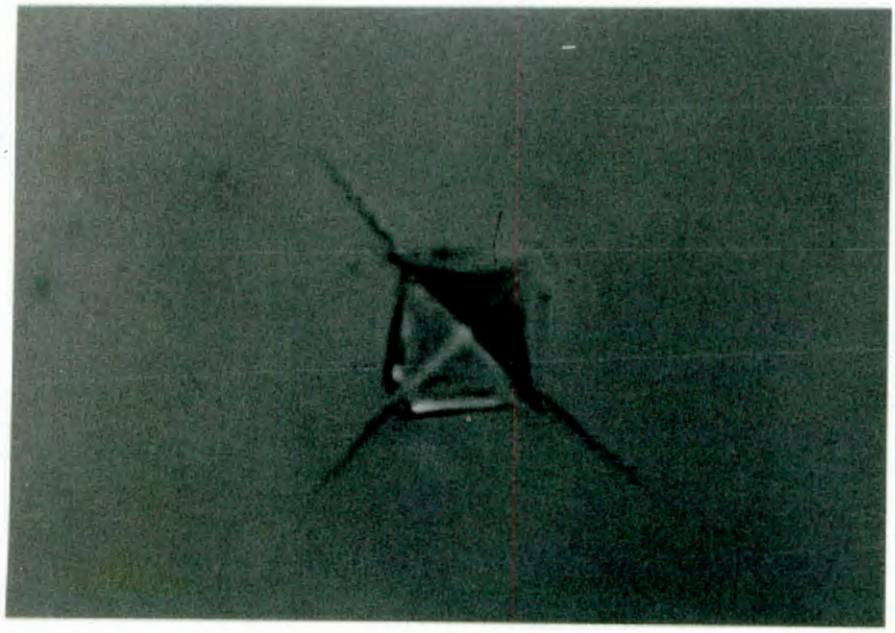

Fig.9.17 100gm Vickers indentation on X-cut plane.

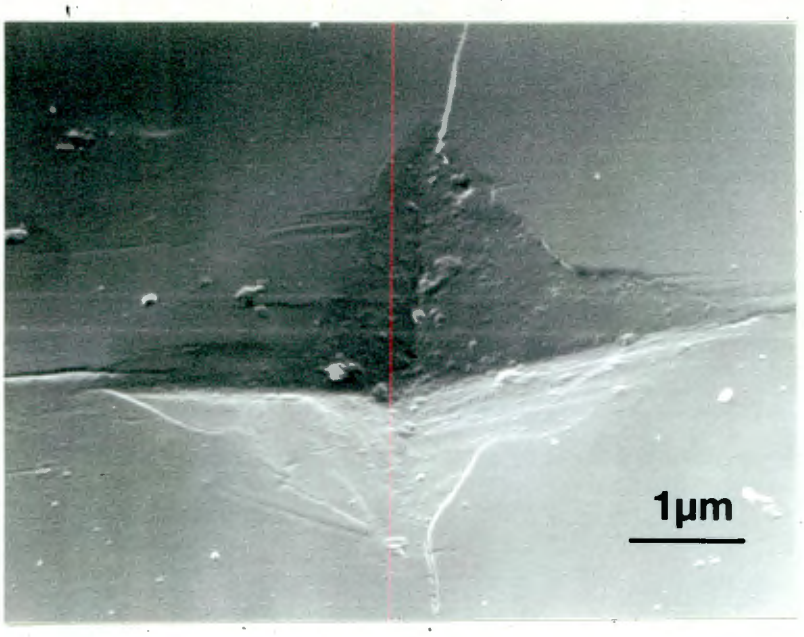

Fig.9.18 SEM of 30gm Vickers indentation made on Z-cut plane.

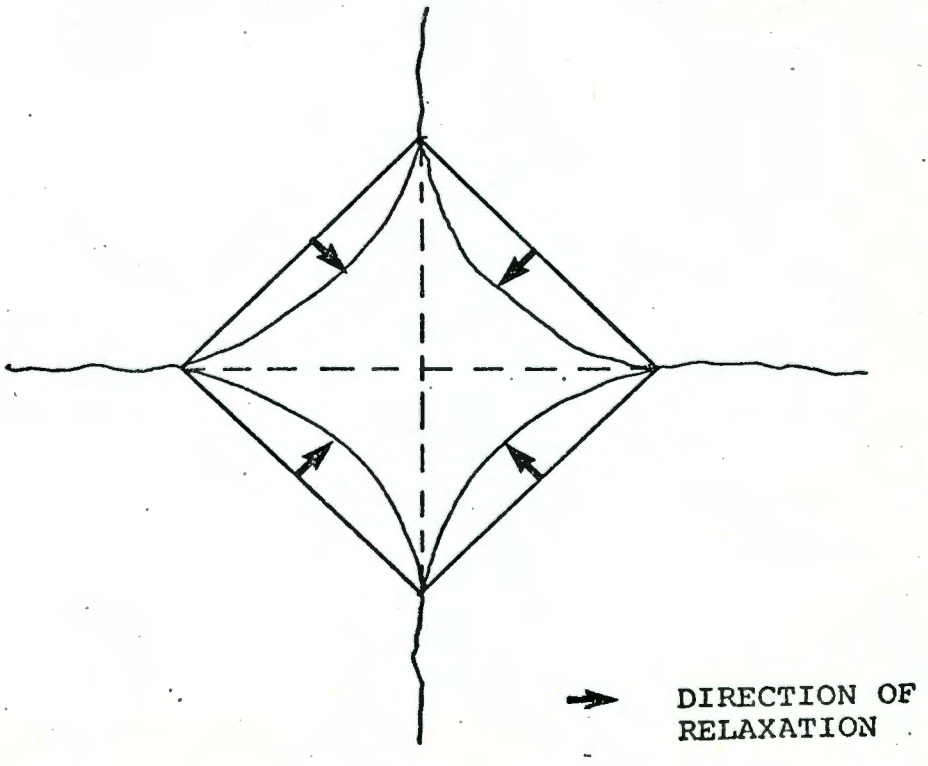

Fig.9.19 Schematic diagram to show relaxation of walls of impression. (see text).

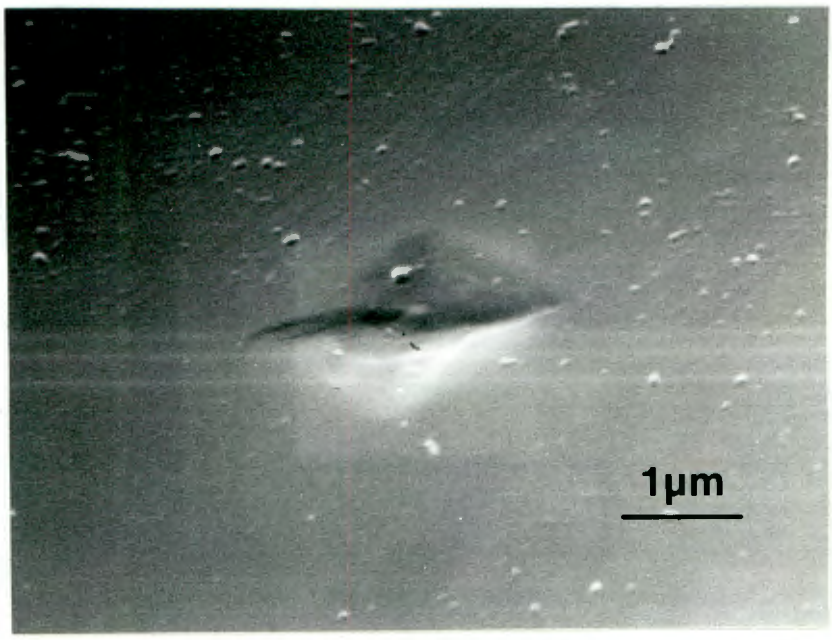

Fig.9.20 SEM of low load (5.4gm) indent on Z-cut plane. Note the indistinct shape and lack of cracks.

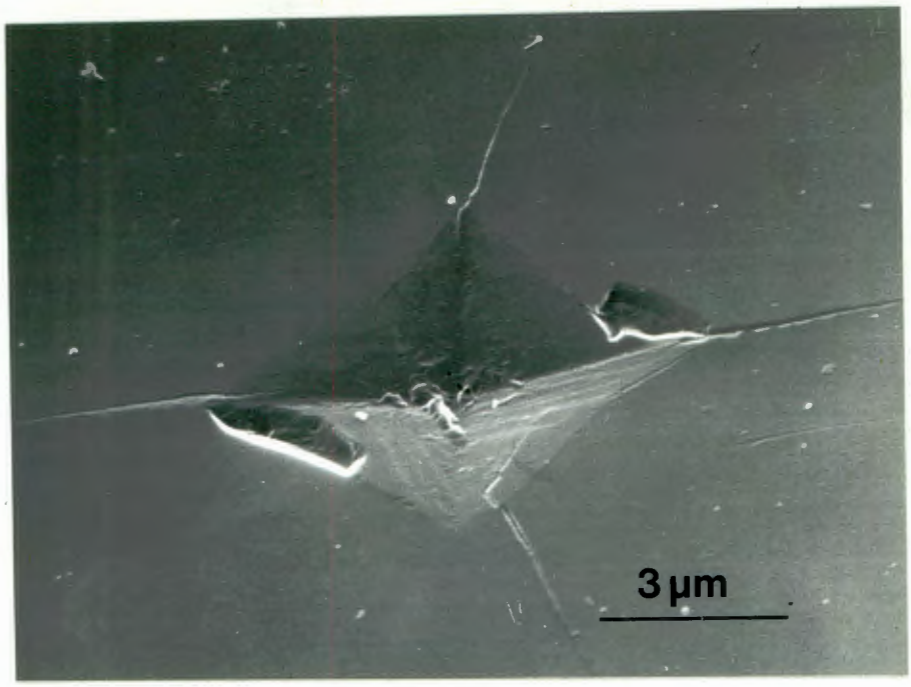

Fig.9.21 SEM of 35gm indentation on the X-cut plane. Note in particular the shallow chips at the edge of the impression.

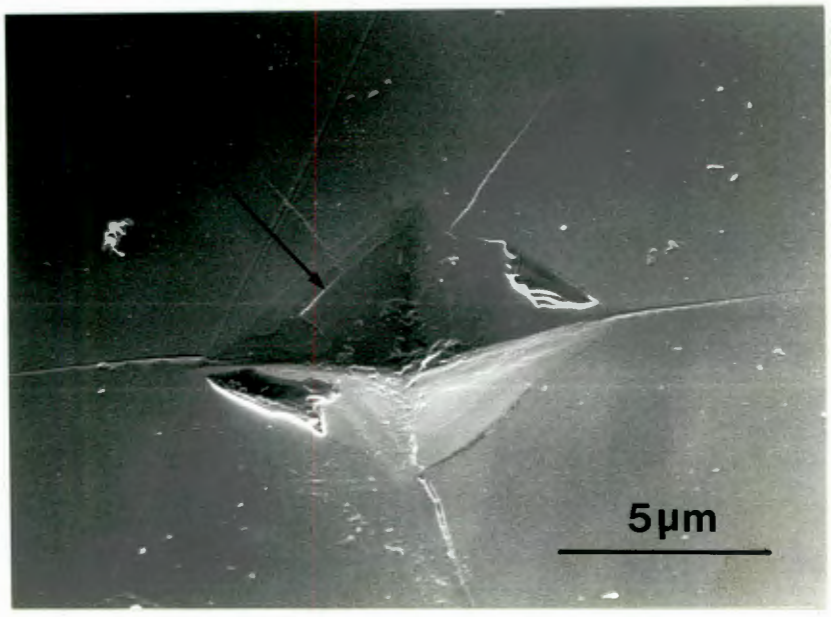

Fig.9.22 SEM of 60gm indentation on the X-cut plane. Micro-cracks within the impression are marked c.

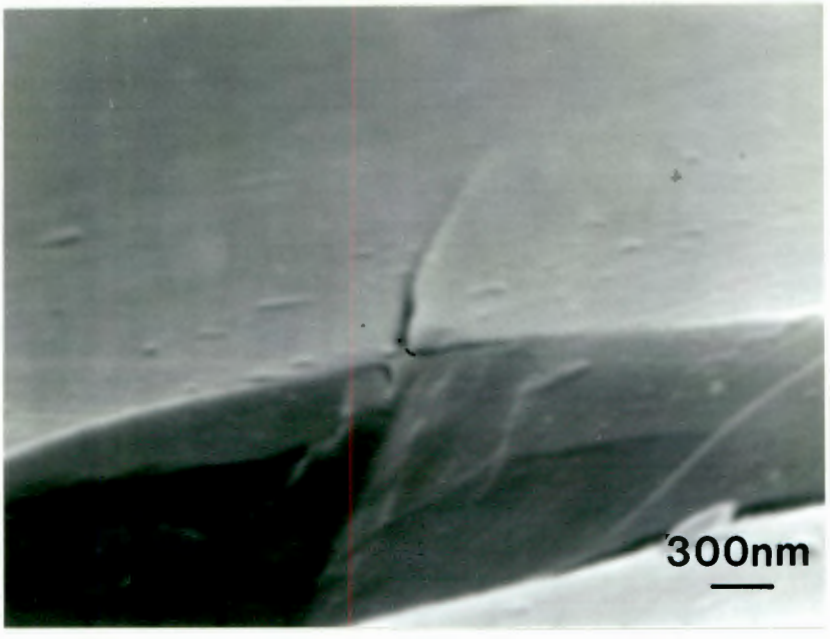

Fig.9.23 High magnification SEM to show microcracks on the walls of the impression.

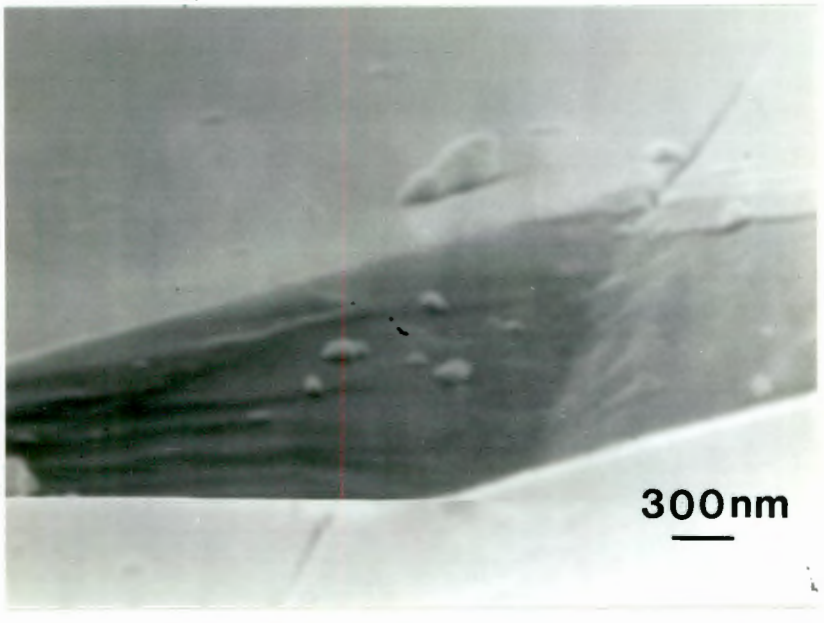

Fig.9.24 Further details of above. The smooth lines on the walls of the impression are reminiscent of slip line outcrops.

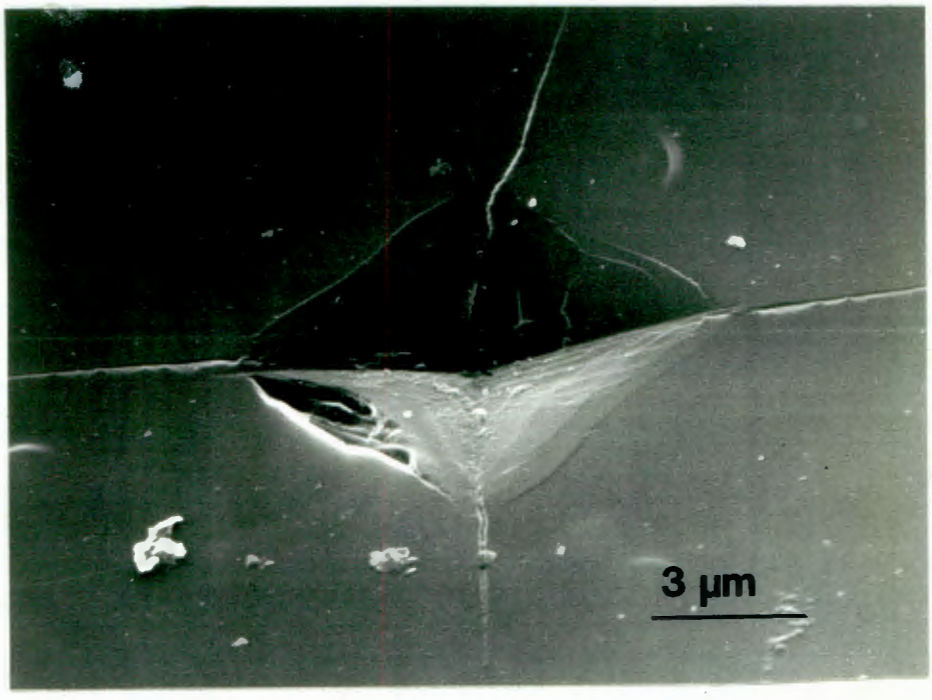

Fig.9.25 A further example of microfracturing during indentation (70gm, X-cut plane).

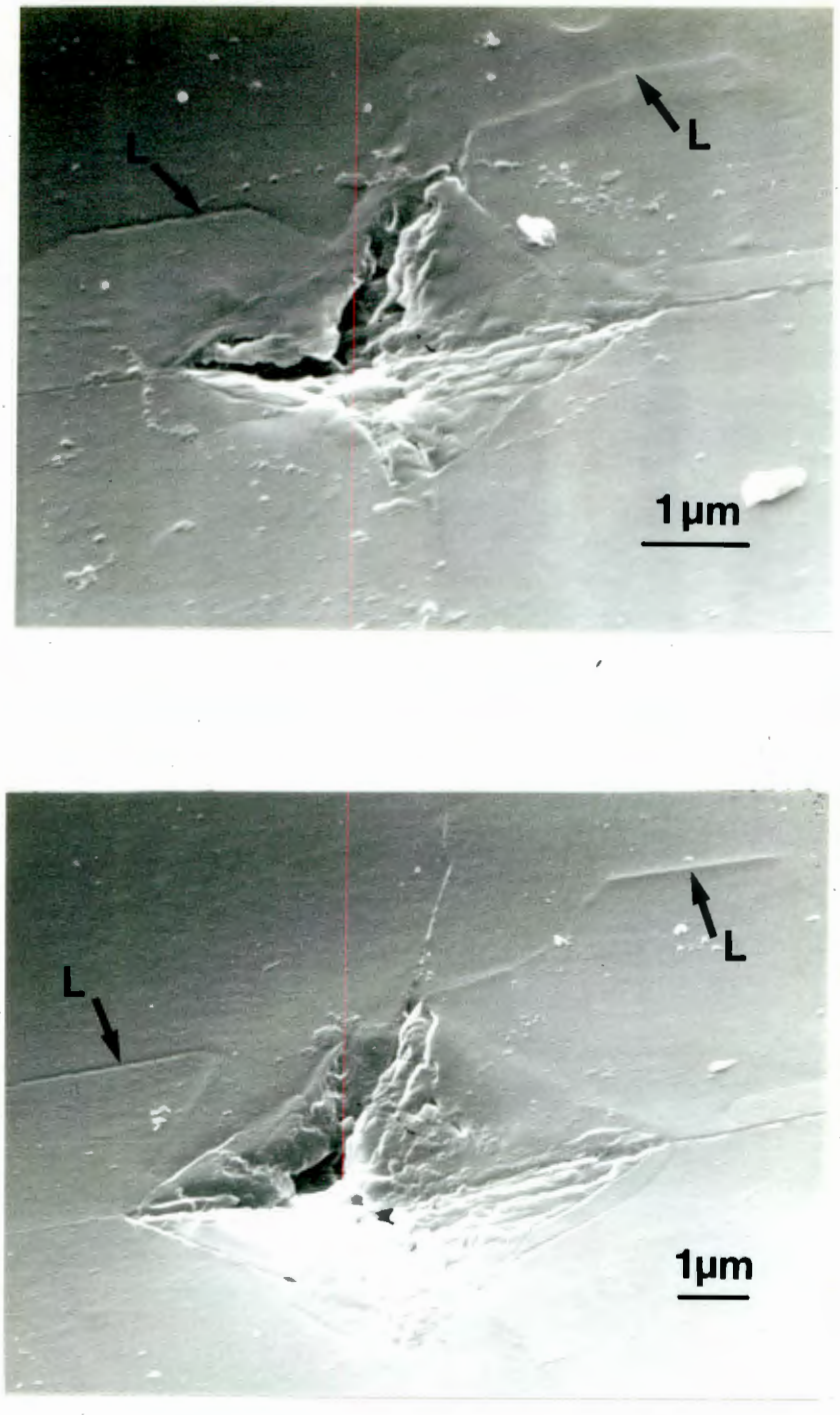

Fig.9.26 Examples of etched indentations examined in the SEM. The features marked (L) are discussed in the text. Z-cut plane.

Fig.9.27 Nomarski light interference micrograph of etched indentations. The features (L) seen in fig.9.26 are clearly visible, and are arrowed.

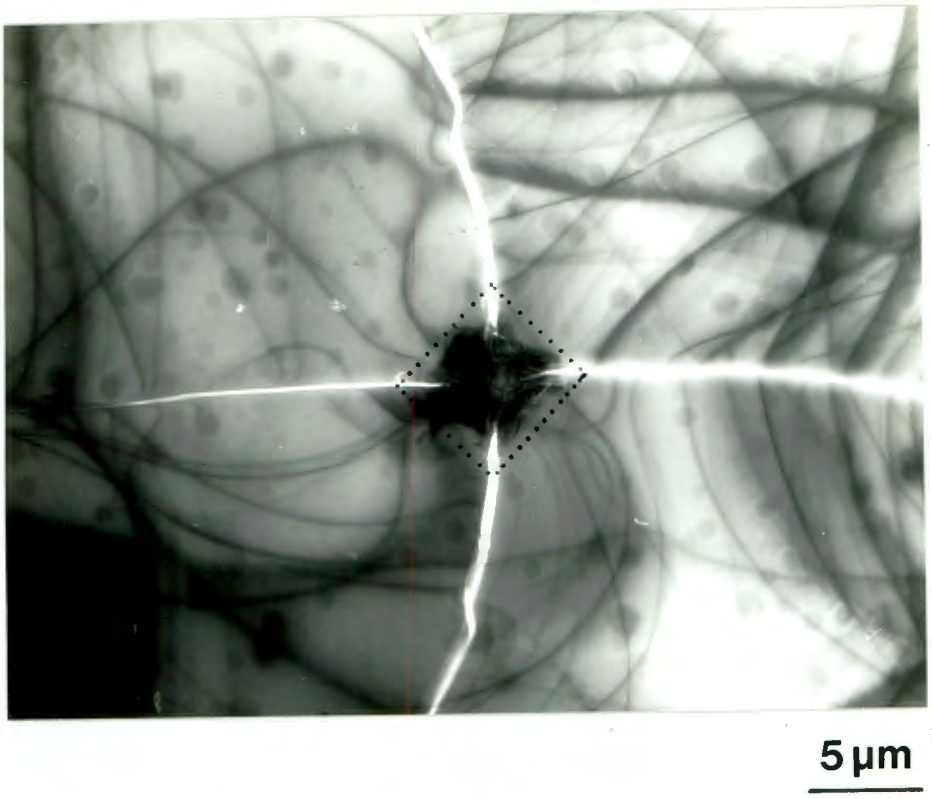

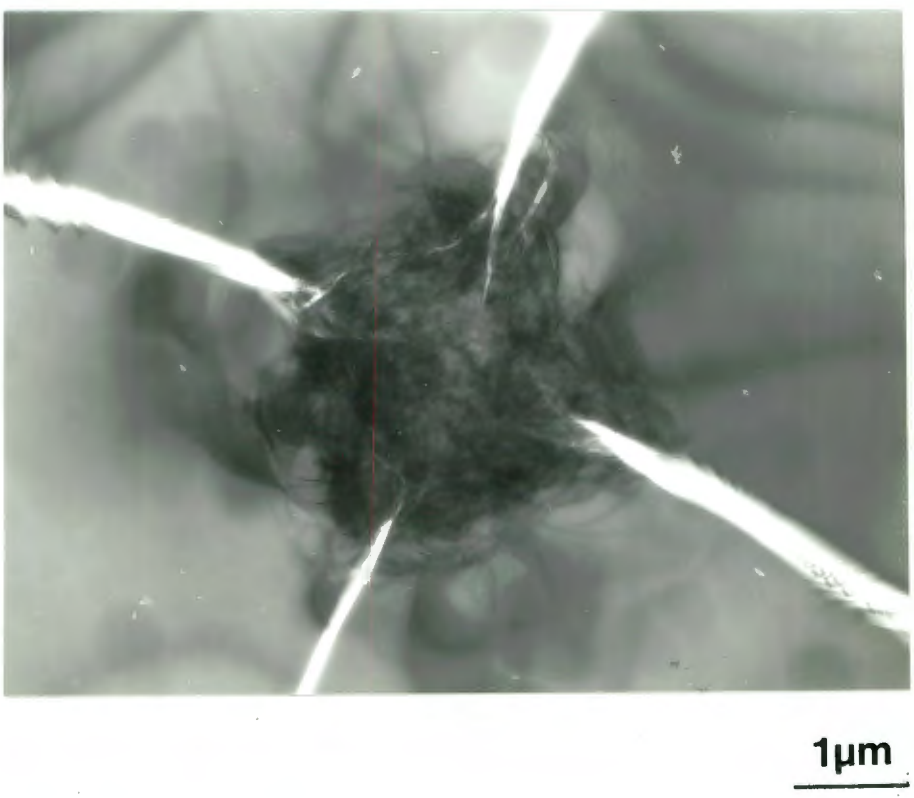

Fig.9.28 Typical examples of micrographs taken using HVEM. The outline of the impression (from optical measurements) is shown by the dotted line. Note the extension of the cracks from the diagonal corners, and also the localized nature of the contrast from the bottom of the impression. (Y-cut plane, 50gm).

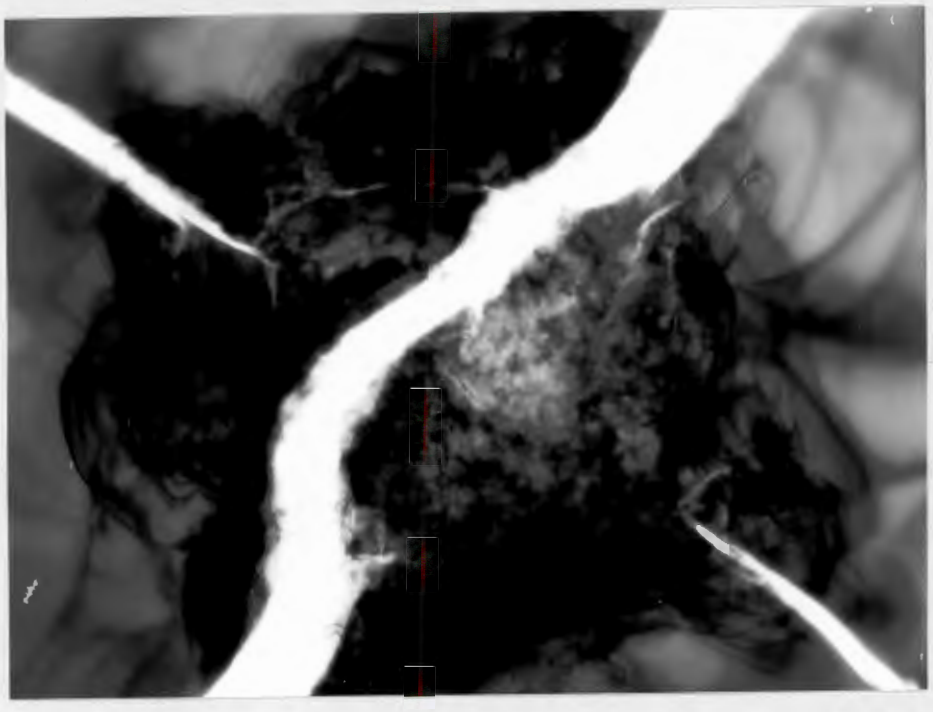

0.5μm

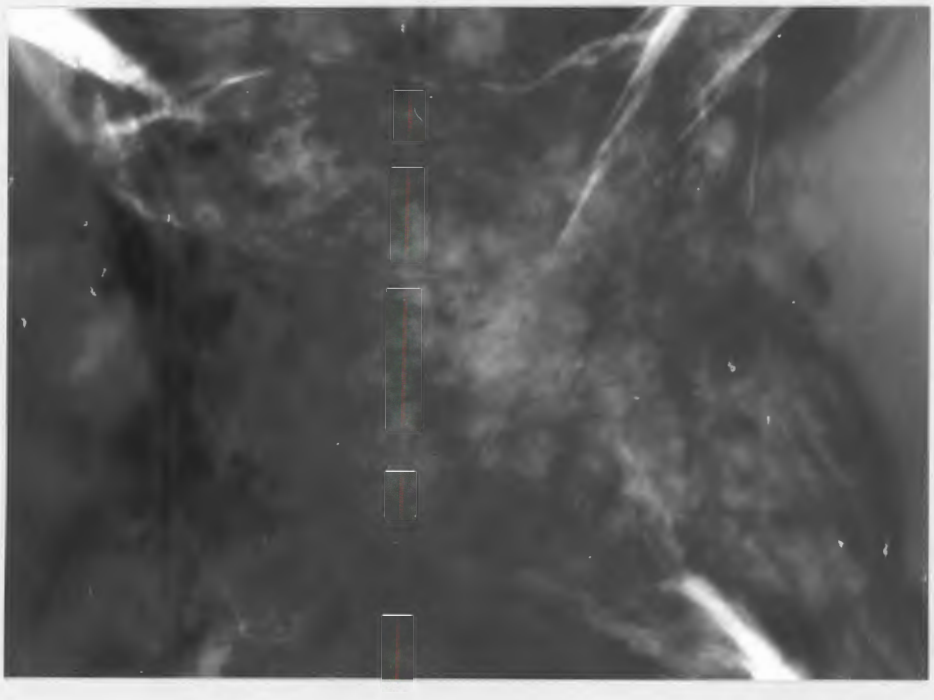

0.5μm

Fig.9.29 Further examples of HVEM micrographs. Individual dislocations cannot be imaged, but it is believed that a high density of dislocations has been produced. (Y-cut plane, 50gm).

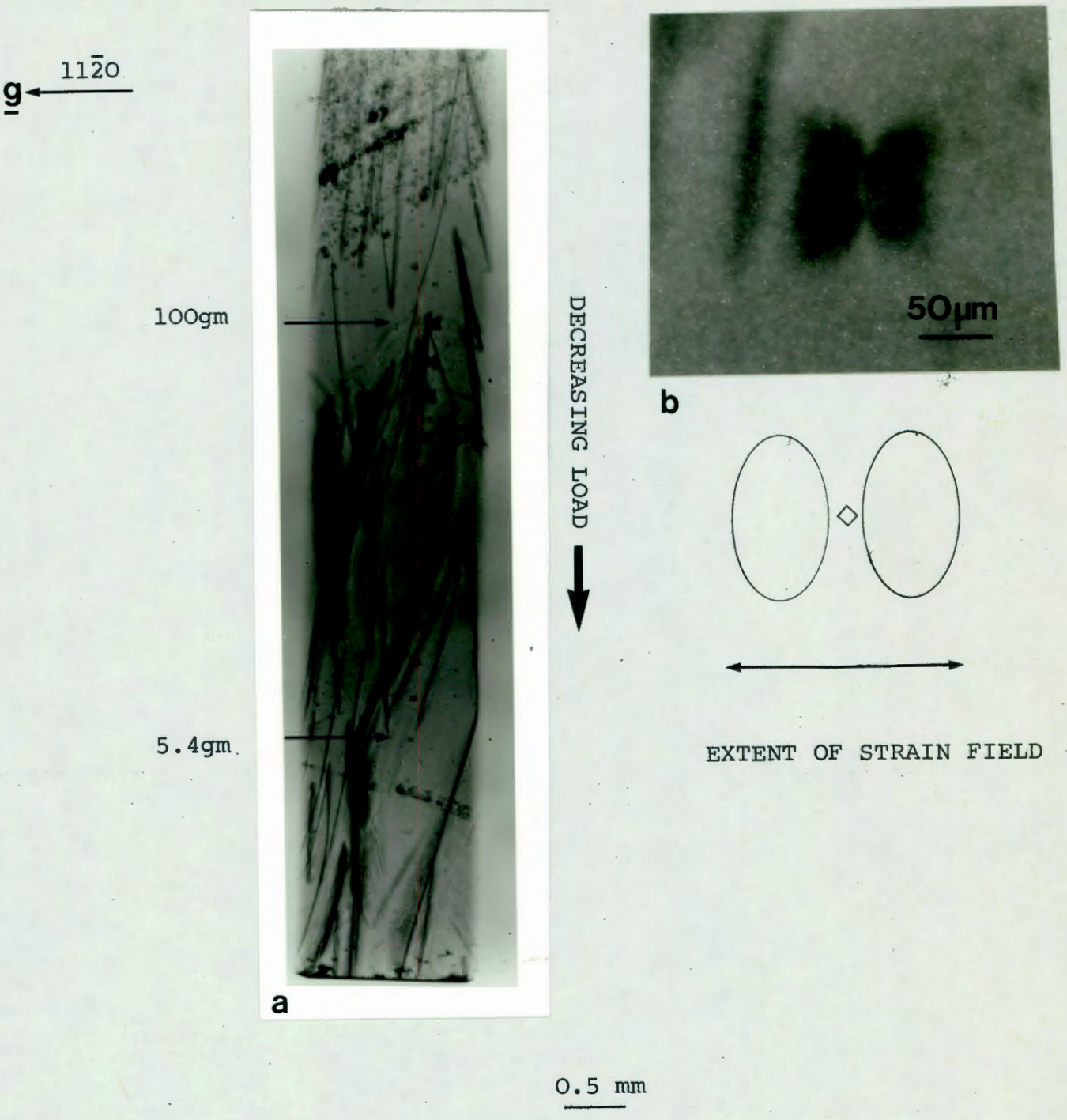

Fig.9.30 X-ray diffraction topograph of a series of indentations (5.4gm-100gm) made on the Y-cut plane. (a) The complete series. (b) High magnification of 100gm indent.

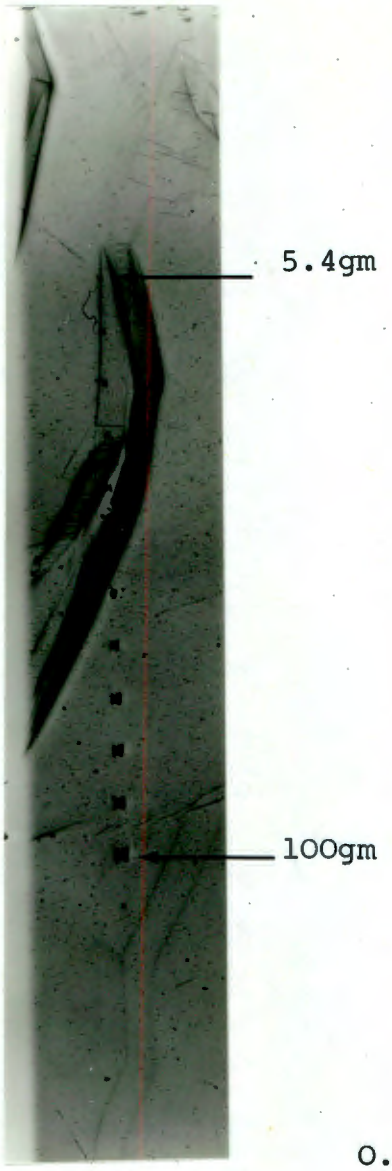

$\underline{g}$ ← $10\bar{1}1$

Fig.9.31 X-ray diffraction topograph of a series of indentations on the Z-cut plane. The asymmetry in the image is a diffraction effect.

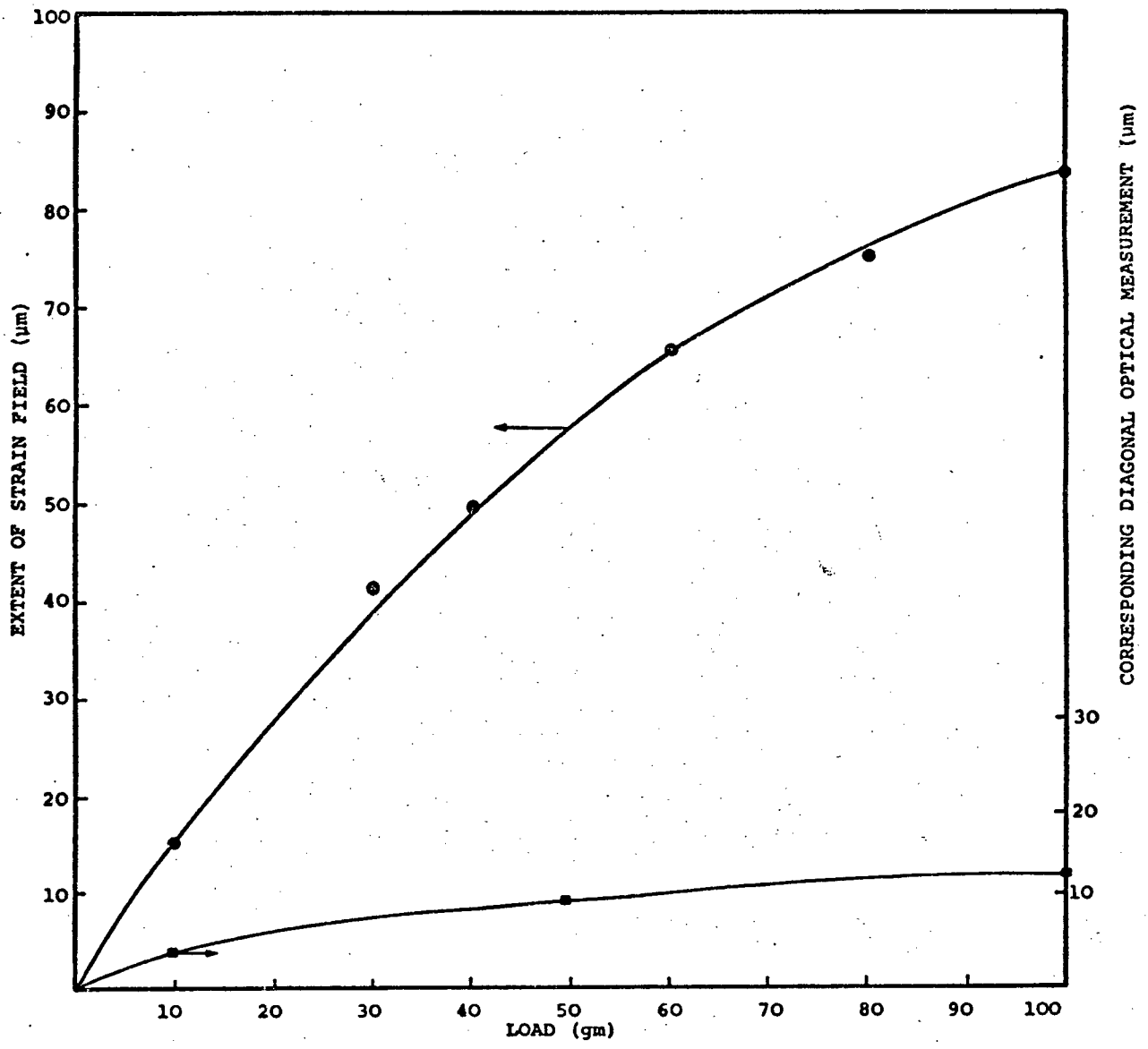

Fig.9.32 Comparison of the Vickers hardness impression diagonal lengths, determined optically with the spatial extent of the X-ray strain field. (Y-cut plane.).

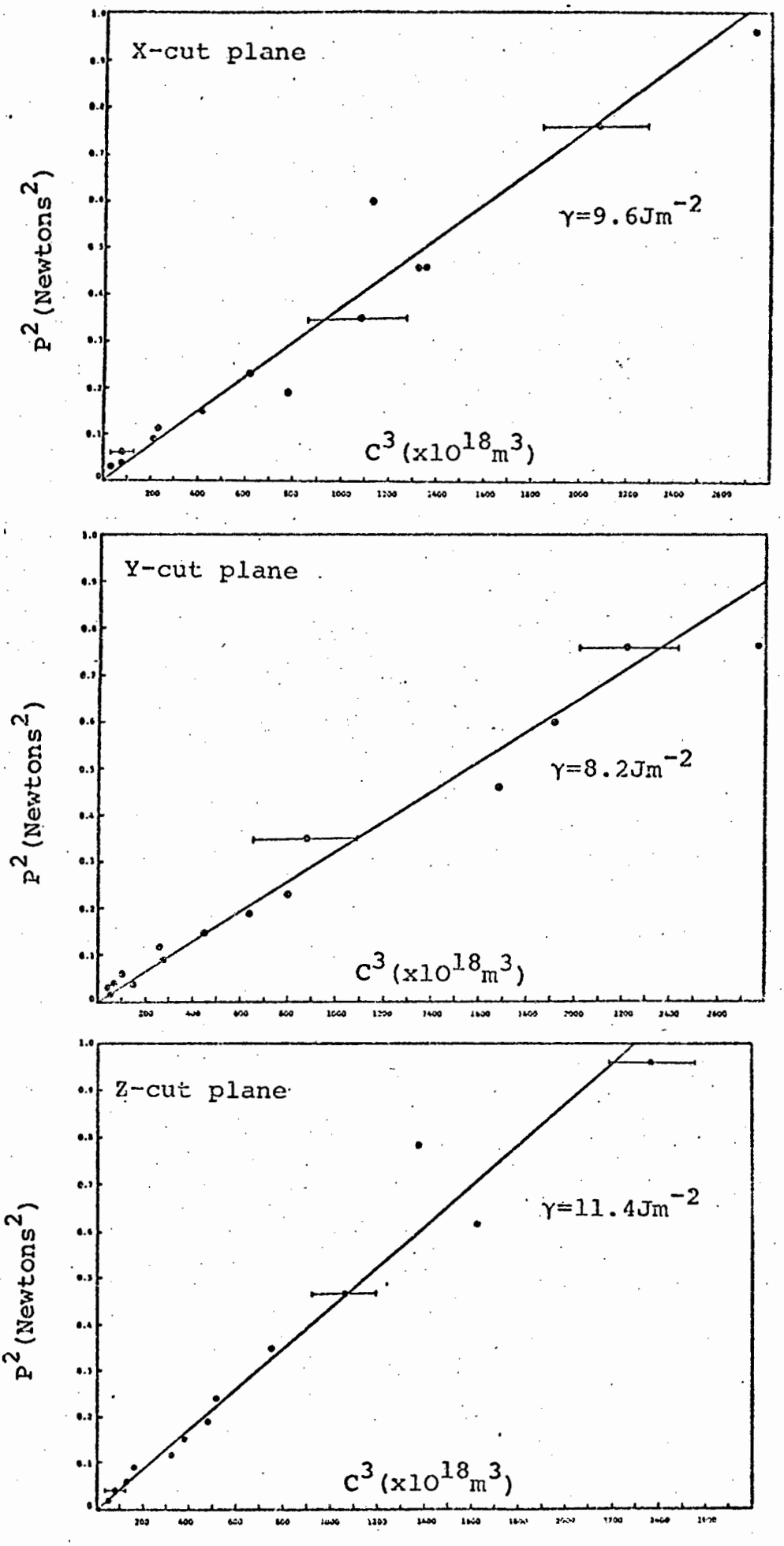

Fig.9.33 Plots of crack length (c^3) as a function of load (P^2) from data obtained from hardness impression measurements. The slopes of these curves give an estimation of γ.

9.8 Discussion

9.8.1 Prior Work on Quartz

The magnitude of the room temperature hardness of quartz has been measured by a number of authors, using both Vickers and Knoop* indentors. In some of the earlier work on natural quartz Taylor (1949) found the Vickers hardness of polished surfaces of $\{10\bar{1}0\}$ to be 1206 Kg mm^{-2}, as compared to 1103 Kg mm^{-2} for (0001). Using a Knoop indentor Winchell (1945) determined that on $\{10\bar{1}0\}$ the indentation hardness is greater parallel, than perpendicular to, the c-axis. Brace (1963) also using a Knoop indentor reported a variation in hardness with load; for example, at a load of 5 gm H_K was equal to 2190 Kg mm^{-2}. At considerably higher loads (1 Kg) the hardness had decreased still further to 670 Kg mm^{-2}. Brace found a directional anisotropy on $\{10\bar{1}0\}$, but in this case the reverse of Winchell's (1945) observation.

Westbrook (1959) determined the Vickers hardness of the $\{10\bar{1}0\}$ face to be $\approx$ 1100 Kg mm^{-2}, harder than the basal plane by $\approx$ 15%. These results were obtained at a load of 50 gm in vacuo. Hartley & Wilshaw (1973) indented the X$(11\bar{2}0)$, Y$(1\bar{1}00)$ and Z(0001) cut planes of synthetic quartz with a Vickers pyramid, but could determine no difference in hardness values between these planes. There was also no difference in hardness between a test made in moist air or dry nitrogen. These authors reported that cracking from the impression corners occurred at loads above 30 gm, although the presence of these cracks did not affect the hardness value.

---

*The Knoop indentor is an elongated pyramid, with a length to width ratio of 7 : 1. It produces a shallower impression than the Vickers indentor, and is hence more suited to hard materials, which may extensively fragment when indented to large depths. The Knoop indentor is also used to study the directional anistropy of hardness. Knoop hardness values are in agreement with results obtained using the Vickers indentor for loads > 100-200 gm; the Vickers pyramid gives more reliable readings in the microhardness regime (Bückle, (1959).)

On the other hand, Westbrook & Jorgensen (1968) also indented (natural) quartz in both dry (anhydrous toluene) and wet (as received, or as polished) conditions and found significant differences in Vickers hardness under these extreme conditions. A natural $(10\bar{1}0)$ plane had a Vickers hardness of 1140 Kg mm^{-2} when dry, but only 870 Kg mm^{-2} when wet, a reduction of 21%. The applied load in these tests was 50 gm, and the authors report that no cracking occurred.

Finally, the impurity concentration can affect the hardness value. Brace (1963) indented both natural and synthetic quartz and found the synthetic quartz to be softer by 10-25%. This softening effect was attributed to a higher impurity concentration in synthetic quartz.

The results obtained in the present study are in agreement (as far as magnitudes are concerned) with this previous work. An increase in hardness with decrease in load has been found. Exact correlations with the Knoop data of Brace is uncertain, because of the different indentor geometry. The present results do show a discrepancy with those of Westbrook & Jorgenson; our hardness results are higher for 'wet' conditions than their data. The reason for this is unlikely to be the impurity effect found by Brace, since we may expect synthetic quartz (our samples) to be softer than natural quartz tested by Westbrook & Jorgensen.

9.8.2 Elastic-Plastic Indentation

The hardness of a solid is a measure of the mean contact pressure acting beneath the indentor. For a plastic indentation the hardness value must in some way be related to the mean uniaxial compressive flow stress (σ_y) of the solid. If the solid behaves in a rigid-perfectly plastic manner then it may be shown (Tabor, 1951) that:

$$H = C' \sigma_y \qquad (9.7)$$

The constant C′ is known as the constraint factor and takes a value approximately equal to 3, the exact value depending upon the indentor geometry (Johnson, 1970). If the solid has no definite yield stress, then the uniaxial stress at a particular level of strain (which corresponds to 8% for the Vickers pyramid) is used.

The values of yield stress predicted by eqn(9.7) have given satisfactory agreement for metals; that is the constraint factor ≈ 3 for this class of solids. However, when solids such as glasses and polymers are indented the hardness values are found to be lower than may be expected from a consideration of the experimental flow stress and the application of eqn.(9.7). Such solids are characterized by low values of Young's modulus, E, and the strain imposed by the indentor can be accommodated to a large extent elastically. This led Marsh (1963) & Johnson (1970) to re-evaluate the theory of indentation, and base it on the analysis of an elastic-plastic solid. The results of such an analysis leads to the relationship (Johnson, 1970):

$$\frac{H}{\sigma_y} = \frac{2}{3}\left[1 + \ell n\left(\frac{(E/\sigma_y)\ \tan\beta + 4(1-2\nu)}{6(1-\nu)}\right)\right] \qquad (9.8)$$

where β is the angle between the indentor face and the surface of the solid. Thus, the hardness is not related simply to the yield stress, but to a more complex function of the mechanical parameters of the material.

The form of the function (eqn.(9.8)) is shown in Fig.9.34. Marsh (1963) visualised the indentation process in terms of an expanding spherical cavity to obtain the relationship between the pressure(hardness)in the cavity and (E/σ_y). Johnson (1970) assumed that immediately below the indentor there was a hemi-spherical hydrostatic core of radius a, surrounded by material which had yielded (Fig.9.35). Outside of the plastic zone the material still behaved in an elastic fashion. Increasing the applied load resulted in an expansion of the elastic-plastic boundary.

The onset of plasticity occurs when the elastic-plastic boundary coincides with the radius of the hydrostatic core. If the radius of the elastic-plastic boundary is ρ, then this condition is equivalent to $\rho/a = 1$, and eqn.(9.8) predicts $H/\sigma_y = 1.1$. The indentation becomes fully plastic at $H/\sigma_y \approx 3$; at this point the elastic plastic boundary is located at $\rho \approx 2.5a$.

While the above is specifically modelled for a conical indentor, Johnson (1970) drew attention to the fact that the majority of the experimental data has been obtained with the Vickers pyramid, and provides a satisfactory correlation with theory. However, the appropriate value of β to use in eqn.(9.8) is 19.7°, which corresponds to an equivalent volume of material displaced both by a cone ($\beta = 19.7^{\circ}$) or a pyramid ($\beta = 22^{\circ}$), indented to the same depth.

The sequence of deformation would be as follows. Plastic deformation would commence in a localised volume at the apex of the indentor, at a pressure $\approx \sigma_y$, and spread with increasing values of (E/σ_y) tan β. With a spherical indentor this spread is brought about by an increasing load, since β increases as the sphere sinks in (Fig.9.36). The material which is displaced by the indentor is accommodated by the elastic-plastic radial expansion of the outer material.

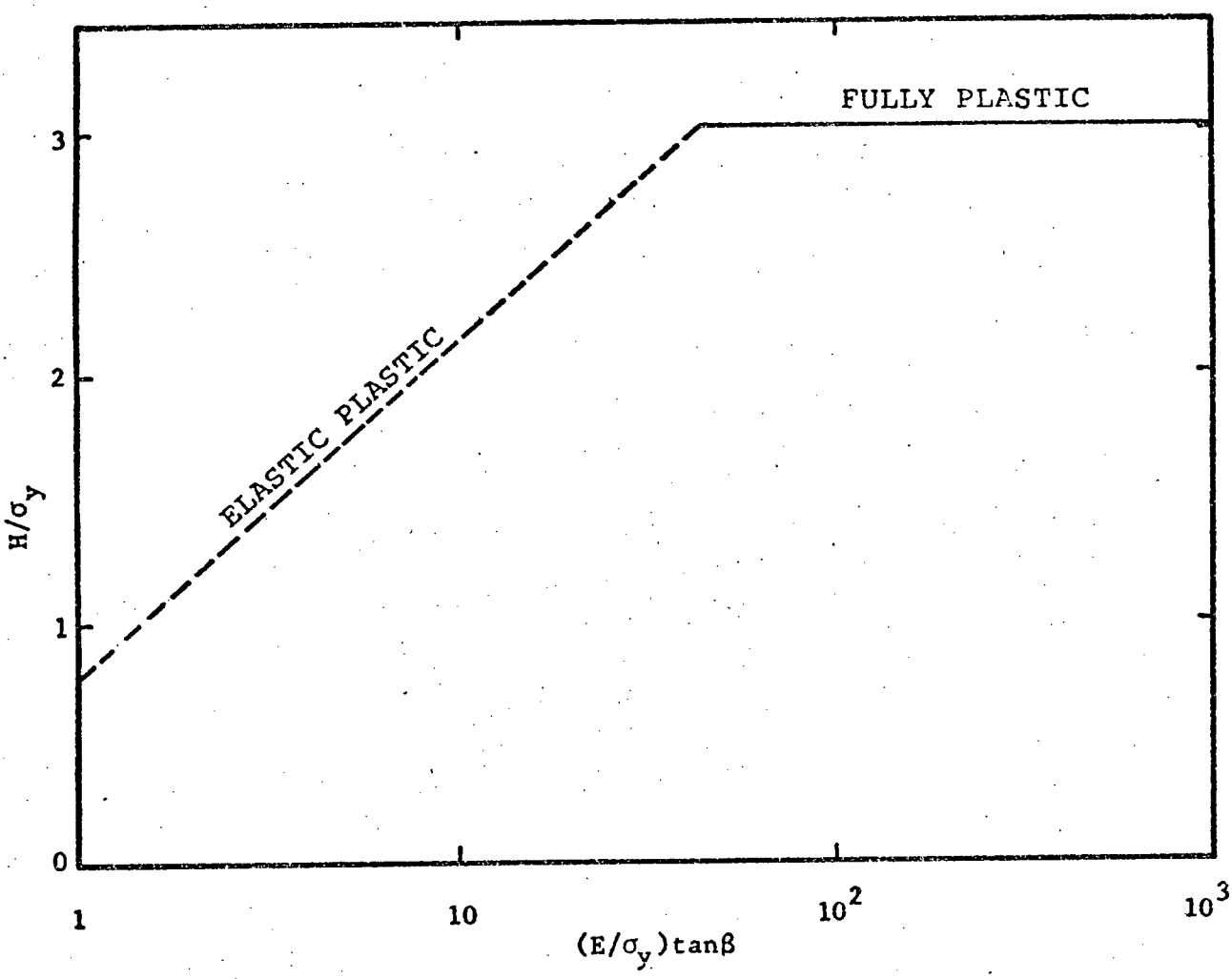

Fig.9.34 Correlation of the constraint factor (H/σ_y) with the parameter $E \tan \beta/\sigma_y$; $\tan \beta$ is the angle which the indentor makes with the surface being indented, E is Young's modulus, and σ_y is the yield stress. The model proposed by Johnson (1970) which corrects the constraint factor ($C'=H/\sigma_y$) for elastic strain is shown by the dashed line.

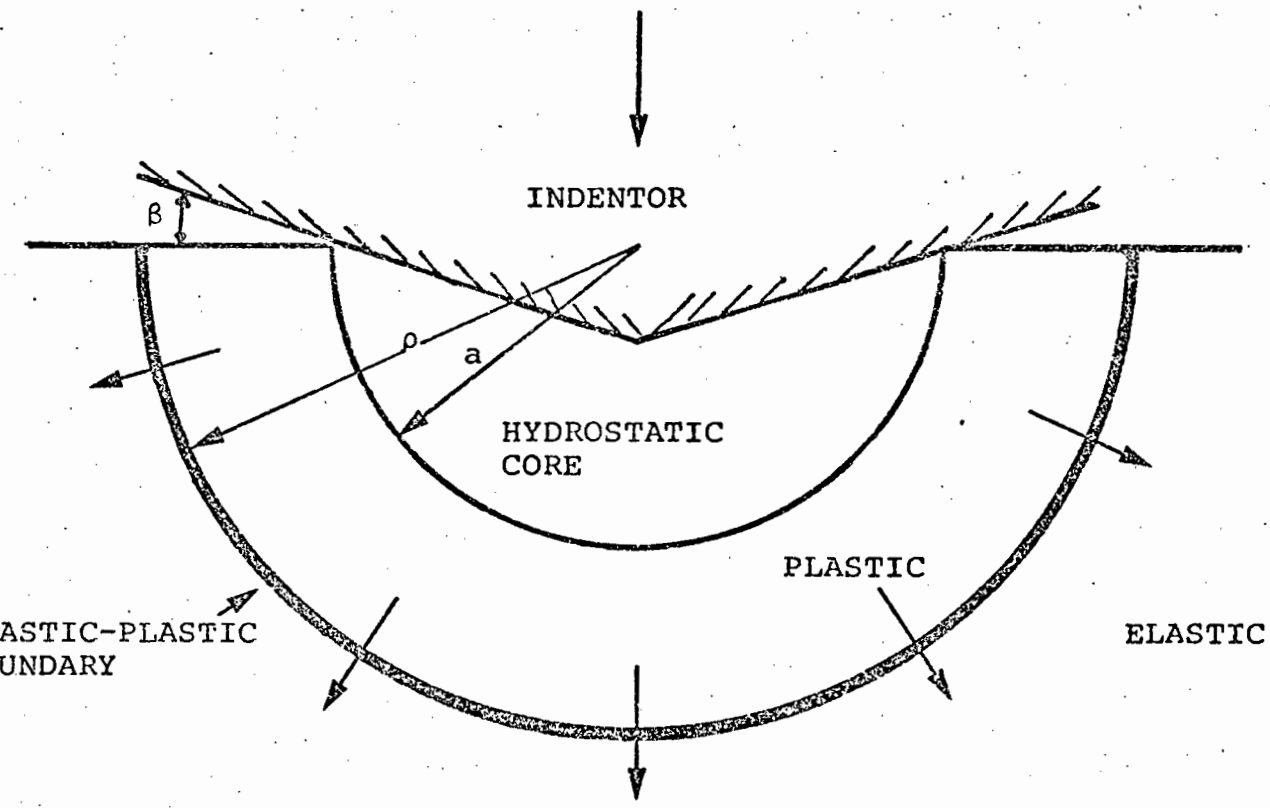

g.9.35 Idealized model of an indentation; a hydrostatic core sur-
unded by an elastic-plastic region in which the deformation is ra-
ally symmetrical. (after: Johnson, 1970).

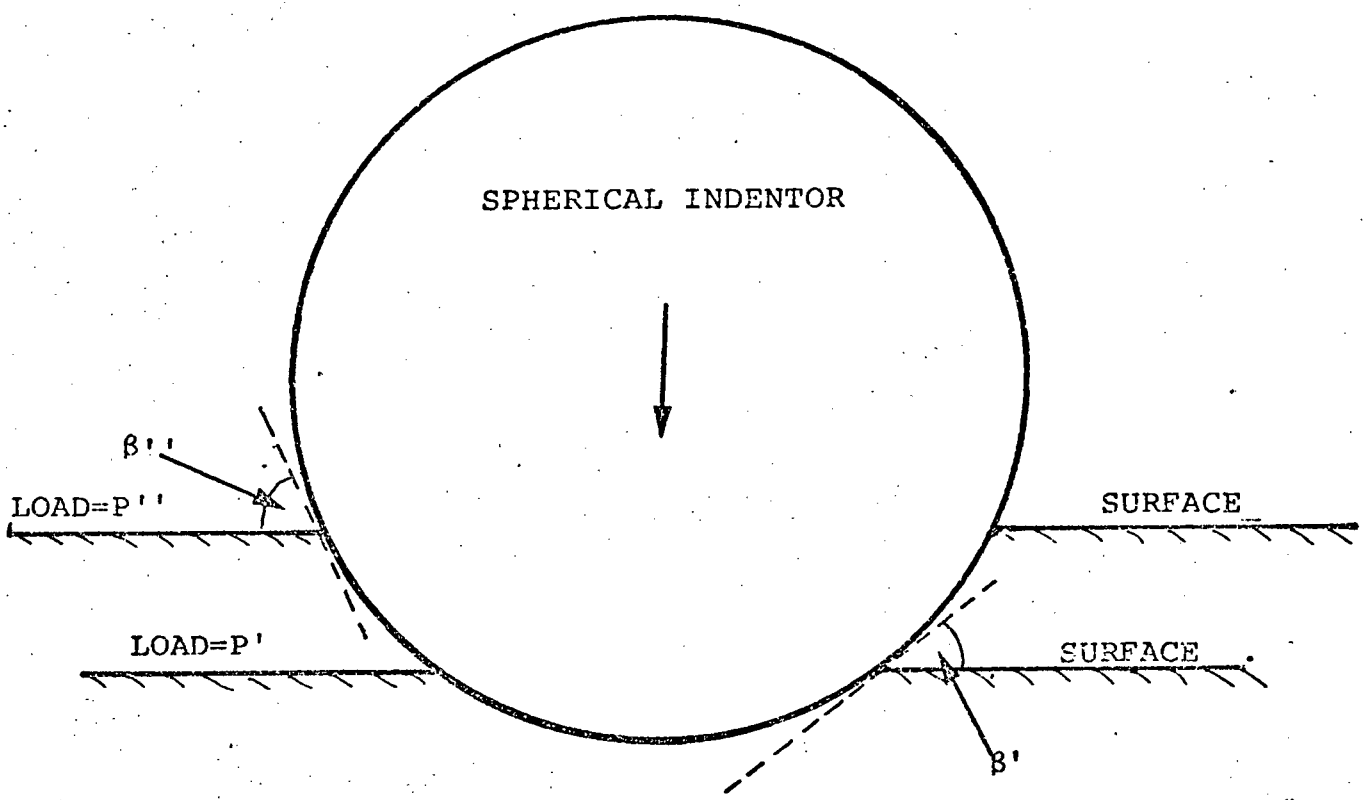

Fig.9.36 Schematic diagram demonstrating the change of the angle β as the load on a spherical indentor increases. P'' >P' and β'' >β'.

When $(E/\sigma_y)\tan\beta \approx 50$, the pressure has increased to $\approx 2.8\,\sigma_y$, and this causes a change in the deformation mode; the displaced material can now pile-up at the sides of the indentor without any further increase in pressure, becoming equivalent to the rigid-perfectly plastic analysis. With a Vickers pyramid a geometrical similar impression is made. For this indentor, changes in deformation must be reflected through the material constants, E or σ_y.

Perrott (1977) also examined the elastic-plastic indentation in an attempt to account for the fracture modes associated specifically with this type of deformation. His analysis gave the relationship

$$\frac{H}{\sigma_y} = 0.494 + 0.577\ \ell n\left\{\frac{E\tan\beta}{\sigma_y(1-\nu^2)}\right\} \qquad (9.9)$$

The transition from fully elastic to elastic-plastic behaviour occurs at $H/\sigma_y = 0.577$. Plastic behaviour results when $H/\sigma_y = 1.155$.

9.8.3 Change of Shape during Indentation

Indentation imposes an arbitrary change of shape upon a solid, and as a consequence the Von Mises (1928) criterion must be met if a plastic impression is to be formed (Rice, 1971 and Gilman, 1973). For materials such as quartz, which do not satisfy Von Mises at room temperature the stresses acting beneath the indentor must generate a sufficient "constraint" to suppress premature fracture and at the same time be high enough to activate the hard secondary slip systems. No general yielding may occur until the stress exceeds the level for secondary slip system operation. If either of these conditions are not met, we may expect gross fragmentation which will result in a indistinct impression, or a pure elastic response which will not leave an impression.

It may be argued that the proximity of the free surface can relax the Von Mises criterion. However, the majority of the experimental evidence clearly indicates that the hardness derived yield stress is more closely related to the polycrystalline yield stress, where hard as well as easy slip systems must be activated for a general change of shape (Rice, 1971).

The experimental evidence obtained from optical microscopy, and scanning electron microscopy in the present study suggests that well developed plastic hardness indentations may be made on the surface of single crystal quartz at room temperature. However, the high voltage electron microscopy has shown that plastic flow processes are localised at the apex of the pyramidal indentation, and do not surround the whole volume about the impression. This clearly suggests that the indentation is elastic-plastic with a constraint factor $C' \approx 1$.

The room temperature constraint factor for quartz was calculated from the Perrott analysis (eqn.(9.9)) by an iterative technique. The procedure was as follows:

(i) Letting $C' = 3$, calculate σ_y using the hardness data, via the expression $H/\sigma_y = C'$.

(ii) Evaluate the new value of C' using the RHS of eqn.(9.9) by substituting for σ_y.

(iii) Using the same value of H and the new value of C', estimate σ_y.

(iv) Re-evaluate C'.

Using this mathematical technique the value of C' soon converged to a constant value. This we take as the constraint factor. We note that a similar analysis has been undertaken by Evans & Goetze (1979) for quartz, using an empirical relationship for H/σ_y.

Using accepted room temperature values for $E(10^{11}\ N\,m^{-2})$ and ν (0.1) for quartz, taking $\beta = 19.7^{\circ}$ for the Vickers pyramid and an average value of hardness ($12GPa \approx 1200\ Kg\,mm^{-2}$) obtained from the present results, then by iteration, $C' = 1.26$. This confirms the HVEM investigation, since we do not expect fully developed plasticity for such a value of the constraint factor.

9.8.4 Microplasticity of Quartz

With a constraint factor of 1.26 we can obtain an estimate of the yield stress σ_y = 9.5 GPa. We now test to ascertain if this value of σ_y is compatible with slip on the secondary slip systems <a + c> of quartz at room temperature. We know from the results of Baëta & Ashbee (1970) that slip on <a + c> is not observed for T $\lesssim$ 1100 K during deformation at atmospheric pressure. Our results on crystals orientated for slip on <a + c> suggest a similar conclusion. Since Evans and Goetze (1979) estimated the strain rate in a hardness test to be ~ 10^{-5} s^{-1}, deformation is possible at these lower temperatures by the climb motions of dislocations. At lower temperatures (T $\lesssim$ 700K) we anticipate that diffusion does not proceed quickly enough to allow the dislocation climb to make any contribution to strain. In this case the stress may be increased to the level necessary for <a + c> operation. To prevent fracture, a high hydrostatic confining pressure must be applied.

The present indentation experiments were carried out on crystals with a grown-in dislocation density $\approx 10^7$ m^{-2}. The scale of the indentation stress field is such that the deformation was concentrated in volumes of the crystals which were essentially dislocation free. In fact no pre-existing dislocation images or other defects such as inclusions or precipitates are visible in any of the electron micrographs (e.g. Fig.9.28). There will therefore be no dislocation multiplication sources within the stress field, and it is anticipated that under these conditions the hardness derived yield stress will approach the theoretical shear stress (Gane, 1970). The theoretical shear strength $\tau_{(th)}$ of a solid can be roughly estimated as $G/2\pi$ (Kelly,1973, page 22), representing the force necessary to slide two adjacent atomic planes over one another, and to form a 'total' dislocation. For quartz we estimate τ_{th} ~ 5 GPa. An estimate of the resolved shear stress on <a + c> during indentation is $\sigma_y.\cos^2 45^\circ$ ~ 5 GPa. Thus the shear stress acting below the indentor is approximately equal to the value of the theoretical shear stress, confirming our contention.

It is to be noted then, in conventional compression testing of single crystal quartz, dislocation multiplication sources must exist within the stressed volume, and the nucleation of glide dislocations is expected at lower stress levels than the theoretical shear stress. However, in the quartz structure the glide of dislocations is expected to be difficult, because of the strong directed nature of the bonding. The extrapolation of yield point data obtained by Hobbs et al., (1972), for $\langle \underline{a} + \underline{c} \rangle$ slip, indicates a room temperature yield stress of ~ 2 GPa. In addition, according to the data of Hobbs et al., the $\langle \underline{a} + \underline{c} \rangle$ slip system shows little variation in yield stress with temperature while the easy slip systems show an appreciable temperature effect, and may become as difficult as $\langle \underline{a} + \underline{c} \rangle$ at low temperatures.

In indentation testing, glide on the primary slip systems is often manifested upon etching as a 'dislocation rosette' phenomenon. The gliding dislocations travel large distances away from the impression. Of interest here is the fact that the indentation on the Y-cut plane involves a high resolved shear stress acting on an easy slip system, viz. $\{10\bar{1}0\}\ \langle 11\bar{2}0 \rangle$. Thus, such dislocations should be visible as slip bands in the electron microscope. We suggest that our failure to observe these features confirms the difficulty of dislocation slip on the easy systems at low temperatures. This cannot be attributed to the constraint of an elastic-plastic indentation, since Evans and Goetze (1979), investigating the hot hardness of Olivine, found dislocation rosettes for a value of $C' \approx 2$. An interesting point to emerge is that while at elevated temperatures the quartz problem revolves around the activation of the $\langle \underline{a} + \underline{c} \rangle$ systems to satisfy Von Mises criterion, at low temperatures all slip systems appear equally difficult and high stresses are necessary to achieve a change of shape.

9.8.5 The Role of Twinning during the Indentation of Quartz

Considering the localised nature of plastic flow, it is perhaps surprising that the extent of elastic recovery is apparently quite low. A constraint factor of ≈ 1.3 indicates a large elastic accommodation of the strain under load. A tentative conclusion was drawn from the optical microscopy of etched indentations that secondary Dauphiné twinning may be associated with the deformation. However, it is important to emphasise that Dauphiné twinning in quartz cannot contribute to any permanent strain. The twinning operation does enable elastic strain to be more effectively accommodated (Thomas & Wooster, 1951) by reducing the stiffness of the quartz structure (Tullis & Tullis, 1972). On unloading recovery would be complete (no change in strain) provided no permanent deformation had occurred.

Several aspects of this deserve further comment. We note that the HVEM analysis gave no indication of twinning. One possible explanation is that the extension of the median cracks after the ion-beam thinning operation, may absorb strain energy from the indentation site and the change in the stress may possibly result in an un-twinning operation. Thus the lack of twinning in the HVEM investigation is peculiar to the necessity for having a thin specimen, and is not representative of the 'bulk' indentation.

It is interesting to note that there was very little strain contrast surrounding the indentation. This should be compared to the X-ray diffraction topograph (Fig.9.30) where strain was particularly extensive, extending for several times the physical indentation size. Although the X-ray technique is more strain sensitive than electron microscopy, we feel that the observed lack of strain in the HVEM may be an indication of the absorption of strain energy by median crack extension. A possibility in that the median cracks which form on indentation, allow the impression to retain its original (loaded) shape.

9.8.6 Extension to High Temperature Indentation Plasticity

Although no high temperature indentation experiments were performed, it is useful to extend the present analysis to elevated temperatures where direct comparisons can be made with single crystal data. We also know from our work on the annealing of quartz, that a heat treatment will produce numerous dislocations and faceted bubbles. It is of interest to see how these processes are reflected in the high temperature hardness data.

The hardness of α-quartz decreases linearly as the temperature is raised (Westbrook, 1958; Nadeau, 1970), while in β-quartz there is a more rapid decrease. At 1150K the Vickers hardness has dropped to 200 Kg mm^{-2}. At the α → β transformation Westbrook found a sudden increase in hardness followed by a decrease, although this could not be confirmed by Nadeau. Nadeau found that a heat treatment at 1700K produced an increase in hardness over the full temperature range (300-1150K), and that this removed the rapid hardness decrease in β-quartz. Fig.9.37 summarizes this information.

Using the appropriate average values of Young's modulus E (Fig.9.38) from Evans and Goetze (1979), the constraint factor C′ was calculated using the Perrott (1977) analysis (eqn.(9.9)), and the hardness data of Nadeau (Fig.9.37). The results (Fig.9.39) indicate that for an annealed sample there is a change from an elastic-plastic, to a fully plastic behaviour (C′ → 3) in the β-quartz field. However, for the pre-annealed sample the deformation remains essentially elastic-plastic.

Nadeau (1970) reports that he observed "two kinds of hardness impression. Those that indicated high hardness values were, of course, small; they showed no sign of 'piling-up' at the periphery ... the second type was larger and displayed considerable pile-up ...". We may interpret this by stating that the high hardness indents were elastic-plastic, and we would expect no pile-up. The low hardness (large) indents were obviously obtained at elevated temperatures where

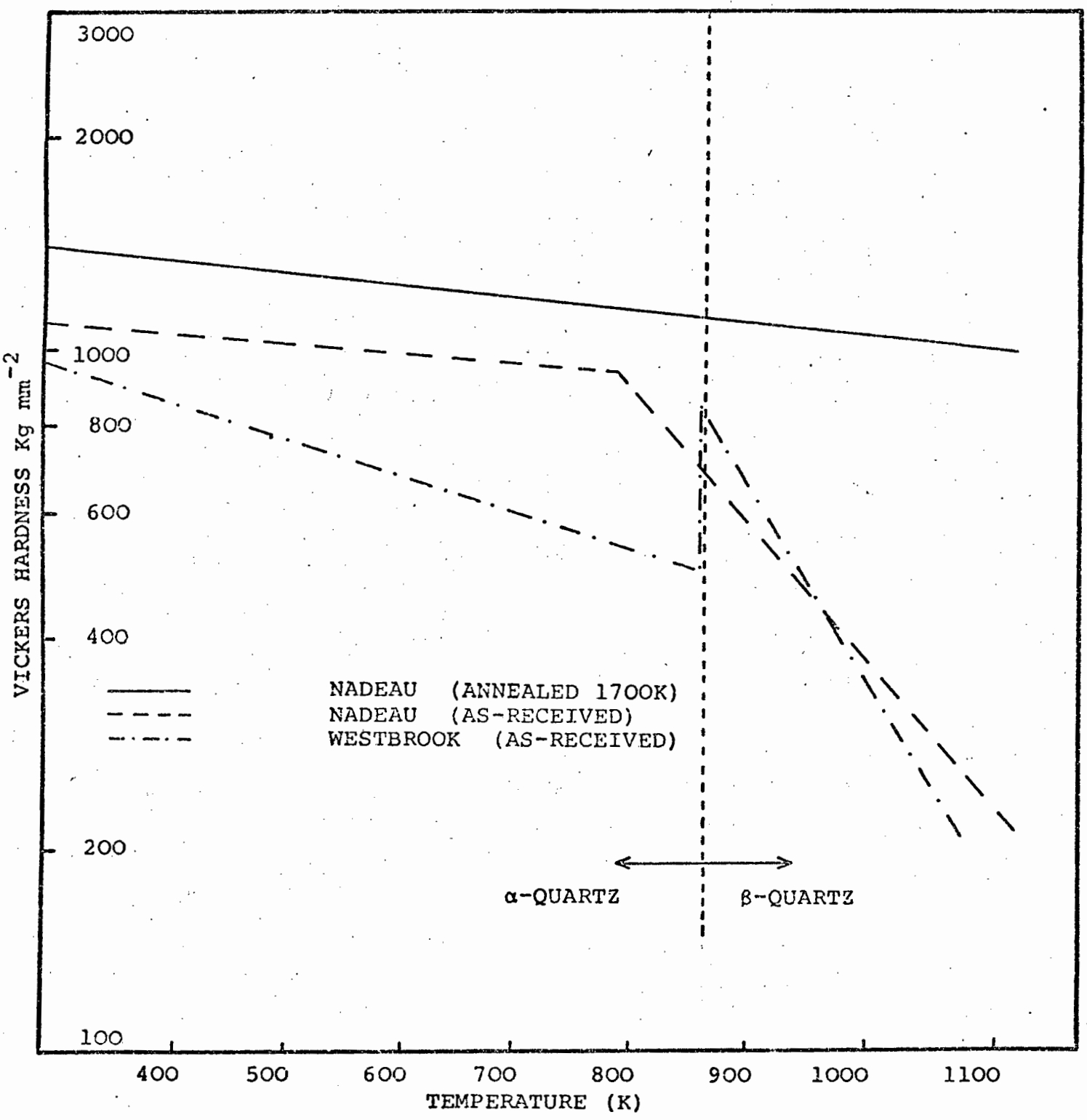

Fig.9.37 Variation in hardness with temperature of single crystal quartz. The results of Nadeau (1970) for as-received and annealed (1700K) samples, and Westbrook (1958) for as-received samples are shown.

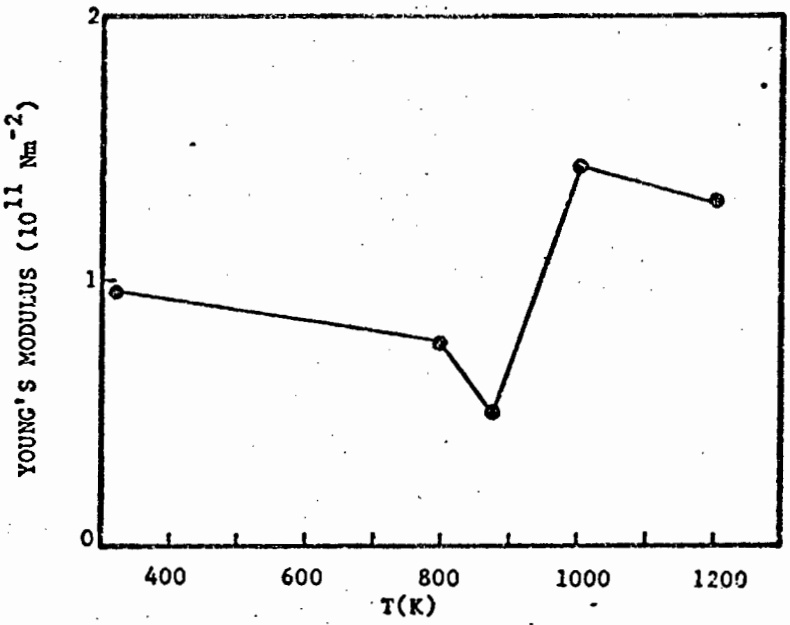

Fig.9.38 Change in Young's modulus (E) of quartz as a function of temperature (data from Evans and Goetze, 1979).

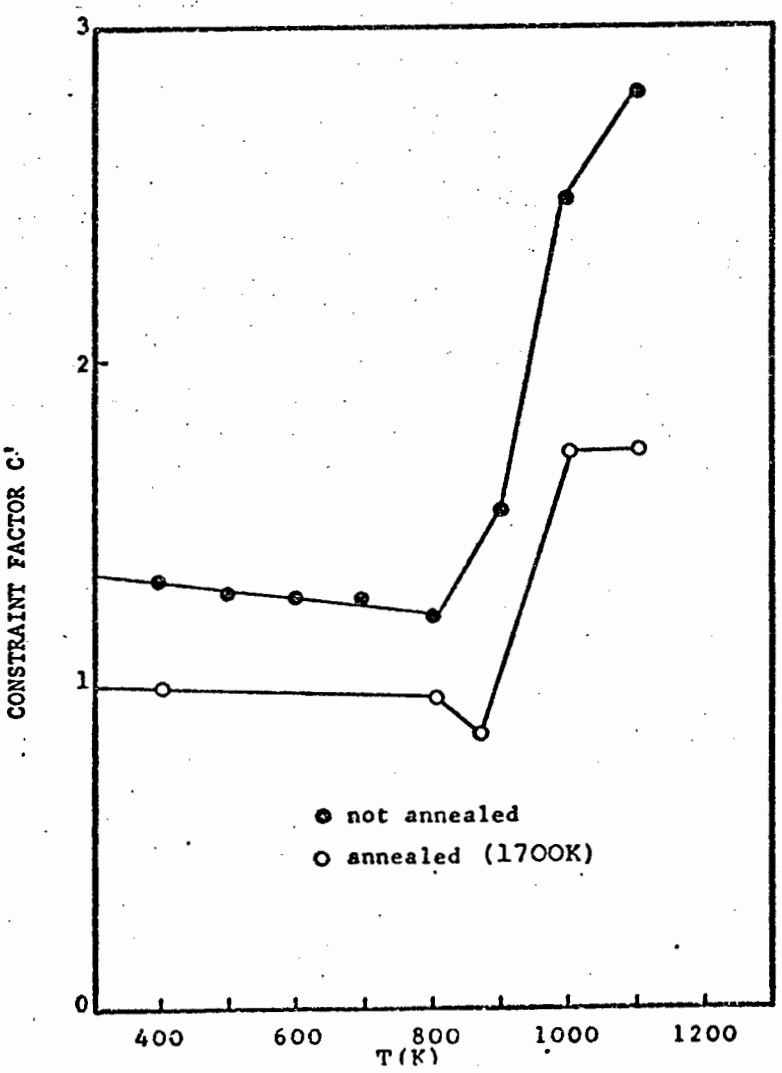

Fig.9.39 Constraint factor (C') calculated from hardness data of Nadeau (1970).

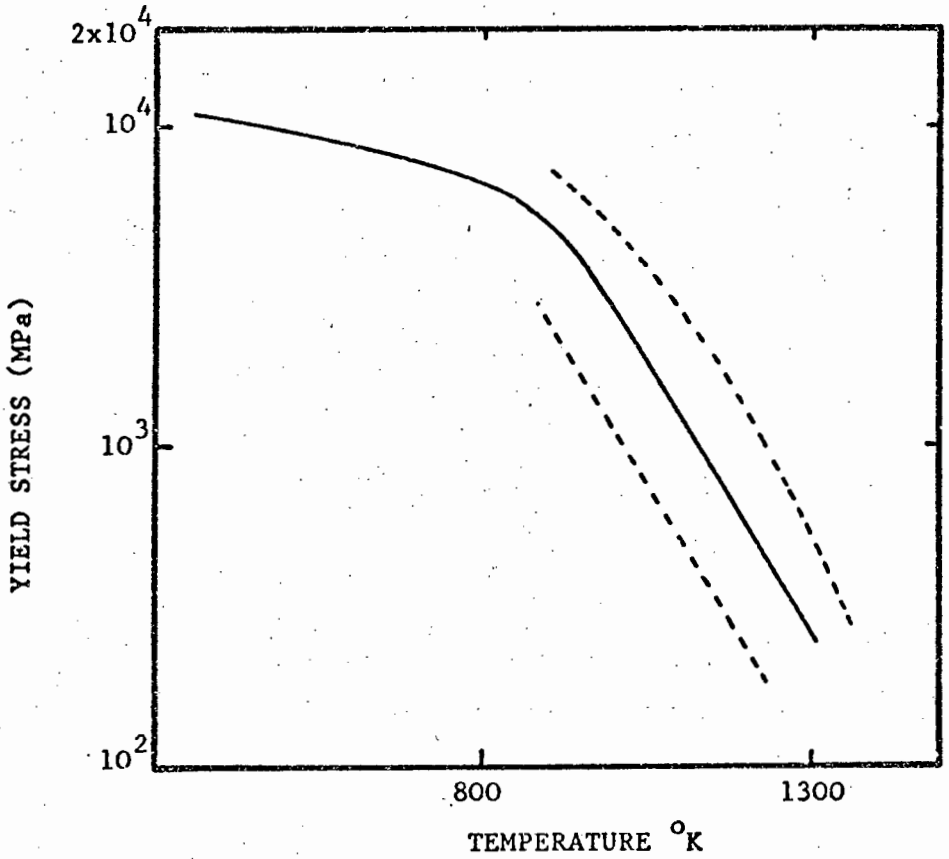

Fig.9.40 Hardness derived yield stress (solid line) compared to the polycrystalline yield stress (bounds of experimental data indicated by dashed line). (after: Evans and Goetze, 1979).

the deformation was fully plastic and pile-up was expected.

At 1100K Baëta & Ashbee (1969b) obtain a critical resolved shear stress ≈ 200 MPa for <a + c> slip. Estimating the shear stress from the hardness derived yield stress (Fig. 9.40) we obtain a value ≈ 400 MPa, in satisfactory agreement with the compression data considering the errors of micro-hardness testing. Since the values of CRSS obtained at 1100 K by Baëta & Ashbee are lower for the easy slip systems, we conclude that at these elevated temperatures the yield stress obtained from a hardness test is related to the ease with which <a + c> operates. Also indicated on Fig.9.40 are the results collated by Evans and Goetze (1979) for the polycrystalline yield stress of quartz obtained from compression tests. The fit is in remarkably good agreement with the hardness derived yield stress.

It can be postulated on the basis of our results that the reduction in yield stress may be related to the easy climb motions of dislocations. Since it is to be expected that a heavy anneal will result in the generation of bubble precipitates (on the scale of the indentation stress field), and a network of dislocations locked by the bubbles (see for example Fig.8.9), the increase in yield stress after such an anneal can be attributed to either:

(1) The removal of the effective water weakening agent.

(2) The pinning of indentation generated dislocations by the precipitates (precipitation hardening).

Nadeau reported that at 1200K the hardness of a previously unannealed crystal suddenly increases. While it may be possible that a phase change to tridymite is occurring, Nadeau considered that the evolution of hydrogen and alkali ions from the surface to be the cause of this increase. An alternative mechanism is that the bubble precipitates formed at this temperature and effectively acted as a hardening mechanism.

The electrolysis of quartz by Nadeau resulted in a slight softening and the removal of the decrease in hardness in the β-quartz field ($T \gtrsim 900K$). Such a softening was also found for an electrolysed pre-annealed sample, although the hardness did not reduce to the room temperature value. Since electrolysis results in the injection of hydrogen and the removal of mobile alkali ions, the absence of the high temperature softening may be attributable to the appearance of precipitates at a lower temperature, since the 'water' content has effectively increased. The room temperature softening (by $\approx$ 30%) is unexpected. The climb motions of dislocations cannot be significant at 300K even in the presence of water.

Interestingly, the results of Westbrook and Jorgensen (1968) show a similar softening effect in wet conditions. Perhaps a distinction needs to be drawn between water incorporated during crystal growth and that added at a later stage; this latter type appears to be extremely reactive at room temperature. It is tempting to assume that the water interacts with the crack system, and this may result in sub-critical crack growth and a relaxation of the residual stress. If a significant relaxation of the stress occurs, then the extent of elastic recovery may be diminished and the impression becomes 'larger', resulting in a lower calculated hardness value. Although Westbrook and Jorgensen reported that during indentation no cracks formed, the present results indicate that microcracks can occur within the indent crater (e.g.Fig.9.23), and into which water may diffuse. Clearly this is an area of further study and consideration.

Finally, Nadeau cast doubt on the effectiveness of water as the high temperature weakening agent (at least in indentation tests). By diffusing in Li^+ after a crystal had been annealed at 1700K, he was able to show that the softening in β-quartz could be restored.

The above microplastic interpretation of hot hardness data must of necessity be speculative. However, it is clear that indentation tests may give some clues as to the expected mode of deformation of quartz on a macroscopic scale, without the need for complex equipment. It is important that the localised nature of the indentation stress field is appreciated, and the use of HVEM to help develop a coherent analysis in such microstudies cannot be over emphasized.

9.8.7 Fractography

The crack system which develops during the indentation of a brittle solid has already been discussed (Section 5.2.1). It may be expected that the development of a substantial degree of plasticity will affect this ideal pattern. In particular, tough materials display only shallow radial cracks (Palmquist cracks) which, although superficially similar to the median cracks observed in the conventional brittle solids such as glass, are fractographically distinct. The analysis of Perrott (1977) is able to predict this type of radial crack. The various types of cracks found in elastic-plastic indentation have been succinctly described by Hagan & Swain (1978).

The cracks extending from the diagonals of the Vickers hardness in the present experiments have been ascribed to median crack formation. Such cracks develop only in the elastic zone. However, Palmquist cracks form within the plastic zone of the indentation (Perrott, 1977). Cracks similar to Palmquist cracks (i.e. the shallow radial cracks) can be formed in brittle solids if the indentor is not overloaded (Hagan & Swain, 1978) and these authors suggested that discrepancies in the fracture mechanics analysis of 'median' cracks may be attributable to the failure to recognize that radial cracks do form preferentially at lower loads.

The small scale of the microhardness indentations in the present work prohibited any sectioning to determine if the cracks extending from the impression corners are true median cracks, but our chance observation that these cracks may form on indentor unloading could indicate that these cracks are akin to Palmquist cracks. Perrott (1977) noted that, for glass, the Palmquist cracks would grow on unloading only.

The origin of the median cracks is still a moot point. Lawn and Evans (1977) postulate a critical sub-surface flaw, while Hagan (1979), indicates that a Stroh pile-up mechanism could generate the crack. We have already calculated that in the presence of a surface flaw, length 1 μm, quartz will fail at 0.25 GPa. In compression the stress will increase to ≈ 3 GPa. Ashby & Verrall (1978) show that a superimposed hydrostatic pressure modifies the fracture criterion. If the shear stress is σ_s the hydrostatic pressure p, and σ_f the fracture strength in tension, then the fracture criterion is given by:

$$\sigma_s \geq \sigma_f + p \qquad (p < \sigma_f) \qquad (9.10a)$$

$$\sigma_s \geq 2(\sigma_f P)^{\frac{1}{2}} \qquad (p \geq \sigma_f) \qquad (9.10b)$$

In the present case $p \approx 8$ GPa ($\approx {}^{2}/_{3}\ H_v$). Let us consider two cases for σ_f:

(i) σ_f equal to the ideal (tensile) strength.
Here $\sigma_f \sim 25$ GPa, and $p < \sigma_f$. Thus using eq.(9.10a) we may show that
$\sigma_s \geq 33$ GPa for fracture.

(ii) σ_f equal to the strength in the presence of a flaw.
Here $\sigma_f \approx 0.25$ GPa and thus $p > \sigma_f$. Using eqn.(9.10b) we may show $\sigma_s \approx 2.8$ GPa for a fracture.

Our estimated shear stress is 5 GPa, and it is clear that the presence of small (< 1 μm) sub-surface flaws may lead to the development of median cracks.

The usual fractographic analysis of cracking about indentations in brittle solids (Lawn & Wilshaw, 1975) suggests that median cracks form on indentor loading while it is the lateral cracks, propagating in planes approximately parallel to the surface, which form on unloading. No lateral cracks of large extent were observed in the present experiments on quartz, but the 'chips' at the sides of some of the indentations (see for example Fig.9.21) are indeed the result of lateral cracks developing and intersecting the surface. These cracks are very similar to those found by Hagan & Swain (1978) on indented soda-lime glass (see their Fig.2a).

The fracture mechanics analysis of Swain & Lawn (1976) leading to the estimation of γ from the length of the median cracks, shows that the crack length is proportional to $(\text{load})^{2/3}$. The Palmquist cracks have a linear dependence on load. The present results are clearly in accordance with the median crack analysis, although the extent of any error, if these cracks are not true median cracks but shallow radial cracks, is not known. However, the agreement of our results for γ ($\approx$ 10 J m^{-2}) with the value obtained by Hartley & Wilshaw (1973) (γ = 11.5 J m^{-2}) is encouraging.

It is not clear if the minor variations between the values of γ obtained from the different indented crystallographic planes reflects differences in the fracture mode. Quartz does not possess any planes of easy cleavage (Bloss, 1957) although the rhombohedral planes are preferred. It is therefore postulated that the cracks extend by fracture along the rhombohedral planes, and not along the crystallographic planes defined by the orientation of the Vickers indentor diagonals. This may explain why γ is higher than the theoretical prediction ($\approx$ 3.5 J m^{-2}). Since the crack extends by a zig-zag motion, the distance travelled by the crack front is greater than if the extension was along a single plane, and the measurements made on the surface of the indented crystal could underestimate the total surface area created, resulting in an overestimation of γ.

CHAPTER 10

THE CUTTING OF QUARTZ *

10.1 Introduction

Our experiments were designed to give a complete understanding of the response of single crystal quartz to the stress field generated by a normally loaded translating indentor. Both room temperature and high temperature scratches were made. Additionally, scratches were made in normal laboratory air, in dry conditions (relative humidity ≈ 0%) and under water, in order to clarify the role of environment on the mode of scratch deformation. Since static fatigue and chemomechanical effects are displayed by many brittle solids it was anticipated that water may facilitate the fracture of quartz and hence favourably enhance material removal rates. A few experiments were made to gain some insight into how the scratch deformation changed as a function of the number of scratches. Additionally, a series of adjacent scratches were made to assess the extent of interaction between closely spaced scratch grooves. Multiple and adjacent scratches are particularly important to an understanding of real cutting operations.

To evaluate the scratching 'efficiency' (specific energy, or the energy required to remove unit volume of material) it is necessary to measure the horizontal force (F_H) acting between the cutting tool and specimen. The specific energy S_e is related to the rate of volume removal (Z) and the power ($\dot{W}$) needed for removal by the expression:

$$S_e = \left(\frac{\dot{W}}{Z}\right) \text{Jm}^{-3} \qquad (10.1)$$

* By cutting in the case of a brittle solid we mean that a track has been produced from which fragments have been produced across the full width and length.

If the cutting tool is moving at a velocity v the rate of volume removal is:

$$Z = A_x v \qquad (10.2)$$

where A_x is the cross-sectional area of the scratch. The power input is given by

$$W = F_H v \quad . \qquad (10.3)$$

Substituting for Z and W in eqn(10.1) using (10.2) and (10.3) we can show:

$$S_e = \frac{F_H}{A_x} \qquad (10.4)$$

Thus, by measuring F_H during scratching, and establishing the cross-sectional area of the resulting scratch, the specific energy can be estimated.

10.2 Experimental Methods

10.2.1 The Scratching Apparatus

An overall view of the scratching apparatus is shown in Fig.10.1 while details of the traversing mechanism, hot stage, and strain sensing element to record the horizontal force, are shown in Figs.10.2a and 10.2b.

The scratching apparatus consists of a counterweighted balance arm, supported on two roller bearings. The cutting tool can be accurately aligned in a detachable head, which is then connected to the strain sensing element. The vertical load is applied by means of weights, and the balance arm can respond to vertical loads of $\approx$ 0.01 N.

To enable the cutting tool to be positioned smoothly onto a specimen, a device was incorporated to lower the balance

B - BALANCE ARM

C - CUTTING TOOL

E - STRAIN SENSING ELEMENT

H - HOT STAGE

L - ARM LOWERING DEVICE

M - TRAVERSE MOTOR

T - TRAVERSE STAGE

S - SPECIMEN

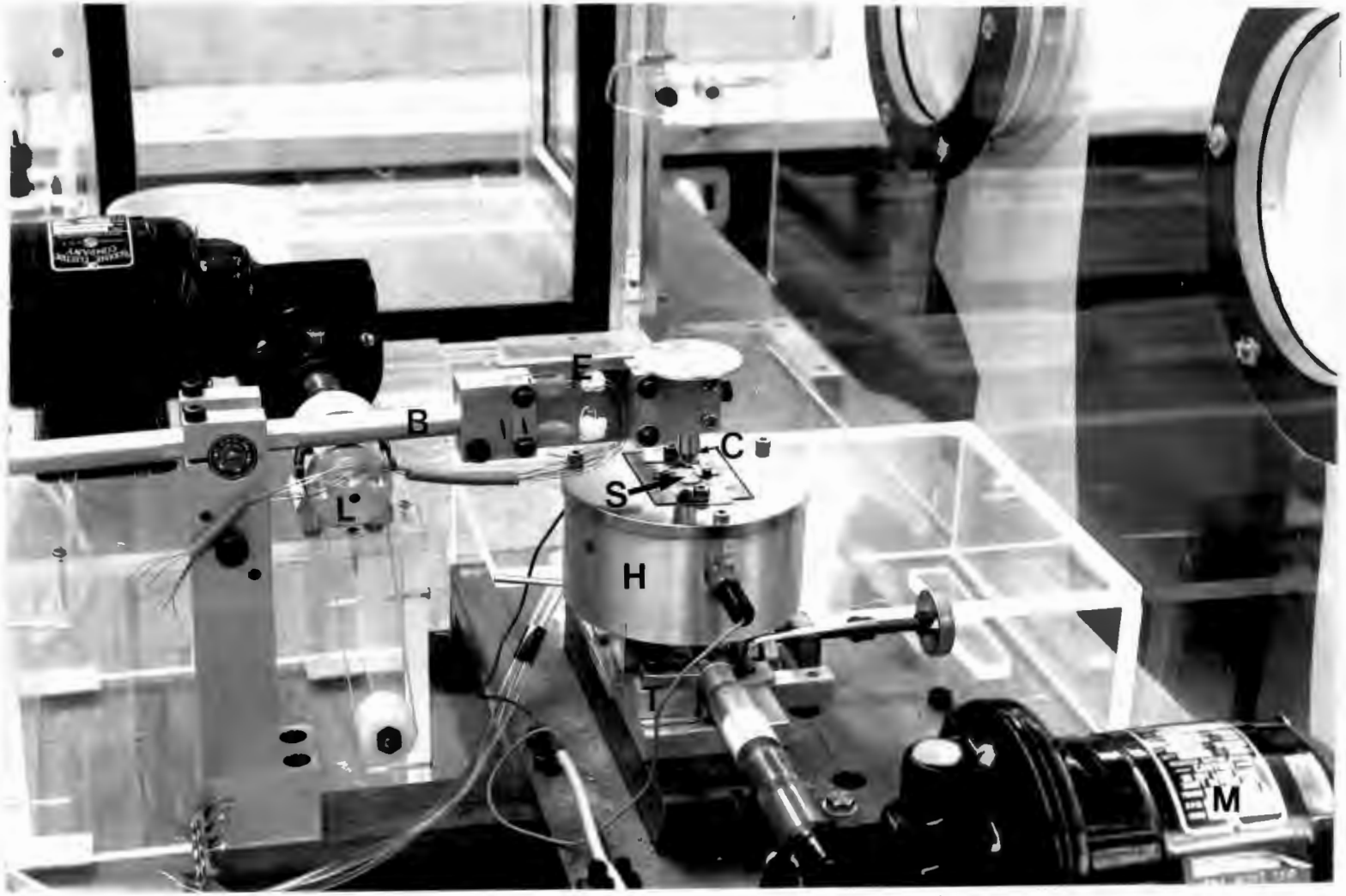

Fig.10.1 Scratching rig.

C - CUTTING TOOL
H - HOT STAGE
M - MICROMETER DRIVE
S - SPECIMEN
T - THERMOCOUPLE
W - WATER COOLING .

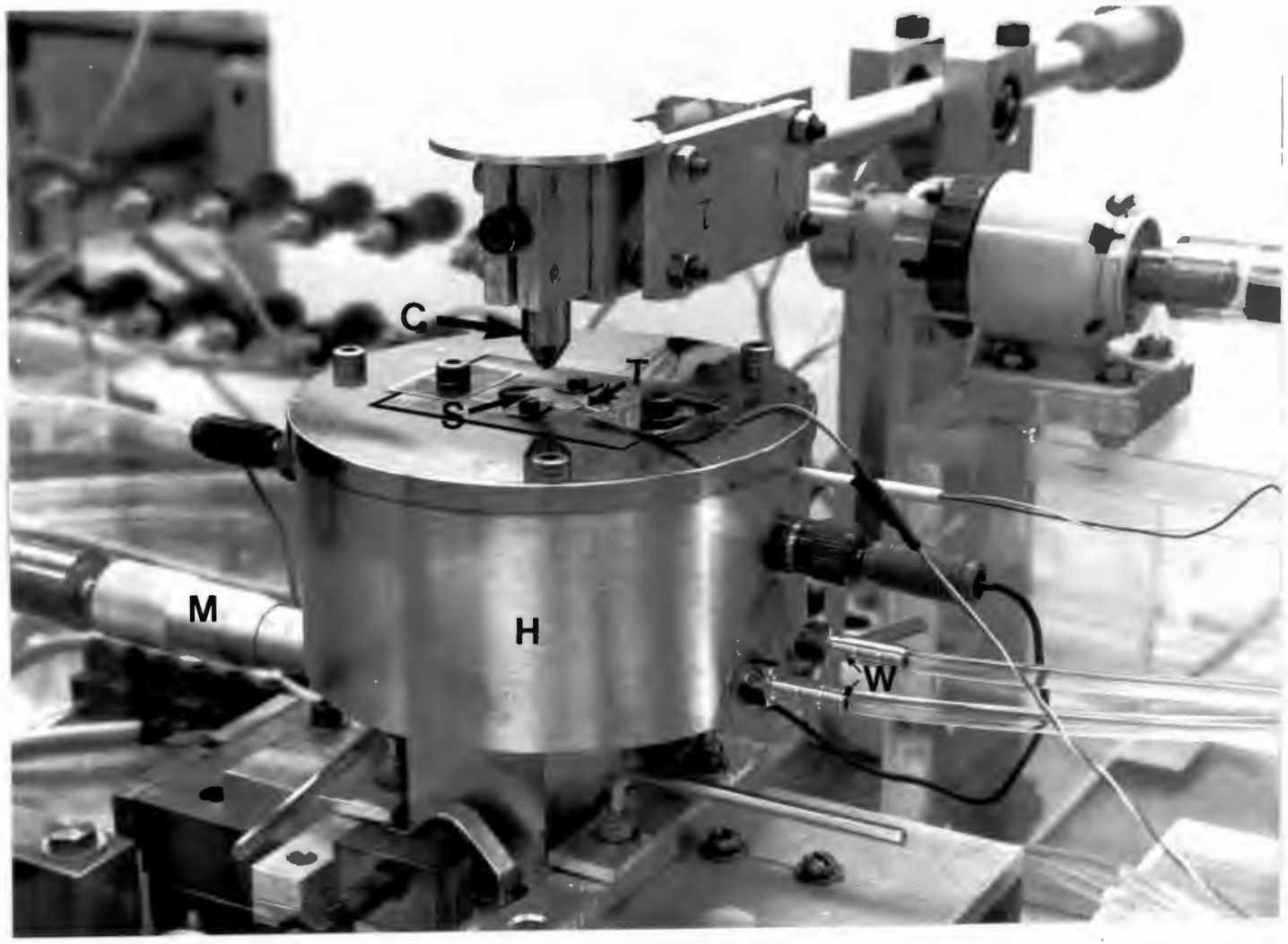

Fig.10.2a Details of the scratching apparatus.

Fig.10.2b Further details of the scratching apparatus. The arrows indicate the directions of motion of the traverse stage.

arm at a pre-determined rate. An eccentric wheel was located below the arm, and rotated by means of an electric motor. The rate of approach of the tool onto the sample was approximately 20 mm min^{-1}.

The traverse stage was driven by a variable speed, reversible electric motor. The motor was coupled to the stage by means of a micrometer. This had two advantages:

1. The rotational motion of the motor was converted to a linear drive.
2. The micrometer scale enabled the specimen on the traverse stage to be accurately positioned below the cutting tool before each scratch.

The traverse stage was a low friction Schneeburger type with no lateral side play. The speed of the motor was controlled by a solid state controller, which was pre-calibrated to give traverse speeds in the range 10-100 μms^{-1}.

10.2.2 The Strain Sensing Element

This sensing element must be elastically stiff to prevent a stick-slip motion and yet give an output signal within the electronic capabilities of the amplifying system. Calculations were performed in the manner below in order to ascertain the optimum thickness of this element.

If the applied voltage to a strain gauge bridge network (Fig.10.3) is V_{APP}, then the output voltage ($V_{o/p}$) due to a strain ε, prior to amplification, is given by

$$V_{o/p} = V_{App}.\varepsilon.\text{ gain factor of gauges} \qquad (10.5)$$

The sensing element is in the form of a cantilever beam, height h, thickness t, and length ℓ (Fig.10.4). Under the action of a bending moment $M = P.\ell$, where P is the applied

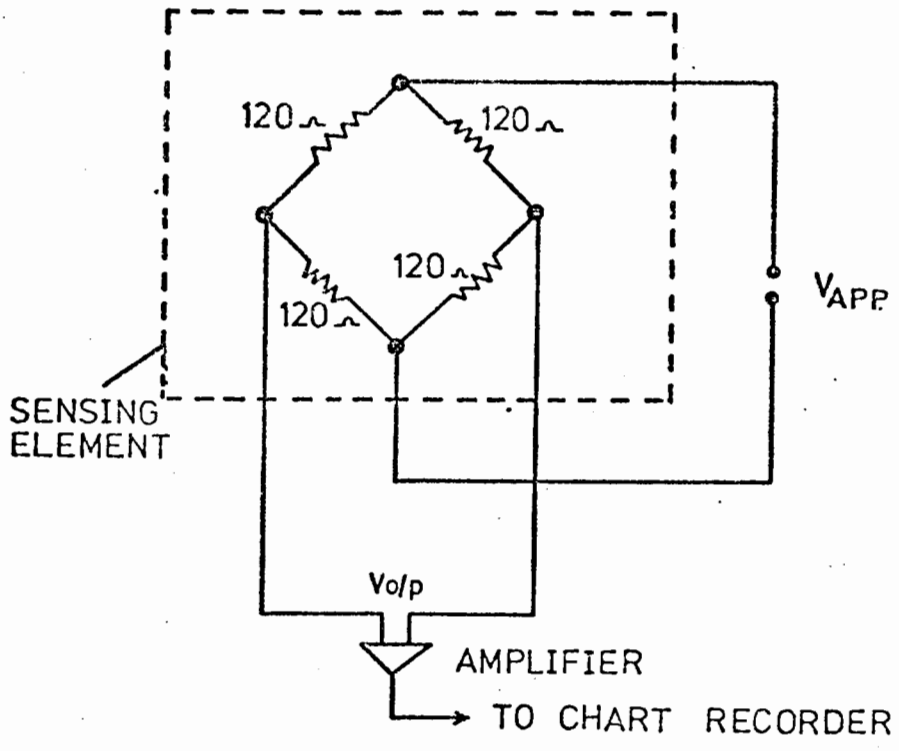

Fig.10.3 The strain gauge network.

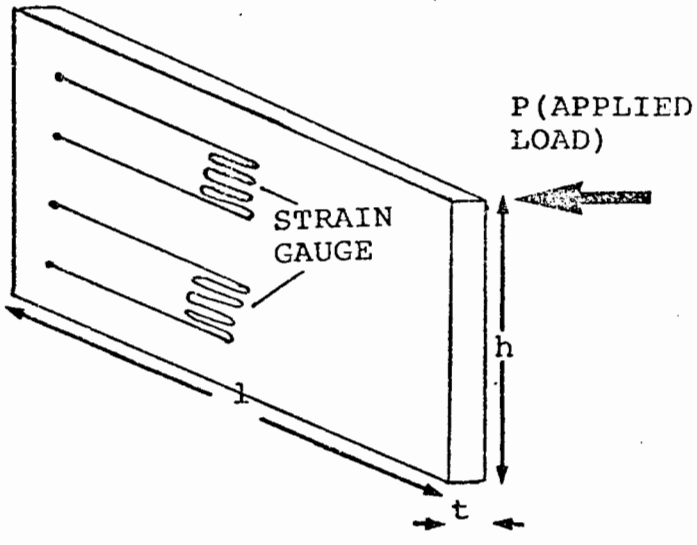

Fig.10.4 Schematic diagram of the strain sensing element.

load, a strain ε is established, given by:

$$\varepsilon = \frac{P.\ell}{I_b} \frac{(t/2)}{E} \qquad (10.6)$$

I_b is the moment of inertia of the beam and equal to $ht^3/12$. Substituting for I_b in eqn.(10.6) we find:

$$\varepsilon = \frac{6P\ell}{Eht^2} \qquad (10.7)$$

Substituting for ε in eqn.(10.5), using eqn.(10.7) we can show

$$V_{o/p} = V_{APP} \cdot \left(\frac{6.P.\ell}{Eht^2}\right) . \text{ gain factor} \qquad (10.8)$$

A strain gauge exciter/amplifier, with an excitation voltage of 5V and a maximum amplification of × 1000, was used. Be-Cu strip (width 3 cm) was chosen as the most suitable material for the strain sensing element. The Young's modulus of Be-Cu is ≈ 120 GPa. The selected strain gauges had a gain factor ≈ 2, and the total length of the element was limited to 6 cm. Inserting the appropriate values of ℓ(6 cm), E(120 GPa), h(3cm) into eqn(10.8), it is possible to show that for a sensitivity of 1 mV/N the appropriate thickness of the strain element should be 1 mm. Thus, with amplification of × 1000, the sensitivity is 1 V/N. This value was considered adequate for the present experiments. The strain element was calibrated experimentally with known weights. The output voltage was found to be a linear function of applied force and to have a calibration slope of 840 mV/N. The output from the strain gauge amplifier was fed directly to a chart recorder, and a permanent trace of the horizontal force during scratching was obtained. The stiffness of the strain element is 4.10^3 N/M.

10.2.3 The Hot Stage

To achieve elevated temperatures a 1 KW hot-stage was constructed. The heat source was a flat ceramic former (machined from pyrophillite) and wound with Kanthal 'A' wire. The stage was provided with a water-cooled base to prevent damage to the Schneeburger stage. Despite the use of heat reflectors and insulation, the large surface area presented problems of excessive heat radiation and the maximum operating temperature was 800 K. Temperature control was achieved using a Eurotherm 070 controller. The thermocouple (Chromel/Alumel) was positioned on the specimen surface and held in position with mica. An initial experiment indicated that the temperature variation over the crystal was better than 10^{o} at 800 K.

10.2.4 The Environmental Chamber

Scratching experiments in dry conditions were made in a specially designed and constructed dry box. The complete scratching equipment was placed within this box and two glove portals enabled this apparatus to be conveniently operated.

The dry box (Fig.10.5) was constructed from 10 mm thick perspex and had overall dimensions of 50 cmx 50 cmx 150cm. Two chambers were incorporated, a main chamber housing the scratching equipment, and a subsidiary chamber which was used as an airlock to prevent moist air from entering the main chamber when passing specimens/equipment through. Electrical lead-throughs, and water services for the hot-stage were also provided. To achieve a low relative humidity, high purity nitrogen (water content 0.006 mg/ℓ) was flushed through the chamber. The change in humidity was monitored using a hair hygrometer positioned inside the main chamber. Additional pre-drying

B=BLOWER

C=CHART RECORDER

G=GLOVE PORTALS

M=MAIN CHAMBER

O=OUTER CHAMBER (AIR LOCK)

S=STRAIN GAUGE EXCITER/AMPLIFIER

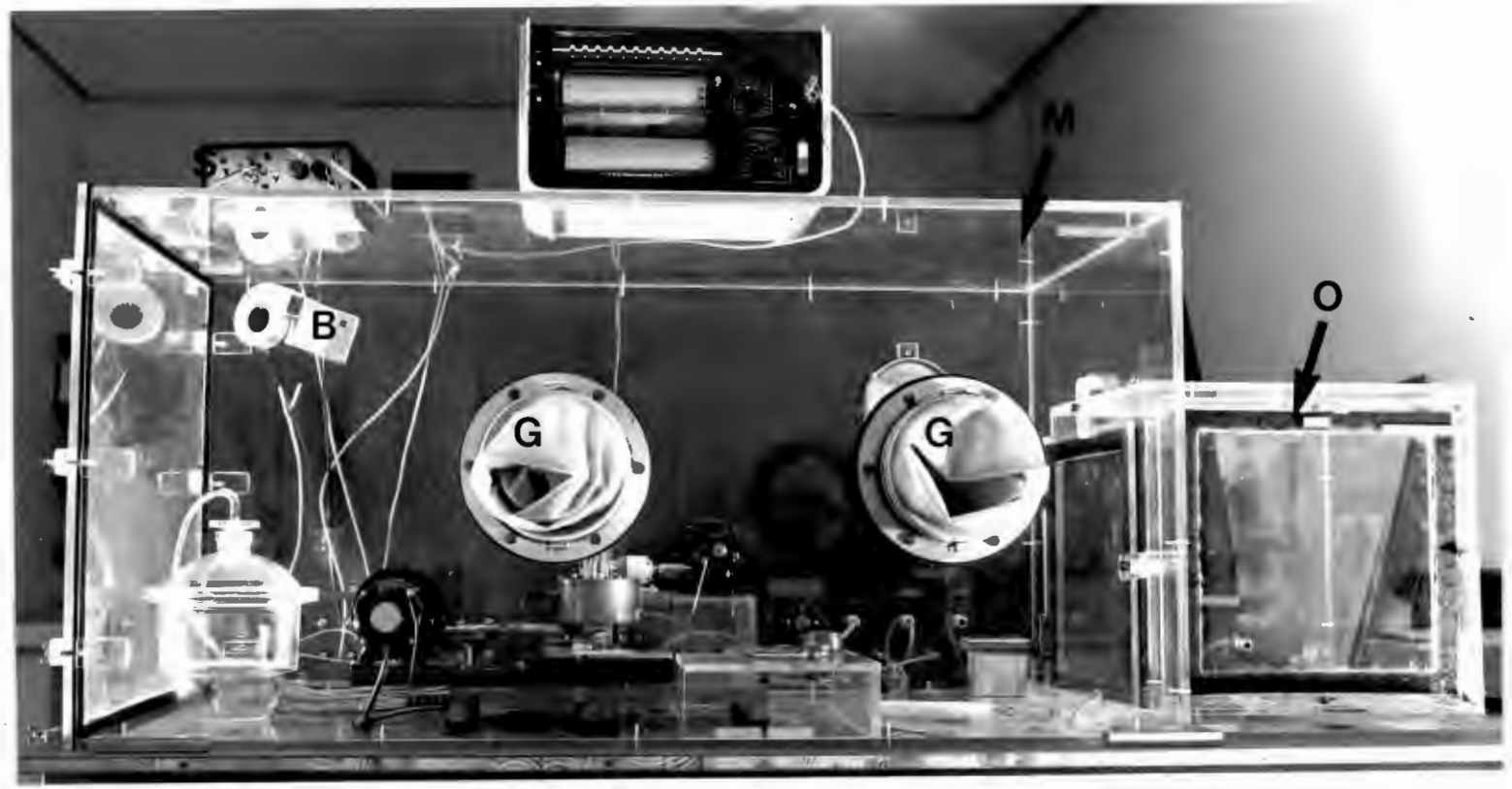

Fig.10.5 The environmental dry box.

of the nitrogen was undertaken using anhydrous magnesium perchlorate crystals. To achieve a good gas circulation within the main chamber, a small blower was incorporated.

It was found that the perspex surfaces had absorbed a considerable quantity of water, and an initial nitrogen flushing operation had to continue for approximately one week to reach a relative humidity level of $\approx 5\%$. P_2O_5 drying agent was then placed within the chamber and this rapidly reduced the humidity to a low value. A small flow of nitrogen, plus frequent changing of the P_2O_5 subsequently kept the humidity low.

10.2.5 Experimental Procedure

Scratches were made on polished and etched sections of the X-, Y- and Z-cut planes of quartz. Surface moisture was removed from the crystals by vacuum annealing at 800K and 10^{-5} torr in quartz glass ampoules for a period of 24 hours. After annealing the ampoules were cooled to room temperature and sealed. They were then placed within the subsidiary chamber of the dry box. Nitrogen was flushed through this chamber for several hours, and the ampoules then moved through into the main chamber and opened. In this way the crystals were not exposed to any moisture after annealing and prior to scratching.

To scratch a crystal the following procedure was adopted:

1. The crystal was lined up using the traverse stage motor and the micrometer drive.
2. The balance arm was loaded with the required weight.
3. The balance arm lever was activated and the cutting tool slowly lowered.
4. The scratch was made, usually for a length of 0.5 or 1 mm. In all cases a scratch speed of 10 $\mu m\ s^{-1}$ was selected.
5. The balance arm was raised and the crystal repositioned for the next scratch.

After each series of tests on a crystal, optical micrographs were taken and used to measure the scratch widths. These measurements were made after the scratch debris had been removed with a piece of sticky tape. Some of this debris was mounted on an SEM stub for subsequent examination in the scanning electron microscope.

It was found difficult to measure the small scratch depths, and two techniques were investigated. A Talysurf instrument was available, but the stylus diameter was large (2.5 μm) and this led to poor results for the scratches made at the lower loads. The alternative method was the use of the optical microscope and the calibrated fine-focus control. By successively focusing on the edge and bottom of the scratch groove, the depth could be determined. This method was effective, provided care was exercised in taking up the backlash of the focusing assembly. Again, for the scratches at low loads difficulties were encountered because of the problem of locating the bottom of the groove.

There was no significant difference in the experimental accuracy of measurements by either technique. In view of the relative ease with which the optical measurements could be made, the depths of the scratches were obtained using the microscope. However, the depth measurements are only accurate to ± 1μm, and the results presented are an average of three readings taken at different positions along the scratch track.

10.2.6 The Cutting Tool

Prior work on the scratching of brittle materials (Broese van Groenou et al., 1975) has demonstrated that it is particularly important to ensure that the geometry of the cutting tool is well defined if results are to be amenable to analysis. Accordingly, it was decided to utilise a Vickers pyramid in these scratching experiments.

Two orientations were used, viz:

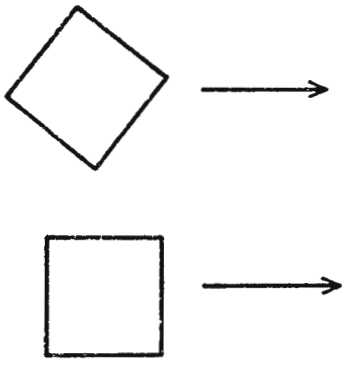

Pyramid position A

Pyramid position B

The use of a Vickers pyramid as the cutting tool has the additional advantage in that it links closely to the series of microhardness tests described previously. The vertical force (F_V) acting on the pyramid (0.1-1.0 N) was also chosen to correspond closely to the range covered in the microhardness experiments. Commercially available Vickers pyramids were obtained and used exclusively in the present work.

It was found, however, during the coarse of these scratching tests that the pyramid tip wore rapidly and became blunt (Fig.10.6). The blunting effect was not anticipated and had a profound influence on the scratch deformation. Consequently a distinction is made between scratching with a blunt and a sharp pyramid, when presenting the results.

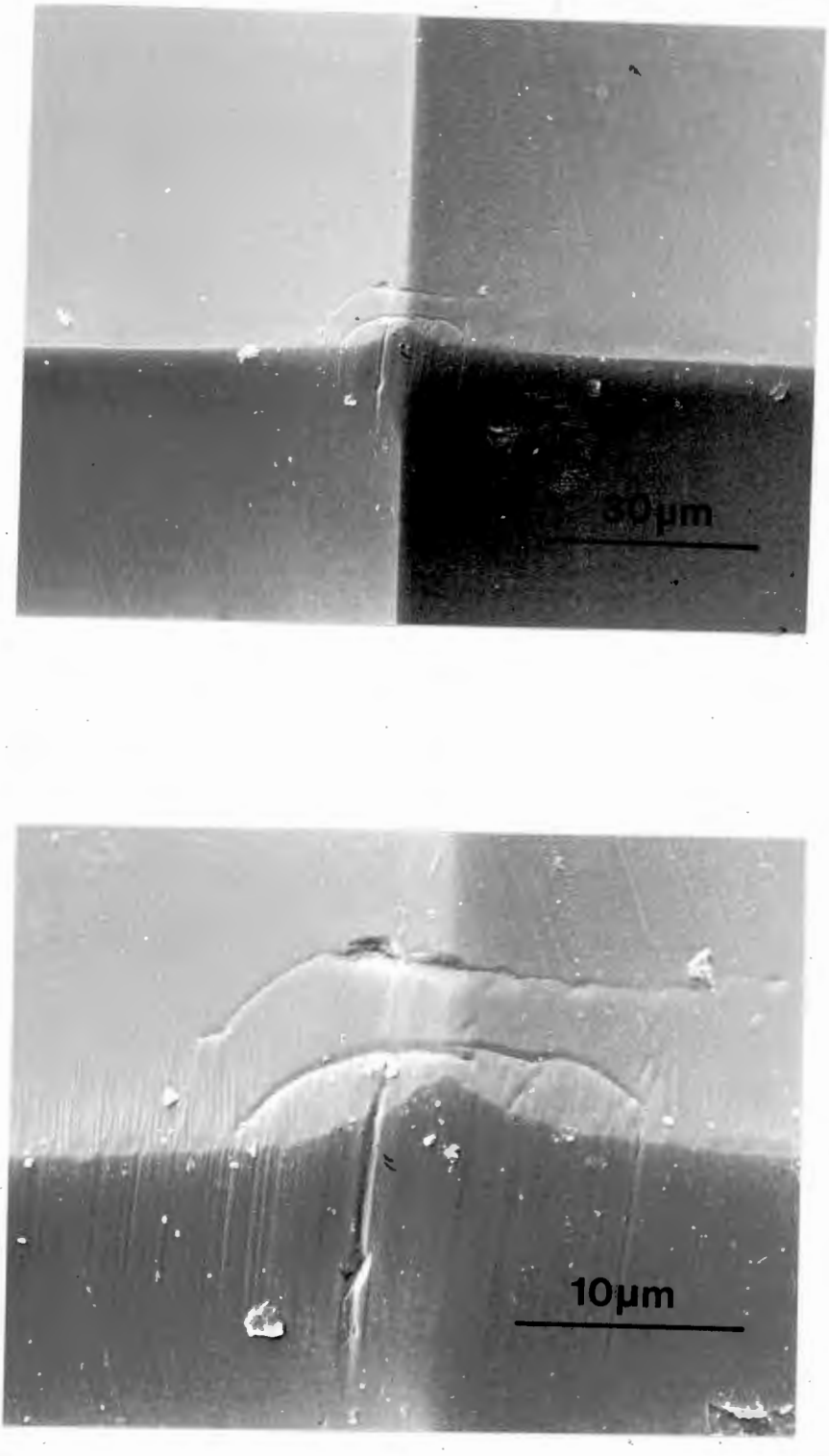

Fig.10.6 SEM micrographs showing the wear of the diamond pyramid.

10.3 RESULTS

10.3.1 Scratches Made at Room Temperature, in a Dry Nitrogen Environment

(a) Scratching with a Sharp Indentor

Scratches were made on the three principal cuts of quartz in the following crystallographic directions:

X-cut $(11\bar{2}0)$: $\langle 10\bar{1}0\rangle$, [0001]
Y-cut $(\bar{1}100)$: $\langle 11\bar{2}0\rangle$, [0001]
Z-cut (0001) : $\langle 10\bar{1}0\rangle$, $\langle 11\bar{2}0\rangle$

The pyramid was aligned in orientation (A).

Fractography

Examples of reflected light optical micrographs of scratches made on the Z-cut plane in the $\langle 11\bar{2}0\rangle$ direction are shown in Fig.10.7. A full cutting action occurs over the entire experimental vertical load range, while the extent of cracking to the side of the scratch increases with load. Similar results were obtained for the X-cut plane. However, for the Y-cut plane, scratched in both the $\langle 11\bar{2}0\rangle$ and [0001] directions, a 'ductile groove' with some chipping and cracking is formed at low loads (Fig.10.8a), and extensive chipping is dominant at higher loads (Fig.10.8b).

Scanning electron microscopy was used to examine the scratch deformation in more detail. Fig.10.9 shows a scratch, made at a load of 1.0 N before the scratch debris was removed. Fig.10.10 is a similar scratch after cleaning. The outline of the scratch is irregular, and consistent with brittle fracture, but there is no evidence for cleavage on preferred crystallographic planes such as r or z.

SEM investigations of the scratch debris (Fig.10.11) gave evidence that the sharp indentor was 'rubbing' over the surface of the crystal, generating partial cone-cracks. The zone in which cutting takes place lies in the sub-surface region, so that material is removed by delamination. This cutting mode is schematically represented in Fig.10.12.

Cutting Parameters

Examples of the horizontal force output trace are shown in Fig.10.13. As the vertical load is increased we note an increasing degree of fluctuation in the horizontal force. In this particular example, at 0.5N, there is a sudden drop in the value of horizontal force, approximately half-way along the scratch track. Attempts to correlate such events optically with a deformation feature (particularly chip formation) along the scratch were not successful.

The average horizontal force (F_H) was plotted as a function of vertical force (F_V) and a linear relationship found for all planes and directions of scratching (Fig.10.14 for the Y-cut plane.) However, is is evident that a best-fit line through the data points does not intercept the origin.

To estimate the specific energy it is necessary to calculate the cross-sectional area of the scratch, A_T. Widths (Fig.10.15) were measured from the optical micrographs, and the depths (Fig.10.16) found optically. It is clear from the SEM micrograph of a scratch (Fig.10.10) that the cross-sectional shape is not an exact copy of the translating pyramidal tool. A sectioning experiment was undertaken to help clarify the exact shape of the scratch track, and it can be seen (Fig.10.17) that the outline approximates to an ellipse. Accordingly this cross-sectional geometry was used to calculate the specific energy as a function of vertical load (Fig.10.18). Specific energy is high at low loads decreasing to a constant value ($\approx$ 8 GJ/m^3) for vertical loads $\gtrsim$ 0.3N. Because of the

experimental difficulties in measuring the scratch depths, and also the inability to account for material removed by chipping at the sides of the scratch groove, this energy data must be treated with some caution.

(b) Blunt Indentor

The X-, Y-, and Z-cut planes of quartz were scratched in the following crystallographic directions:

X-cut $(11\bar{2}0)$: $\langle 10\bar{1}0\rangle$, [0001]

Y-cut $(\bar{1}100)$: $\langle 11\bar{2}0\rangle$, [0001]

Z-cut (0001) : $\langle 10\bar{1}0\rangle$, $\langle 11\bar{2}0\rangle$

The pyramid was aligned in orientation (A).

Fractography

Z-cut plane

Optical examination (Fig.10.19) revealed that there was a definite crystallographic effect between scratching in $\langle 11\bar{2}0\rangle$ and $\langle 10\bar{1}0\rangle$. Cutting is easier in $\langle 11\bar{2}0\rangle$, (commencing at a vertical load of 0.2N), while in $\langle 10\bar{1}0\rangle$ full cutting is not achieved until a load of 0.8N is exceeded. Note also that Hertzian cracking is visible on the scratch deformation tracks for the 'harder' $\langle 10\bar{1}0\rangle$ direction (see, for example, the 0.5N scratch). One puzzling feature is that only one half of the track has been removed for some scratches in $\langle 10\bar{1}0\rangle$; the remaining half shows the characteristic Hertzian cracking. In transmitted light (Fig.10.20) we note that the median crack oscillates from one side of the groove to the other. This effect has recently been observed by Swain (1979).

In the SEM these findings are confirmed (Fig.10.21). The Hertzian deformation track is particularly well defined, showing a heavily deformed central zone, with microcracks extending out from the central region. Side views of the Hertzian deformation (Fig.10.22 & 23) indicate that the central zone may have undergone plastic deformation. The surface has evidently been heavily distorted, but rather than the appearance been angular and consistent with brittle fracture, some of the deformation is smooth in outline and indicative of the operation of inelastic processes. However, confirmation of dislocation nucleation and slip using HVEM could not be obtained (Fig.10.24a) since extensive distortion about the scratches precluded any dislocation contrast experiments. An X-ray diffraction topograph (Fig.10.24b) indicated that strain contrast was extensive about scratches in quartz.

X-cut plane

Scratching in the [0001] direction was found to be harder than $\langle 10\bar{1}0 \rangle$. In [0001] no cutting action was found up to the highest load, although at 1.0N the extent of subsurface deformation was increased and occasional chips were formed (Fig.10.25a). In $\langle 10\bar{1}0 \rangle$ cutting occurred at loads $\geq$ 0.6N, and chipping was predominant (Fig.10.25b).

Y-cut plane

Similar results to the X-cut plane were obtained. Scratching in the [0001] direction was hard, and no cut was observed over the experimental vertical load range. These tracks show the characteristic Hertzian cracking (Fig.10.26a). In the $\langle 11\bar{2}0 \rangle$ direction cutting occurred for loads $\geq$ 0.6N. At higher loads cracking and chipping was evident (Fig.10.26b).

Summarising these results of scratching with a blunt pyramid in dry conditions we may state:

1. For scratching on the basal (0001) Z-cut plane the $\langle 10\bar{1}0 \rangle$ direction is 'harder' than $\langle 11\bar{2}0 \rangle$. By harder we mean that a full cutting action (material removal by delamination) requires a higher vertical load than the 'easier' direction.

2. For scratching on the X- and Y-cut planes scratching parallel to [0001] is harder than in directions perpendicular to [0001].

Cutting Parameters

We may expect that these effects of crystallographic orientation dependence would be shown up on the horizontal force data. However, this is not the case (Fig.10.27, for the Z-cut plane), and all orientations, whether 'hard' or 'easy' show the same F_H/F_V relationship. Again, it is noted that the best fit line through the data does not intercept the origin.

The variation in the width of the scratches for the Z-cut plane as the vertical load is increased (Fig.10.28) illustrates the change in deformation. For the hard direction the width measured is that of the Hertzian deformation zone. A sudden increase in width at $F_V = 0.5N$ is the point at which cutting commences. We note that the scratch width is the same for both the hard and easy directions when cutting occurs.

Similar results were obtained for scratches on the Y- and X-cut planes. In the hard [0001] direction the values of width reflect the measured deformation zone, while in the easy directions, cutting is observed for loads $\geq 0.6N$; again

a sudden increase in width was noted when a cut is produced.

A value of depth could only be measured when a physical cut was produced, and it was found that under these conditions the depths are exactly the same as for a cut with a sharp pyramid.

Values of specific energy are obviously infinite when no cut is produced, but, in general, the trends are similar to the sharp pyramid scratches. For the case of Z-cut quartz scratched in the easy <11$\bar{2}$0> direction, the specific energy increases as F_v is reduced to below 0.3N (Fig.10.29).

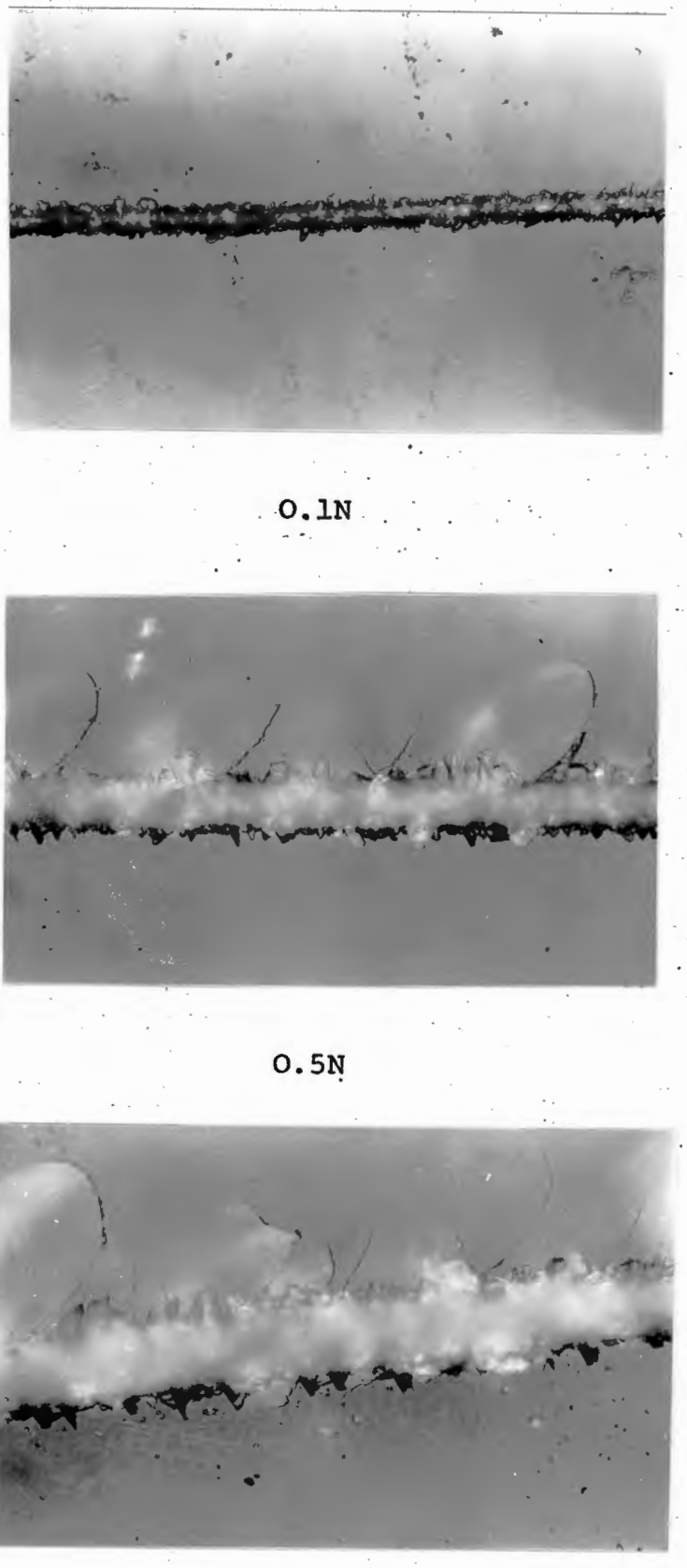

Fig.10.7 Optical micrographs showing the change in scratch deformation as the vertical load is increased. (Z-cut plane, $[11\bar{2}0]$ scratching direction, sharp pyramid, RH~0%).

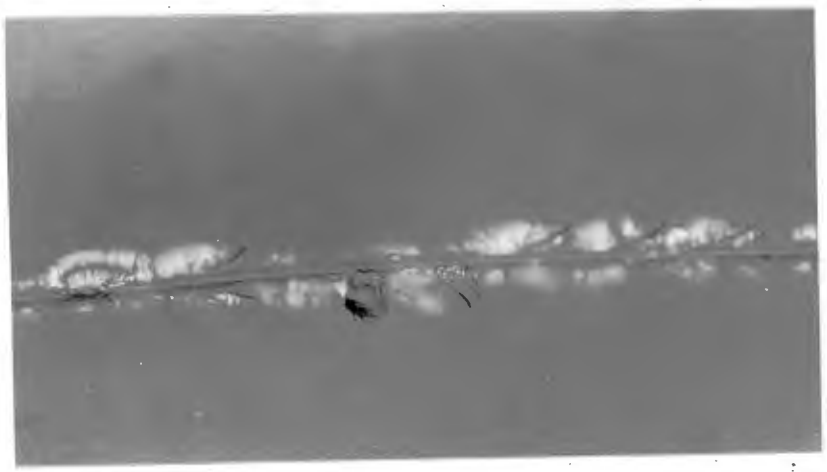

(a)

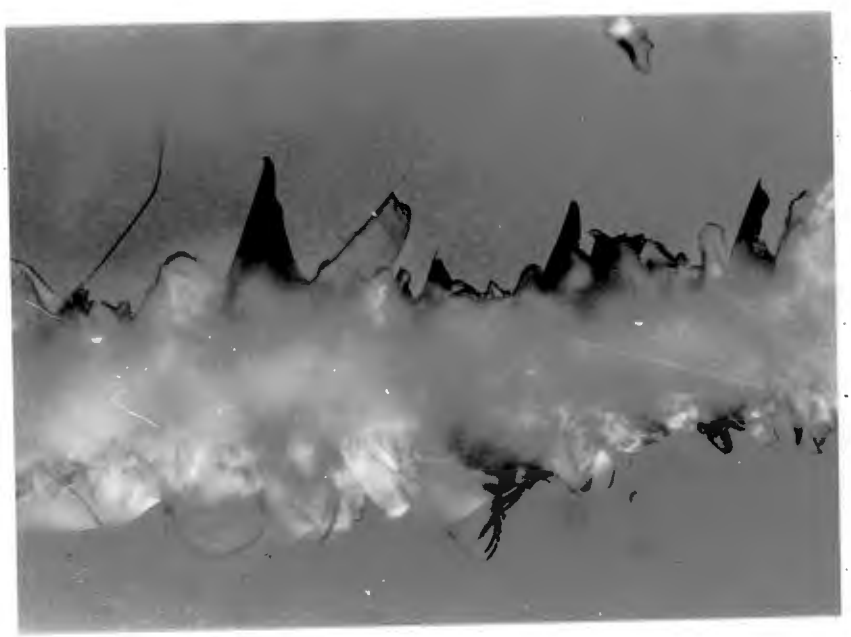

(b)

Fig.10.8 Scratches on the Y-cut plane (sharp pyramid, dry conditions). (a) Low load (0.1N). Note the ductile groove. (b) High load (1.0N). The extent of chipping is more pronounced than the Z-cut plane.

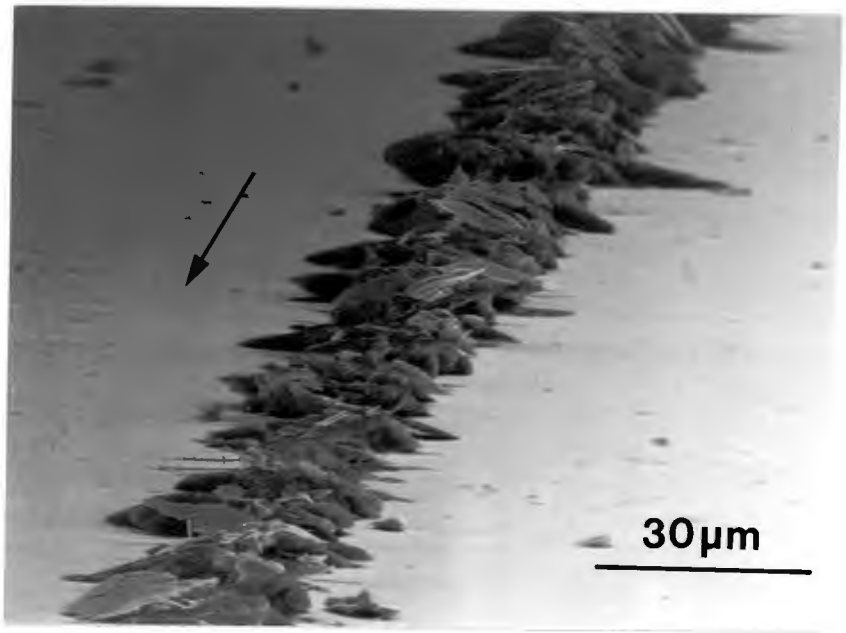

Fig.10.9 Example of a scratch prior to removal of debris. (Z-cut plane, [0001] scratching direction, dry conditions).

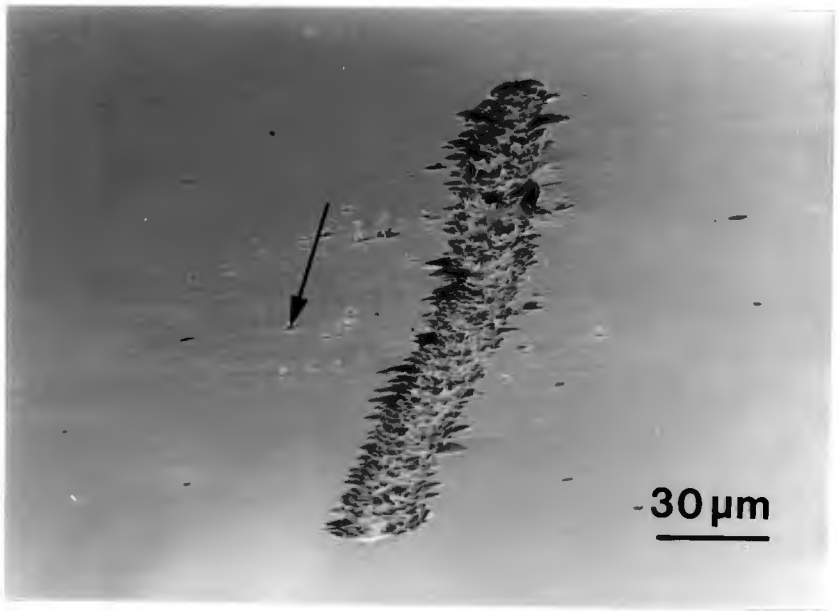

Fig.10.10 Similar scratch to fig.10.9, but after scratch debris was removed.

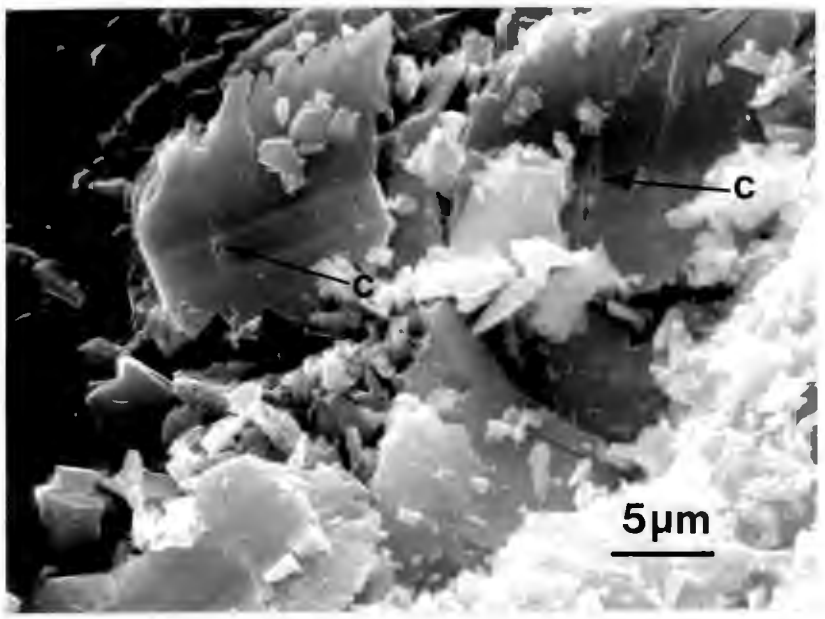

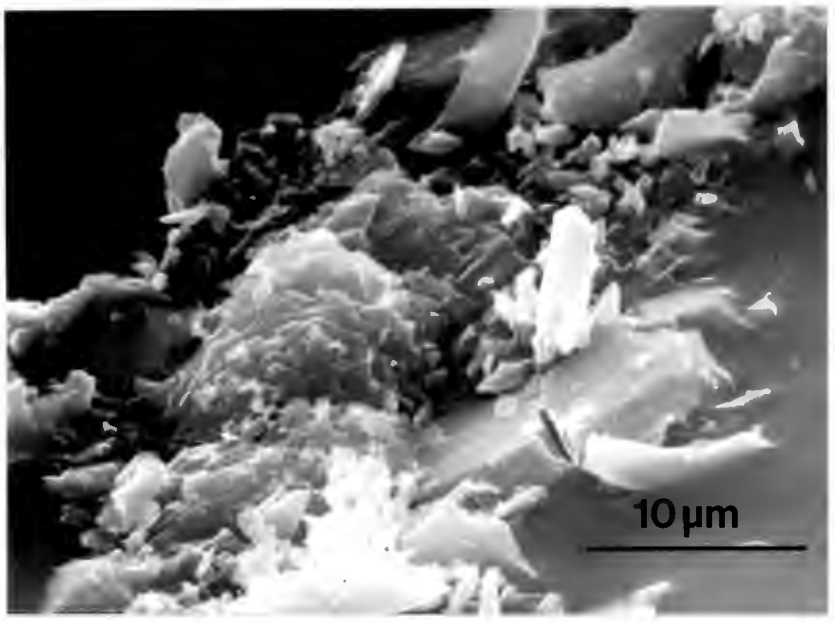

Fig.10.11 Examples of the scratch debris. Note the fact that the sharp pyramid appears to have rubbed over the surface, generating cone cracks (c) yet a cutting action has occured in the sub-surface layer.

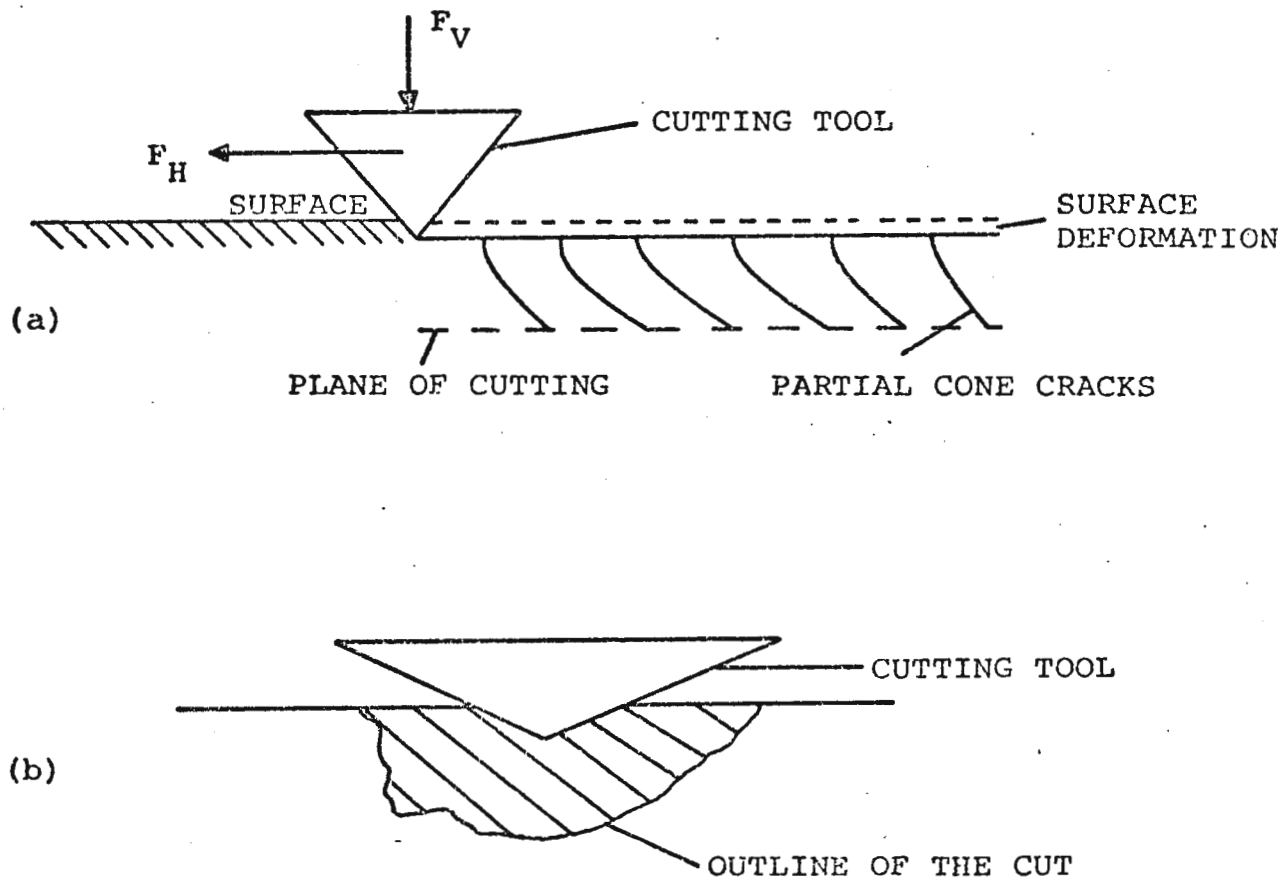

Fig.10.12 Schematic diagram of the cutting action. (a) Side view. (b) End view.

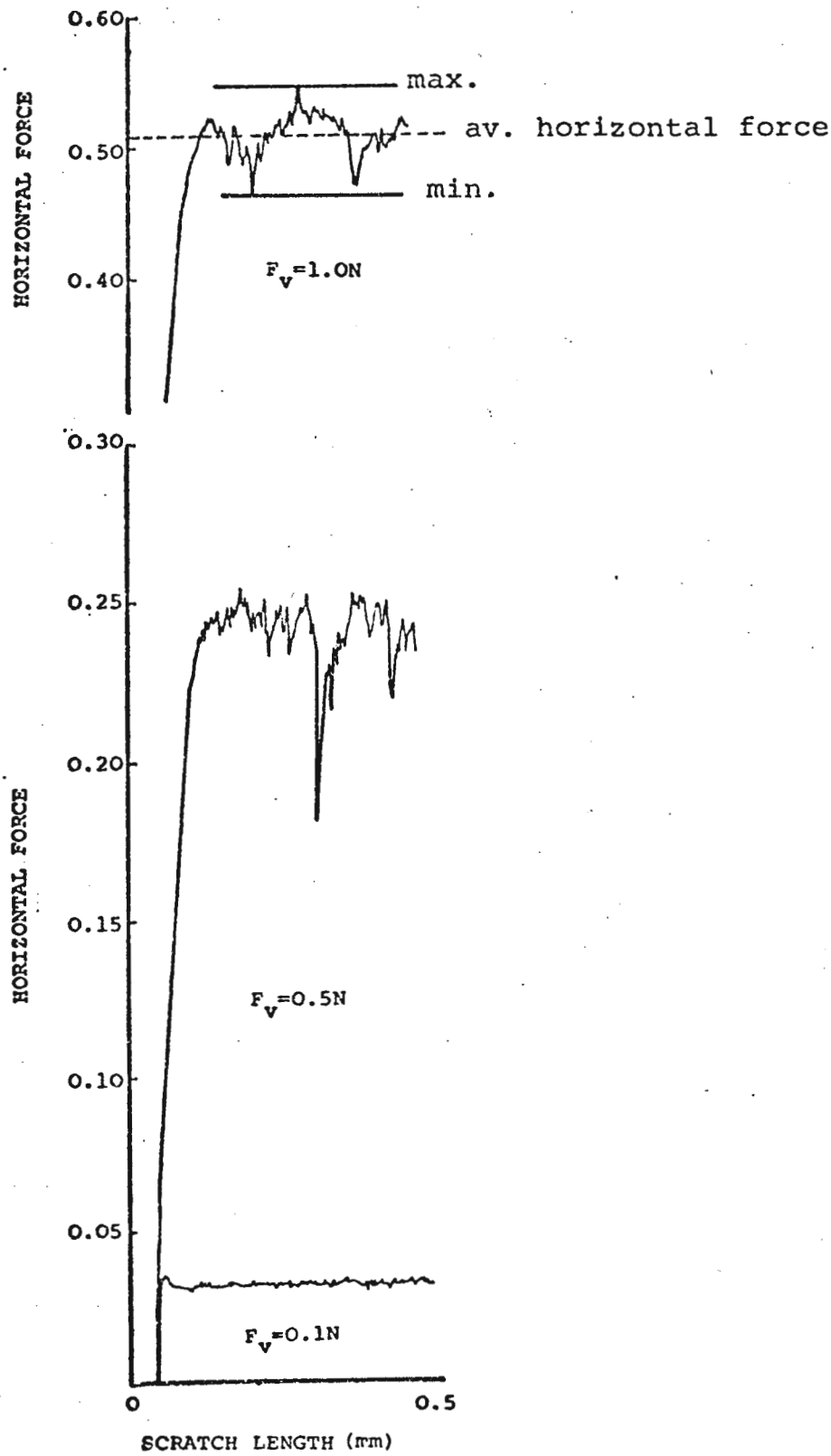

Fig.10.13 Examples of horizontal force output trace (0.1, 0.5 and 1.0N scratches). Note change of scale for 1.0N scratch. The fluctuations in horizontal force increase as the vertical force (F_V) is increased.

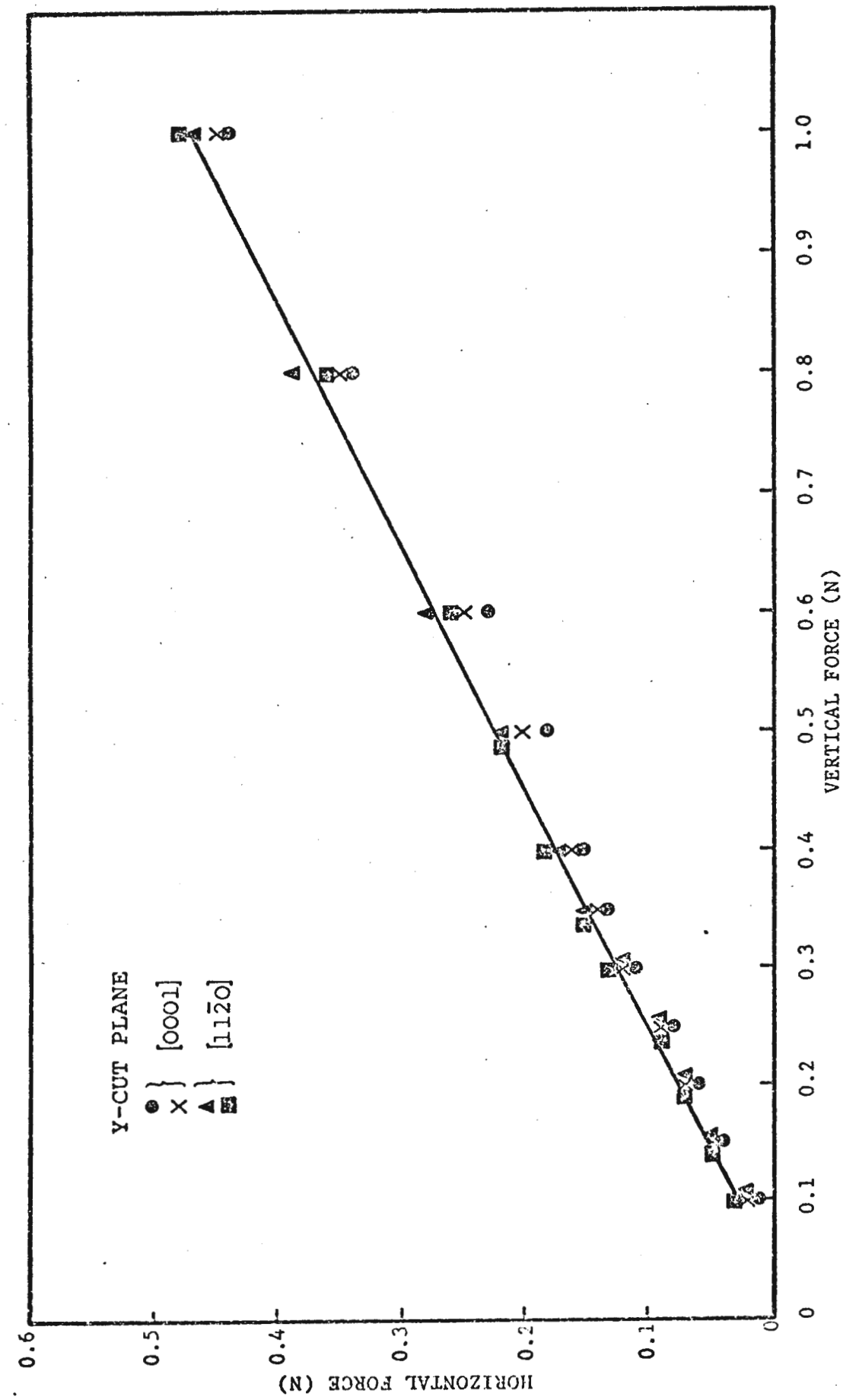

Fig.10.14 Average horizontal force as a function of vertical force. (Y-cut plane, sharp pyramid, dry conditions RH~0%).

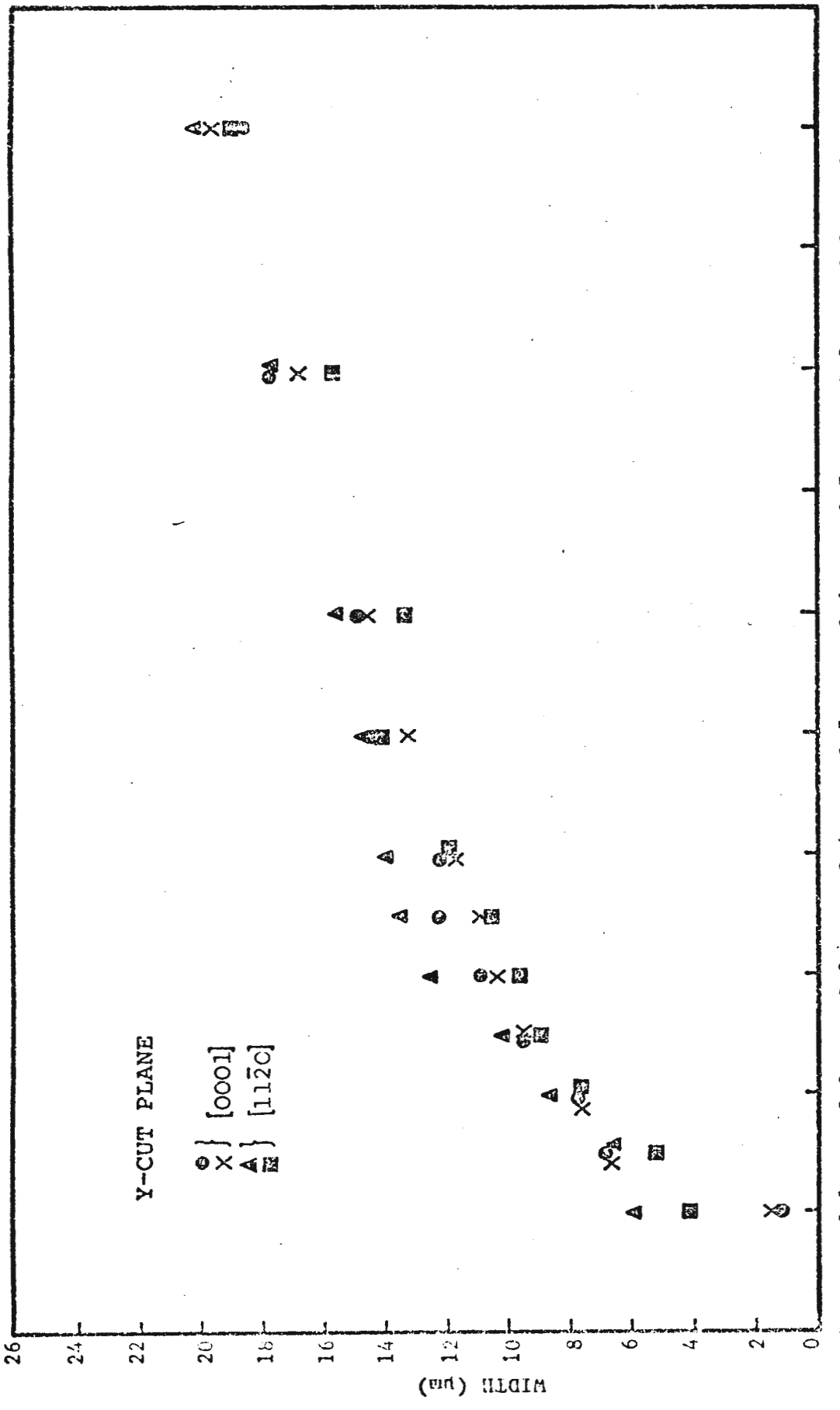

Fig.10.15 Scratch widths as a function of vertical force. (sharp pyramid, dry conditions, RH~0%).

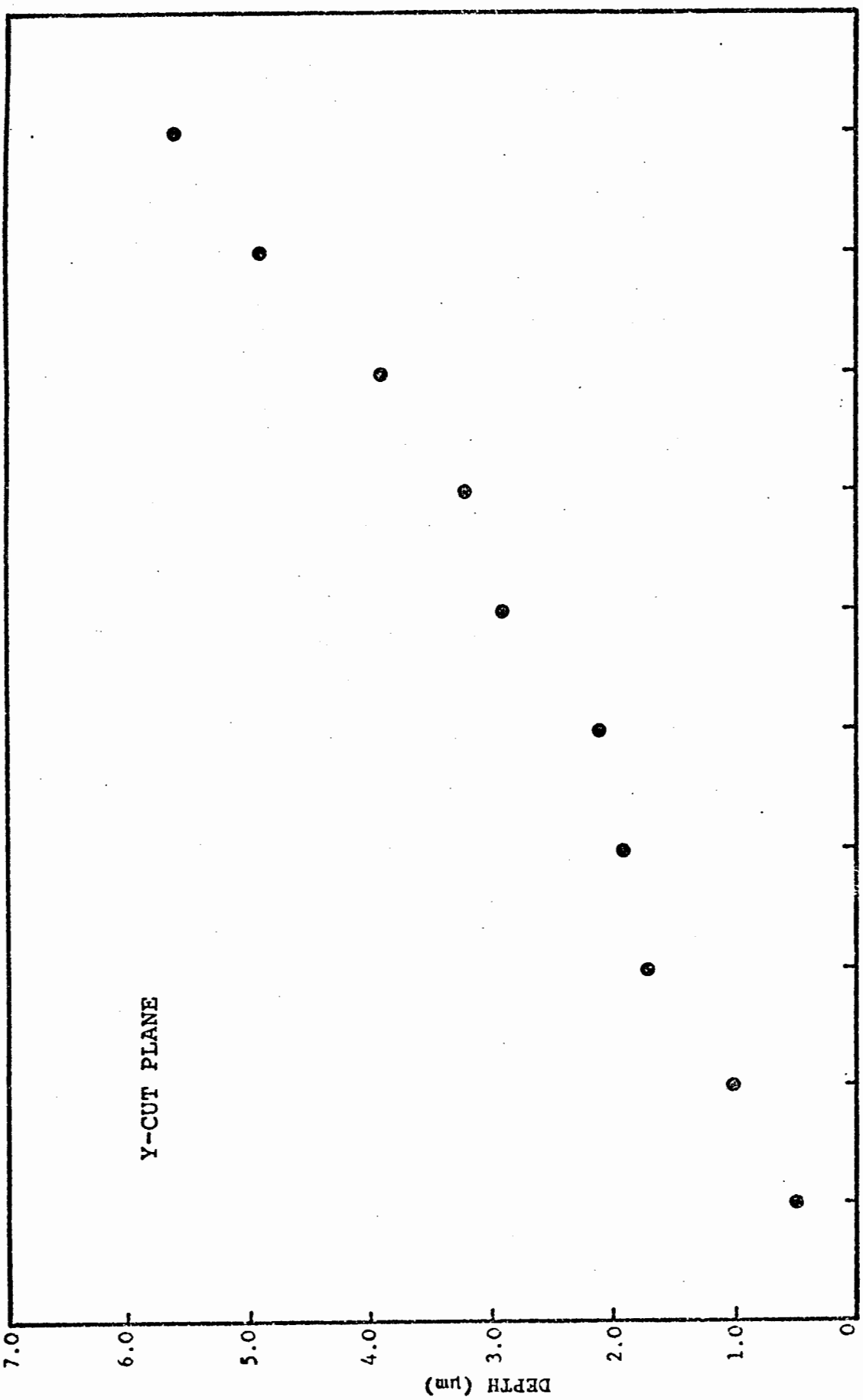

Fig.10.16 Scratch depths as a function of vertical force. (sharp pyramid, dry conditions, RH~0%).

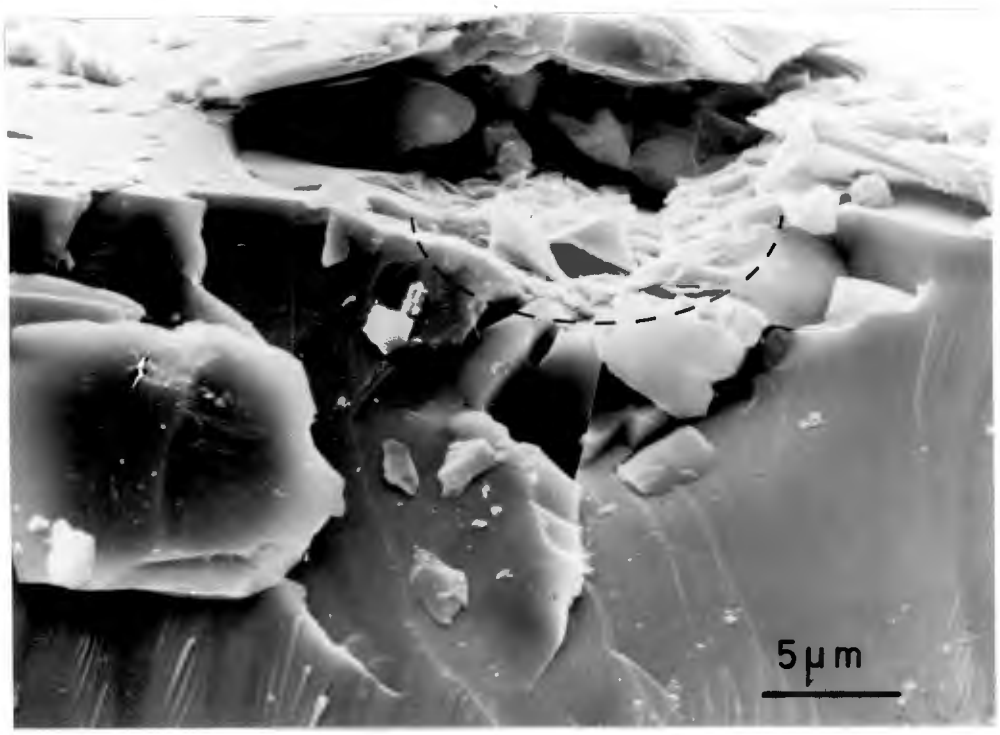

Fig.10.17 Cross section of a scratch.

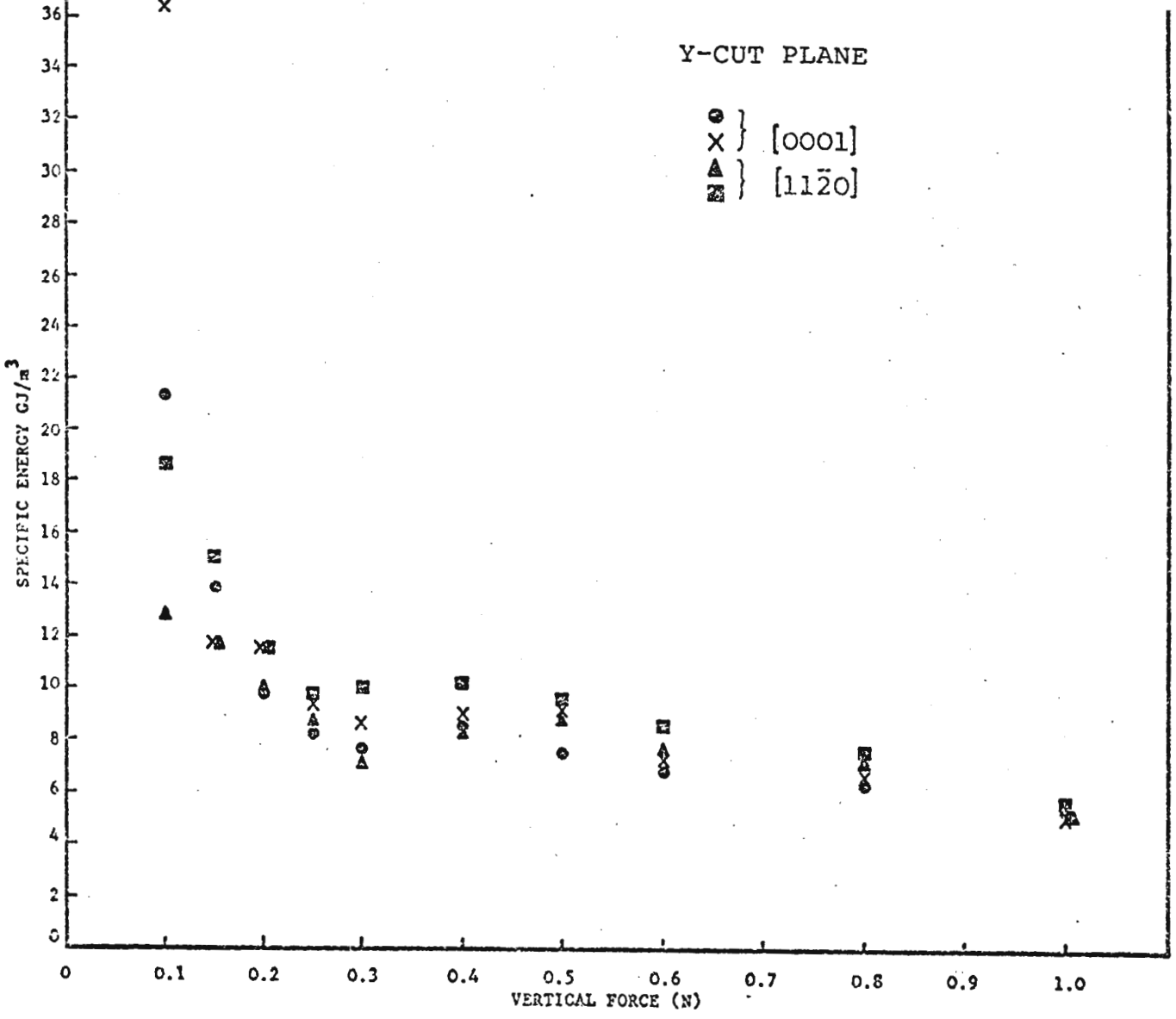

Fig.10.18 Specific energy as a function of vertical force (sharp pyramid, dry conditions, RH~0%).

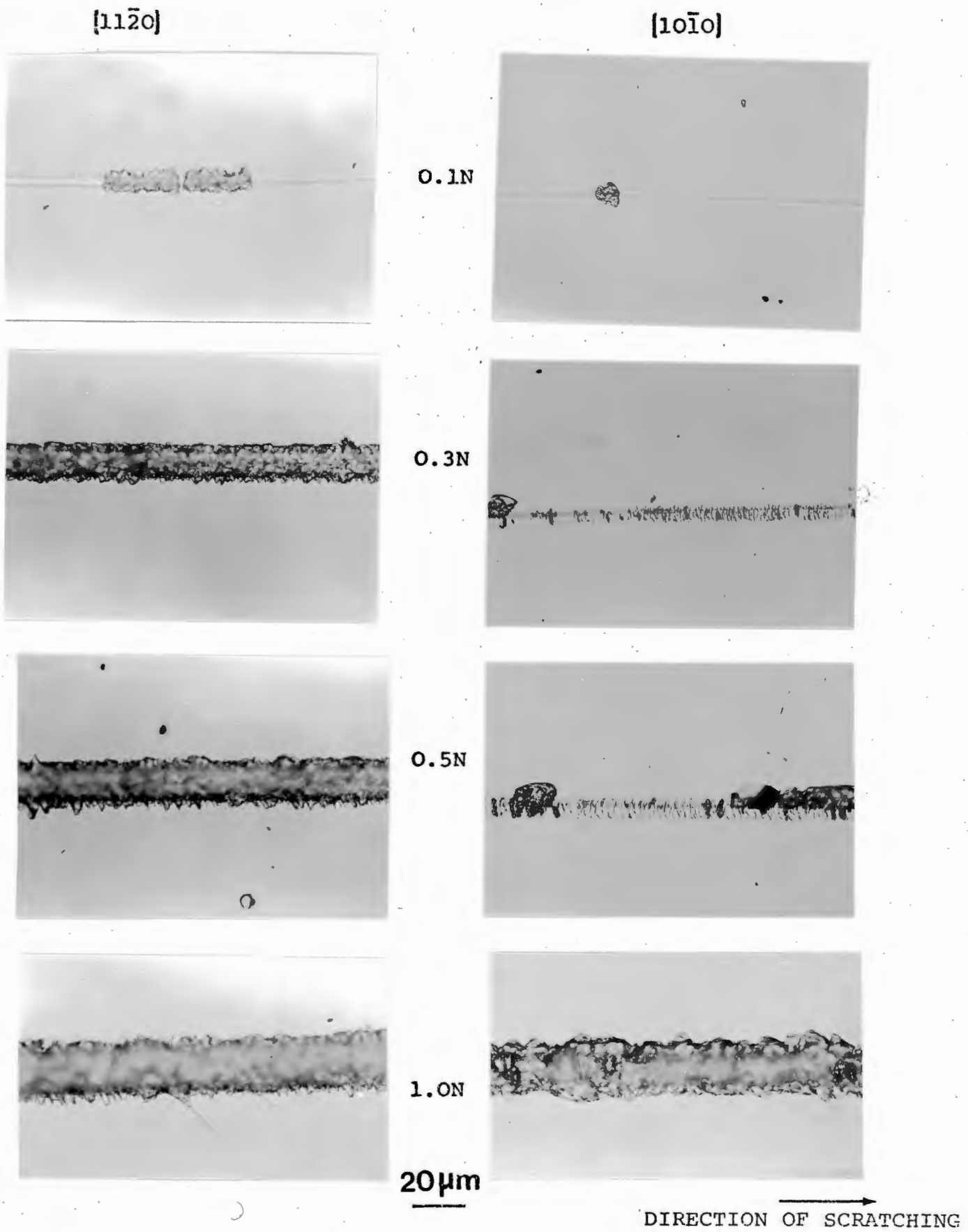

Fig.10.19 Series of optical micrographs illustrating the directional anisotropy of cutting with a blunt pyramid. (Z-cut plane, 10$\bar{1}$0 and 11$\bar{2}$0 direction, dry conditions).

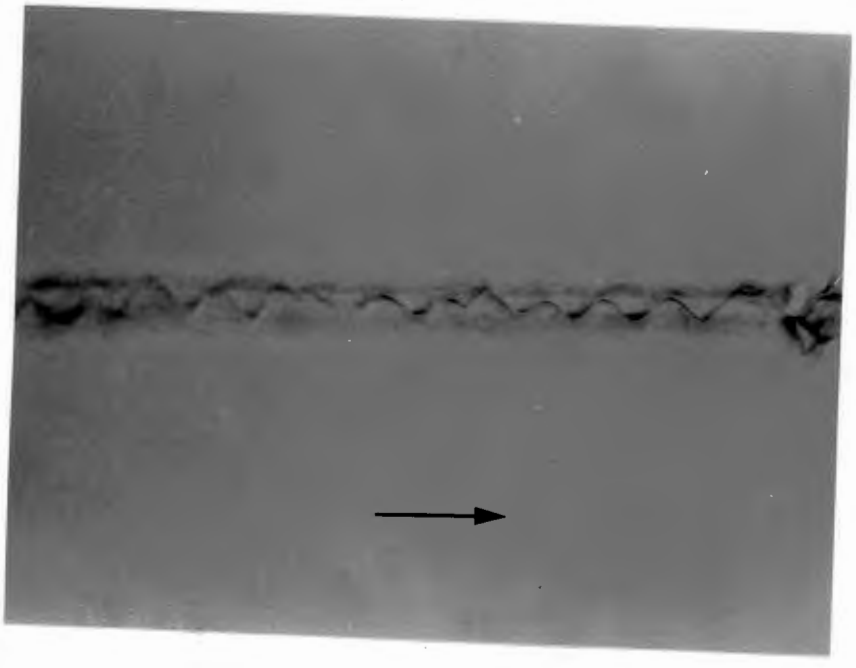

Fig.10.20 Transmitted light optical micrograph showing the median crack oscillating from one side of the track to the other. (Z-cut plane, [10$\bar{1}$0] direction).

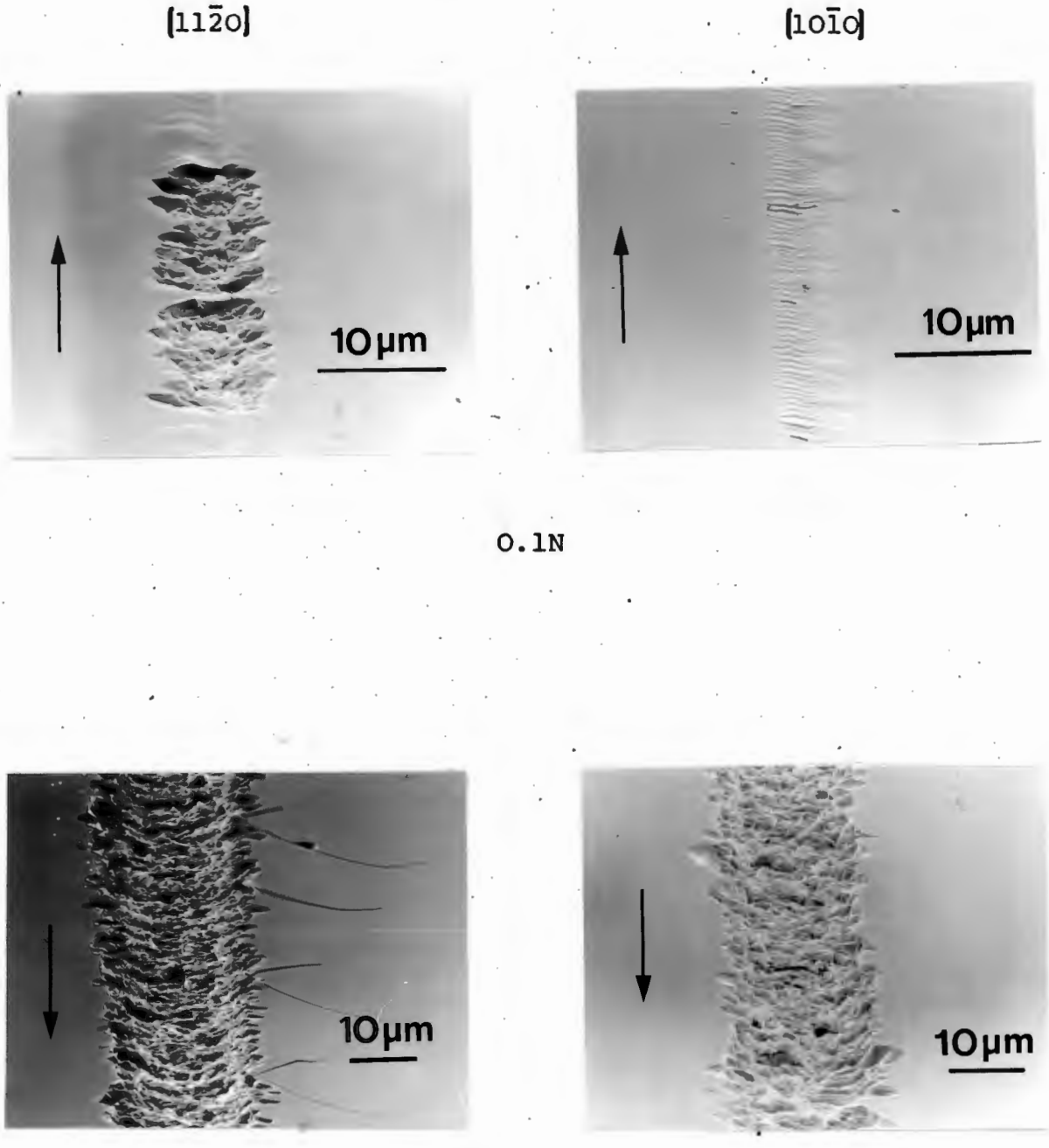

Fig.10.21 The effect of scratching with a blunt pyramid. These SEM micrographs show the directional anisotropy of scratching. (Z-cut plane, dry conditions).

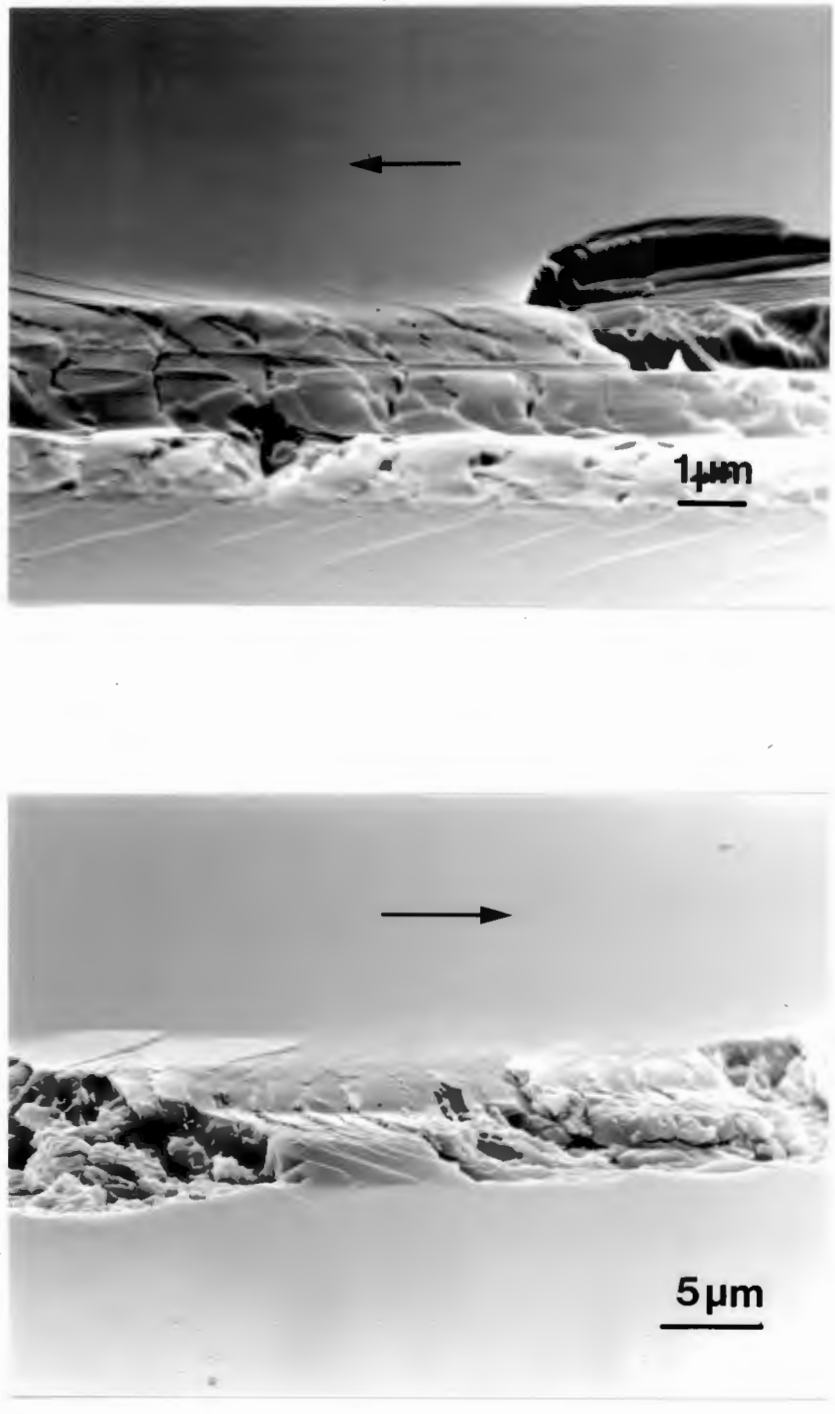

Fig.10.22 SEM micrographs of a Hertzian deformation track. (Z-cut plane, vertical load, 0.2N).

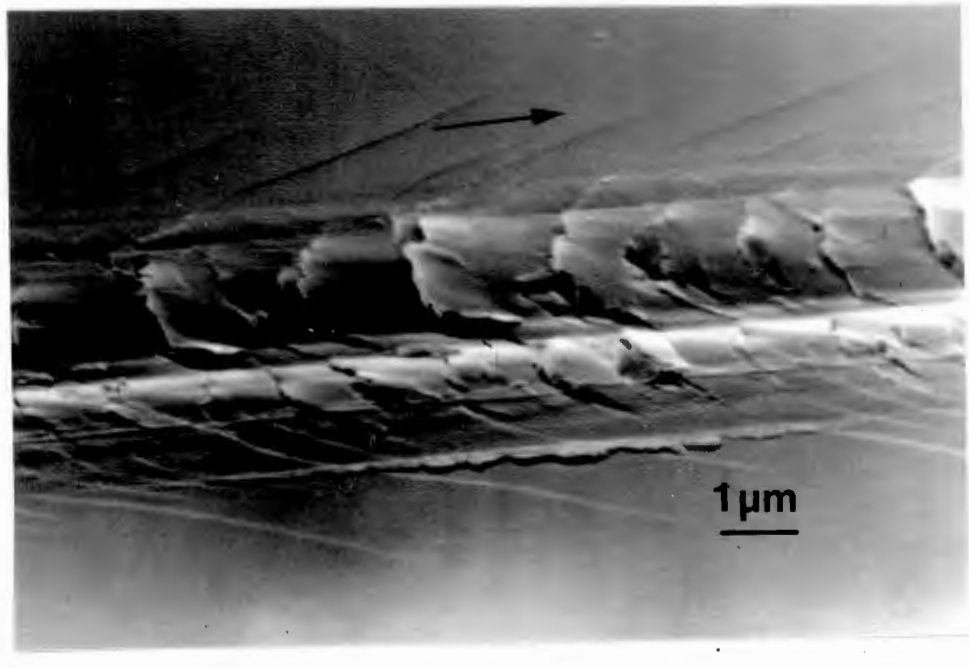

Fig.10.23 SEM micrograph of a Hertzian deformation track. (Z-cut plane, vertical load, 0.2N).

Fig.10.24(a) HVEM of a scratch on quartz. (Z-cut plane, vertical load 0.5N).

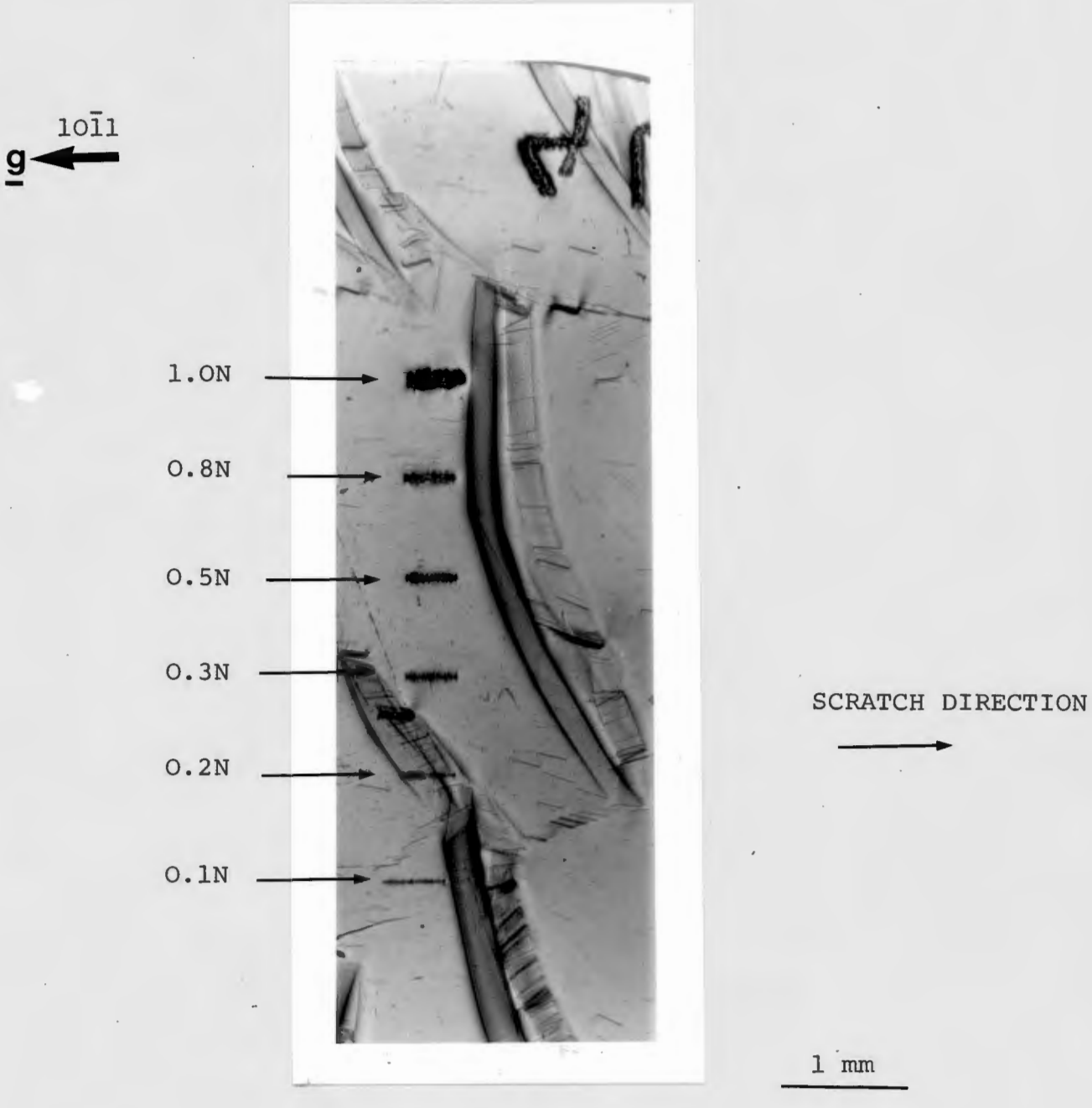

Fig.10.24(b) X-ray diffraction topograph of a series of scratches on quartz. (Z-cut plane).

(a)

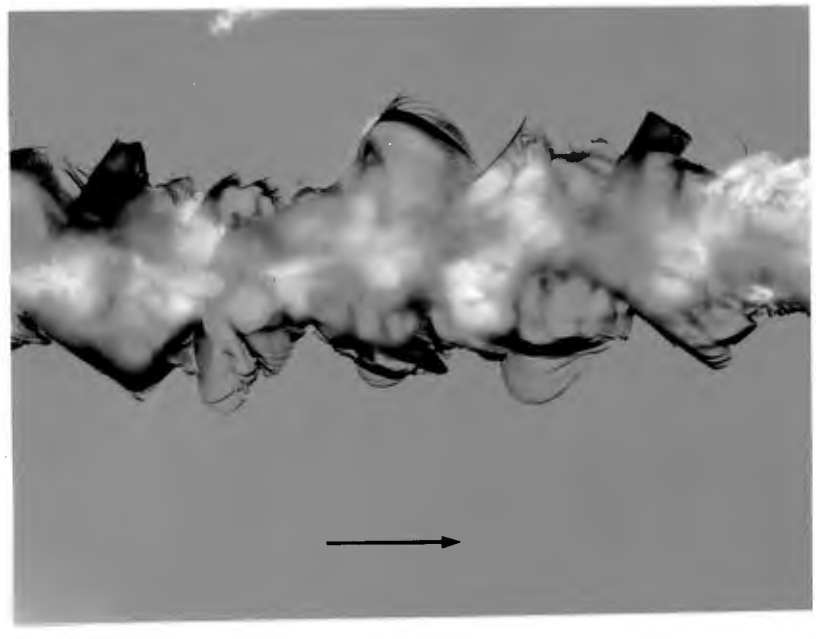

10 µm

(b)

Fig.10.25 The directional anisotropy of cutting with a blunt pyramid. (X-cut plane). (a) Scratch made at a vertical load of 1.0N in the 'hard' [0001] direction. Note the Hertzian deformation track. (b) Same conditions as fig.10.25, but in the 'easy' [10$\bar{1}$0] direction. A full cut has resulted.

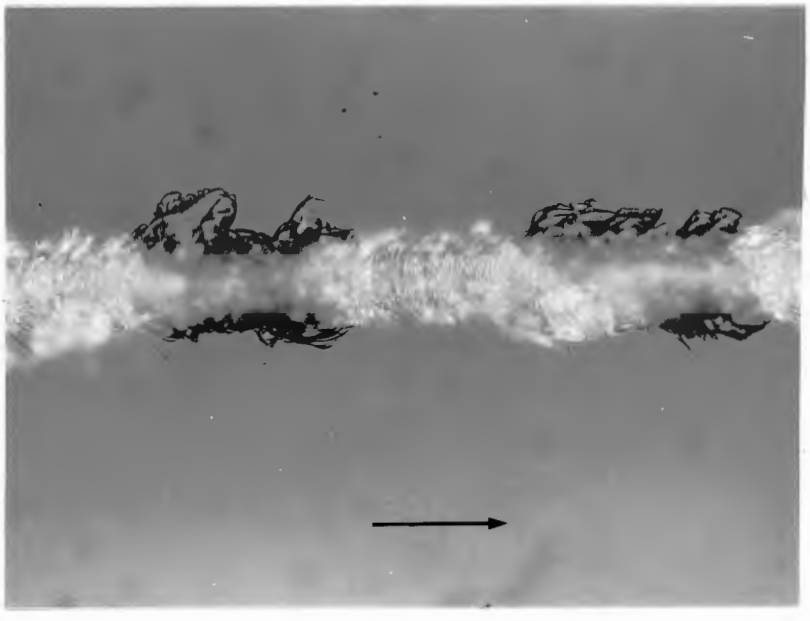

(a)

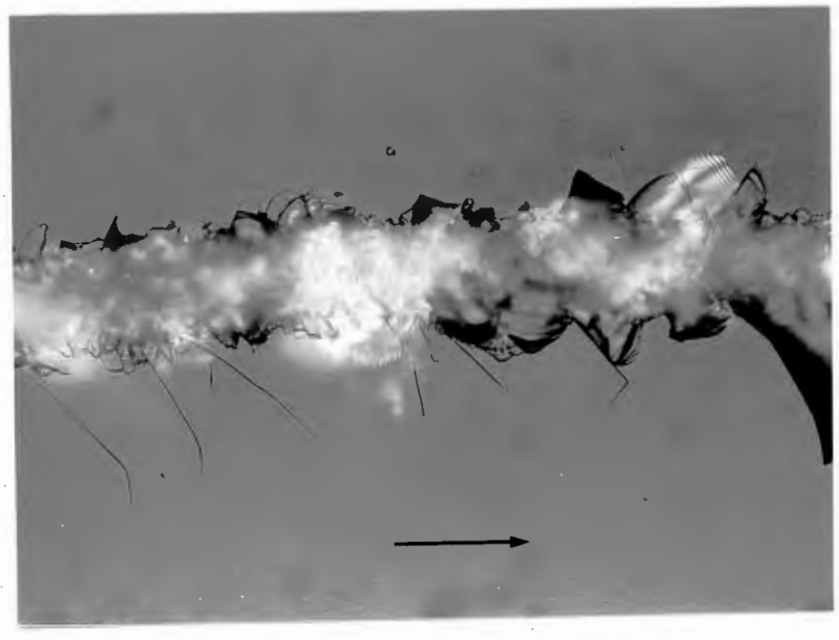

10μm

(b)

Fig.10.26 The directional anisotropy of cutting with a blunt pyramid. (Y-cut plane). (a) Scratch made at a vertical load of 1.0N in the 'hard' [0001] direction. (b) Same conditions as above (fig:10.26(a)), but in the 'easy' [11$\bar{2}$0] direction.

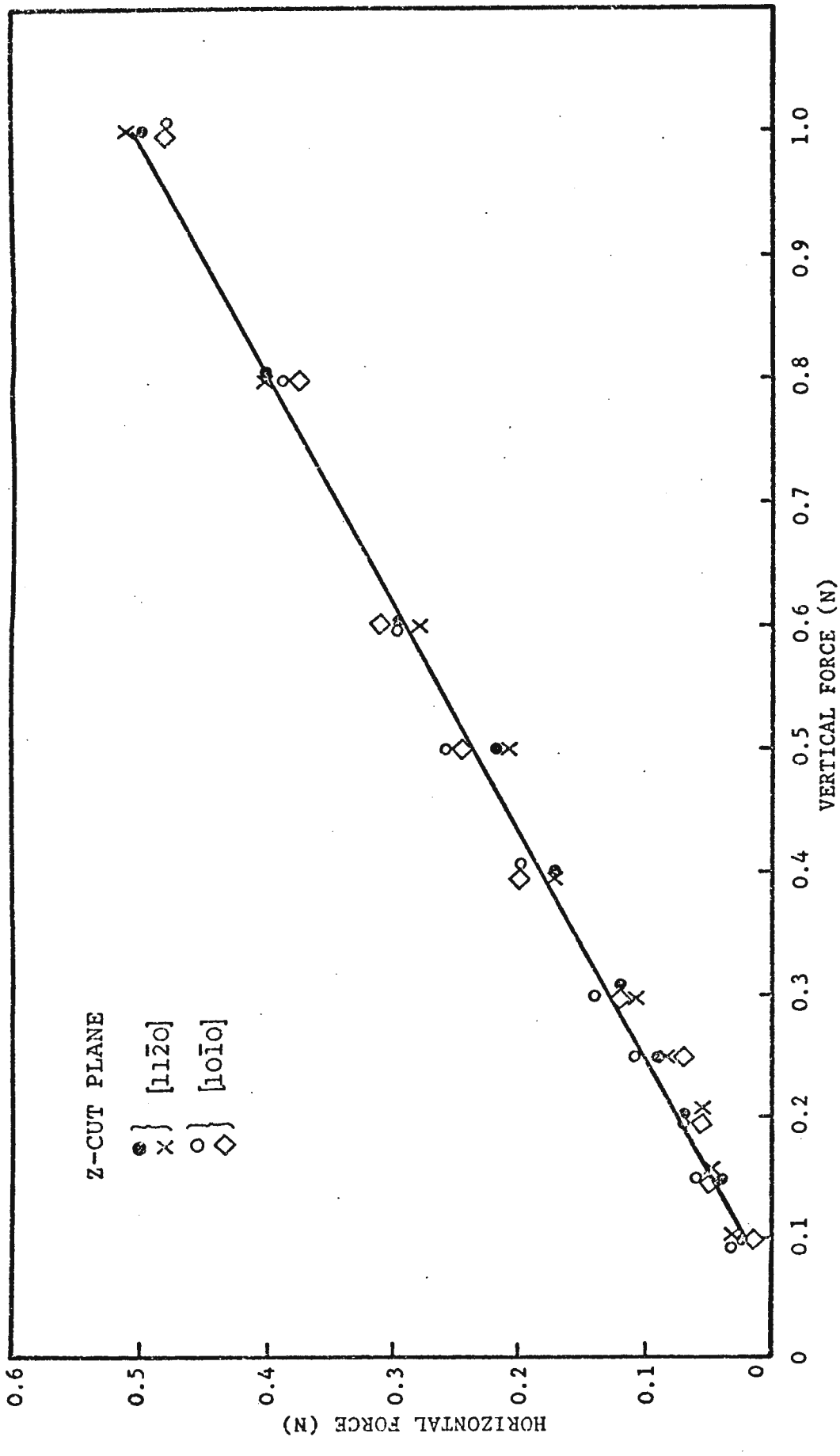

Fig.10.27 Horizontal force as a function of vertical force. Although a directional anisotropy of scratching is apparent these variations are not reflected in this data. (Z-cut plane, blunt pyramid, dry conditions).

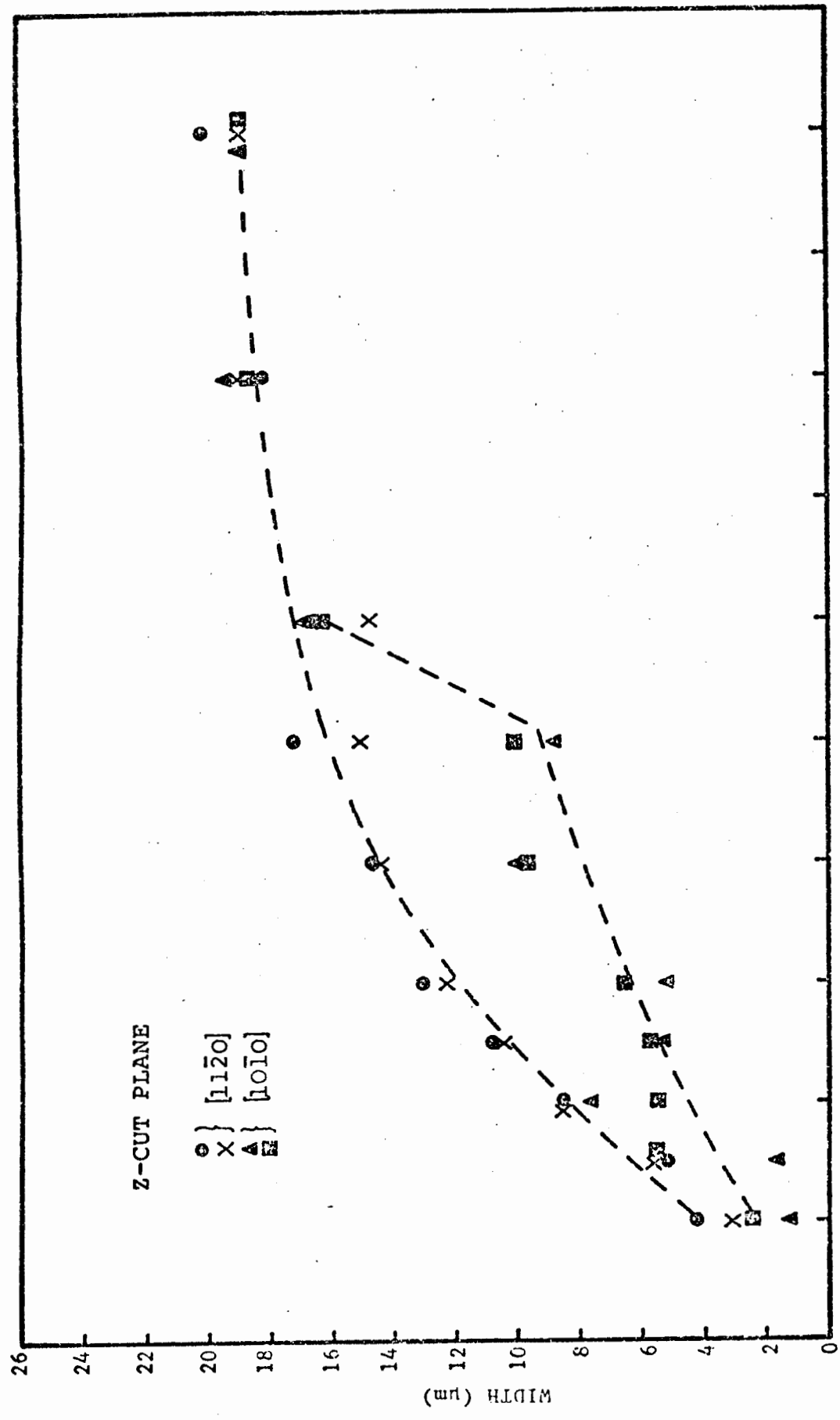

Fig.10.28 Variation in width of scratches as a function of the vertical force. Note that in the hard [10$\bar{1}$0] direction a change from a Hertzian deformation zone to a cutting action results in a sudden increase in width. (Z-cut plane, blunt pyramid, dry conditions).

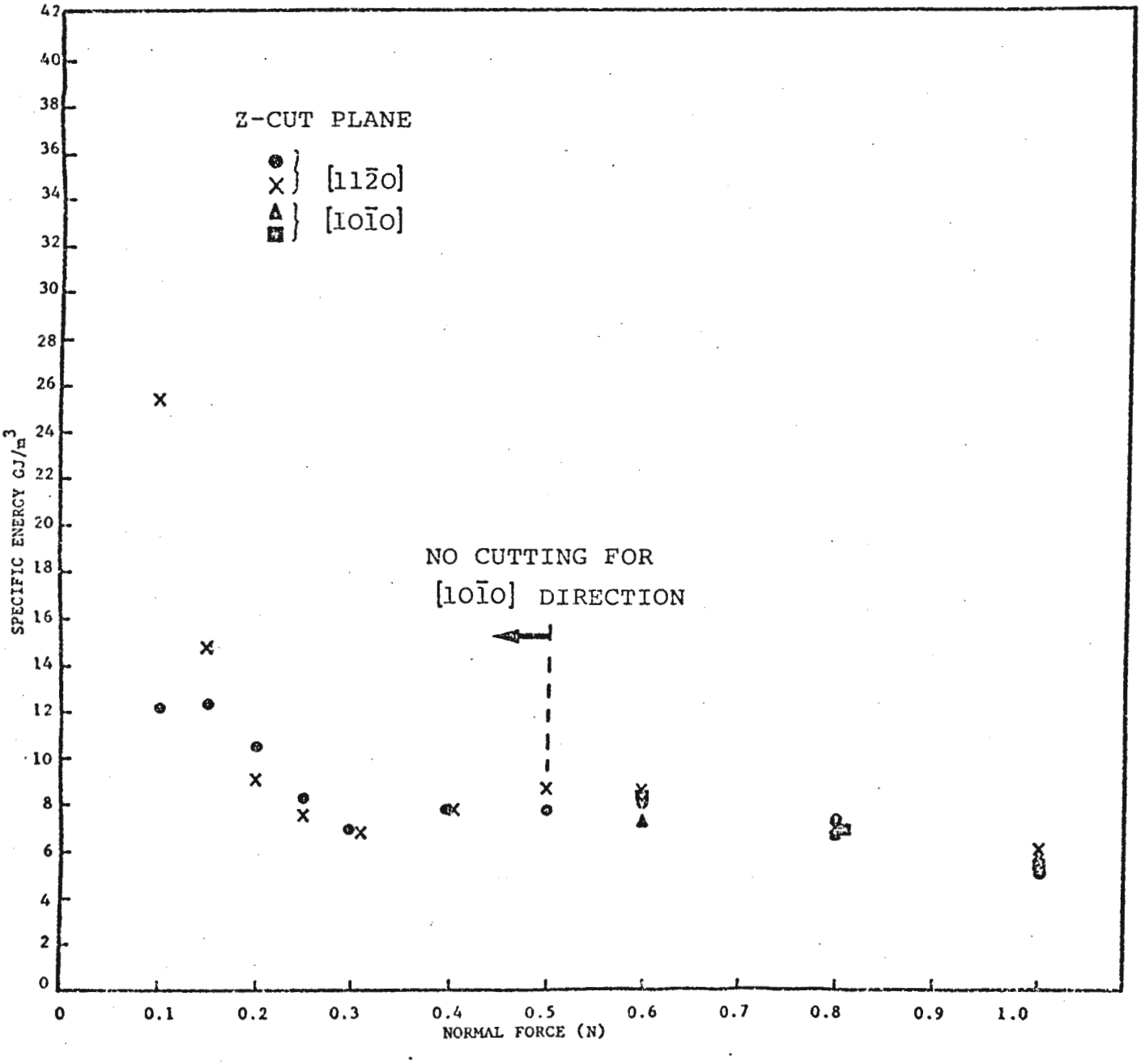

Fig.10.29 Specific energy as a function of vertical force. (Z-cut plane, blunt pyramid, dry conditions).

10.3.2 Scratches Made at Room Temperature in a Wet Environment

In this series of tests the three principal cuts of quartz was scratched in the following crystallographic directions:

X-cut $(11\bar{2}0)$: [0001] , $\langle 10\bar{1}0\rangle$

Y-cut $(\bar{1}100)$: $\langle 11\bar{2}0\rangle$, [0001]

Z-cut (0001) : $\langle 10\bar{1}0\rangle$, $\langle 11\bar{2}0\rangle$

The diamond pyramid was aligned in orientation (A).

Effect of the State of the Tool Tip

Both sharp and blunt pyramids were utilised, but while a profound effect on scratch deformation was found for the blunt tool, no difference existed between wet and dry conditions with the sharp tool. This was true of both the deformation and the scratching parameters. Results obtained for the sharp pyramid in water are thus exactly the same as for scratching in dry conditions, and are thus not presented.

Blunt Pyramid

The principal effect of scratching with a blunt pyramid on a crystal flooded with water was to generate a full cutting action in place of the Hertzian deformation track, which occurred when the crystal was scratched in dry conditions.

This effect is amply demonstrated by the series of optical micrographs (Fig.10.30) for the Z-cut plane, showing the differences between dry and wet scratching. At the lowest load, the effect of water is to produce chip formation at intervals along the length of the track. As the vertical load is increased ($\gtrsim$ 0.3N) a full cutting action takes place. At the highest

load (1.0N) it should be noted that the appearance of a dry scratch and a wet scratch are identical.

Scanning electron micrographs of these differences in deformation are presented for the Z-cut plane scratched in $\langle 10\bar{1}0 \rangle$ (Fig. 10.31), and for the Y-cut plane scratched in [0001] (Fig. 10.32). Note that the mode of cutting is apparently by delamination.

Cutting parameters

The effect of scratching in water is to considerably reduce the average horizontal force from the dry values. Comparisons are presented for wet and dry conditions for the X, Y and Z-cut planes (Figs. 10.33, a-c, respectively). This reduction in F_H occurs over the full load range, but is greater at low loads ($\simeq$ 60% reduction) than at high loads ($\simeq$ 25% reduction).

The differences in scratch widths are shown in Fig. 10.34 for the Z-cut plane. For vertical loads > 0.8N a cut was formed when dry, and hence the effect of water is negligible for these loads. At lower loads (< 0.8N) the width of the wet scratch is greater than the width of the dry scratch Hertzian zone. It is to be noted that the scratch widths for a blunt pyramid in wet conditions are the same as for a sharp pyramid in dry conditions.

However, the values of specific energy are slightly lower for wet scratching. This is, of course, a consequence of the lowering in the values of F_H. There is the usual increase in specific energy as the load is reduced.

Finally, to ascertain if the increased cutting efficiency was due purely to the effects of water, some scratches were made in glycerol (water content $\simeq$ 10%) and heptanol. A full cutting action was found, and the cutting parameters (width, depth and reduction in F_H) were approximately the same as for scratching in water. (Fig. 10.35).

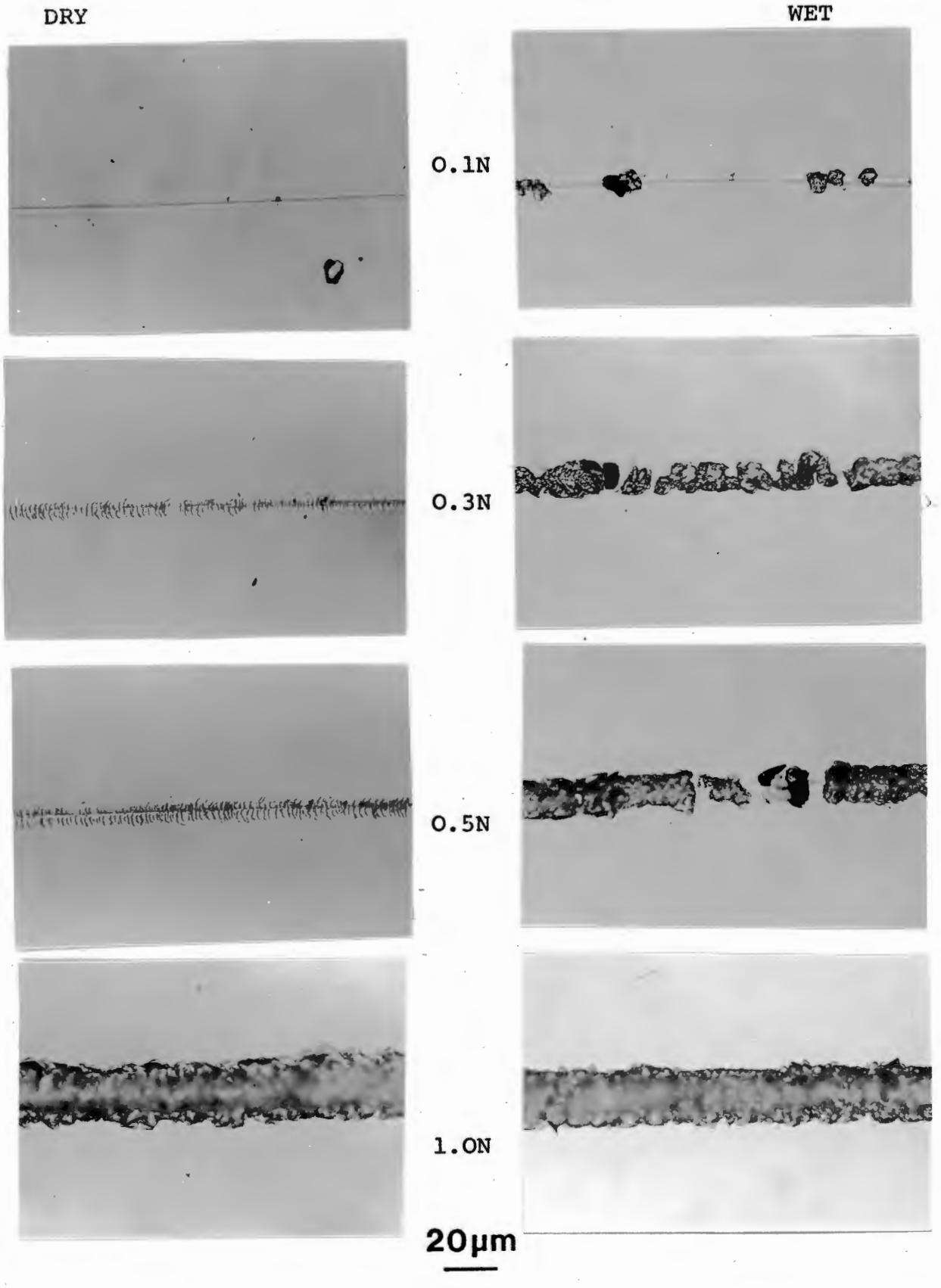

Fig.10.30 Comparison of scratches made in dry and wet conditions. (Z-cut plane, $10\bar{1}0$ direction)

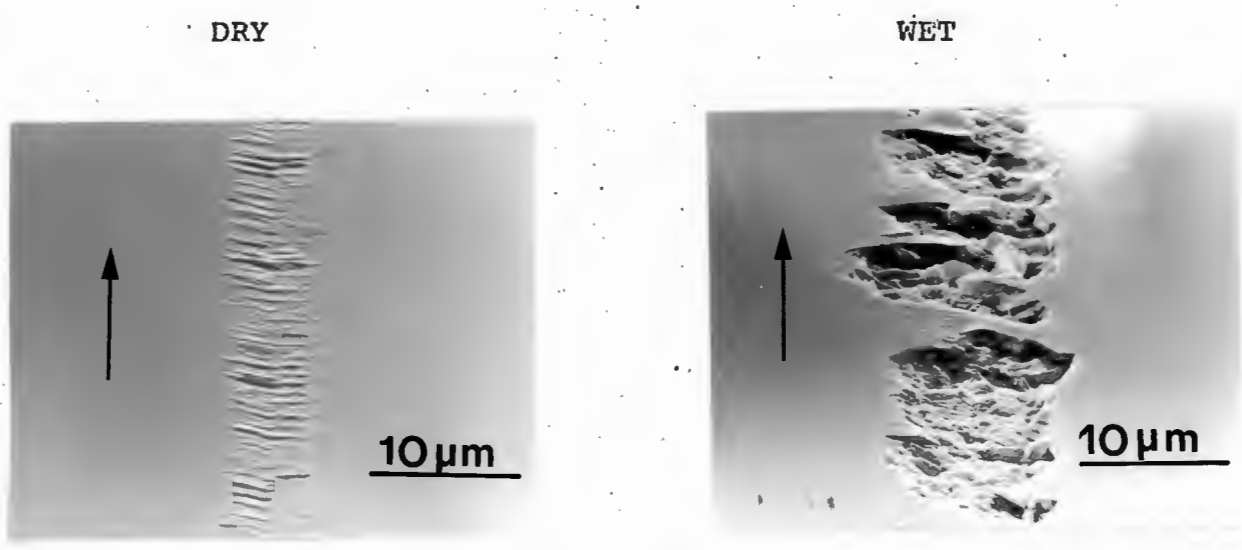

0.3N

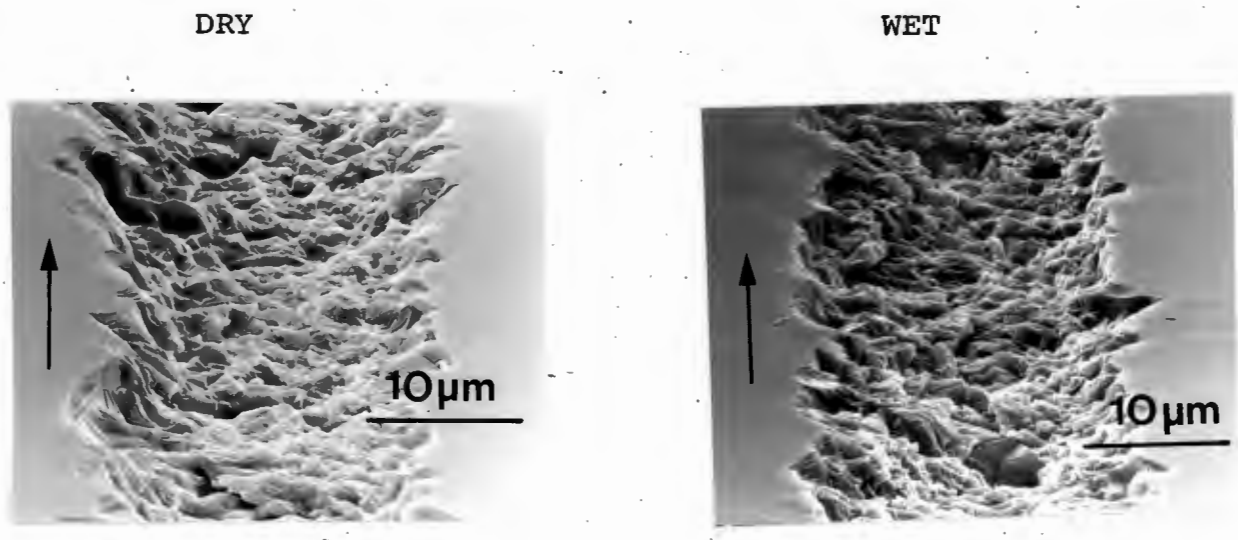

1.ON

Fig.10.31 Comparison of scratches made in dry and wet conditions. (Z-cut plane, [10$\bar{1}$0] direction, blunt pyramid).

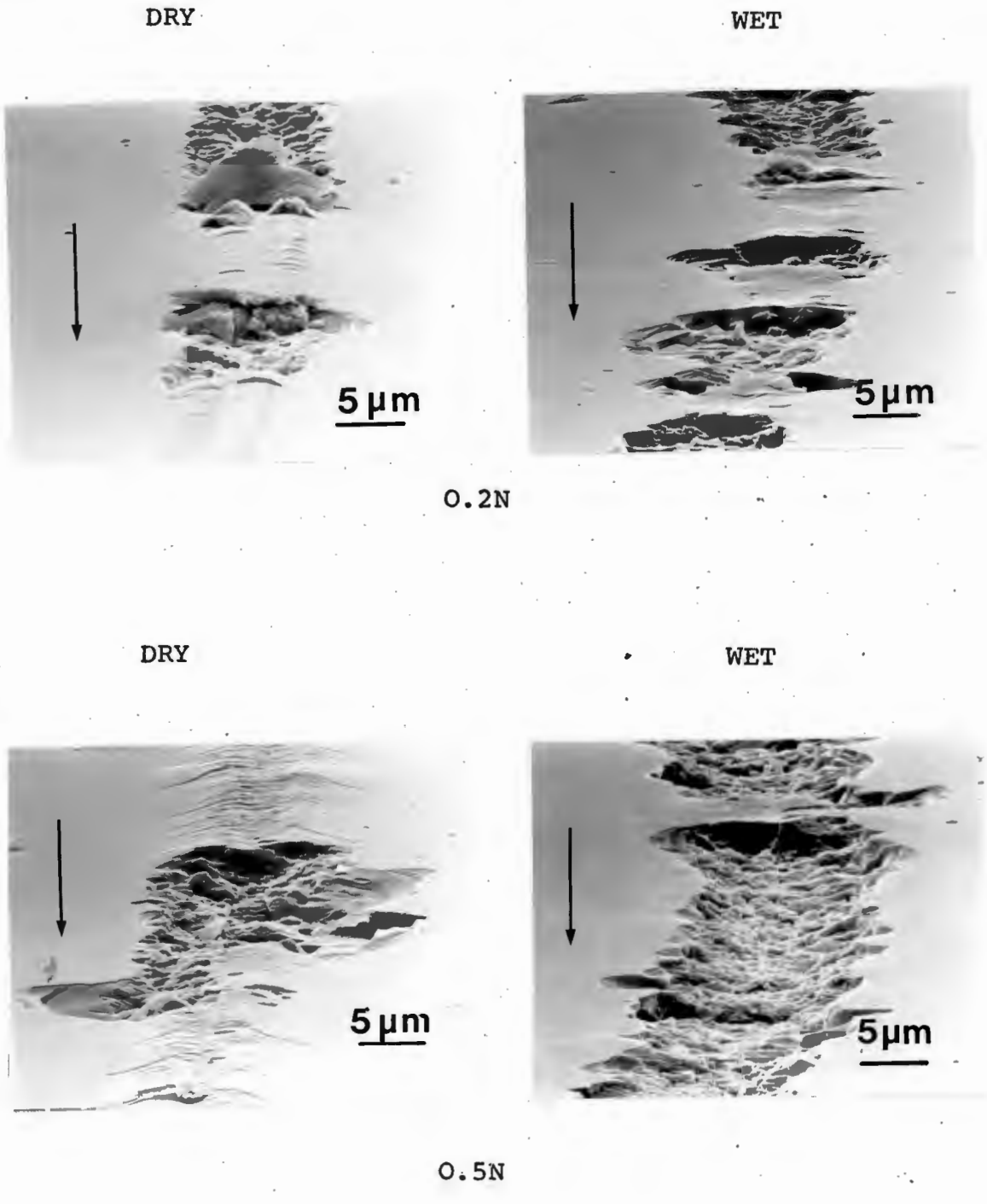

Fig.10.32 Comparison of scratches made in dry and wet conditions. (Y-cut plane, [0001] direction, blunt pyramid).

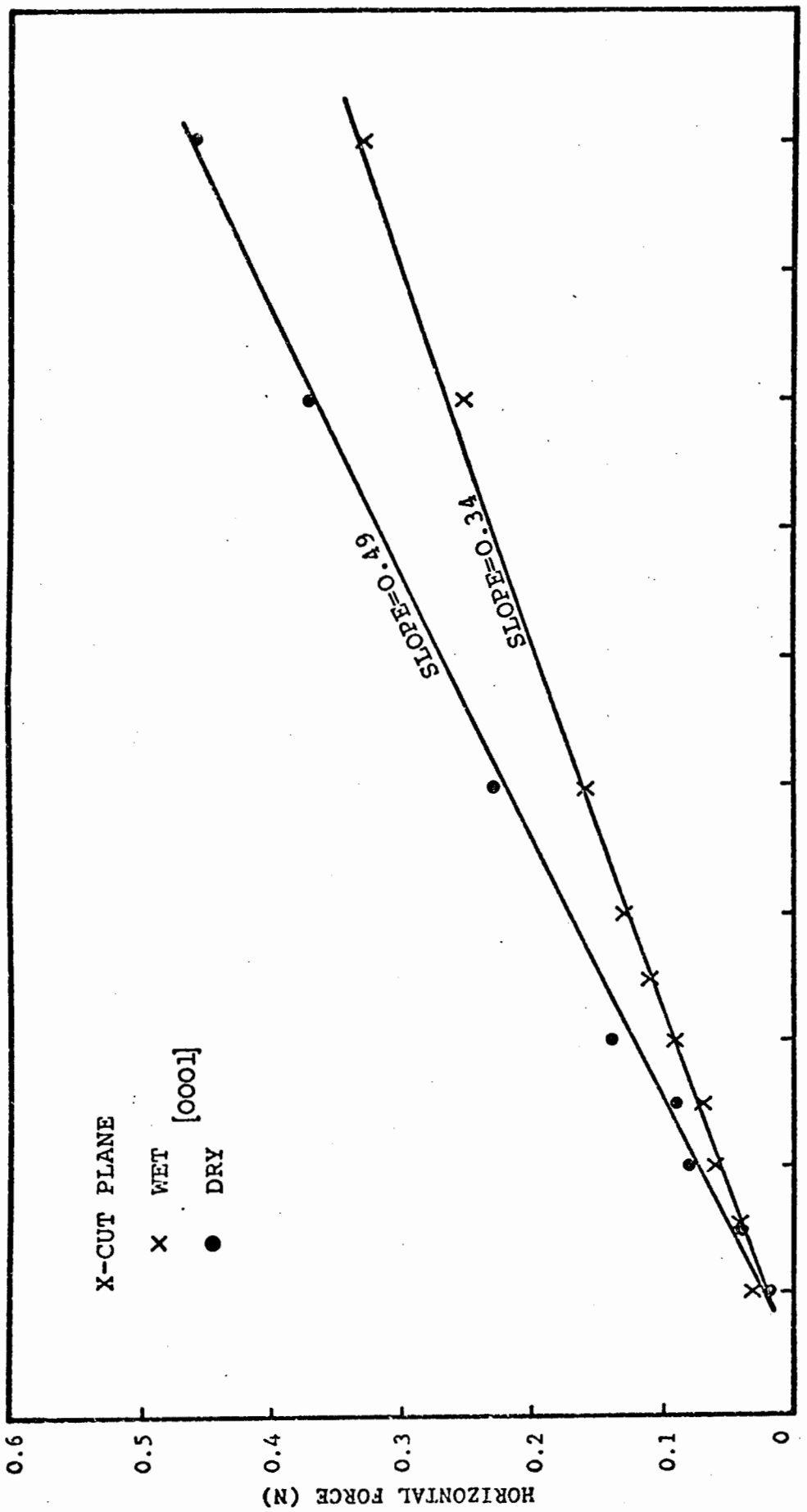

Fig.10.33(a) Comparison of the horizontal force in dry and wet conditions. (X-cut plane, blunt pyramid).

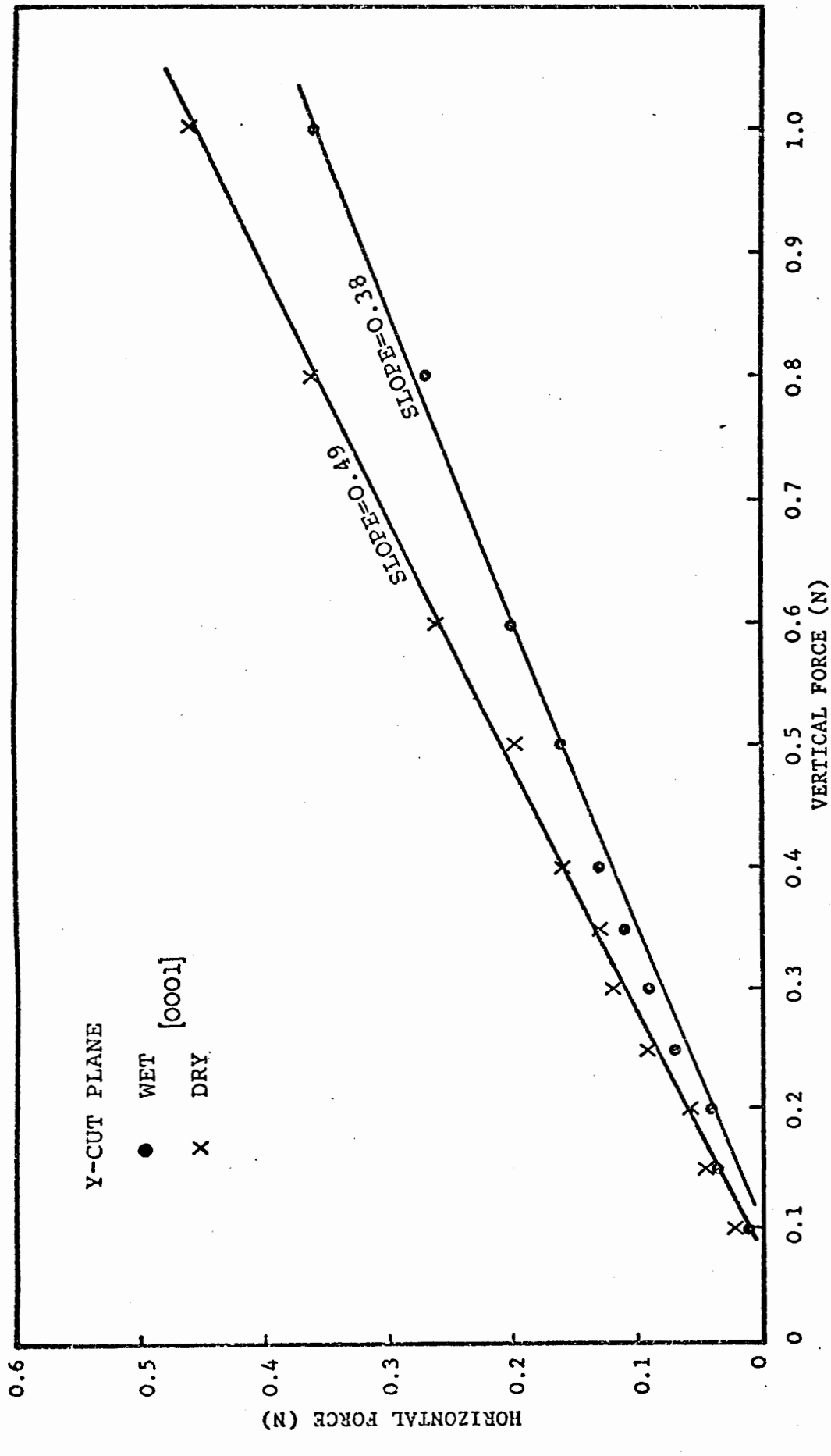

Fig.10.33(b) Comparison of the horizontal force in dry and wet conditions. (Y-cut plane, blunt pyramid).

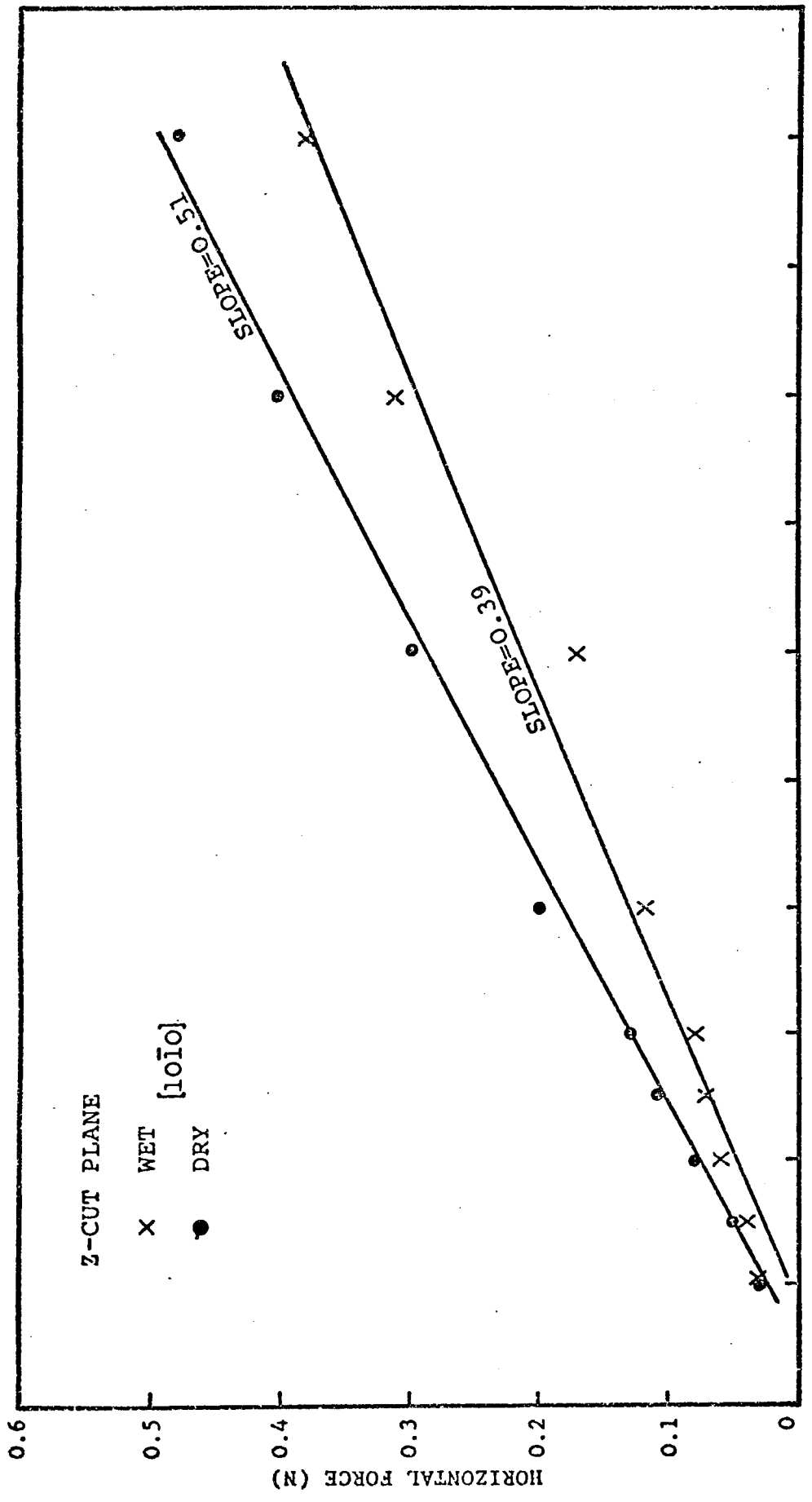

Fig.10.33(c) Comparison of the horizontal force in dry and wet conditions. (Z-cut plane, blunt pyramid).

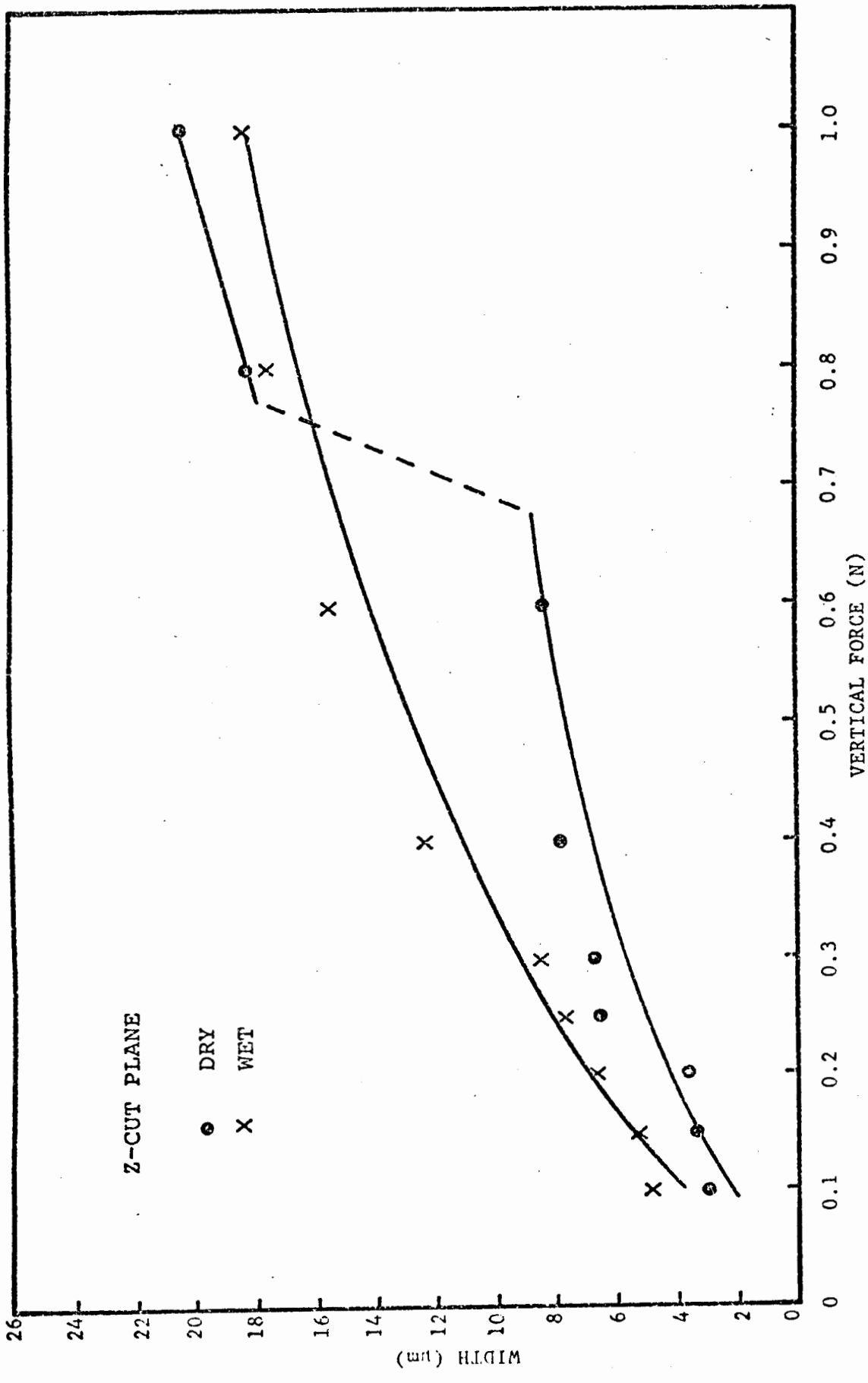

Fig.10.34 Variation in scratch width as a function of vertical force, in dry and wet conditions.

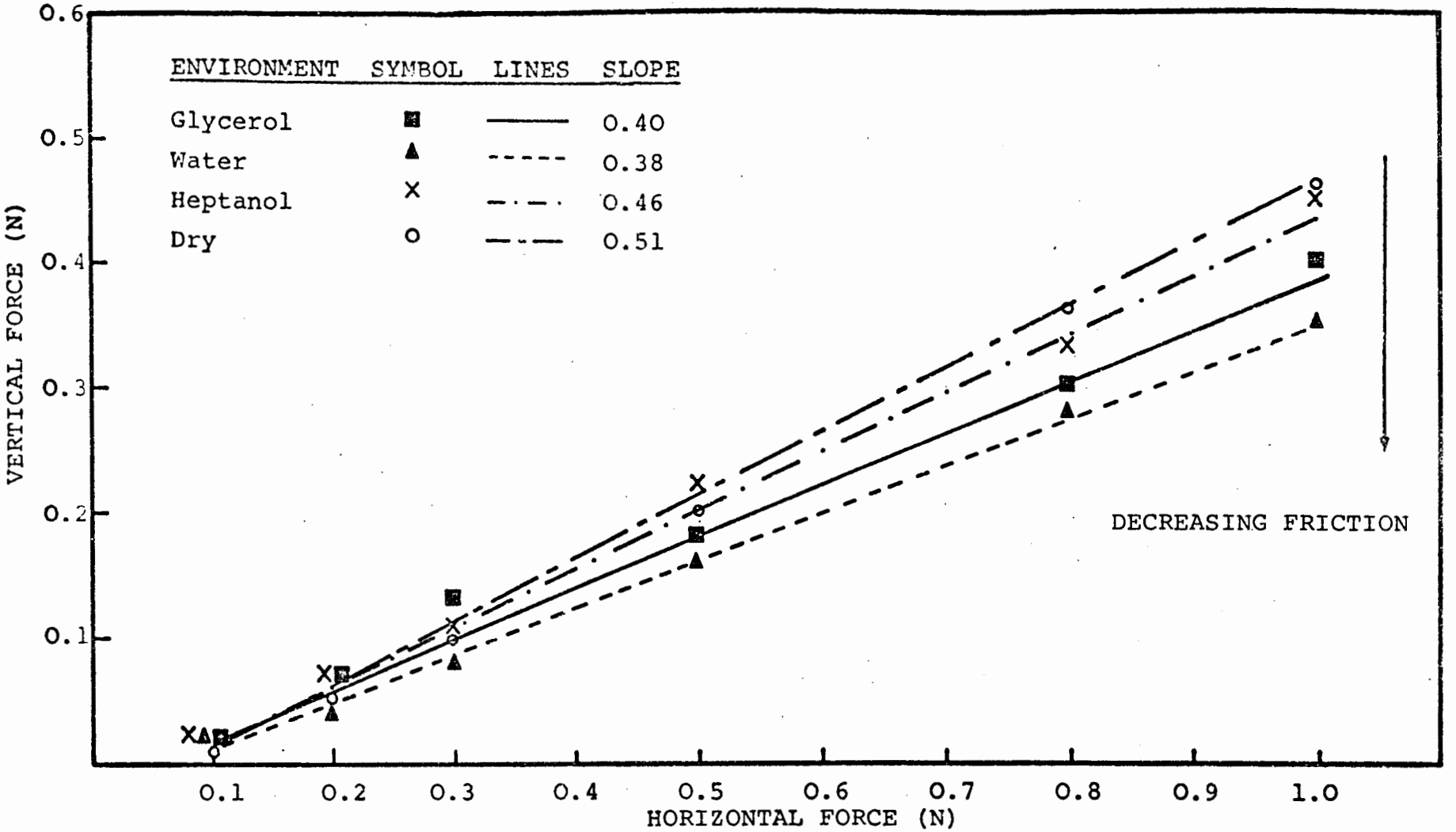

Fig.10.35 Results of scratching with a blunt pyramid in water, glycerol and heptanol. Results are compared to dry scratches. A reduction in the horizontal force is apparent in the presence of 'lubrication'. (Y-cut plane).

10.3.3 Scratches Made at Elevated Temperatures in Dry (RH ≈ 0%) Conditions

Scratches were made with a sharp pyramid, aligned in orientation (A). Tests were conducted at 373K, 523K, 623K and 723K on the X, Y and Z-cut planes in the following crystallographic directions:

X-cut $(11\bar{2}0)$: $\langle 10\bar{1}0 \rangle$

Y-cut $(\bar{1}100)$: $\langle 11\bar{2}0 \rangle$

Z-cut $(000l)$: $\langle 10\bar{1}0 \rangle$

Fractography

At the lowest vertical loads $\leq$ 0.2N the major effect of increasing temperature was to curtail the cutting action, and to replace this with a Hertzian zone, typical of the blunt pyramid. Such behaviour was found for all T $\geq$ 373K. Fig. 10.36 illustrates this phenomenon for the Z-cut plane. It is important to note that the 'blunting' action cannot be attributed to the diamond pyramid tip undergoing permanent deformation since a scratch made at room temperature, following the high temperature scratch, shows the return to a full cutting action. Similar observations were made for the X- and Y-cut planes. Figs.10.37 & 10.38 show low load (0.1N) scratches made on the X-cut plane at 523K. It is evident that the scratch deformation is 'plastic' in appearance. Fig.10.39 shows the region at the end of a 0.1N scratch.

At intermediate vertical loads (0.3 - 0.5 N) there was an increasing tendency towards material removal by delamination. Fig.10.40 shows clearly an area of a scratch where there has been a transition from Hertzian deformation to a cutting mode. As the temperature was raised the extent of sub-surface deformation increased (Fig.10.41), and deep side spalls were produced

0.1N T=300K

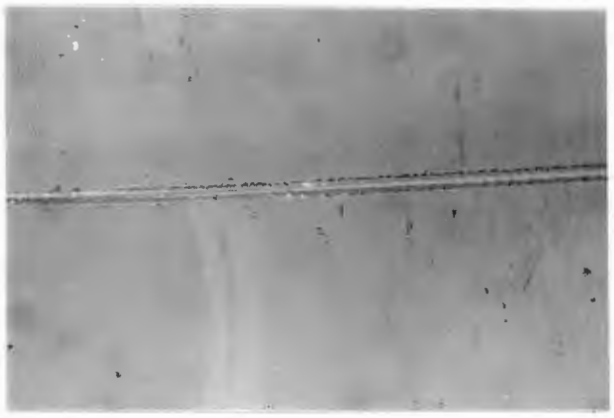

20μm

0.1N T=373K

0.1N T=723K

DIRECTION OF SCRATCHING

Fig.10.36 Examples of scratches made at elevated temperatures. Note the increased cracking at 723K and the appearance of a ductile groove. (Z-cut plane, sharp pyramid, dry conditions).

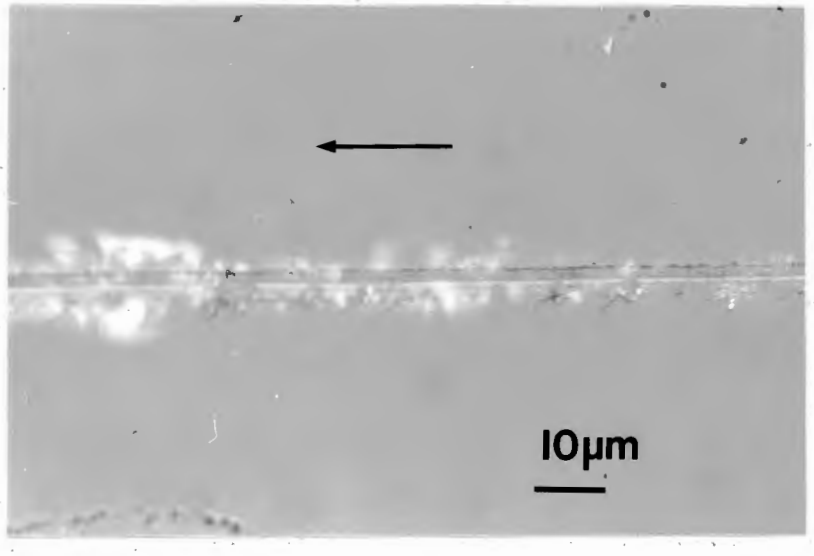

(a)

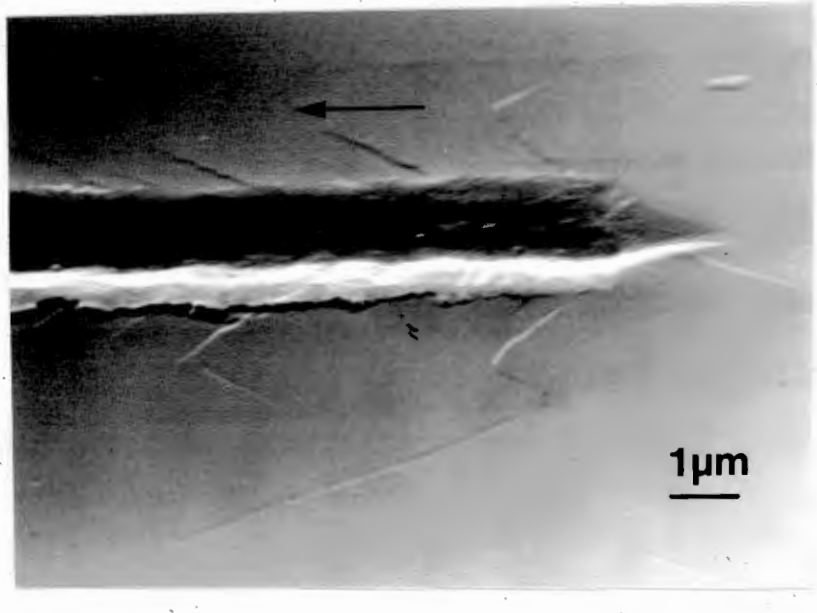

(b)

Fig.10.37 Elevated temperative scratches. (a) Optical micrograph. (b) Same scratch examined in the SEM. (0.1N, X-cut plane).

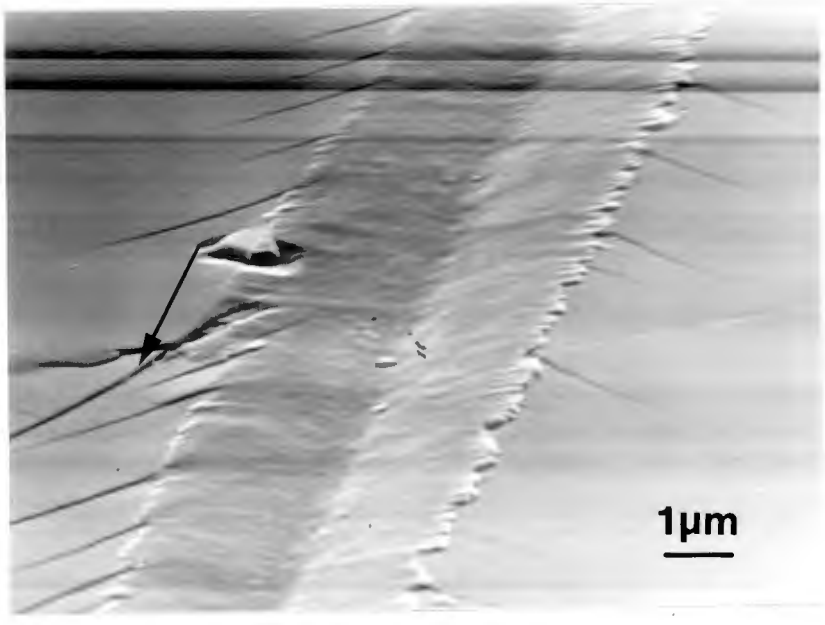

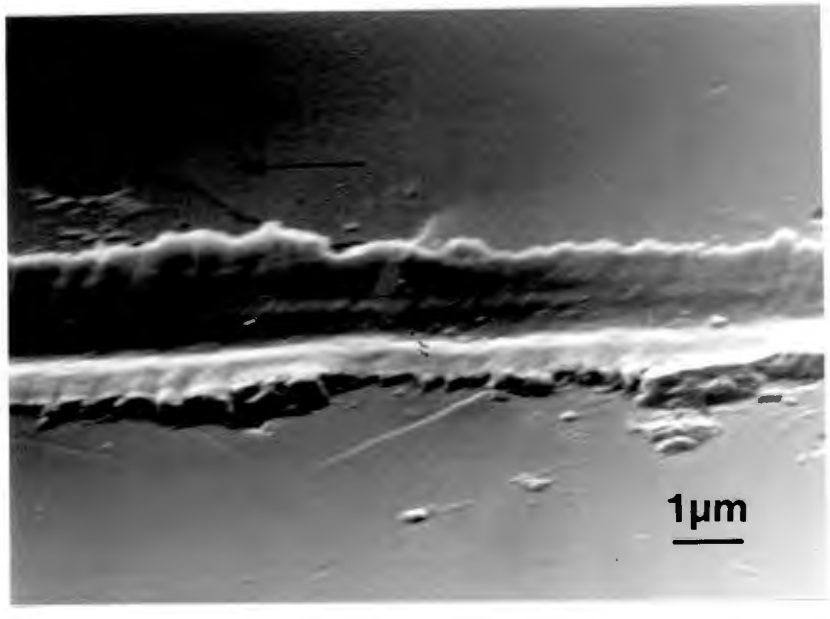

Fig.10.38 High temperature (523K) low load (0.1N) scratches. (X-cut plane, [10$\bar{1}$0] direction).

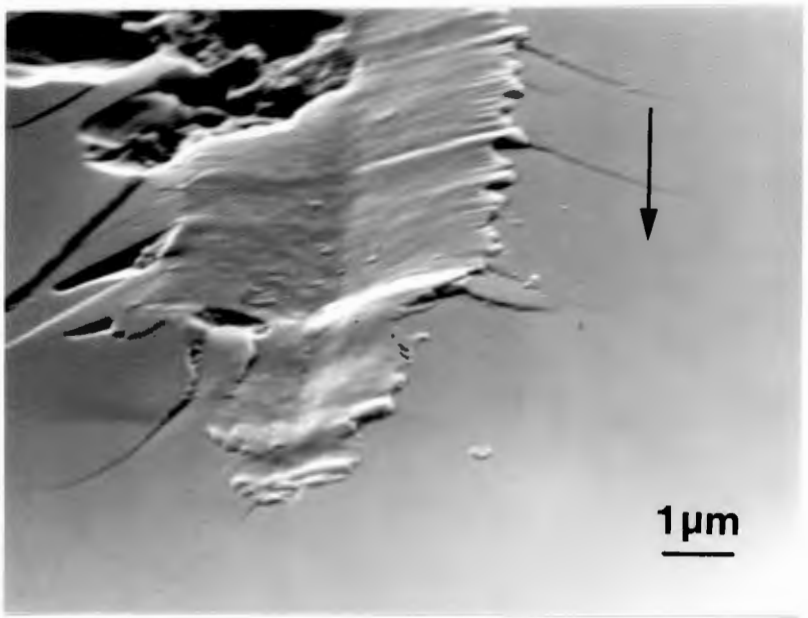

Fig.10.39 The end of the track of a high temperature (523K), low load (0.1N) scratch. (X-cut plane, $[10\bar{1}0]$ direction).

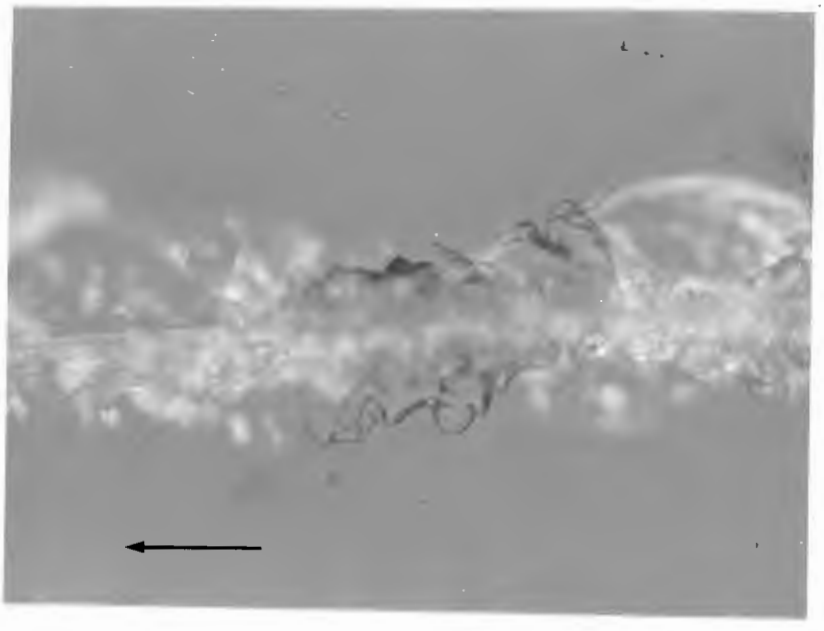

(a)

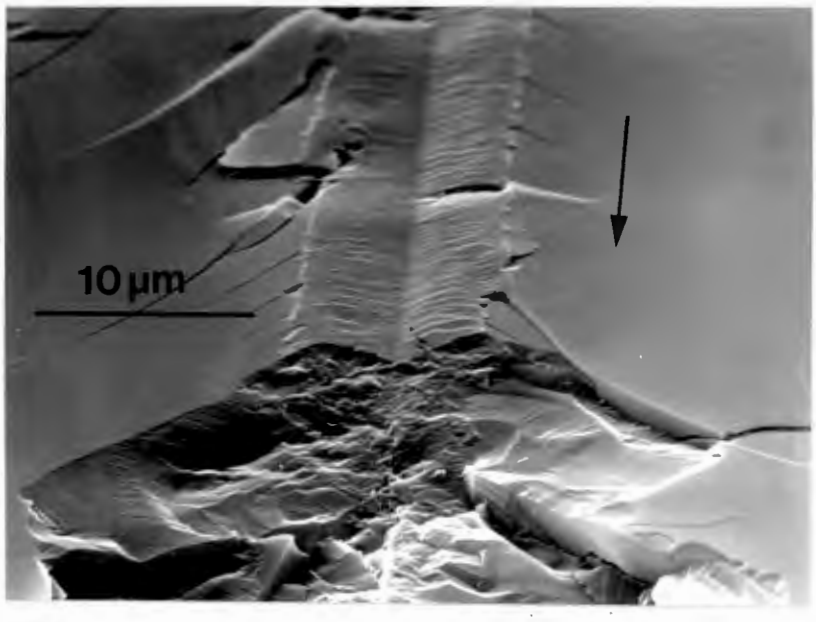

(b)

LOAD 0.3N

Fig.10.40 High temperature (623K) scratch (X-cut plane). (a) Optical. (b) SEM.

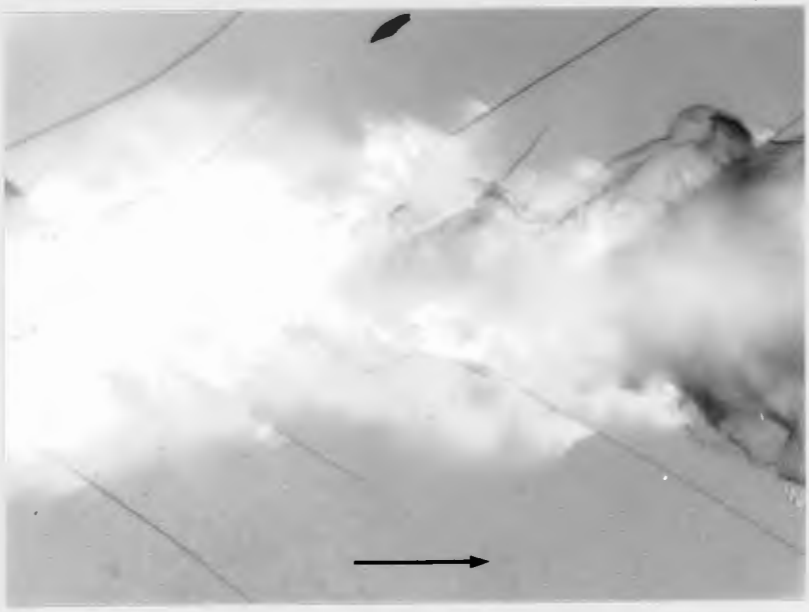

Fig.10.41 High temperature scratch showing the development of sub-surface deformation (white contrast).

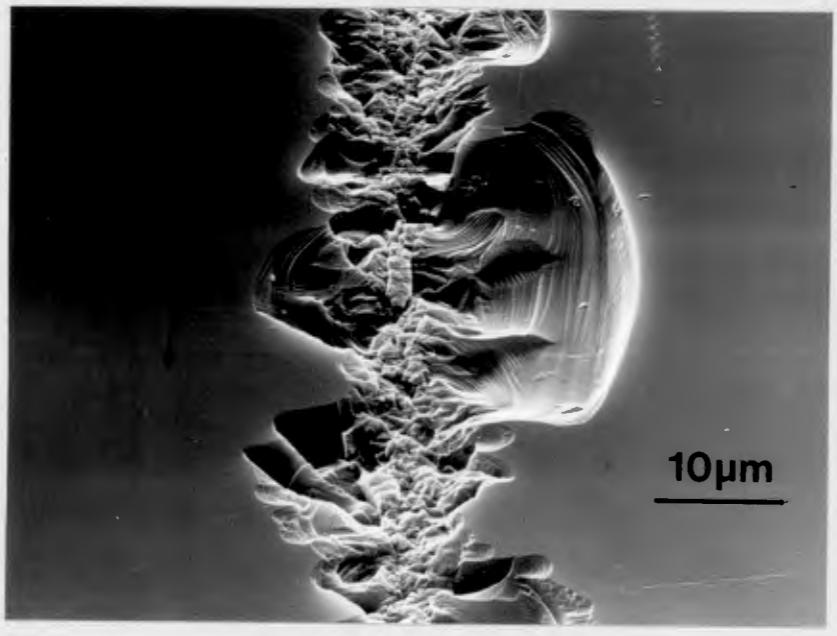

Fig.10.42 Production of deep side spalls at high temperatures. (623K, 0.5N).

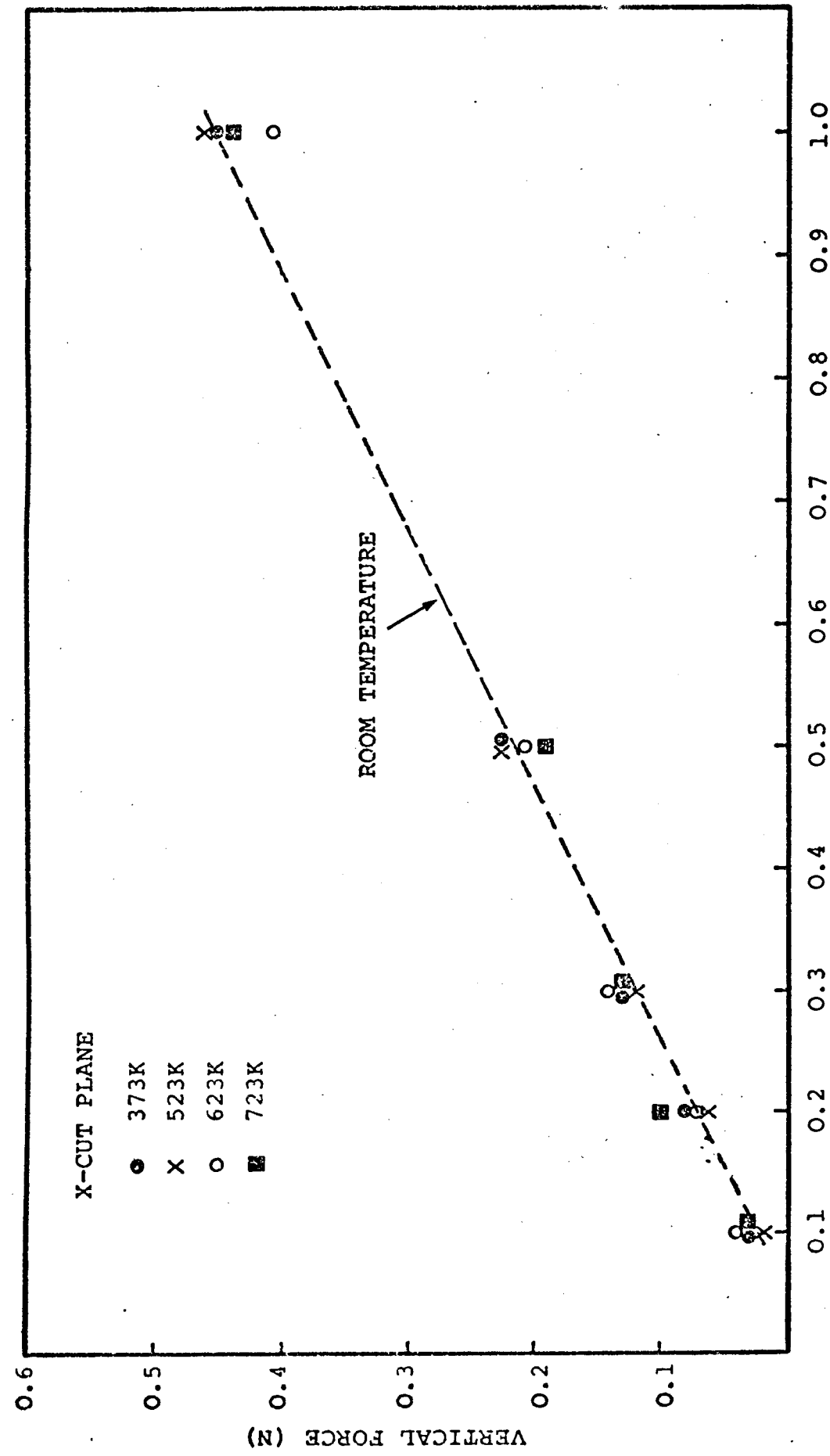

Fig.10.43(a) Vertical force as a function of horizontal force. High temperature scratches. (X-cut plane, dry conditions, sharp pyramid).

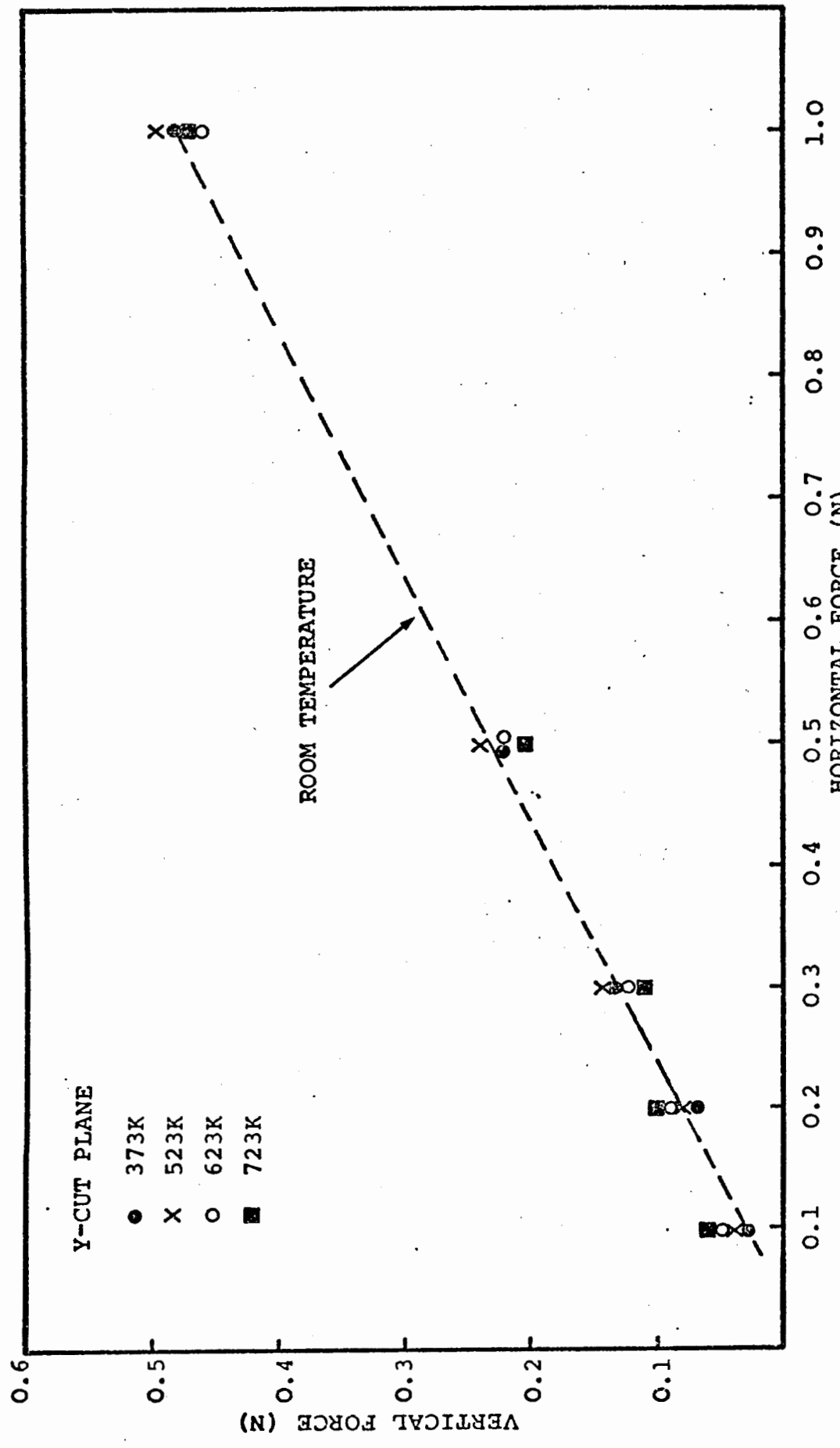

Fig.10.43(b) Vertical force as a function of horizontal force. High temperature scratches. (Y-cut plane, dry conditions, sharp pyramid).

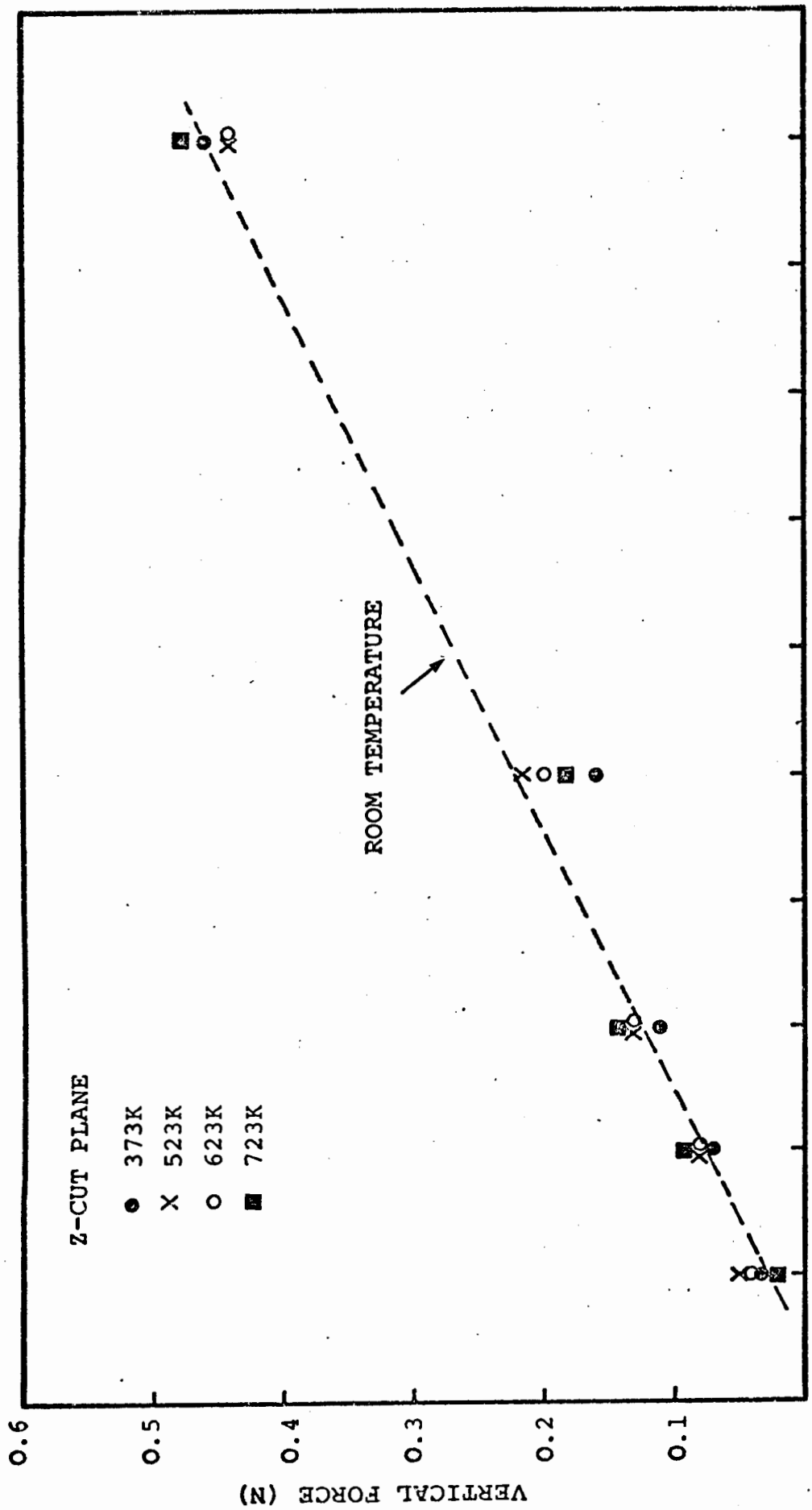

Fig.10.43(c) Vertical force as a function of horizontal force. High temperature scratches. (Z-cut plane, dry conditions, sharp pyramid).

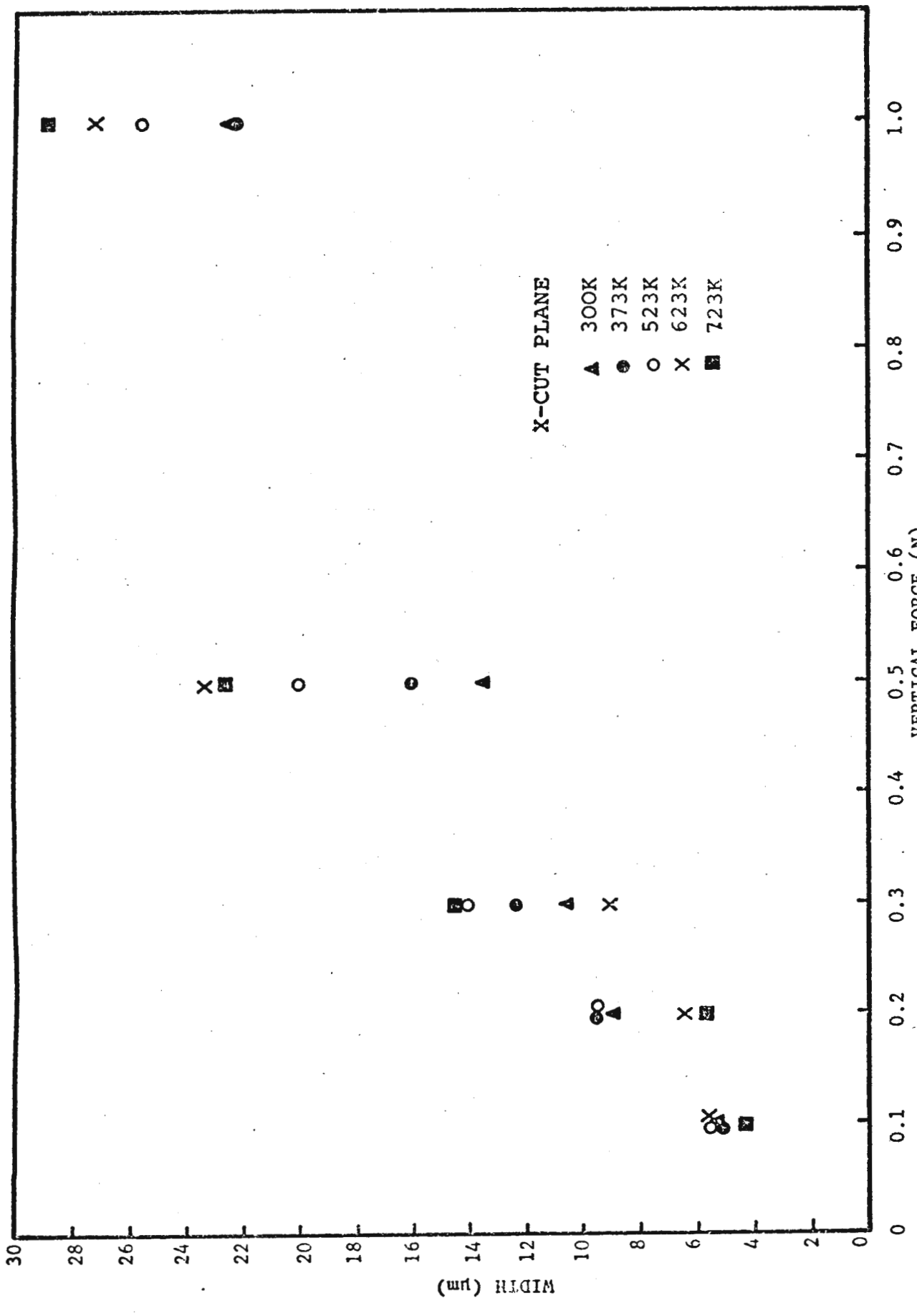

Fig.10.44(a) Change in scratch width as temperature is increased. (X-cut plane).

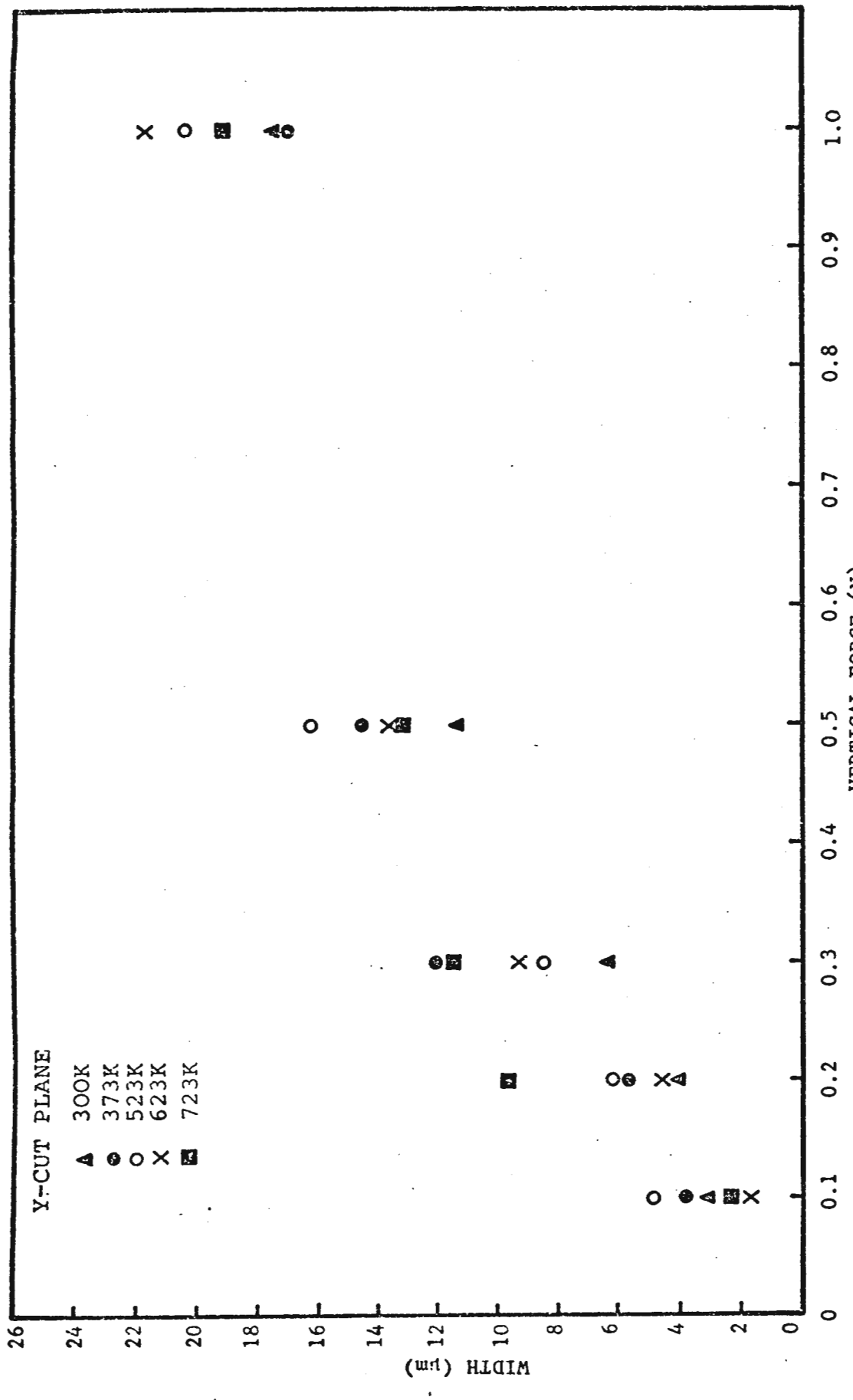

Fig.10.44(b) Change in scratch width as temperature is increased. (Y-cut plane).

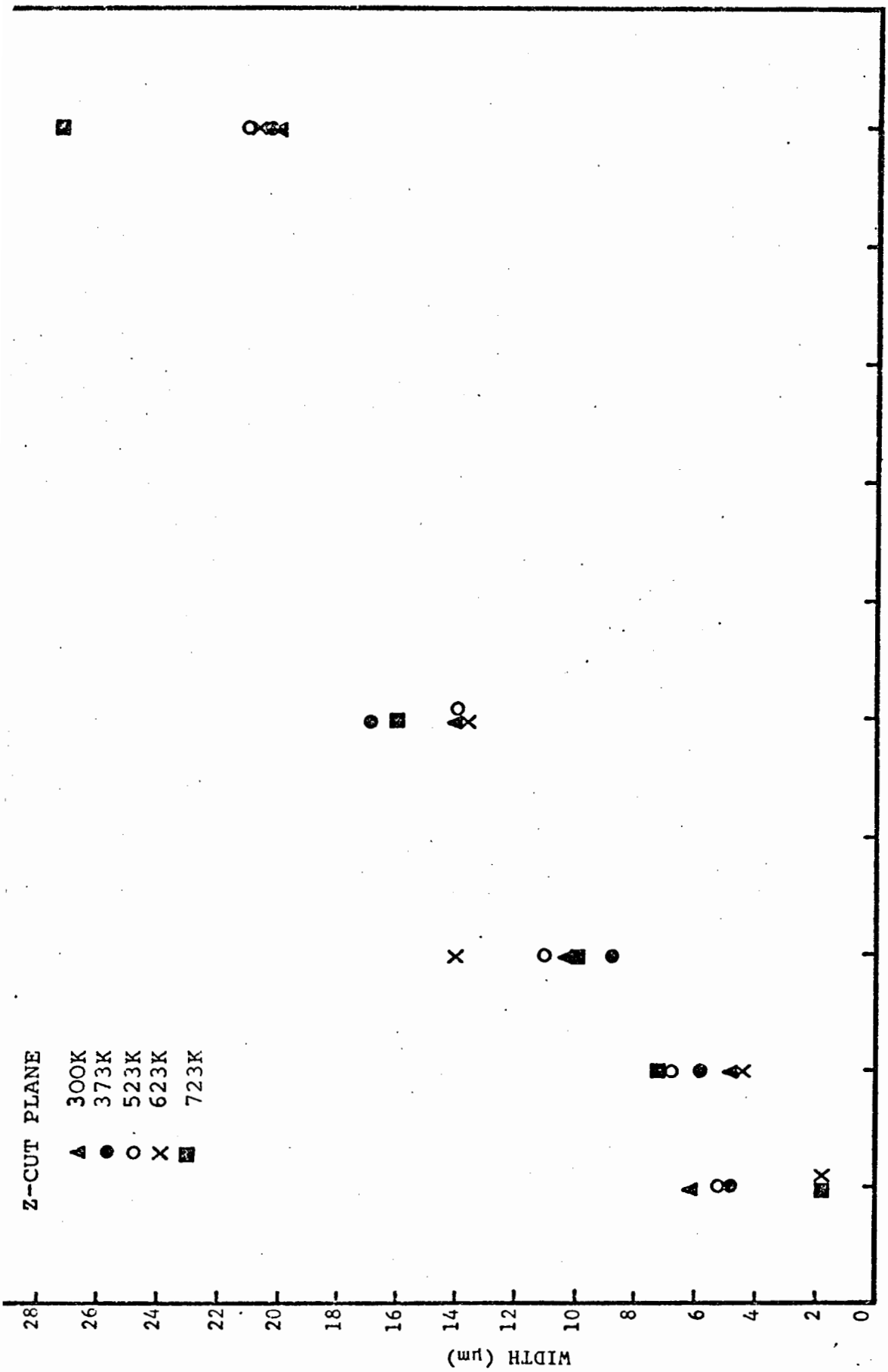

Fig.10.44(c) Change in scratch width as temperature is increased. (Z-cut plane).

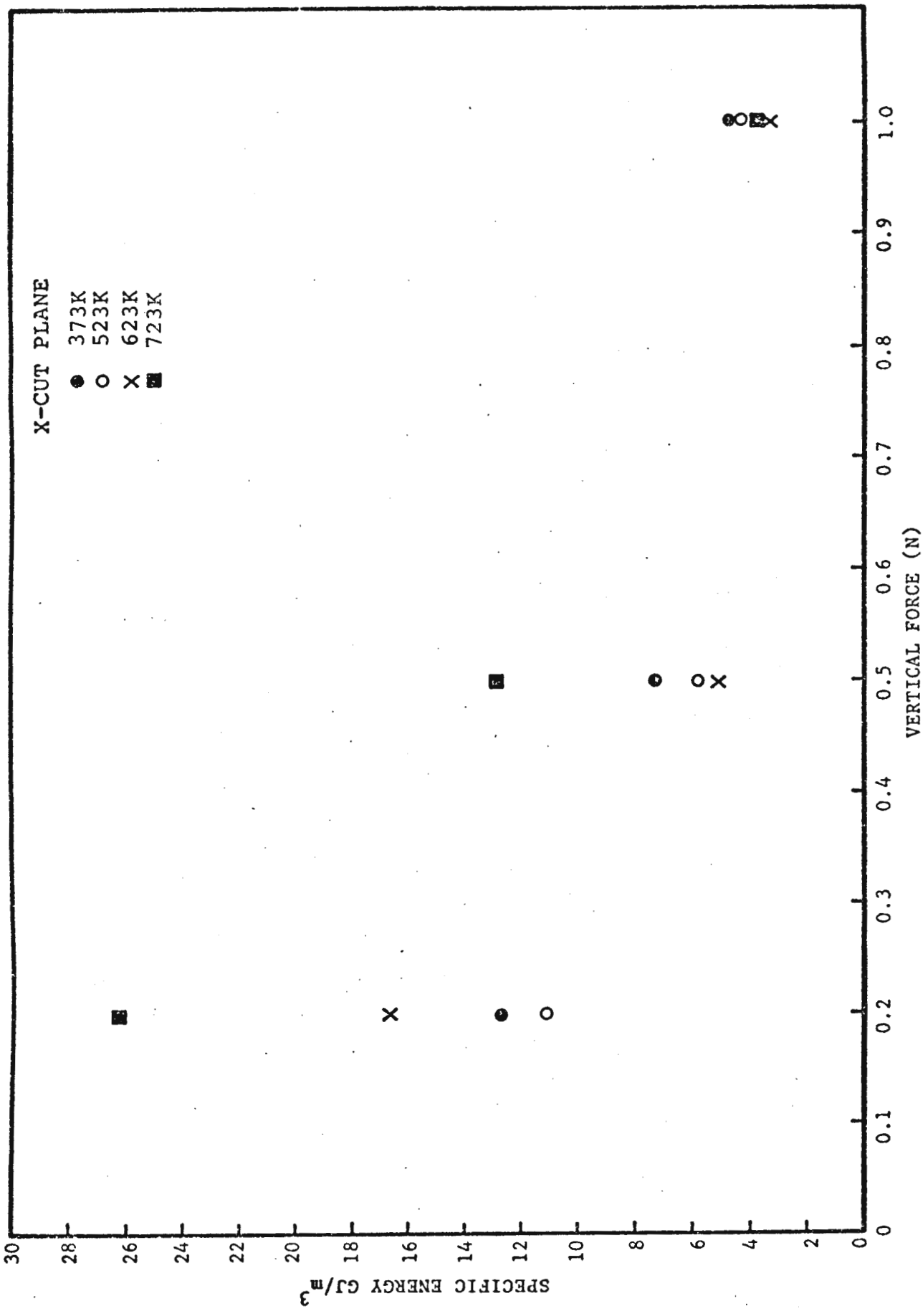

Fig.10.45 Effect of temperature on specific energy.
(X-cut plane).

10.3.4 Scratches made at Room Temperature in Moist Laboratory Air (RH ≈ 70%)

This series of scratching tests was made at room temperature with a sharp pyramid on the Z-cut plane only. The directions $<10\bar{1}0>$ and $<11\bar{2}0>$ were scratched. Both orientations (A and B) of the diamond pyramid were used. The environment was moist laboratory air which had a relative humidity of ≈ 70%.

Fractography

Optical examination (Fig.10.46) of these scratches showed that the scratch deformation was a function of the pyramid orientation and also the direction of scratching. At low loads it is apparent that it is more difficult to form a cut with the pyramid in orientation (B). The differences between the $<11\bar{2}0>$ and $<10\bar{1}0>$ directions should also be noted for the pyramid in orientation (A). At the highest experimental load the extent of chipping at the sides of the scratch is greater for pyramid in orientation (B). Cracks propagating to the side of the scratch are predominant for scratching in the $<10\bar{1}0>$ direction.

Cutting Parameters

An example of the horizontal force data for different scratch directions and pyramid orientations is shown in Fig.10.47. A best-fit line is drawn through the experimental points. The least-squares fit to the data does not pass through the origin, an effect found in previous sections of this work, and which now seems typical of such data on quartz.

Examples of the scratch width and depth are shown in Fig.10.48. Scratches with the pyramid in orientation A produce wider grooves than orientation B. This is expected from a

geometrical consideration of the pyramid. The depths of the scratches were found to be independent of pyramid orientation and crystallographic direction of scratching.

As with previous sections, we note that the value of specific energy rises as the vertical load is reduced (Fig. 10.49). Specific energy is higher for the pyramid in orientation B, although the inability to measure accurately the contribution to material removal by chipping at the sides of the grooves will reduce these values.

Previous results in this section were obtained with a diamond pyramid tool which had a well defined sharp tip. During preliminary scratching experiments, before it was known that the pyramid tip would blunt and produce such diverse behaviour, some scratches were made in a moist air environment with a pyramid that may be described, somewhat unscientifically, as not completely sharp. Since it is evident that a blunt pyramid can, in fact, become effectively sharp at higher loads, the fairly sharp pyramid enables us to explore this transition at lower loads. The pyramid was aligned in orientation (A).

This series of scratches produced some quite remarkable scratch deformation events. At a vertical load of 0.2N, a high degree of spalling is evident (Fig.10.50), showing spectacular deformation features. At high magnification (Figs. 10.51 and 10.52) these spalls show three distinct deformation zones. There is a central raised region (width $\approx$ 3 μm-10 μm) with an irregular fracture surface. To either side of this central feature, the crack dips downwards to a flat surface running parallel to the crystal surface. At the edge of the spall the crack runs upwards at a steep angle to intercept the crystal surface. The total width of these spalls are $\approx$ 20 μm (load = 0.1N) and $\approx$ 60 μm (load = 0.2N).

Note the interesting fact that spall uplift has occurred after coating for SEM examination (Fig.10.53). Clearly this spalling action is time-dependent and it is probable that it is environmentally assisted by atmospheric moisture.

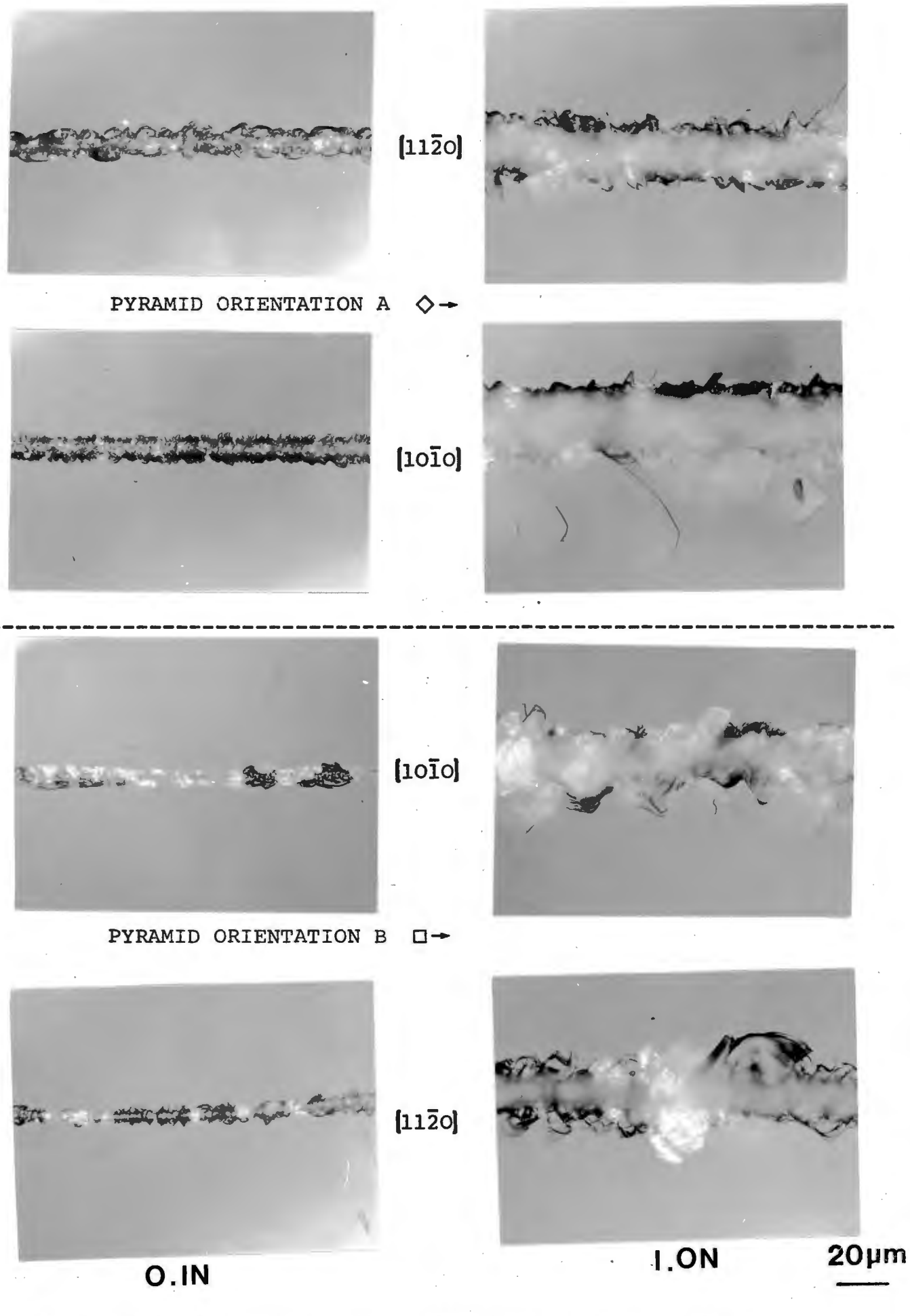

Fig.10.46 Scratches made at room temperature in moist laboratory air. (sharp pyramid).

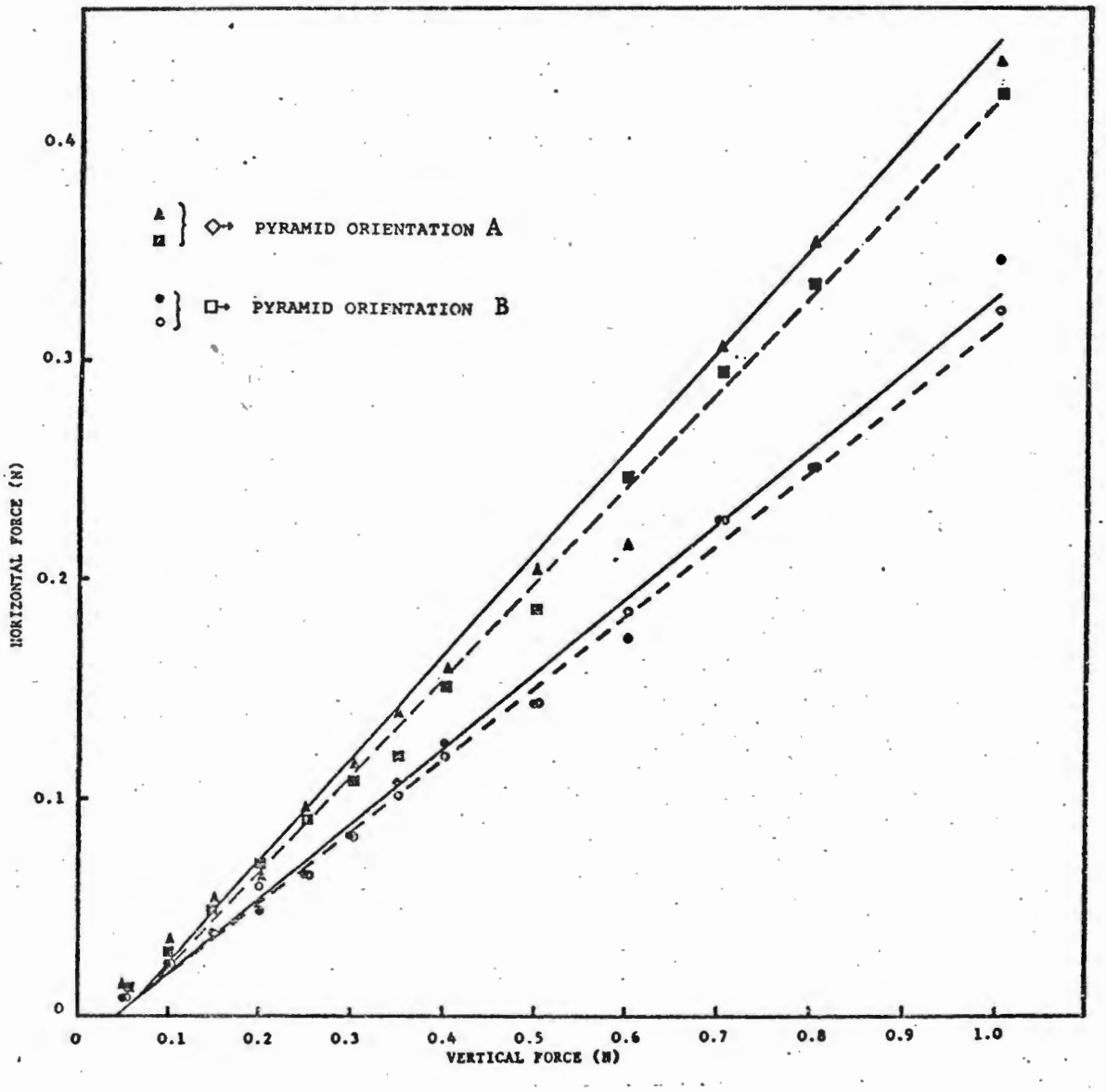

Fig.10.47 Horizontal force data. Two pyramid orientations are shown. (moist laboratory air, room temperature, sharp pyramid, Z-cut plane, $[10\bar{1}0]$ direction).

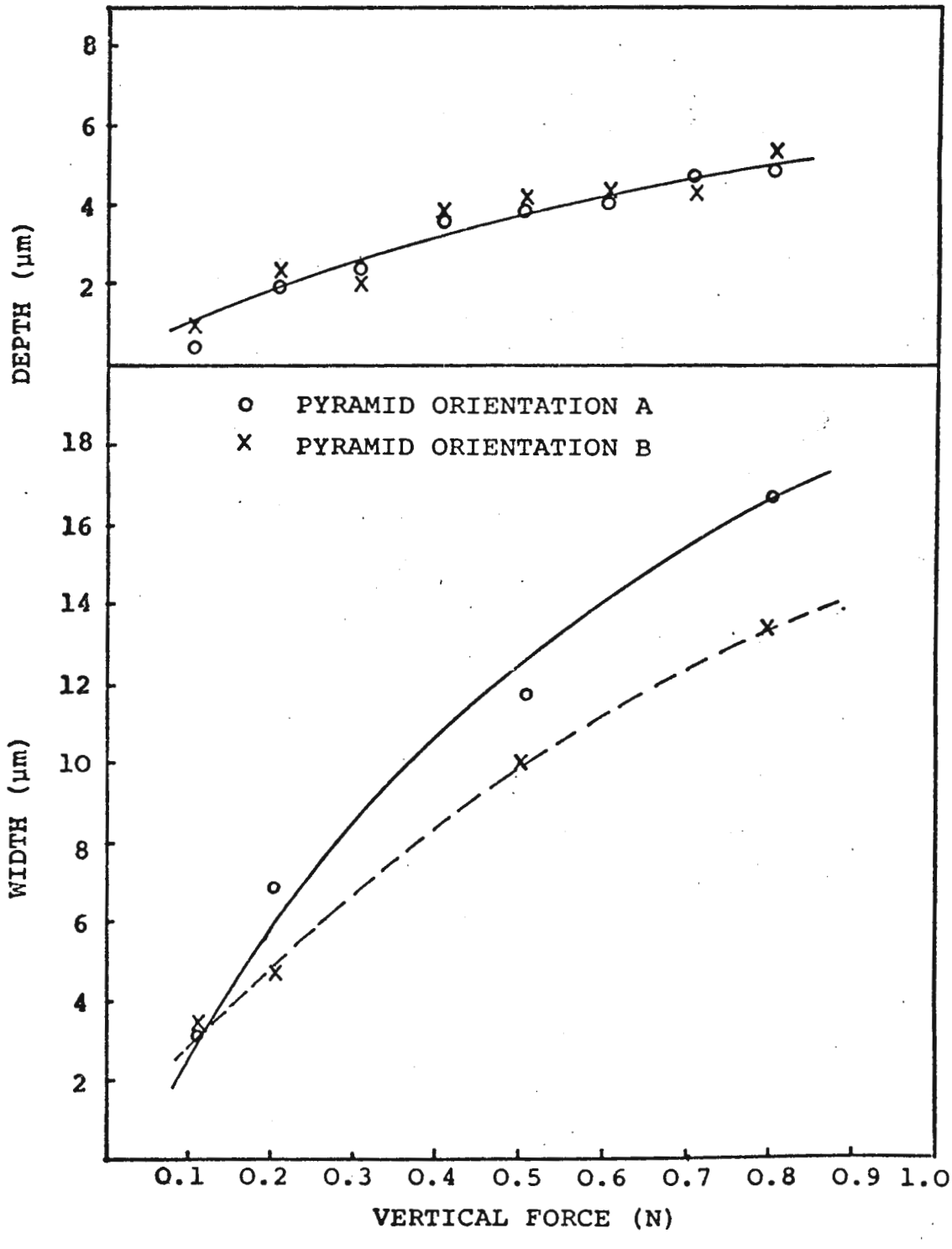

Fig.10.48 Variation in scratch width and depth with vertical force. (moist laboratory air, room temperature, sharp pyramid).

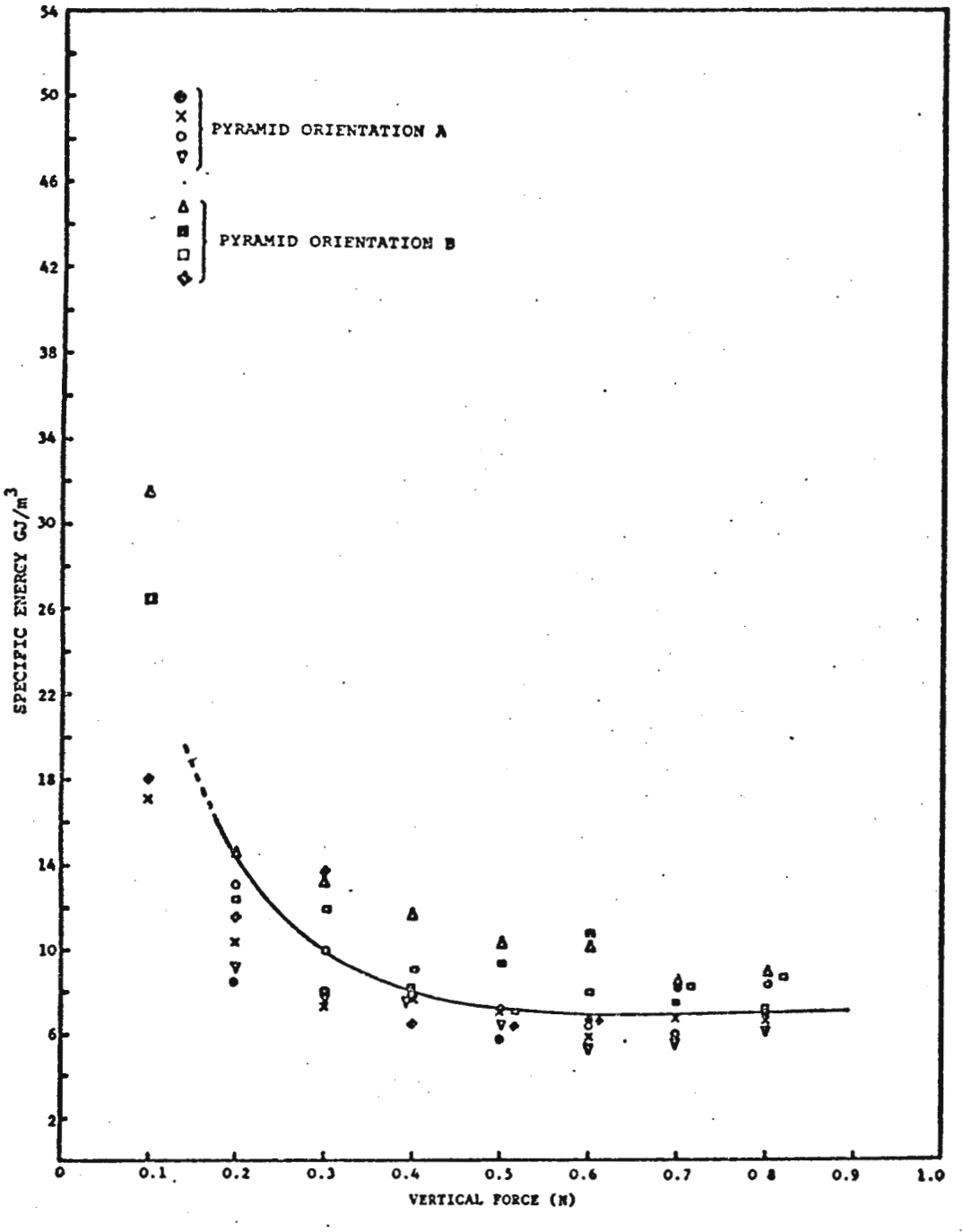

Fig.10.49 Specific energy as a function of vertical force. (moist laboratory air, room temperature, sharp pyramid).

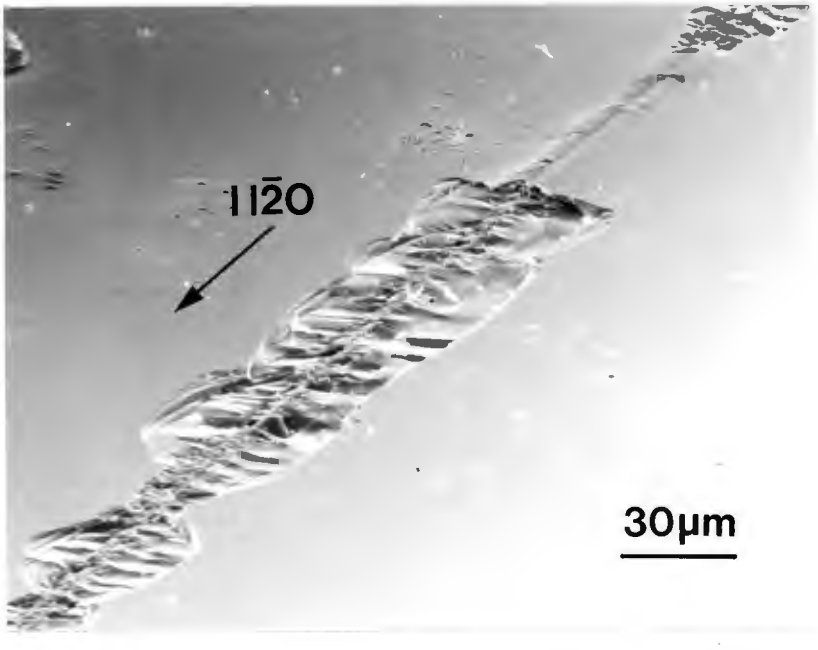

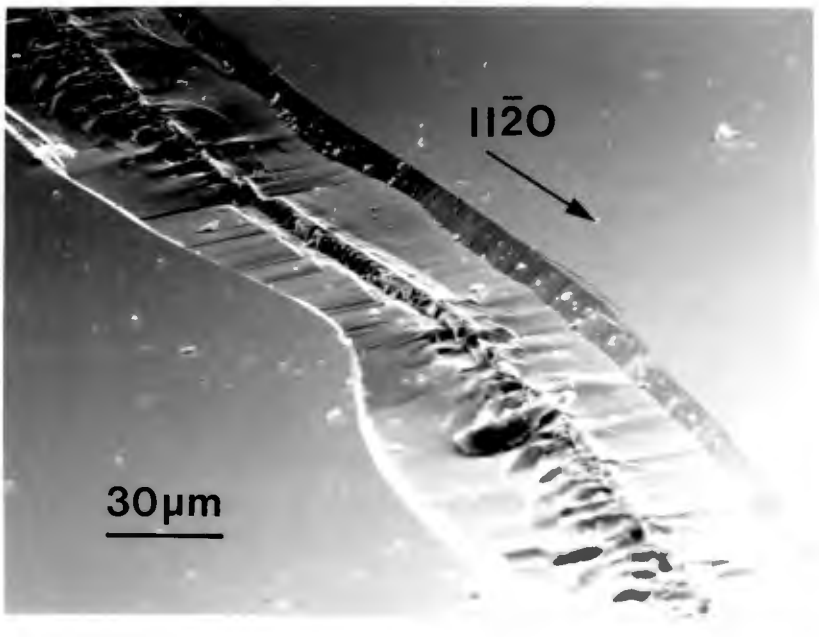

Fig.10.50 Examples of spalls produced when cutting quartz.

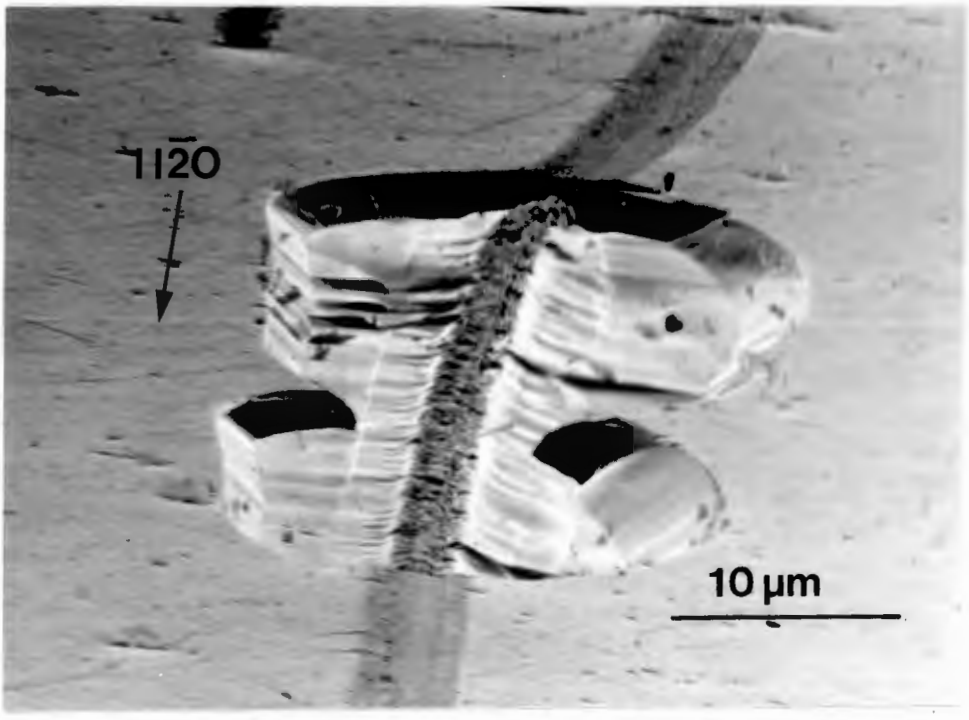

Fig.10.51 Example of a spall on quartz.

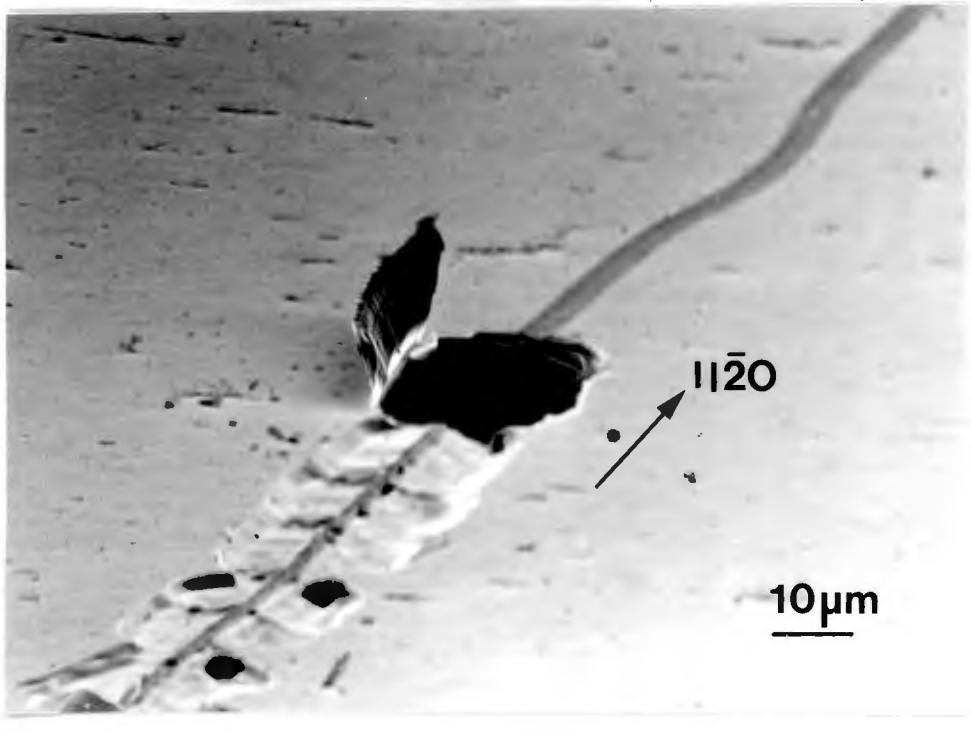

Fig.10.53 Example of time dependent spall uplift. This has occured after coating for the SEM.

10.3.5 Scratches made at Elevated Temperatures in Moist Laboratory Air (RH ≈ 70%)

Only the Z-cut plane was scratched, in the <10$\bar{1}$0> direction. Both pyramid orientations were used, and scratches made at three vertical loads (0.2, 0.5, and 0.8N) as a function of temperature (473K, 573K, 673K and 773K). A sharp pyramid was used.

Fractography

Pyramid aligned in orientation (A):

At low vertical loads there is a change from a cutting action to the Hertzian deformation zone, as the temperature is increased (Fig.10.54). The change is evident even for temperatures as low as 373K. No physical deformation of the diamond pyramid tip occurred during scratching, since a scratch made at room temperature after high temperature testing showed a return to a full cutting action. At higher vertical loads ($\gtrsim$ 0.5N) full cutting occurs, associated with considerable cracking and chipping (Fig.10.55). However, there is again evidence to suggest that the pyramid rubs over the surface, generating partial cone-cracks, yet cutting in the sub-surface region (Fig.10.56).

Pyramid aligned in orientation (B):

The same general features of a curtailment in cutting, replaced by the Hertzian deformation zone, was observed (Fig. 10.57) for all vertical loads $\lesssim$ 0.5N, and temperatures $\gtrsim$ 373K. Increasing the load at elevated temperatures resulted in the more extensive development of a sideways extending crack system (Fig.10.58). At higher loads there was extensive cracking, and chip formation (Fig.10.59).

Cutting Parameters

The variation in horizontal force (Fig.10.60) as the temperature is increased shows little temperature dependence and within experimental error is the same as the room temperature data. Scratch width and depth as a function of vertical load and temperature are presented in Figs.10.61 a & b for pyramid orientations A and B respectively. On the width curves the regimes of cutting and no cutting are dilineated, while for the depth of cut, data points are only included where cutting occurred. There is a trend for increasing scratch width as the temperature is raised, while the depth of cut is temperature independent.

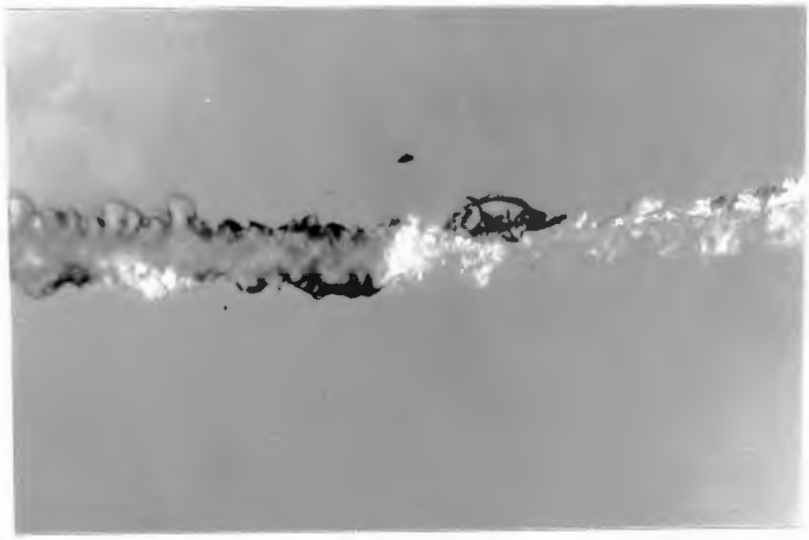

0.2N T=300K

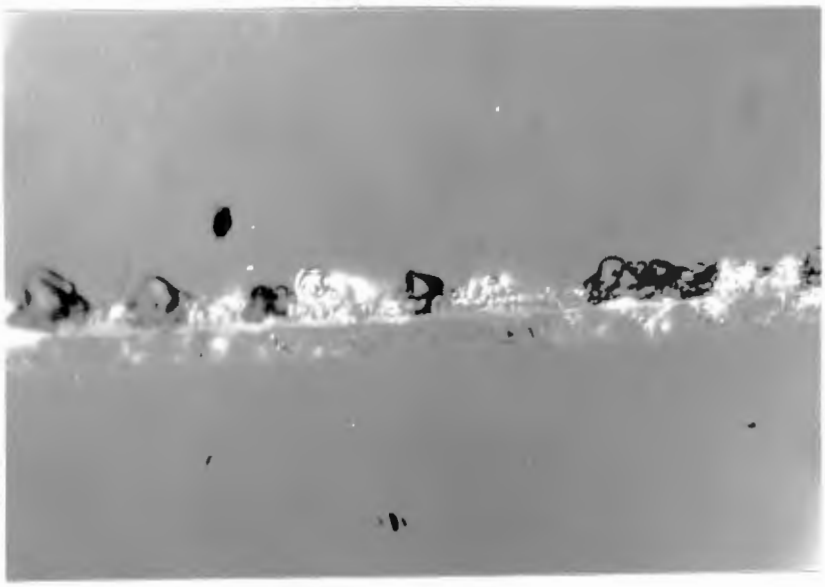

0.2N T=473K

0.2N T=773K

10μm

DIRECTION OF SCRATCHING

Fig.10.54 High temperature, low load (0.2N) scratches made in moist laboratory air. The development of a Hertzian deformation track is apparent as the temperature is raised. (Z-cut plane, sharp pyramid, orientation A).

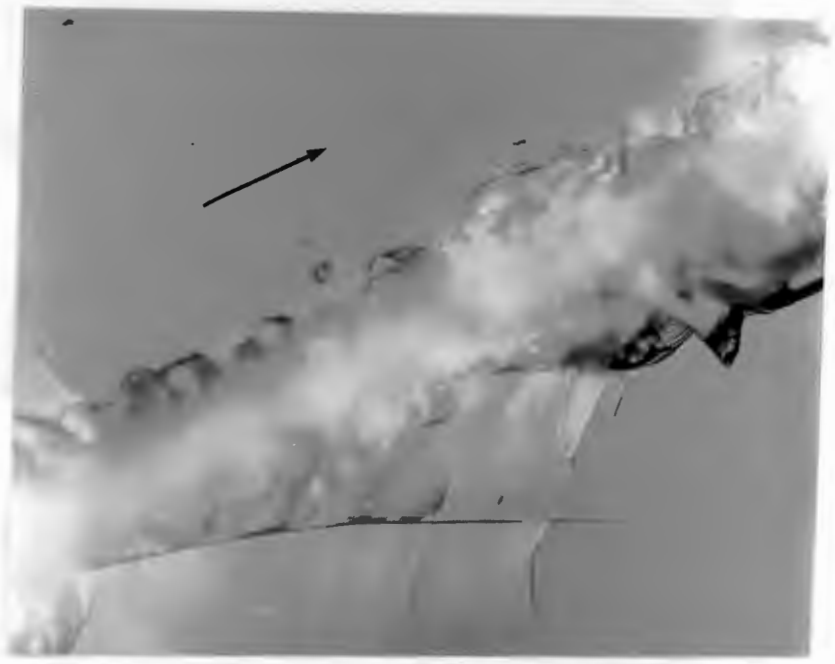

Fig.10.55 Optical micrograph of a high temperature scratch. Note the extensive cracking to the side of the groove. (Z-cut plane, sharp pyramid, orientation A, T=773K, load=0.8N)

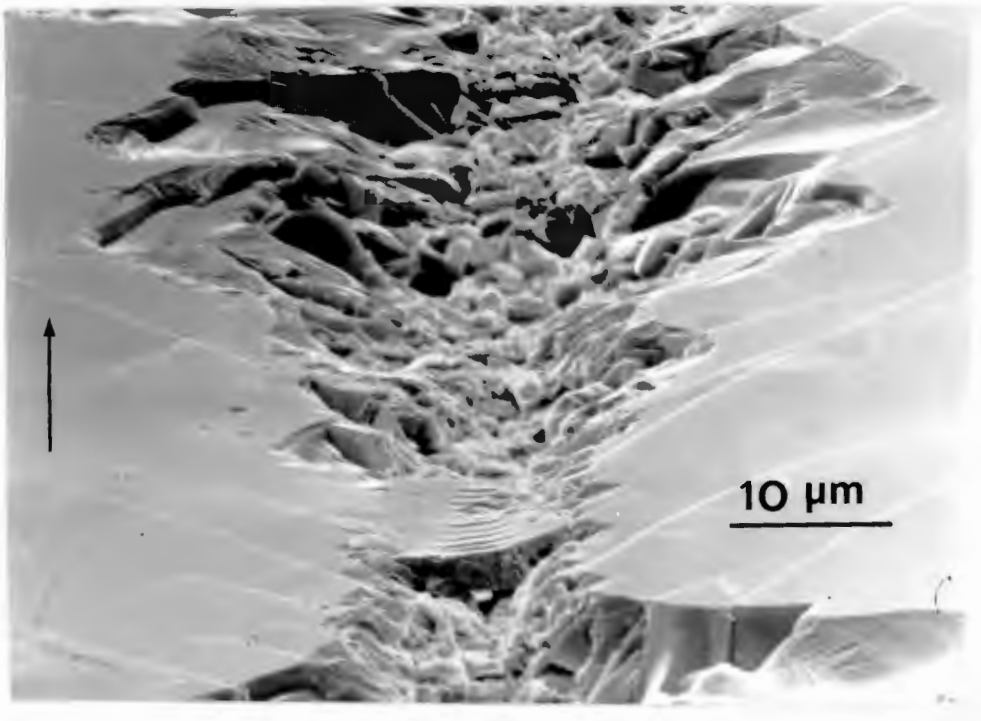

Fig.10.56 SEM micrograph of similar scratch to above. Note in particular the material which has remained within the groove and which displays the characteristic Hertzian cracking.

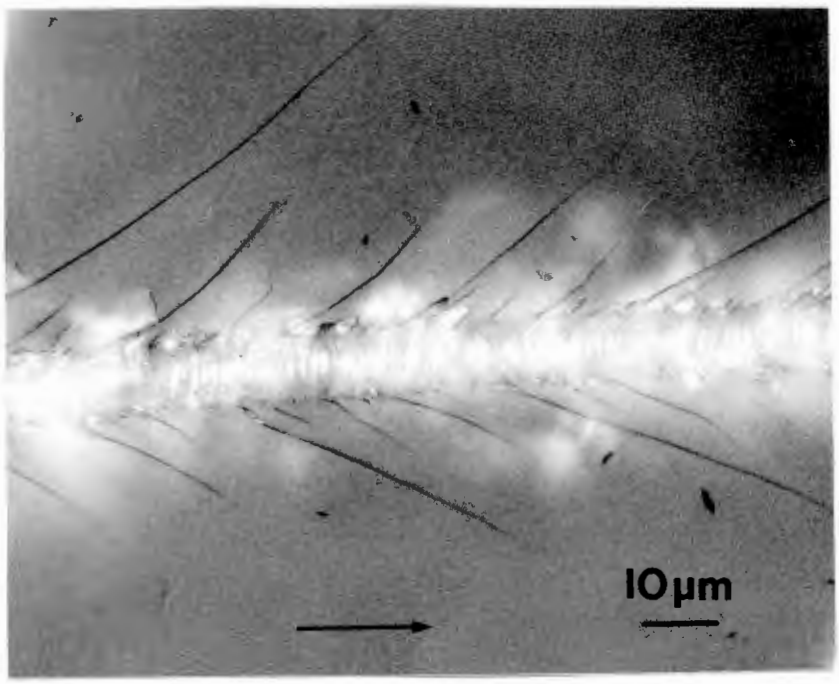

Fig.10.58 High temperature (773K) scratch made at 0.5N. Note the cracks propagating from the sides of the Hertzian zone. (Z-cut plane, sharp pyramid, orientation B).

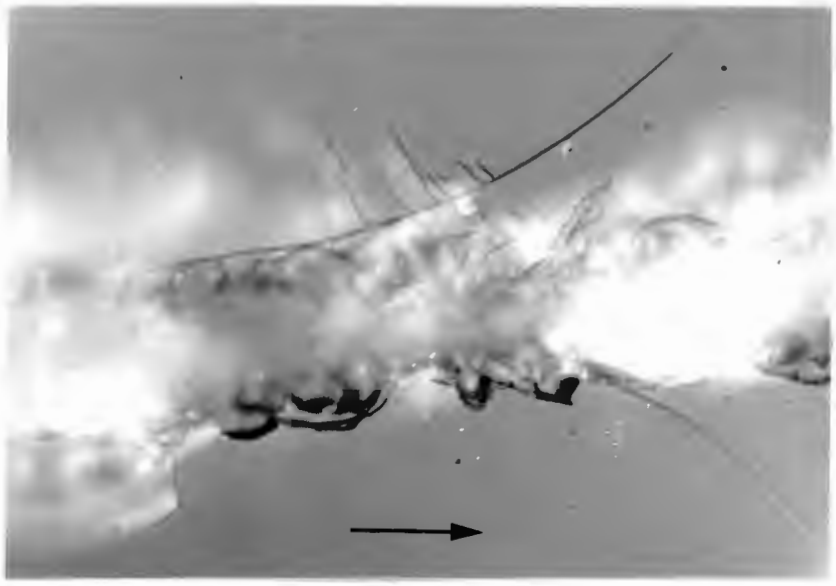

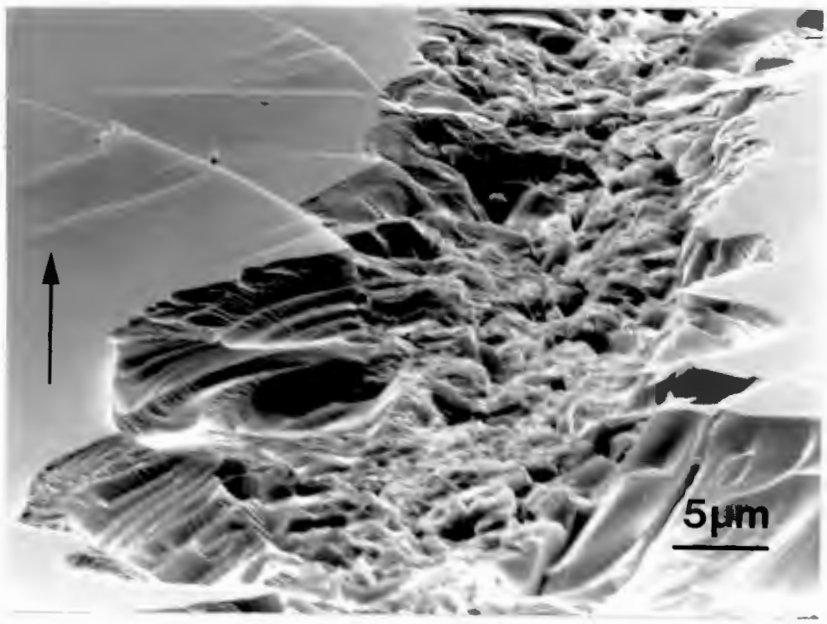

Fig.10.59 High temperature (773K) scratch made at 0.8N, showing extensive chipping and cracking. (Z-cut plane, sharp pyramid, orientation B).

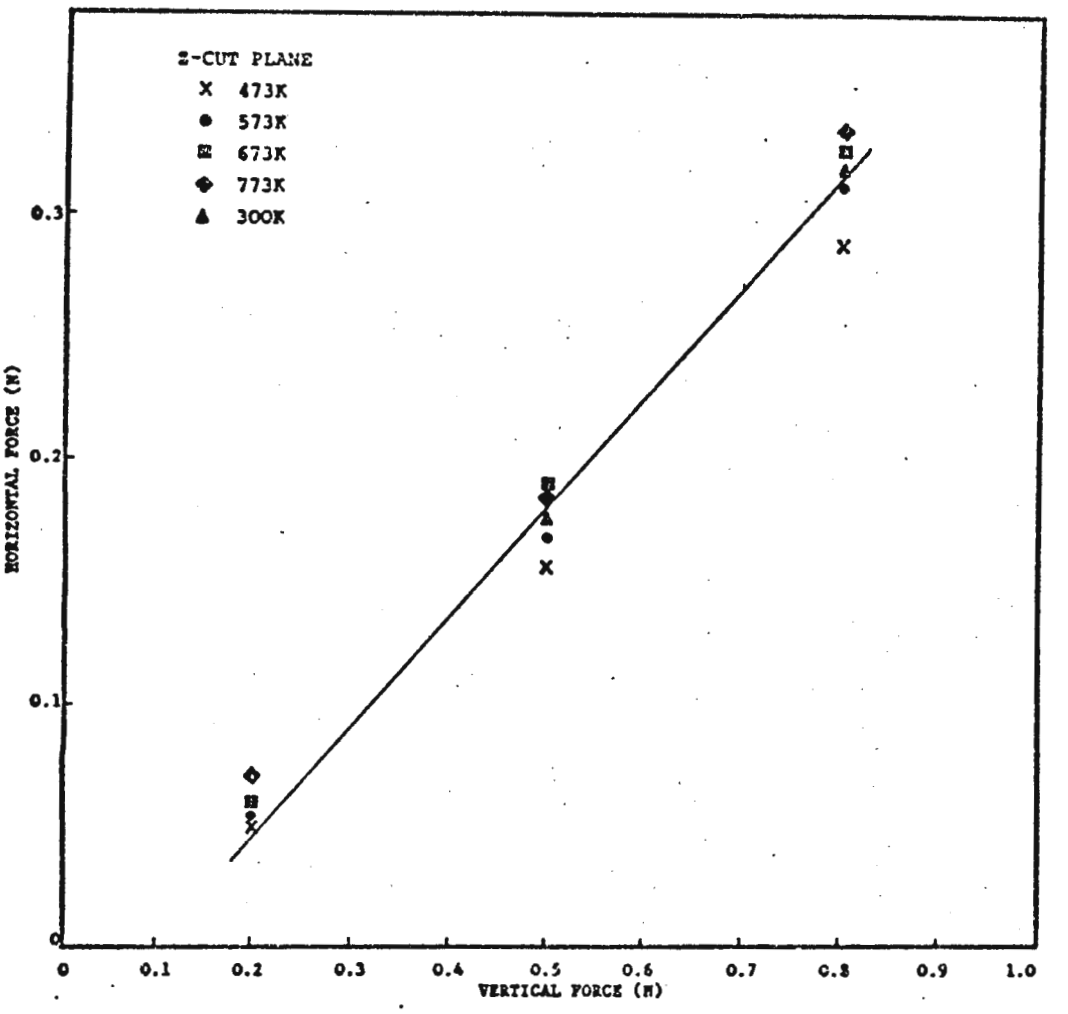

Fig.10.60 Variation in horizontal force as a function of vertical force for high temperature scratches. (Z-cut plane, moist laboratory air, sharp pyramid).

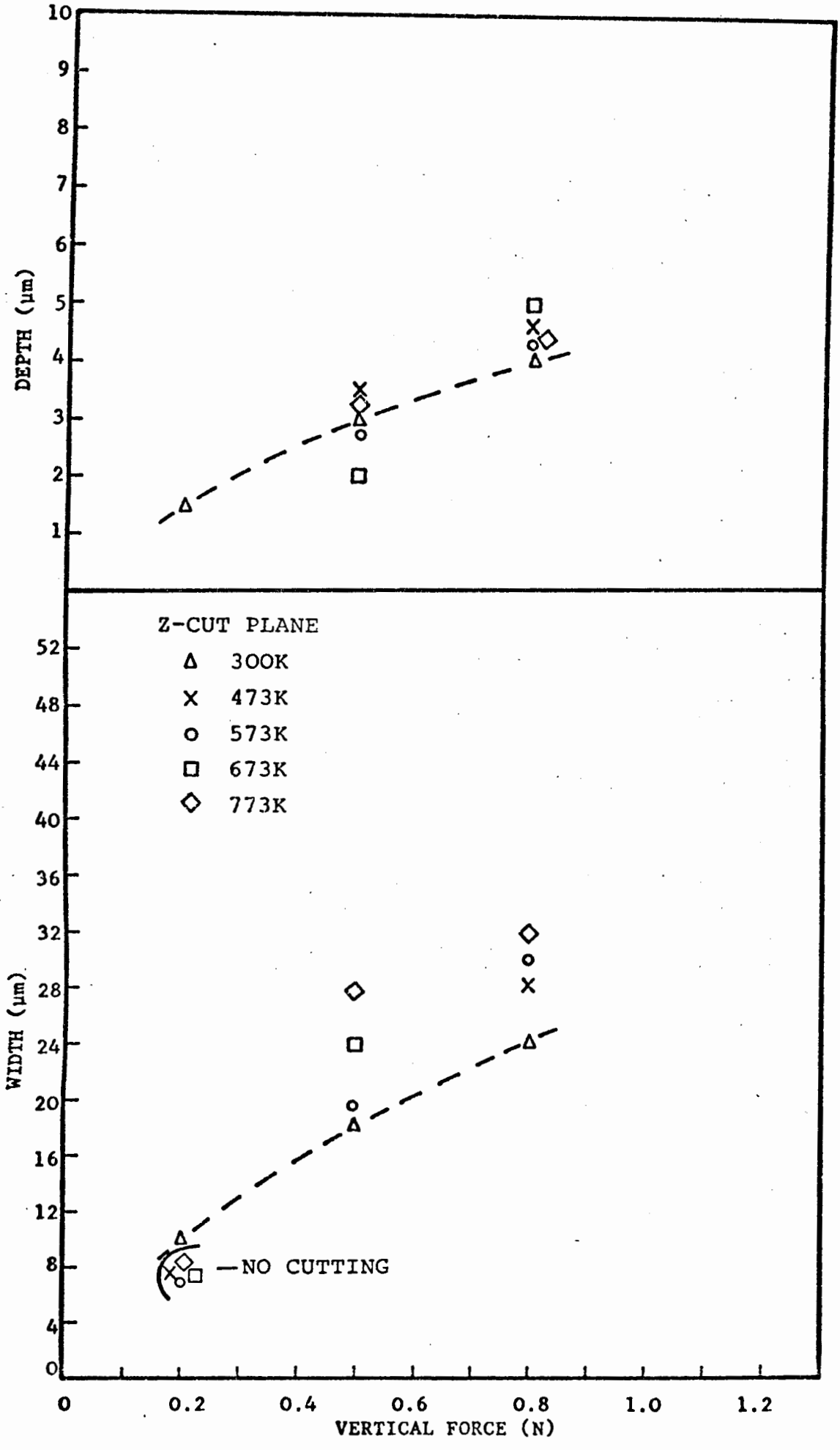

Fig.10.61(a) High temperature scratches. Variation in width and depth. (Moist laboratory air, sharp pyramid, orientation A).

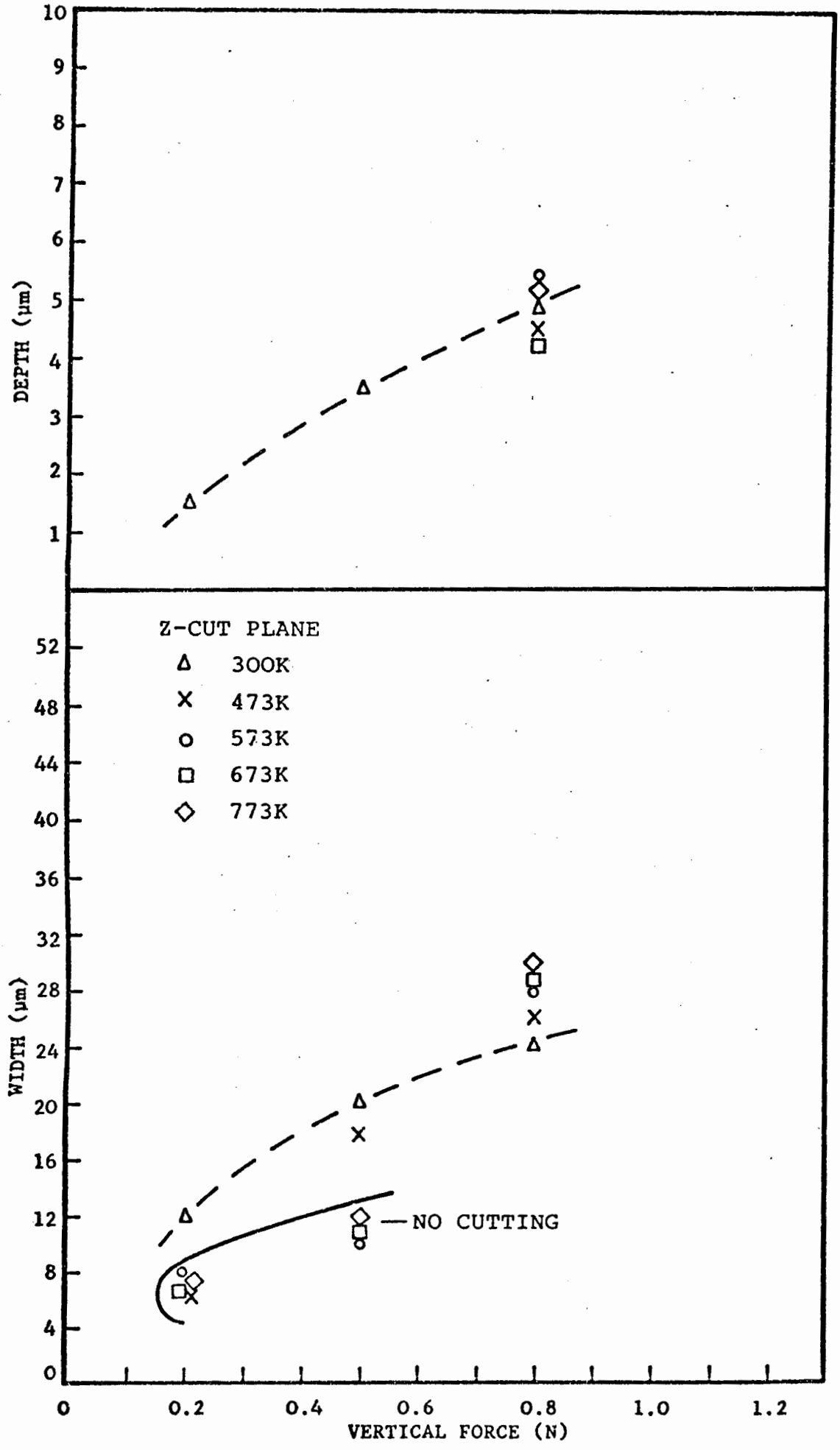

Fig.10.61(b) High temperature scratches. Variation in width and depth. (Moist laboratory air, sharp pyramid, orientation B).

10.3.6 Multiple Scratches with a Blunt Pyramid

(a) X-Cut Plane Scratched in the <10$\bar{1}$0> Direction in Dry Conditions

Up to five passes of the diamond pyramid were made, as a function of the vertical load. At the lowest load (0.1N) the effect of multiple scratching is to eventually produce a well defined scratch track (Fig.10.62). There is an increase in spalling after four scratches. At a vertical load of 0.5N just three scratches suffice to produce a well defined cut (Fig.10.63). In this case there is no spalling action but proper cutting.

(b) Y-Cut Plane Scratched in the [0001] Direction

Dry Conditions

Fig.10.64a shows a low load (0.1N) multiple scratch (10 passes); it should be compared to the deformation for the single scratch (Fig.10.64b). It is evident that a low load multiple scratch can eventually cause the formation of a rather irregular groove. Fig.10.65 shows the deformation for intermediate loads (0.5N). This time the groove outline is more regular. At 1.0N (Fig.10.66) this trend continues, and of interest is the appearance of additional 'plastic' deformation within the scratch track. This may suggest that the "asperities" of preceding scratches can be plastically deformed by the pyramid as it advances.

Wet Conditions

In wet conditions up to five passes of the cutting tool were made. Similar results to the dry multiple scratches were obtained (Figs.10.67-10.69). The plastic deformation within the grooves is more in evidence, but overall there are no significant changes in deformation between dry and wet multiple scratches.

Cutting Parameters

We depart from previous sections and present the cross-sectional area of the groove (for those scratches where cutting did occur) as a function of the number of passes (N) (Fig. 10.70) for the Y-cut plane. This is shown for the 0.5N and 1.0N scratches. It is clear that water enhances the cutting action for this load range. We have also attempted to find a relationship between the depth of the scratch and N. If this data is plotted logarithmically (Fig.10.71) a straight line can be drawn through the data points. The slopes of the fitted lines vary from 0.5 - 0.7.

An estimate was made of the specific energy of cutting, as a function of the number of passes, for both the low (0.1N) and high (1.0N) load scratches in wet conditions. It is apparent (Fig.10.72) that the specific energy reduces after the first few scratches, and tends to a constant value after $\approx$ 5 passes. From this it may be concluded that the single pass scratching test may not be a reliable indicator of cutting energies.

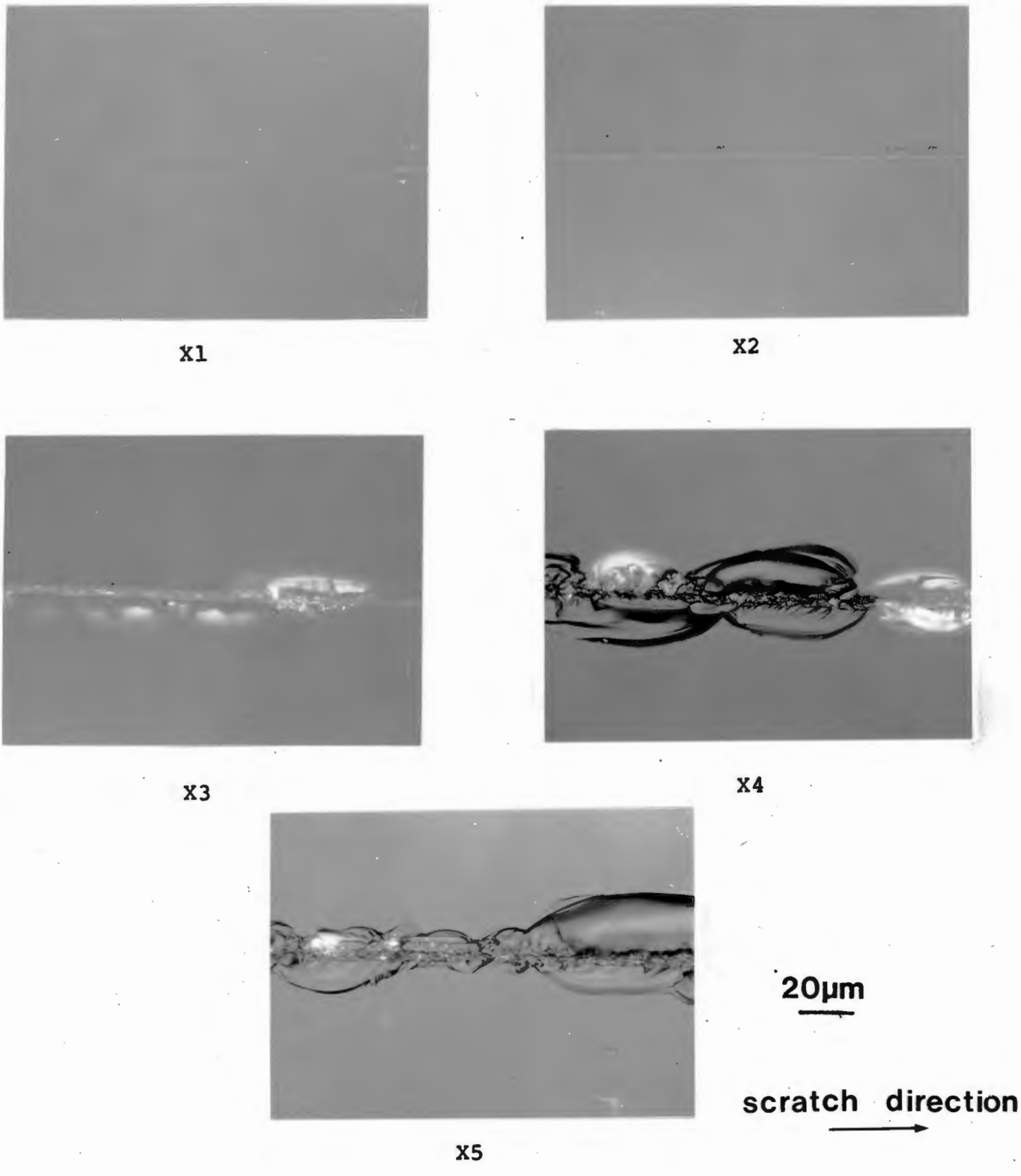

Fig.10.62 Examples of multiple scratches at low loads (0.1N). Note the development of spalling as the number of passes increases. (X-cut plane, dry conditions, blunt pyramid).

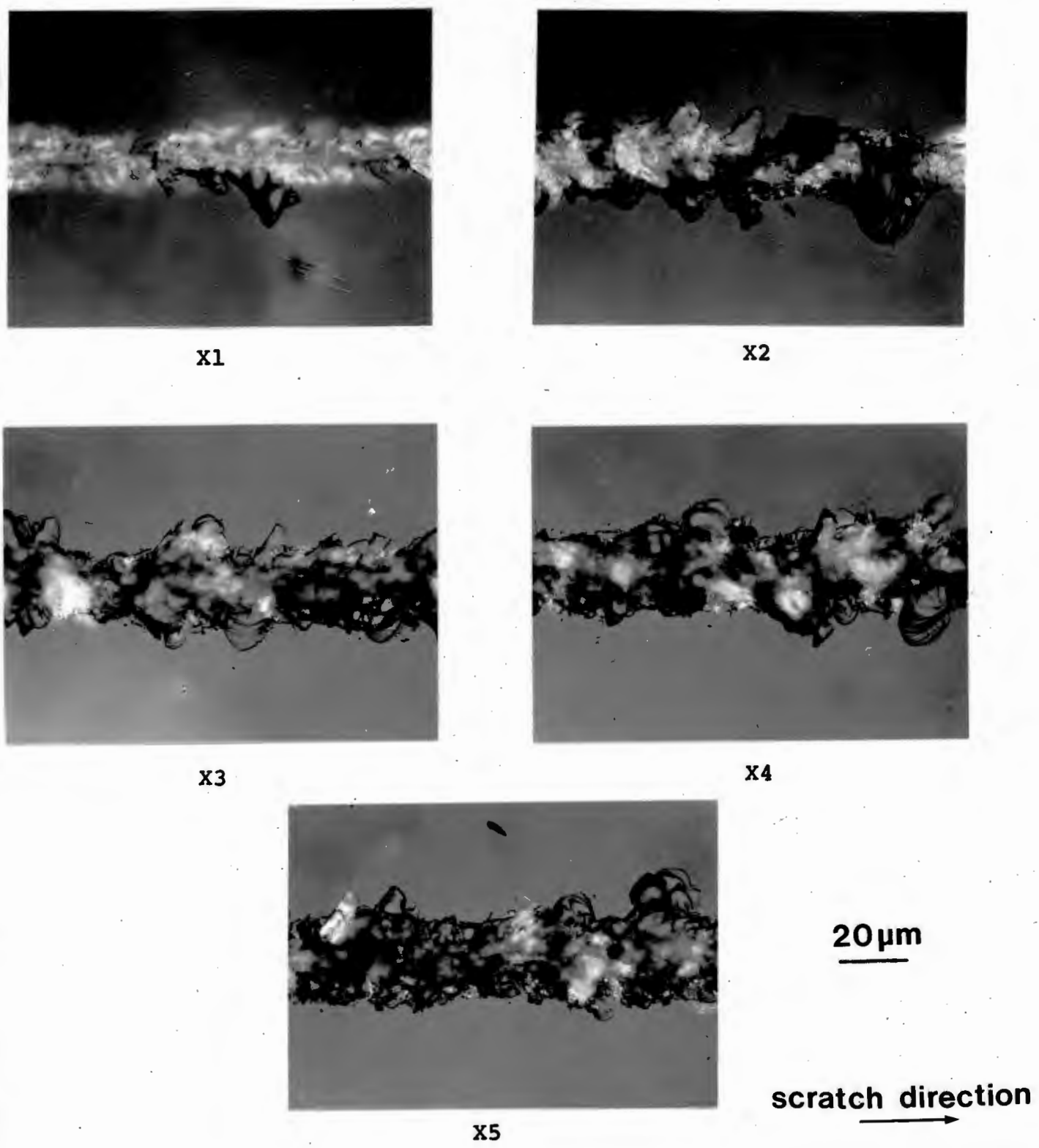

Fig.10.63 Examples of multiple scratches at intermediate loads (0.5N). A full cutting action is apparent after three scratches. (X-cut plane, dry conditions, blunt pyramid).

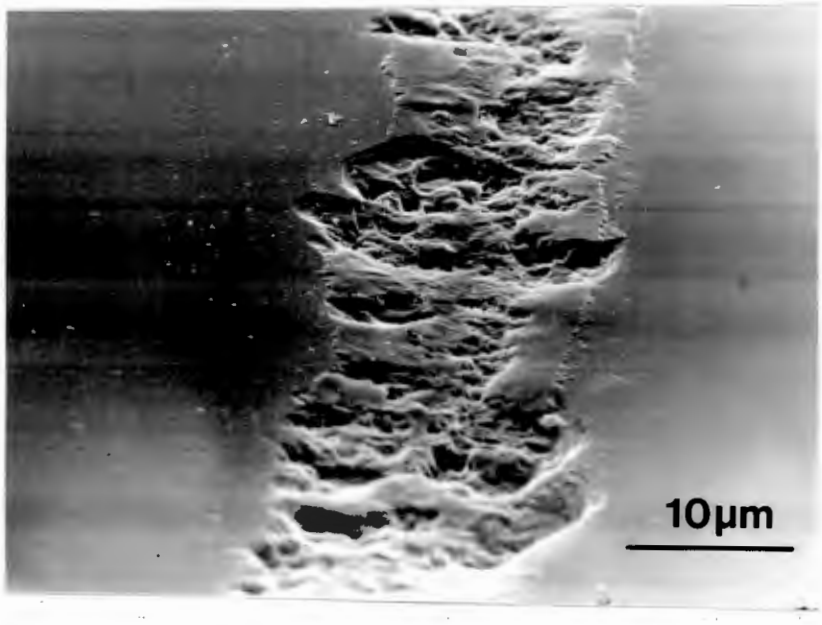

(a)

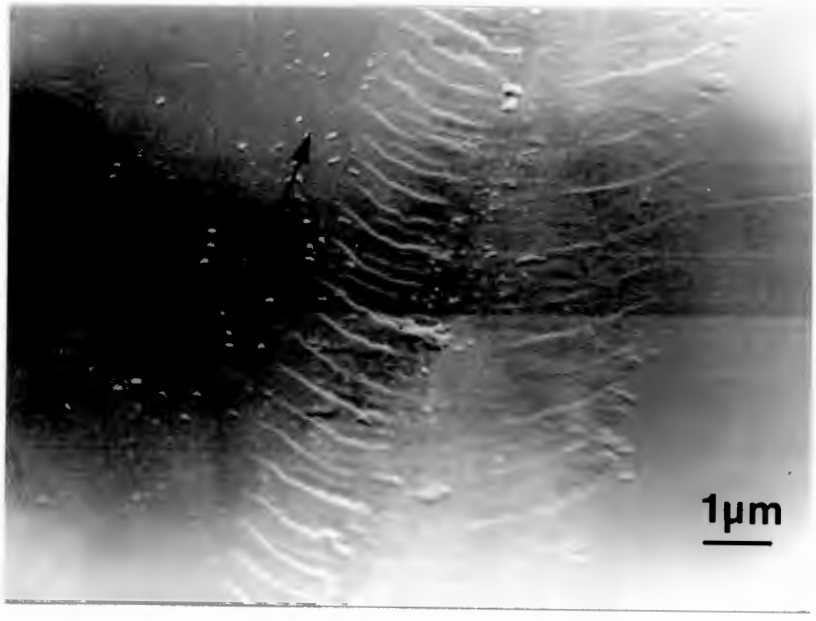

(b)

Fig.10.64 Multiple scratches at low loads (0.1N). (a) After ten passes. (b) After one pass. (Y-cut plane, dry conditions, blunt pyramid).

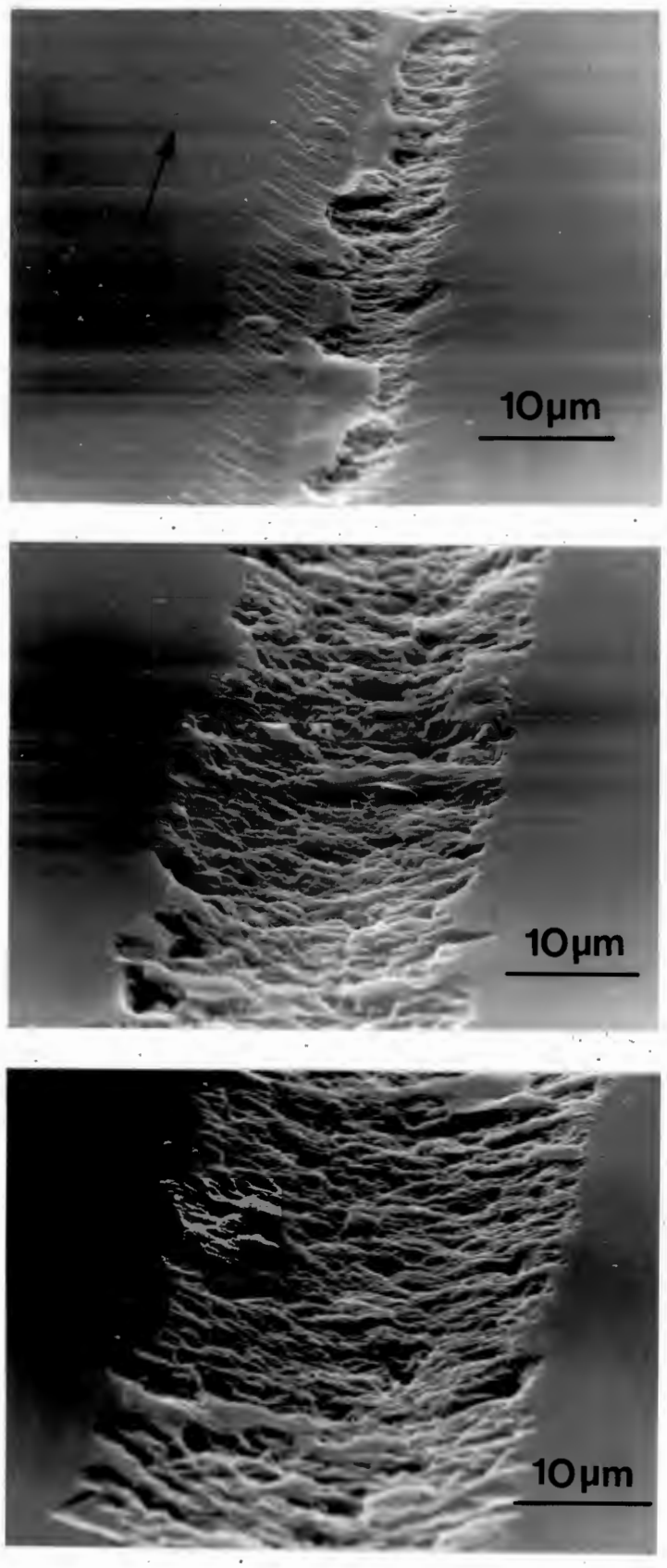

Fig.10.65 Multiple scratches at intermediate loads (0.5N). (Y-cut plane, dry conditions, blunt pyramid).

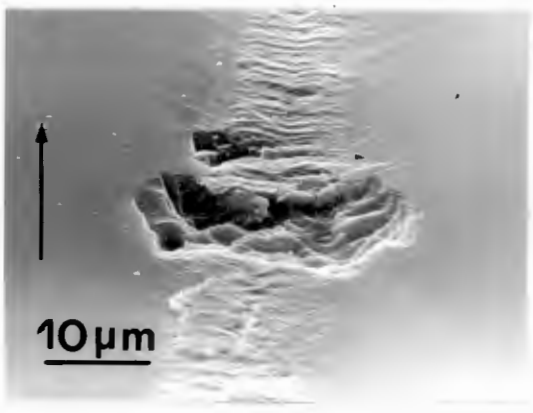

X1

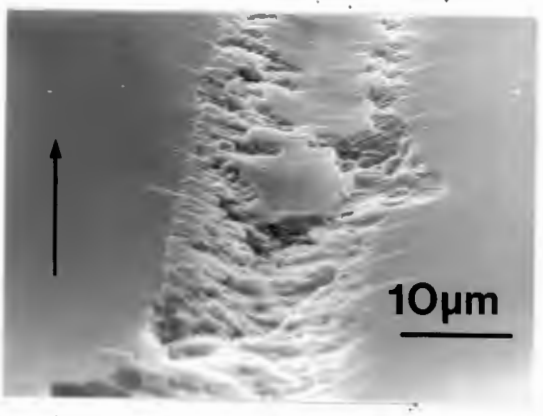

X2

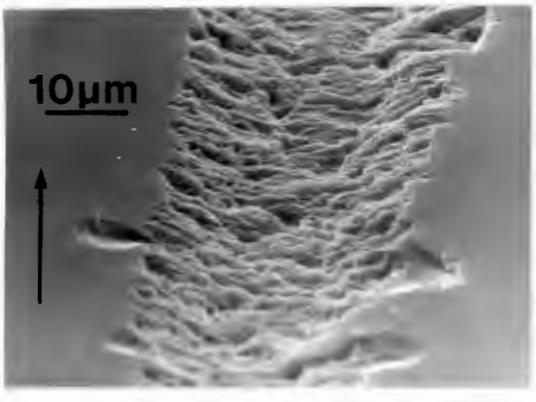

X5

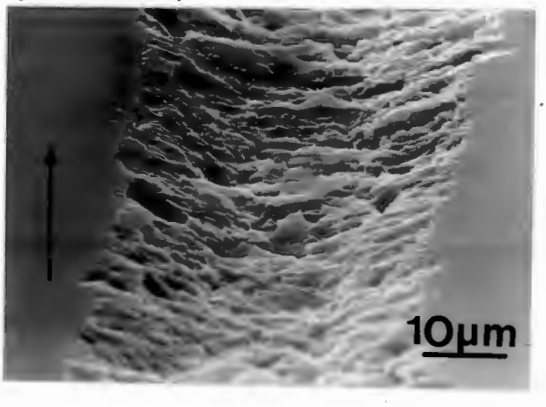

X10

Fig.10.66 Multiple scratches at high loads (1.0N). The development of plastic deformation of the asperities within the scratch track is of interest. (Y-cut plane, dry conditions, blunt pyramid).

X1

X2

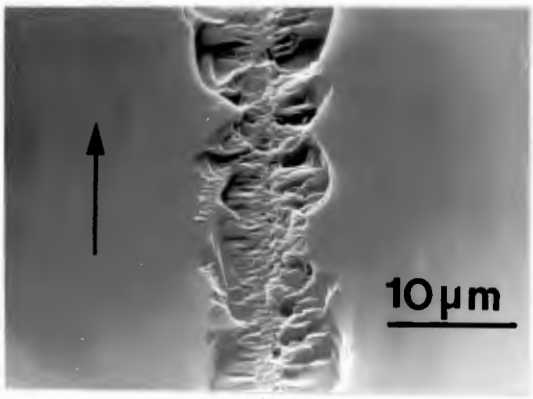

X3

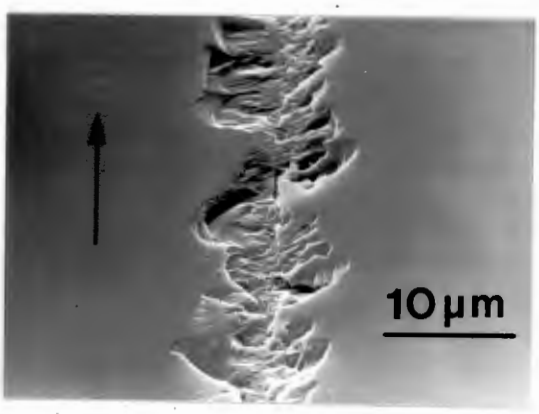

X4

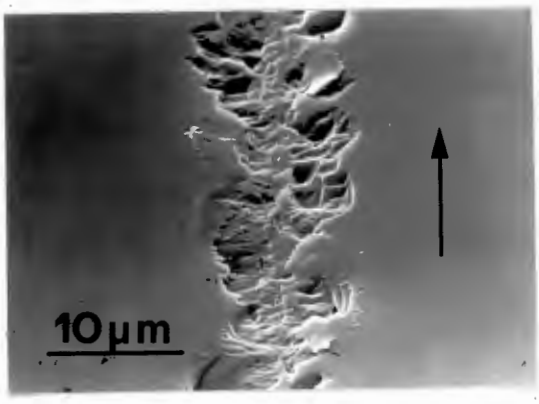

X5

Fig.10.67 Multiple scratches in wet conditions at low loads (0.1N). (Y-cut plane, blunt pyramid).

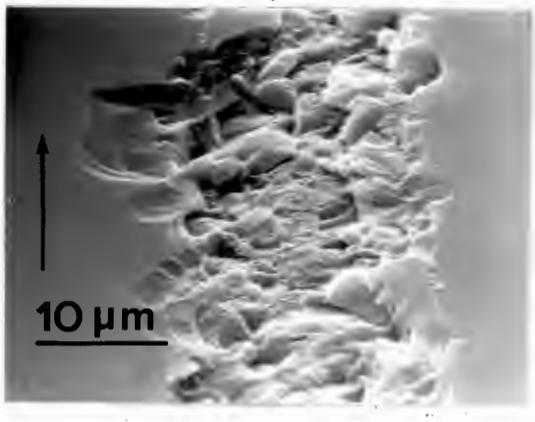

X2

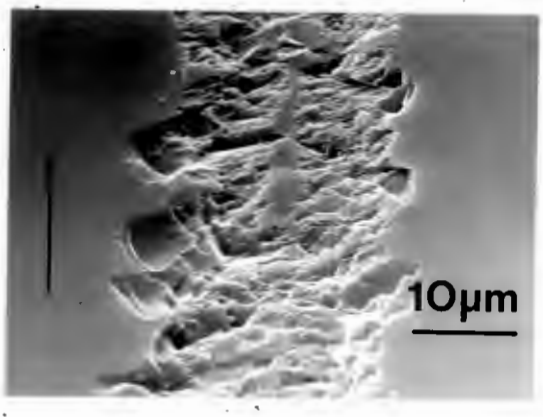

X3

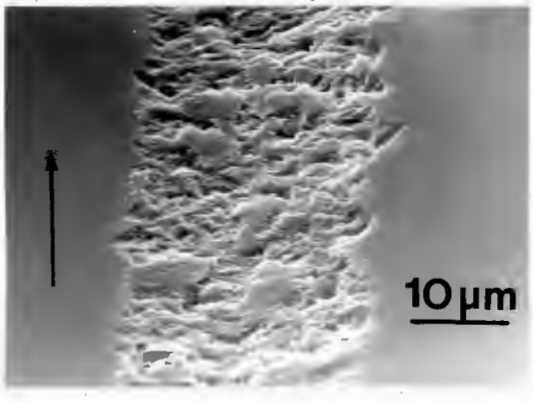

X4

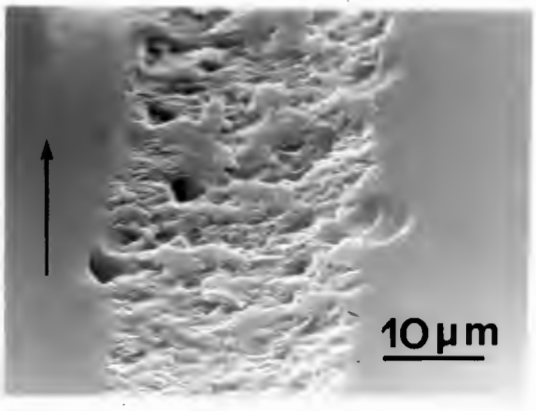

X5

Fig.10.68 Multiple scratches in wet conditions at intermediate loads (0.5N). (Y-cut plane, blunt pyramid).

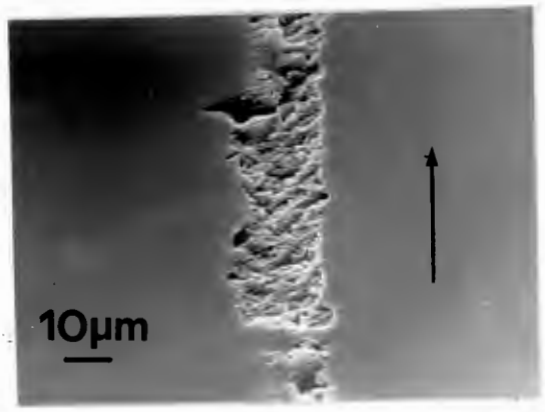

X1

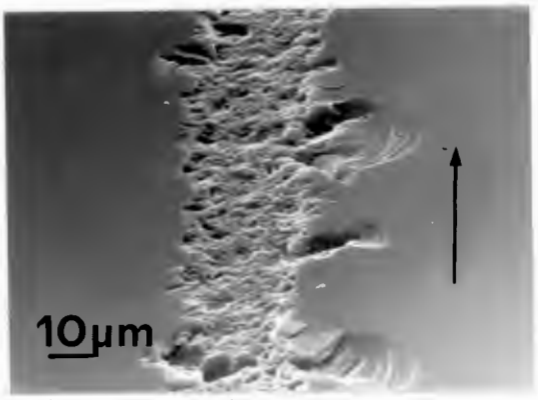

X2

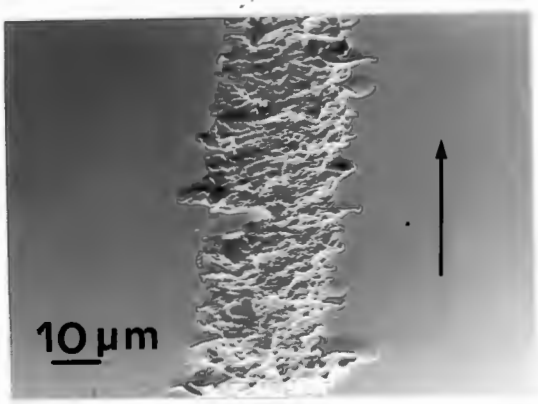

X3

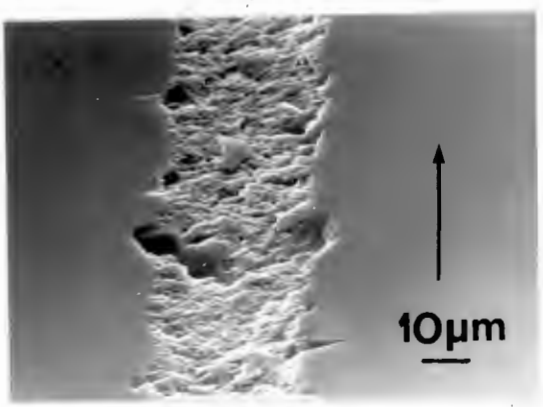

X4

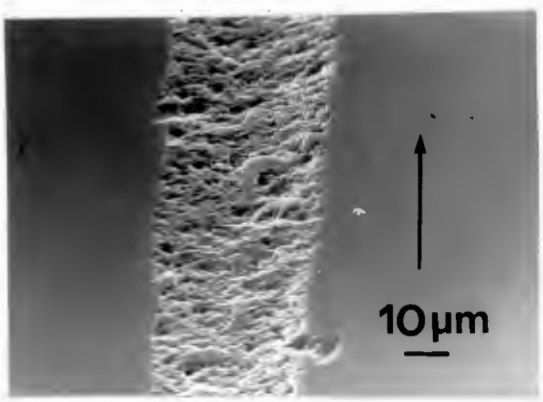

X5

Fig.10.69 Multiple scratches in wet conditions at high loads (1.0N). (Y-cut plane, blunt pyramid).

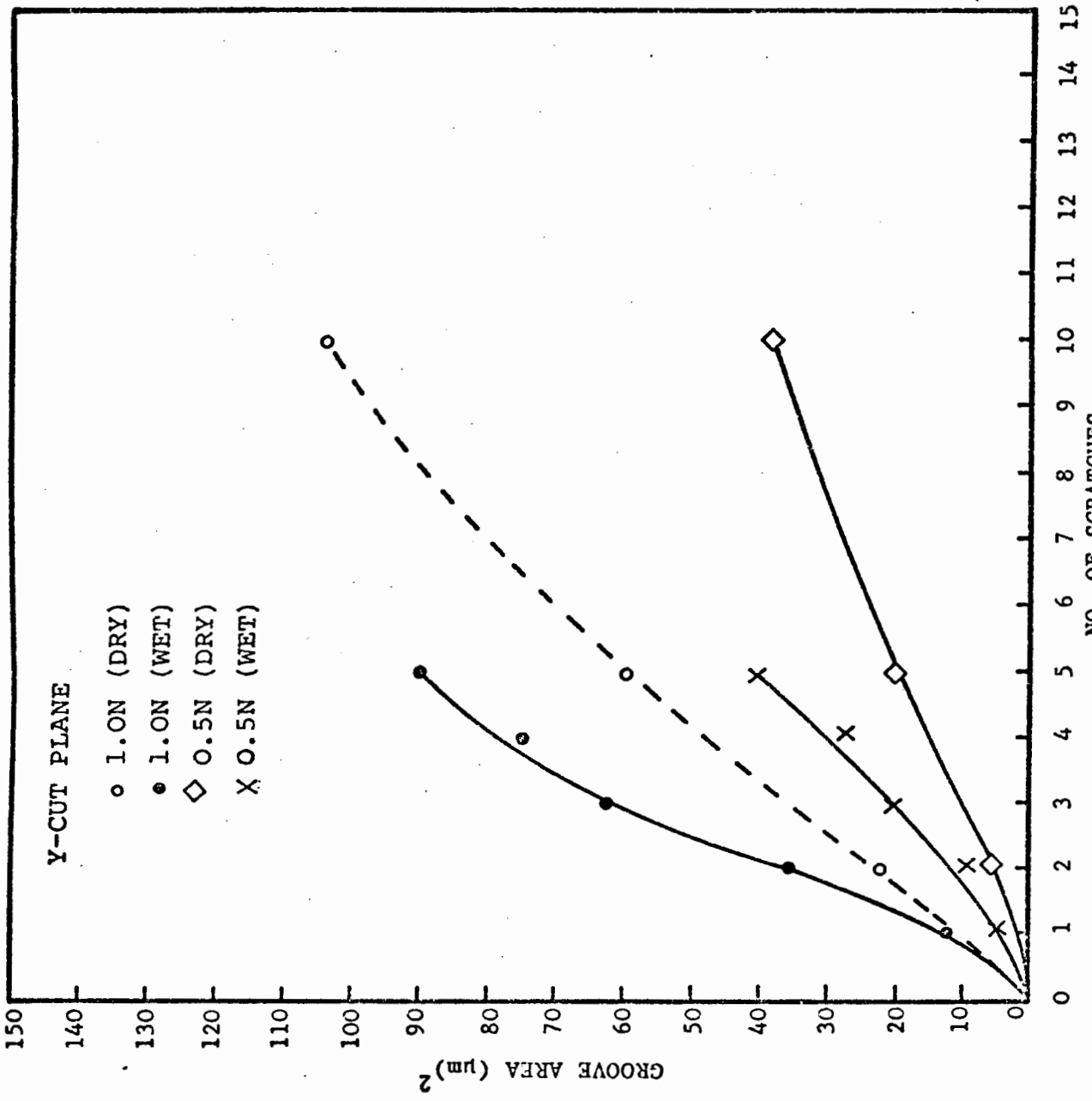

Fig.10.70 Cross sectional area of a scratch groove as a function of the number of passes. Comparison of dry and wet conditions. (Y-cut plane, blunt pyramid, [0001] direction).

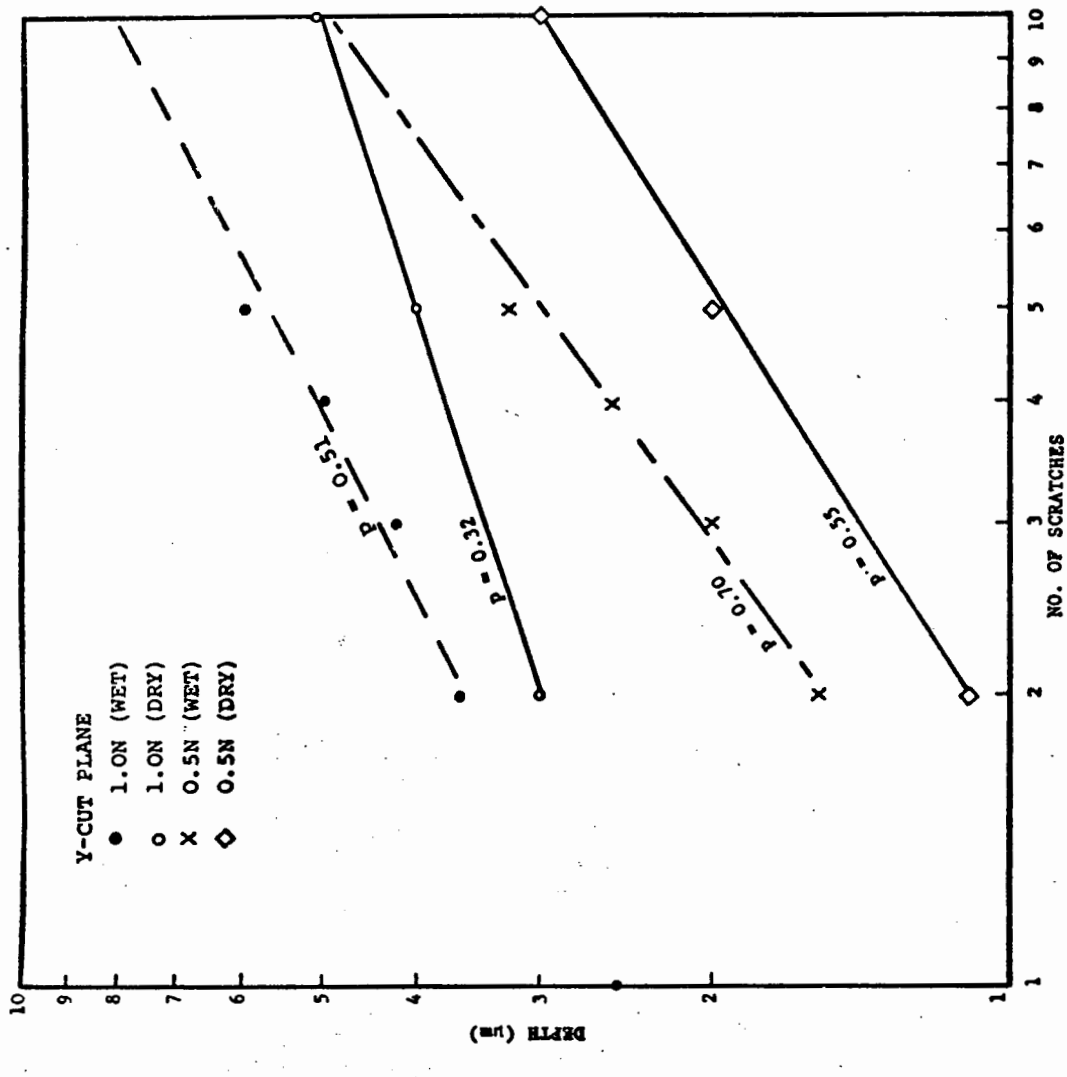

Fig.10.71 Logarithmic plots of the increase in depth of a scratch as a function of the number of passes. Both dry and wet scratches are shown. (Y-cut plane, blunt pyramid, [0001] direction).

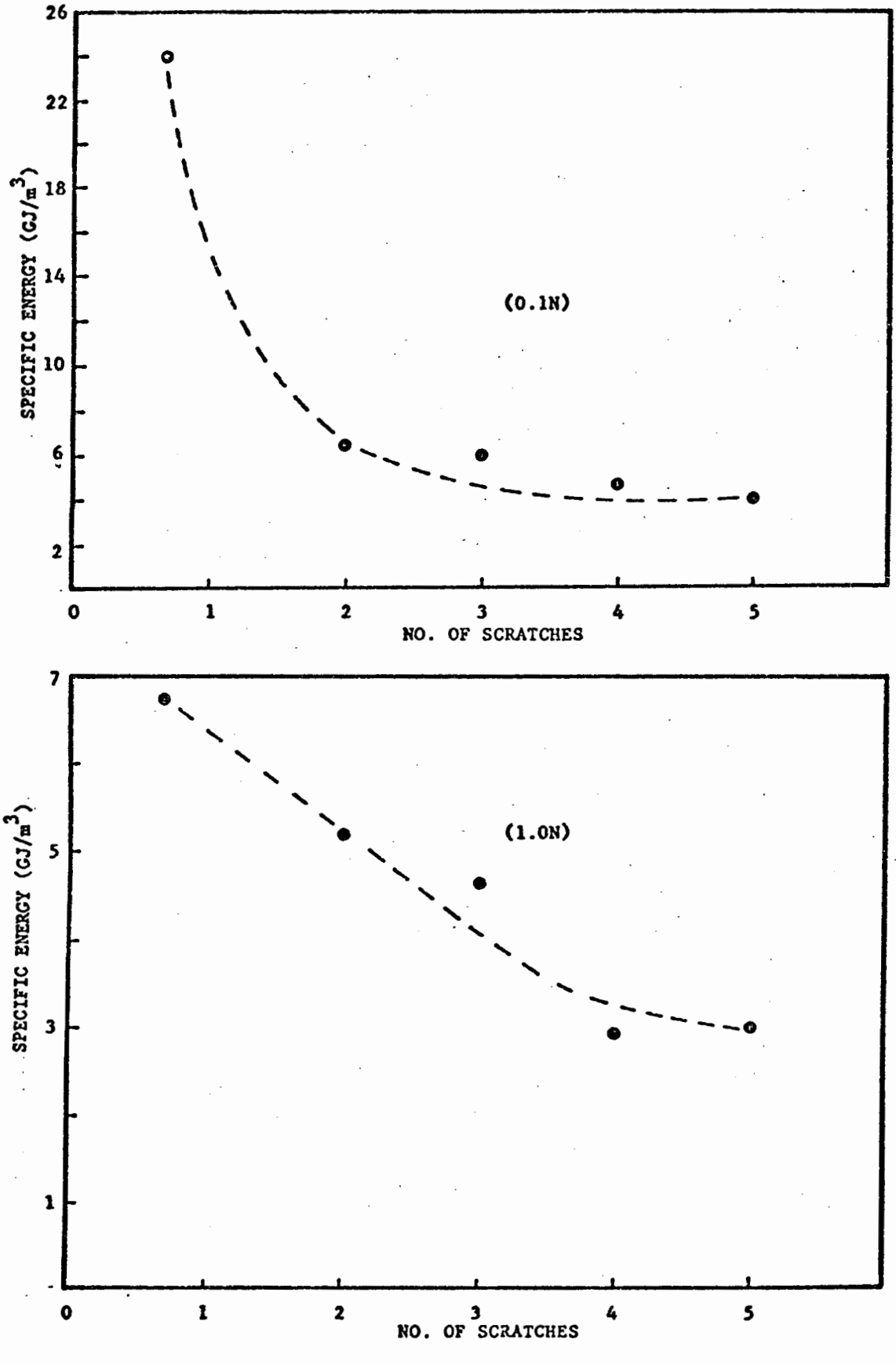

Fig.10.72 Specific energy as a function of the number of tool passes in a multiple pass scratch experiment. (Y-cut plane, wet conditions).

10.3.7 Adjacent Scratches

An attempt was made to assess the extent of the interaction between adjacent scratch tracks. However, little coalescence of the cracks was observed (Fig.10.73), and to all intents and purposes the tracks are independent of each other. These scratches were made sequentially. It would be worthwhile to attempt scratching with two cutting tools running simultaneously next to each other, to ascertain if this can produce some interaction.

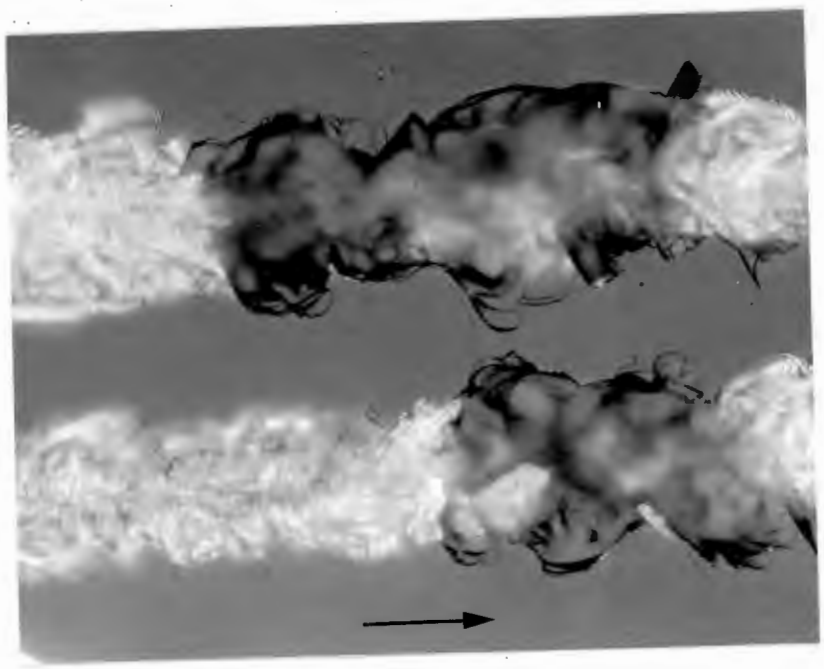

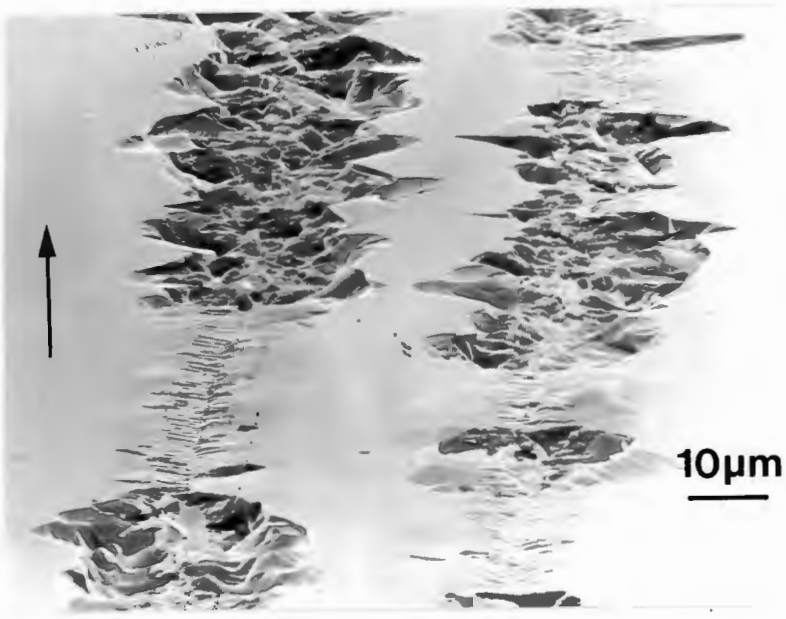

Fig.10.73 An example of adjacent scratching. (a) Optical micrograph. (b) Corresponding SEM micrograph. Note the low extent of interaction between the scratch grooves either by chipping, cracking or sub-surface cracking.

10.4 Summary of Scratching Results

1. The state of the tool tip has a significant effect upon the scratch deformation. With a sharp tip a full cutting action occurs over the complete experimental load range. With a blunt tip a Hertzian deformation track is observed at low loads while at higher loads there is a change to a full cutting action.

2. With a blunt pyramid a directional anisotropy of cutting is noted. That is, a particular crystallographic direction may be either 'hard' to cut (a full cut is not produced until high vertical loads) or 'easy' to cut (a full cut is produced at lower loads). The hard and easy directions for cutting quartz is as follows:

Crystal Plane	Scratching Direction	Cutability
X-cut plane $(11\bar{2}0)$	$\langle 10\bar{1}0\rangle$	Easy
	[0001]	Hard
Y-cut plane $(\bar{1}100)$	$\langle 11\bar{2}0\rangle$	Easy
	[0001]	Hard
Z-cut plane (0001)	$\langle 11\bar{2}0\rangle$	Easy
	$\langle 10\bar{1}0\rangle$	Hard

3. The effect of scratching a crystal flooded with water was to change the extent of cutting, but only for a scratch made with a blunt pyramid. In this case the Hertzian deformation track was replaced by a full cutting action. This significant change was also found for scratches made on crystals flooded with heptanol and glycerol. Scratching in water also reduces the horizontal force from its 'dry' value.

4. The cutting action appears to result from a delamination of a surface layer over which the cutting tool has passed. This type of 'cut' was observed for both a sharp and a blunt cutting tip.

5. The effect of scratching at elevated temperatures is to replace the cutting action by the Hertzian deformation track (this is particularly true of lower loads). The extent of the sideways extending cracks is enhanced, and a greater degree of chipping results. There is evidence of an increased plastic response at high temperature.

6. Large scale spalling can occur if the transition from a 'blunt action' to 'sharp cutting' occurs at lower loads ($\lesssim$ 0.3N). Time dependent spalling can be observed in this case.

10.5 Discussion

10.5.1 The Cutting of a Brittle Solid

The efficient cutting of a brittle solid requires the generation of a system of microcracks which can combine to achieve fragmentation. In this respect the degree and type of fragmentation will depend upon the sub-surface stress distribution, and hence the geometry of the cutting particle. For a sharp contact the median and lateral cracks will translate along with the particle generating a linear fissure and a system of sideways extending chips (Lawn & Wilshaw, 1975). In the case of a blunt contact, a strong dependence on the radius of the particle tip is expected (Evans, 1976). For a large tip radius a pure elastic response will be dominant and the translating indentor will develop a series of partial cone-cracks on the surface. As the tip radius is reduced, the indentor will sink in; a substantial plastic zone (elastic-plastic indentation) results. In this case, as we have previously noted (Fig.5.5) the blunt indentor shows a crack geometry which is remarkably similar to the sharp indentor. The brittle and plastic response of a brittle solid are both apparently important in determining the mode of cutting. The largest indentor tip radius for elastic-plastic deformation increases as the hardness of the material decreases, and as the fracture toughness increases (Moore and King, 1980).

Experimental observations (Broese van Groenou et al., 1975) have shown that the scratching response of brittle ceramic materials (such as ferrites and $A\ell_2O_3$) results in the following sequence of deformation as a function of the vertical load:

1. Low loads ($F_v \lesssim 0.2N$) : A well defined ductile groove is formed.

2. Intermediate loads ($0.2N \lesssim F_v \lesssim 0.5N$) : Cracking in the material adjacent to the groove occurs.

3. High loads ($F_v \gtrsim 0.5N$) : Brittle chipping becomes a mode of deformation in addition to cracking and grooving.

Comparison of our results (for example Fig.10.7 & 10.8) with the above indicates that the scratching of quartz shows a similar behaviour.

Veldkamp & Klein Wassink (1976) suggest that three material properties determine the scratching behaviour of a brittle solid:

1. The yield stress (and hence hardness)

2. Crack resistance (fracture toughness)

3. The defect density of the material (that is, the chance that the stress field associated with the cutting particle meets a defect and generates a microcracking event).

With regard to (1) above, it is known that an increase in strain rate ($\dot{\varepsilon}$) results in an increase in yield stress. Static hardness measurements may not correctly reflect the scratching response, since the hardness derived yield stress corresponds to $\dot{\varepsilon} \approx 10^{-5}\ s^{-1}$ (Evans & Goetze, 1979). Veldkamp & Klein Wassink (1976) estimate the strain rate within a deformed zone of 10 μm extent in front of a cutting particle moving at a speed of 10 m s^{-1} to be $\approx 10^{5}\ s^{-1}$, and this will result in a considerable increase in hardness. However, it must be appreciated that at the higher scratching speeds frictional heating effects become important and this will result in a lowering of hardness (from the high strain rate value). The significant parameter must be the net change in hardness due to both of these processes.

The crack resistance is also speed dependent. At low scratching speeds, the cracks (travelling along with the cutting particle) may be influenced by environmental interaction. This indicates a lowering of the fracture toughness parameter (K_c). However, at high cutting speeds (say $\gtrsim$ several tens of $m\,s^{-1}$) the cracks are propagating unstably (i.e. at the Griffith criterion) and environmental interaction is not anticipated (Wiederhorn, 1967). Slow crack growth may, however, still take place regardless of the speed of cutting because the lateral cracks form as a result of the residual stress field about the scratch groove. X-ray topography (Fig.10.24b) has indicated that the extent of this strain field may be considerably greater than that about a hardness indentation (Fig.9.30).

At high cutting speeds the temperatures generated by frictional heating may also blunt the microcracks, and hence reduce the efficiency of cutting. As eqn.(4.5) shows, the fracture stress is sensitive to the crack tip radius, and dislocation generation in this region (Fig.10.74) will increase ρ and hence σ_f.

The lateral cracks are the major source of material removal during cutting. Evans (1976) finds that the extent of lateral cracking is similar for both static indentation and cutting. He is able to show that the volume of material removed per unit length of sliding is given by the expression:

$$\frac{V}{\ell} \alpha F_v^{7/6} K_c^{-2/3} H_v^{-\frac{1}{2}} , \qquad (10.9)$$

Swain (1979) from a consideration of lateral cracking about scratches shows that:

$$\frac{V}{\ell} \alpha H_v^{\frac{1}{2}} F_v^{3/2} K_c^{-2} \qquad (10.10)$$

while from a three dimensional analysis of lateral cracking about hardness impressions derives the same expression (eqn. 10.9) as Evans (1976). The three dimensional analysis applies to those cutting modes where lateral cracking proceeds ahead of the cutting particle.

10.5.2 Geometrical Ploughing Theory

The use of a well defined cutting particle geometry enables the response of a material at a cutting tool interface to be predicted by ploughing theory. This theory applies only to the flow properties of materials and is able to predict the values of force ratio $f(= F_H/F_V)$ or coefficient of sliding friction, for a specific cutting tool geometry. Ploughing theory has been used, and modified, by Broese van Groenou et al. (1975), for the analysis of their scratching experiments made on ceramic materials. The following analysis is based on their work.

We shall consider three specific cutting particle geometries:

1. Pyramid with one leading plane in contact with the material;
2. Pyramid with two planes in contact;
3. Spherical indentor.

The average stresses perpendicular to, and in the interface are the compressive (σ) and shear (τ) stresses, respectively. The shear or friction stress can be defined as $\tau = \mu\sigma$, where μ is the Coulomb friction coefficient (note that μ is not the same as f). The exact direction of the friction stress at the interface is determined by the relative motion of material flow as the cutting tool traverses across the surface. There are two cases to consider:

1. The indentor moves over the material without any flow processes occurring;
2. Material is ploughed out and moves over the indentor, both upwards and sideways.

An example of the first case would be a lightly loaded sphere rubbing across the surface. If the vertical load on the sphere is increased, the sphere sinks in and material is 'ploughed'; this would represent the second case.

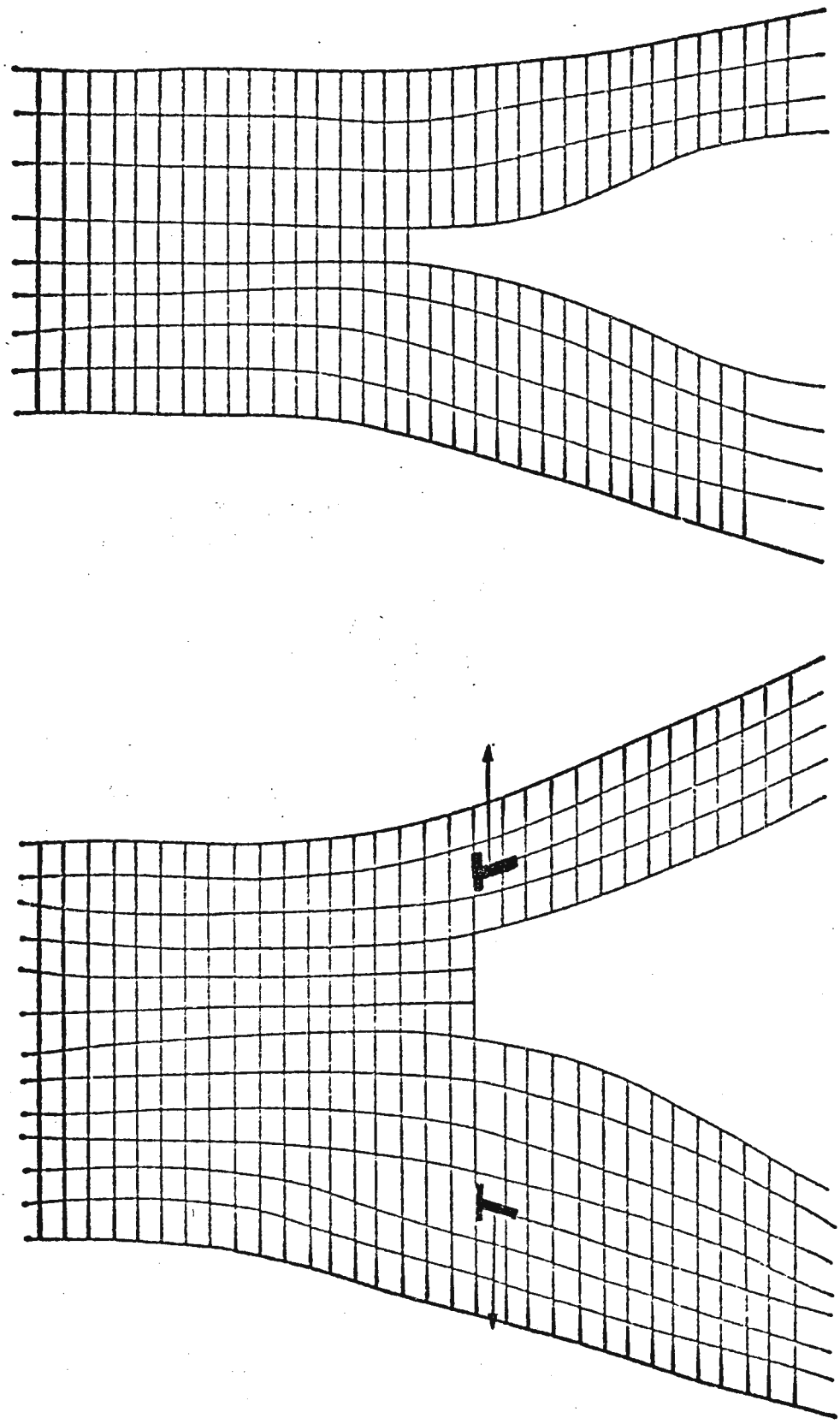

Fig.10.74 The blunting of an atomically sharp crack via two mobile dislocations.

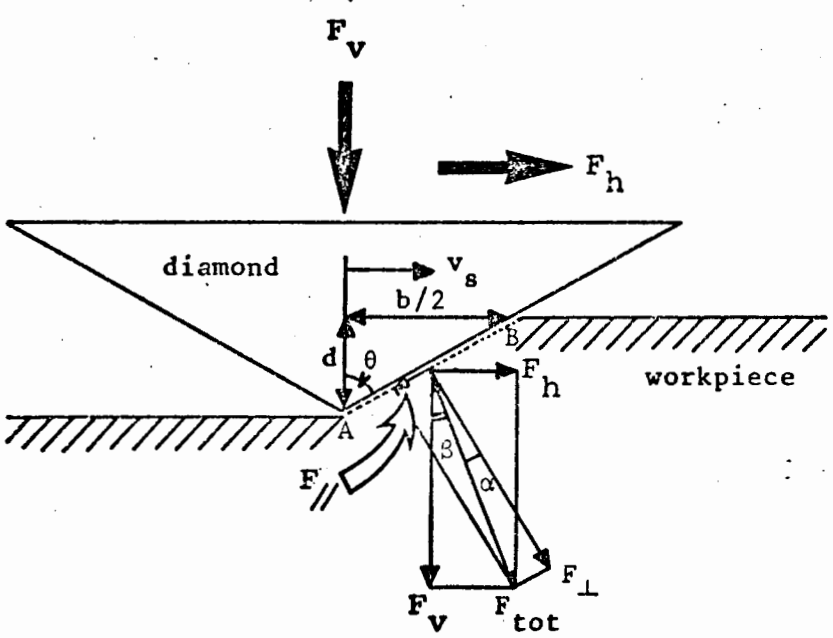

Fig.10.75 Cutting pyramid with one leading plane in contact with the workpiece. (after: Broese van Groenou et al., 1975).

Consider that we have a pyramid (semi-angle θ) with only one leading plane in contact (Fig.10.75). The analysis made by Broese Van Groenou et al., (1975) assumed that the two side faces did not carry any load. If the material is moving upwards with respect to the indentor (case 2) the friction force on the material points downwards (as shown in Fig.10.75.) We can resolve the vertical (F_V) and horizontal (F_H) force components into a total force (F_{TOT}). F_{TOT} is then resolved into two forces, both perpendicular ($F_\perp$) and parallel ($F_{,,}$) to the interface. The compressive $F_\perp$ force leads to failure of the material in front of the indentor, while the $F_{,,}$ force is the Coulomb friction between the material and indentor.

The friction coefficient μ is equal to $\tan \alpha (= F_{,,}/F_\perp)$. β is the angle between F_V and F_{TOT}, so that the force ratio f is:

$$f = \frac{F_H}{F_V} = \tan \beta = \cot(\theta+\alpha) = \frac{\cot \theta - \mu}{1+\mu \cot \theta} \qquad (10.10)$$

It is important to appreciate that a <u>reduction</u> in the Coulomb friction results in an <u>increase</u> in f for the assumed mode of material removal. Since $f = \cot(\theta+\alpha)$ the sign of angle α is critical. If there is no friction force $\mu = 0$, $\alpha = 0$ and hence $f = \cot \theta$. A positive value of α means that f is smaller than $\cot \theta$ (material flow opposite to the analysis presented here).

For the pyramid with two leading planes in contact, assuming pure Coulomb friction <u>without</u> flow ($\alpha < 0$) it can be shown that:

$$f = \frac{\cos \theta + \mu (1+\sin^2\theta)^{\frac{1}{2}}}{2^{\frac{1}{2}} \sin \theta \, [1-\mu \cos \theta (1+\sin^2\theta)^{-\frac{1}{2}}]} \; . \qquad (10.11)$$

f increases with increasing friction at the interface, and conversely decreases with decreasing friction.

For a sphere it may be shown that:

$$f = \frac{(4/3\pi)\alpha + \mu}{1-(4/3\pi)\alpha\mu} \qquad (10.12)$$

$\alpha = \sin^{-1}(b/2R)$ where b is the width of a groove, and R the radius of the sphere. For negligible penetration $\alpha \to 0$ and hence $f = \mu$. Thus, to evaluate the Coulomb friction coefficient μ for a particular material/lubricant interface, measurements are conveniently made using a lightly loaded sphere traversing across a surface.

Knowing the compressive stress σ at the interface and evaluating μ it can be shown that the specific energy S_e is given by:

$$S_e = \sigma(1-\mu \tan \theta) \qquad (10.13)$$

(Pyramid with one leading face)

$$S_e = \sigma[(1+\mu(1+\sin^2\theta)^{\frac{1}{2}})/\cos \theta] \qquad (10.14)$$

(Pyramid with two leading faces)

Since in practical grinding or cutting operations of a brittle solid, chipping and cracking are predominant leading to extensive material removal to the sides of the grooves, the theoretical values of S_e above, are likely to be inaccurate.

We now use out experimental scratching data to determine if and to what extent the present results can be explained by the ploughing theory. In particular, it is of interest to ascertain the direction of material flow at the interface. There are several reasons for this:

1. If a delamination mode of cutting is occurring, then we expect no flow of material over the tool interface, and hence f should be greater than cot θ.

2. In the high temperature scratching experiments, evidence was found for a substantial plastic response. If there is significant flow the deformed material should move upwards with respect to the indentor and a decrease in f(< cot θ) is anticipated.

3. The addition of water, glycerol and heptanol resulted in a reduction in horizontal force from the dry values. A true lubrication action should be reflected by a reduction in interfacial friction μ.

Values of the force ratio, f, were calculated using the data obtained from the scratches made with a sharp pyramid at room temperature (Fig.10.47). The corresponding change in force ratio as a function of vertical load is shown in Fig.10.76.

The data points are the experimental values found, while the full lines are calculated from the least squares analysis of the horizontal force data (Fig.10.47). The value of f at the higher loads (where f tends to be a constant value) is lower for the pyramid in orientation B. The limiting values of f are as follows:

Pyramid Orientation	f (Experimental)	f (Theoretical)
A	0.40	0.285
B	0.31	0.404

For pyramid orientation (A), f(expt) > f(theo.) and this suggests that there should be no upwards flow of material at the interface. The reverse is true of pyramid orientation (B). Unfortunately, no evidence could be obtained from the experiments with the (B) orientation to confirm any different mode of cutting. Certainly, the optical micrographs (Fig. 10.46) do not indicate any significant differences in the appearance of the grooves between the two pyramid orientations. Similar experimental values of force ratio to the present ones were found by Broese van Groenou et al. (1975) for scratches on ceramic materials. These workers also found a similar decrease in f as the vertical load was reduced when scratching Al_2O_3. This was attributed to the influence of a finite tool tip radius (estimated to be $\approx$ 0.5 μm). At low loads this blunting effectively results in a higher value of θ and thus cot θ

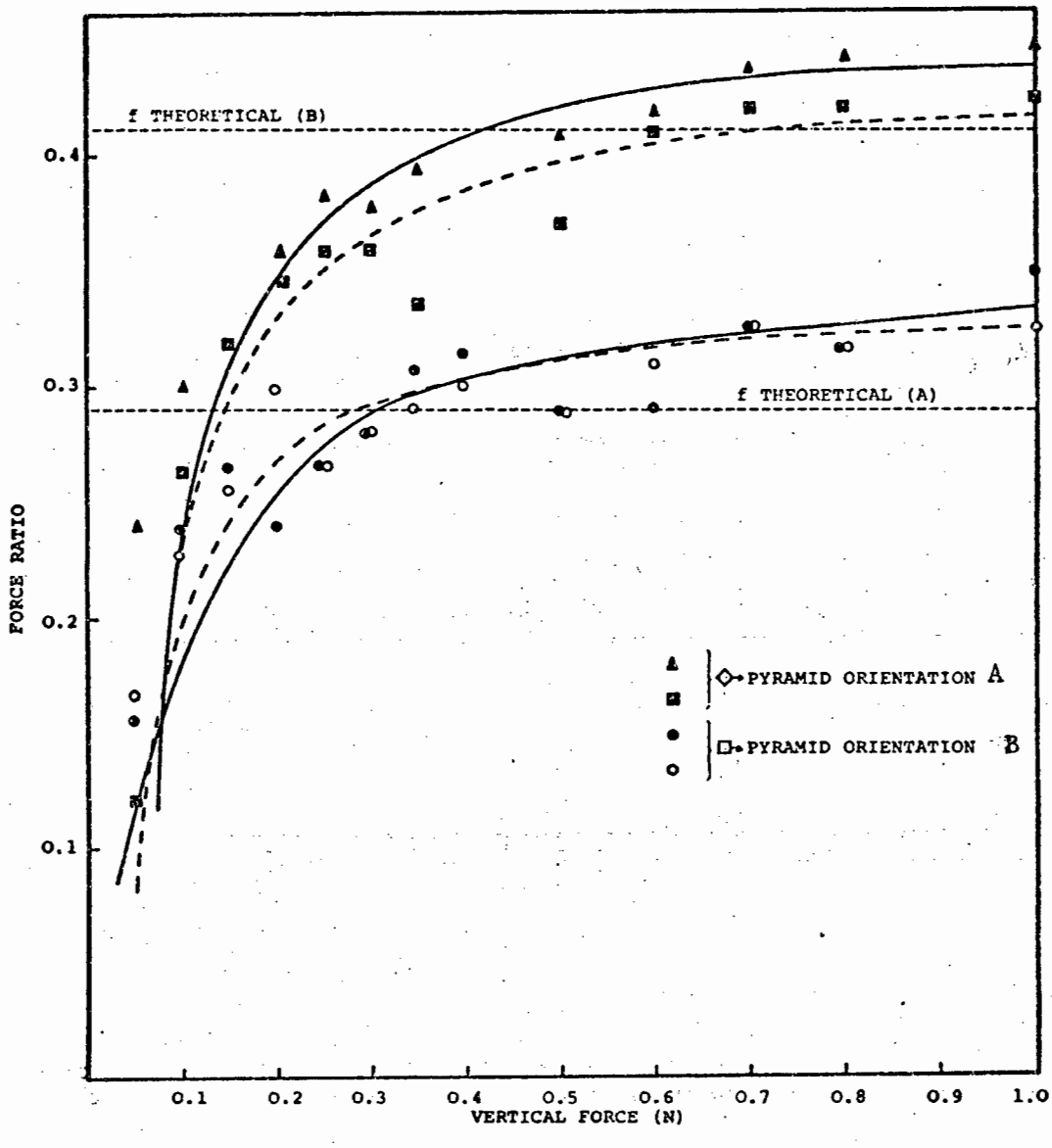

Fig.10.76 Values of force ratio (f) calculated for the two pyramid orientations. The theoretical value of f is also shown. For each orientation, two opposite directions of scratching are indicated. (Z-cut plane, [10$\bar{1}$0] direction).

reduces. It is evident that such an effect will only be manifested on hard materials.

There is some indication that the values of force ratio are higher for scratching with the blunt pyramid. (For example, using the horizontal force data for a blunt pyramid in orientation (A), we can calculate a value $f \approx 0.5$ at a vertical load of 1N. This should be contrasted to the sharp pyramid results which gave $f \approx 0.4$ at 1N). A higher value of f suggests a sharper pyramid ($\theta < 68^{\circ}$). However, if the interfacial friction (μ) is included then from eqn.(10.11), it is possible to show that (for a constant θ) a higher value of μ results in a higher force ratio f. This could well be the mechanism accounting for increased values of force ratio with the blunt pyramid in these experiments.

For the sharp pyramid we may calculate using eqn.(10.11) that at the highest vertical load, (where f is constant ≈ 0.4 and $\theta = 68^{\circ}$) that the friction coefficient (μ) ≈ 0.1. At the lowest load $f \approx 0.1$. Making the assumption that $\theta \rightarrow 90^{\circ}$ in eqn.(10.11) (an effectively blunt pyramid) then $f \approx \mu \approx 0.1$ Thus the value of μ at low loads is approximately equal to the value of μ at the highest loads. If it is assumed that the mode of material removal remains unchanged (i.e. delamination) over the complete load range then we may not expect μ to vary. The experimental results are consistent with such an interpretation.

Values of the force ratio obtained when scratching in dry and water flooded conditions are shown in Fig.10.77. The value of f is lower for wet cutting, and clearly indicates a reduction in friction between the tool interface and crystal. Similar results were obtained for scratching in glycerol and heptanol.

There was little evidence (within experimental error) for changes in the horizontal force as the temperature was increased (see Fig.10.43). This implies that f did not change even though a substatial plastic response was found (Fig.10.38), and that there is no change in material flow direction.

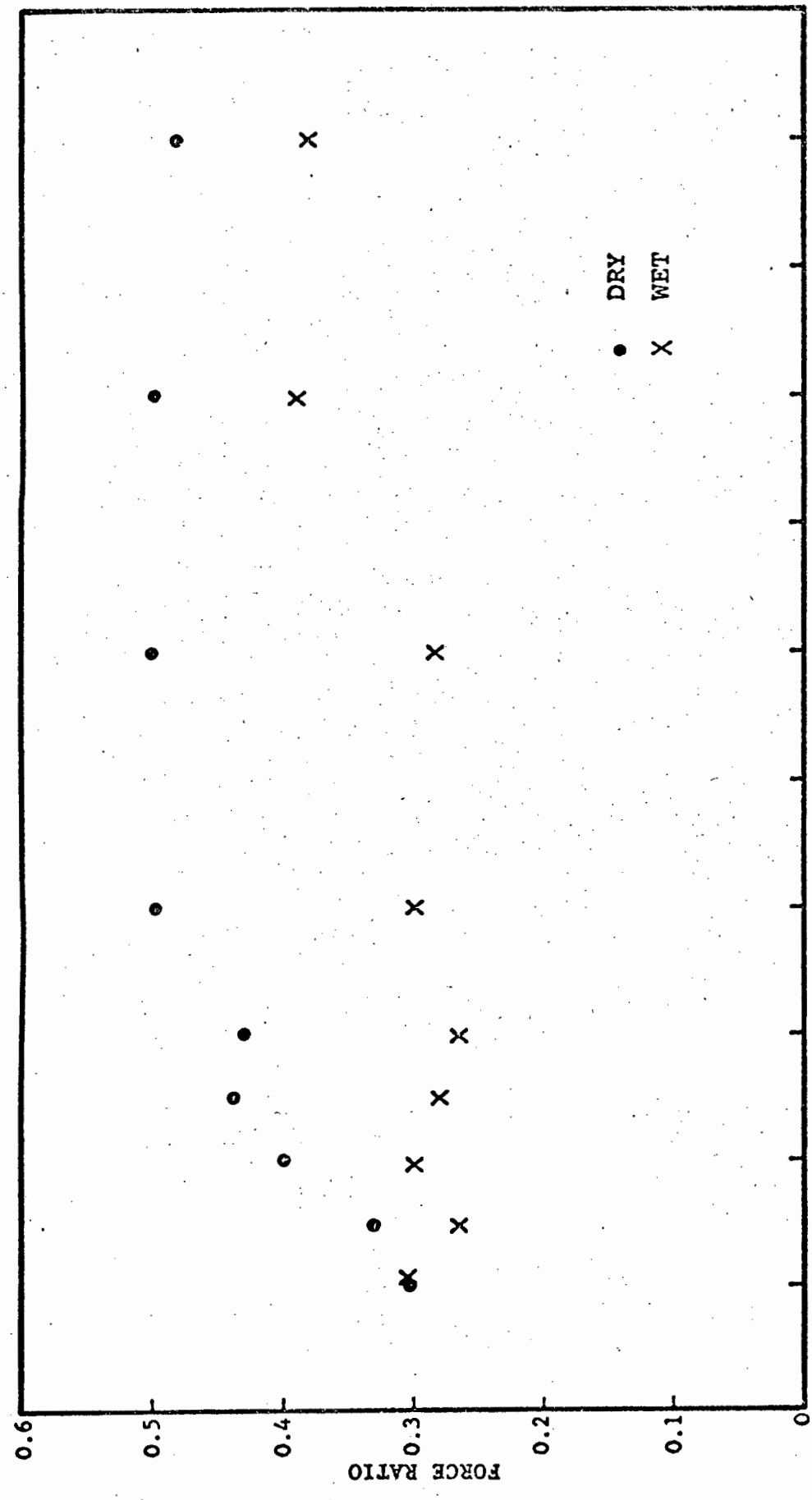

Fig.10.77 Calculated values of the force ratio ($f=F_H/F_V$) for scratches made in dry and wet conditions. Note the reduction in f for wet conditions. (Z-cut plane, blunt pyramid).

10.5.3 A Proposed Theory of Cutting Quartz

Based on our experimental observations, there would appear to be a competition between the generation of partial cone-cracks and the development of a sub-surface 'shear' crack. It is proposed that the fundamental factor controlling cutting is the ease with which cone-cracks (strictly partial cone-cracks in the case of a sliding contact) can be induced in a brittle material. If such cracks can readily be produced then this creation of new surface area absorbs a considerable fraction of the input energy.* Less energy is then available to produce a sub-surface crack. Cutting in this case would be 'hard' and a characteristic Hertzian deformation track would result. If, on the other hand, the generation of partial cone-cracks is difficult, the input energy goes into the development of the shear crack, cutting is 'easy' and occurs by delamination.

The ease of cutting is sensitive to the presence of a lubricant, the ambient temperature and crystallographic direction of scratching. The proposed theory must account for these facts. The most dramatic cutting effects were found when scratching with a blunt or flattened pyramid. With a sharp pyramid it could be that the blunt → transition occurs at loads below the experimental range (< 0.1N). Since delamination was also observed when scratching with a sharp pyramid it is suggested that this interpretation is correct.

This proposed theory should be contrasted to the currently assumed mode of cutting a brittle material, in which material is removed by chip formation in front of the indentor and chipping to the sides of the groove by lateral cracking.

We shall now develop the theory but first it is necessary to examine the static cone-crack fracture data obtained on α-quartz by Hartley & Wilshaw (1973). The stress analysis of Hamilton & Goodman (1966) for a sliding circular contact zone has previously been described (Section 5.5). Although the contact area of our blunt pyramid was not circular, we believe that the stress analysis for a circular Hertzian contact can be broadly applied to our results.

*Footnote on the end of page 360

10.5.4 The Static Fracture of Quartz

The work of Hartley & Wilshaw (1973) demonstrated that the critical load P_c to produce a well-defined cone-crack in α-quartz depends upon the crystallographic face being indented, the temperature and also whether the indentation is made in dry, or moist conditions.

In moist air (Fig.10.78a), at room temperature, the Z-cut plane had a considerably higher fracture load than X or Y. These differences were attributed to differences in Poissons ratio for the various crystal planes. As the temperature was increased, the critical fracture load for Z dropped rapidly, but showed evidence for a peak at ≈ 500 K. By contrast, the X and Y planes showed little temperature dependence. In dry nitrogen (Fig.10.78b) the fracture load for all the planes was increased, relative to moist air. The Z-cut plane again gave the highest value of fracture load, followed by Y and then X. As the temperature was increased the fracture load dropped for all indented planes, but a pronounced peak at ≈ 700 K was found for the Z-cut plane.

To explain their results, Hartley & Wilshaw considered that both lattice 'water' and external atmospheric water could affect the fracture load. Atmospheric moisture could diffuse to the crack tip and hence reduce the strength of the Si-O bond; this effect could operate over the full temperature range. The peaks in the the fracture data were considered to be associated with lattice water, and the mechanism advanced was stress enhanced diffusion of OH^- ions to the crack tip, which could subsequently attack the Si-O bond. Heat treatment experiments (annealing in the range 400-1100 K) showed that the room temperature fracture load increased as the annealing temperature was raised.

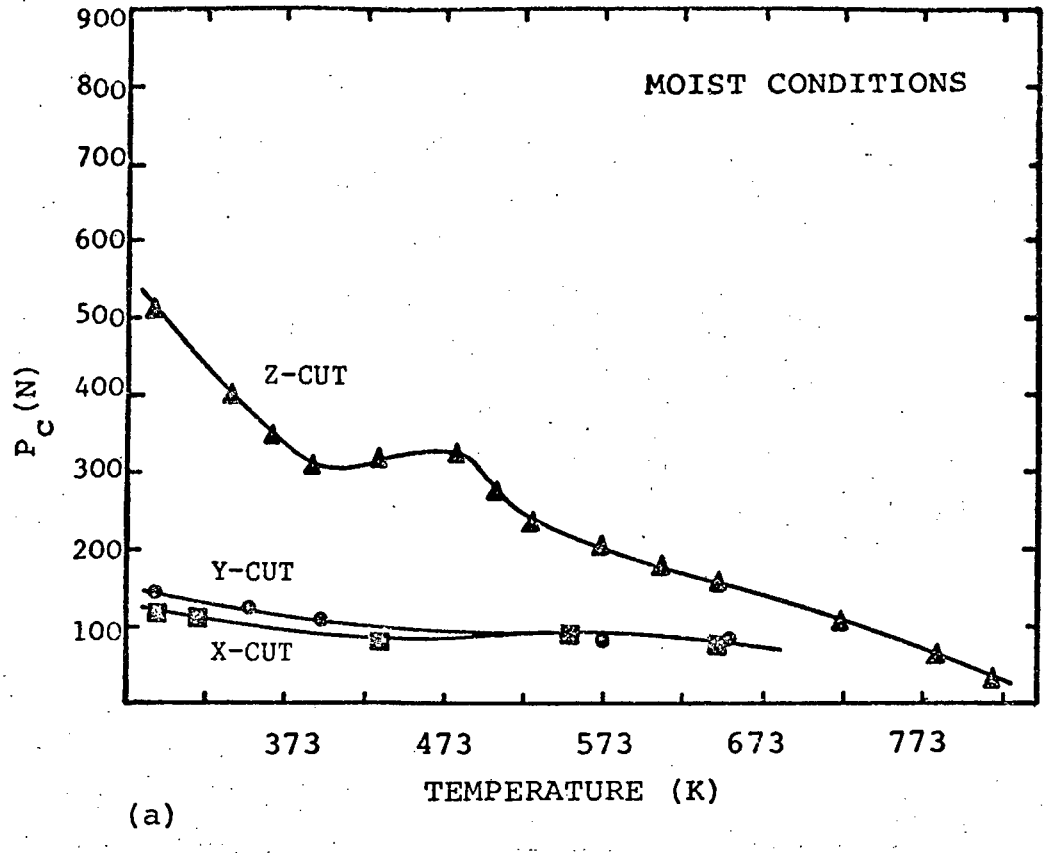

(a)

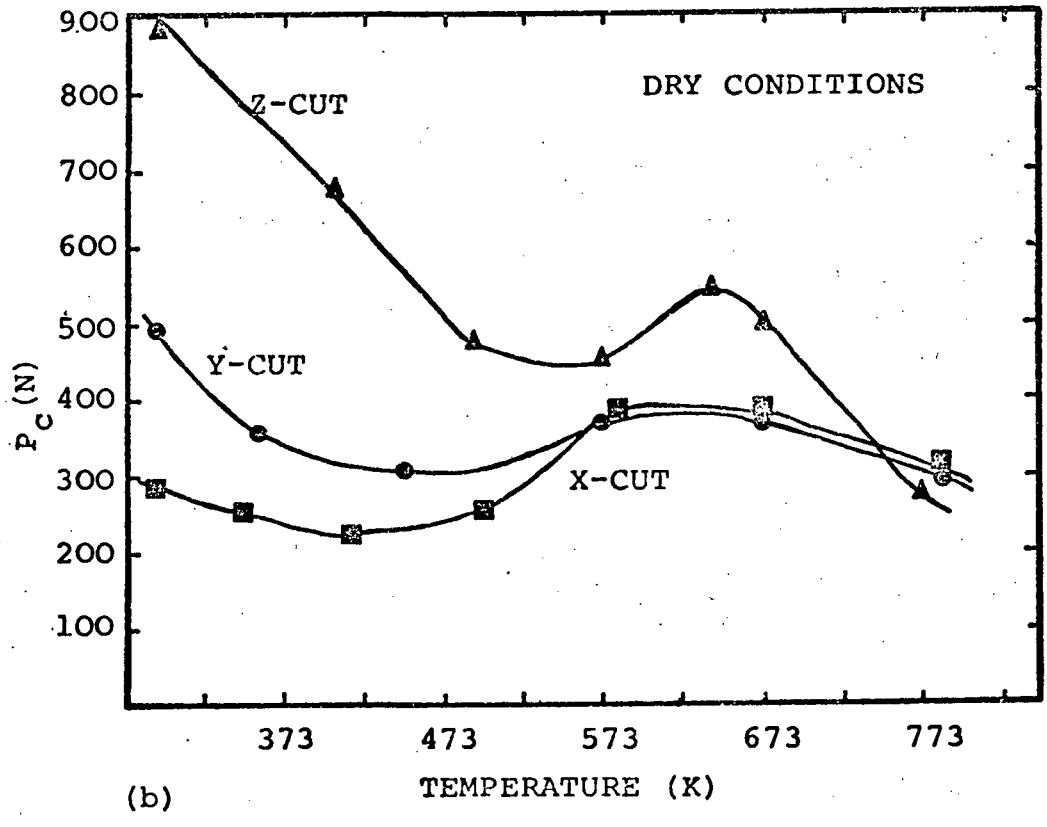

(b)

Fig.10.78 The variation in the critical load (P_c) form a cone crack in synthetic quartz as a function of temperature. (a) Moist laboratory air environment. (b) Dry nitrogen environment. (after: Hartley and Wilshaw, 1973).

10.5.5 The Directional Anisotropy of Scratching

We have proposed that the ease of cone-crack formation determines the mode of cutting and the results of Hartley & Wilshaw (1973) obtained at room temperature in dry conditions suggest that the ease of cutting (i.e. this corresponds to the development of a shear crack) should be:

$$Z(0001) > Y(1\bar{1}00) > X(11\bar{2}0)$$

Our experimental results show that the ease of cutting is sensitive to the crystallographic direction of scratching. We found that on the Z-cut plane cutting was hard in $\langle 10\bar{1}0\rangle$ and easy in $\langle 11\bar{2}0\rangle$. For both the X- and Y- cut planes scratching was harder for the direction [0001], parallel to the c-axis. Similar results have been found by Graham (1972), for scratches made on quartz with a spherical indentor. This author found that more damage (more Hertzian cracking) was found when the direction of scratching was parallel to c[0001]. Thus this corresponds to a 'hard' cutting. Frondel (1962) reports the work of Berndt who found that on planes other than (0001) the scratch hardness is greater parallel to the trace of [0001] than perpendicular to [0001].

Hartley & Wilshaw suggested that since the surface energy γ for quartz is ill-defined, γ is independent of orientation, and cannot account for variations in fracture load for different planes. Instead they proposed that it is the variation in Poisson's ratio ν which controls the initiation tangent of the surface ring crack. Figure 10.79 shows the lines of constant tensile stress acting in the plane of contact of the Hertzian stress distribution for the sliding indentor. Clearly the most intense stress is to the rear, and the arrows indicate the directions of the stress. The magnitude of Poisson's ratio in these highly stressed regions must control fracture initiation.

Once the cone-crack has formed, however, fracture is controlled by preferred cleavage on the rhombohedral planes. A cone-crack fracture analysis by Heavens & Ashbee (1975) showed that, contrary to expectations, fracture is initiated on the z-minor $\{01\bar{1}1\}$ rhombohedral planes, rather than the r-major $\{10\bar{1}1\}$ rhombohedra. The exact orientation of these z-minor planes, with respect to the tensile stress field created by the sliding indentor, may also account for the observed anisotropy of scratching. Thus, in this case, a z-minor $\{01\bar{1}1\}$ plane that is favourably orientated within the Hertzian stress field will be the preferred fracture plane, and a high density of partial cone-cracks will be generated as the indentor translates. In this situation we do not expect 'easy' cutting. It is therefore suggested that a full analysis of the hard and easy cutting directions in quartz must include both the initiation condition (and hence Poisson's ratio) and the subsequent fracture on crystallographic planes.

---

* It is possible to estimate the fraction of input energy going into the formation of these cone-cracks. From the present results (eg. Fig. 10.30), we can estimate a crack density of 10^6/m, and a typical crack size of 10μm wide and 10μm in depth. Assuming the surface energy to be $10 J/m^2$ then only ~0.3% of the input energy (~0.3J) goes into the production of cone-cracks. This implies that the inelastically deformed zone may absorb the remainder of the input energy. If the bulk of the input energy goes into such a plastically deformed zone then, assuming a dislocation line energy of 10^{-9} J/m, in quartz a dislocation density of $10^{18} m^{-2}$ is anticipated, outside of the resolution of the HVEM. This could be a reason for the failure to resolve individual dislocations below the scratch tracks (Fig. 10.24(a)).

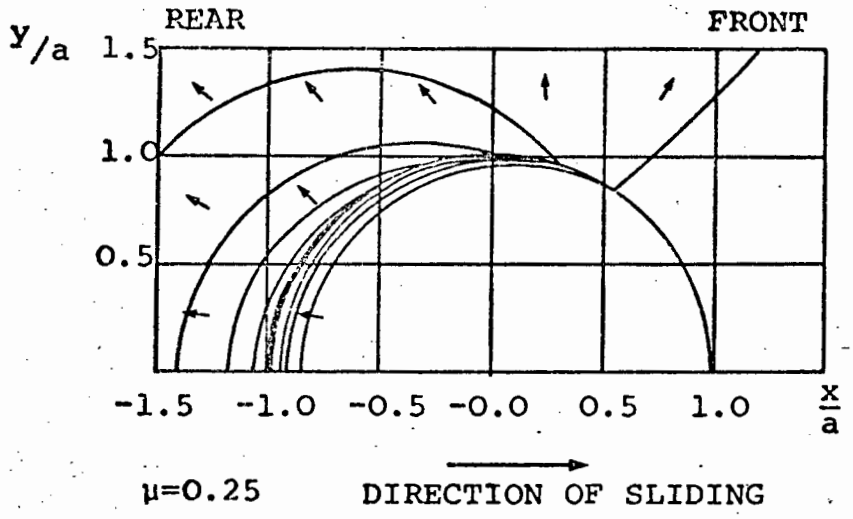

Fig.10.79 Lines of constant tensile stress acting in the plane of contact. (after: Hamilton and Goodman, 1966).

10.5.6 Scratching in Water

To explain why cutting should be considerably enhanced when scratching in water, it is necessary to consider the role of the force ratio (f) on the sub-surface stress field. The data of Hartley & Wilshaw shows that the critical load to form a cone-crack decreases in moist air. In wet conditions we may expect a further reduction in the fracture load (Swain et al. 1973). On the basis of our discussion so far, a reduction in P_c facilitates the generation of partial cone-cracks and hence cutting should be reduced. This is in direct contradiction to our cutting results. Furthermore, we found that scratching in glycerol increased cutting, and we are thus inclined to interpret our result in terms of a stress field effect, rather than to seek explanations in stress corrosion cracking phenomena.

The stress analysis of Hamilton & Goodman (1966) demonstrated that as the coefficient of friction decreases, the magnitude of the tensile stress acting at the rear of the indentor is reduced. In other words cone-cracks are not as likely to form in low friction conditions. Our scratching data (Fig.10.77) shows a clear decrease in f (and hence μ) when the surface of the crystal was flooded with water (or glycerol), and we believe that this reduction, in the likelihood of cone-crack generation is responsible for enhanced cutting. It is consequently more accurate to talk about a 'lubricant' rather than 'environment', and to achieve a good cutting action it is desirable to choose a lubricant which results in the lowest value of interfacial friction at the tool/workpiece interface.

10.5.7 High Temperature Scratching

When scratching at elevated temperatures with a sharp pyramid we noted that in moist conditions (RH ≈ 70%) an increase in temperature to 473 K was sufficient to curtail cutting at low vertical loads. The characteristic Hertzian deformation track was produced instead. The cone-crack data of Hartley & Wilshaw (Fig.10.78a) shows a reduction in the critical fracture load for the Z-cut plane of approximately 50% over this temperature increase. These observations fit our proposed theory because the reduction in P_c allows preferential Hertzian cracking, a reduction in shear cracking and hence negligible cutting. Thus even a sharp indentor is capable of creating a Hertzian field, and this is in accordance with the stress analysis of Swain (1979). Similar trends were also found when scratching at elevated temperatures in dry conditions, and must be related to the same reduction in the critical load as the temperature is increased (Fig.10.78b).

The more extensive cracks extending to the sides of the grooves made in a moist environment (Fig.10.54) may be enhanced stress corrosion cracking, due to a combination of heat and moisture.

The occurrence of an enhanced plastic response is not expected on the basis of our consideration of high temperature microhardness maeasurements, where a constraint factor of 3 was not achieved until $T \gtrsim 900$ K. Examination of Fig.10.37b, shows that at the origin of the track (which is in effect, a static hardness impression) material has not 'piled up'. As the indentor translates, material is pushed to either side of the track (Fig.10.38). A plastic response on the surface and the sub-surface shear crack occur as two distinct phenomena (Fig.10.40), so it is suggested that the surface placticity is a response to the high shear stresses generated at the tool/solid interface. This plasticity is enhanced by the zone of high hydrostatic pressure in the surface regions. The fact that a sub surface crack is observed indicates that dislocation nucleation and slip are still extremely difficult at these temperatures.

10.5.8 The Delamination Theory of Wear

Fig.10.80 compares the widths and depths of some scratches with the microhardness data. It is clear that both the depth and widths of the scratches are greater than may have been expected from the hardness data alone. Hence, the scratch groove cross-section is not a copy of the translating pyramid.

We have demonstrated that the Hertzian contact stress system is applicable to these results on the cutting of quartz. In particular, we now examine the position of maximum 'shear' stress which lies below the contact circle, since it is from here that we may expect sub-surface failure to originate.* We know that the actual position of this maximum depends upon the coefficient of friction (Fig.5.9). For low values of friction this maximum is located at a depth $Z = 0.5a$, where 2a is the contact circle diameter. The corresponding magnitude of the shear stress is $0.35\ p_o$. (p_o is the maximum pressure at the centre of the contact and is given by $3P/2\pi a^2$). Examining the experimental cutting results (Fig. 10.80) we find that at a vertical load of 1N, the depth of cut is $\approx 5\mu m$. If the cut is located at the position of maximum shear stress then this indicates that the contact diameter is 20 μm and the maximum pressure p_o is 4.8 GPa.

Since $\sigma_y/p_o = 0.35$ (Hamilton & Goodman, 1966) we obtain a yield stress of 1.7 GPa. This value is close to the theoretical shear stress of quartz. Clearly, however, the magnitude of the stresses must depend critically upon the contact geometry details, as well as the coefficient of friction. Our calculation does give the correct order of magnitude and hence indicates that this line of attack may have some merit; in other words, dislocation nucleation and slip may be occurring below the translating indentor.

Suh and co-workers (Suh, 1977) have developed a delamination theory of wear which has found applicability primarily to metals. This theory indicates that cracks are nucleated

*By shear crack we mean a crack which develops due to Mode II loading.

preferentially below the surface during asperity contact, because the component of hydrostatic pressure in the surface contact zone suppresses fracture. The sub-surface crack can eventually propagate to the surface and wear sheets delaminate. The actual thickness of the wear sheet is controlled by the coefficient of friction and material properties.

The following sequence leading to delamination is postulated (Suh, 1977):

(a) Two sliding surfaces come into contact. The asperities of the softer surface are easily deformed or fractured by the repeated loading action.

(b) The rough surface becomes smoothed; there is a change from asperity-asperity contact, to asperity-plane contact.

(c) Cracks are now nucleated below the surface.

(d) Further loading and unloading (fatigue) propagates these cracks parallel to the surface.

(e) The cracks can reach the surface. The propagating end of the crack is situated behind the moving asperity, and the crack reaches the surface after the asperity has moved over the crack. Thus, the wear sheet lifts up from the surface as shown schematically in Fig.10.81.

Bearing the above in mind, and considering the present experimental results on quartz we can make the following remarks:

(1) Our multiple scratching tests show that on repeated loading the asperities within the scratch groove show evidence for plastic deformation (Fig.10.66). The rough surface will eventually become smooth and polished. Also, a cut could be produced on multiple scratching where in the single pass scratching experiment, only the Hertzian deformation zone occurred. There is thus a 'fatigue' effect in quartz.

(2) The wear particles do lift up as shown in the schematic diagram (Fig.10.81). The side view of a scratch (Fig.10.23) shows this clearly.

(3) Examination of scratch debris (Fig.10.11) amply demonstrates that quartz can wear by delamination. The essential difference between the wear by delamination of a metal to a brittle solid, is the formation of partial cone-cracks in the latter class of solid.

The exact origin of the shear crack remains a problem. In quartz only a single pass is sufficient to generate this crack, whereas in the metallic case it is evidently seen as a fatigue effect. The generation of dislocation and their subsequent slip can presumably lead to pile-ups and the formation of cracks. Sub-surface flaws may also develop into propagating cracks. For the low load scratches made on quartz, multiple passes are necessary to generate wear sheets. Only at higher loads does one pass suffice to produce the crack. We lack any evidence for dislocation processes in the maximum shear stress region during the cutting of quartz, but postulate that the magnitudes of the stresses are high enough to nucleate dislocations. This is analogous to the hardness observations. The way in which the stress distribution changes as the indentor translates across the surface may then be responsible for the development of dislocation pile-ups and crack nucleation. Finally we should note that the shear crack may interact with the partial cone-cracks, and hence aid material removal.

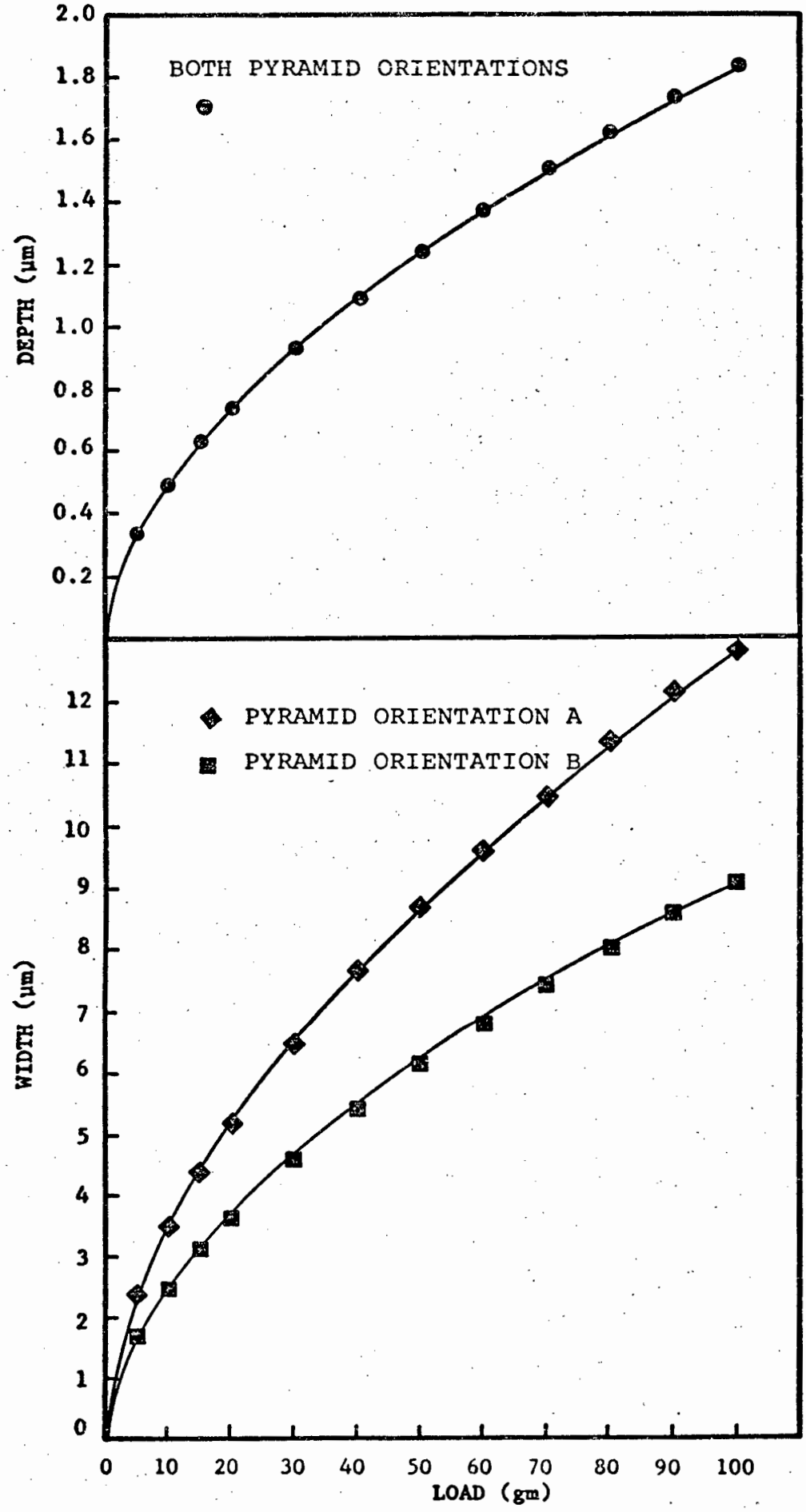

Fig.10.80 The widths and depths of scratches which are to be expected if the scratch groove is a perfect 'copy' of the vertically loaded pyramid tool. These values should be compared to actual scratching results. (eg. figs. 10.15, 10.16, 10.28 and 10.48).

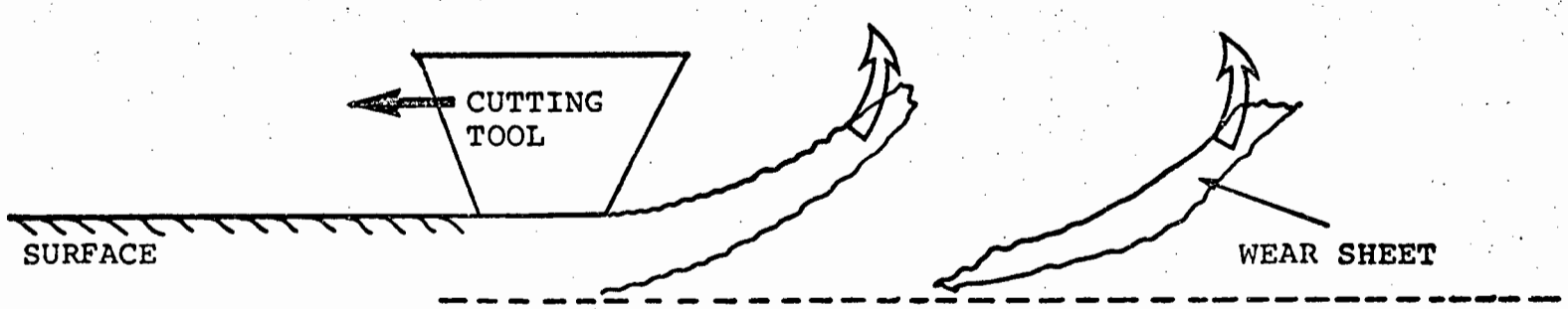

Fig.10.81 The delamination theory of wear. Observed mode of wear sheet uplift. (see Suh, 1977, fig.4).

10.5.9 Lateral Cracks-Spalling

In the discussion so far, we have adopted the theme that when quartz is cut with a vertically loaded Vickers pyramid, delamination rather than lateral cracking is the mechanism of wear. Swain (1979) finds that when soda-lime glass is cut by a similar (sharp) pyramid, the extent of lateral cracking is reduced at higher loads. (We should note that Swain assumes the mode of cutting to be by a lateral crack formation). From the micrographs he presents (see his Fig.10) we suggest that there may be a change to delamination at these higher loads (≈ 4N). Our results indicate that lateral cracking may be extensive at lower loads, but specifically when scratching with a pyramid which is just developing a blunt tip.

If the total width of a scratch track is 2a, and the total extent of lateral cracking is 2c then it may be shown (Swain, 1979) that

$$\frac{K}{\beta\, Ha^{\frac{1}{2}}} = \frac{1}{\pi^{\frac{1}{2}}} \left(\frac{a}{c}\right)^{\frac{1}{2}} \left[1 - \left(\frac{a}{c}\right)^2\right]^{\frac{1}{2}} \qquad (10.15)$$

where K is the stress intensity factor and β is related to the residual stress about the scratch.

For quartz, a value of γ = 10 J m^{-2} leads to a (c/a) ratio, according to expression (10.15) of 5. Swain (1979) indicates that quartz does indeed show these experimental values during scratching.

Fig.10.51 is a lateral crack produced during a scratching test on quartz. A value of c = 12 μm and a = 2.5 μm yields (c/a) ~ 5, in agreement with Swain. In this case the value of K is at the K_{IC} catastrophic crack propagation limit (Atkinson, 1979). Fig 10.52 is another lateral crack. Here c = 30 μm, a = 2.5 μm and hence (c/a) ≈ 12. This yields an effective value of $\gamma \approx 1.5$ J m^{-2} using expression (10.15).

We postulate that in this latter case stress corrosion cracking must have assisted the growth of the crack. Recent results of Atkinson (1979) examining slow crack growth in quartz using the double-torsion test configuration, suggest that a value of γ(1.5 J m^{-2}) corresponds to a crack velocity $v \approx 0.01$ μm s^{-1} (tested in air, RH ≈ 68%, at 20°C). Thus our spalls would take ≈ 60 minutes to develop fully. The observation that spall uplift can take place long after the pyramid passed over the surface is thus explained.

No evidence was obtained during the majority of the scratching tests for lateral crack formation. These cracks must be extensive and well developed for such a designation. Instead the results confirm that quartz cuts by a delamination mode of wear.

The reason why spalling is only observed at low loads ($\lesssim$ 0.3N) during a blunt → sharp cutting transition is unknown, but may be related to the residual stress field being particularly intense under these circumstances.

CHAPTER 11

GENERAL DISCUSSION

11.1 Review

Quartz is a complex material, and it is evident that the lattice impurities have a major influence on both the brittle and plastic responses. Hydrogen, either in the form of H^+ or bonded to the oxygen sub-lattice, appears to be the most active impurity, although alkali ions (Li^+, Na^+) will take part in the overall defect structure. Unfortunately, the exact way in which these impurities are incorporated is poorly understood, although certain generalisations have assisted in explaining their influence upon the mechanical properties of quartz. It is clear that the interpretation of plasticity experiments has been hampered by the apparent inability to homogenize the 'water' content of the crystals, so that deformation is concentrated in certain zones of the sample. Only by careful consideration of these zones and their different, or similar impurity and deformation structures can one hope to understand the precise role of impurities. As an aid to the correlation of results from different laboratories it would be worthwhile to consider specifying the impurity content (hydrogen, alkali ions) from different zones of a deformed crystal, rather than the average content as is currently the case.

Turning now to the Von Mises problem in quartz, we have found that the exact mechanical response will be affected by this slip system criterion. The plastic response can only be facilitated if five independent slip systems are activated, but under conditions where dislocation climb processes can

operate this restriction is relaxed. Favourable deformation parameters for climb are elevated temperatures and slow strain rates. At room temperature climb will be too slow to allow Von Mises to be relaxed, and consequently placticity at low temperatures is associated with the operation of the necessary slip systems. Favourable conditions for this include an applied hydrostatic pressure and a constraint of the deforming material, both of which are typical under indentation. If five independent slip systems cannot operate or if temperatures are too low to allow dislocation climb, then quartz will fracture.

11.2 Geological Implications

In the earth's crust a rock may deform by elastic, plastic or brittle processes, and the exact response depends on the differential stress, temperature and also time. At the lowest temperatures we may expect shear failure to be dominant. Since quartz shows a static fatigue effect, then the presence of water located in fissures or pores must result in a reduced strength on the geological time scale. It is not expected that intrinsic hydrogen defects can diffuse rapidly enough within the quartz lattice at low temperatures, so that the influence of lattice water on the strength at these temperatures will be small.

As the temperature increases we may expect dislocation glide processes to make a contribution to deformation. For quartz this means that the hard <a + c> slip system must operate if a general change of shape is to result. However, only under conditions of high hydrostatic pressure does it appear that quartz will satisfy the Von Mises criterion at low temperature, and it is expected that brittle failure, rather than dislocation slip, will predominate under crustal conditions.

At temperatures approaching 800K diffusional processes become significant, permitting the climb of dislocations. It is in this regime that the Von Mises restriction is relaxed, and a change of shape can occur. The strain rate supported is dependent upon the diffusion coefficient of ionic species, the differential stress and the temperature.

It is apparent that the hydroxyl ion diffusion controls deformation in quartz. Fig.11.1 shows a deformation map for quartzite, grain size 1 mm, derived by White (1977). On this map lines of constant stress are drawn, as a function of temperature and differential stress. The dominant mode of deformation is also indicated. Grain boundary deformation (Coble or Nabarro-Herring creep) is only significant at low differential stresses. The Nabarro creep field was calculated using the diffusivity of OH ions in the quartz lattice. Grains orientated favourably within the polycrystalline matrix will deform by dislocation creep (slip plus climb), while in the case of a grain with the [0001] axis parallel to the maximum stress axis, only a climb mechanism can provide a change of shape. Since Nabarro creep is slower than dislocation creep it is anticipated that the pure climb process will be rate determining, and the strain rate in the crust will reflect that predicted by the Nabarro equation. On Fig.11.1 the dashed line indicates the boundary where Nabarro creep is one order of magnitude slower than dislocation creep, and can accommodate 10% of the strain. A component of strain must also come from the grain boundary diffusion processes. It is therefore concluded that quartzite in the earth's crust deforms by the mechanism of slip plus climb, pure climb and grain boundary diffusion. The strain rates supported by these mechanisms are $\approx 10^{-10} - 10^{-18}\ s^{-1}$.

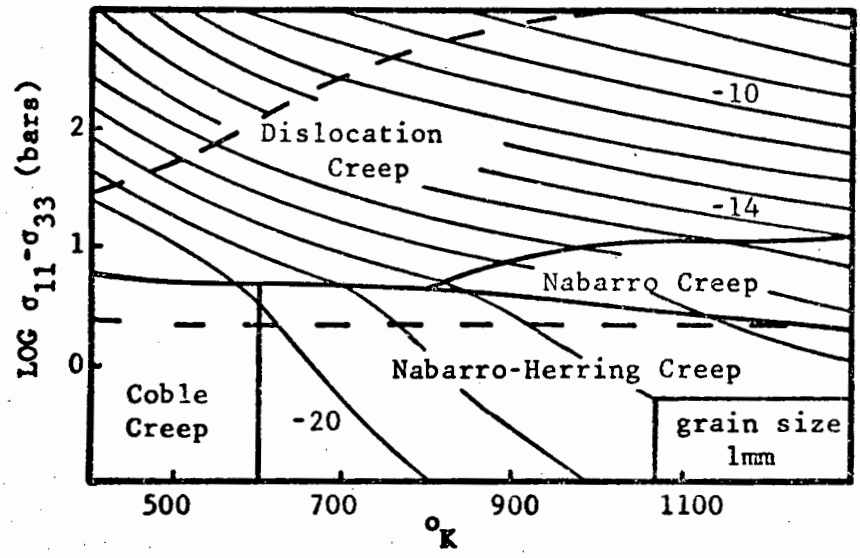

Fig.11.1 Deformation map for quartz showing the field for dominant Nabarro creep. The upper dashed line marks the limit where Nabarro creep is one order of magnitude slower than dislocation creep. The bottom dashed line marks a similar limit for dislocation creep in the diffusion creep fields. Strain rate contours, log sec^{-1} are shown. The values of Log $\sigma_{11}-\sigma_3$ are based on values of the shear modulus at 1200K. (after: White, 1977).

11.3 Practical Application

The present work has demonstrated that much relevant information on the diamond drilling process may be obtained from a study of single and multiple pass scratching experiments. In this particular case single crystal quartz was cut; the extension to a study of polycrystalline quartz, where the influence of grain boundaries introduces another variable is now warranted.

The basic mechanism of cutting, or wear, depends critically upon the state of the individual diamonds which comprise the tool bit, and a complex interplay of the vertical load per diamond and degree of lubrication. Unexpectedly, chemo-mechanical effects were found to be unimportant, but we return to this point later.

It is anticipated that the diamond cutting points will be running in a blunt condition during a drilling operation. In this case, in order to achieve a full cutting action (delamination) the vertical load per point must be high enough to generate a sub-surface shear crack propagating parallel to the surface. This is assisted by the presence of a lubricant, since the tensile stresses to the rear of each cutting point will be diminished and there will be fewer partial cone-cracks formed to absorb the available input power.

It is to be noted that high temperatures caused by frictional heating are expected in the vicinity of the tool bit/workpiece. This will create a substantial plastic zone at low strain rates (low rotational speeds of the drill bit). Experimental results at high temperatures (obtained up to and including 800K) indicate that elevated temperatures have no significant effect on cutting performance, provided the partial cone cracks can be suppressed. This suggests that water is <u>not</u> a good lubricant since a severe environmental interaction is anticipated.

There is much evidence in the literature which indicates that normal alcohols are effective chemo-mechanical cutting agents. However, our results show no significant benefits to be gained from cutting in heptanol, a normal alcohol which in contact with quartz gives a zero ζ-potential, a maximum in the pendulum hardness and hence a favourable brittle response. Recent work by Ishido and Mizutani (1980) indicates that at $\zeta = 0$, the compressive strength of quartzite is a minimum. This is attributed to the influence of the ζ-potential on slow (sub-critical) crack growth. However, we have indicated that slow crack growth is probably not an important contributor to material removal at high rates of cutting.

The specific energy showed an increase with decreasing vertical load. When scratching in dry conditions with a blunt diamond, the cutting action was negligible after one pass of the tool, but after several passes, a cut did develop. With the addition of a lubricant a full cut was produced after a single pass. Clearly the effect of the lubricant is to generate a cutting action in the low vertical load regime. In dry conditions the specific energy is high, tending to an infinite value for the single pass scratch. Thus, a drilling experiment, undertaken such that the vertical load per cutting point is low will be extremely sensitive to the lubrication conditions. At a higher vertical load, where a cut is produced in both dry and wet conditions, the rate of bit penetration and consumption of energy should be independent of whether there is lubrication or not. However, we recognise that the effectiveness of any particular lubrication will shift the vertical load at which the transition from the Hertzian cracking to shear cracking occurs. Thus a drilling experiment which runs over a long time period could well result in significant differences in drilling rates for the different lubricants. The single point scratching experiment is not sensitive to small changes in such conditions.

This may also explain why there is a correlation between the ζ-potential and drilling rate. It is important to recognise that relatively small differences in cutting behaviour can lead, at a practical level, to large and significant variations in performance.

However, Cooper and Berlie (1976) suggest that a different interpretation of environment on cutting rate is plausible. They deduce that drilling in normal alcohols reduces the wear of the diamonds on the drill bit, whereas in water the diamond wear is more rapid and the rate of bit penetration quickly slows. Our scratching tests convincingly demonstrated that a sharp pyramid can rapidly blunt when in contact with quartz after a short sliding distance (estimated to be ~ 15cm). Diamond wear is hence a significant feature in the total drilling analysis.

The above mechanisms of cutting quartz with a diamond pyramid have to some extent been recognized by Spink (1972). This author examined the nature of the diamond drilling process in rocks. Of significance is the fact that the Hertzian fracture mode was proposed as a possible mechanism of material removal in real drilling operations. The alternative mechanism Spink suggested was abrasion, by which the diamond indentor sinks into the rock and material is displaced and detached. On the basis of our results an abrasive mode is not important whiledelamination as a mode of cutting is the significant feature.

In diamond drilling energy is consumed in the following ways:

(a) Surface energy of new surfaces produced.
(b) Elastic strain energy.
(c) Plastic work at crack tips and in the bulk.
(d) Friction between the indentor (diamond) and workpiece.

In real rock drilling two additional processes consume energy (Spink, 1972):

(a) Friction of the bit matrix on the rock.
(b) Secondary breakage of detached particles.

Spink suggests that in Hertzian fracture, below a cutting bit, friction on the indentor is reduced, since the overall contact area per diamond is less, and in addition, friction between the bit matrix and rock is smaller. Secondary breakage will also be diminished because of lower bit pressures.

From a consideration of experimental results achieved with a diamond drilling bit cutting different types of rock, Spink also indicated that his abrasive mode of fracture consumes three to four times more energy than Hertzian fracture. However, while the energy consumption is an important consideration in drilling operations, the rate of penetration of the bit may be of more economic significance. Our results indicate that when Hertzian fracture is significant, then this is not a favourable load regime to cut in. The material removal rate is low, and specific energy high. It is of benefit to increase the vertical force per diamond to achieve cutting by delamination.

Finally, we wish to point out the significance of the Auerbach law and suggest that a consideration of this empirical relationship may be of importance to the design of diamond drilling bits.

We have found that to promote cutting by delamination, the partial cone-cracks must be suppressed. This means that the friction between the indentor and workpiece should be low. We have already indicated that in the Auerbach regime the static Hertzian fracture load (P_c) is proportional to the radius (R) of the indentor, while at higher loads the fracture load obeys the Hertzian analysis, for which $P_c \alpha R^2$. It is clearly

desirable that the fracture load should depend on a high power of the radius.

In a sliding contact the Auerbach fracture criterion is modified and depends upon the coefficient of friction μ, (Gilroy and Hirst, 1969). For high values of coefficient of friction the Auerbach law is obeyed up to large indentor radii. For a low μ system the $P_c \propto R^2$ behaviour sets in at lower radii. In the intermediate range of coefficient of friction, it is possible to compensate for a fairly high value of μ by increasing the effective radii of the diamonds. This approach may also be of significance to mechanised methods in the mining industry where large tungsten carbide wear bits are used to cut rock. Because of the empirical nature of the Auerbach law, the ideal combination of diamond radius and lubricant should be selected on the basis of controlled experimentation such as single point sliding tests.

CHAPTER 12

CONCLUSIONS

1. The deformation of quartz crystals compressed along their c[0001] axes at temperatures between 800-1000 K occurs by the climb of a$\langle 11\bar{2}0\rangle$ and c[0001] dislocations, and can be analysed by the model of Nabarro (1967). No evidence for the operation of slip systems involving dislocation of the type a + c $\langle 11\bar{2}3\rangle$ was obtained.

2. The use of experimental and published data suggests that the diffusion coefficient of the rate-controlling ionic species during creep deformation can be expressed as

$$D = 8\ 10^{-17} \exp(-82/RT)\, m^{-2}\, s^{-1} \quad .$$

The activation energy (0.85 eV) is close to that reported for hydroxyl ion diffusion.

3. It is evident that impurities incorporated within the quartz lattice play an important role in the plastic deformation behaviour. The principle impurity is a hydrogen defect, probably involving an hydroxyl ion and an oxygen vacancy.

4. Annealing experiments have shown that the hydrolytic weakening phenomenon in quartz may be visualized as a surfeit of dislocations (or potential dislocation sources) and their rapid climb by a vacancy absorption mechanism.

5. It has been discovered that dislocations in quartz can scatter light. It is probable that impurity or vacancy clouds in the vicinity of dislocations are responsible for the optical milkiness seen on annealing 'wet' quartz at low temperatures ($T < 1100$ K).

6. The room temperature Vickers indentation of quartz is elastic-plastic, with a constraint factor C' ~ 1.3. HVEM analysis indicated a high density of dislocations at the apex region of the impression, consistent with the above.

7. During room temperature the resolved shear stress was calculated to be approximately equal to the theoretical shear stress (~ 5GPa). There was no evidence for slip band formation by the glide of dislocations of the easy slip systems.

8. An analysis of published data on the high temperature hardness of quartz, coupled with a consideration of the heat treatment and creep deformation results has shown that the hardness test is a convenient method to obtain data on deformation mechanisms at elevated temperatures. It is emphasized that the localised nature of the indentation stress field must be appreciated, and that the use of HVEM is an essential tool in such studies.

9. In view of the above, this study has clarified the Von Mises (1928) change of shape problem in quartz. Three distinct deformation regimes can be discerned.

(i) For temperatures below approximately 800 K all slip systems are equally difficult to activate and will only operate at high applied stress levels. To achieve a change of shape without shattering, a high confining pressure must be applied.

(ii) For temperatures in the range 800 - 1100 K the climb motions of dislocations begin to make an important contribution to deformation. A change of shape may now occur by the climb of $\underline{a}\langle 11\bar{2}0\rangle$ and $\underline{c}[0001]$

dislocations without the necessity for the operation of the hard <a+c> slip systems.

(iii) At temperatures in excess of 1000 K, <a+c> systems can be activated at reasonable pressures. A general change of shape can be accomplished solely by dislocation slip processes, without the need for a confining pressure.

The frequent observation that quartzite from the earth's crust shows the development of a dislocation climb structure is thus adequately explained.

10. It has been established that the mode of scratch deformation, when cutting quartz, is a function of the cutting tool geometry and also the degree of lubrication.

11. A sharp diamond cutting point was found to wear and blunt rapidly. Under these cutting conditions a directional anisotropy of cutting quartz was found. It is suggested that this effect is due to the directional variation in the value of Poisson's ratio, and also the orientation of the rhombohedral z-minor cleavage planes with respect to the sub-surface stress distribution below the sliding contact.

12. Cutting results obtained using a vertically loaded Vickers pyramid have been interpreted in terms of the sub-surface stress distribution of a sliding Hertzian contact. In such an analysis the coefficient of friction and position of maximum shear stress determine the cutting response. A low coefficient of friction is found to be beneficial for cutting since this reduces the likelihood of the development of partial cone cracks in the wake of the contact, and the

available input energy is used to generate a sub-surface shear crack. Quartz thus cuts by the mechanism of delamination.

13. It is believed that chemo-mechanical and environmentally active agents may be of secondary importance to the dominant effect of lubrication efficiency.

14. The single point scratching test, performed under controlled conditions enables the efficiency of cutting to be determined. However, multiple pass tests have indicated that the energy to remove unit volume of material is high for the first scratch and that this gradually reduces to a steady state value after a number of scratches along the same track. A full analysis of such tests must therefore include some information on multiple pass scratching to be of any practical benefit.

15. Information obtained from high temperature scratches in a dry environment suggests that both plastic and brittle behaviour occur together. A zone of enhanced placticity is located in the near surface region but does not appear to hamper the development of the sub surface shear crack. However, water at elevated temperatures is particularly reactive with quartz and this increases cone-crack formation during scratching. This reduces the development of the shear crack and hence the cutting efficiency falls. Water may thus not be a good lubricant in real rock drilling operations, where elevated temperatures are anticipated at the bit/workpiece interface.

REFERENCES

ASHBY, M.F., VERRALL, R.A.: In: Creep of engineering materials and of the earth. The Royal Society, London, (1978).

ATKINSON, B.K.: A fracture mechanics study of subcritical tensile cracking of quartz in wet environments. Pure and Appl. Geophys., 117, 1011-1024, (1979).

AYENSU, A., ASHBEE, K.H.G.: The creep of quartz single crystals, with special reference to the mechanism by which water accommodates dislocation glide. Philos. Mag., 36, 713-723, (1977).

BAËTA, R.D., ASHBEE, K.H.G.: Slip systems in quartz: I., Experiments. Amer. Mineral., 54, 1551-1573, (1969a).

BAËTA, R.D., ASHBEE, K.H.G.: Slip systems in quartz: II., Interpretation. Amer. Mineral., 54, 1574-1582, (1969b).

BAËTA, R.D., ASHBEE, K.H.G.: Mechanical deformation of quartz, I. Constant strain-rate compression experiments. Philos. Mag., 22, 601-624, (1970).

BALL, A., WHITE, S.: On the deformation of Quartzite. Phys. Chem. Minerals, 3, 163-172, (1978).

BAMBAUER, H.U., BRUNNER, G.O., LAVES, F.: Light scattering of heat-treated quartz in relation to hydrogen-containing defects. Amer. Mineral., 54, 718-724, (1969).

BASTIN, J.A., MITCHELL, E.W.J.: Light scattering from heat treated synthetic quartz. Amer. Mineral., 46, 1227-1244, (1961).

BLOSS, F.D.: Anistropy of fracture in quartz. Am. J. Sci., 225, 214-225, (1957).

BRACE, W.F.: Behaviour of quartz during indentation. J. Geol., 71, 581-595, (1963).

BROESE VAN GROENOU, A., MAAN, N., VELDKAMP, J.D.B.: Scratching experiments on various ceramic materials. Philips Res. Repts., 30, 320-359, (1975).

BÜCKLE, H.: Progress in micro-indentation hardness testing. Met. Revs., 4, 49-100, (1959).

BÜCKLE, H.: In: The science of hardness testing and its research applications. eds. Westbrook, J.H., Conrad, H. American Society for metals, Ohio, (1973).

BURTON, B.: In: Vacancies'76. eds. Smallman, R.E., Harris, J.E. The Metals Society, London, (1977).

CADY, W.G.: Piezoelectricity. McGraw-Hill, New York, (1946).

CANNON, W.R., SHERBY, O.D.: Third power stress dependence in creep of polycrystalline nonmetals. J. Am. Ceram. Soc., 56, 157-160, (1973).

CHANG, R.: Creep of Al_2O_3 single crystals. J. Appl. Phys., 31, 484-487, (1960).

CHOUDHURY, A., PALMER, D.W., AMSEL, G., CURIEN, H., BARUCH, P.: Study of oxygen diffusion in quartz by using the nuclear reaction $O^{18}(p,\alpha)N^{15}$. Sol. St. Comm., 3, 119-122, (1965).

COE, R.S., PATERSON, M.S.: The α-β inversion in quartz: A coherent phase transition under nonhydrostatic stress. J. Geophys. Res., 74, 4921-4948, (1969).

COOPER, G.A., BERLIE, J.: On the influence of the flushing fluid during diamond drilling. J. Mats. Sci., 11, 1771-1775, (1976).

DODD, D.M., FRASER, D.B.: The 3000-3900 cm^{-1} absorption bands and anelasticity in crystalline α-quartz. J. Phys. Chem. solids, 26, 673-686, (1965).

EVANS, A.G.: Quasi-static solid particle damage in brittle materials. Rockwell international rpt. No. N00014-75-C-0669, (1976).

EVANS, A.G.: In: Fracture mechanics applied to brittle materials. A.S.T.M. special publication 678. A.S.T.M., Philadelphia, (1979).

EVANS, B., GOETZE, C.: The temperature variation of hardness of Olivine and its implications for polycrystalline yield stress. J. Geophys. Res., 84, 5505-5524, (1979).

EVANS, H.E., KNOWLES, G.: A model of creep in pure materials. Acta. Met., 25, 963-975, (1977).

EVANS, H.E., KNOWLES, G.: Dislocation creep in non-metallic materials. Acta. Met., 26, 141-145, (1978).

FATHERS, D.J., TANNER, B.K.: Line defects in Barium Titanate observed by polarized light microscopy. Philos. Mag., 28, 749-770, (1978).

FRASER, D.B.: Impurities and Anelasticity in crystalline quartz. In: Physical Acoustics, V.5, 1968, ed. Mason, W.P., Academic Press, New York.

FRONDEL, C.: The system of mineralogy. Vol.III: Silica minerals. John Wiley & Sons, New York, (1962).

GANE, N.: The direct measurement of the strength of metals on a sub-micrometre scale. Proc. Roy. Soc. Lond., (A) 317, 367-391, (1970).

GILMAN, J.J.: In: The science of hardness testing and its research application, eds. Westbrook, J.H., Conrad, H. American Society for metals, Ohio, (1973).

GILROY, D.R., HIRST, W.: Brittle fracture of glass under normal and sliding loads. Brit. J. Appl. Phys. (J.Phys. D), 1784-1787, (1969).

GRAHAM, J.: Damage induced by a sliding diamond - An approach to hard rock drilling. Rock Mechanics, 4, 191-202, (1972).

GRIFFITH, A.A.: The phenomenon of rupture and flow in solids. Phil. Trans. Roy. Soc. Lond., A 221, 163-198, (1920).

GRIGGS, D.T.: Hydrolytic weakening of quartz and other silicates. Geophys. J.R. Astr. Soc., 14, 19-31, (1967).

GROVES, G.W., KELLY, A.: Change of shape due to dislocation climb. Philos. Mag., 19, 977-986, (1969).

HAGAN, J.T.: Micromechanics of crack nucleation during indentations. J. Mats. Sci., 14, 2975-2980, (1979).

HAGAN, J.T., SWAIN, M.V.: The origin of median and lateral cracks around plastic indents in brittle materials. J. Phys. D., 11, 2091-2102, (1978).

HAM, R.K.,: The determination of dislocation densities in thin films. Philos. Mag., 6, 1183-1184, (1961).

HAMILTON, G.M., GOODMAN, L.E.: The stress field created by a circular sliding contact. J. Appl. Mech., 33, 371-376, (1966).

HARRISON, J., WILKS.: The Hertz indentation test and Auerbach's law. J. Phys. D., 11, 73-81, (1978).

HARTLEY, N.E.W., WILSHAW, T.R.: Deformation and fracture of synthetic α-quartz. J. Mats. Sci., 8, 265-278, (1973).

HAUL, R., DÜMBGEN, G.: Diffusion of O^{18} in crystalline quartz. Z. Elektrochemie, 66, 636-641, (1962).

HEAVENS, J.W., ASHBEE, K.H.G.: On the relative fracture surface energies of the major and minor rhombohedra in low-quartz. J. Mats. Sci., 10, 1938-1942,(1975).

HERTZ, H.: J. Für die reine und angewandte mathematik, 92, 156-171, (1981). See: Hertz's miscellaneous papers, chapter V, MacMillan, London, (1896).

HILLIG, W.B., CHARLES, R.J.: In: High strength materials, ed. Zackay. John Wiley, New York, (1964).

HIRSCH, P.B., HOWIE, A., NICHOLSON, R.B., PASHLEY, D.W., WHELAN, M.J.: Electron microscopy of thin crystals. Butterworths, London, (1965).

HIRTH, J.P., LOTHE, J.: Theory of dislocations. McGraw-Hill, New York, (1968).

HOBBS, B.E.: Recrystallisation of single crystals of quartz. Tectonophysics, 6, 353-401, (1968).

HOBBS, B.E., McCLAREN, A.C., PATERSON, M.S.: Plasticity of single crystals of synthetic quartz. J. Geophys. Res., 16, 29-53, (1972).

INGLIS, C.E.: Stresses in a plate due to the presence of cracks and sharp corners. Proc. Inst. Naval Archit., 55, 219, (1913).

ISHIDO, T., MIZUTANI, H.: Relationship between fracture strength of rocks and ζ-potential.Tectonophysics, 67, 13-23, (1980).

JAYATILAKA, A. DE. S.: Fracture of engineering brittle materials. Applied Science Publishers, London, (1979).

JOHNSON, K.L.: The correlation of indentation experiments. J. Mech. Phys. Solids, 18, 115-126, (1970).

JONES, M.E.: The influence of hydrostatic pressure on the precipitation of structure-bound water in micro-inclusions in quartz. Philos. Mag., A 37, 703-706, (1978).

KATS, A.: Hydrogen in Alpha-quartz. Philips Res. Repts., 17, 201-279, 133-195, (1962).

KEITH, M.L., TUTTLE, O.F.: Significance of variation in the high-low inversion of quartz. Ann. J. Sci., 203, 203-280, (1952).

KEKULAWALA, K.R.S.S., PATERSON, M.S., BOLAND, J.N.: Hydrolytic weakening in quartz, Tectonophysics, 46, T1-T6, (1978).

KELLY, A.: Strong solids, Clarendon Press, Oxford, (1973).

KIRBY, S.H., McCORMICK, J.W.: Creep of hydrolytically weakened synthetic quartz crystals oriented to promote $\{2\bar{1}\bar{1}0\}$ <0001> slip: a brief summary of work to date. Bull. Mineral., 102, 124-137, (1979).

KNOTT, J.F.: Fundamentals of fracture mechanics. Butterworths, London, (1973).

LANG, A.R.: Studies of individual dislocations in crystals by X-ray diffraction microradiography. J. Appl. Phys., 30, 1748-1755, (1959).

LANG, A.R.: Mapping Dauphiné and Brazil Twins in quartz by X-ray topography. Appl. Phys. Letts., 7, 168-170, (1965).

LANG, A.R., MIUSCOV, V.F.: Dislocations and fault surfaces in synthetic quartz. J. Appl. Phys., 38. 2477-2483, (1967).

LANGITAN, F.B., LAWN, B.R.: Hertzian fracture experiments on abraded glass surfaces as definitive evidence for an energy balance explanation of Auerbach's Law. J. Appl. Phys., 40, 4009-4017, (1969).

LAUDISE, R.A.: In: Crystal growth: An introduction. ed. Hartman, P., North-Hollan, Amsterdam, (1973).

LAWN, B.R.: Partial cone crack formation in a brittle meterial loaded with a sliding spherical indentor. Proc. Roy. Soc. Lond., A 299, 307-316, (1967).

LAWN, B.R.: A model for the wear of brittle solids under fixed abrasive conditions. Wear, 33, 369-372, (1975).

LAWN, B., EVANS, A.G.: A model for crack initiation in elastic/plastic indentation fields. J. Mats. Sci., 12, 2195-2199, (1977).

LAWN, B., WILSHAW, R.: Indentation fracture : Principles and applications. J. Mats. Sci., 10, 1049-1081, (1975).

MARSH, D.M.: Plastic flow in glass. Proc. Roy. Soc., A 279, 420-435, (1964).

MARTIN, J.W., DOHERTY, R.D.: Stability of microstructure in metallic systems. Cambridge Univ. Press, Cambridge, (1976).

MARTIN, R.J.: Time dependent crack growth in quartz and its application to the creep of rocks. J. Geophys. Res., 77, 1406-1419, (1972).

McCLAREN, A.C., PHAKEY, P.P.: A transmission electron microscope study of bubbles and dislocations in amethyst and citrine quartz. Aust. J. Phys., 19, 19-24, (1966).

McCLAREN, A.C., RETCHFORD, J.A., GRIGGS, D.T., CHRISTIE, J.M.: Transmission electron microscope study of Brazil twins and dislocations experimentally produced in natural quartz. Phys. Stat. Sol., 19, 631-644, (1967).

McCLAREN, A.C., RETCHFORD, J.A.: Transmission electron microscope study of the dislocations in plastically deformed synthetic quartz. Phys. Stat. Sol., 33, 657-668, (1969).

McCORMICK, J.W.: Computer simulation of dislocation images in quartz. In: Electron microscopy in mineralogy, ed. Wenk, H.R., Springer-Verlag, Berlin, (1976).

MINDLIN, R.D.: Force at a point in the interior of a semi-infinite solid. Physics, 7, 195-202, (1936).

MITCHELL, T.E., HOBBS, L.W., HEUER, A.H., CASTAING, J., CADOZ, J., PHILIBERT, J.: Interaction between point defects and dislocations in oxides. Acta. Met., 27, 1677-1691, (1979).

MOORE, M.A., KING, F.S.: Abrasive wear of brittle solids. Wear, 60, 123-140, (1980).

MORIYA, K., OGAWA, T.: Observation of growth defects in synthetic quartz crystals by light scattering tomography. J. Cryst. Growth, 44, 53-60, (1978).

MORIYA, K., OGAWA, T.: Observation of dislocations in a synthetic quartz crystal by light scattering tomography. Philos. Mag., A 41, 191-200, (1980).

MORRISON-SMITH, D.J., PATERSON, M.S., HOBBS, B.E.: An electron microscope study of plastic deformation in single crystals of synthetic quartz. Tectonophysics, 33, 43-79, (1976).

MOTT, B.W.: Micro-indentation hardness testing. Butterworths, London, (1956).

NABARRO, F.R.N.: Steady state diffusional creep. Philos. Mag., 16, 231-237, (1967).

NABARRO, F.R.N.: Theory of crystal dislocations. Clarendon Press, Oxford, (1967,b).

NADEAU, J.S.: Influence of hydrogen and alkali impurities on the high-temperature indentation hardness of natural quartz crystals. J. Am. Ceram. Soc., 53, 568-573, (1970).

NYE, J.F.: Physical properties of crystals. Clarendon Press, Oxford, (1957).

PATERSON, M.S., KEKULAWALA, K.R.S.S.: The role of water in quartz deformation. Bull. Minéral., 102, 92-98, (1979).

PERROTT, C.M.: Elastic-plastic indentation : hardness and fracture. Wear, 45, 293-309, (1977).

PLINT, C.A., GREIG, M.L.: Temperature dependence of light scattering in some alkali halides. J. Appl. Phys., 35, 2745-2749, (1964).

RICE, R.W.: The compressive strength of ceramics. Mat. Sci. Res., 5, 195-229, (1971).

SAADA, G.: Dislocations dans les cristaux piézoélectriques. Phys. Stat. Sol., 44, 717-731, (1971).

SCHOLZ, C.H.: Static fatigue of quartz. J. Geophys. Res., 77, 2104-2114, (1972).

SMITH, G.S., ALEXANDER, L.E. : Refinement of the atomic parameters of α-quartz. Acta cryst., 16, 462-471, (1963).

SPINK, K.: The nature of the diamond drilling process. Ind. Dia. Rev., 230-242, (1972).

SUH, N.P.: An overview of the delamination theory of wear. Wear, 44, 1-16, (1977).

SWAIN, M.V.: Microfracture about scratches in brittle solids. Proc. Roy. Soc. Lond., A 366, 575-597, (1979).

SWAIN, M.V., LATANISION, R.M., WESTWOOD, A.R.C.: Further studies on environment sensitive hardness and machinability of Al_2O_3. J. Am. Ceram. Soc., 58, 373-376, (1975).

SWAIN, M.V., LAWN, B.R.: Indentation fracture in brittle rocks and glasses. Int. J. Rock. Mech. Min. Sci. and Geomech. Abstr., 13, 311-319, (1976).

TABOR, D.: The hardness of metals. Clarendon Press, Oxford, (1951).

TANNER, B.K.: X-ray diffraction topography. Pergamon Press, Oxford, (1976).

TANNER, B.K., FATHERS, D.J.: Contrast of crystal defects under polarised light. Philos. Mag., 29, 1081-1094, (1974).

TAUREL, L., HUMPHREYS-OWEN, S.P.E.: Study of quartz imperfection by light scattering. Proc. Phys. Soc., 75, 473-488, (1960).

TAYLOR, E.W.: Correlation of Moh's scale of hardness with Vickers hardness numbers. Mineral. Mag., 28, 718-721, (1949).

THOMAS, L.A., WOOSTER, W.A.: Piezocrescence - the growth of Dauphiné twinning in quartz under stress. Proc. Roy. Soc., (A) 208, 43-63, (1951).

TIMOSHENKO, S.P., GOODIER, J.N.: Theory of Elasticity. McGraw-Hill, New York, (1970).

TULLIS, J., TULLIS, T.: Preferred Orientation of quartz produced by mechanical Dauphiné twinning : Thermodynamics and Axial experiments. Geophys. Monog., 16, 67-82, (1972).

VAND, V., VEDAM, K., STEIN, R.: The Laser as a light source for ultramicroscopy and light scattering by imperfections in crystals. Investigation of imperfections in LiF, MgO and Ruby. J. Appl. Phys., 37, 2551-2557, (1966).

VELDKAMP, J.D.B., KLEIN WASSINK, R.J.: Grindability of brittle materials : a theoretical and experimental investigation. Philips Res. Rpts., 31, 153-189, (1976).

VERHOOGEN, J.: Ionic Diffusion and Electrical conductivity in quartz. Amer. mineral., 37, 637-653, (1952).

VON MISES, R.: Mechanik der plastischen Formanderung von Kristallen. Z. angew. Math. Mech., 8, 161-185, (1928).

WARSHAW, S.I., NORTON, F.H.: Deformation behaviour of polycrystalline Aluminium oxide. J. Am. Ceram. Soc., 45, 479-486, (1962).

WEERTMAN, J.: Steady-state creep through dislocation climb. J. Appl. Phys., 28, 362-364, (1957).

WENDEN, H.E.: Ionic diffusion and the properties of quartz I. The direct current resistivity. Amer. Mineral., 42, 859-886, (1957).

WESTBROOK, J.H.: Temperature dependence of strength and brittleness of some quartz structures. J. Am. Ceram. Soc., 41, 433-440, (1958).

WESTBROOK, J.H.: In: The science of hardness and testing its research applications. eds. Westbrook, J.H., Conrad, H. American Society for metals, Ohio, (1973).

WESTBROOK, J.H., JORGENSEN, P.J.: Effects of water desorption on indentation microhardness anisotropy in minerals. Amer. Mineral., 1899-1909, (1968).

WESTWOOD, A.R.C.: Tewkesbury Lecture: Control and application of environment sensitive fracture processes. J. Mats. Sci., 9, 1871-1895, (1974).

WESTWOOD, A.R.C., MACMILLAN, N.H., KALYONCU, R.S.: Environment-sensitive hardness and machinability of Al_2O_3. J. Am. Ceram. Soc., 56, 258-262, (1973).

WHITE, S.: Electrical conductivity of quartz; a reply. Nature, 233, 63-64, (1971).

WHITE, S.: The effect of strain on the microstructures, fabrics and deformation mechanisms in quartzites. Phil. Trans. Roy. Soc., A 283, 69-86, (1976).

WHITE, S.: Geological significance of recovery and recrystallisation processes in quartz. Tectonophysics, 39, 143 - 170, (1977).

WIEDERHORN, S. M.: Influence of water vapour on crack propogation in soda-lime glass. J. Am. Ceram. Soc., 407 - 414, (1967).

WILLIAMS, J. S., Lawn, B. R.: Slow crack growth in proton- and deuteron- irradiated quartz. J. Mats. Sci., 8, 1059 - 1061, (1973).

WINCHELL, H.: The Knoop microhardness tester as a mineralogical tool. Amer. Mineral., 30, 583 - 595, (1945).

YOUNG, R. A., POST, B.: Electron density and thermal effects in α-quartz. Acta cryst., 15, 337 - 346, (1962).